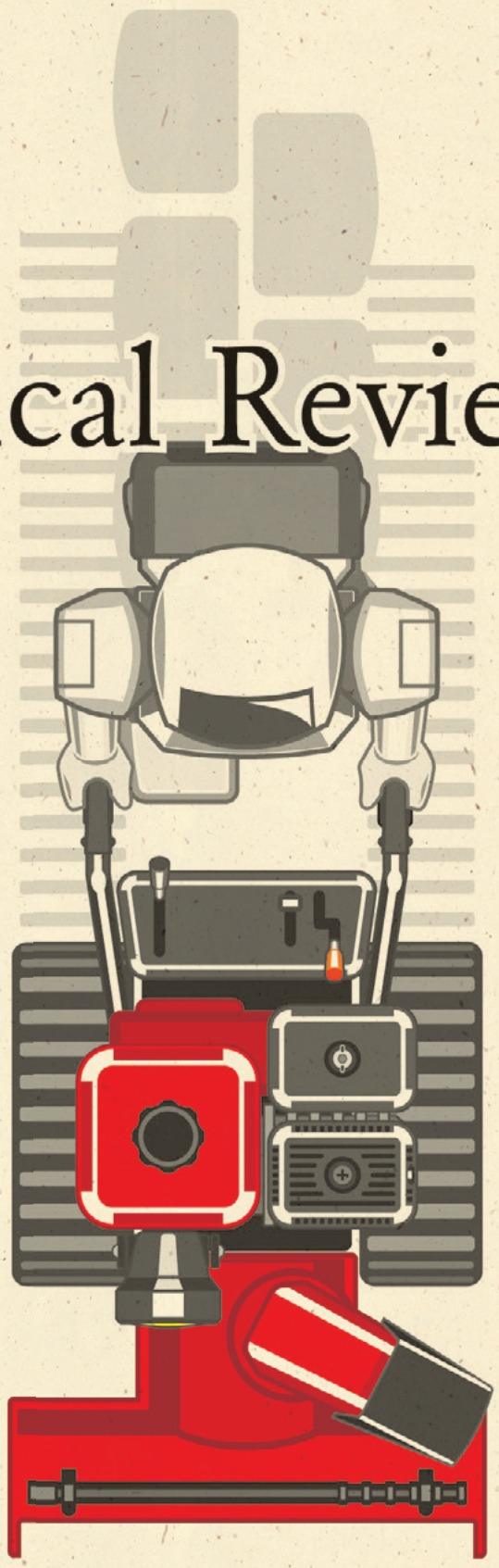
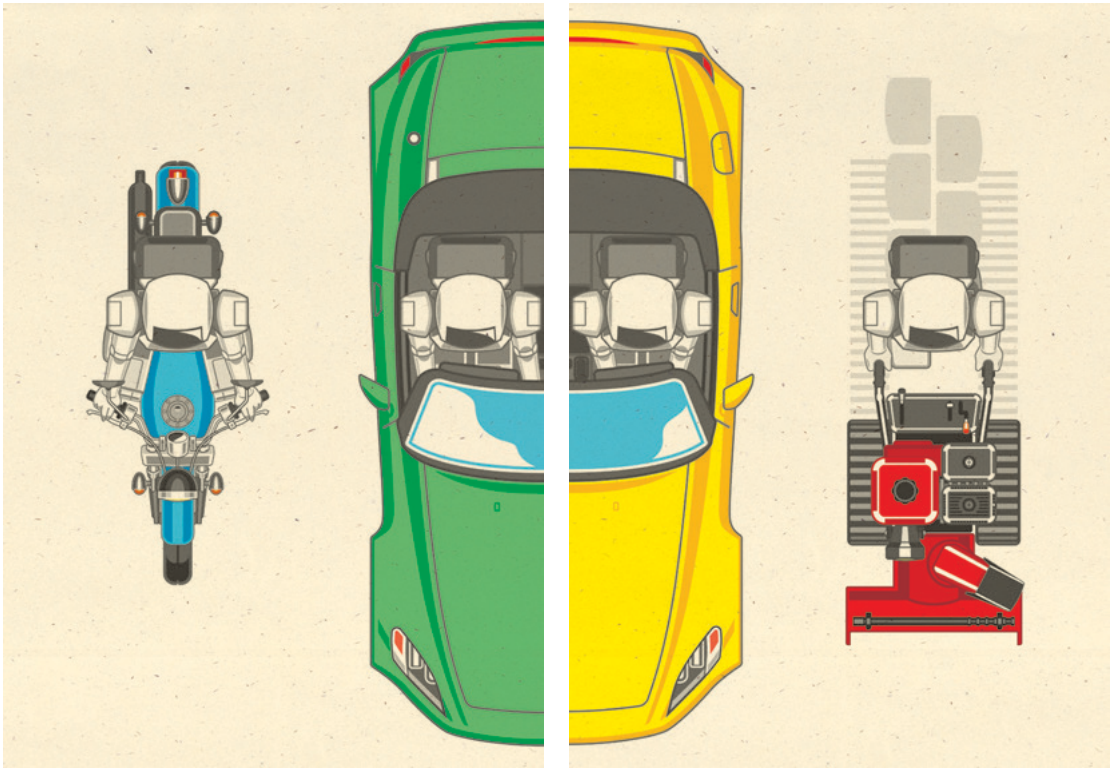
Honda R&D

Technical Review



April 2002



Comment on the Cover



We have many products at Honda that allow users to directly sense the sounds, colors, and scents of the season.
Making products that appeal to the physical sense is important to us, and I intend to maintain this sensory value in what I do.
This cover expresses my sense of the way Honda products fit in perfect comfort with people's live in the open air.

Asaka Higashi R&D Center
Koichi Azuma

Introduction of Personal Watercrafts AquaTrax F-12/F-12X Installing a 4-Stroke Engine

Hajime SHOGASE* Takaharu KUROSAKI* Masahiko TSUCHIYA*
Takao KOCHI* Mamoru URAKI* Noboru YOKOYA*

ABSTRACT

The AquaTrax F-12 and F-12X Personal Watercraft (PWC) were developed with design goals of excellent driveability and environmental suitability superior to the existing 2-stroke engine PWCs. A 4-stroke engine and turbo charger were installed for the first time in PWCs. As a result, they passed the EPA 2006 emission regulation and the CARB 2004 emission regulation for the first time in PWCs, and driveability exceeded that of the existing 2-stroke engine PWCs. The turning ability of these PWC, like that of a motorcycle, was realized through a newly developed water jet pump suitable for the characteristics of a 4-stroke engine, and the hull bottom of Honda's original shape. Thus, the level of existing PWCs was changed completely.

1. Introduction

Personal watercraft (PWC) are presently marketed for one to four riders. PWCs are popular for offering a greater degree of maneuverability than boats, and in 2001, approximately 110,000 units were sold in the US market. In response to concerns about the environment and market trends demanding increased controllability and stability and higher speeds in PWC, Honda has developed a PWC fitted with a 4-stroke engine.

The 2002 AquaTrax F-12 (F-12X) is shown in Fig. 1. The AquaTrax is highly stable, and offers a level of rider comfort new to PWC. It is a three-person PWC, which takes into account the needs of inexperienced users, and is fitted with an Off-Throttle-Steer (OTS) system[(1)], and features a limit mode that controls the maximum speed of the engine. The F-12X is fitted with a turbo-charger, and is the most powerful three-person PWC on the market. This paper will describe the major technologies utilized to achieve the performance targets set for these PWC.



Fig.1 AquaTrax F-12

* Asaka R&D Center

2. Development Concept

Development of the AquaTrax F-12/F-12X did not restrict itself to the conventional paths taken in PWC design. Designers adopted a users' perspective and considered the requirements of a PWC for family use and the features of a PWC which most contribute to rider enjoyment. The development concept established for the craft was to achieve a product which is safe, friendlier to the environment, sporty, and easy to use. Fig. 2 shows details of the development concept.

3. Engine

In addition to the existing U.S. Environmental Protection Agency (EPA) marine exhaust emissions regulations, the California Air Resources Board (CARB) has recently issued a set of strict regulations, and the US Water Quality Bureau has also commenced consideration of regulations. All of these regulations place severe restrictions on marine engine design. Given these environmental considerations, Honda has chosen a 4-stroke engine as its PWC engine. The base engine is a CBR1100XX motorcycle engine. This engine was modified for aquatic use, and the stroke was increased by 5 mm. The engine has a displacement of 1,235 cm^3. Table 1 shows the main engine specifications for the F-12/F-12X. A target of 100 PS/L at 7,000 rpm was set for the natural aspiration AquaTrax F-12. Reduction of pressure loss and mechanical loss in the exhaust system has enabled the achievement of performance in the middle class of the PWC market. The AquaTrax F-12X adds a turbo-charger to the F-12 engine, and features the highest power output of any PWC on the market. A biaxial secondary balancer ensures safe, comfortable high-speed cruising.



Fig. 2 Development concepts and features for AquaTrax

Table 1 Major specifications of engines

Items		AquaTrax F-12X	AquaTrax F-12
Engine type		4-stroke inline 4 cylinder	4-stroke inline 4 cylinder
Valve train		DOHC 16 valve	DOHC 16 valve
Displacement	(cm^3)	1 235	1 235
Bore x stroke	(mm)	79 x 63	79 x 63
Compression ratio		8.5	11
Cooling system		Water cooled, open loop	Water cooled, open loop
Lubricating system		Dry sump	Dry sump
Fuel supply system		Programmed fuel injection	Programmed fuel injection
Intake system		Turbocharger and intercooler	–
Balancer shaft		Applied	–
Maximum power	(kW/ r/min)	121.4 / 6 100	91.9 / 7 000
Maximum torque	(N·m/ r/min)	191.8 / 5 500	125.5 / 7 000

Despite their numerous advantages, 4-stroke engines generally have a lower specific power than 2-stroke engines. To achieve top performance, high engine speed and high output, supercharging, and a large displacement were each examined as possibilities in the design of the F-12X engine. At high engine speeds, cavitation in the water jet pump causes a noticeable decline in pump efficiency. Reduction was therefore examined as a method of ensuring that engine speed did not exceed the limit for impeller use, but it was not adopted due to the fact that it caused over revving feel. Higher displacement would increase weight, and the power/weight ratio would prevent the achievement of performance targets. Supercharging, through the adoption of an exhaust turbo-charger, proved to be the method allowing achievement of the targets set for the F-12X.

Fig. 3 shows an external view of the F-12X engine, Fig. 4 shows a cutaway drawing of the same engine, and Fig. 5 gives an idea of the power performance of the F-12/F-12X. Both engines are set to deliver maximum power under 7,000 rpm, and the engine and water jet pump are coupled by a simple direct crank connection. To prevent a drop in intake efficiency in the jet pump intake duct, it was necessary to position the propeller shaft as far as possible below the bottom surface of the hull. For this reason, the crank center height has been lowered by fitting a dry sump with a shallow oil pan. The oil tank has been integrated with the front cover, and the oil pump has been built in. The oil pump is directly driven by a semi-Oldham coupling from the tip of the ACG flywheel, and features a simple mechanism dispensing with a chain and drive gears.



Fig. 3 F-12X Engine appearance

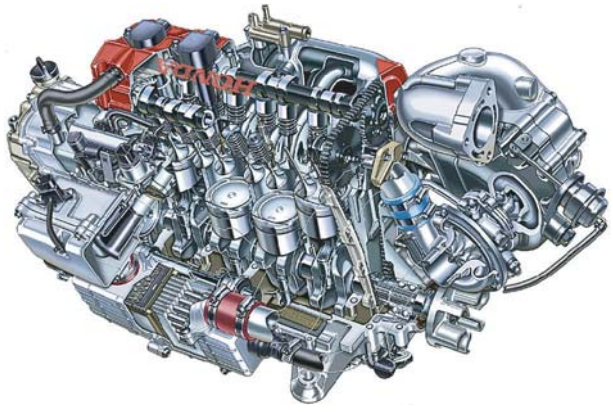


Fig. 4 Cutaway drawing F-12X engine

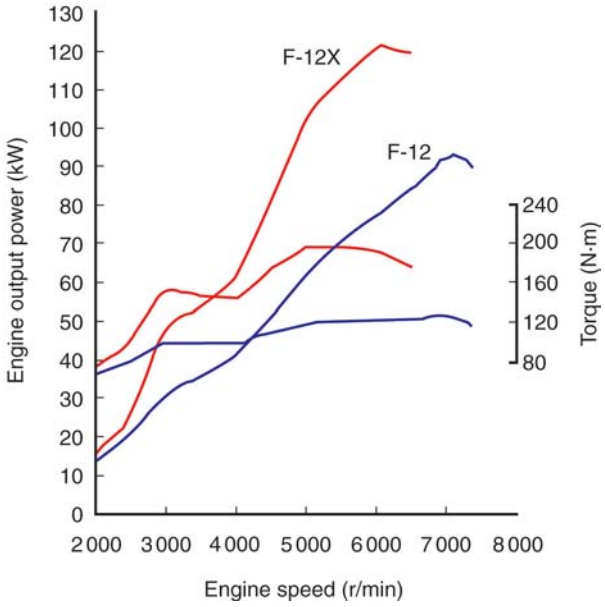


Fig. 5 F-12/F12X Engine performance

The turbo-charger utilized in the F-12X was designed specifically for this craft, and is manufactured by IHI. It is the world's first seawater direct cooling exhaust turbo-charger with an attached waste gate in this class. Fig. 6 shows a structural diagram of the turbo-charger. Because a high level of throttle response was required from the engine, low inertia mixed flow turbine blades were adopted. As Fig. 7 shows, this enabled a 22% reduction in turbine weight, and a 20% increase in acceleration of turbine speed. It has also been possible to significantly decrease turbo lag. The turbine housing is made of seawater corrosion-resistant niresist cast iron, and is provided with a water jacket which maintains surface temperature below 85 °C, even at full power with the throttle fully engaged. Turbo supercharging generates a mean effective pressure in cylinder of 2.14 MPa. To resist this pressure, the high-rigidity, fully rounded pistons are made of forged aluminum. An oil jet cooler positioned below the pistons maintains low piston temperature, and alumite treatment of the top ring channels ensures continuous high-load operation.

It was necessary to adopt measures to deal with oil flow from the breather, because of the possibility that a PWC may overturn. As Fig. 8 shows, in the AquaTrax F-12/F-12X, vertical breather chambers are located within the vertical type oil tank on the engine side and the tank side. When the craft is overturned, the oil level in the breather chambers falls below the height of the separator. This configuration ensures that oil does not flow into the breathers even when the craft is not immediately righted. Because this is a simple structure utilizing no special devices, it is highly reliable. The engine cooler is a direct-cooling type utilizing jet pump water pressure rather than a cooling water pump. The same resin top-coating corrosion-resistant treatment used for outboard motors is applied to the inner surface of the water jacket. To ensure that the cooling water jet injected into the exhaust system does not flow back when the craft is overturned, the mechanism shown in Fig. 9 was adopted to prevent flow-back from the water muffler into the engine.

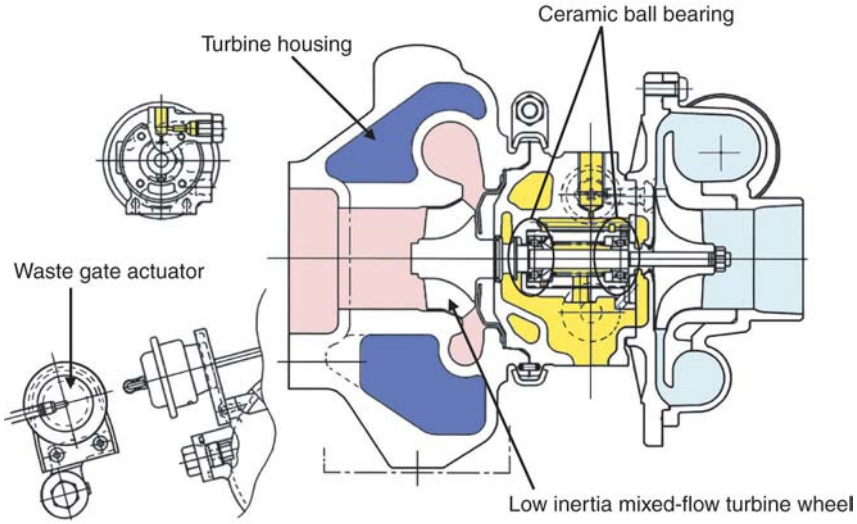


Fig. 6 Layout of turbo charger for F-12X

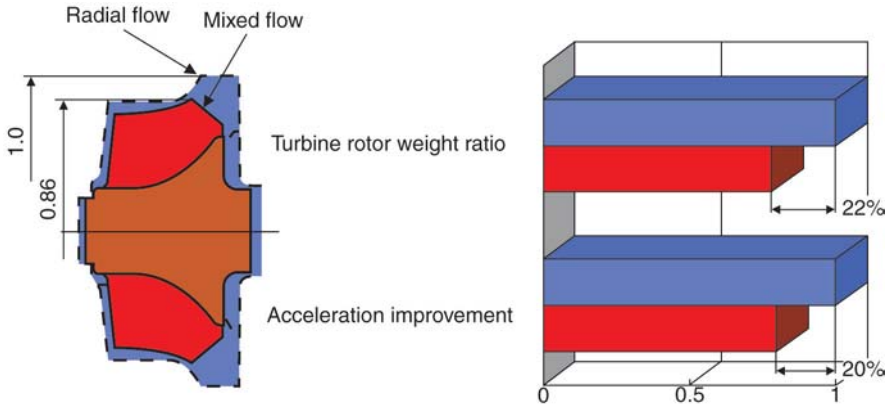


Fig. 7 Improvement of acceleration

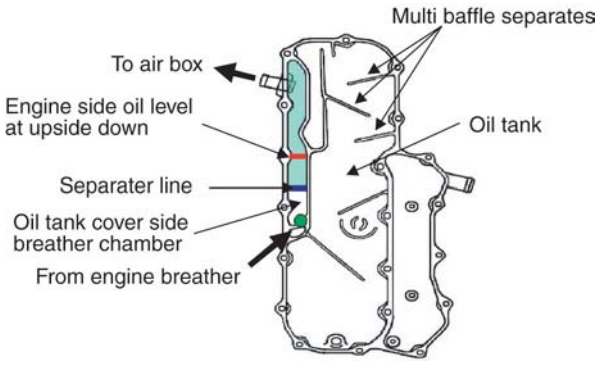


Fig. 8 Engine breather system

4. Hull

To give the craft a banking turn similar to a motorcycle, a multi-chine deep-V hull shape was adopted for the basic rise of the hull bottom (dead rise) as shown in Fig. 10. The dead rise angle was established with consideration of a balance between maneuverability and running resistance. The two left and right strakes generate buoyancy while the craft is running, and contribute to the reduction of running resistance in the hull. The design of the keel, positioned in the center and representing the lowest point of the hull, is different than that found in conventional PWCs. The curvature of the section connecting the left and right sides of the hull has been increased to enable the craft to bank easily when turning, and

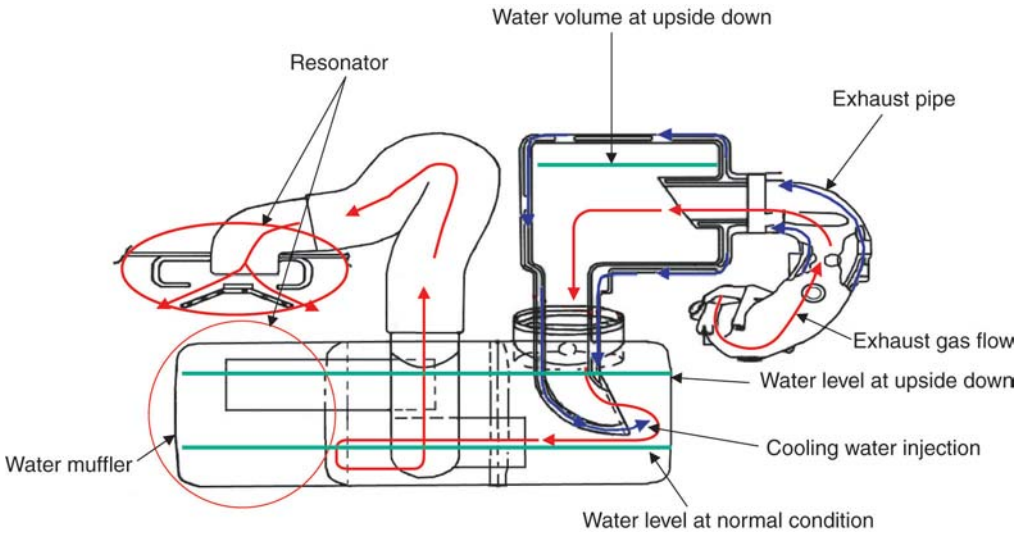


Fig. 9 Layout of exhaust system



Fig. 10 3-D Hull design

to ensure that the direction of yaw is not excessively affected by transversal waves, etc., when the craft is in operation. The sponson fitted at the rear of the hull is effective in ensuring static stability and grip when turning. Fig. 11 shows the side flow sponson. This configuration allows the current produced under the lower surface of the sponson when the craft is turning to flow freely around the side flow section. This prevents the occurrence of sudden excess yaw rate when the craft commences its turn, and balances slide and grip during turning.

5. Deck

5.1 High Nose Form Design

To reduce the amount of splashing of the rider during operation, the craft was designed so that the bond line at the front is higher than the bond line at the rear. This design makes the external appearance of the AquaTrax different to other PWCs, giving the craft an individual identity.

5.2 Side Panels

As shown in Fig. 12, a section of the deck underneath the seats on both sides has been designed to make it removable for easy access to the inside of the hull for maintenance. This design enables a higher level of maintenance to be carried out than has been the case in the available 2-stroke PWC.



Fig. 11 Sponson



Fig. 12 Side panel

5.3 Riding Position

To enable safe, comfortable steering with a sporty feel, the seat on the new PWC has been positioned higher than on other models. Fig. 13 shows the riding position for the new PWC. The height of the seats gives a riding position which makes the craft easier to control, and has increased hull turning ability, realizing the above mentioned safe, comfortable steering with a sporty feel.

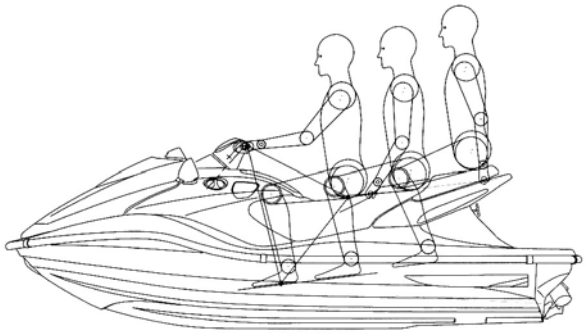


Fig. 13 Riding position



Fig. 14 Glove box

5.4 Storage Space

The AquaTrax F-12/F-12X features a 74.6 liter storage space at the front of the craft, and a 10.3 liter glove box in front of the rider. The glove box, shown in Fig. 14, has the largest capacity of any PWC, increasing ease of use.

5.5 Stern Deck

The long stern deck of the F-12/F-12X, has a flat surface making it easier to board the craft from the water, and is also convenient for towing and a variety of other uses.

6. Water Jet Pump

The AquaTrax F-12/F-12X is propelled by a single-stage axial flow water jet pump[(2)] independently designed by Honda. Fig. 15 shows the structure of the water jet pump. The intake section was designed to achieve a balanced performance from low to high speeds using cavitation tunnel tests and computational fluid dynamics (CFD). The pump section features a three-blade stainless steel impeller, with a stainless steel housing. This steel has excellent wear durability. The stator has six vanes; the vanes and the impeller blades were designed with careful consideration of cross-sectional characteristics. The size of the rear internal bearings in the F-12X has been increased to accommodate the greater engine power, and these bearings also receive thrust. The jet nozzle is a straight type, and the craft is also provided with a bilge pump operating on negative pressure.

Pump matching was optimized on the basis of running tests. To respond to rapid pickup from the 4-stroke's characteristic idling to high engine speeds and sudden increases in power generated by the turbo-charger, the engine was tuned to increase absorption power in the transients. In combination with changes in engine power characteristics, this was intended to allow for the continuousness of acceleration and the feeling of initial acceleration.

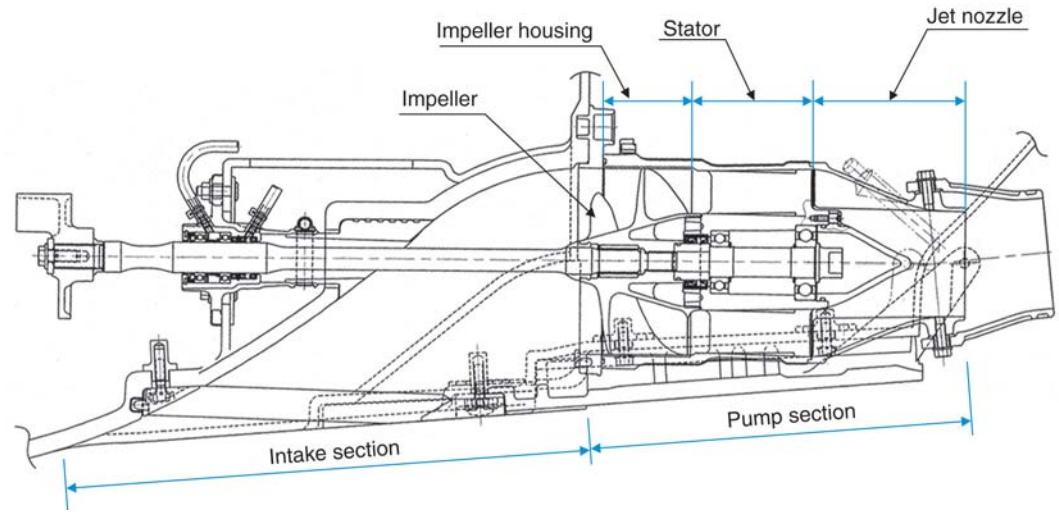


Fig. 15 Water jet pump for AquaTrax

7 Off-Throttle-Steer (OTS) System

The structural characteristics of PWC cause thrust to drop when the throttle is closed (off throttle). There are therefore situations in which riders may not be able to turn the craft in the intended direction. To provide a solution, the new PWC has been designed with an OTS system to help eliminate this possibility when turning with the throttle off. Fig. 16 shows a structural diagram of the AquaTrax F-12/F-12X throttle body.

There are two types of OTS systems: the rudder type, and the type which increases engine speed. The type adopted for the AquaTrax F-12/F-12X makes turning possible by increasing engine speed at full steering with the throttle closed. Fig. 17 shows an operational diagram for the OTS system. In this system, full turning of the steering handle with the throttle released switches on a steering switch located on the handle shaft, which activates a solenoid valve. A diaphragm releases the negative pressure built up in the surge tank, which opens the throttle valve, increasing engine

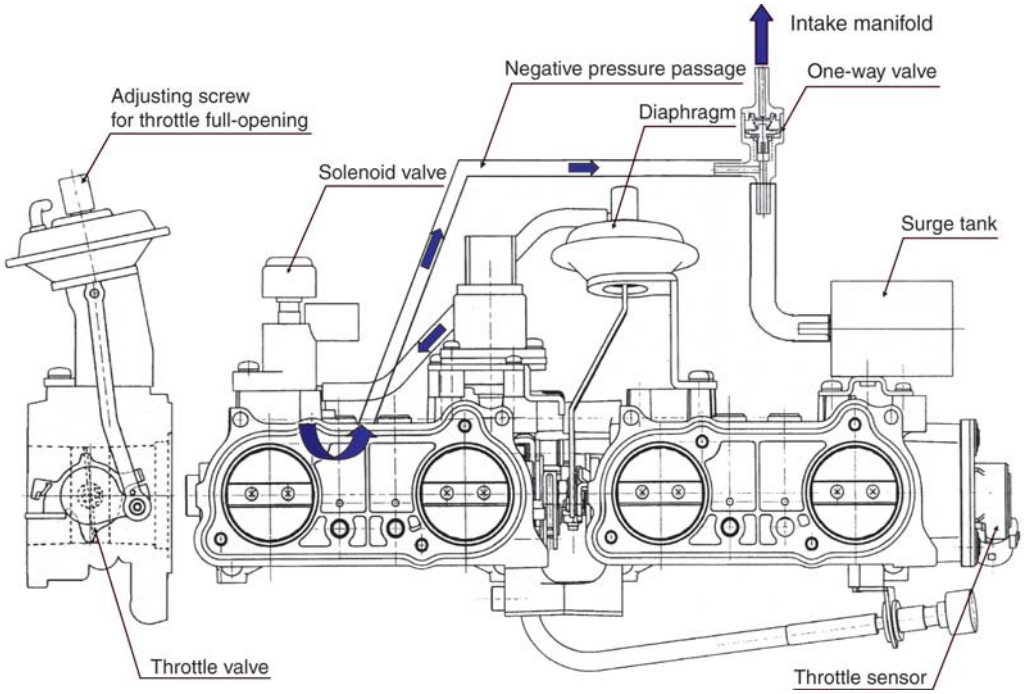


Fig. 16 OTS Construction

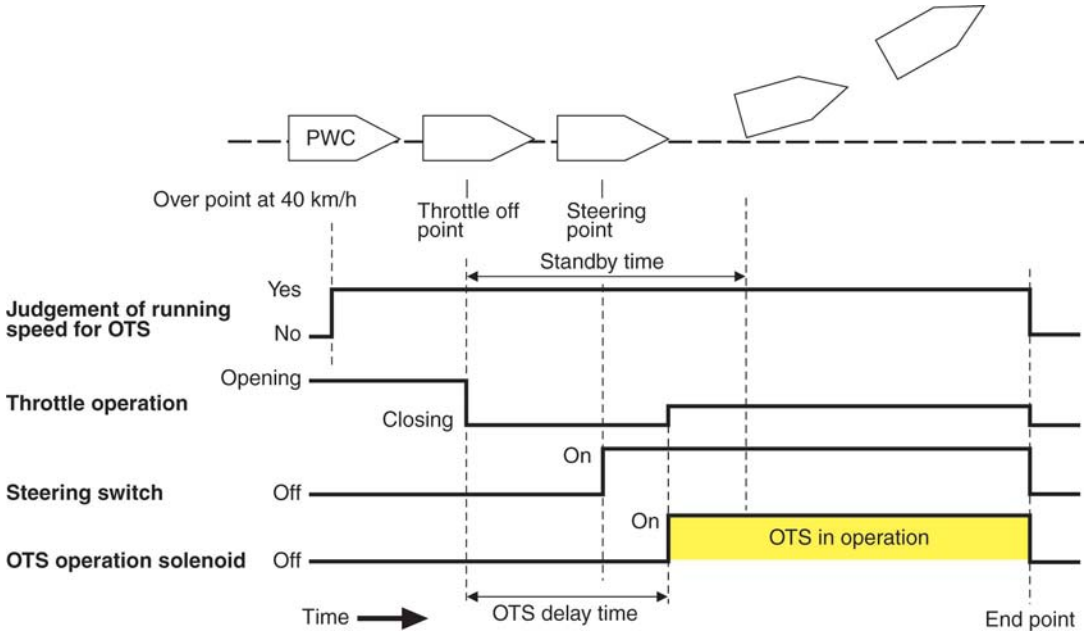


Fig. 17 OTS System operation

speed and therefore ensures turning ability. The estimated craft speed at which control will take effect is calculated in the ECU on the basis of engine speed and the degree of openness of the throttle. The craft running locus with and without OTS is shown in Fig. 18. Utilization of the OTS system ensures that the craft will continue to turn when the steering handle is being turned with the throttle closed.

8. Electrical System

The AquaTrax F-12/F-12X has achieved a balance between excellent throttle response on the one hand and high power and low emissions on the other by utilizing electronically controlled fuel injection and ignition to provide optimal control of fuel injection and ignition timing in response to running conditions. In the AquaTrax F-12X, fine waste gate control provides stress-free transients from natural aspiration at low engine speeds to high engine speeds with turbo-charger-enhanced power, in addition to incredible power at high engine speeds. The AquaTrax F-12 engine has been provided with settings to ensure ease of handling and a high level of response across the entire range of engine speeds, and offers a different but no less pleasurable experience than the turbo-charged F-12X.

The AquaTrax F-12/F-12X features a limit mode to help inexperienced users in learning to control the craft. This function can be engaged using the mode button on the multi-function meter shown in Fig. 19. Setting the limit mode limits the maximum engine speed, enabling inexperienced users to gain an understanding of the behavior of the craft under limited speed. The combination meter shows running speed, engine speed and remaining fuel on an LCD display. The multi-function meter shows time, total running time, time over a section and distance over a section. Various warnings are displayed on red LED indicators and also appear on the LCD display. At the same time, the rider's attention is attracted by a buzzer. The types of warnings include fuel remaining, low battery level, abnormal oil pressure and fuel injection system malfunction. When a malfunction is detected in the fuel injection system, the LCD warning symbol and the red LED display a diagnostic code.

To provide added security, the user can also freely choose an ID number for keyless ignition, enabling him or her to lock the electronic system and prevent unauthorized use.



Fig. 19 Multi function meter

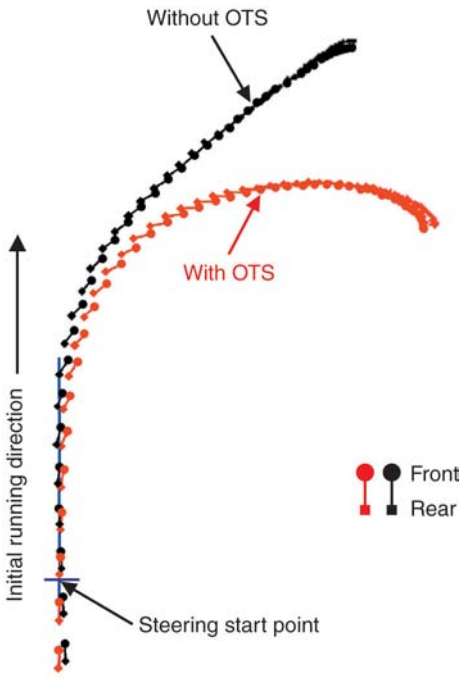


Fig. 18 Comparison of running locus

9. Sound Management

The AquaTrax F-12X is fitted with a biaxial secondary balancer, which in combination with the rubber mounting of the engine offers an extremely quiet and vibration-free riding experience. The turbo-charger contributes greatly to the quietness of the craft by absorbing exhaust energy, but the effect tends to be mitigated at low engine speeds until supercharging takes effect by sympathetic resonance in the water lock hose fitted to prevent infiltration of water into the exhaust system, which is a persistent difficulty encountered in PWC. To prevent these vibrations, the new PWC has been provided with a large-capacity 16.7 liter water muffler, one-third of which acts as a resonator to stop sympathetic resonance, and a water chamber fitted to the exhaust system outlet. Fig. 20 shows the water chamber when fitted, and Fig. 21 shows the resonator section. The form of the water chamber and the structure of the outlet were designed not merely to enhance driveability, but to prevent infiltration of water and increase ease of pump maintenance.

In order to achieve target performance in the natural aspiration engine of the AquaTrax F-12, it has not been fitted with a balancer. Because of this, the hardness of the rubber engine mounts has been reduced to decrease vibration. The mounts fit on to FRP plates which function like speakers to transmit vibration and noise, and therefore vibration cannot be isolated and generates noise in each section of the engine. Therefore the plate thickness of the hull side surface, the plate thickness and rib shape of the post cover, the plate thickness of the side panels and the structure and plate thickness of the rear grip were all reexamined to reduce vibration and noise.



Fig. 20 Installed appearance of water chamber (Resonator)



Fig. 21 Upper view of water chamber (Resonator)

10. Conclusion

In designing its first PWC, the AquaTrax F-12/F-12X, Honda was not limited by the concepts utilized in the design of existing PWCs, and adopted a user's perspective to focus on safety, sportiness and ease of use.

(1) A 4-stroke engine has been utilized in a PWC for the first time. This engine has been optimized for use with a jet pump, and balances superior drivability to other PWCs with environmental suitability which meet or exceed current regulations.
(2) Honda's original hull design has realized a turning feeling like that of a motorcycle.
(3) The F-12/F-12X features OTS and limit mode to help users to control the craft.
(4) The F-12X engine is fitted with a turbo-charger and a biaxial secondary balancer. These features make the F-12X extremely quiet and vibration-free, giving the rider a comfortable high-speed cruising experience.
(5) The F-12 engine's high throttle response at all engine speeds makes it easy to handle, and offers a different type of enjoyment to the turbo-charged model.

11. Acknowledgments

The authors wish to sincerely thank all concerned at Ishikawajima-Harima Heavy Industries Co., Ltd. for their generous cooperation in the development of the turbo-charger used in the AquaTrax F-12X engine.

References

(1) Kochi, T., et al: "Development of an Off-Throttle-Steer System for Personal Watercraft", Honda R&D Technical Review Vol. 14, No. 1. pp. 125–130 (2002)

(2) Tsuchiya, M., et al.: "Establishment of a Development Method of Water Jet Pump for 4 stroke Personal Watercraft", Honda R&D Technical Review Vol. 14, No. 1. pp. 117–124 (2002)

■ Authors ■


Hajime SHOGASE


Takaharu KUROSAKI


Masahiko TSUCHIYA


Takao KOCHI


Mamoru URAKI


Noboru YOKOYA

Development of Honda Flagship Outboard Motor "BF225/200"

Masaki TSUNODA* Masayuki OHSUMI* Makoto YONEZAWA*
Kentaro FURUYA* Sadafumi SHIDARA* Ryuichi KIMATA*

ABSTRACT

Honda has developed 225 and 200-horsepower outboard motors powered by a 3.5-liter V-type 6-cylinder (V6) engine, the largest such outboard motors in the world, as the flagship models in its 4-stroke outboard motor series. The BF225/200 models are the first 4-stroke outboard motors to use the VTEC (variable valve timing and lift electronic control system), a variable intake and O_2 feedback system. The resulting engine performance also makes them the world's first outboard motors in the 200-hp class to achieve emissions levels that satisfy the year 2008 values for marine engine exhaust emissions set by the California Air Resources Board (CARB). At the same time, they have achieved a highly balanced performance improvement, with a maximum torque that is 10% greater and fuel consumption that is approximately 15% lower than previous models. The adoption of non-chrome coating methods for exterior parts on these motors has achieved the environmental compliance while maintaining coating quality on a par with previous models. In terms of comfort, their low vibration and low noise place them at the top of their class. The out bank exhaust manifold design with the same construction as V6 automotive engines and the use of a plastic inlet manifold makes these models lightweight and compact enough to replace conventional 2-stroke outboard motors without requiring any modification to the boat. Honda has achieved these performance levels while maintaining high reliability and simultaneously reducing cost by standardization of basic specifications and communizing parts with it's automotive V6 engines.

1. Introduction

The US represents the largest market for outboard motors in the world. From 2001, California Air Resources Board (CARB) emissions regulations were instituted in the US alongside the existing Environmental Protection Agency (EPA) regulations. In addition to the importance of complying with the CARB 2008 regulations, another factor influencing the design of outboard motors is the move away from conventional two-stroke motors and the rapidly increasing demand for four-stroke motors with clean emissions, high fuel economy, and low levels of noise and vibration.

Honda has engaged in continuous production of four-stroke outboard motors exclusively since 1964. In 1998, the company announced the development of the BF130/115[(1)], a

* Asakahigashi R&D Center

motor with the highest horsepower of any four-stroke outboard motor at that time. Honda has now developed the BF225/220, shown in Fig. 1, to complete its full line-up of outboard motors, and to increase its competitiveness in the U.S. market, the main market for large outboard motors, accounting for 80% of yearly world unit sales.



Fig. 1 External view of BF225

2. Aims of the Development

The BF225/200 maintains the commitment of Honda's outboard motor series to user friendly and environmentally friendlier four-stroke motors of the highest quality at an economical price. In addition, the new model represents a world first in featuring the following new technologies for the first time in an outboard motor:

· Variable valve timing and lift electronic control (VTEC)[(2)]
· A variable intake system
· External non-chrome finish

It also features the following technologies for the first time in a four-stroke outboard motor:

· An O_2 feedback system
· A knock control system

The new outboard motor has the highest horsepower in the Honda series, and is friendlier to the environment and more economical and reliable than competitors' two-stroke direct injection (2stDI) outboards or existing four-stroke outboards. It was developed with the aim of creating Honda's flagship outboard motor, the leader of the next generation.

The development also aimed to minimize the effect of the larger engine cover necessitated by the four-stroke's more extensive valve system, and to create a package size and weight enabling the outboard to be fitted to a boat capable of fitting a comparable two-stroke motor without modification.

3. Main Specifications and Outline

Table 1 shows the main specifications of the BF225, and Fig. 2 shows a cutaway view of the newly developed outboard. The motor shares the components of it's main dynamic system (crankshaft, connecting rods, etc.) with a 3.5-liter 60° V6 engine.[(3)] In the interests of compactness, components from an SOHC-VTEC engine have been used for the valve system. Lubrication and cooling systems have been modified to allow utilization in a vertically mounted

Table 1 Specification

Code name	BF225 X-type
Overall length (mm)	920
Overall width (mm)	625
Overall height (mm)	1 800
Transom height (mm)	635
Dry weight (kg)	272
Engine type	4 stroke 60° V-type 6 cylinder
Displacement (cc)	3 471
Bore (mm) × stroke (mm)	89 × 93
Compression ratio	9.4 : 1
Valve train	SOHC VTEC 24 valves
Valve number	4/cylinder
Maximum power (kW/rpm)	165 / 5 500 (225 hp / 5 500 rpm)
Maximum torque (N·m)	295
Recommended engine rpm range	5 000 ~ 6 000
Fuel supply system	Programmed Fuel Injection
Ignition system	Programmed Ignition (with Plug Hole Coil)
Charge output (A)	60
Cooling system	Water cooling (with 2 thermostats)
Exhaust system	Through propeller hub

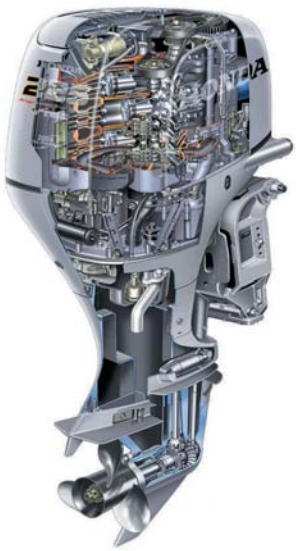


Fig. 2 Cutaway view of BF225

configuration. The oil filter and alternator have been located in the front of the engine as viewed from the direction of motion. The intake and fuel systems are located in the in bank at the rear of the engine, and the exhaust system is in the out bank. The ECU is located on the starboard side of the motor, with the starter on the port. This configuration gives the new outboard a slim external appearance.

The engine is the first four-stroke outboard motor engine to have VTEC, a variable intake and O_2 feedback system with knock control system. The engine follows previous models in featuring programmed fuel injection (PGM-FI), but represents an improvement in power, maneuverability, fuel economy and exhaust emissions over previous models. The control system is based on a proven automotive engine system. The alert system and other systems have been modified to match the characteristic functions and use requirements of an outboard motor.

4. Component Technologies

4.1 Use of Automotive Engine Components

Fig. 3 shows the relation between Honda automobiles and outboard motors. After having shared crankshaft and connecting rods of an automotive engine with the BF90/75, Honda went on to increase the number of parts shared in the BF130/115, which included an automotive valve train system and balancer mechanism. In addition to further increasing the amount of shared parts, the development of the BF225/200 also focused on sharing automotive production facilities for the cylinder block and cylinder heads, and thus adopted an engine layout different from that of previous outboard motors.

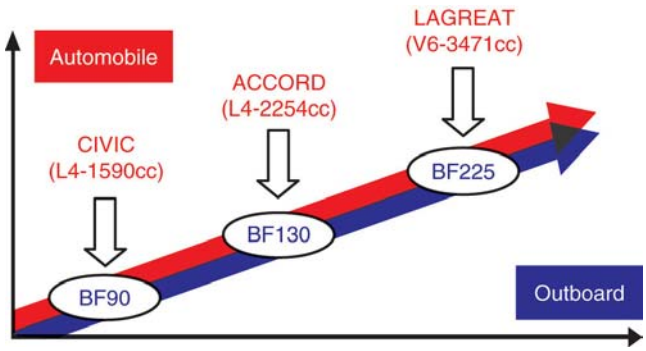


Fig. 3 Relation of automobile and outboard engine

Previous layouts have integrated the exhaust passage with the cylinder heads and cylinder block, in a configuration unique to outboard motors. To enable the BF225/200 components to share a mechanical processing line with automotive cylinder heads and cylinder blocks, the exhaust passage has been separated from these components, and has the same dimensions as an automotive engine. A full jacket has been adopted for the periphery of the exhaust port. The separate exhaust passage is composed of an exhaust guide supported by a water-cooled aluminum exhaust manifold fixed to the head and mount case. Exhaust gas from the head does not pass through the cylinder block, but is guided directly to the extension case below the mount case. This configuration has made it possible to utilize the same head gasket as an automotive engine. The crankshaft is supported by sintered alloy bearing caps of the type used in automotive engines. By these means high reliability has been balanced with cost reductions in the new outboard. Fig. 4 compares the structure of the power head in the new motor with a previous motor.

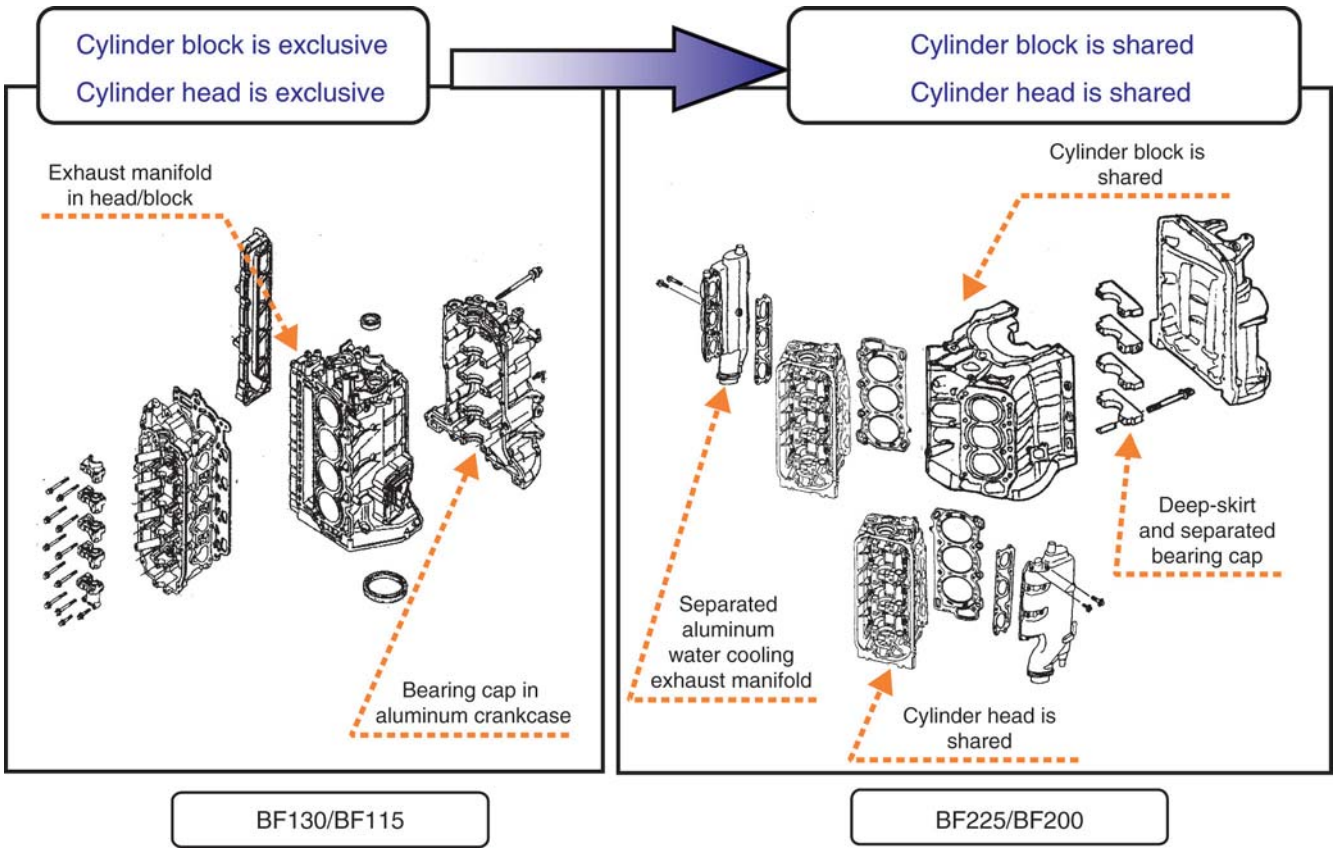


Fig. 4 Structure of power head

4.2 VTEC/Variable Intake System

The displacement of the BF225 was established with the output power of the BF200 as a base. The BF225 is the first outboard motor engine to utilize VTEC, which has resulted in the increased output power.

The VTEC system used in the BF225 is variable only on the intake side, and the high-speed valve timing setting enables maximum output at 225 horsepower. Valve timing settings at low to medium speeds were established with consideration of idling stability and ease of use in the normal operating range of the engine. Adoption of the variable intake system has increased low to medium speed torque. By opening and closing the valve separating the right and left chambers of the intake manifold, the variable intake system is able to use resonance effects below 4,000 rpm and inertia effects above 4,000 rpm, increasing the volumetric efficiency. This valve is located inside the aluminum upper cover on the back surface of the inlet manifold chamber.

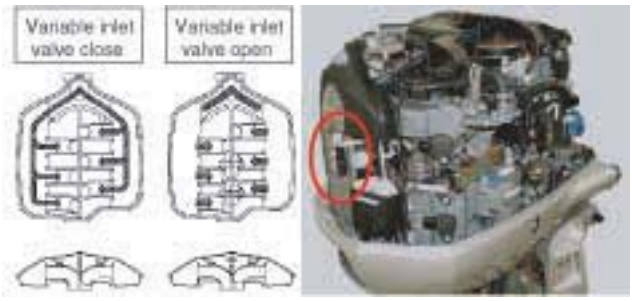


Fig. 5 Variable inlet valve

Fig. 5 shows a conceptual diagram and a cross-sectional view of the variable inlet valve, and Fig. 6 is a graph of the output characteristics of the BF225.

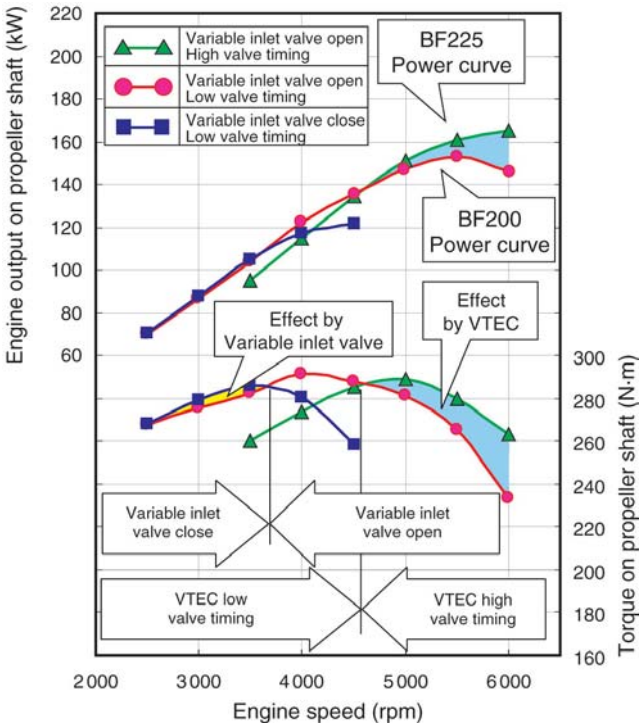


Fig. 6 Power curve of BF225/200

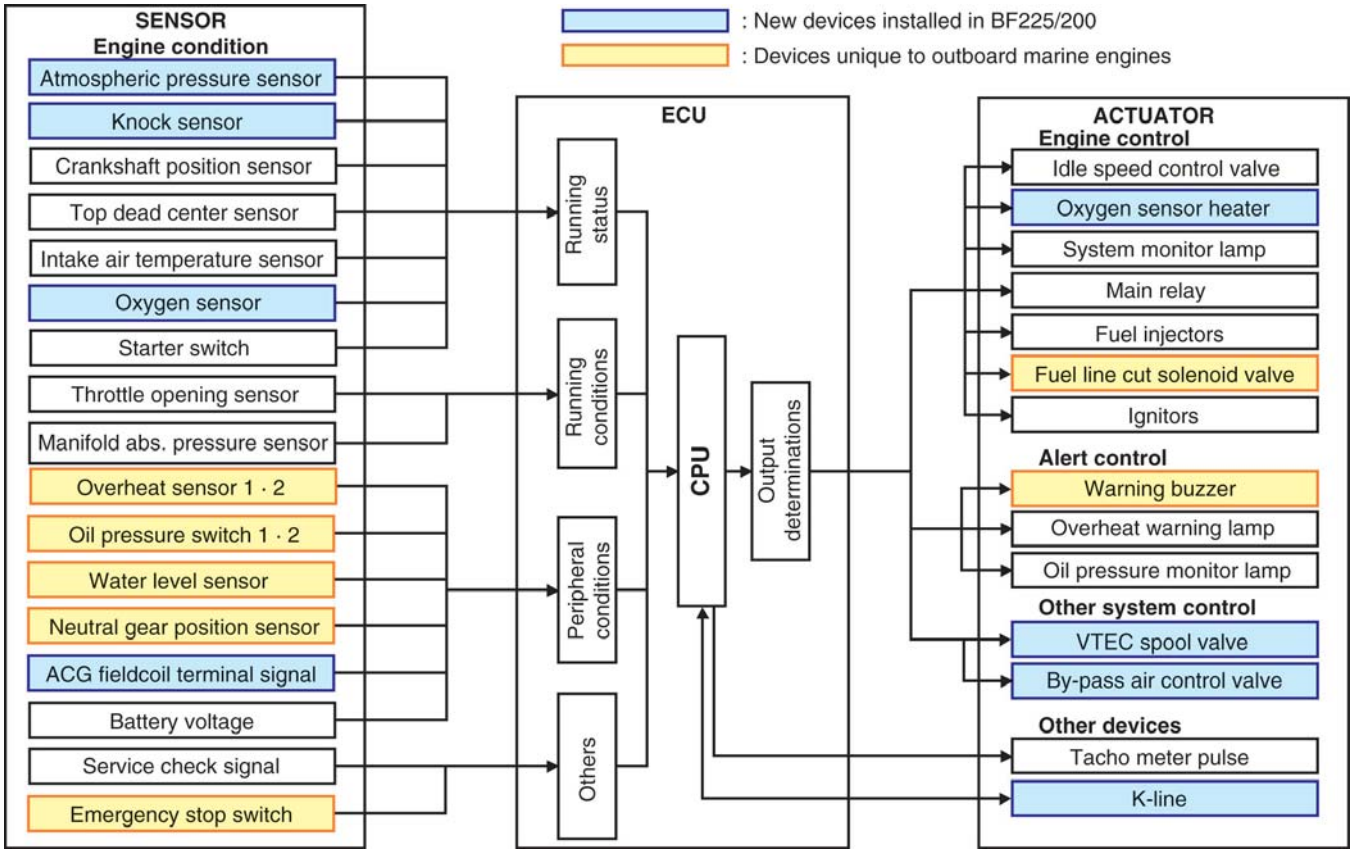


Fig. 7 BF225/200 Engine control system

4.3 Engine Control System

4.3.1 Total system outline

Honda’s previous outboard motor, the BF130/115, was it’s first to be provided with PGM-FI, and the resulting ease of starting and reliability became an important selling point. Basic performance of the BF225/200 has been taken to a still higher level, as befits the flagship of Honda’s Outboard series. It features an O_2 feedback system to increase fuel economy and decrease exhaust emissions; a knock control system to increase power; and improved alert control systems (overheating, oil pressure, PGM-FI, ACG, water separator alert) to increase reliability. The systems are based on automotive control systems, but the alert systems were newly designed with consideration of the requirements for outboard motor use. The heat, vibration, corrosion and water immersion resistance of each component has also been increased on the basis of the same considerations. Fig. 7 shows a diagram of the engine control system.

4.3.2 O_2 feedback system

To balance high fuel economy and low exhaust emissions, the new engine has been provided with PGM-FI for the intake and fuel systems and, an O_2 feedback system was adopted for the first time in a four-stroke outboard motor. These systems have enabled the achievement of an 8% decrease in fuel consumption against our competitors’ 2stDI outboard motors of the same power. The engine has cleared the CARB marine engine (2008) exhaust emissions standards, becoming the first 200 horsepower class outboard motor to achieve an ULTRA-LOW emissions level. Fig. 8 shows BSFC figures, and Fig. 9 shows exhaust emission levels.

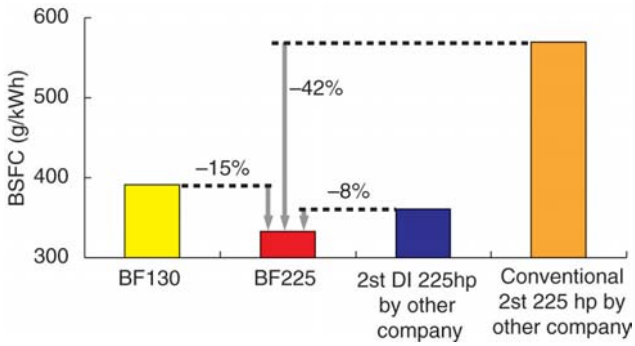


Fig. 8 BSFC on the emission-measuring mode

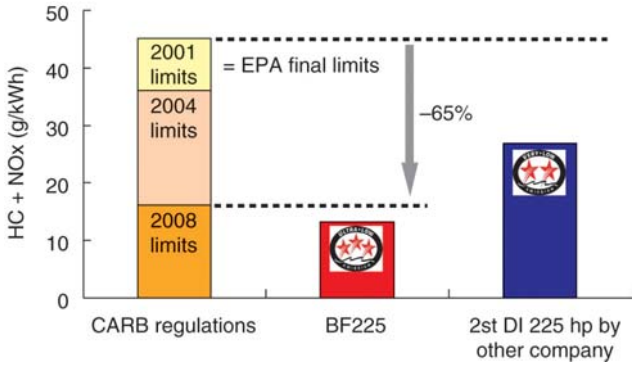


Fig. 9 Exhaust emissions comparison

When an outboard motor clears the CARB marine engine regulations, it earns the right to bear one of the CARB environmental labels shown in Fig. 10. The BF225/200 will bear the three-star (ULTRA-LOW) label shown at the bottom of Fig. 10.



Fig. 10 CARB environmental label

4.3.3 Knock control system

To obtain the rated output horsepower of 165 kW at 5,500 rpm from the propeller shaft, it was necessary for the engine itself to produce 200 kW, requiring specific output horsepower to be increased to 57 kW/l. Therefore, in addition to the use of the VTEC system and the tuning of the intake and exhaust systems, a knock control system was adopted to maximize the potential output horsepower. The knock sensor is a resonance vibration type, and controls the optimum ignition timing within the 80–90 RON octane number. The adoption of this system has increased power output by 5-6 kW with the throttle fully opened.

4.3.4 Alert control system

(1) Overheat Alert

Because outboard motor cooling systems are operated by direct intake of seawater, etc., into the engine, foreign matter floating on the surface of the water can block the inlet and cooling water channels creating potential for engine overheat and serious engine damage. Overheat sensors, which accurately detect blockages in the water channels, are installed in both banks of the V6 engine providing a system which gives early warning of overheating. The control algorithms are based on those used for the BF130/115. The alert signal is transmitted to the rider by means of a buzzer and a lamp, and then fuel supply and ignition is cut down.

(2) Oil Pressure Alert

The oil pressure alert control algorithm is based on the algorithm used for the BF130/115. Oil pressure is monitored by low and high oil pressure switches, and the alert is set to function in response to engine speed and oil temperature, which has improved the engine protection function. The alert signal is transmitted to the rider in the same way as for the overheat alert described above.

(3) Other Alert Systems

The outboard motor has been provided with warning buzzers and lamps to warn the rider in advance of abnormalities in alternator function and infiltration of water in the fuel tank or fuel lines.

4.4 Weight Saving Technology

4.4.1 Resin inlet manifold

Considerations of strength and rigidity lead to a change in material for the inlet manifold from aluminum to nylon. Fig. 11 shows an external view of the inlet manifold.

As Fig. 12 shows, the inlet manifold is composed of three injection-molded components formed from nylon 6 and joined by vibration welding. Accurate control of the welding surface to form a single unit was achieved by setting all the joint surfaces on a single plane, enabling consistent welding quality.

The inlet manifold utilized in the BF225/200 was made flat to enable reduction of the front and rear length of the engine cover, which created the necessary opening for installation of the variable intake valve cover. To improve pressure resistance with this configuration, strength is ensured by simultaneously vibration welding six supports around the opening for installation of the cover.

Support and rib configurations were optimized by analyzing pressure resistance and vibration using CAE, which included analysis of the welded sections. This enabled designers to ensure sufficient strength, with a Nominal thickness of under 4 mm. Application of these technologies has resulted in significant weight savings, with the new manifold approximately half the weight of the previous aluminum inlet manifold.



Fig. 11 External view of inlet manifold



Fig. 12 Structure of inlet manifold

4.4.2 Resin ECU case

ECU's normally generate a great deal of heat due to built-in ignition igniters. And the ECU case is typically made of aluminum to dissipate radiant heat, but this increases weight significantly. The igniter has subsequently been built in to the ignition coil, and the heating circuits have been positioned on the base plate to improve radiation of heat. This has controlled the ambient temperature around the ECU when installed in the engine, making it possible to use nylon resin for the ECU case. The height of the electronic components has also been reduced, and the former bath tub shape of the case has been changed to an envelope shape, enabling the use of less plastic material in the injection molding process and resulting in a weight reduction of more than 30% over the previous model. The new low profile of the ECU has also improved mounting flexibility. The ECU is shown in Fig. 13.



Fig. 13 ECU

4.4.3 Optimization of bracket system components

To achieve weight savings in the stern bracket system, CAE analysis models (Fig. 14) of the stern bracket which fixes the outboard to the boat and the swivel case which supports the steering shaft were used to examine the relationship between static and dynamic breaking loads in actual brackets. The high load-bearing sections were identified, enabling the form to be optimized to balance strength with weight savings.

As a result, the weight of the bracket system has been reduced 20% compared to the previous model (BF130/115).

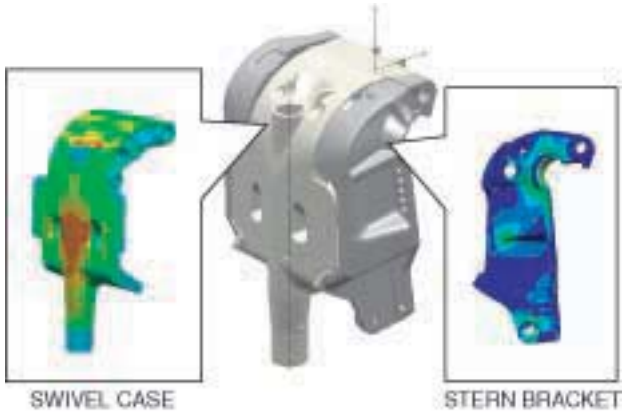


Fig. 14 CAE model of strength

4.5 Engine Cover With Center Handle

Four stroke outboards require that the user check the engine oil level periodically. A burden is placed on the user when removing the engine cover, as they are large, heavy, and difficult to carry. A lightweight, easy to carry engine cover was therefore developed for the new outboard. The engine cover of the previous model was designed with a combined tilt-up handle and an air intake at the rear. Because the new engine is larger, a special carrying handle was designed in the center of the upper surface of the cover. The rim molding previously utilized in the BF130/115 was adopted, resulting in an engine cover 7.1 kg lighter than a 2stDI engine cover. Fig. 15 shows an external view of the engine cover and an image of how it is carried.



Fig. 15 Center handle engine cover

4.6 New Anti-corrosion Painting

As previously mentioned, the low exhaust gas emissions and high fuel economy of the BF225/200 make it friendlier to the environment. In addition, to make the production process environmentally friendlier, a non-chrome paint was adopted for the external components of the new outboard.

To ensure corrosion resistance when outboards are used in saltwater, aluminum alloy external components are treated with an anodic oxidation coating, to which paint is then applied.

The anodic oxidation coating leaves porous layer that can act as starting points for corrosion. Previously, a molybdenum disulfide and nickel acetate treatment was applied to seal this porous layer, and reinforce the anodic oxidation coating. However, when deep scratches occur to the paint surface, the molybdenum disulfide crystallizes, allowing the advance of corrosion without the formation of a passive state film to protect the aluminum surface.

To prevent this, a primer containing chrome, which has been proven effective against corrosion, is typically applied between the aluminum and the topcoat to form a passive state film. Chrome has been entirely eliminated in the new anti-corrosion paint utilized for the BF225/200 by impregnation of the porous layer with phosphate zirconium and sealing with nickel acetate to reinforce the anodic oxidation coating. Because phosphate zirconium does not crystallize, it forms a passive state film between the aluminum surface and the paint which prevents corrosion even when deep scratches occur to the paint surface. The addition of a primer containing molybdenum phosphate has further strengthened the film. This has done away with the necessity of utilizing chrome in the painting process, while at the same time achieving a level of corrosion resistance equivalent or superior to that of the current method. Fig. 16 shows a cross-sectional image of the paint layers formerly used and those used on the new outboard motor.

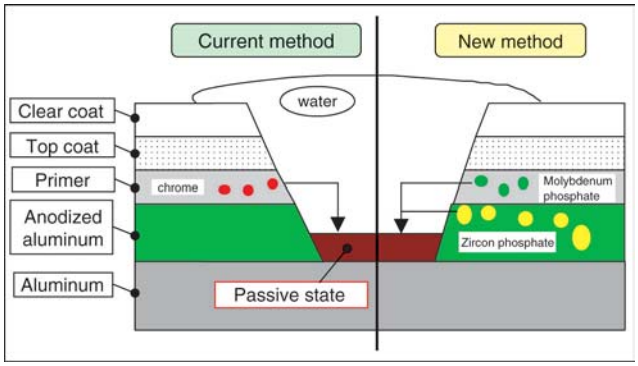


Fig. 16 Cross-sectional image of outboard paint

5. Results of Development

5.1 Performance

The adoption of power-enhancing technologies such as VTEC a variable intake system and a knock control system, combined with weight-saving technologies such as plastic inlet manifold and analysis of the bracket system, have enabled acceleration performance of the BF225/200 equivalent to that demonstrated by competitors’ 2stDI outboard motors, as shown in Fig. 17.

5.2 Low Vibration

The adoption of a 60° V6 engine, natural torque axis support mounts (center axis of rotational motion established by reactive force of combustion), and rubber mounting with non-linear spring characteristics have reduced the level of vibration of the new outboard to less than half that of competitors’ 2stDI outboard motors. Fig. 18 shows craft vibration levels, which are shown as non-linear rubber mount spring characteristics in Fig. 19.

5.3 Low Noise

To maintain compactness, a large capacity intake silencer has been installed to the upper section of the engine. As Fig. 20 shows, this has reduced engine noise more than 3 dBA against competitors’ 2stDI outboard motors.

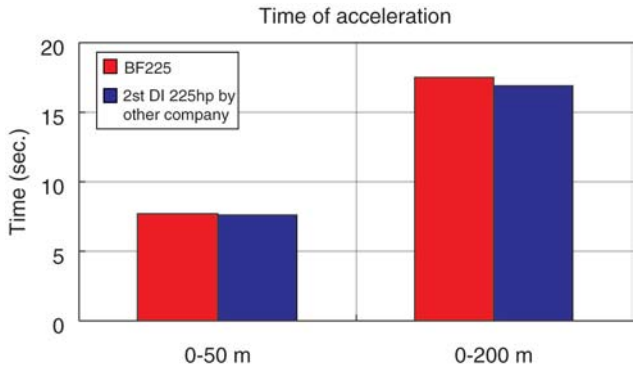


Fig. 17 Comparison of acceleration time

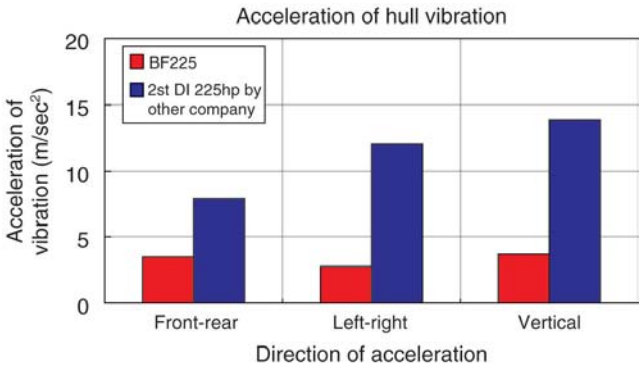


Fig. 18 Comparison of vibration level

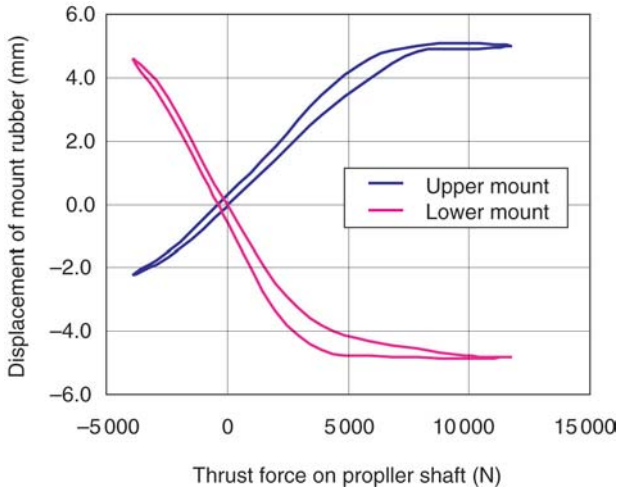


Fig. 19 Displacement of mount rubber

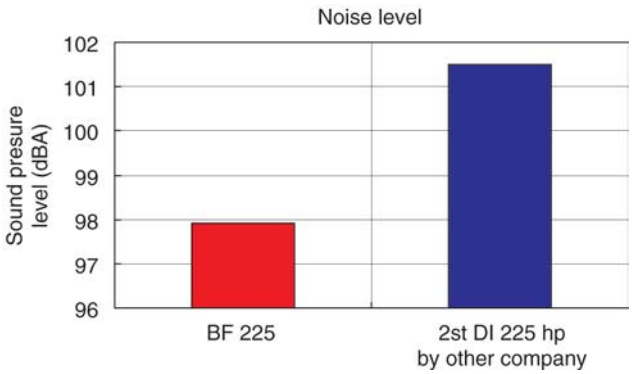


Fig. 20 Comparison of noise level

5.4 Ease of Installation

Frequently, users of outboards in the power class of the BF225/200 choose to install two motors on a single boat (twin installation). When twin outboards are installed, it is normal to position the motors as close as possible to the center of the boat, to prevent the propellers from leaving the water when turning. Four-stroke outboard motors conventionally have a larger size than two-stroke outboards of equivalent power. In addition, the valve system of V6 engines tends to increase their total width. The BF225/200 features a "V-wing Form", in which the width of the front of the engine cover is reduced. This allows twin outboards to be installed in a 660 mm span, the smallest mounting span in the market, and a world first for 200 HP class four-stroke outboard motors.

This means that users making the transition from competitors' two-stroke outboard motors do not need to increase the installation space on their boats.

Fig. 21 compares twin installation of the BF225/200 and another company's two-stroke outboard. Fig. 22 shows a bird's-eye view of twin BF225/200s at full steering.

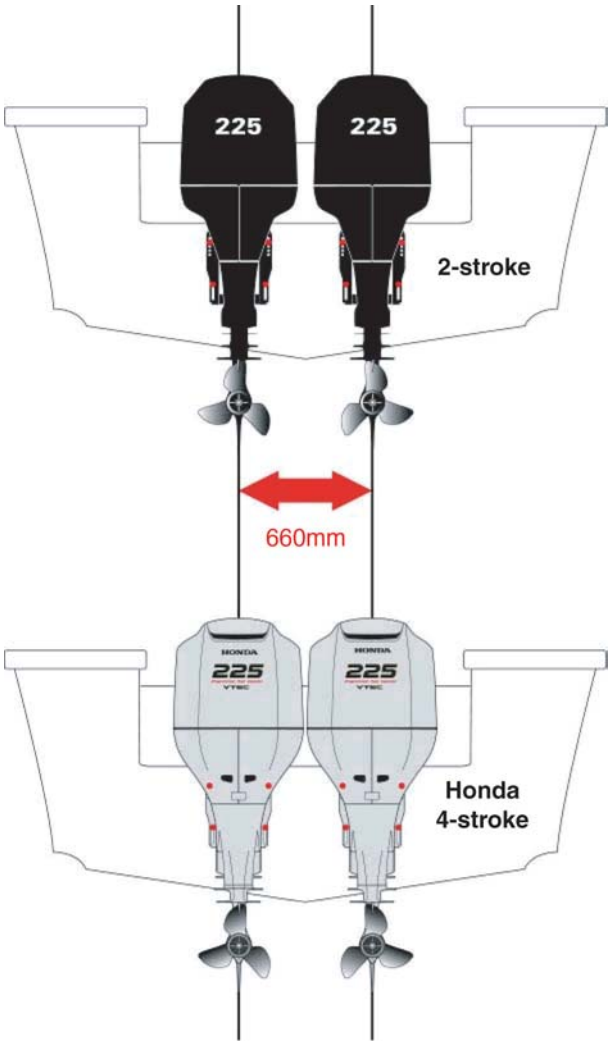


Fig. 21 Installation of twin outboard motors

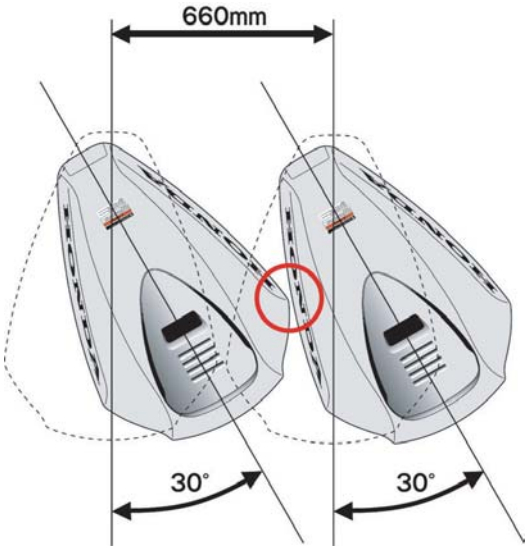


Fig. 22 Twin installation at full steering

6. Conclusion

The BF225/200 has been provided with VTEC, a variable intake system, a plastic inlet manifold, a knock control system, and a water-cooled exhaust manifold to ensure equivalent power and ease of mounting to existing 2stDI outboard motors in the same class. At the same time, PGM-FI and an O_2 feedback system enable high power and fuel economy with a low level of exhaust gas emissions. Parts sharing with an automotive engine and the sharing of an automotive production line for cylinder blocks and cylinder heads has further achieved high reliability and reduced costs.

These technologies have enabled Honda to present the BF225/200 (Fig. 23) to the market as its flagship model, with the world’s highest power for a four-stroke outboard motor, and to expand its four-stroke outboard line-up from 2 HP to 225 HP models.

In closing, the authors wish to express their sincere thanks to the many people, at factories both in Japan and overseas, representing both Honda and other companies, who generously offered their assistance in the development of this new outboard.



Fig. 23 Boat with twin BF225s at cruising speed.

References

(1) Tsunoda, M., Shidara, S., Shimazaki, H., Hayashizaki, S.: “Development of Large 4-Stroke Outboard Motor BF115/130”, HONDA R&D Technical Review, vol. 11, No. 1, p. 15–22 (1999)

(2) Hosaka, T., Hamazaki, M.: “Development of the Variable Valve Timing and Lift (VTEC) Engine for the Honda NSX”, SAE Paper 910008

(3) Otsu, K., Nakahara, K., Sakamoto, Y., Imai, Y.: “Development of 3.0LV6 Engine for ’97-model Acura CL”, HONDA Technical Review vol. 9, p. 51–60 (1997)

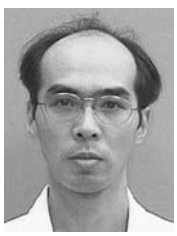
■ Authors ■


Masaki TSUNODA


Masayuki OHSUMI


Makoto YONEZAWA


Kentaro FURUYA


Sadafumi SHIDARA


Ryuichi KIMATA

Introduction of CRF450R Equipped with 4-Stroke Engine

Norio HOSHI* Yasuo SHIMURA* Takanori OKUMA*
Akifumi NOMURA* Kazuhiko GOGO*

ABSTRACT

The first 4-stroke engine motocrosser (CRF450R) in Honda was developed focussing on the fastest motocrosser for all motocross races and to enable riding without stress according to the rider's intention. The development targets were to obtain a linear characteristic in torque and traction, which was controlled easily by adopting the 4-stroke engine, and to achieve the equivalent power-weight ratio to the 2-stroke engine motocrosser of the same race class. A lightweight forged piston with an extremely short skirt, a valve train of SOHC 4-valve engine (UNICAM system), titanium inlet valves, and a separated lubrication system for both the crankcase and the transmission were adopted in the engine as means to get a liner characteristic in torque and high power. As a result, 29.5 kg of engine mass and 41 kW of maximum power were achieved. Engine startability via the kick-starter was also improved by adopting a newly developed auto-decompression system. A total vehicle mass of 102 kg was realized by lightening each part of the frame body and suspension through techniques such as a newly shaped aluminum frame and a titanium exhaust pipe.

1. Introduction

The 2-stroke motocrosser is presently the mainstream for motocross racers. However, in light of the demand for a cleaner motocrosser Honda has developed a new type of motocrosser equipped with a 4-stroke engine.

2. Development Concept

Since motocross has jump sections and series of tight corners, the greatest emphasis is placed on a compact frame body and low weight. No matter how superior its engine's power characteristics, a motocrosser that is large and heavy will be difficult to race. Motocross also involves riding on slippery offroad surfaces, so even though maximum power is required, it is also of great importance to have linear torque and traction characteristics that allow easy handling. In order to satisfy these requirements, the aim was to achieve a vehicle body size and power-weight ratio on a par with 2-stroke motocrossers, together with the power characteristics of a 4-stroke engine, which make for easy handling in a motocrosser.

This development concept for the CRF450R, Honda's first 4-stroke motocrosser, was further defined as follows:

- A motocrosser that is the fastest even beyond its class
- Easy to handle and refreshingly fun to ride

* Asaka R&D Center

3. Model Overview and Objectives

Fig. 1 shows an external view of the CRF450R, and Table 1 gives the major specifications. The vehicle was made equivalent to the 2-stroke motocrosser CR250R in size. In determining the vehicle mass and maximum power, the positioning of the power-weight ratio in relation to various classes of displacement, comparison of the mixed racing results and lap times in every class were taken into account. A target of 102 kg was set for vehicle mass and 41 kW for maximum power, in addition to the goal of linear torque characteristics. Fig. 2 shows the power-weight ratio comparisons. The 4-stroke engine has a higher compression ratio and fewer igniting chances, firing once out of every two crankshaft revolutions, so it was necessary to improve the startability using the kick-starter. It was desirable to provide fast restarting to recover from stalls due to over-braking or falls during motocross races. The goal was set for startability using the kick-starter on a par with 2-stroke engines in order to make the bike enjoyable for a wider range of riders.



Fig. 1 External view of CRF450R

Table 1 Major specifications

Items		Specifications
Overall length	(mm)	2187
Overall width	(mm)	825
Overall height	(mm)	1254
Wheelbase	(mm)	1488
Seat height	(mm)	945
Ground clearance	(mm)	331
Vehicle dry mass	(kg)	102
Engine type		Liquid cooled 4-stroke OHC single cylinder
Engine displacement	(cm^3)	449
Bore x Stroke	(mm)	96 x 62.1
Compression ratio		11.5 : 1
Valve train		SOHC 4valve
Max.power	(kW/r/min)	41/9000
Max.torque	(Nm/r/min)	49.8/7000
Carburetor type		FCR40
Fuel capacity	(L)	7.4
Clutch type		Wet multi-plate type
Transmission		5 speed constant mesh
Caster angle		27° 50'
Trail length	(mm)	114
Tire size	Front	80/100-21 51M
	Rear	110/90-19 62M
Brake system	Front	Single 240mm disc with twin-piston caliper
	Rear	Single 240mm disc
Suspension	Front	Telescopic
	Rear	Pro-link
Frame type		Aluminum twin-tube

4. Engine

The width, length, and height of the engine were set to make it a size that could be mounted on the CR250R platform. In terms of mass, the target mass for the completed vehicle was set, and the various individual targets for engine, frame body, suspension, and electric equipment were then assigned accordingly. The target engine mass was set at 29.5 kg. Fig. 3 shows a cutaway drawing of the engine as a whole.

The engine speed at maximum power was held to a low 9,000 r/min to emphasize rear wheel traction and instantaneous acceleration characteristics. The bore/stroke was set to 96 mm × 62.1 mm and the engine displacement to 449 cm^3 in order to achieve the target power of 41 kW. Fig. 4 shows the engine performance curve.

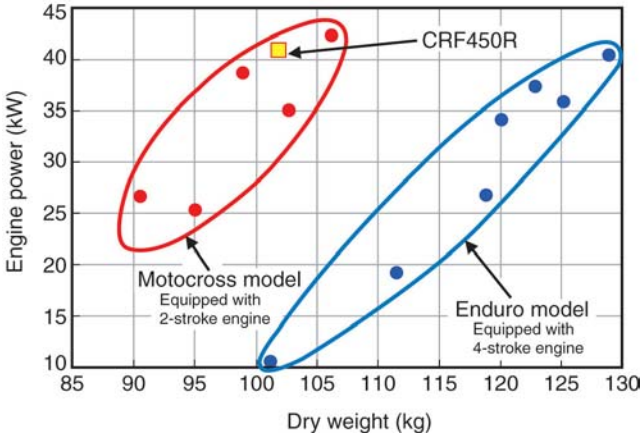


Fig. 2 Comparison of power-weight ratio between motocross models and enduro models

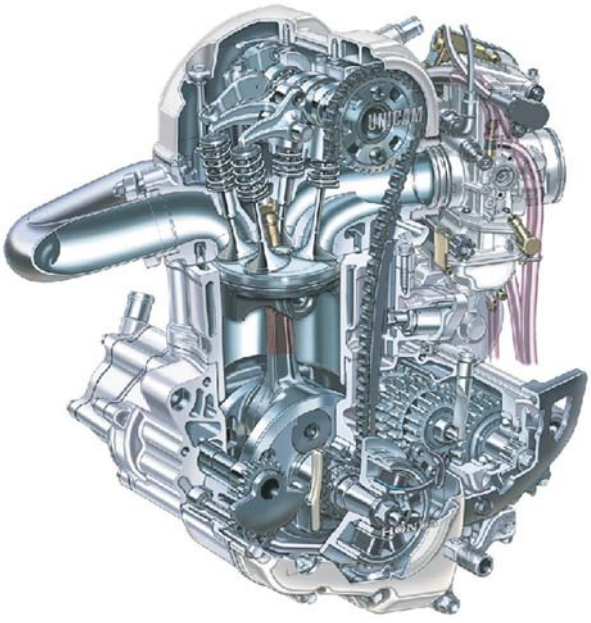


Fig. 3 Cutaway drawing of CRF450R engine

Fig. 5 presents a comparison of engine size with the XR400R, an earlier 4-stroke engine with the same displacement. The CRF450R achieved an engine weight reduction of 23% relative to the XR400R, an improvement of 53% in maximum power, and an improvement of 31% in maximum torque.

The valve timing and intake-exhaust assembly were optimized, friction was reduced, and other such measures were taken to enhance power and speed without degrading the linear torque characteristics of the 4-stroke engine. A torque contour that included partial gate opening ranges was used as a guide for linear torque characteristics. Torque characteristics allowing for easier handling were achieved by selecting those characteristics that yielded a contour with uniform pitch. Fig. 6 presents a comparison of torque contours with the 2-stroke CR250R.

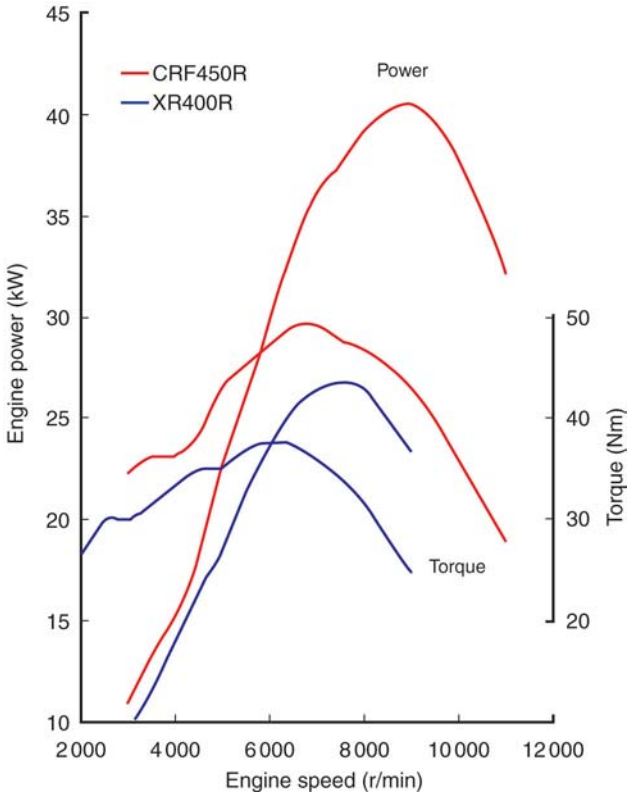


Fig. 4 Engine performance curve

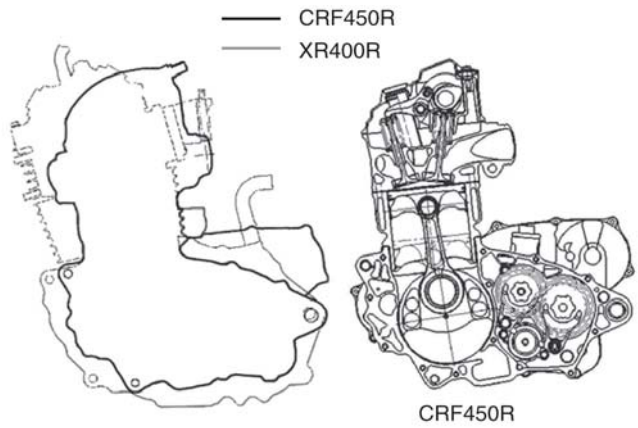


Fig. 5 Comparison of engine size

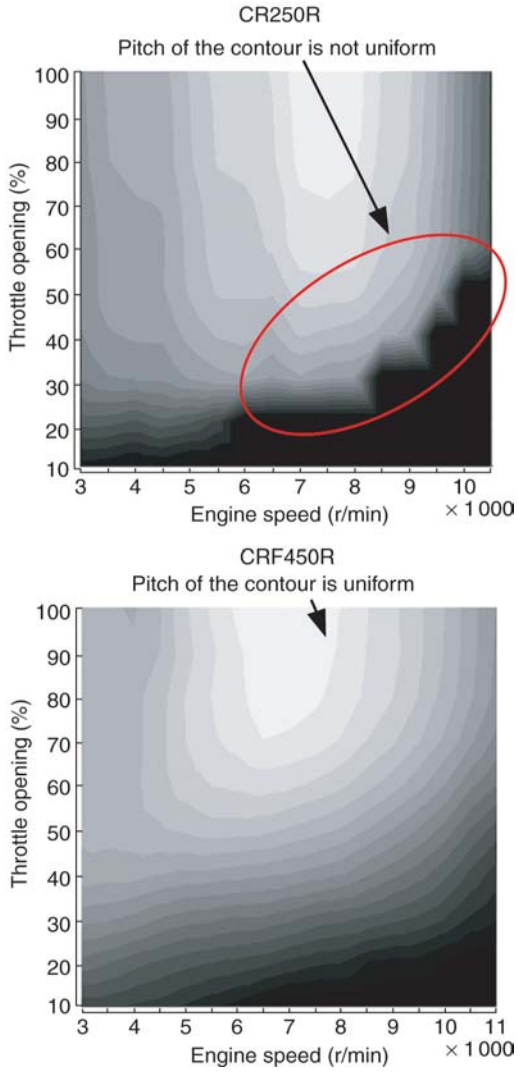


Fig. 6 Torque contour

4.1. Valve Train System

Fig. 7 gives an overall view of the valve train system. Adoption of DOHC for the valve train system is one method for achieving higher speed than in conventional single-cylinder engines. With DOHC, however, separate camshafts become necessary for intake and exhaust assemblies, which is inappropriate in terms of weight reduction. For the CRF450R, titanium valves were used on the intake side where the large valve diameter is disadvantageous at high speeds, and they were made directly actuated for greater stability of behavior. The exhaust side was given an SOHC configuration that uses a rocker arm. The cam holder was made as a single diecast unit with the valve lifter hole and rocker arm shaft supports. This is called the UNICAM system, for unit-type cam. The camshaft shown in Fig. 8 uses SCM carburizing and quenching rather than the conventional FC to increase fatigue strength while thinning the walls to the limit. The overall valve train system achieved a 376 g weight reduction relative to a DOHC layout.

The rocker arm is a roller type with a forked structure. The spark plug hole is located between the forks so that the spark plug can be centered for greater flame spread speed. This valve train system allows the valves to be set at a narrower angle than the DOHC layout, at 21.5°. This makes the combustion chamber more compact, and contributes to the higher compression ratio and higher output power.

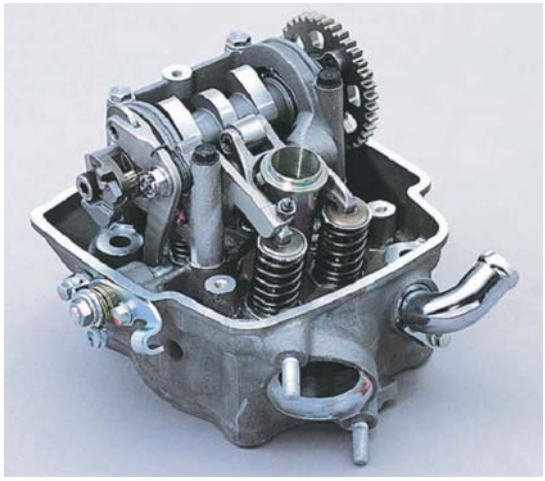


Fig. 7 UNICAM system



Fig. 8 External view of camshaft

4.2. Dual Lubrication Systems

As shown in Fig. 9, the crankcase was developed as an extension of the closed crankcase used in the XR650R.[1] The balancer is placed outside the crankcase and the pressure inside the crankcase is allowed greater variation in order to improve oil discharge performance. Taking advantage of the closed construction of the crankshaft, which has oil seals at both ends, a dual lubrication system was adopted that separates the lubrication on the crankshaft and piston side from that on the transmission and clutch side. For the crankshaft, piston, and valve train system, a trochoid pump similar to those in conventional engines is used for pressurized oil delivery. Fig. 10 shows the structure of the oil pump. An oil bath lubrication like that in a 2-stroke engine is used for the transmission and clutch side. Despite the compactness of the crankcase, the space between the left side crankcase and the cover on that side is used as an oil tank so that stable lubrication can take place even throughout the severe changes in frame body angle that occur during motocross races. A housing was created on the crankcase joint surface and used as the oil pump body to make it 147 g lighter than the conventional structure.

4.3. Shorter Piston Skirt and Lighter Forged Piston

In order to make the engine more compact, it was necessary to reduce the mass of the reciprocating parts. The slipper-shaped, ultra-short skirt piston shown in Fig. 11 is 36 mm in height with a bore of 96 mm, and achieved a weight of 267 g, or a reduction of 108 g over a piston with a conventional design. Fig. 12 shows the relationship between piston bore and piston mass for conventional models. Optimization of the piston profile, correct adjustment of lubrication, reduction in lateral pressure of the piston skirt, and correct adjustment of the clearance between the small end of the connecting rod and the piston pin boss made it possible to use this short skirt.

4.4. Automatic Decompression System

The heavy force on the kick pedal and insufficient igniting chances had been existing issues for the conventional 4-stroke engine. In order to address them, a unique pin-rotational type automatic decompression system was adopted. Fig. 13 shows the system structure, and Fig. 14 shows the decompression cam. This system provides improved cold starting and hot restarting on a par with 2-stroke engines.

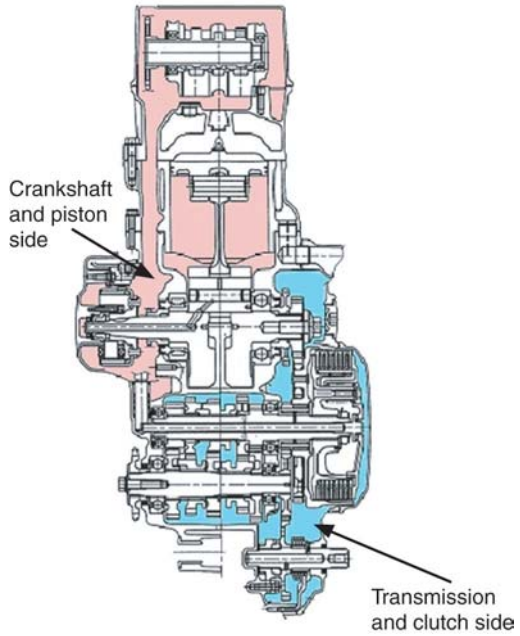


Fig. 9 Structure of dual system lubrication

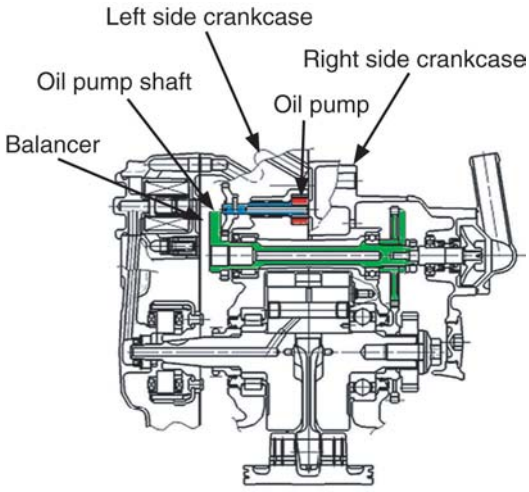


Fig. 10 Structure of built-in oil pump

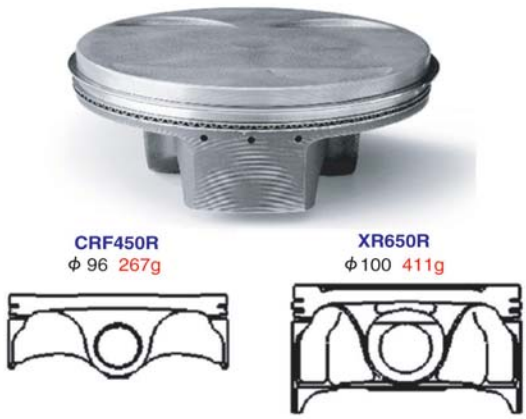


Fig. 11 Short skirt piston

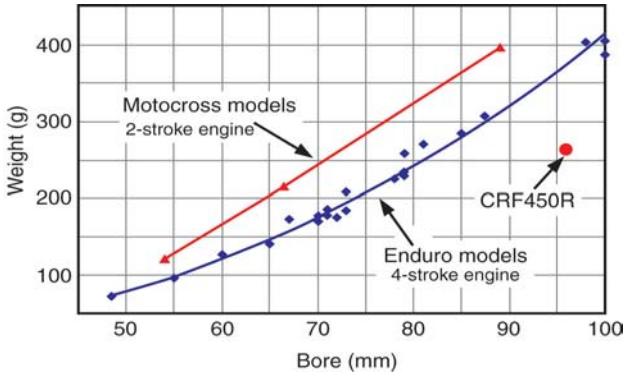


Fig. 12 Relation between piston bore and weight

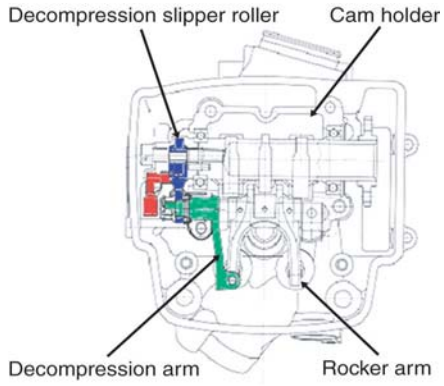


Fig. 13 Structure of automatic decompression system

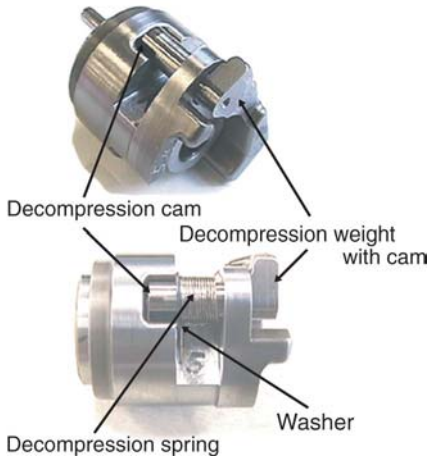


Fig. 14 Decompression cam

Fig. 15 shows the operation of the system. When starting, the decompression cam formed from a pin, works through the decompression slipper roller to press the rocker arm on the exhaust side. This reduces the pressure inside the cylinder and reduces the amount of force on the kick pedal. After starting, centrifugal force causes the decompression weight, which is integrated with the pin, to turn and release the decompression cam. The issue of igniting chances is addressed by adjusting the operating range and the lift of the decompression cam to the proper amount, which provides a significant improvement compared to operation without a decompressor. Fig. 16 shows the relationship between the force on the kick pedal and the crank turning force for different crank angles with and without the decompression system.

4.5. Crankshaft and Connecting Rod

The crankshaft was changed from the conventional S48C induction hardened material to SCM420H carburization and quenching hardened material in order to reduce the weight while providing the same fatigue strength. The connecting rod has different requirements for fatigue strength at the big end and the small end, and a balance between fatigue strength and weight reduction was sought by varying the depth of heat treatment in these areas. This achieved a reduction of 262 g in the mass of the crankshaft alone compared to conventional crankshafts. Fig. 17 gives an external view of the crankshaft.

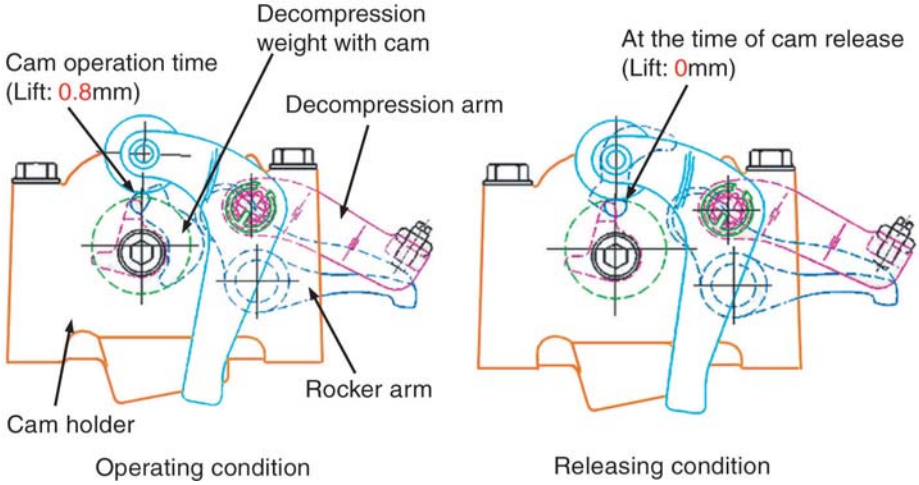


Fig. 15 Operation of automatic decompression system

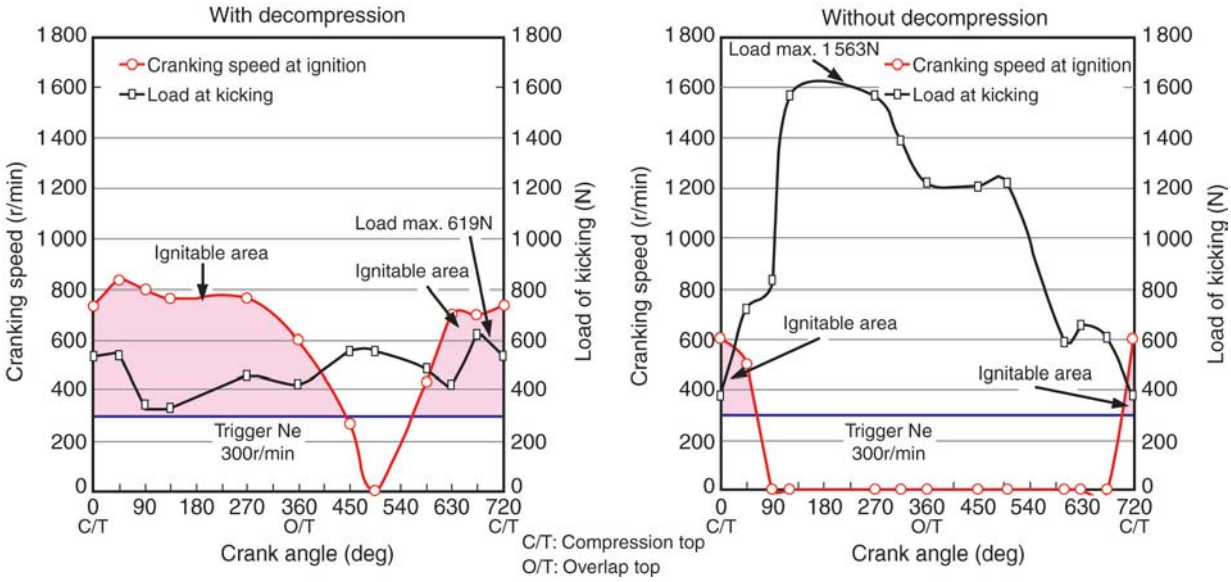


Fig. 16 Comparison of ignitable area, with or without decompression system

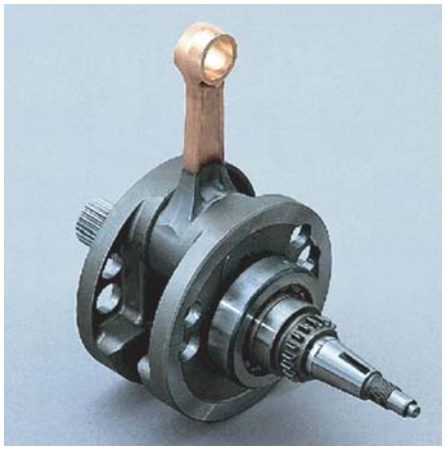


Fig. 17 External view of crankshaft



Fig. 18 FCR carburetor

4.6. Flat Slide Valve Carburetor

The flat slide valve of the FCR carburetor made by Kehin is equipped with four rollers on both sides to provide sharp response and enable light, smooth throttle operation. A separate route is also provided as a fresh air induction path in order to improve startability by adjusting the air-fuel ratio to the proper level when hot starting the engine or starting after a fall. Fig. 18 shows an external view of the carburetor, and Fig. 19 shows the geometry of the fresh air induction path.

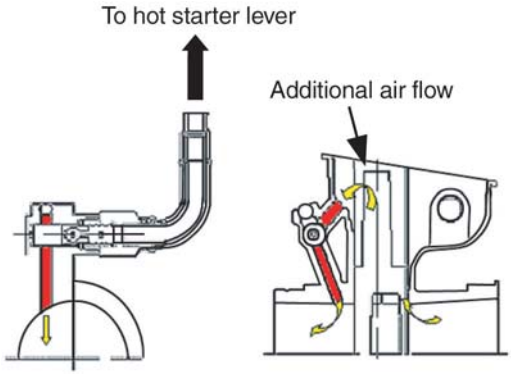


Fig. 19 Fresh air induction path

4.7. Hot Start Lever

A hot start lever is provided for easier starting of a hot engine and restarting after a fall as described in section 4.6. This device opens a fresh air induction path to the carburetor in order to adjust the air-fuel ratio to the proper level when starting a hot engine or restarting after a fall. This lever was previously an integral part of the carburetor. For the CRF450R, the hot start lever is connected through a cable to the carburetor and mounted coaxially with the clutch lever in a location where riders can operate it without removing their hands from the handlebars. Not only does this help avoid operating mistakes, but it also makes it possible to operate the hot start lever simultaneously with the clutch lever when restarting after a fall, so that the bike can be restarted quickly in any gear. Fig. 20 shows how the hot start lever is mounted.



Fig. 20 Hot start lever

4.8. Ignition System

The ignition system utilizes a highly accurate 8-bit electronic control unit (ECU) that incorporates capacitive discharge ignition (CDI). This provides the optimum ignition timing suited to throttle opening and engine speed. Fig. 21 shows the map of the ignition timing.

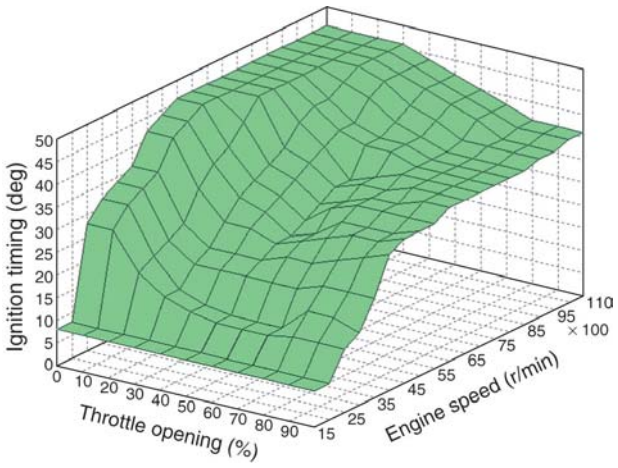


Fig. 21 3-D map of ignition timing

5. Vehicle Body

In order to realize the development concept of a motocrosser that is easy to handle and refreshingly fun to ride, the objective was to attain a body size and vehicle mass equal to the CR250R 2-stroke motocrosser, which has a high competitiveness that has been developed over many years. Further objectives were easy-to-control turning characteristics and reduction of bump impact.

5.1. Vehicle Dimensions

In order to provide free maneuvering performance, the engine mounting position was determined using the dimensions of a 2-stroke motocrosser as a basis and with consideration for the optimum location of the engine center of gravity, ground clearance in order not to interfere with rough-road running ability, fuel tank capacity sufficient to complete a race, and other such conditions. This resulted in vehicle dimensions generally the same as the CR250R and realization of stability when going straight that takes advantage of the traction characteristics of a 4-stroke engine, turning characteristics equal to a 2-stroke motocrosser, and good handling characteristics resulting from a compact body. Fig. 22 shows the vehicle dimensions.

5.2. Frame Body

The CRF450R frame body was enhanced based on the aluminum semi-double-cradle twin-tube frame used for the CR250R. Fig. 23 shows an external view of the frame body. In order to have an optimum balance of rigidity and strength, a tapered tube fabricated by the swaging process used for swing arms was selected for the down tube. A cross member was added to the center part of the frame, and this cross member was integrated with the rear cushion bracket. This created the space required for mounting a 4-stroke engine without altering the frame width and size. Not only does this structure provide the space layout, but it also contributes to the proper degree of deflection. Together with the down tube described above, this optimizes longitudinal rigidity, lateral rigidity, and torsional rigidity, and realizes high stability and easy-to-control turning characteristics.

The compact steering head pipe made of forged aluminum was newly designed following reevaluation of the joint structure on the 2001 model of the CR250R. In order to reduce weight and reduce bump impact while riding, a large opening was also made in the inside wall, as shown in Fig. 24, and the frame was given the proper rigidity balance. This made it possible to achieve a high-order balance of agile steerability and stability. The mass of the frame body was reduced by 200 g.

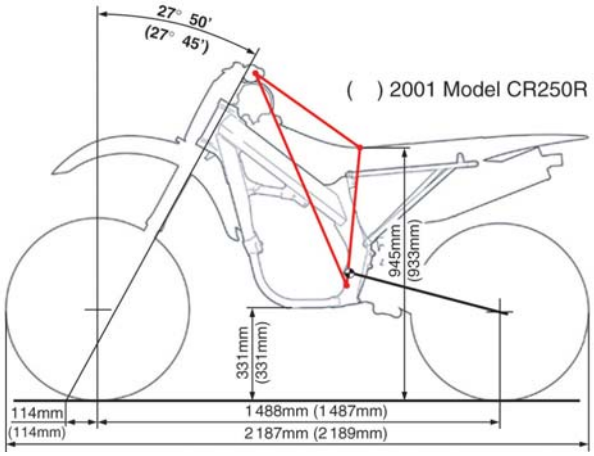


Fig. 22 Geometric dimension of CRF450R



Fig. 23 External view of frame



Fig. 24 Forging aluminum steering head pipe

6. Suspension System

Suspension performance, strength and durability are of great importance for motocrossers, which ride on rough roads, jump, and so on. In terms of performance, the suspension is required to undergo constant improvement for maneuverability, stability, and rough-road running ability. Continuous efforts are being made to reduce weight and increase rigidity as one means for achieving this end.

In general, mounting a 4-stroke engine will cause higher traction and a heavier engine so that the suspension will have a higher spring rate and becomes heavier. The CRF450R suspension, however, has been optimized for rigidity and strength, yielding a weight reduction of 1,260 g over the CR250R. This has realized a mass of 45.8 kg, which is on a par with 2-stroke motocrossers.

6.1. Rear Suspension

The rear suspension is of the swing-arm type with an axle stroke of 315 mm. A single shock absorber of the remote reservoir gas presser risen type, with a piston that is 50 mm in diameter, is located at about the center of the frame body. It is equipped with adjusters that allow separate tuning of low-speed and high-speed compression damping force, and tuning of the tension damping force. The shock absorber is attached to the swing arm by means of a linking device known as the PRO-LINK, which changes the shock absorber stroke progressively according to changes in the axle. This PRO-LINK was given shanks with a low-load design and was optimized for link ratio, yielding a superb ride feel and rough-road running ability. In order to provide ground clearance and to achieve low weight and low positioning of the rear caliper, the swing arm was shaped with a vertically asymmetrical taper. Fig. 25 shows the layout of the rear suspension.

6.1.1. Swing arm

The objectives for the swing arm were in the direction of increasing torsional rigidity, lateral rigidity, and weight reduction. The front portion of the structure utilizes AC4CH-T6 cast aluminum, which allows design freedom and high durability, and the rear portion utilizes tapered tube with tensile strength of 380 MPa that has been processed by non-rotating dies swaging manufacturing method. The target rigidity was achieved with the minimum mass by applying CAE to perform repeated calculations of rigidity and mass. This made it possible to optimize the thickness of each part of the swing arm and to locate the ribs properly so that the torsional rigidity was improved by 15%, the lateral rigidity was improved by 4%, and the weight was reduced by 200 g compared to the CR250R. As a result, the CRF450R achieved an improvement of 18% in the mass-rigidity ratio, a figure that shows design efficiency. Fig. 26 shows an external view of the swing arm.

6.2. Front Suspension

The front suspension is a telescopic type with a 305-mm axle stroke and inverted front forks with an inner tube 47-mm in diameter. The front forks have internal shock absorbers of the low-friction remote reservoir spring presser risen type equipped with adjusters that allow the damping force to be tuned on both the compression and extension sides. A review was conducted of the materials used for bolts, nuts, damper rods, and springs in the front forks, the margin of thread engagements, and other such factors. As a result, a weight saving of 300 g relative to the CR250R was achieved, despite the higher spring constant. Fig. 27 shows the front fork structure.



Fig. 25 Structure of rear suspension



Fig. 26 External view of swing arm

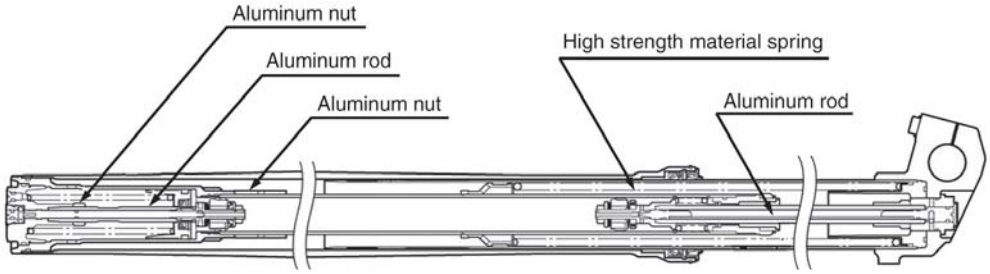


Fig. 27 Structure of front fork

6.3. Brakes

Hydraulic disc brakes with a 240-mm disc are used for both the independent front and rear brakes. Since their caliper bodies and caliper brackets are unsprung parts, they are made using light cast aluminum. The front brakes have two-pot calipers using aluminum pistons, while the rear brakes use newly-designed one-pot calipers.

6.3.1. Rear brake system

Issues involved in the brake system include the objectives of improved maintainability and reduced weight as well as two design issues specifically related to the 4-stroke engine:

- The mufflers located on the upper part of the rear calipers require a larger capacity than in 2-stroke engines. Therefore, it was necessary to give the mufflers a larger cross-section. It was a challenge to realize the enlarged cross-section, however, because of insufficient clearance between the caliper and muffler when the rear suspension is fully stroked.
- The exhaust pipe for a 4-stroke engine reaches higher temperatures than that of a 2-stroke engine. This causes a challenge with placement of the brake fluid sub tank that belongs to the master cylinder and with arrangement of the tubing between the master cylinder and sub tank.

Calipers with a compact piston 22.65 mm in diameter and a master cylinder integrated with an ultra-compact reserve fluid tank and a cylinder 9.52 mm in diameter were developed in order to address these issues. Making the caliper piston 22.65 mm in diameter not only made it possible to reduce the caliper size, but also reduced the reserve tank size with reduction of the amount of brake fluid compensation required when the pad is worn, and this allowed considerably greater freedom of layout for the reserve tank. As a result, it was possible to reduce the caliper size and position it lower down, so that the muffler could be given a diameter 25 mm larger than the XR400R. In addition, protective parts such as the disc cover and caliper guard could be made more compact so that the rear brake system achieved a weight reduction of 300 g. Fig. 28 shows an external view comparison of the developed caliper and master cylinder with previous components for the CR250R.

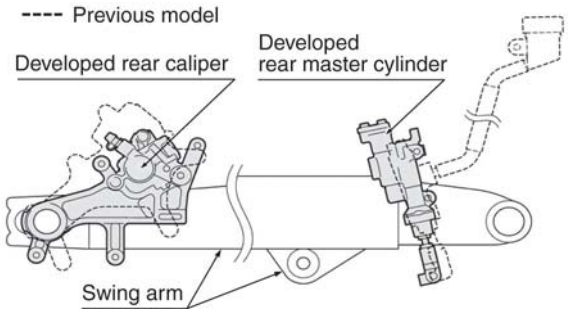


Fig. 28 Developed rear caliper and master cylinder

6.4. Wheels

Offroad vehicles generally use spoked wheels for their rigidity, strength, and mass.

Super-duralumin nipples were used for both front and rear wheel spoke nipples. A weight reduction of 180 g relative to conventional SWCH material was sought for the front and rear wheels together.

The rims are required to be lightweight with wheel rim compression strength, wheel rim flange strength, strength of spoke hole, and crack toughness against stress and corrosion. When the bike is being ridden, in particular, the rim may strike rocks or other objects with great force, causing permanent deformation of the rim in the direction of the opening. Increasing the strength of the flange opening was an issue for weight reduction. A high-strength Al-Zn-Mg-Cu material of 520-MPa grade has been used as the rim material for some time, and no further improvement could be expected in this regard. Instead, therefore, the rear wheel rim was given a section that is not JIS-specified but had been under study for use with a works motocrosser. This rim section raised the angle of the rim flange, giving it a shape that minimized the moment generated when a load was applied to the flange and made the flange less likely to deform. This rim has strength equal to conventional rims while achieving a 150-g reduction in weight. Fig. 29 shows a comparison of the conventional and developed wheel sections.

The size of the bolt used to attach the brake disc, the method of attaching spokes, and other aspects of the rear wheel hub were reviewed. This yielded a weight reduction of 50 g.

7. Other Lightweight Technologies

7.1. Titanium Exhaust Pipe

Use of titanium material for the exhaust pipe resulted in a weight reduction of approximately 400 g compared to conventional materials. Fig. 30 shows the exhaust pipe attached to the engine.

7.2. Engine Covers

A magnesium alloy was used for the cylinder head cover and clutch maintenance cover.

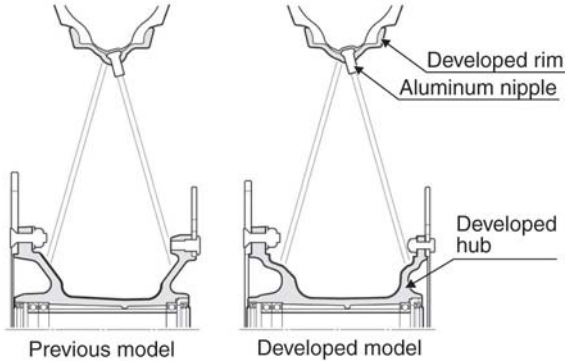


Fig. 29 Comparison of wheel structure

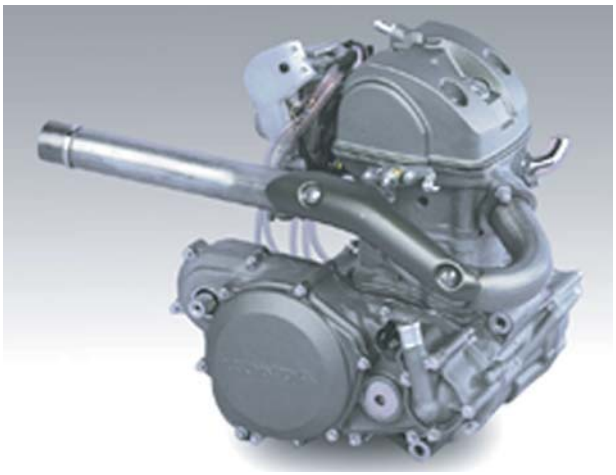


Fig. 30 External view of engine with titanium exhaust pipe

8. Conclusion

Taking advantage of the easy-handling traction characteristics of the 4-stroke engine, the CRF450R achieves a compact, lightweight engine and performance enhancements that include startability, a vehicle mass of 102 kg, maximum output of 41 kW/9,000 r/min, and maximum torque of 49.8 Nm/7,000 r/min. It is hoped that the CRF450R, as the flagship high-performance motocrosser that is also engineered with consideration for the environment, will help to improve the image of offroad vehicles as a whole.

References

(1) Osamu KUDO, Yasuo SHIMURA, Koji TERADA, Nobuaki INUMARU, “Development of a closed crankcase system engine for motorcycles,” Honda R&D Technical Review, Vol. 12, No. 1, pp. 27–32 (2000).

■ Authors ■



Norio HOSHI



Yasuo SHIMURA



Takanori OKUMA



Akifumi NOMURA



Kazuhiko GOGO

Development of Hybrid HS1390i Snow Thrower

Jitsumi HANAFUSA* Tsutomu WAKITANI*
Takahiro YAMAMOTO* Tsutomu INUI*

ABSTRACT

Honda has developed the HS1390i hybrid snow thrower for general consumer use based on the key concept of enhanced handling and operability. The snow clearing system is driven by an engine that simultaneously generates power for two drive motors. Computer-controlled travel motion combined with automatic load sensitive speed control make travel motion and work smooth. Operator load has been reduced by mounting the driving levers on the driving system frame and placing the operating controls in a fixed location. In addition, the use of an electric operating system reduces the amount of force required to operate the various controls. Fuel consumption per volume of snow removed is also better than previous models, making this product strongly competitive in the market.

1. Introduction

Snow clearing is a difficult task that imposes hard labor on people who live in regions with heavy snow. Honda sought to lighten the burden of that hard labor when it entered this market in 1981 with development of the HS35 compact snow thrower for consumer use in America. In Japan, it placed the consumer-use HS50 (5-HP class) compact snow thrower on the market in 1982. Honda snow throwers are now used by customers in some twenty countries around the world, and their cumulative sales have passed the 500,000-unit mark.

In Japan today, Honda has a line-up of snow throwers ranging from gasoline-engine-powered models (6 HP) to those with diesel engines (25 HP). It now leads the industry as the top manufacturer, having acquired a 40% share of the overall market for snow throwers.

In recent years, what has been termed a phenomenon of global warming has caused increased snow coverage. Larger regions have been experiencing falls of heavy snow (snow with a high specific gravity), and the removal of heavy snow is coming to be an increasingly difficult task.

There has been growing demand for a mid-sized snow thrower (10-HP class) that will satisfy the desire to make snow clearing faster, easier, and simpler to accomplish.

The circumstances of snow clearing are also under change, influenced by the recent transition to an aging society and the lack of workers to perform the labor, among other factors.

It was in order to meet the demands of this market that the HS1390i was developed, and this model will be introduced here.

2. Development Goals

The development concept for this product was defined as a high-performance snow thrower that anyone can easily use. In specific terms, the goals were as follows:

(1) Use a 2-motor driving system in order to improve turning and slow speed control which simplifies operation.
(2) Increase the efficiency of snow clearing work by using electric power and linking it with the engine.
(3) Utilize electric control to reduce the load on the operating system and improve operability.

* Asakahigashi R&D Center



Fig. 1 External view of HS1390i

3. Basic Configuration and Major Specifications

In general, the drive train of the conventional snow thrower is made up of the snow clearing system and the driving system. The snow clearing system has an auger that fragments the snow and gathers it in a central location, and a blower that blows the snow up to distances of nearly 20 m. It is driven by a belt from the engine. The driving system is made up of a transmission that is either gear drive transmission or a hydro static transmission (HST), and a crawler that generates traction to provide performance on rough surfaces as well as to force the snow clearing system into contact with the snow.

The present HS1390i has a hybrid drive train that, when it is clearing snow, uses the engine to drive the snow clearing system, which requires large amounts of power, and uses two independent motors on the left and right to power the driving system, which must be capable of more delicate operation. Fig. 1 shows an external view of this product, and Fig. 2 shows a schematic drawing of the hybrid system. The use of a computer to control the driving system makes it possible to achieve smooth travel motion and smooth work operations geared to the load. This makes it easier even for beginners to perform snow removal operations that require experience when handling a conventional snow thrower. There is also an auger automatic rise function that automatically lifts up the auger housing, when the machine moves in reverse. A height mechanism maintains the operating controls at a fixed height regardless of changes in the auger height setting, and the amount of force required to operate the various controls has been reduced. The use of these mechanisms reduces the load on the operator. Table 1 shows the major specifications.

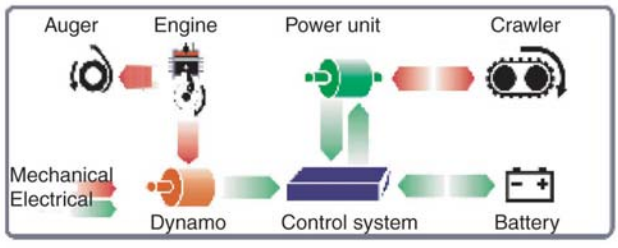


Fig. 2 Hybrid system

Table 1 Major specifications

Items		Specifications
Overall length	(mm)	1 650
Overall width	(mm)	920
Overall height	(mm)	1 350
Dry weight	(mm)	250
Engine model name		Gx350
Engine type		Air cooled, 4-stroke, single cylinder gasoline engine (OHV)
Maximum power	(kW)	9.6
Snow-clearing wideth	(mm)	920
Snow-clearing height	(mm)	680
Maximum Snow-clearing volume	(ton/h)	80
Drive system		Independent left and right drive motors
Speed control		Revolution feedback PWM

3.1. Driving System Configuration

The driving system power unit consists of the motor, magnetic brake, reduction gear, wheel shaft, revolution sensor, and thermo sensor. The source of driving power is electricity supplied by a battery and an alternator. The reduction gear is used to reduce motor revolutions. The crawler is driven by the wheel shafts via the wheels.

Two independent power units are installed as configured above, one each on the left and right. Fig. 3 shows the driving system, and Fig. 4 shows the layout of the motor and reduction gear.

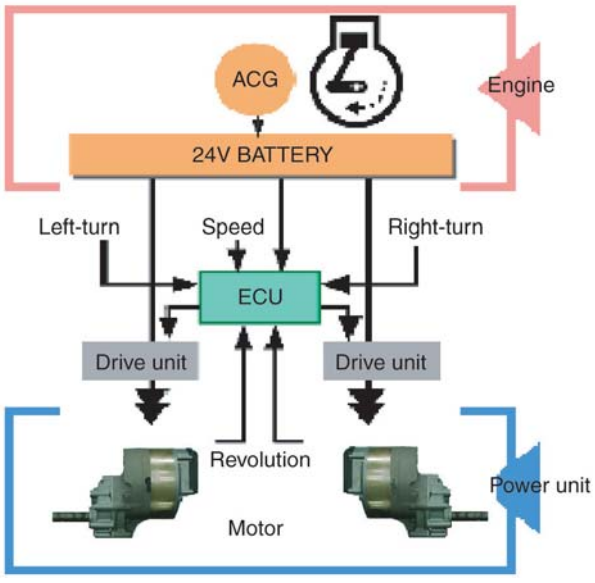


Fig. 3 Driving system

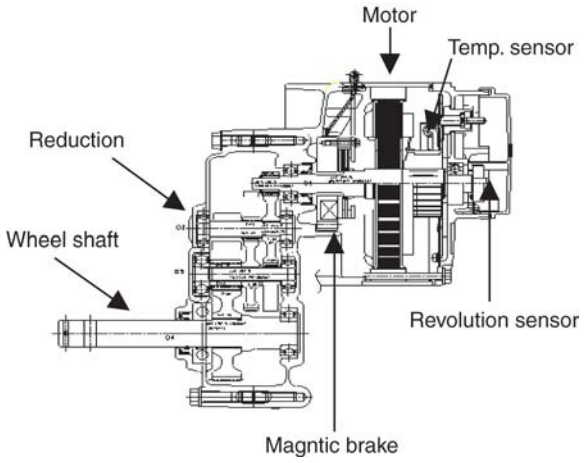


Fig. 4 Power unit layout

3.2. Snow Clearing System Configuration

The snow clearing system of the snow thrower is made up of an auger that fragments the snow and gathers it in a central location, and a blower that blows the snow to a maximum distance of nearly 20 m. This system is required to be capable of being raised and lowered independently of the frame of the driving system in order to control the amount of work and the depth to which snow is cleared.

The snow clearing system is ordinarily attached to the frame on which the engine is mounted in order to make use of the engine's power directly. In conventional models, the limitations of the drive train meant that the driving levers were also fixed to this frame, and as a result they would move up and down around the fulcrum of the crawler drive shaft together with the snow clearing system as it was raised and lowered. With the HS1390i, the driving levers are instead attached to the driving system frame and the operating system is fixed in place. This reduces the load on the operator. Fig. 5 shows a conceptual view comparing the operator posture with these different models.

The fulcrum for raising and lowering the snow clearing mechanism was located near the attachment point for the driving levers, thus greatly increasing the range of vertical movement of the snow clearing system. Table 2 shows the lift height of the snow clearing system and the height of the handle. The snow clearing system is raised and lowered by the telescopic motion of a hydraulic unit that is built into the motor and operated by a lever on the control panel.

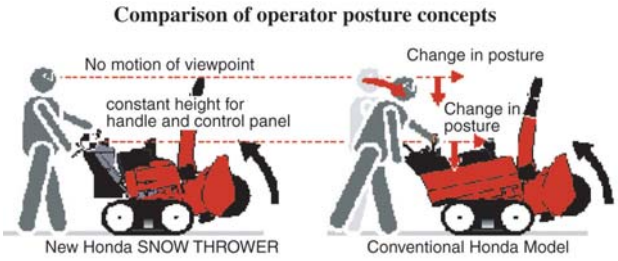


Fig. 5 Outline of figure

Table 2 Comparison of operation posture (Unit: mm)

	Lift height Auger	Handle height (Max/Min)
HS1390i	220	830/830
Conventional	125	890/620

3.3. Operating System Configuration

During snow clearing work, the operating system engages simultaneously during several activities. It operates the clutches for both travel motion and snow clearing, while also controlling the amount of snow clearing (by varying speed and depth), it also determines the snow-throwing direction. Previously operation required experience and most of the operations involved rods and wire-operated clutches. This required greater operation force, and imposed more load on the operator. (Sequential travel speed control with the engine load was used as described above for the purpose of making operation less complicated and difficult.) For the HS1390i, the two points described below were implemented to resolve these issues.

3.3.1. Improved layout of controls

The turn control levers, conventionally located on the control panel, were attached to the left and right handlebar grips. In the past, the running speed control lever had an H-gate because there was a sub-transmission with two speeds as well as the HST. With the adoption of electric power, this has become a continuously variable arrangement with just one gear that is basically in the form of an I-gate. These changes allowed considerable freedom to rearrange the control panel layout, and the controls, including the shooter and auger control levers, have been placed for greater ease of use.

Fig. 6 shows the layout of the control panel.



Fig. 6 Control panel

3.3.2. Reduction of operation force

The change to electric power for the driving system made it possible to reduce the force required for operation of controls to a great extent. The running speed control lever and the turn control levers are now controlled by voltage volume. A magnetic clutch that operates as an on/off switch was adopted for the snow clearing system, and the clutch lever for travel motion was also replaced with an electrically operated switch.

Table 3 shows the force required to operate the various controls.

Table 3 Force required to operation control (Unit: N)

	Speed lever	Turn lever	Driving lever
HS1390i	11	16	15
Conventional	41	46	43

4. Component Technologies

4.1.Motor

The flat disk type motor was given a flat ratio of 1:8.75 compared to the cumulative thickness and armature outer diameter ratio of 1:1 in ordinary motors. The motor installed in the Monpal ML100 electric scooter[(1)] was used as the base. Table 4 shows the major specifications. The power and durability of the motor were enhanced relative to the Monpal ML100 by changing the winding specification from wave winding to lap winding and by increasing the number of brushes from two to six.

Thermistors placed close to the brushes monitor the temperature and guard against overheating in the motor.

A magnetic brake was placed on the motor output shaft. The motor case was integrated with the reduction gear case.

Table 4 Specifications of motor

Motor	Rated power (V/W)	24/600
	Armature (mm)	Φ140 × 16 (31 slots)
	Winding	Wave class B
Sensor	Revolution	2-phase magnetic pickup
	Temperature	Thermistor

4.2.Control System

The system uses an electric control unit (ECU) with a 16-bit microprocessor and two 8-bit microprocessor drive units, one each on the left and right, to perform linked control of the left and right motors.

Apart from the above travel motion control, the ECU is used for an on/off control for the magnetic clutch that transfers power from the engine PTO shaft to the snow clearing system, an interlock control for the starter motor, and controls for the various other devices. Together these make up the total control system.

4.2.1.Drive unit

The forward/reverse direction and speed of the motor are controlled by two field effect transistors (FET) in parallel used in a full-bridge configuration. Cooling fins are formed on the aluminum case for improved cooling efficiency, and this extends motor power. Pulse width modulation (PWM) control is used to control the motor, with signals from the ECU passed through an interface to be processed by the 8-bit microprocessors. The voltage, temperature, and current monitoring functions were added, and they output signals to the ECU in case of malfunction. Fig. 7 shows the drive unit.

4.2.2. ECU

(1) Travel motion control functions

The ECU works with voltage detection sensors installed on the speed control lever, which regulates running speed, and on the left and right turn control levers, which are used for turning. It determines the travel motion control mode using the engine speed and the setting of the i-control switch (control mode selector).

Fig. 8 shows the control unit. Fig. 9 shows a diagram of the control system.

Travel speed control operates by digital proportional integral (PI) control that feeds back the speed and turning direction from the hole IC turn sensor built into the motor. Fig. 10 shows the speed control system.

The ECU evaluates separate speed signals from the left and right motors and performs linked control of the two motors. The categories of linked control are straight forward movement control, forward and reverse movement control, turn control, and travel speed control linked to the engine load.

(a) Straight forward movement control

There are conditions in which straight forward movement cannot be assured by speed control of the independent left and right motors alone. This is the case, for example, while climbing over a bump when the weight is unbalanced, or when the motors become overloaded while climbing a slope, and so on.

Such situations when the motors run at different speeds can be handled by synchronizing the speed of the faster motor with the one that is running more slowly. For cases when the motor on one side is running at a slower speed while climbing a slope, the system incorporates a control that instructs both motors to slow down to the speed prescribed for direct forward movement. The resolution of the speed control lever has also been changed to allow finer speed adjustment within the snow clearing speed range.

(b) Forward and reverse movement control

Given the form of snow clearing work, there are occasions when forward and reverse movements are frequently repeated. In such cases, the machine may move in a skewed manner because variations between the two motors causes one motor to lag behind the other when shifting between forward and reverse movement by independent motor control.

This is handled by having the system constantly compare the speeds of the left and right motors. The timing of the shift between forward and reverse is then synchronized between the two according to the speed level of a running stop.

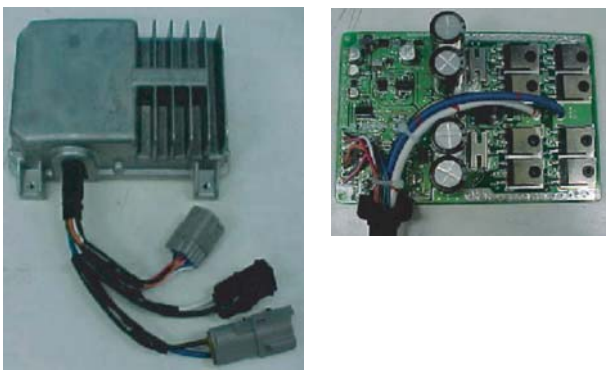


Fig. 7 Drive unit

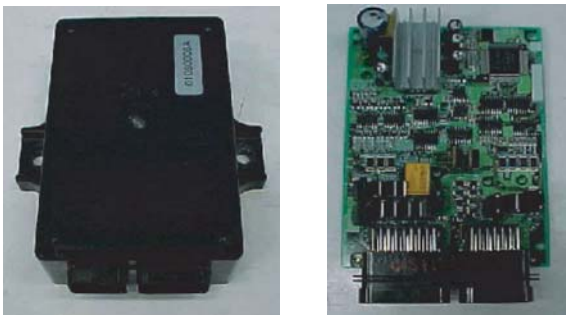


Fig. 8 Control unit

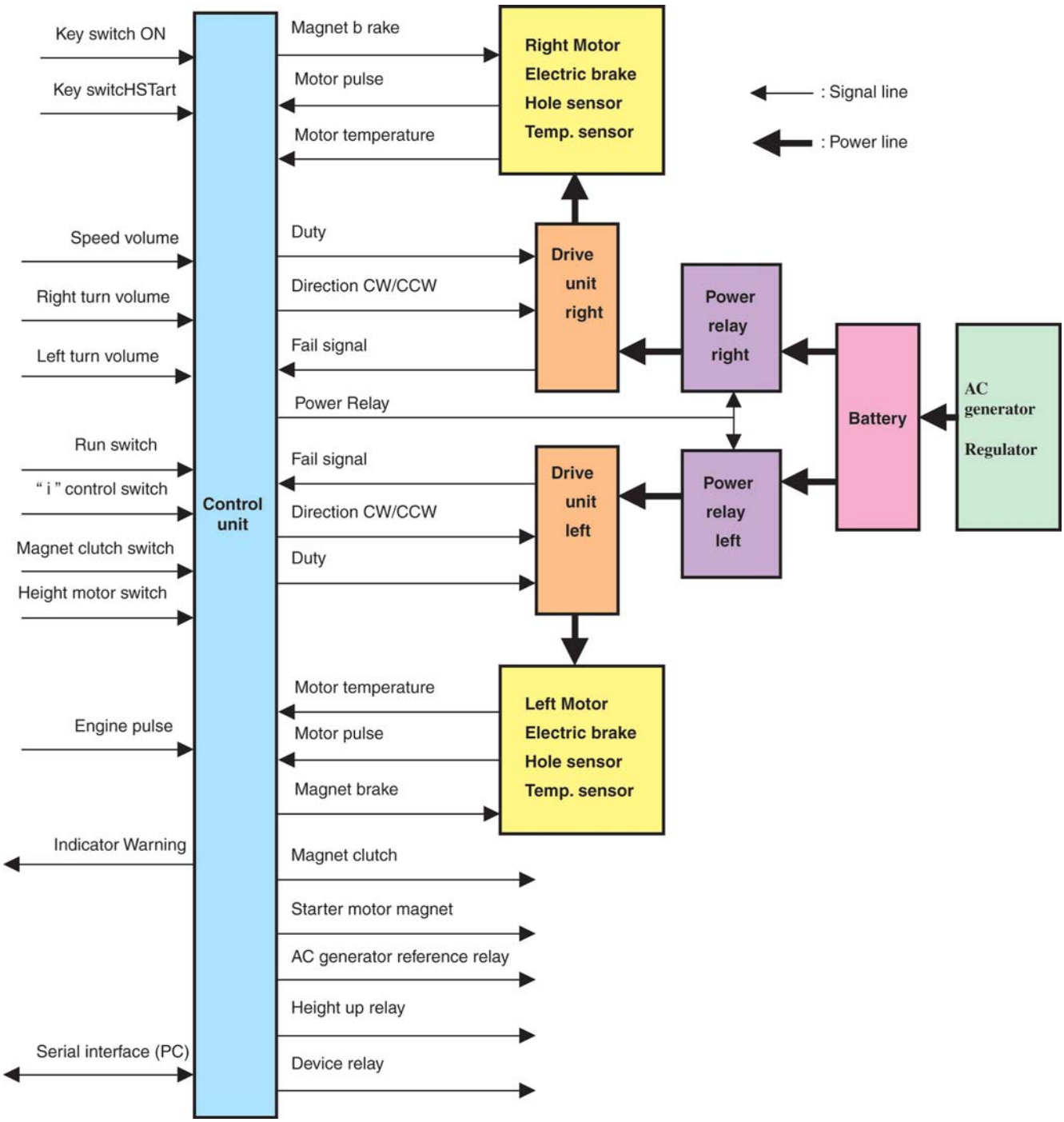


Fig. 9 Control system diagram

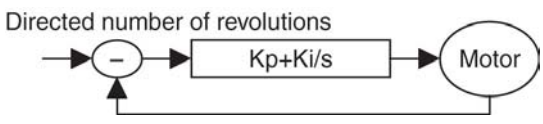


Fig. 10 Speed control system

(c) Turn control

Turn control adjusts the speed of the left and right motors to their optimum level according to the amount of grip pressure on the speed control lever and turn control levers. This has enabled smooth, easy turns within the traveling speed range, and axis turns (zero turns) within the working speed range.

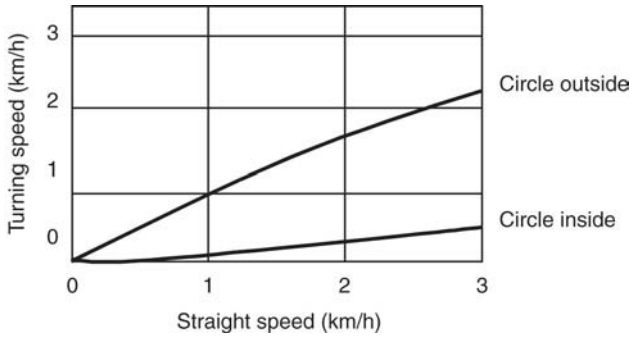


Fig. 11 Turn control

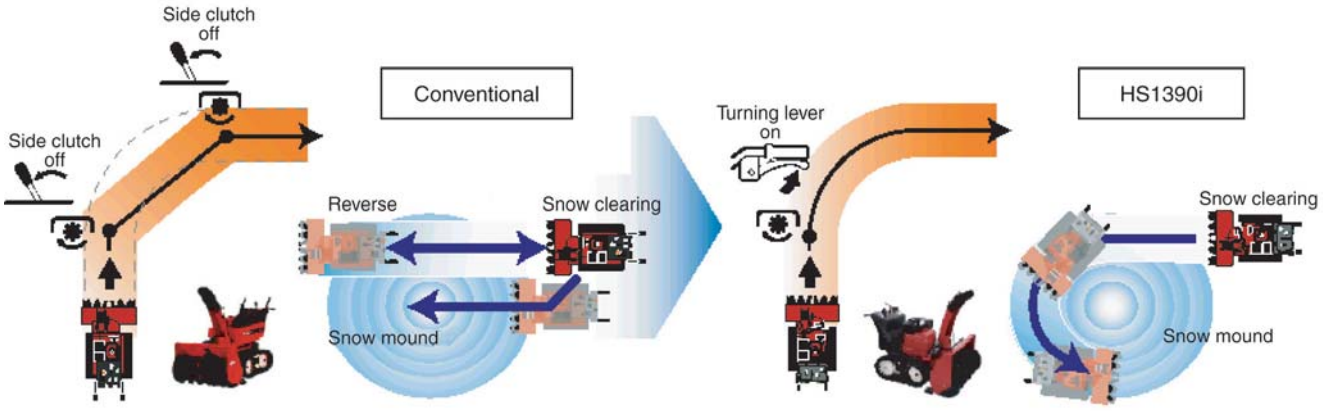


Fig. 12 Outline of turn control

Fig. 11 shows the running speed characteristics for the motor on the outside and inside of a turn made using only one of the turn control levers. At a travel speed of 3 km/h, smooth, easy turning is obtained by reducing the traveling speed on the outside of the turn. In the low speed range (1 km/h or less), the speed on the inside of the turn is reduced to zero.

Fig. 12 shows a comparison of turns with conventional snow throwers.

(d) Sequential travel speed control with the engine load

When clearing snow with the i-control switch turned on, the control system links the travel speed adjustment with the engine speed. Specifically, the control links travel speed with the engine speed so that it reduces travel speed to as little as 10% of the set value.

This function inhibits the reduction of snow clearing capability that occurs when the engine stops or slows down.

Fig. 13 shows the characteristics of the slowdown rate of the running speed when the engine running speed set by control is 3,500 rpm and the engine speed drops. For example, when travel speed while clearing snow is 0.5 km/h and the engine speed drops to 2,400 rpm, then the travel speed will be 0.05 km/h.

As shown in Fig. 14, the travel speed when clearing snow is adjusted automatically according to the depth of the snow being cleared. This has reduced the necessity for the operator to use the running speed lever. It has been confirmed that the use of this function by a beginning operator when clearing snow will bring about a maximum improvement of approximately 10% in snow clearing fuel consumption (amount of snow cleared/amount of fuel consumed) over conventional models.

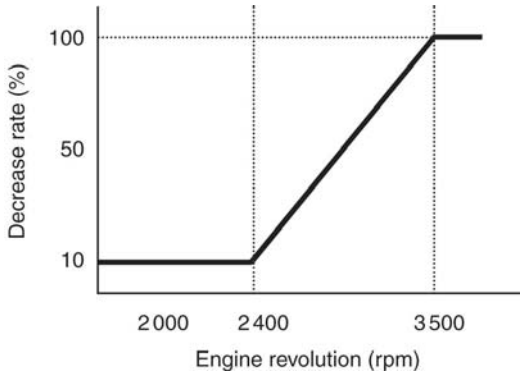


Fig. 13 Speed control

(e) Parking brake

A magnetic brake is built into the axle of the driving system motor. Power is supplied during travel motion, and it is cut off when the travel motion clutch is turned off, or when the running speed lever is placed in neutral, then the parking brake is activated, in that sequence. When snow clearing involves frequent forward and backward movement, operation of the magnetic brake is cancelled when the running speed lever passes through the neutral position. This makes for smoother shifting between forward and backward movement and improves usability.

(2) Sensor position correction function

The ECU has a function that collects the initial values from the voltage sensors installed on the running speed lever and the left and right turn control levers. This corrects for mechanical error.

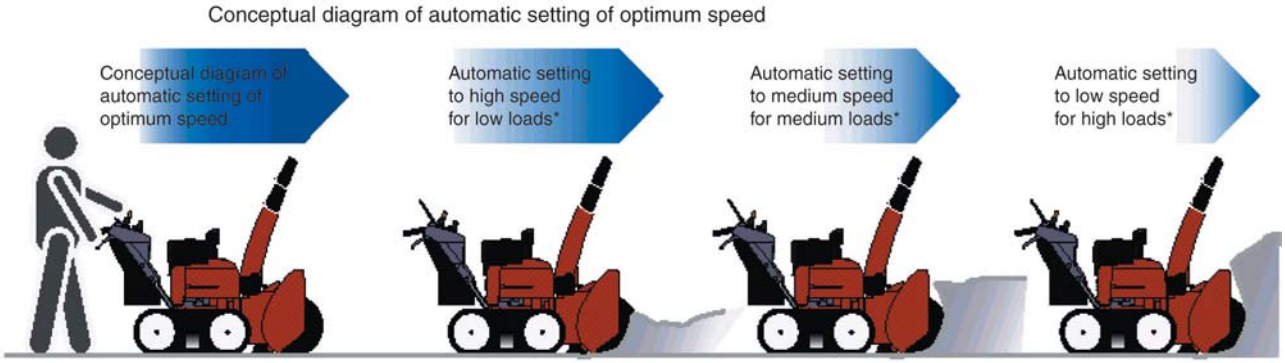


Fig. 14 Outline of speed control

(3) Protective functions and malfunction detection functions

A protective function was set up to prevent damage to the motors and drive unit. Notice of the operation of this protection is provided by red and orange lights installed on the left side of the control panel. The operator is alerted by the light in orange flashing mode. The protective function has two modes, reduced power and power off. In reduced power mode, low-speed travel is possible. When a malfunction occurs, the system turns on the red light on the control panel, and indicates the location of the malfunction by the number of times the orange light flashes. Fig. 15 shows the control panel with the key turned on and the lights illuminated during the self-diagnosis process.

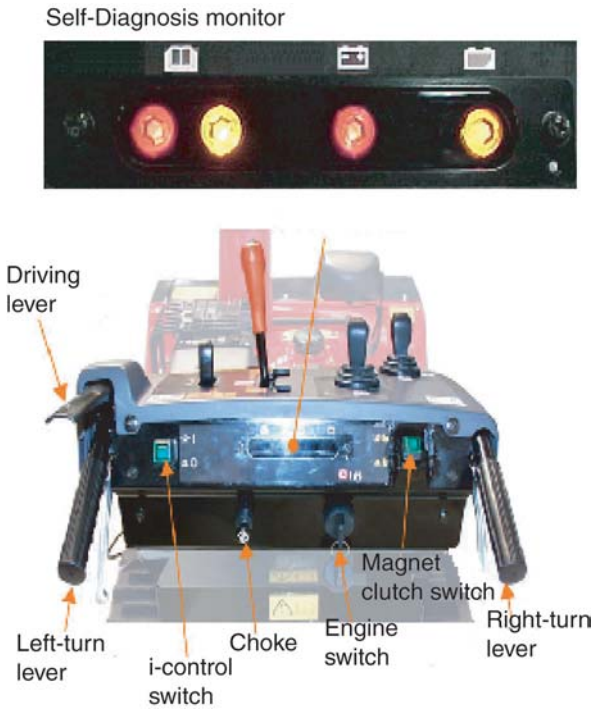


Fig. 15 Control panel

(4) Starter and magnetic clutch control functions

By using both a starter interlock and a magnetic clutch interlock, smooth and correct snow clearing is provided. The ECU controls the on/off status of the starter magnet and magnetic clutch.

(5) Height motor control function

(a) Automatic height function

A hydraulic height motor was installed to raise and lower the snow clearing part in order to control the amount of work and the depth to which snow is cleared. An auxiliary function for frequent raising and lowering operations was provided by incorporating a function that will automatically raise the snow clearing part for two seconds when the running speed lever is set to reverse while the i-control switch is turned on. Lowering it requires a manual operation by the operator. Fig. 16 shows a comparison of snow clearing operations with the conventional snow thrower.

(b) Timer function

The system was given a timer function to limit the electric current consumption when the height motor is operated for long periods of time. Specifically, one timer was set up so that the ECU would add up the operation inputs to the height switch, and another timer was set up that would stop when the switch is operated continuously.

(6) Personal computer monitor port

A port has been included to allow verification of motor control output and voltages of the various operating controls during shipment inspections of completed units. This makes it possible to evaluate the load current in the motor transmissions, which also contributes to quality improvement. The port was designed to allow for the possibility of future use as a tool for inspection using a personal computer.

4.3.Power Supply System

In light of motor efficiency, a 24-V power supply system was adopted and all devices from the starter motor to the engine electric devices were designed to run on 24 V. The charging system uses a new 24-V alternator to assure balanced consumption during travel, and the output was set to a 24-V, 40-A specification.

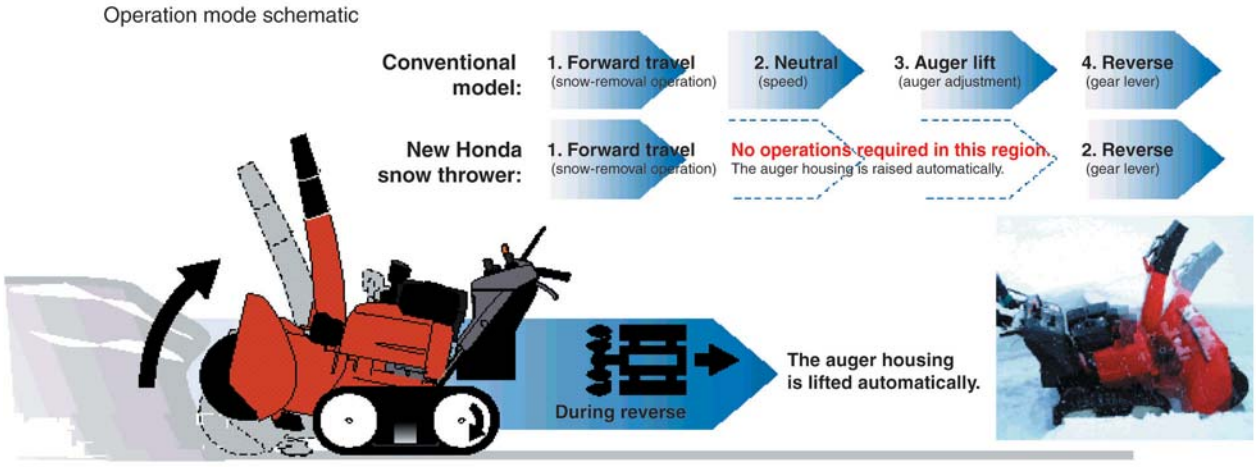


Fig. 16 Outline of HIT control

5. Summary

In development of the HS1390i hybrid snow thrower equipped with a two-motor driving system using electric power supplied from the engine, the following achievements were made:

(1) Two independent motor power units were installed on the left and right to power the driving system, each was equipped with its own drive unit, and a control system was established with an ECU. This allowed for better turning control and made it possible to adjust low speeds, thus achieving simple operation.
(2) Computer control was instituted for engine load and the driving system. This allowed automatic adjustment of travel speed during snow removal work, and it has been confirmed to reduce the necessity for the operator to use the running speed lever, lower the load on the operator, and enhance the snow clearing fuel consumption.
(3) Enhancements in the operating position have reduced the load on the operator and improved performance on difficult surfaces by increasing the range of vertical movement of the snow clearing mechanism.
(4) The use of electric control made it possible to arrange the operating system for greater ease of use and to reduce the amount of force required to operate the controls.
(5) Shifting the running speed lever into reverse causes the snow clearing components to be raised automatically. This simplifies the operation procedure and enhances usability.
(6) The ECU monitors the various functions and indicates the location of malfunctions when they occur, thus enhancing maintainability.

6. Conclusion

The HS1390i achieved a new concept of driving system known as hybrid, which combines an engine and machinery with motors and electricity. This came about through the pursuit of ease of use and efficient snow clearing for the customer. This system was combined with an automatic control system run by a CPU, thus making it possible to take full advantage of the strengths of a hybrid system and to make the product easier to use. The power unit has also created new possibilities for further application to general-purpose power products.

This snow thrower hopes to reduce the burden on customers who live in regions with heavy snow. This development project received substantial cooperation from people inside and outside the company. Here, in closing, the authors express their heartfelt gratitude.

References

(1) Jun HOSAKA, Tsutomu INUI, Kiyotomi MAESAKA, “Electric scooter Monpal ML100 wheelchair,” Honda R&D Technical Review, No. 12, No. 1, pp. 21–26 (2000).

■ Authors ■


Jitsumi HANAFUSA


Tsutomu WAKITANI


Takahiro YAMAMOTO


Tsutomu INUI

Development of a New Power Train for the Civic Hybrid

Masato MATSUKI* Teruo WAKASHIRO* Toshihiro KAMIYAMA*
Toshiyuki SATO* Toshiaki KAKU* Masahiro KANDA*

ABSTRACT

The Civic Hybrid was developed as a compact passenger hybrid car that achieves both low fuel consumption and cleaner operation from the viewpoints of preserving the global environment and conserving resources. The engine has lean-burn countermeasures added to the base i-DSI 4-cylinder 1.3-liter SOHC 2-ignition plugs/cylinder engine mounted in the “Fit”. In addition, the cylinder idling system has been adopted to increase the regenerated energy during deceleration. The hybrid system is based on the Honda IMA system, and the maximum regenerative torque has been increased by approximately 30% by improving the magnetic circuits of an ultra-thin DC brushless motor and adopting a new rotor manufacturing method. Fuel economy is improved by a new hybrid power train incorporating a CVT that further improves transmission efficiency, thus achieving the low fuel consumption of 29.5 km/l in the 10-15 mode. New emission technologies applied are a new exhaust system with a NOx adsorption reduction type three way catalyst and air-fuel ratio control achieved 75% reduction from the 2000 emission standards in Japan. The power control unit, which is the IMA system control unit, was downsized and located behind the rear seat, thus ensuring comparable trunk capacity to the base vehicle of the Civic Ferio.

1. Introduction

The demand for low fuel consumption, low emission automobiles is growing ever stronger, due to the direction of preserving the global environment and conserving resources. For gasoline engines, in addition to lean-burn, there has been research into different types of engines, including direct injection and Miller cycle engines, and the creation of new products. At Honda, research and development has continued since 1992 into lean-burn engines[(1)–(5)] adopting technologies such as the VTEC device (VTEC: Variable Valve Timing and Lift Electronic Control).

The possibilities are great for hybrid systems, too, that combine electricity (motors) with engines. At Honda, an IMA (Integrated Motor Assist) system was developed as a hybrid technology. IMA entered the market in 1999 fitted to the ultra low fuel consumption vehicle “Insight”[(6)].

Now a new IMA system, based on the previous IMA system, has been developed with improved motor torque and efficiency. A new 1.3 L lean-burn engine (LDA model) has been developed based on the L13A i-DSI (DSI: Dual and Sequential Ignition) engine[(7)] installed in the “Fit” with an added cylinder idling system. These were installed in the “Civic”. This paper introduces the new IMA system and the engine technology.

* Tochigi R&D Center

2. Aims of Development

Honda's first hybrid vehicle, the "Insight," achieved the lowest fuel consumption for mass production passenger vehicles worldwide, demonstrating the potential of hybrid technology. Now, based on the hybrid technology fostered with the Insight, the development aim was a 5-passenger, compact sedan hybrid vehicle that realizes "low fuel consumption and environmental measures." The engine was modified on the foundation of a compact hybrid power train design that corresponds to the vehicle package, achieving low fuel consumption through higher efficiency of the DC motor and CVT. In addition, adopting a lean NOx catalyst and modifying the exhaust system achieved lower emissions.

The concrete development targets are as follows.

(1) No. 1 in fuel economy, in the 5-passenger compact sedan class
(2) Low emission performance
Japanese J-ULEV "Ultra Low Emissions" certification
USA ULEV: Ultra Low Emission Vehicle
(3) A compact IMA design that can be fitted in the Civic to maintain trunk space capacity
(4) Highly responsive performance in the normal range

3. Hybrid Systems and Low Fuel Consumption Technology

As a hybrid system, a simple, lightweight, compact IMA system was adopted. As shown in Fig. 1, the IMA system construction has a DC brushless motor between the engine and transmission and has a nickel metal hydride battery and power control unit (PCU) at the rear of the vehicle. It is a parallel hybrid power train that uses the engine as the major power source. The motor is used as a supplementary power source during acceleration, while during deceleration regenerative braking only is used. The engine is based on the i-DSI (L13A model) having output characteristics that satisfy, in combination with the motor, drive performance required of a Civic. Fig. 2 shows a view of the power train.

Development focused on increasing regenerated energy, making each system more efficient and lighter. In addition, efforts were made to improve the transmission efficiency. Against the base vehicle Civic iE[5] (10-15 mode fuel consumption rate of 20 km/L), the ratio of contribution of each system towards lower fuel consumption is as shown in Fig. 3.

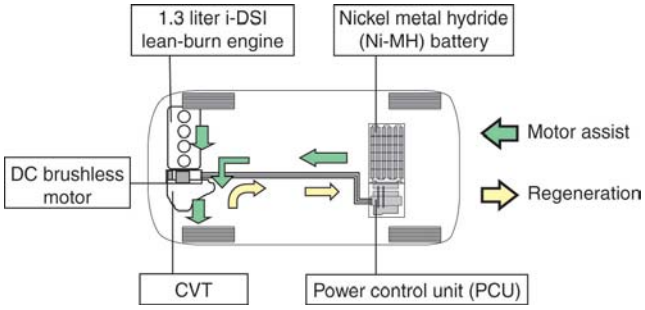


Fig. 1 IMA system construction

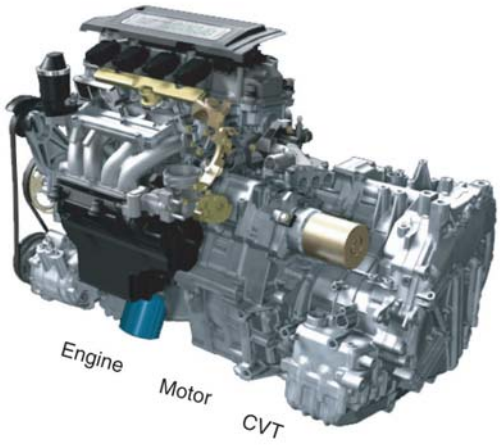


Fig. 2 View of IMA power train

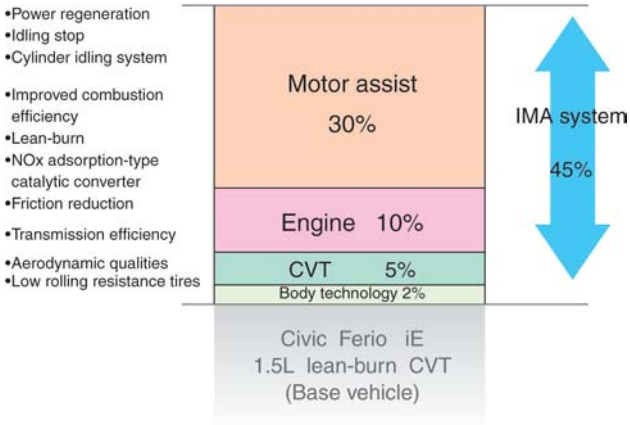


Fig. 3 Ratio of contribution to improve 10-15 mode fuel economy

Table 1 Engine specifications

Engine code		LDA
Cylinder configuration		In-line 4-cylinder
Bore × stroke (mm)		73 × 80
Displacement (cm^3)		1 339
Compression ratio		10.8 : 1
Valve train		SOHC Cylinder Idling System (CIS)
Number of valves		2 per cylinder
Valve diameter (mm)	Inlet	32
	Exhaust	28
Ignition system		Dual and Sequential Ignition (DSI)
Exhaust manifold		Stainless steel
Catalytic converter		Under floor 2 bed Front: TWC Rear: Lean NOx
Max. power (kW/rpm)	Without	63 / 5 700
Max. torque (N·m/rpm)	Motor assist	119 / 3 300

4. Engine

4.1. Engine General Specifications

Table 1 gives the engine's general specifications. The fundamental spec is based on the i-DSI 4-cylinder, 1.3 liter SOHC 2-plug engine installed in the Fit, with additional IMA system modifications and measures to fit it to the Civic body.

In addition, the valve train adopted a cylinder idling system (CIS) to increase the regenerated energy during deceleration. Details are outlined below.

4.2. Output Characteristics

Decreasing engine capacity is effective in reducing fuel consumption, but is a problem when also trying to maintain vehicle dynamic performance. The output of the 1.3 L engine plus the motor is an output roughly equivalent to that of the D15B model 1.5 L VTEC-E engine (maximum output 77 kW, maximum torque 139 N·m) fitted to the base Civic iE. It is notable that the motor characteristics give high torque in the low speed range, providing a 20% improvement over the iE at 2,000 rpm torque (Fig. 4).

4.3. Cylinder Idling System (CIS)

4.3.1. Aims of CIS

Engine friction can be roughly divided into mechanical loss and pumping loss. The CIS developed in this project is a system that pauses inlet and exhaust valves in three cylinders during deceleration fuel cut. This reduces pumping loss and allows the friction energy to be stored through the motor as regenerated energy. Accompanying the increase in regenerated energy, there is an increase in the amount of motor assistance during acceleration, and as a result, fuel consumption is lower. Fig. 5 shows the engine friction during deceleration (throttle fully closed). Pumping loss is reduced by approximately 50% by CIS.

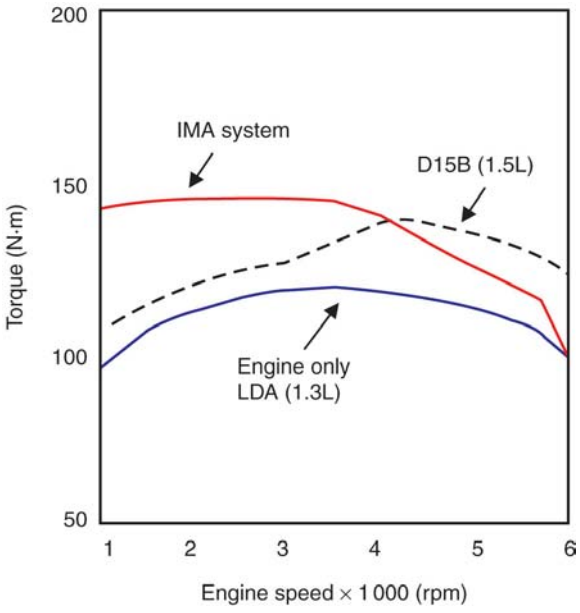


Fig. 4 Output performance of IMA system

Pumping loss would be almost zero when all valves in all four cylinders are paused. This would be effective in increasing regenerated energy. However, in order to maintain driver performance if there were a failure of CIS system parts, it was decided to apply the CIS mechanism for three cylinders.

4.3.2. CIS configuration

Fig. 6 shows the CIS hardware configuration. In the same way as with a conventional VTEC, it is a system hydraulically controlling the spool valve and pistons in the rocker arm, switching between inlet and exhaust valve lift and complete stop. This CIS rocker arm is used in cylinders No. 2 through No. 4. The No. 1 cylinder uses a rocker arm without a switching device.

Fig. 7 shows the CIS rocker arm construction. For one valve, construction is such that there are rocker arms A and B, pistons A and B, and a return spring. Conventional VTEC is a system that connects with hydraulic pressure and separates with spring reaction force. With the CIS, however, in order to maintain switching ability through the low rev range where hydraulic pressure is low (around 1,000 rpm), a hydraulic pressure to hydraulic pressure switching method is adopted to switch between connection and separation. Fig. 7-(c) shows a cross section of the rocker shaft. It is a 2-hole type adopted in the 3-stage VETC[(2)].

A hydraulic pressure to hydraulic pressure switching method requires two hydraulic paths. The oil supplied from the main carrier switches between the valve-active side and the valve-inactive side paths, through the three-way type spool valve as shown in Fig. 8.

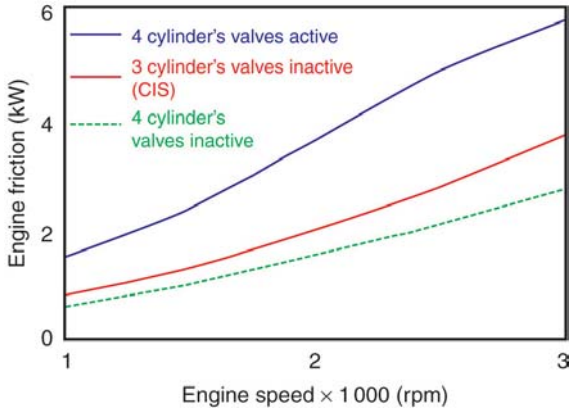


Fig. 5 Engine friction reduction effect by CIS

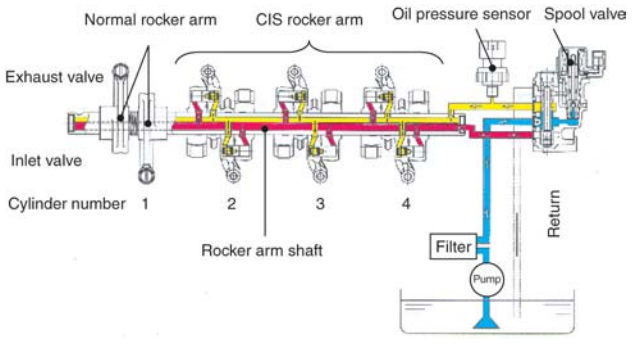


Fig. 6 CIS valve train and hydraulic passage

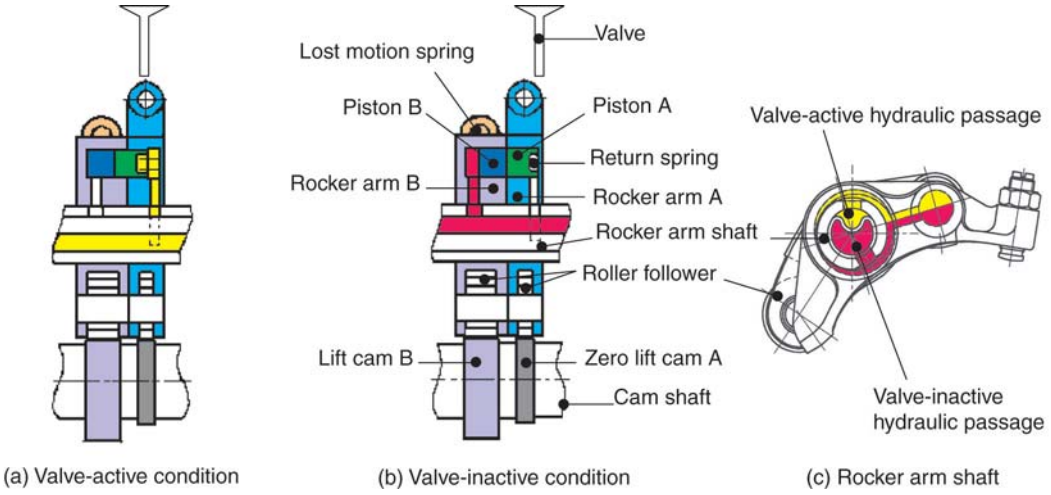


Fig. 7 CIS rocker arm and rocker arm shaft construction

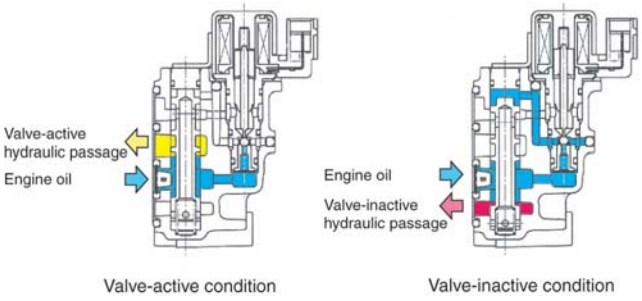


Fig. 8 Spool valve construction

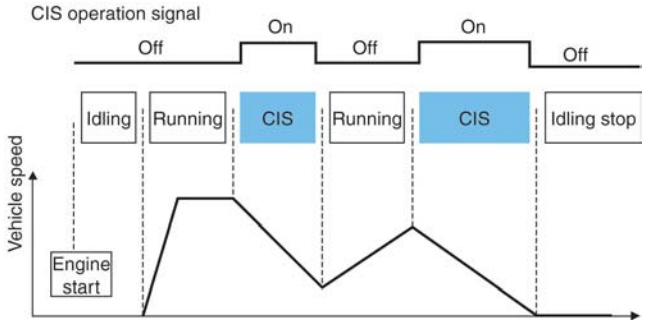


Fig. 9 CIS operation pattern during actual driving

The normal valve-active condition is shown in Fig. 7-(a). Hydraulic pressure is applied to rocker arm A, so rocker arm A and rocker arm B are connected by piston A. According to the profile of lift cam B, the connected rocker arms operate, and the valve is driven.

The valve-inactive condition is shown in Fig. 7-(b). With the spool valve switching, the hydraulic pressure is supplied to rocker arm B, and with the shifting of piston B, rocker arms A and B separate. Rocker arm A enters the valve-inactive state according to the profile of the zero-lift base circle cam A.

4.3.3. CIS operation range and control

The CIS is a system that increases regenerated energy by reducing engine friction during deceleration, and so works towards lower fuel consumption. It only runs under fuel injection cut conditions during deceleration, as shown in Fig. 9. Fig. 10 shows the system components. Under conditions of high oil temperature or low engine revs, hydraulic pressure drops. In order to improve CIS control accuracy with low hydraulic pressure, an oil pressure (Poil) sensor and oil temperature (Toil) sensor were adopted. CIS switching implementation is judged, combining information on engine revs and vehicle speed, high-pressure battery residual amount, etc. The motor regeneration amount is controlled according to the CIS operation state, and the deceleration feeling is the same as with an ordinary gasoline vehicle.

When the vehicle accelerates again after deceleration, the control system switches the spool valve over to the active side, starts operation of the intake and exhaust valve, then initiates fuel injection, in that order. This achieves smooth acceleration performance.

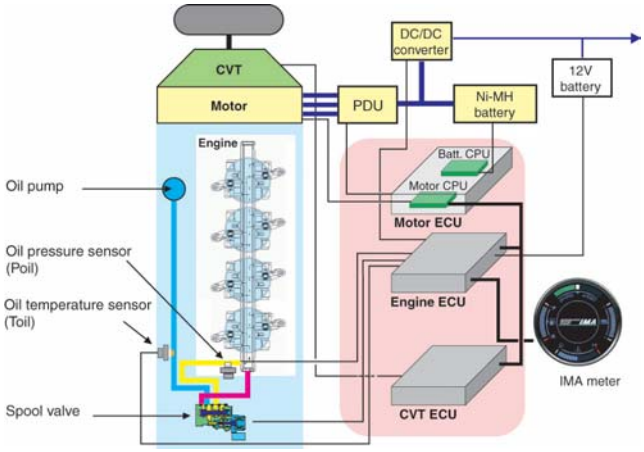


Fig. 10 CIS components

4.3.4. Cylinder pressure when valves are paused

Fig. 11 shows the maximum cylinder pressure when switching from valve operation to valve pause. The throttle is fully closed; No. 1 cylinder operates normally; and No. 2–No. 4 cylinders switch from valve operation to pause. The amount of air remaining in the cylinder differs according to the paused cylinders' inlet valve and exhaust valve pause timing. Cylinders that pause from the inlet valve immediately after the exhaust process (No. 4 cylinder in Fig. 11) have reciprocating action with TDC portion air capacity tightly closed. Cylinders that are paused from completion of inlet

process (No. 2 and No. 3 in Fig. 11) have reciprocating action with process portion air capacity tightly closed. According to valve pause switching timing, cylinder pressure immediately after switching differs according to the amount of air remaining in the cylinder, but at some dozens of cycles, cylinder pressure becomes saturated and equivalent.

The No. 1 cylinder, which is operating normally, has a rise in cylinder pressure, as inlet air amount increases in line with inlet pipe pressure rise due to the valves in the other three cylinders being paused.

4.4. Engine Friction Reduction

In addition to the low friction technologies adopted in the base engine L13A, plateau honing was adopted to smooth the cylinder sleeve surface roughness and to reduce piston sliding resistance (Table 2). Plateau honing is a machining method that forms oil pools to maintain the oil film, and at the same time improves surface smoothness. Fig. 12 compares surface states with conventional honing and plateau honing. Plateau honing achieves a reduction of 8% in mechanical friction at 1,500 rpm, and of 4% of friction, including pumping loss (inlet pipe pressure = -53 kPa).

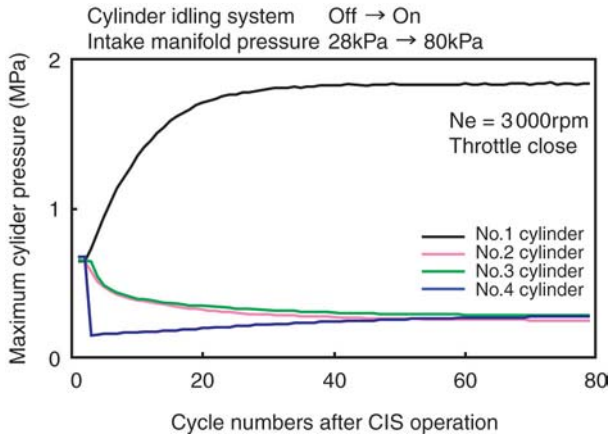


Fig. 11 Change in cylinder pressure patterns after CIS operation

Table 2 Engine friction reduction technology

○=Adoption

Engine code	LDA	L13A
Roller rocker arm	○	○
Off-set cylinder arrangement	○	○
Low tension piston ring	○	○
Streak crank bearing	○	○
MoS_2 processing of piston skirt	○	○
Cam shaft chain drive system	○	○
Low-viscosity engine oil	○	○
Cylinder sleeve plateau honing	○	
Two mode cooling system	○	○

4.5. Reduction in Fuel Consumption Rate

The combustion concept adopted by the L13A model i-DSI engine installed in the Fit is a rapid combustion concept using dual-point ignition[7]. A homogenous air-fuel mixture is formed through inlet port shape and combustion chamber shape, and together with dual-point ignition precision control, a high compression ratio was achieved. The LDA model specifications contributing to combustion are shared, but a lean-burn combustion method was adopted. Fig. 13 shows BSFC (brake specific fuel consumption) and co-variation of indicated mean effective pressure (IMEP) characteristics against air-fuel ratio. Against stoichiometric air-fuel ratio, through lean-burn a 10% BSFC reduction was achieved.

Honda adopted lean-burn combustion methods using VTEC-E for 4-valve engines. In the low rev range, one of the 2 inlet valves is almost completely paused (lift 0.5 mm), and due to high swirl (swirl ratio 2.5–3.4)[1–6], it is a stratified lean-burn combustion[5, 8]. The i-DSI engine (swirl ratio 1.6) does not use this variable device, but rather actualizes homogenous lean-burn combustion through modified cylinder flow that includes a modified combustion chamber shape, and a dual-point ignition system. Fig. 14 shows the relationship between BSFC and engine displacement at 1,500 rpm, output power = 2.94 kW load. The LDA model achieved a BSFC level equivalent to the D15B that used the VTEC-E, and to the ECA1.

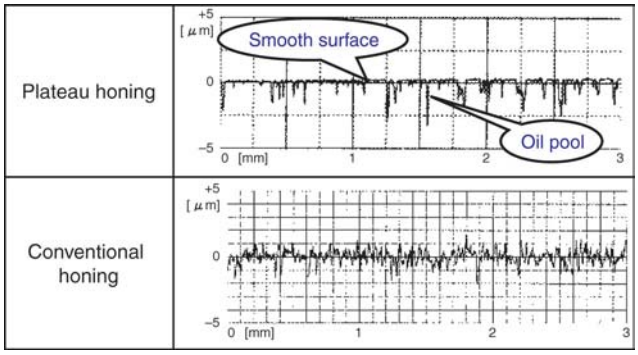


Fig. 12 Comparison of cylinder sleeve surface between plateau honing and conventional honing

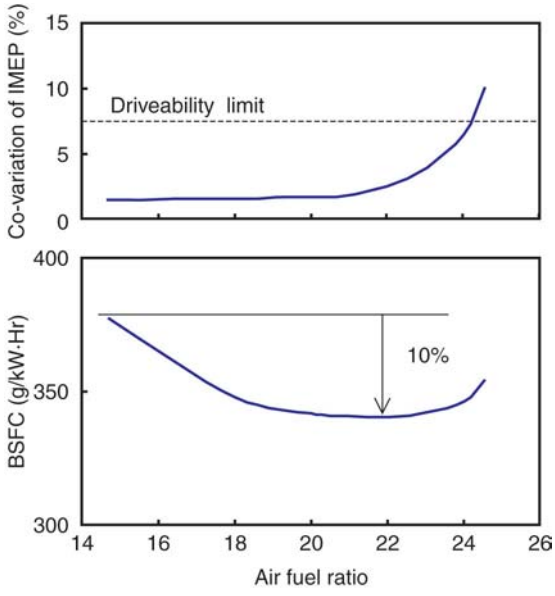


Fig. 13 Lean-burn effect on BSFC

Fig. 15 shows the simulation results of an engine in-cylinder air-fuel distribution with the LDA and the D15B. As for the calculation conditions, an average air-fuel ratio of A/F = 22 (excess air ratio = 1.5) was used, and fuel injection period and image crank angle (= ignition time) were actual engine driving conditions for both engines. The image surfaces were sections horizontal and vertical to the spark plug center electrode position. The LDA model has both vertical sections to the dual sparkplugs. In comparison with the D15B, the LDA forms a homogenous mixture.

5. CVT

5.1. Lightweight and Compact CVT

The transmission adopted was Honda's own Multi Matic S (CVT)[9, 10]. This is a carryover of the basic framework of the transmission used in the Fit, made more compact. In comparison with the Civic iE, there is a reduction in total length of 5%, which makes it possible to fit the IMA motor in a Civic body. There is also a 5% reduction in weight, making it lightweight and compact. (Table 3)

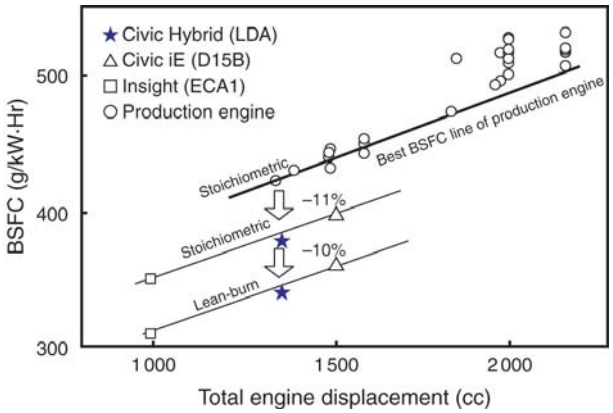


Fig. 14 Improvement of BSFC

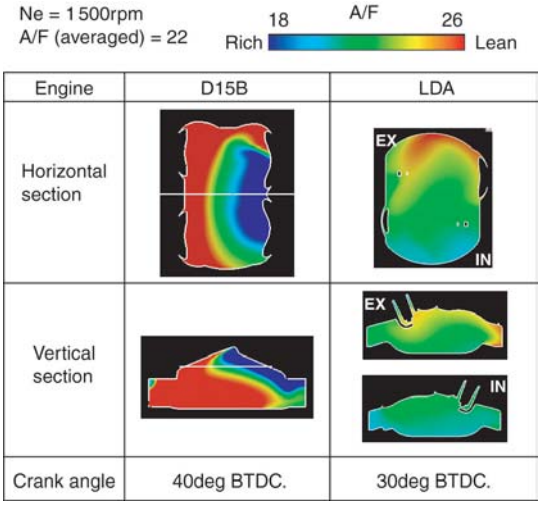


Fig. 15 Comparison of in-cylinder A/F distribution between LDA and D15B (VTEC-E)

5.2. CVT Low Fuel Consumption Technology

5.2.1. Friction reduction

Reducing pulley clamp hydraulic pressure through improved accuracy of engine torque estimates and a reduction in hydraulic pressure control variation has reduced friction by 20% over that used in the Civic iE. (Fig. 16)

5.2.2. CVT electronic control

In order to realize low fuel consumption, revisions were made to control system settings, making them even more accurate. The main items were as follows:

- Set optimum shift characteristics for low fuel consumption.
- Improved start clutch control method that achieves both high drivability and low fuel consumption.
- Refined start clutch feedback control during deceleration in order to increase regeneration amount.
- Increased accuracy of pulley clamp pressure.

Fig. 17 shows a characteristic comparison of pulley clamp hydraulic pressure command values during driving. By making the calculations of required hydraulic pressure more accurate, there is a reduction in hydraulic pressure command values. Through the above, a 5% reduction in fuel consumption was achieved, in comparison with conventional CVT control.

Table 3 CVT specifications

	Civic Hybrid	Civic iE
Belt axis length (mm)	143	155
Transmission length (mm)	352	372
Transmission weight [wet] (kg)	65.3	68.6

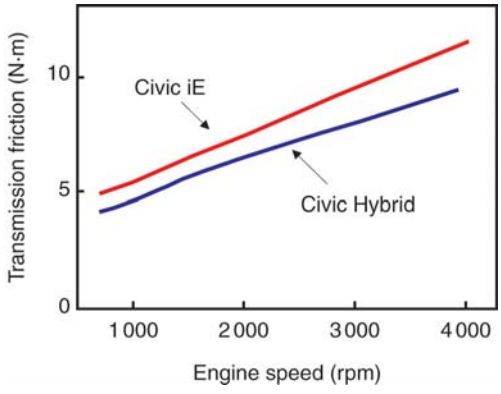


Fig. 16 CVT friction reduction effect

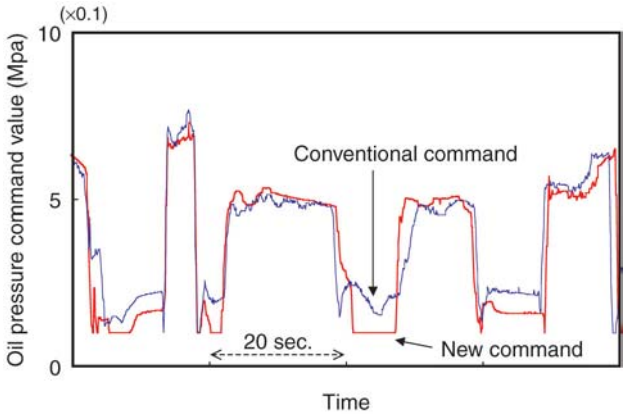


Fig. 17 Comparison of pulley clamp oil pressure command values

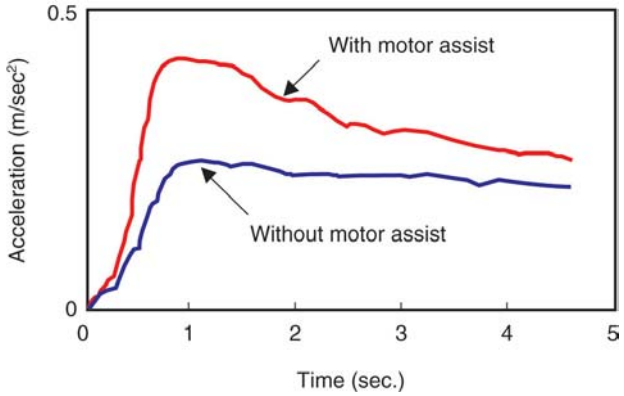


Fig. 18 Motor assist effect on vehicle starting performance

5.3. High Marketability through Combination with IMA

Fig. 18 shows start-off characteristics with and without motor assistance. Pending issues include an increase in vehicle weight due to installing the hybrid system, and a drop in acceleration performance due to smaller engine capacity. However, using motor assistance, it is possible to achieve 1.5 L class start-off performance without lowering the gear ratio.

In addition, by combining CVT and IMA, optimum prosmatec control is adopted, and even on mountain roads it is possible to achieve a high level of drivability.

6. New IMA, in the Pursuit of High Efficiency and Compact Size

To create a motor that responds to an increase in vehicle weight or an increase in regenerative energy, it is necessary to improve maximum regenerative torque and efficiency. The motor's external dimensions are equivalent to the Insight[6], and it has improved performance with modifications to electromagnetic circuits.

Volume is reduced by making the electrical units, such as the power control unit (PCU) driving the motor, the battery, etc., centralized and compact; and by placing them behind the rear seats in a sedan type passenger vehicle, it is possible to maintain a practical trunk space.

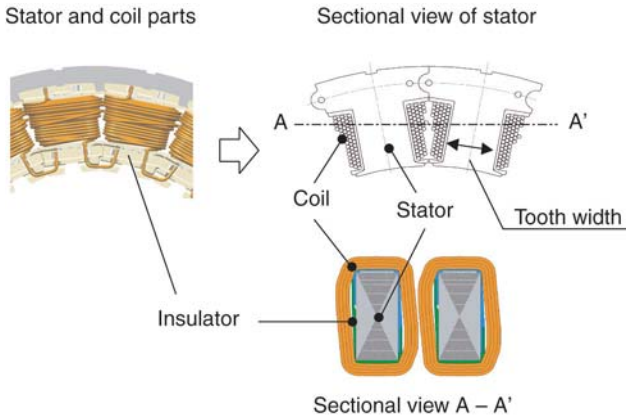


Fig. 19 Construction of stator and coil

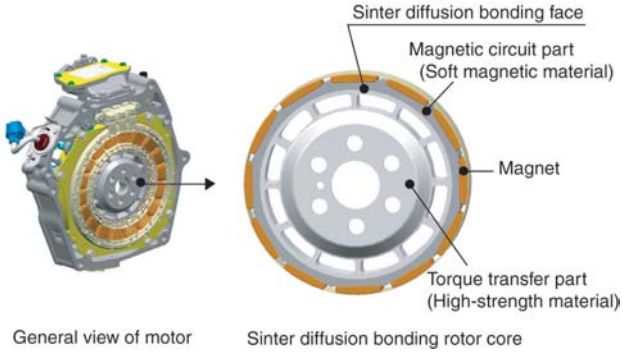


Fig. 20 Sinter diffusion bonding rotor core

6.1. Thin DC Brushless Motor

6.1.1. Motor performance improvements

As a means of improving motor performance with modifications to electromagnetic circuits, reductions in copper loss and iron loss, and improvements to torque constant (Nm/A) can be considered. Reductions in copper loss and iron loss can be made through measures expanding the diameter of the coil wire (+0.2 mm) and increasing the width of the teeth (+0.5 mm).

Winding the coil in the conventional method in the same space leads to contact between adjoining coils, and insulation performance cannot be maintained. As countermeasures, the insulator on the inner side of the coil was made thinner, and a shape adopted so that the thick part of the coils do not overlap at the center. The coil winding method was also modified. By adopting a non-symmetrical winding that effectively utilizes coil part space, a reduction in copper loss of approximately 30% was achieved, without changing the stator's external dimensions (Fig. 19).

There was an improvement of approximately 16% in torque constant, by expanding the magnetic circuit area (+5.5 mm) in the motor's axial direction. The space required for this is obtained by integrating functions of the parts inside the motor, keeping the external dimensions equivalent to those of the conventional unit.

Thanks to these improvements, the maximum regenerative torque was improved by approximately 30%, and efficiency in the normal range was improved by approximately 3%.

6.1.2. New rotor manufacturing method

A rotor must have the function of fixing magnets to the perimeter and creating electromagnetic circuits, and must

have the strength to transfer torque by being connected to the crankshaft. Conventionally, the rotor has been formed by applying the lost wax method, using carbon steel, giving priority to connection strength. In order to work towards both maintaining connection strength and at the same time improving motor efficiency, a high strength material was used on the inner side of the rotor, and a soft magnetic material on the outer side (Fig. 20). The rotor is formed by sinter diffusion bonding, which firmly bonds different metals. Through this, motor efficiency was improved, and weight reduced by 15% in comparison with the conventional unit.

6.2. Making Electrical Units Compact

Modifying the layout of the PCU controlling motor drive, the Ni-MH battery, and high pressure peripheral devices, as shown in Fig. 21, led to the creation of a compact electrical unit IPU (Intelligent Power Unit).

Modifications were also added to the IPU's cooling path. With the Insight, the PCU system and battery system had independent cooling paths, but with innovations in layout inside the IPU, a single path was realized. With these modifications, a compact shape was achieved, as well as a reduction of 42% in IPU volume, in comparison with the IPU fitted to the Insight.

As shown in Fig. 21-(b), the IPU is placed behind the rear seats, and trunk capacity is maintained that is no worse than gasoline based vehicles.

From the above, engine, transmission, and motor efficiencies are improved, achieving the target fuel consumption of 29.5 km/L in Japanese 10-15 mode.

7. Low Emission Technology

Conventionally, under the lean-burn condition, there is no expectation for NOx cleaning with a three-way catalyst, and so achieving low emissions is an issue.

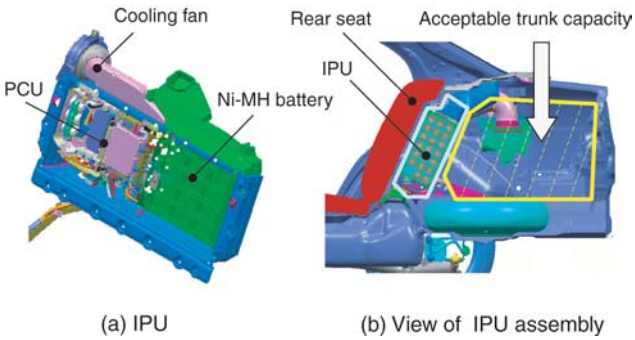


Fig. 21 View of IPU assembly



Fig. 22 View of exhaust system

In studying the emissions system for this engine, the target for domestic (Japanese) sales models was set at a 75% reduction from the 2000 emission standards in Japan (approval as "ultra-low emissions").

7.1. Exhaust System

The exhaust system for this engine is shown in Fig. 22. In order to maintain low emissions in the cold range and in stoichiometric air-fuel ratio range, a lightweight stainless steel exhaust manifold was adopted, reducing thermal capacity. Placing a 2-bed catalyst under the floor, in the front a 900 cell three-way catalyst was used, and in the rear a 600 cell NOx adsorption reaction three-way catalyst for lean burn[11] was used. By making the converter high density and thin walled, the catalyst's temperature rise characteristics are improved. By increasing the surface area in contact with the exhaust gases, there is improved emission conversion. A rolling type canning process was selected to achieve both high density and high contact surface area.[12]

7.2. Achieved Emission Values

In addition to the exhaust system, a multi-hole injector having a 6-hole nozzle and an electric EGR valve were adopted. Furthermore, the engine control systems outlined below were also adopted. This made possible an emission reduction level of 75% from the 2000 emission standard.

- STR (Self Tuning Regulator)[13]
- Quick Warm-up System[14]
- Lean control of air-fuel ratio for a low temperature start

In addition, in the North American spec, a 900-cell three-way catalytic converter was placed in the stainless steel closed-couple exhaust manifold integrated with the converter, and a 2-bed 400 cell three-way NOx adsorption reaction catalyst was placed under-floor. This meets the US ULEV, which is the global standard.

8. Summary

The following high fuel economy and emissions performances were achieved, thanks to the development of a new 1.3 L i-DSI lean burn engine of the LDA type adopting the cylinder idling system; the development of a new IMA system that improved motor efficiency by approximately 30%; and the development of a hybrid power train comprising a CVT with improved transmission efficiency.

- Japanese 10-15 mode fuel consumption rate 29.5 km/L
- A 75% reduction of the 2000 emission standards, gaining approval as "J-ULEV"

References

(1) Oura, S., Miura, K.: "Making Gasoline Engine More Efficient, using Variable Structures," Automotive Technology, Vol. 45, No. 8, pp.93–98 (1991)

(2) Matsuki, M., et al.: "Development of a Lean Burn Engine with a Variable Valve Timing Mechanism," SAE Paper 960583

(3) Hayashi, A., Sakurahara, Y., Takabayashi, T., Endo, T.: "1.8 L Lean Burn Engine Development for Accord and Torneo," Honda R&D Technical Review, Vol. 10, pp. 49–57 (1998)

(4) Niizato, T., Hayashi, A.: “New 2.0 L Lean Burn Engine Development,” Honda R&D Technical Review, Vol. 12, No. 2, pp. 45–54 (2000)

(5) Matsuki, M., Oura, S., Watanabe, K., Kinoshita, Y.: “Development of a 1.5 L Lean Burn Engine for 2001 model ‘Civic’”, Honda R&D Technical Review, Vol. 12, No. 2, pp.29–36 (2000)

(6) Aoki, et al.: “Development of Motor Type Hybrid Power Train,” Automotive Technology Conference Proceedings, No. 98–99 (1999)

(7) Nakayama, Y., Suzuki, M., Iwata, Y., Yamano, J.: “Development of a 1.3 L 2-plug engine for 2002 model Fit”, Honda R&D Technical Review, Vol. 13, No. 2, pp. 43–52 (2001)

(8) Hardalupas, Y., et al.: “Influence of Injection Timing on In-cylinder Fuel Distribution in a Honda VTEC-E Engine,” SAE Paper 950507

(9) Yamaguchi, T.: “CVT control in Honda Hybrid ‘IMA’”, No. 9908 JSAE Symposium Power Transmission Latest Technology ’99, pp. 37–40 (1999)

(10) Sumi, M., Fujimoto, S.: “Development of Compact CVT for Hybrid Automobiles,” Automotive Technology Vol. 54, No. 4, pp. 48–54 (2000)

(11) Ono, H., Takahashi, T., Takaoka, N., Sakanushi, M., Sugiura, K.: “Development of a three-way NOx adsorption reaction catalyst System,” Honda R&D Technical Review, Vol. 11, No. 2, pp. 45–50 (1999)

(12) Kitagawa, H., et al.: “Ultra-low Emission System for ‘Accord SULEV’”, Honda R&D Technical Review, Vol. 12, No. 2, pp. 37–44 (2000)

(13) Maki, H., et al.: “Real Time Control Using STR in Feedback System,” SAE Paper 950007

(14) Ueno, M., et al.: “Engine quick warm-up system during fast idle, with application controls for intake air amount and ignition timing,” Honda R&D Technical Review, Vol. 11, No. 1, pp. 73–78 (1999)

■ Authors ■


Masato MATSUKI


Teruo WAKASHIRO


Toshihiro KAMIYAMA


Toshiyuki SATO


Toshiaki KAKU


Masahiro KANDA

Development of a 1.7 L CNG Engine for the 2001 Civic GX

Takushi TODA* Masato MATSUKI*
Tadanobu OHMORI* Yuji YAMAMOTO*

ABSTRACT

Honda has upgraded the Civic GX, which has been in production since 1998, with a newly developed CNG engine for the 2001 model. Based on the gasoline engine in the 2001 model Civic, this CNG engine was given larger displacement and an improved air intake system for better torque at low to medium speeds. A layout that integrates the air intake system and the CNG regulator was adopted to make the power plant more compact. The new Civic GX is the world's first vehicle to be qualified as an AT P-ZEV by the CARB. In order to satisfy the AT P-ZEV requirements, the vehicle was given the capability for quick light-off of the catalyst from a cold start, high-precision air-fuel ratio control, and reduced exhaust emissions. It has certified for Japan ULEV status. This model also achieved a 7% improvement in city driving fuel economy over the 1998 model by changing the transmission that is paired with the CNG engine from a 4AT to a CVT.

1. Introduction

As deterioration of air quality due to exhaust emission from automobiles is recognized as a global issue, development work is being carried out on power plants that use alternative fuels other than gasoline in order to reduce the pollutants in exhaust emissions. Among alternative fuels, compressed natural gas (CNG) with CH_4 (methane) as its main component is a fuel that has little impact on air quality, and is viewed as having excellent prospects due to the possibility of easy supply with vast amounts of reserves of natural gas using city gas networks as infrastructure.

Honda has mass produced the Civic GX since 1998. The Civic GX uses a dedicated CNG engine, and features an output performance equivalent to that of a gasoline vehicle while at the same time achieving the lowest exhaust emission performance in the world. With the full model change to the Civic series in 2001, further efforts were made to reduce exhaust emissions in order to comply with newly enacted exhaust emission regulations. In addition, a power plant for CNG was developed with the aim of longer driving distances. This paper introduces the details of these developments.

2. Development Aims

The following target performances were set in order to realize the highest level of environmental countermeasures in the world while at the same time achieving an ease of use equivalent to gasoline vehicles as a mass production passenger vehicle fueled by CNG.

(1) The lowest exhaust emissions performance in the world

US: Complying with the California State AT P-ZEV (Advanced Technology Partial-Zero Emission Vehicle) category, which is considered to be the most severe in the world.

Japan: Complying with the "Ultra-Low Emission Vehicle" certification standards which are a 75% reduction from the 2000 standard level, and complying with the exhaust emission technology guidelines for compressed natural gas vehicles.

* Tochigi R&D Center

(2) Longer driving distance

Improving fuel economy by 5% or more focusing on city driving in order to lengthen the driving distance without changing the tank capacity.

3. Outline and Specifications

3.1. Engine

The engine is based on the gasoline engine of the 2001 model Civic with CNG support added. The main engine unit features valve recession countermeasures[(1)] (changed intake and exhaust valve and valve seat materials) like the 1998 model and an increased compression ratio.

The intake system up to the air cleaner and resonator is mounted to the power plant, and the fuel system described hereafter is also integrated to reduce the power plant size and facilitate engine mounting during factory production.

The displacement was increased and the intake system was also changed to increase the torque at medium to low speeds. Combined with a continuously variable transmission (CVT), driveability in urban areas was improved, which mainly use the medium to low engine speed range.

The main specifications of the CNG engine are shown in Table 1, the output characteristics in Fig. 1, and the engine appearance in Fig. 2.

3.2. Fuel Supply System

Fig. 3 shows the CNG cylinder and fuel supply system layout in the vehicle body.

The CNG cylinder is based on the 100 L capacity (20 Nm^3 when filled at 20 Mpa) all-composite tank developed for the 1998 model. The cylinder was mounted between the rear seat and the trunk. A new rear suspension layout allowed the cylinder to be mounted in a forward and lower position. The front-to-back space in the trunk, which presents a concern for CNG vehicles, is therefore larger by 82.5 mm than in the 1998 model.

Table 1 Engine specifications

Engine code		D17A
Cylinder configuration		In-line 4-cylinder
Bore x stroke (mm)		75.0 x 94.4
Displacement (cm^3)		1 668
Compression ratio		12.5 : 1
Valve train		SOHC
Number of valves		4 per cylinder
Valve diameter (mm)	In.	30
	Ex.	26
Fuel supply system		Multi-point injection
Ignition system		Programmed ignition (Plug hole coil)
Max. power (kW/rpm)		74 / 6 100
Max. torque (N·m/rpm)		132 / 4 000

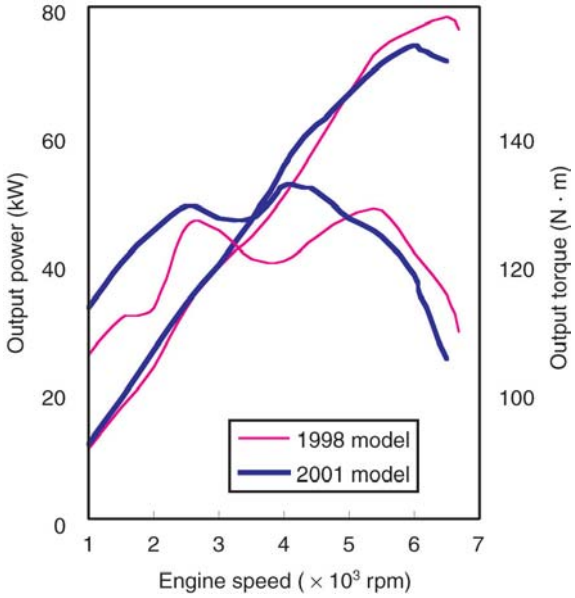


Fig. 1 Engine performance

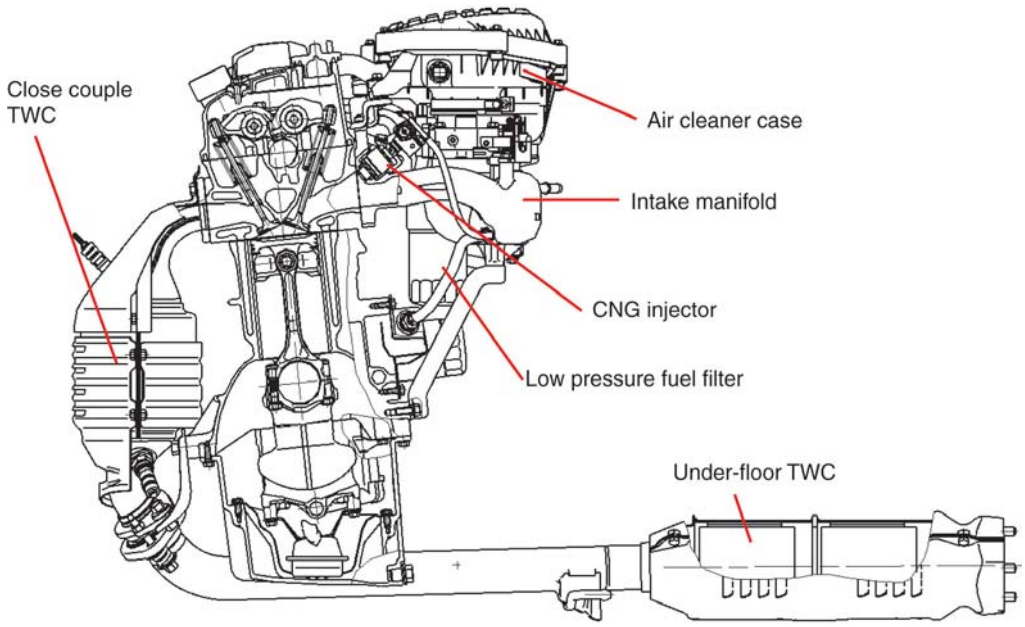


Fig. 2 2001 model CNG engine

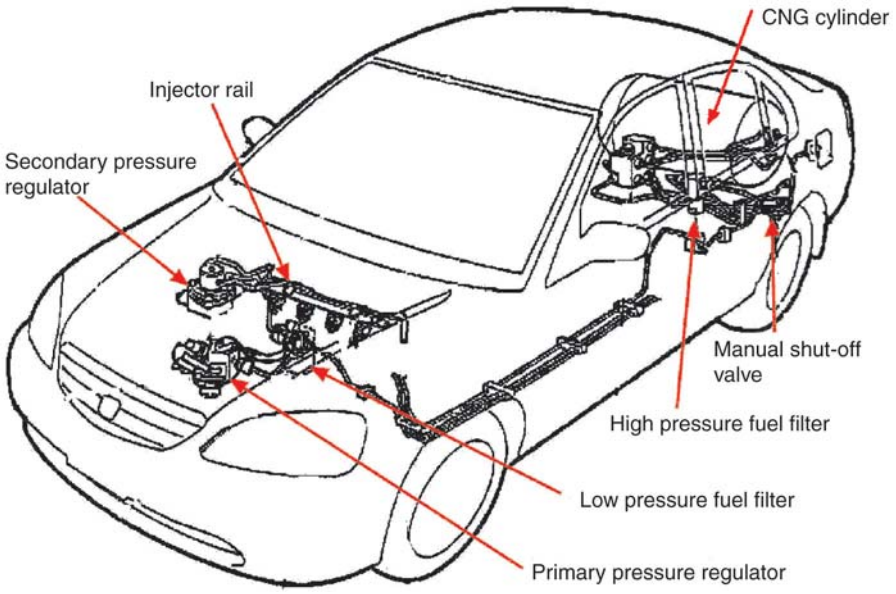


Fig. 3 Overview of Civic GX CNG fuel supply system

The regulator for adjusting the fuel pressure performs pressure reduction in two stages in order to provide stable fuel pressure. The 1998 model combined the primary and secondary stages in an integrated regulator structure, but the regulator in the 2001 model has a split structure. A low pressure fuel filter is located between the primary and secondary regulator. This filter removes any oil and water contained in the fuel. The primary stage regulator is located at the chassis side below engine room toe board, and the secondary stage regulator and the low pressure fuel filter are mounted on the engine. The layout flexibility of the engine compartment was increased by splitting the regulator, which has a large volume.

Fuel is supplied to the engine using the multi-point injection (MPI) method, which positions a special injector[(2)] at each cylinder and sprays fuel into the intake ports. In this layout, the injector and injector rail are mounted on the intake manifold. The intake manifold was designed specially for a CNG engine, making it different from the intake manifold for the base gasoline engine.

4. Low Emission Technology

The emission system was designed in order to comply with the US California State P-ZEV category, which is considered to be the most severe exhaust emission regulation in the world.

As a result, the 2001 model Civic GX was qualified as the world's first AT P-ZEV by the California Air Resources Board (CARB).

4.1. AT P-ZEV

The P-ZEV category is required to have the exhaust emission levels (tail pipe emissions) of a Super Ultra Low Emission Vehicle (SULEV), the evaporative emission (fuel vapor emissions) of the zero evaporative emission category, and a durability guaranteed distance of 240,000 km (150,000 miles).

Non-methane organic gas (NMOG) in the hydrocarbons (HC) are subject to P-ZEV regulations. CH_4 has little impact on air quality (extremely low photochemical reactivity), so other types of HC are subject to regulation, while CH_4 is excluded. In addition, approximately 80% of hydrocarbons emitted in a non-combusted state from engines using CNG as fuel are CH_4. CNG engines have an advantage compared to gasoline engines when reducing NMOG to the P-ZEV level.

Therefore, reducing NO_x is the main issue for achieving P-ZEV level exhaust emission performance using CNG as a fuel. In addition, the NO_x emissions level of 1/10 ULEV (80,000 km equivalent) achieved by the 1998 model must be guaranteed over an even longer driving range (240,000 km) (Fig. 4).

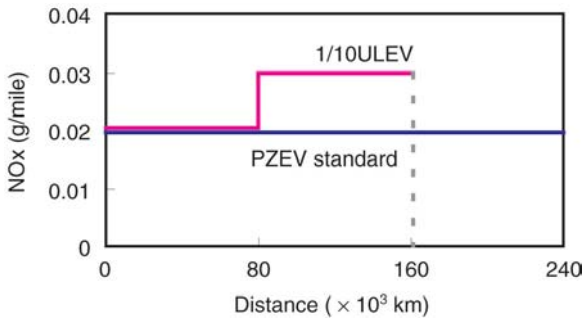


Fig. 4 P-ZEV emission standard and 1998 model Civic GX emission target (1/10 ULEV)

Evaporative emissions do not apply because the fuel system is sealed using a pressure vessel and the main fuel component is CH_4. Furthermore, CNG fuel can minimize its influence on air quality throughout the fuel manufacturing and distribution cycle. For these reasons, the AT P-ZEV (Advanced Technology P-ZEV) category is applied to P-ZEV using CNG as fuel.

The 240,000 km durability guarantee was subjected to similar verification testing as other Honda vehicles, by extending the concentrated durability method from the equivalent of 160,000 km (100 k miles) to the equivalent of 240,000 km (150 k miles). As a result, the emission system was verified to have maintained P-ZEV exhaust emission performance even after running for 240,000 km.

Among the emission system technologies that make it possible to achieve AT P-ZEV, the following low emissions technologies are described below. (1) Exhaust system and catalytic converter which have a large influence on quick light-off of the catalyst after engine start, (2) O_2 sensors which are the key to air fuel ratio feedback, and (3) air fuel ratio control for reducing NO_x after catalyst light-off.

4.2. Exhaust System and Catalytic Converter

The exhaust system uses the same close coupled and under-floor catalytic converter layout as in the 1998 model (Fig. 5). The close coupled converter has superior temperature rise characteristics, so the time until catalyst light-off can be shortened, which is effective for reducing exhaust emissions after engine start. The under-floor converter aims to reduce exhaust emissions after warming-up.

The exhaust manifold was changed from the conventional cast iron type to pressed and welded stainless steel materials, and was welded together with the close coupled converter. The under-floor converter and exhaust pipe, which had been connected with a flange, were welded together to form an integrated unit and thus reduce their weight. The close coupled converter outlet and the exhaust pipe were connected using a spherical flexible joint. These enhancements were intended to reduce the thermal capacity by reducing the weight of the exhaust system from the engine outlet to the under-floor converter by 1.5 kg over previous models.

The 2001 model sought to improve fuel economy by adopting a continuously variable speed transmission (CVT) and controlling engine speed to keep lower than the 1998 model (Fig. 6). This is disadvantageous for heating the catalyst after starting the engine. However, the reduction in the thermal capacity of the exhaust system provided compensation in the temperature rise characteristics, which achieved levels on a par with the 1998 model (Fig. 7).

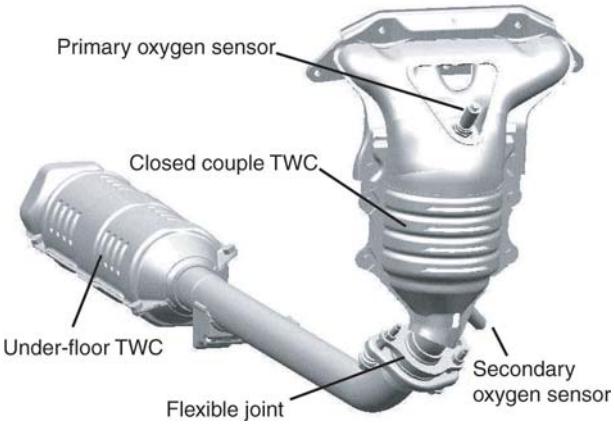


Fig. 5 Exhaust and catalytic converter system

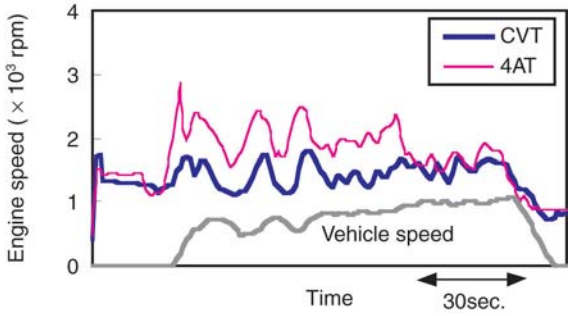


Fig. 6 Engine speed comparison between CVT and 4AT

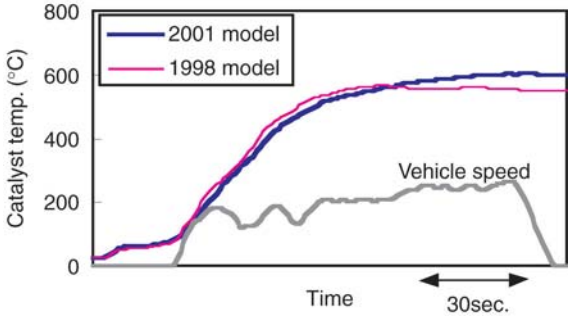


Fig. 7 Catalyst temperature after engine start

4.3. O_2 Sensors

Air fuel ratio control uses two O_2 sensors. A primary O_2 sensor is located at the exhaust manifold, and a secondary O_2 sensor is located at the close coupled converter outlet (Fig. 5). These O_2 sensors were developed specially for CNG[3]. CNG engine exhaust emissions contain a large amount of hydrogen (H_2). As a result, when the air-fuel ratio is close to the theoretical optimum, the primary O_2 sensor controlled air-fuel ratio (λ point) shifts to the lean side so that the NO_x emissions level increases. This is countered by adding a catalytic coating to the element surface of the sensor and eliminating the influence of H_2 to increase the λ point detection accuracy. On the other hand the CH_4 in the exhaust emission following the catalyst undergoes oxidation on the sensor element, causing the sensor output to invert between the rich and lean sides quickly. This was suppressed by adding silver (Ag) to the secondary O_2 sensor element located after the close coupled converter.

4.4. Air Fuel Ratio Control

Air fuel ratio control is performed using two O_2 sensors in order to reduce NO_x after catalyst light-off. Here, air fuel ratio compensation according to the secondary O_2 sensor output is added to the $\lambda = 1.0$ feedback using the primary O_2 sensor. This enables control that maintains constantly low NMOG and NO_x emissions levels for any engine operating state.

Control is performed at λ = 1.0 when cruising normally and accelerating to suppress CO and NMOG. On the other hand, when excess oxygen is present inside the catalyst, there is insufficient capacity for reducing NO_x. Therefore, when excess oxygen passing through the catalyst causes the secondary O_2 sensor output to indicate the lean side (0 V side), the O_2 feedback center (the control air fuel ratio) is shifted to the rich side (λ < 1.0). (Fig. 8) The catalyst interior is adjusted to a state suited for NO_x reduction by shifting the control air fuel ratio to the rich side to consume the excess oxygen. When there is excess oxygen inside the catalyst such as after fuel cut operation during deceleration for reducing fuel consumption, momentary rich control is performed to reduce NO_x emissions by consuming oxygen in a short time (Fig. 9). These control modes make it possible to reduce NO_x after catalyst light-off and balance it with NMOG at low values (Fig. 10).

Unlike gasoline engines, CNG engines do not need to increase the amount of fuel immediately after starting the engine at normal temperatures. However, the air fuel ratio prior to starting O_2 feedback is controlled to a level richer than λ = 1.0 in order to shift the inside of the catalyst to the rich side beforehand and reduce NO_x emissions.

4.5. Achieved Exhaust Emission Values — US/Japan

P-ZEV category exhaust emission levels were achieved as a result of reducing NO_x by enhancement of the exhaust system and air fuel ratio control. Table 2 shows the P-ZEV standard values and the achieved values, and Fig. 11 compares NO_x emission values in each LA-4 mode phase with those of the previous model.

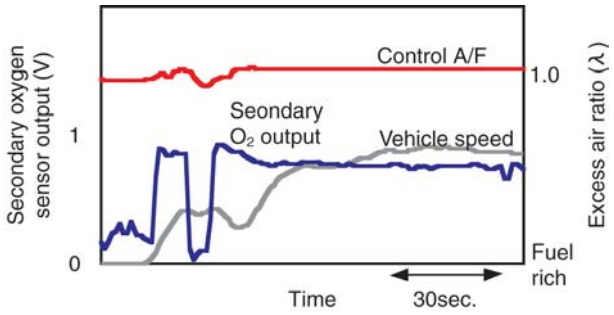


Fig. 8 A/F feed back control with secondary oxygen sensor

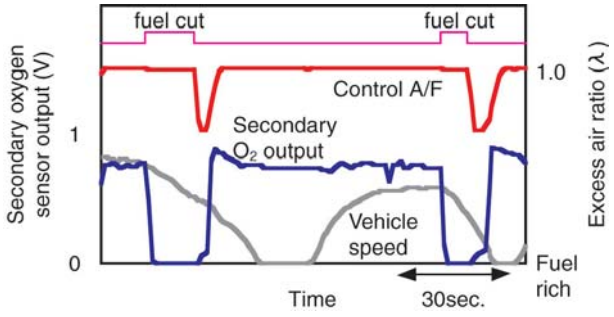


Fig. 9 A/F control after fuel cut

The 2001 model satisfied the Japanese exhaust emission technology guidelines for compressed natural gas vehicles, and also acquired "Ultra-Low Emission Vehicle" certification, which is a 75% reduction from 2000 standard values. Table 3 shows the 10-15 mode emissions values, and Table 4 shows the 11 mode emissions values.

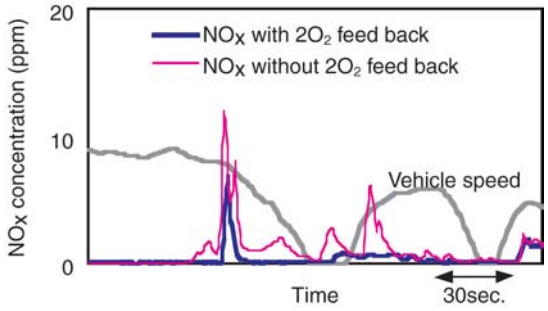


Fig. 10 NO_X reduction from use of $2O_2$ feed back system

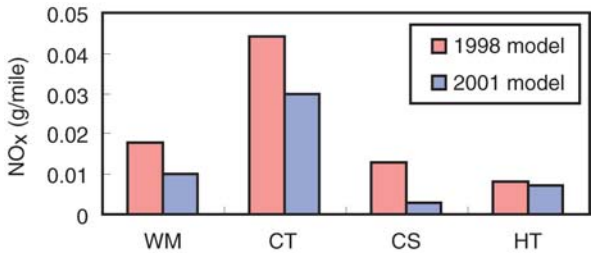


Fig. 11 NO_X emission comparison between 2001 and 1998 model

Table 2 USA emission values (in-house test result)

	CO	NMOG	NO_X	Highway NO_X
P-ZEV standard	1.0	0.01	0.02	0.03
Achieved Value	0.088	0.001	0.008	0.011

(g/mile)

Table 3 Japan 10-15 mode emission values

	CO	THC	NMHC	NO_X
2001 Civic GX	0.06	0.01	0.01	0.01
J-ULEV standard	0.67	0.02	–	0.02
CNG standard	0.67	0.04	0.03	0.04

(g/km)

Table 4 Japan 11-mode emission values

	CO	THC	NMHC	NO_X
2001 Civic GX	0.3	0.4	0.1	0.1
J-ULEV standard	19.0	0.55	–	0.35
CNG standard	19.0	1.10	0.88	0.70

(g/test)

5. Low Fuel Consumption Technologies

5.1. Reduced Engine Friction

In order to reduce the friction of the engine, MD (Micro Dimple) treatment[4] was applied to the surface of the piston skirt portions, a lower-viscosity engine oil was used, the pin metal width of the crank shaft was reduced, and the valve spring load was reduced. As a result, in spite of increase in the displacement, the same engine friction was achieved as the 1998 model (1.6 L).

5.2. CVT

The CVT changes the pulley ratio in a step-less manner, making it possible to continuously use the engine in the low fuel consumption ratio range. As shown in Fig. 12, the 4-speed automatic transmission accelerates while shifting up, resulting in use at high revolutions and low load. In contrast to this, the CVT is capable of accelerating at continuously low revolutions and high load, therefore reducing engine friction and pumping loss. As a result, the CVT makes it possible to reduce fuel consumption during city driving which has frequent acceleration and deceleration. CVT internal control uses hydraulic pressure. The hydraulic control solenoid valve and hydraulic circuit were improved with the aim of improving the pulley ratio and starting clutch control accuracy. In addition, the transfer efficiency was improved by reducing the metal belt side pressure.

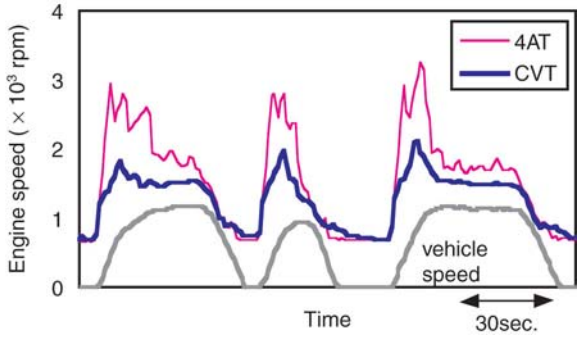


Fig. 12 Engine speed comparison between CVT and 4AT

Table 5 USA fuel economy (Label FE)

	City	Highway
2001 model	30	34
1998 model	28	34

(mile/GGE)

Table 6 Japan 10-15 mode fuel economy

	10-15 mode
2001 model	18.8
1998 model	17.0

(km/Nm³)

5.3. Achieved Fuel Economy

These low fuel consumption technologies focused on adoption of a CVT, reduced fuel consumption by 7% in the US City (LA-4) mode compared to the 1998 model (Table 5). In addition, in the Japanese 10-15 mode, a 10% reduction in fuel consumption resulted in the achievement of a driving range of 380 km (Table 6).

In the United States, the labeled amount of CNG fuel consumed is shown converted to the gasoline gallon equivalent (GGE). On the other hand, the Japanese figures show the amount of CNG using volume (Nm^3) in the standard condition.

6. Deterioration of the CNG Emission System in the Market

Exhaust emission measurement tests were conducted on vehicles that were actually driven for long distances in the market. This was done to investigate the deterioration of the emission system in the 1998 model Civic GX which is the first CNG vehicle mass produced and sold by Honda. The test vehicles were five taxis used in the State of Connecticut, US. All vehicles had been driven the durability guaranteed distance of 160,000 km (100 k miles) or more, with the longest driving distance reaching 222,000 km (138 k miles).

Fig. 13 shows the result of the measurement. These results confirmed that all vehicles satisfied the development targets for exhaust emission levels, with NMOG and NO_x levels 1/10 of the ULEV values (with respect to standard levels when driving 160,000 km). It was also found that no change took place in the rate of degradation of exhaust emission levels even after driving 160,000 km.

These results showed that there was no difference between the emission system deterioration verified in-house by actual driving and the concentrated durability method and that occurring in the course of actual use. They also verified that the same deterioration was maintained at 160,000 km and beyond.

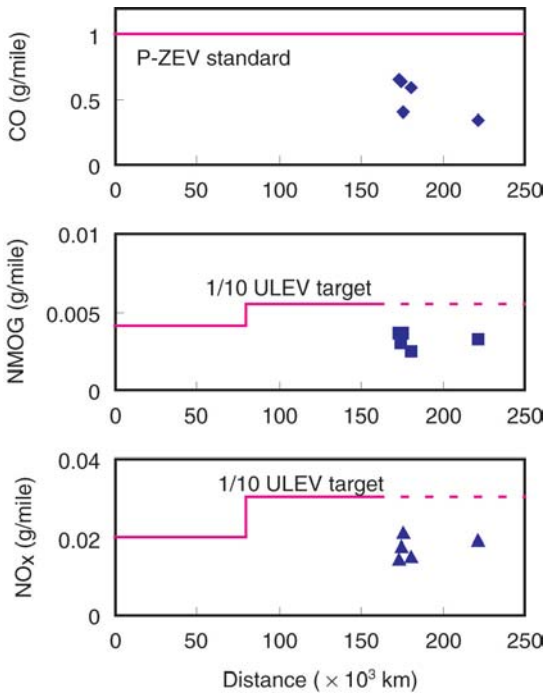


Fig. 13 Emission test results for 1998 Civic GX obtained on market

7. Conclusion

The 2001 model Civic GX achieved the lowest exhaust emission performance in the world by improving temperature rise characteristics of the exhaust system and air fuel ratio control. As a result, the 2001 model Civic GX received the world's first AT P-ZEV qualification in the State of California, U.S.A. And in Japan, it received "Ultra-Low Emission Vehicle" certification.

In addition, fuel economy during city driving was improved by 7% using low fuel consumption technologies centering on adoption of a CVT.

On the other hand, the exhaust emission of 1998 models actually driven in the market was measured, and these results confirmed that the exhaust emission performance of 1/10 ULEV, which was the development target, is maintained even in vehicles that had been driven in excess of 160,000 km.

8. Afterword

CNG is a gaseous fuel, so when used in an internal combustion automobile engine, stable combustion is possible even in low temperatures or immediately after starting. In addition, CNG has little influence on durability and deterioration of the emissions system. Therefore, low exhaust emission performance can be maintained throughout the total course of vehicle usage. Furthermore, the effects of CNG fuel on air quality can be kept to a minimum including in the manufacturing and distribution processes. For these reasons, CNG vehicles hold promise as alternative fuel and low pollution vehicles. Urban air quality can be improved by increasing the ratio of CNG vehicles. For CNG vehicles to achieve widespread adoption, it is necessary to create the proper environment such as increasing the number of CNG filling stations (constructing infrastructure) so that CNG vehicles can be used without worrying about driving range, etc. In addition, CNG fuel price settings and preferential tax systems for CNG vehicles must also be investigated.

References

(1) Sato, K., Takahashi,T.: "Development of Valve Seat Material for CNG Fueled Engines," IANGV, NGV 2000 Proceedings, p.195–204 (2000)

(2) Matsuura, H., Kato, A., Yamashiro, M., Fujii, I.: "HONDA Dedicated CNG Passenger Vehicle," Conference Proceeding of NGV '96, Vol. 2 (1996)

(3) Hosokai, S., Kubota, H.: "Super-Low Emissions Technology for Natural Gas Vehicles," Automotive Technology Association 1998 Autumn Conference Proceedings (No. 87-98) pp. 1–4 (1998)

(4) Matsuki, M., Oura, H., Watanabe, K., Kinoshita, Y.: "Development of a 1.5 L Lean Burn Engine for the 2001 Model Civic," HONDA R&D Technical Review Vol. 12, No. 2, pp. 29–36 (2000)

■ Authors ■



Takushi TODA



Masato MATSUKI



Tadanobu OHMORI



Yuji YAMAMOTO

Research of Hydrostatic CVT for Passenger Vehicles

Takashi IINO* Akihito OKUDA* Kazuaki SAKAI*
Mikihiro TAKANO* Tetsushi ASANO* Koichi FUSHIMI*
Masashi TANAKA*

ABSTRACT

Hydraulic Continuously Variable Transmissions ("CVT") have a large capacity for power transmission and have achieved proven results in industrial machines. Research was conducted on hydraulic CVT for use in passenger cars with large engine displacement, particularly in the areas of fuel economy performance, high-speed performance and quietness where passenger cars have higher demands compared to industrial machines. An HMT (Hydro Mechanical Transmission), which has the highest efficiency of all hydraulic CVT, was adopted to improve efficiency at cruising which greatly affects fuel economy when cruising at high speeds. In addition, the lock-up brake mechanism and the hydraulic pump and motor portions were improved to reduce agitation, resulting in a 6% improvement in efficiency when cruising at 50 mph. The hydraulic motor rotates at high speed during high-speed cruising, but centrifugal force has little effect and prospects for durability were obtained by adopting a bowl type slipper and improving the cooling method. A method for reducing noise was also derived by focusing on fluctuations of swash plate movement, which are correlated with noise.

1. Introduction

Continuously variable transmissions (CVT) have gained attention as an attractive technology for increasing fuel efficiency. Since Honda began mass production of a CVT for the Civic in 1995, its use has been expanded into many other models. The basic structure of this CVT is a metallic belt running between two pulleys to provide a continuously variable set of speed ratios. At present, however, there are limits to the torque which can be carried by this transmission, and it has been a challenge to apply it to large-displacement engines.

Oil hydraulics CVT consisting of hydraulic pumps and motors are widely used in industrial machinery. These provide high torque transmission, but they have several issues preventing their application to passenger automobiles (cars): their efficiency is low, they cannot withstand high-speed operation, and they are very noisy.

Honda has had an interest in overcoming these issues and has continued development of oil hydraulics CVT. Products have been developed for motorcycles and other small vehicles. Honda introduced the JUNO scooter in 1962, a lawn mower in 1989[(1)] and, more recently, in 2000, a series of all-terrain vehicles[(2)]. These technologies were used as a basis for the present research on automotive oil hydraulics CVT.

* Tochigi R&D Center

2. Aim of Research

The aim for this research was application of a CVT for cars with large-displacement engines. Thus, it was assumed that the transmission would be mounted on cars of the currently dominant front-wheel drive (FFD) design featuring transverse-mounted engines. Also, in addition to the requirement of fuel efficiency, which grows with engine size, higher operating speed and lower noise level are also essential; therefore, the following points were emphasized in this research:

(1) Technologies for higher efficiency;
(2) Technologies for higher rotational speed;
(3) Technologies for less noise.

3. Technologies for Higher Efficiency

CVT have been anticipated to offer higher fuel economy than staged automatic transmissions (AT). Due to its wide range of speed ratios, the CVT can be set to allow the engine to operate continually in its range of peak thermodynamic efficiency, despite the high frequency of acceleration and deceleration and the low speeds usually encountered in city driving. In suburban and freeway driving, with their lower frequency of acceleration and deceleration but high speeds, the CVT is again at an advantage due to its higher top-end speed ratio, which allows lower engine speeds. Both features are expected to improve fuel economy. However, AT have recently been equipped with a greater number of speed ratios; some cars with large-displacement engines now have 6-speed AT. Although CVT still offer the capability of operating the engine in the range of peak thermodynamic efficiency, their advantage in ratio range has been eroded. Therefore, it is important to improve the cruise efficiency at the top ratio in order to improve fuel mileage during high-speed driving.

3.1. HMT

Hydrostatic transmissions (HST), which convert all the power of the driving engine to hydraulic power, are commonly used for industrial equipment due to their simplicity of operation and installation. Honda's lawn mower used this type[(1)]. However, HST have a low power transmission efficiency, so are unsuited to automotive use.

Hydro-mechanical transmissions (HMT) are one method of raising the efficiency of oil hydraulics CVT (see Fig. 1). Power from the engine is split; an efficient mechanical connection is used to transmit some of the power from the engine, while the rest of the power is carried by an inefficient but continuously variable hydraulic transmission, and the two power streams are combined at the output for a high-efficiency, continuously variable speed output. HMT were used in the JUNO scooter and ATVs mentioned above to obtain higher efficiency[(2)].

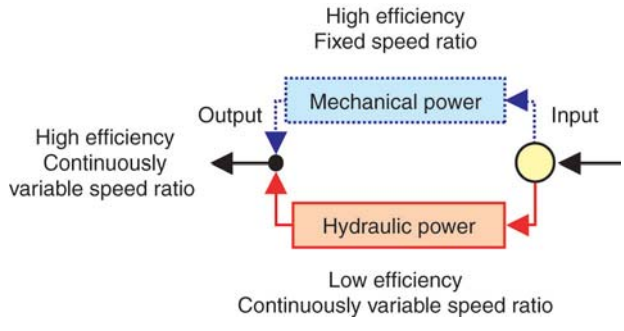


Fig. 1 Concept of HMT

3.1.1. Structure

The highly efficient HMT was used as the CVT in this study since it would provide the high fuel efficiency demanded of cars. There are many configurations of HMT; the configuration in Fig. 2 was chosen for its adaptability to the transverse engine in a FFD car. Here, the oil hydraulic pump lies parallel to the oil hydraulic motor. Both the pump and the motor are the variable displacement, axial-piston swash plate type; the angle of the swash plate can be adjusted and set to change the suction and discharge volumes. The power divider mechanism uses double sun planetary gears, which allow for a wide range of ratios.

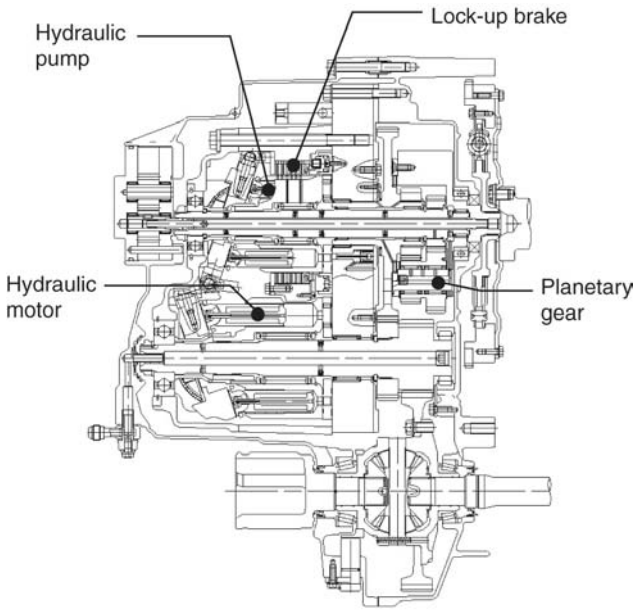


Fig. 2 Section of HMT

3.1.2. Power flow path

Fig. 3 shows the path by which power is transmitted through the HMT. Power enters from the engine to the carrier of a planetary gear, and is divided by two sets of pinion gears and sun gears into hydraulic power and mechanical power. Each path is shown below.

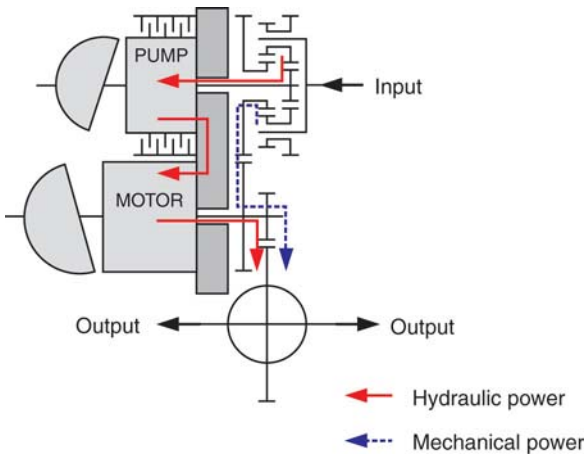


Fig. 3 Power transfer path of HMT

(1) Hydraulic power

Power passes through a large pinion gear and a small sun gear to an oil pump. Here, it is converted to oil pressure and flow, which is transmitted through passages to the hydraulic motor, and from that to the motor shaft.

(2) Mechanical power

Power passes through a small pinion gear, a large sun gear and a pair of gears to the motor shaft.

Thus, the two separate power flows are re-united at the motor shaft and are output from there through the differential to the car's wheels.

3.1.3. Principles of operation

The variation in the swash plate angle ratio of the pump and the motor with respect to the output:input speed ratio of the HMT (I/O speed ratio) is shown in Fig. 4, and the ratios of motor and pump speeds with respect to the same parameter are given in Fig. 5. The 'swash plate angle ratio' is defined as the dimensionless ratio of the maximum angles of each swash plate. The 'rotation speed ratio of pump and motor' is defined thus: for the pump, it is the dimensionless pump speed when the I/O speed ratio is zero; for the motor, it is the dimensionless maximum motor speed. Fig. 5 shows the case when the input speed of the HMT is held constant. The operating principles of the HMT will be explained by relating these figures to vehicle motion.

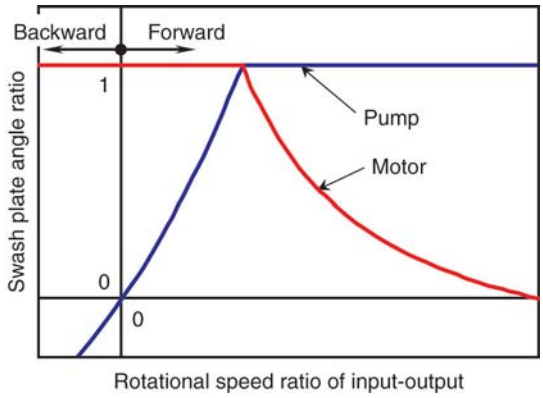


Fig. 4 Swash plate angle ratio of pump and motor

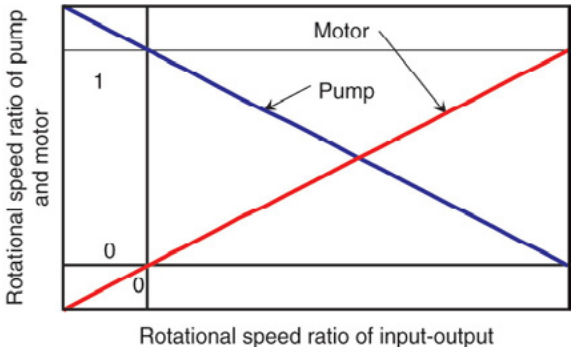


Fig. 5 Rotational speed ratio of pump and motor

(1) Vehicle is stopped

When the I/O speed ratio between input and output speeds is zero, the motor swash plate angle is set at its maximum value and the suction volume is maximized. Meanwhile, the pump swash plate is set at 0° and the discharge volume is 0. Thus, even when the pump is turning, there is no discharge, and the motor does not turn, so the vehicle wheels that are connected to the motor do not turn.

(2) Vehicle starts

As the I/O speed ratio is increased from zero, the motor swash plate angle remains at a maximum and the pump swash plate angle increases from 0°, so that oil is discharged from the pump. This oil causes the hydraulic motor to turn, causing the wheels to turn and setting the vehicle in motion. Then, the pump rotational speed begins to diminish. Once the pump swash plate angle reaches its maximum value, the motor swash plate angle is reduced. As the pump rotational speed diminishes, the motor rotational speed increases, increasing the vehicle speed. Once the I/O speed ratio reaches a maximum, the motor swash plate angle is 0°; since the motor suction volume is now zero, the pump is no longer able to discharge fluid, and it stops rotating. Here, the fluid power transfer is zero, and all power transfer is mechanical.

(3) Reverse

As the I/O speed ratio is decreased from zero, the motor swash plate angle remains at a maximum and the pump swash plate angle is set from 0° to a negative angle. In this situation, the discharge direction is the opposite of that of the forward direction, causing the motor to revolve in the reverse direction, and the vehicle moves in reverse.

3.2. Lock-up Brake

The condition where the I/O speed ratio is maximum (i.e., at the top gear ratio) is the most commonly used condition in cars, so the efficiency at this ratio is critical to obtaining good fuel mileage. The pump is stopped and power is only transmitted mechanically, so this system is more efficient than a HST. However, in this condition, even though the pump is stopped and the oil is not flowing, the oil is still pressurized. There is oil leakage and frictional losses at sliding parts of the motor (between the slipper and swash plate, between the cylinders and valve plate, etc.) Thus, this system incorporated the lock-up brake shown in Fig. 2 in order to further improve efficiency.

Once the pump has been stopped after the I/O speed ratio is maximized, the lock-up brake is activated, fixing the pump cylinders and case. Then, the torque which was acting on the pump shaft is borne by the case. This stops the pressurizing of the oil and further improves efficiency. Fig. 6 shows the variation of efficiency with input torque at a speed of 2,000 rpm. The effect of the lock-up brake improves with increasing torque, resulting in a maximum 8% increase in efficiency.

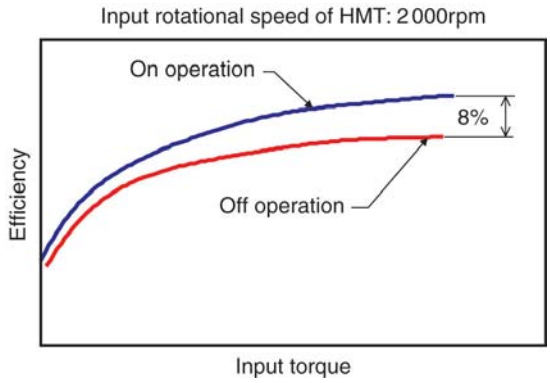


Fig. 6 Effect of lock-up brake

3.3. Part Lubrication

Most oil hydraulic pumps and motors are operated inside a case filled with oil in order to use the oil itself for lubrication and cooling. This design results in considerable agitation loss, however, so a new design was developed which supplies oil only to the necessary locations. The pump and motor are the same structure. As shown in Fig. 7, oil was supplied from the shaft directly to the sliding parts (between the slipper and swash plate, between the cylinders and valve plate, etc.)

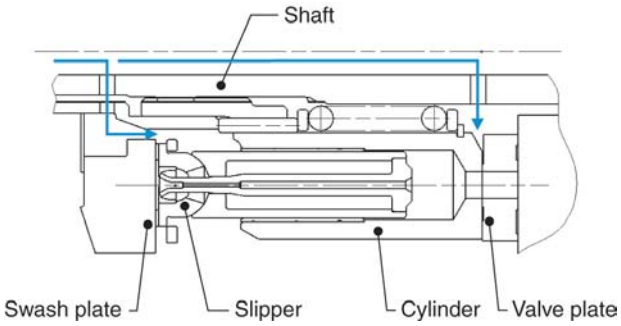


Fig. 7 Part lubrication

Fig. 8 shows the benefit of part lubrication for oil agitation loss in the motor alone. The higher the speed, the greater the benefit.

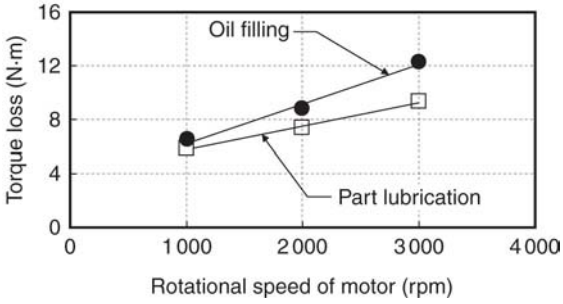


Fig. 8 Agitation loss

3.4. Cruise Effect

The effects of the lock-up brake and part lubrication on cruise efficiency are shown in Fig. 9. At 50 mph, the cruise efficiency was improved by 6% due to the two features.

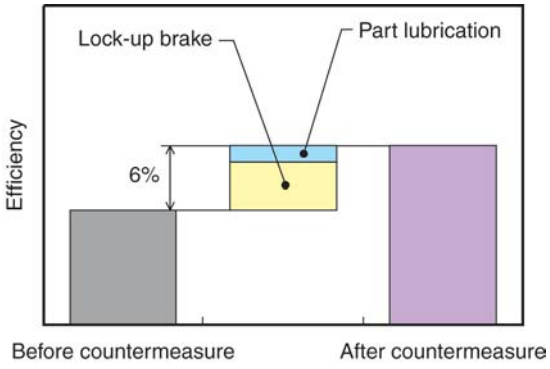


Fig. 9 Efficiency when cruising (50 mph)

4. High-speed Technology

In Fig. 10, the rotational speed of the pump and motor are shown when the accelerator is opened all the way. Initially, the pump speed rises with vehicle speed, then reaches a maximum and falls off. Meanwhile, the motor speed rises in direct proportion to vehicle speed and is maximum at top speed. The actual top motor speed depends on the engine driving the HMT and the vehicle itself. In the sample used for this study, the top pump speed was on a par with that in industrial equipment, 3,500 rpm, but the top motor speed was 7,000 rpm. Thus, technology is needed for handling high rotational speeds.

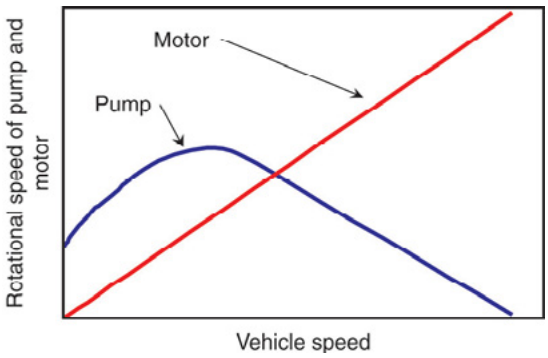


Fig. 10 Rotational speed of pump and motor

4.1. Bowl Type Slippers

At the tips of the pistons in axial swash plate piston pumps and motors are hydrostatic pressure bearings called ‘slippers’. The joint between a slipper and a piston has a spherical shape in order to allow the piston to follow the swash plate. There are many configurations for this joint[3], but the caulking type and with ball type shown in Fig. 11 are common.

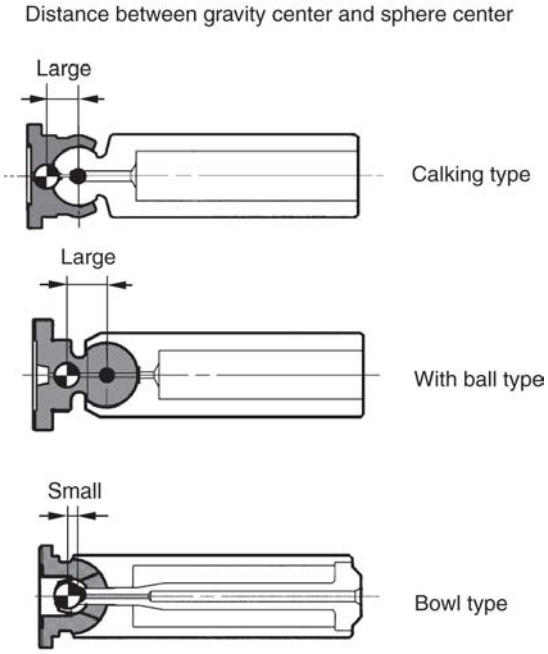


Fig. 11 Type of slipper

However, in the upper two designs in Fig. 11, the center of mass of the slipper is far from the center of the sphere in the joint. A large moment is developed about the center of the sphere when the motor is operated at high speeds, due to the centrifugal force on the mass center. This moment tends to tip the sliding face of the slipper out of contact with the swash plate. This causes an abrupt increase in oil leakage in conventional slippers when they are operated above a certain speed, as shown in Fig. 12. Not only is leakage increased by tipping of the sliding part, the uneven contact gives rise to wear and seizing, greatly lowering durability.

The larger the displacement of the motor, the greater the distance between the motor axis and the slipper, and the greater of the mass of the slipper, magnifying the centrifugal force on the slipper and the concerns with durability. Adopting a 'bowl type slipper' resolved these issues. The center of mass is very close to the center of gravity in this slipper.

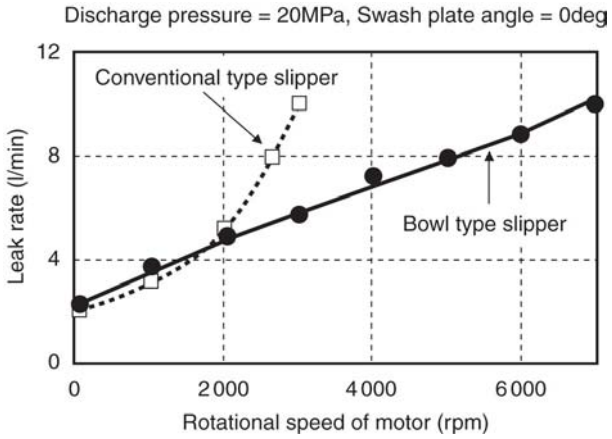


Fig. 12 Leak rate of motor

4.2. Improving Part Lubrication

Part lubrication, mentioned in Section 3.3 as lessening agitation loss, was further refined in order to augment durability at high operating speeds. As shown in Fig. 13, the sliding part is divided from the swash plate. Oil is introduced via the swash plate (not shown) through the back of the sliding component in order to cool them, and then, to the slipper. An oil filling area was created using an oil guide, which ensures that the volume between the slippers and the sliding component is always full of oil. An oil guide was also designed into the cylinder-valve plate region to create an oil filling area there.

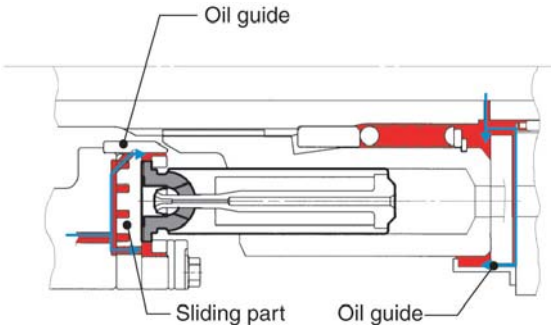


Fig. 13 Improvement of part lubrication

4.3. Results in Durability

The high-speed technologies described above were used in a 160 cc/rev displacement motor to provide high durability at 7,000 rpm (swash plate angle 0°). These results point to application of these technologies in cars with 4-L class engines.

5. Low Noise Technologies

One of the issues in adopting oil hydraulic CVT is the noise from piston pumps and motors. There has been vigorous research into reducing noise from piston pumps for many years[4]. It has been reported that swash plate vibration due to axial-direction thrust loads from the pistons on the swash plate accounts for a large part of the noise from pumps and motors[5]. Experiments by the authors have shown that transfer of swash plate vibration into the cabin is the main factor in noise. However, progress in reducing noise has been thwarted by the nearly unpredictable variations in pressure and flow rate that arise during pumping. Therefore, the authors estimated the swash plate vibration level at the design stage and used those results to modify the specifications in order to reduce swash plate vibration. Experiments were then performed to verify the results.

5.1. Noise Generation Mechanisms

The main cause of swash plate vibration is the violent fluctuations of the pressure in the cylinders (cylinder pressure) in pumps and motors due to pumping, which bring about violent fluctuations in the moment and thrust load on the swash plate. As shown in Fig. 14, the vibrations transfer from the case to the mounts to the vehicle frame, appearing eventually as noise in the cabin.

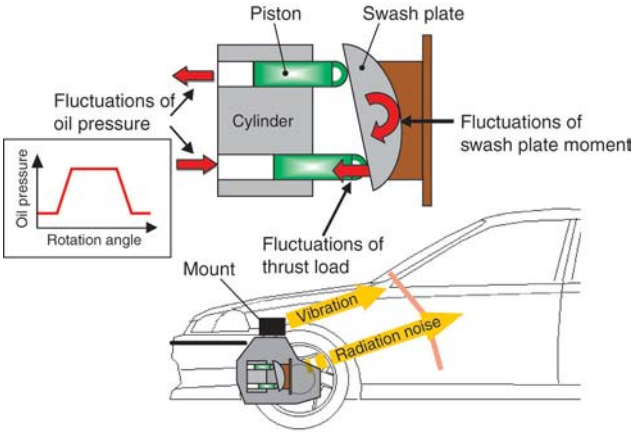


Fig. 14 Mechanism of noise

It is well known that reducing the displacement at the transmission mounting point (hereafter "Mt point") lowers the noise in the cabin. These experiments established a correlation between displacement at the Mt point and fluctuations in moment on the swash plate, as shown in Fig. 15. On the basis of this finding, research was continued with the objective of reducing the fluctuations of the moment on the swash plate.

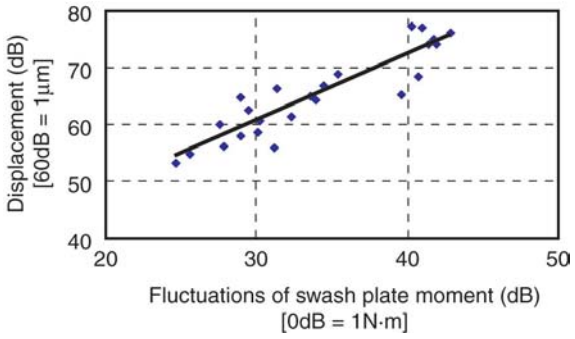


Fig. 15 Relation between fluctuations of swash plate moment and mounting point displacement

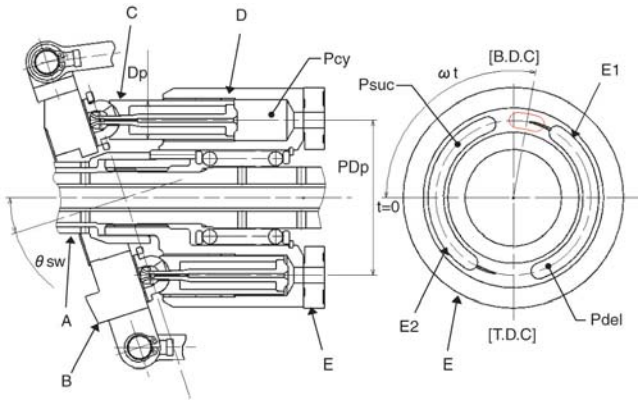


Fig. 16 Pump structure

5.2. Calculation of Cylinder Pressure and Moment on Swash Plate

Because the pressures developed in variable displacement pumps vary with the discharge volume even if the input torque is constant, it has been more difficult to establish an effective method for reducing noise from these motors under the full range of operating conditions than in the case of motors whose pressures do not vary. There is an established method of calculating the cylinder pressure and the moment on the swash plate from the specifications of the pump[6]. That method is explained in detail in the following section.

5.2.1. Nomenclature and structure

Fig. 16 shows the structure of the pump. Here, when axis A turns, the swash plate B vibrates, causing a reciprocating motion of piston C and its cylinder D, and, in turn, pumping the oil through the mechanism. The valve plate E consists of two parts, the discharge port E1 and the suction port E2. During the discharge process of the pump, the cylinder ports are aligned with the discharge port E1, and during the suction process, they are aligned with the suction port E2.

The symbols have the following meanings:

Pcy: Cylinder pressure
Pdel: Discharge pressure
Psuc: Suction pressure
V: Volume of oil in cylinder
V0: Volume of oil in cylinder at t=0
V1: Fluctuation in oil volume due to piston stroke
V2: Volume of oil entering cylinder at discharge port
V3: Volume of oil entering cylinder at suction port
V4: Volume of oil leaking from cylinder
Dp: Piston diameter
PDp: Piston pitch circle diameter
θsw: Swash plate angle
Cdel: Flow coefficient for passage connecting discharge port and cylinder
Csuc: Flow coefficient for passage connecting suction port and cylinder
Adel: Area of restrictor in passage connecting discharge port and cylinder
Asuc: Area of restrictor in passage connecting suction port and cylinder
g: Gravitational acceleration
γ: Oil specific gravity
β: Oil compressibility
ω: Angular speed of pistons
t: Time
Fcyk: Thrust of kth piston
αk: Angle of kth piston
Pcyk: Cylinder pressure of kth piston
α0: Angle of piston #1 at t=0
n: Number of pistons

5.2.2 Equations

The change in cylinder pressure dPcy is found from the following equations:

$$dPcy = \frac{1}{V\beta}(-dV1+dV2+dV3-dV4)$$

$$dV1 = -\frac{\mathrm{Dp}^2\pi \cdot \mathrm{PDp} \cdot \omega \cdot \tan\theta sw \cdot \cos\omega t}{8}\,dt$$

$$dV2 = \pm\,\mathrm{Cdel} \cdot \mathrm{Adel} \cdot \sqrt{\frac{2g}{\gamma}\,|\,Pdel-Pcy\,|}\cdot dt$$

(Right side is positive when Pdel ≥ Pcy, negative otherwise)

$$dV3 = \pm\,\mathrm{Csuc} \cdot \mathrm{Asuc} \cdot \sqrt{\frac{2g}{\gamma}\,|\,Psuc-Pcy\,|}\cdot dt$$

(Right side is positive when Psuc ≥ Pcy, negative otherwise)

$$V = \mathrm{V0} + \frac{\mathrm{Dp}^2 \cdot \pi \cdot \mathrm{PDp} \cdot \tan\theta sw \cdot \sin\omega t}{8}$$

The moment (M) acting on the swash plate around its rotational axis is given by:

$$M = \sum_{k=1}^{n} \frac{Fcyk \cdot \mathrm{PDp} \cdot \sin\alpha k \cdot \sec^2\theta sw}{2}$$

$$Fcyk = \frac{\mathrm{PDp}^2 \cdot \pi \cdot Pcyk}{4}$$

$$\alpha k = \frac{2\pi(k-1)}{\mathrm{n}} + \alpha k \cdot t + \alpha 0$$

Fig. 17 provides a comparison of the calculated pressures and the actual measured pressures in a cylinder of a pump with the basic specifications; the two curves matched quite well. There was also a good match of the pressure variations during the $\theta 1$ range, over which the pressure was building to the maximum, and during the $\theta 2$ range, over which it was falling to the minimum. Fig. 18 shows the calculated fluctuations of moment on the swash plate using calculated cylinder pressure and actually measured values of the moment. The peaks at each order frequency matched well, allowing an estimate of the noise level of improved pump designs.

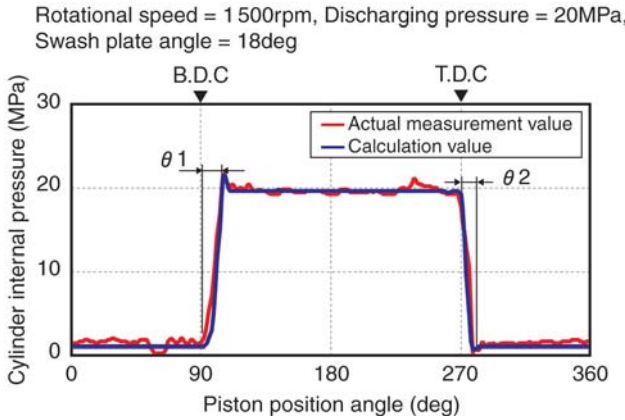


Fig. 17 Cylinder internal pressure

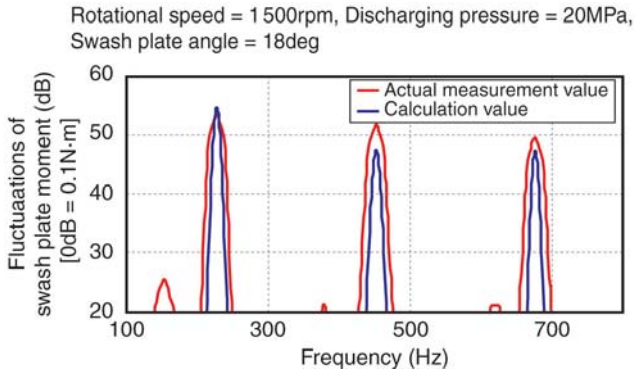


Fig. 18 Fluctuations of swash plate moment

5.3. Methods for Reducing Noise

Methods for reducing pump noise were derived using the equations just explained above and the results of experiments with those designs are described here. Fig. 19 shows the experimental device. The cylinder pressure was measured with a pressure sensor attached to the cylinder. The moment applied to the swash plate was calculated by measuring the loads on the two piston rods and converting these values.

5.3.1. Optimization of cylinder pressure

Fig. 20 shows the relation of the θ of the cylinder pressure θ (= $\theta 1$ = $\theta 2$) and fluctuations of moment on the swash plate in a 9-piston pump. This figure makes it plain that, if θ is 20° or 40°, the swash plate moment fluctuations will be small. There are two particular values of $\theta 1$ and $\theta 2$, which result in low swash plate moment fluctuation. These angles were optimized to take advantage of this tendency of the swash plate moment fluctuation.

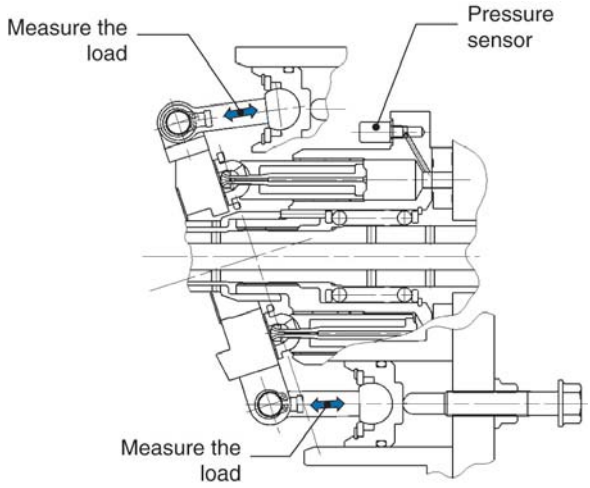


Fig. 19 Experimental equipment

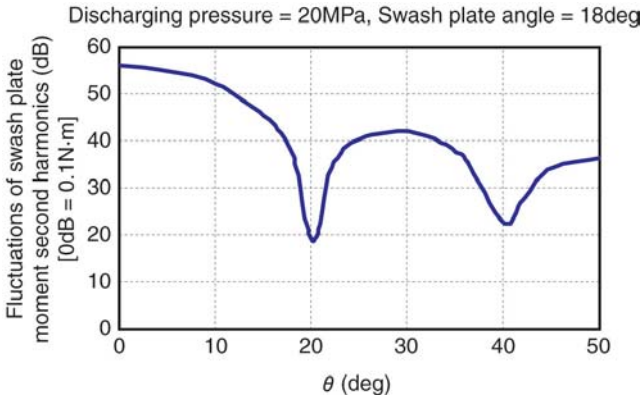


Fig. 20 Relation between θ and swash plate moment

Fig. 21 displays an improved valve plate for a pump with the basic specifications (9 pistons) whose port timing has been adjusted to provide $\theta 1$ and $\theta 2$ near 20°. The cylinder port is connected with the discharge port 20° before bottom dead center (B.D.C.). By introducing the high pressure of the discharge port into the cylinder while the cylinder volume is still in the process of being increased, there results a smoother pressure transition. Again, the cylinder port is connected with the suction port at 20° before top dead center (T.D.C.), while the cylinder volume is still being decreased, by introducing the cylinder pressure into the suction port to allow a smooth pressure transition.

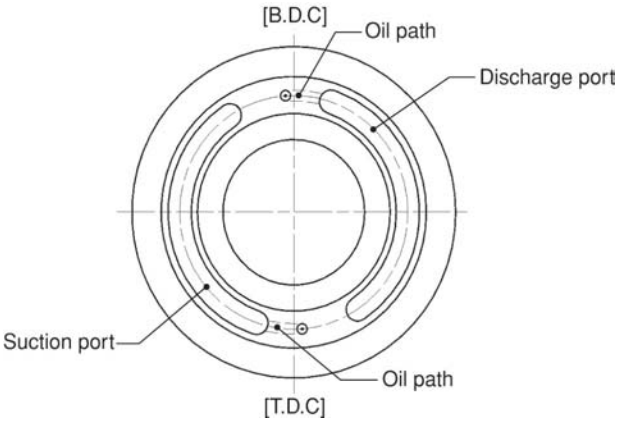


Fig. 21 Port timing change valve plate

Figs. 22 and 23 show experimental measurements of the cylinder pressure and of the fluctuations of moment on the swash plate, respectively. The specifications of the valve plate for the new port timing enable control of both $\theta 1$ and $\theta 2$ at about 20°. The fluctuations of the moment on the swash plate have been reduced and compared with the basic model, showing a beneficial effect of adjusting $\theta 1$ and $\theta 2$ to 20°.

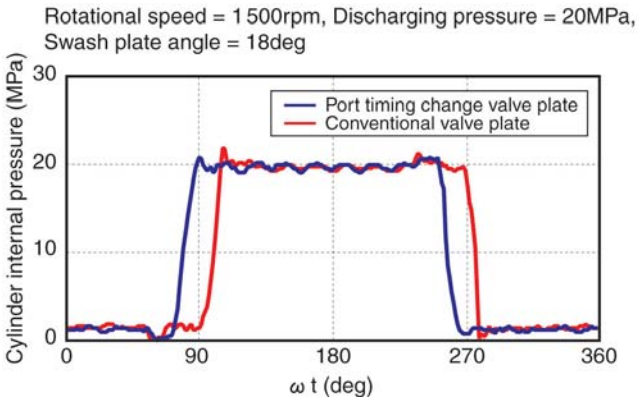


Fig. 22 Cylinder internal pressure with port timing change valve plate

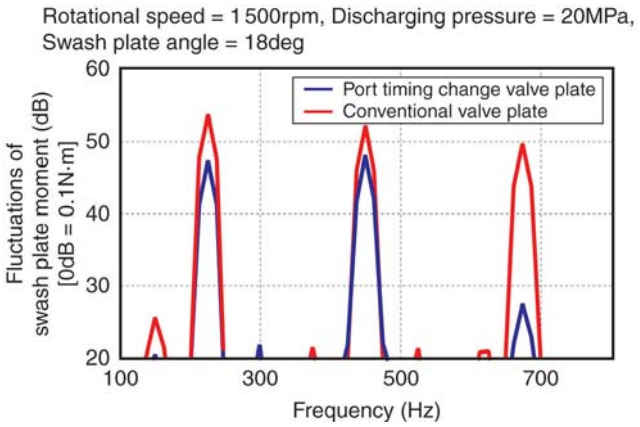


Fig. 23 Fluctuations of swash plate moment with port timing change valve plate

5.3.2. Number of pistons

This section describes the reduction of noise by increasing the number of pistons. Fig. 24 shows the relation of altered piston number with θ (= $\theta 1$ = $\theta 2$) and swash plate moment fluctuation. Increasing the number of pistons from 9 to 11 lowers the swash plate moment fluctuation.

Fig. 25 shows test results for the displacement at the Mt point. The peak displacement has been reduced, indicating a benefit from increasing the number of pistons to 11.

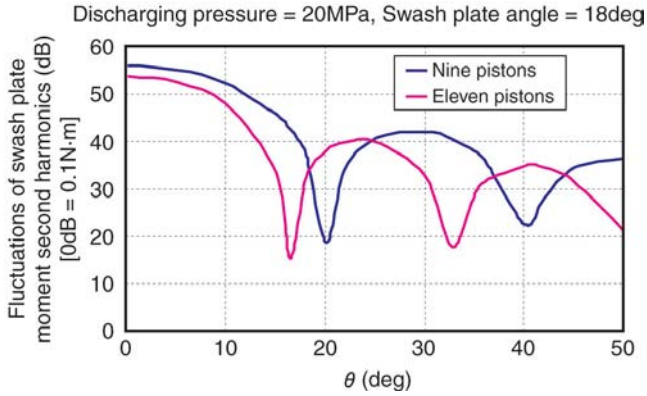


Fig. 24 Relation between number of pistons and fluctuations of swash plate moment

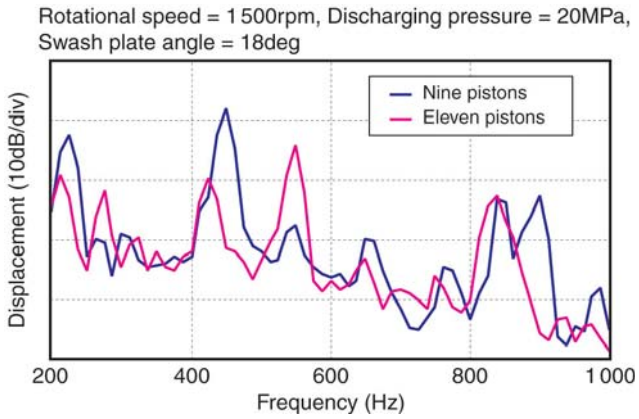


Fig. 25 Relation between number of pistons and displacement of mounting point

5.3.3. Mechanism for variable port timing

Fig. 26 shows a proposed mechanism for variable port timing in order to optimize the cylinder pressure for pumping conditions (pressure, swash plate angle, pump speed). This controls the timing of connections of the cylinder ports with the discharge and suction ports in order to maintain the $\theta 1$ and $\theta 2$ of the cylinder pressure in the neighborhood of 20° under differing operating conditions.

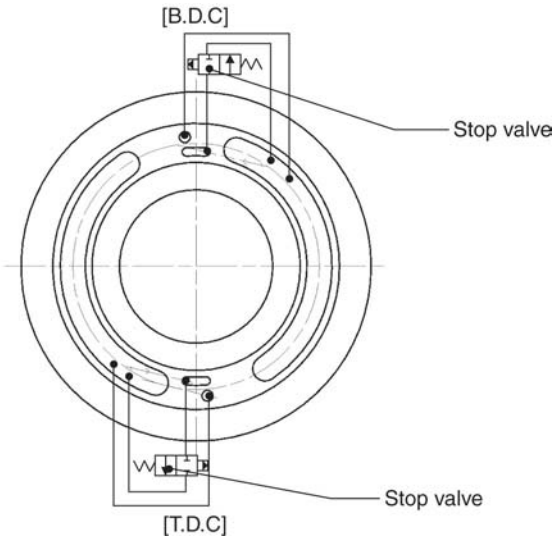


Fig. 26 Variable port timing system

Fig. 27 shows an estimate of mount displacement when the vehicle is traveling at a low speed and these conditions: swash plate angle, 6°; pump speed, 700 rpm; and pressure, 10 MPa. Displacement is predicted to be lower if the variable ports are closed. Fig. 28 shows an estimate of mount displacement while the vehicle is being accelerated, under the following conditions: swash plate angle 18°; pump speed 1,500 rpm; and pressure, 20 MPa. Here, mount displacement is lower if the variable ports are open. Thus, the closed or open condition of these ports may be selected on the basis of the operating conditions in order to minimize noise.

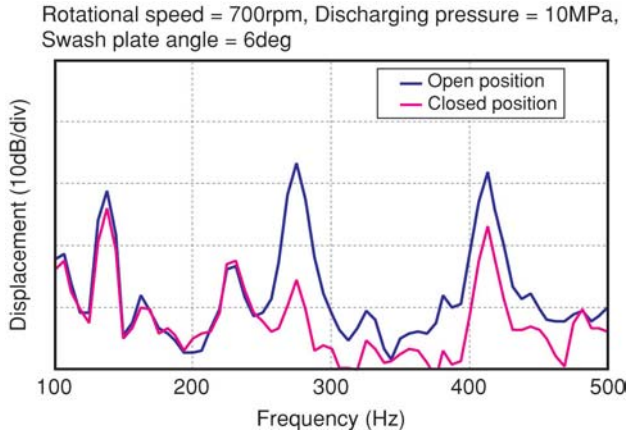


Fig. 27 Displacement of mounting point at low vehicle speed

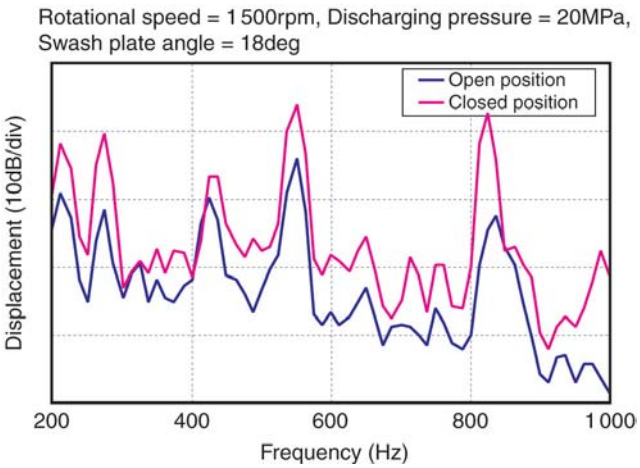


Fig. 28 Displacement of mounting point when accelerating

5.3.4. Cylinder ports with unequal pitch

Cylinder ports with unequal pitch were employed with the goal of reducing the prominence of both the fundamental order and the harmonic component of pump vibration (Fig. 29). By leaving the piston pitch even while introducing variation in the port pitch, variations in the cylinder pressure timing were introduced. Specifications were chosen on the basis of calculations in order to avoid large increases in the fluctuations of moment on the swash plate or in the fluctuations in specific frequencies.

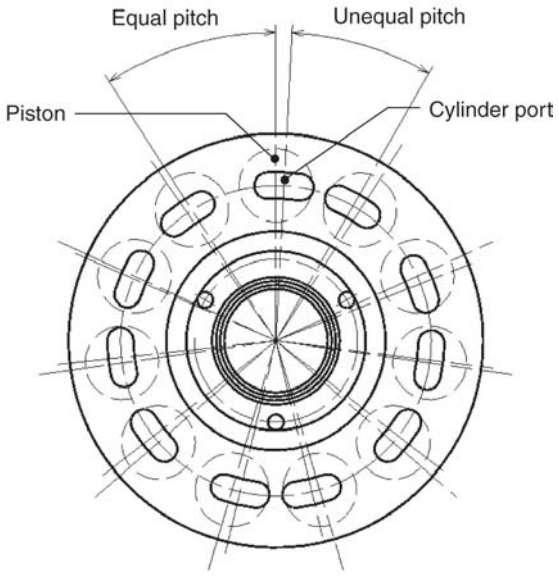


Fig. 29 Unequal pitch cylinder port

Fig. 30 shows a comparison of mount displacement in pumps with even-pitch cylinder port spacing and uneven-pitch cylinder port spacing. Not only did the change to uneven pitch result in a lower peak mount displacement, in the high-frequency region, no large displacement of specific frequencies was observed. These effects mean that the sound quality becomes much less annoying. Thus, the anticipated pump noise in an actual cabin has been reduced more than expected from the data.

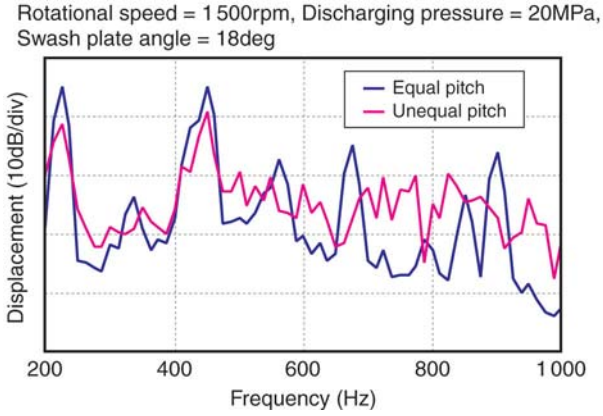


Fig. 30 Displacement of mounting point when unequal pitch cylinder port

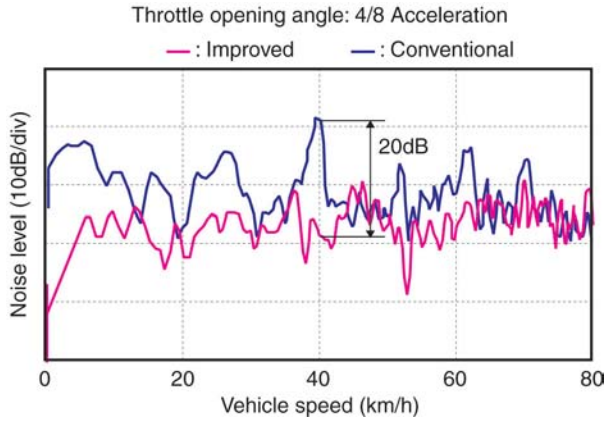


Fig. 31 Pump noise level in the cabin

As shown in Fig. 31, adoption of the above measures against noise has resulted in a reduction of pump noise in the cabin of, at a maximum, 20 dB below the noise from the current pumps. These measures can also be expected to reduce hydraulic motor noise.

6. Summary

Research was carried out on automotive oil hydraulics CVT for adoption in large-displacement, transverse engines for FFD vehicles. The following results were obtained:

(1) A high cruise efficiency was obtained in an oil hydraulics CVT by using a high-efficiency HMT equipped with a lock-up brake and with part lubrication in the pump and motor to reduce the agitation loss.

(2) The speed of the motor reaches 7,000 rpm at the peak speed of the vehicle, but by using bowl type slippers, which are exposed to lower centrifugal force, and by adding a sliding part to the slipper to aid cooling, better prospects for durability were realized.

(3) It was shown that there is a correlation between the noise in a real vehicle and the fluctuations in moment on the swash plates in pumps and motors. The pump was used as an example to verify that a calculated value for fluctuations in moment on the swash plate closely matched observed fluctuations. Then, a design was developed for varying port timing to adjust cylinder pressure in accordance with driving conditions, and the number of pistons was increased to 11; these measures reduced swash plate moment fluctuations. Also, a cylinder port design with unequal cylinder pitch was tested; no large displacement of characteristic frequencies was observed and pump noise was reduced, so that the quality of pump noise was no longer annoying.

7. Acknowledgements

The writers would like to use this space to express their deep appreciation to the many people inside and outside Honda for their assistance.

8. References

(1) Nishimura, S., et al.: “An Oil-Based Continuously Variable Transmission for Small Lawn Mowers”, HONDA Technical Review, Vol. 2, pp. 67–77 (1990)

(2) Saito, M.: “Introduction of PGM-HMT System for ATV”, Autumn Seminar 2001, Japan Fluid Power System Society, pp. 43–50 (2001)

(3) Ishihara, S.: PISTON PUMPS AND MOTORS Theory & Practice, Tokyo, OHM, pp. 127–133 (1979)

(4) Yamauchi, K., Yamamoto, T.: “The Noise of Hydraulic Pump and a Method for Reducing the Noise Level”, Mitsubishi Heavy Industries Technical Review, Vol. 12, No. 4, pp. 78–85 (1975)

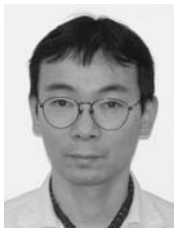
(5) Inoue, K., Nakazato, M.: “A Study on Noise Characteristics of a Swash Plate Type Variable Delivery Axial Piston Pump”, Kayaba Industry Technical Review, Vol. 9, pp. 10–17 (1994)

(6) Ebara, C., Sano, M.: “Vibrative Force of a Piston Pump”, Transactions of the 236th Lecture Meeting, the Japan Society of Mechanical Engineers Kansai Division, pp. 37–40 (1976)

■ Authors ■


Takashi IINO


Akihito OKUDA


Kazuaki SAKAI


Mikihiro TAKANO


Tetsushi ASANO


Koichi FUSHIMI


Masashi TANAKA

The Development of a New Compact CVT for the Fit

Makoto SUMI* Hisashi KUNII* Shuichi FUJITOMO*
Shuji ICHIJO* Takashi HASEGAWA* Yukihiko FUKUSHIMA*

ABSTRACT

Honda has developed a new continuously variable transmission (CVT) for use with new-generation power plants, and this compact, lightweight CVT, known as the Multimatic S, has been installed on the Fit. The redesigned flywheel, oil pump, clutch, and transmission case used in this CVT reduce the number of parts by 15% while simultaneously lowering friction and improving transmission efficiency by 5% over the 1999 model Logo. The new electronic control also provides creep control optimized for cruising conditions and automated switching of the shift schedule. These have yielded both improved fuel economy and a feeling of responsiveness to a wide range of driver demands.

1. Introduction

Year by year there has been increasing demand for better automotive fuel economy, with the focus being protection of the global environment and conservation of resources. The Honda Multimatic, which has excellent fuel efficiency, was used in the ’96 Civic and the ’98 Logo. Then, for the ’99 Hybrid car “Insight”, an even more highly efficient, compact CVT Multimatic was used.(1)

Now, a new CVT has been developed for the new generation, a New Small “Fit”, which replaces the Logo. The technology for making the CVT compact is based on that adopted for the Insight, and further modified.

This paper introduces the new technology.

2. Aims of Development

In order to actualize the Fit’s concept, the following performance enhancements and ease of manufacturing improvements were pursued.

(1) A compact design that responds to a short nose package layout, to achieve both “a spacious interior” and “best-in-class collision safety performance.”
(2) Making the CVT low friction and highly efficient, and modifying CVT controls, all to contribute to “best fuel economy in the world for its class.”
(3) Start-off and shift controls that give “smooth driving pleasure,” matching the driver’s senses.
(4) Improve ease of manufacture by reducing the number of parts.

3. Basic Layout and Principal Specifications

Fig. 1 and Fig. 2 show the main section of the CVT and an outside view, while Table 1 gives the major specifications.

The main changes from the ’99 Logo (referred to as previous model, hereafter) include a shorter pulley axis length, elimination of the oil pan (a structure without an oil pan), changes to control system layout, adoption of a trochoid pump and elimination of the drive chain, and adoption of a single mass flywheel.

* Tochigi R&D Center

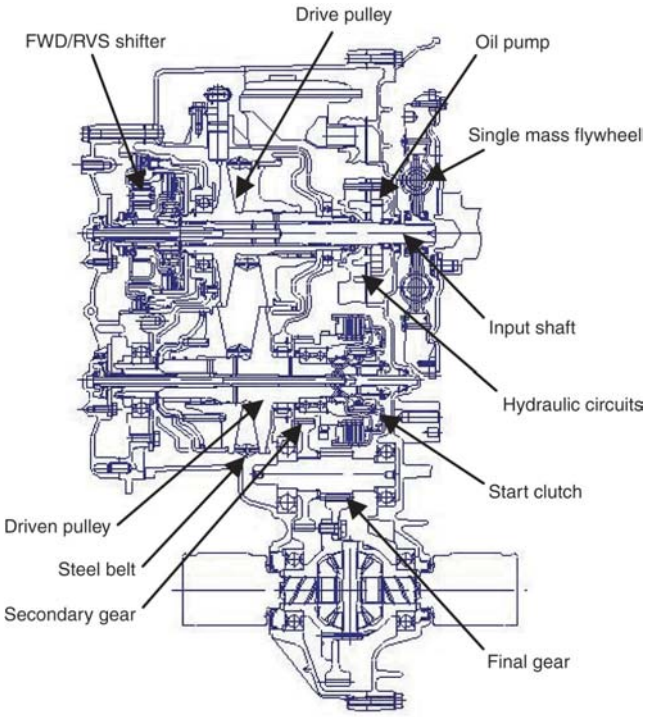


Fig. 1 Main section

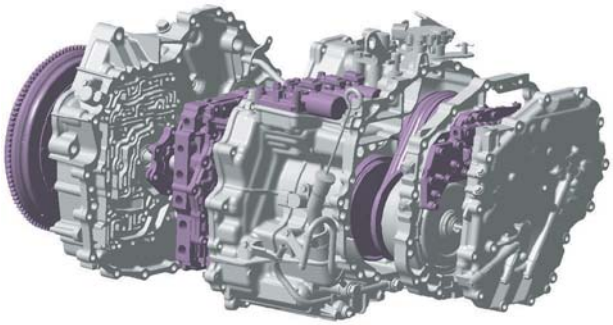


Fig. 2 Outside View

Table 1 Major Specification

		2002 model Fit	1999 model Logo
Engine Specification	Type	1.3L 2VLV	1.3L 2VLV
	Max. power (kW/rpm)	63/5 700	49/5 500
	Max. torque (N·m/rpm)	119/2 800	103/2 500
Ratio	LOW ≀ OD	2.367 ≀ 0.407	2.466 ≀ 0.449
	Secondary	1.333 (52/39)	1.333 (52/39)
	Final (2WD)	4.333 (65/15)	4.357 (61/14)
	Final (4WD)	4.714 (66/14)	
	Reverse	4.226～2.367	2.466
Dimension	Overall length (mm)	349	372
	Pulley axis length (mm)	143	155
Weight (Wet)	2WD (kg)	74.5	80.4

With these changes, in comparison with the previous model, a 6.2% reduction in total width, and a 7.3% reduction in weight were achieved. The number of parts was reduced by 15%, from 770 to 655. Fig. 3 shows parts and weight comparison to the previous model.

Fig. 4 shows an external shape comparison with the previous model (contour profile).

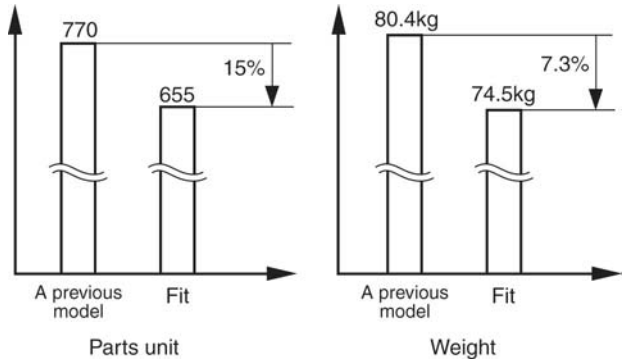


Fig. 3 Comparison of complete parts unit and weight

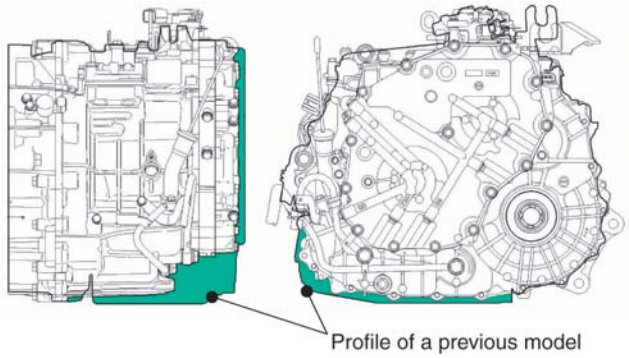


Fig. 4 Comparison of external shape

4. Technologies Adopted

4.1. Single Mass Flywheel

4.1.1. Background to application

The previous model used a high damping performance dual mass type flywheel, in order to prevent gear rattling noise during reverse idling, generated by the planetary gear

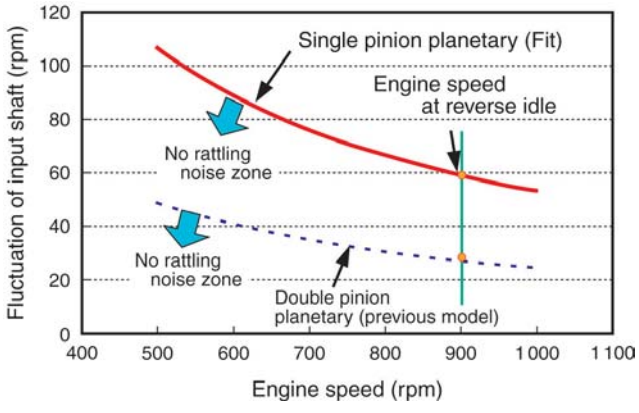


Fig. 5 Rattling noise zone chart

for reverse mechanism. However, with the change in planetary gear from a double pinion type to a single pinion type, and with a reduction in pulley inertia by shortening the pulley axis length, the generation limit for gear rattling noise due to rev fluctuation is more than twice what it has been conventionally, so it became possible to change to a single mass flywheel. Fig. 5 shows the reversing gear rattling noise generation limits with single and with double pinion planetary gears.

4.1.2. Basic structure

Because the inertial mass is not divided in a single mass flywheel, it is a simpler structure than the dual mass flywheel. Comparing the number of parts, a dual mass flywheel has 39 parts, while a single mass type has 29 parts. Fig. 6 shows the structure of the single mass flywheel.

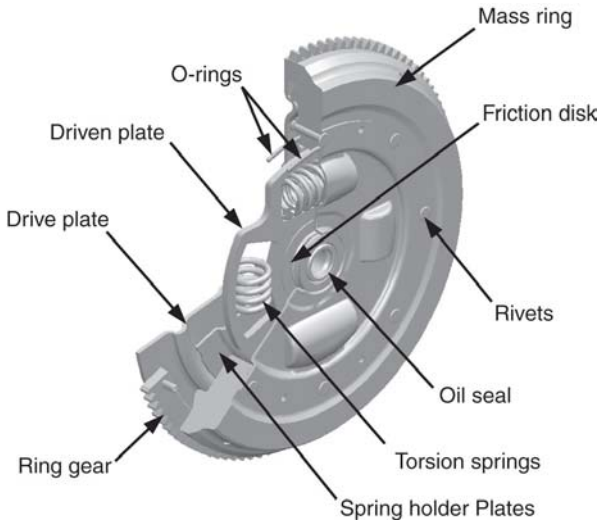


Fig. 6 Structure of single mass flywheel

Regarding torsion characteristic, as shown in Fig. 7, with 3-stage characteristic using two of each 3 types of springs, maximum torsion angle ±25°, and torque capacity is a 207 Nm long travel type.

In addition, in order to generate hysteresis torque, plastic friction disks were added to each space between spring holder plates and driven plates, and utilizing spring holder plate's elastic deformation, pressing load on friction disks is generated.

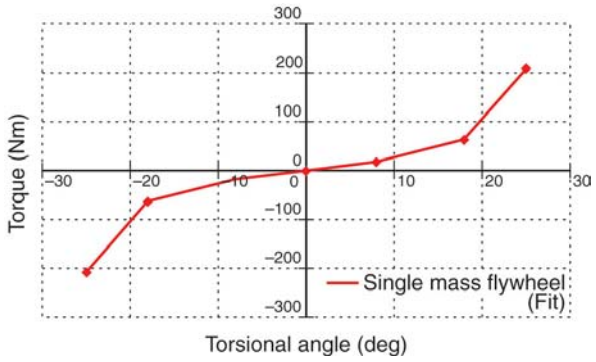


Fig. 7 Torsion characteristics

4.1.3. NV improvements

With a dual mass flywheel, inertial mass is divided into primary and secondary, while with a single mass flywheel, the inertial mass is one piece, so it became possible to increase engine side inertial mass. As a result, engine rev fluctuations are reduced, and there is an improvement in NV performances, such as surge and booming noise.

Fig. 8 shows engine rev fluctuation with both flywheels.

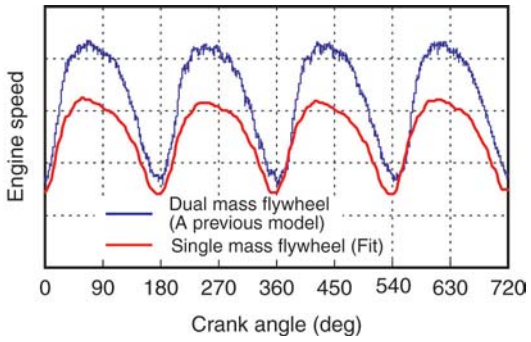


Fig. 8 Cycle irregularity

4.2. Direct Driven Trochoid Oil Pump

4.2.1. Reduction in number of parts (rational design)

With the previous model, the input shaft drove the pump shaft with a chain. With this CVT the input shaft directly drives the pump, so parts such as the chain, sprockets, etc., were eliminated, reducing the number of parts.

The pump itself is a trochoid pump using a sintering rotor, with the inner rotor driven by input shaft spline.

A comparison with the previous model is shown in Fig. 9.

4.2.2. High pressure measures

As this CVT uses a discharge pressure of 3.5 MPa or more, there is a drop in discharge performance due to deformation of the pump body. FEM analysis was used for carrying out optimization of each pump part's shapes, at the same time, pump body was changed to cast iron to reduce deformation. By these effects, discharge performance in a high pressure state can be maintained.

Fig. 10 shows the results of the FEM analysis.

In addition, because the pump rotor's and body's coefficients of thermal expansion are roughly equal, there is little side clearance changes due to temperature changes, and stable discharge performance is obtained.

4.2.3. Discharge performance

The oil pump discharge performance is shown in Fig. 11. With a theoretical discharge amount of 9 cc/rev, at high oil temperature, low rev speed, the pump discharge amount can be maintained at a level equivalent to that with previous model, or better.

4.2.4. Friction reduction

Many trochoid pumps have a hub on the inner rotor, and the structure is supported by a bush. With that particular structure, hydraulically there is a load on the inner rotor, and momentum load is generated by the offset of rotor and hub.

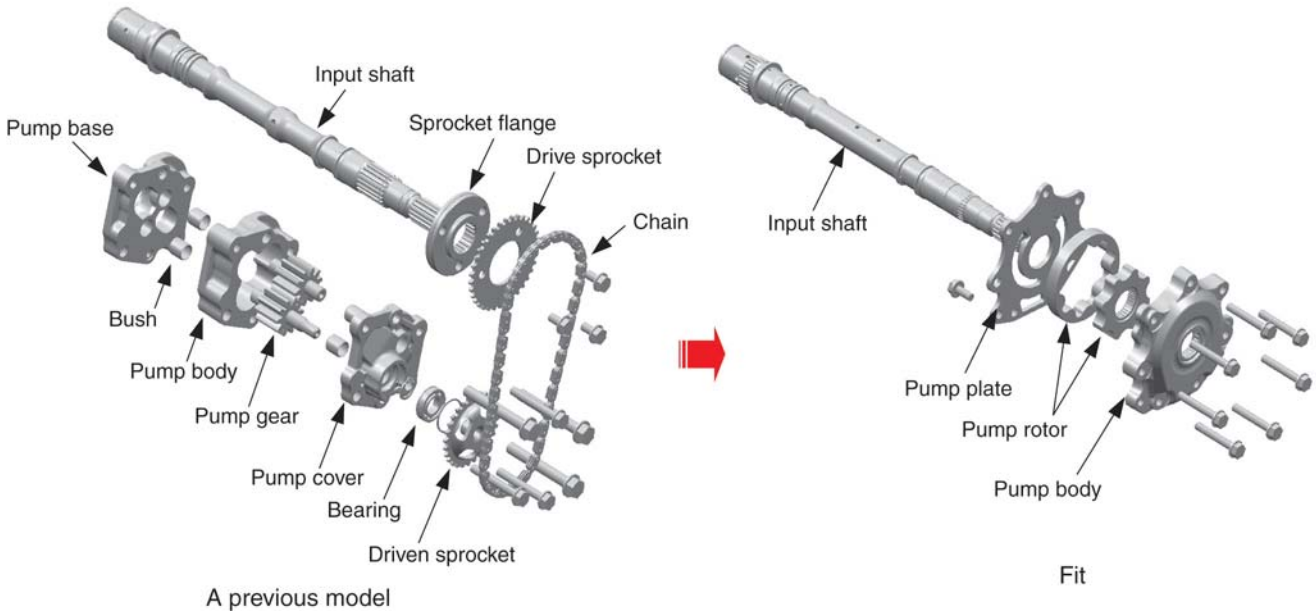


Fig. 9 Oil pump structure

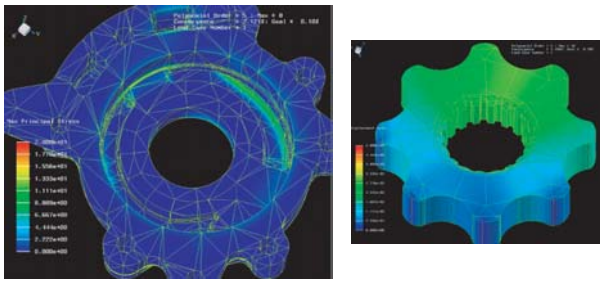


Fig. 10 Pump body stress analysis with FEM

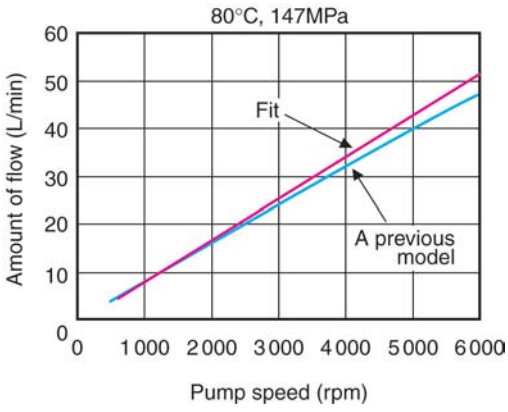


Fig. 11 Oil pump delivery performance

With this oil pump, in order to eliminate the friction caused by the offset load, the structure is such that the inner rotor is supported by the input shaft, and there is a needle bearing on the pump body that determined the position of the input shaft.

Fig. 12 shows a comparison with the conventional structure.

In addition, by eliminating the chain to drive the pump, both drive friction and the friction caused by oil agitation has been reduced.

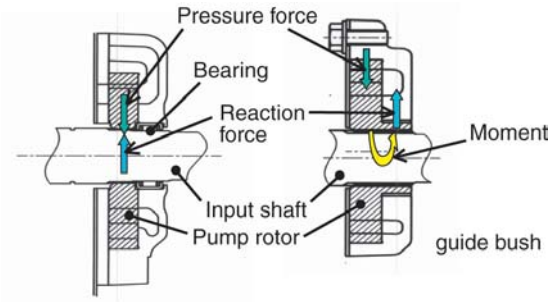


Fig. 12 Reduction of oil pump rotor friction

4.2.5. Reduction in pump noise

To improve pump noise, it is necessary to reduce radiation noise generated by the pump itself, and reduce the transmission of pump vibration to the vehicle body.

As a modification for pump unit radiation noise, the intake port timing advance angle is established to balance manifold vacuum and discharge performance. Discharge noise countermeasures were established by setting the pressurization compression amount between intake port and discharge notch and by setting the timing, width, and depth of the discharge notch 1st stage flat part. Furthermore, by setting the 2nd stage cone shape, pressure change during discharge is made gentler, and generation of cavitation sound is prevented. Fig. 13 shows the discharge notch shape.

As a transmission noise countermeasure, a rib was added to the rear mounting part of the flywheel case to reduce the pump vibration transmission to the body, and as a result, body cabin noise was reduced.

4.2.6. Improved ease of manufacture

(1) Ease of Machining

Because the inner rotor does not have a hub, it is possible to grind both sides of the rotor at the same time, using a double head grinding machine, thereby improving dimensional accuracy and machining speed.

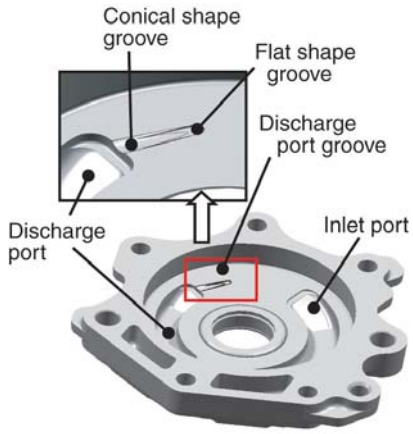


Fig. 13 Shape of discharge port notch

(2) Ease of Assembly

With this CVT, the valve body that was fitted to the oil pump is directly placed on the flywheel case, and is directly driven from the input shaft.

Thanks to this, ease of assembly is improved, as there is no assembly of the drive chain or sprockets, etc. Also, by making the pump body, rotors, and plate a sub-assembly, it is possible to guaranty function with the pump unit parts.

4.3. Structure without an Oil Pan

By creating a layout where the starter motor, conventionally on the CVT side, is moved to the engine side, and moving the control body that had been in the center of the oil pan into the space created by the starter motor shift, the oil pan was eliminated, and the number of case parts was reduced.

Fig. 14 is a comparison with the conventional CVT with an oil pan. As shown in the diagram, integrating the 3 linear solenoid valve bodies that control the drive and driven pulleys and the start clutch control, they are placed on the top of the CVT. The reverse inhibitor solenoid valve, too, is placed on the outside, improving the ease of maintenance of electronic control parts. Other hydraulic control parts, in combination with an oil pump, are placed so that they are directly mounted to the flywheel case. As for the space between the flywheel case and the pulley chamber to its left, conventionally the oil pump and drive parts are located there, but the drive chain and sprockets have been eliminated. By combining the pump with the control body, it was possible for the hydraulic system to be placed in the space conventionally occupied by the oil pump.

From these changes, oil-filling capacity is increased, and oil level can be set at a lower level, thereby reducing agitation resistance.

4.4. Start Clutch Modifications

4.4.1. Bonded seal

Conventional clutch pistons are inserted into separate oil seals, but with this clutch the pistons and the oil seals are integrated using a bonded seal piston.

As a result, the start clutch is more compact, and the number of parts is reduced. Fig. 15 shows as comparison with the previous model's start clutch pistons.

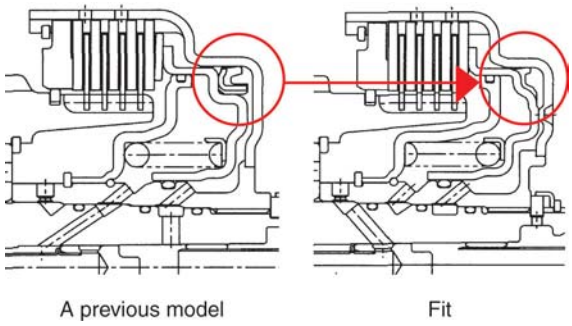


Fig. 15 Structure of start clutch

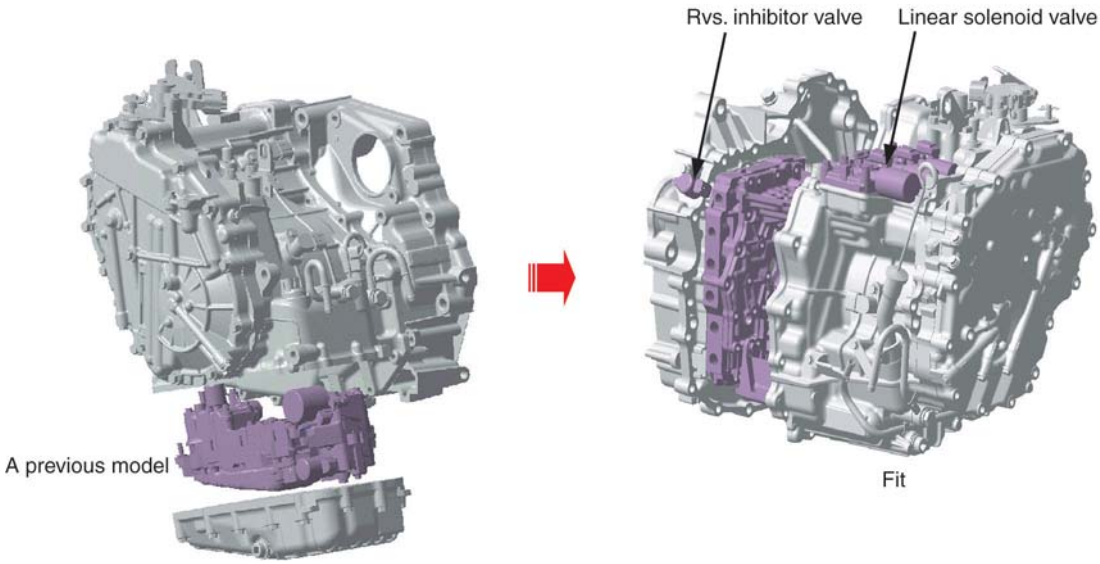


Fig. 14 Casing without an oil pan and valve body layout

4.4.2. Modifications to friction material

The friction material adopted at this time has highly heat resistant fibers added in comparison with the conventional friction material, and other component proportions were revised. Through these measures, durability was enhanced and at the same time good friction characteristics were maintained.

By adopting this material an even smoother start-off performance was achieved. Fig. 16 is an enlargement of the friction material surfaces, and Fig. 17 compares friction characteristics. There is an improvement in friction characteristics throughout the whole range.

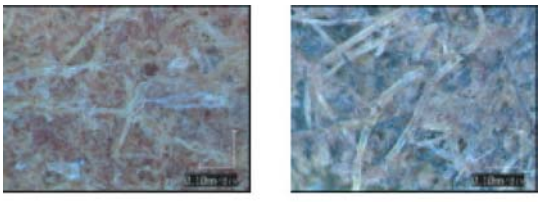


Fig. 16 Magnified disc surface

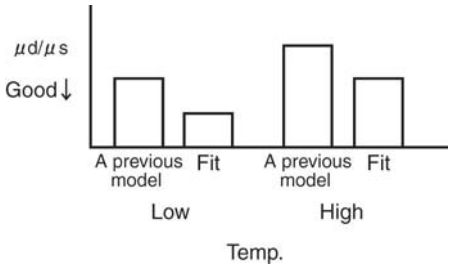


Fig. 17 Disc characteristic

4.5. Creep Control

Creep is an essential function of the automatic transmission vehicles (including CVT), from the point of view of start-off smoothness and ease. On the other hand, because traction force is generated when stopping with brakes, it affects fuel consumption and body vibration. With the new CVT the start clutch creep control is revised, maintaining the creep function only when it is necessary to reduce fuel consumption and body vibration during idling.

When modifying the control it was established that the following driving states require creep when starting off.

- Starting off partway up a hill
- Driving slowly, or starting and stopping repeatedly along in a traffic jam.
- Inching forward in a garage or when parallel parking.

In order to be able to distinguish these situations, the following were established.

(1) Grade judgment
(2) Speed history judgment
(3) Shift position judgment

For conventional inclined road detection methods, a certain amount of speed is necessary (start-off clutch completely tightened), so at low speeds judgment is not possible. With this new control, transmitted torque is calculated from start-off clutch control pressure, and by assuming the clutch slip range drive power it is possible to make a grade judgment even in the low speed range.

Fig. 18 is a flow chart of grade calculation.

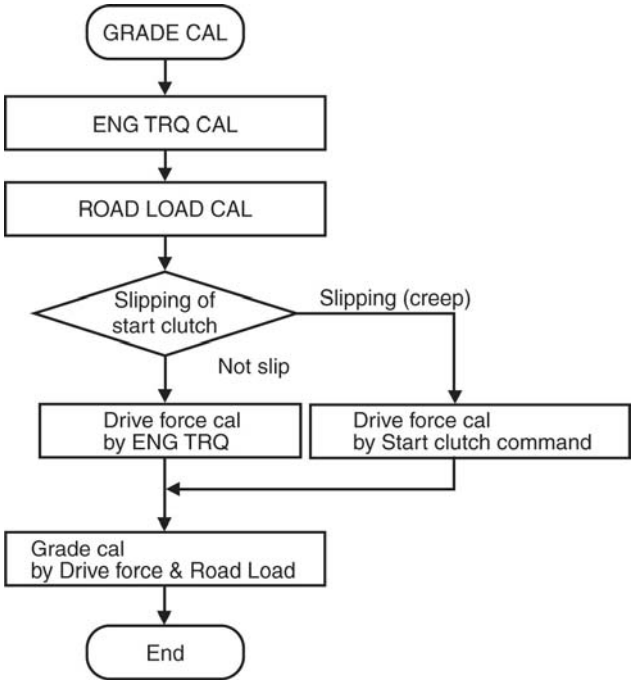


Fig. 18 Flow chart of grade calculation

As outlined above, by appropriately distinguishing the condition that needs creep, it became possible to reduce fuel consumption and body vibration during idling, while maintaining creep performance.

4.6. Shift Control

4.6.1. Enhancements to shift responsiveness

The Fit uses the same pulley pressure direct control method[(1)] as that in the Insight. Drive and driven pulley pressures are controlled separately, and shift speeds can be set freely. Due to this, rapid kick-down response is possible, and from gentle acceleration to sudden acceleration a linear acceleration feeling is actualized, matching the driver's senses. (Fig. 19)

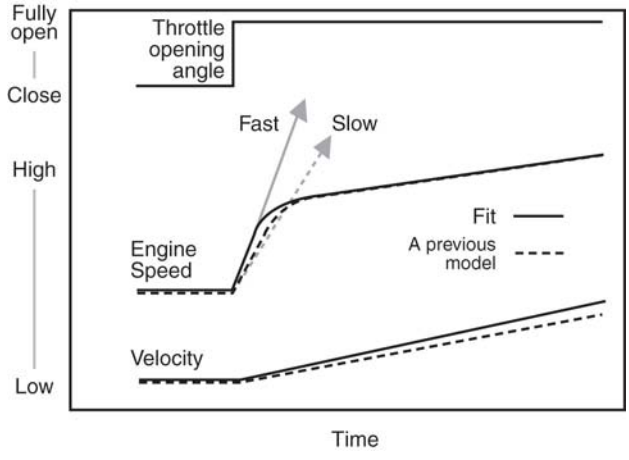


Fig. 19 Kick down response

4.6.2. Shift schedule

The shift schedule in the drive range is established to provide comfortable driving, whether on ordinary roads or joining traffic flow on a highway. However, when driving in the suburbs or on mountain roads, the driver wants to drive with more positive acceleration (aggressive driving), and in this state, it is desired that shift schedule with engine revs is set higher (low ratio side) than the normal drive range shift schedule. Therefore, with the Fit, two shift schedules have been established in the drive range — D1 and D2. Controls have been adopted that automatically switch between them, according to the driver's driving indication.

(1) D1 Schedule

With a shift schedule that focuses on fuel consumption, the throttle opening is in the low to medium range, engine revs are restricted, and the vehicle is running mainly on engine torque.

In the medium range of throttle opening and higher, responsiveness is maintained using the kick-down mode where shifting is quick.

(2) D2 Schedule

Rev speed in the medium throttle opening range is set higher than the D1 schedule to increase drive power, while in the low throttle opening range, the difference from D1 is set small to prevent throttle operation busyness and fuel economy drop due to excessive effectiveness of engine brake during cruising.

Fig. 20 shows a comparison between D1 and D2 shift schedules.

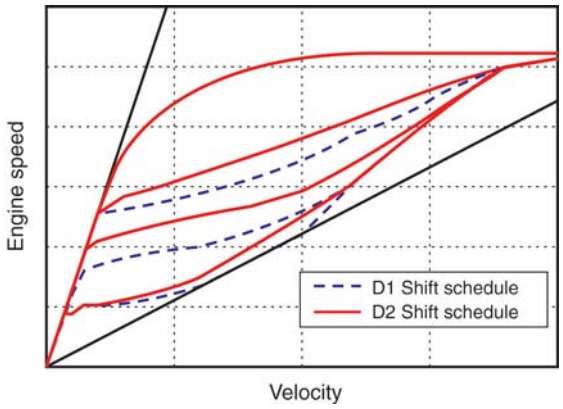


Fig. 20 D1 and D2 shift schedule

4.6.3. Automatic switching between shift schedules

Fig. 21 is a concept diagram showing the relationship between driver driving intent and throttle opening.

When the driver is driving along in a normal flow of traffic, the state is like that in the range at the bottom right of the diagram with low throttle opening. In contrast, when the driver frequently accelerates and decelerates, for example on winding mountain roads, the throttle operation state jumps to the top left range in the diagram.

Fig. 22 shows actual measurements of vehicle speed and throttle opening, as well as the relationship with shift schedule.

The circle on the bottom left is around normal city driving distribution, and the D1 shift schedule is selected.

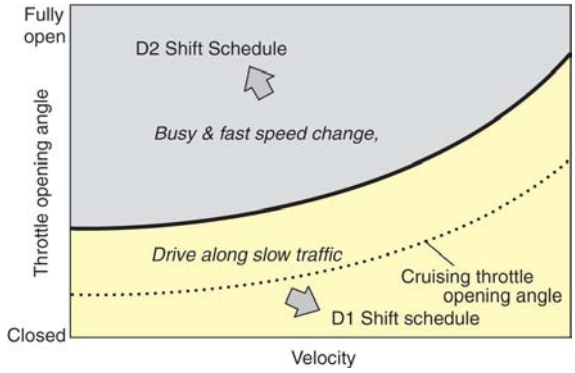


Fig. 21 Condition of shift schedule

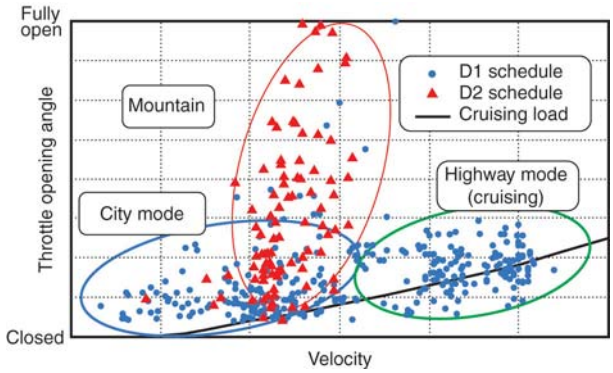


Fig. 22 Throttle distribution chart by shift schedule

The circle on the bottom right is around normal highway driving, as when there is driving with the traffic flow and no overtaking, then the D1 shift schedule is selected.

The circle in the center encloses the distribution of driving on mountain slopes, and because the throttle opening when stepping on the acceleration is greater than on a flat surface, the D2 schedule is selected.

As above, because the shift schedule automatically switches in response to the driver's driving pattern, in comparison with when it doesn't switch, a drive feeling with little uneasiness is obtained.

4.7. Efficiency Improvements[2]

Loss torque, causing a drop in transmission efficiency, involves resistance of metal belt rotation in drive and driven pulleys, oil pump drive torque, oil agitation resistance, etc., and measures were taken to reduce these factors.

4.7.1. Metal belt rotation resistance reduction

With a metal belt, there is friction between layered rings and elements due to the distance between rocking edges and saddles, and rotation resistance generated due to bend load, while rotating in drive and driven pulleys. As a result of optimum design of transmission capacity in line with engine output characteristics, it became possible to change the ring spec from the conventional 12 rings in 2 rows to 9 rings in 2 rows, thereby reducing belt transmission loss.

4.7.2. Oil pump load reduction due to line pressure reduction

The previous model's hydraulic control involved a linear

solenoid valve creating two pulley side pressures of high and low, and with a four-way valve, the high-pressure side level is adjusted, and shifting control is carried out. However, because this method always generates the maximum pressure necessary to shift normally for the minimum pulley required pressure, when the ratio is stable, such as during cruise driving, there is excess pressure, and the oil pump load is increased. With this new CVT, the drive and driven pulley pressures are separately and directly controlled by linear solenoid valves, making it possible to freely control pulley pressure in response to shift demands, and making it possible to reduce excess pressure during cruise driving. In addition, by adopting this control method, it is possible to have the drive and the driven pulley piston diameters be different, enlarging the piston surface area on the drive pulley side which in most case is the high pressure side when driving (1.3 times that of the driven side), so line pressure can be reduced even further.

Fig. 23 shows the pulley side pressure direct control system.

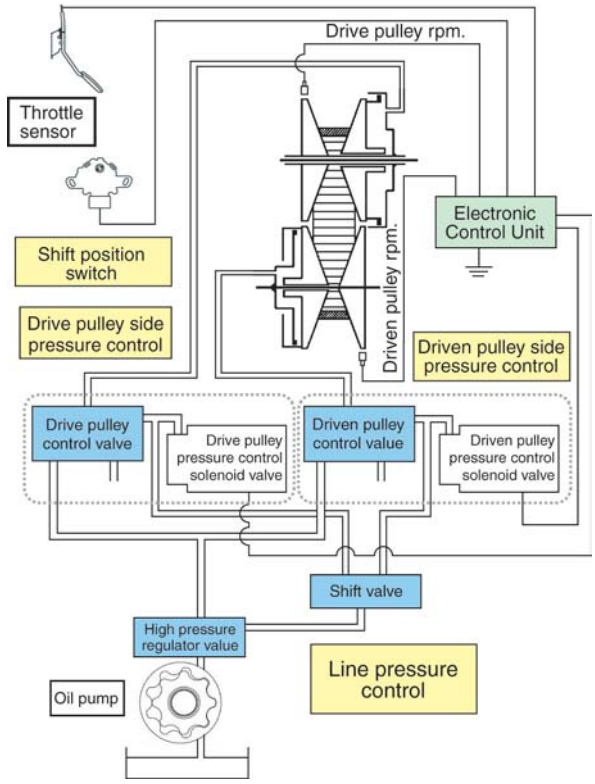


Fig. 23 Pulley side-pressure direct control

4.7.3. Reduction in oil agitation resistance

Agitation resistance is generated by contact between rotating parts and oil. The smaller the oil level, the less the agitation resistance.

As outlined in section 4.3, the oil level is reduced by adopting the new casing structure without an oil pan. In order to reduce it further, low oil temperature aeration measures were taken.

When operating at low oil temperatures, oil viscosity is increased, so there is a delay in return of the oil supplied to each lubricating part and the oil dispersed by agitation. Therefore, the oil level drop is even larger. Because of this, establishing oil levels is carried out according to a low temperature aeration limit, and in the opposite way, at high oil temperatures oil level rises and is a cause of agitation resistance increase. Therefore, a lubrication pressure switching control was added to reduce the lubrication pressure at low temperatures, thereby reducing the amount of oil supplied to each lubricating part, and that directly recirculates any excess to the oil pump. This results in reducing the amount of oil taken in from the strainer at low temperatures, thereby reducing the drop in oil level. Thanks to these measures, it was possible to set the oil level for filling 12% lower (filling amount 8% lower), at the drive pulley shaft center standard.

Agitation resistance is reduced due to this reduction in oil level, and due to the elimination of the oil pump drive-chain.

As a result of reduction of the 3 loss torques as described in sections 4.7.1 to 4.7.3, there is a 5% transmission efficiency improvement at 60 km/h cruising.

Fig. 24 shows a transmission efficiency improvement.

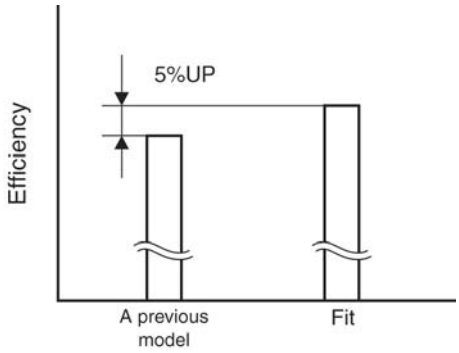


Fig. 24 Cruise efficiency at 60 km/h

5. Summary

A new CVT necessary to actualize the Fit concept was developed, with the following results.

(1) A design more compact than the previous model, incorporating a structure with no oil pan and a changed control system layout, which resulted in a reduction of 6.2% in overall length.
(2) By reducing agitation resistance, oil pump drive loss, and operation hydraulic pressure, transmission efficiency at 60 km/h was increased by 5% in comparison with the previous model. In addition, new creep control was developed to contribute to fuel consumption reduction.
(3) By enhancing shift responsiveness and introducing automatic switching of shift schedules, both fuel economy and linear acceleration performance that can respond to various situations were achieved.
(4) By adopting a structure without an oil pan, a single mass flywheel, and a direct driven pump, etc., there is a 7.3% reduction in weight, and a 15% reduction in the number of parts in comparison with the previous model.

6. In Conclusion

The new compact CVT developed in this project, the "New Honda Multimatic S", is the basic design of a transmission that can handle not only 1.3L class vehicles, but also those of even greater capacity. In the future, while expanding its application to more models, research will be continued toward even higher efficiency.

Finally, the authors would like to extend their sincere thanks and appreciation for the cooperation and support they received in the development of this transmission, from members of the development team and all of those at Honda.

References

(1) Ota, S., Kunii, H., Sumi, M., Fujimoto, S., Yamaguchi, T.: "Development of a Compact CVT for the Hybrid Car 'Insight' ", Honda R&D Technical Review, Vol. 12, No. 2, pp. 61–70 (2000).

(2) Sumi, M., Fujimoto, S.: "Development of a Compact CVT for Hybrid Automobiles", Automotive Technology, Vol. 54, No. 4, pp. 48–54 (2000).

■ Authors ■


Makoto SUMI


Hisashi KUNII


Shuichi FUJITOMO


Shuji ICHIJO


Takashi HASEGAWA


Yukihiko FUKUSHIMA

Development of Engineering BOM Data Management System

Masataka YAMAMOTO* Hideyuki TANAKA* Wataru FUJITA*

ABSTRACT

A new engineering bill of material (BOM) system was developed in order to shorten the development cycle and improve BOM accuracy. This BOM can perform integrated management of basic product information of all vehicle models, all types, and combinations of frame, engine, transmission, and so on. It also improves drawing release efficiency and facilitates connection with other systems. Based on a commercially available product data management package, this system has a three-tier system architecture for easier data linkage, and it runs on the sophisticated Windows NT Server for improved operation performance. This not only allows management of basic product information for all vehicle models, but also makes it possible to centrally manage information sharing and drawing data from the initial development stage through to mass production. Significant improvements have been made in the efficiency of design drawing release and reception work flow as a result.

1. Introduction

From 1980 through the mid 1990's, the System Department at the Tochigi R&D Center carried out extensive system development, including that of the engineering-BOM — the Honda Structure System (HSS hereafter) — in order to shorten the period of drawing issue and to improve the accuracy of BOM information. Examples include a part application indication processing system that made it possible to automatically calculate feature application indications for part data and product variation application (the Honda Feature System; HFS hereafter), a drawing release support system that carries out checks of application, of drawing history, and of configuration from CATIA drawing data, and a drawing distribution system that distributes drawings to suppliers and plants. In the development of the HSS, there was one development facility, five manufacturing facilities, 8 models, and approximately 400 product variations, and the system incorporated all of their needs. However, as the scale of development has grown in recent years, the number of models now is almost four times that of when the system was developed, and the number of product variations is now approximately 10 times what it had been. With the existing system capacity, it is now difficult to carry out processing. In addition to this capacity problem, because it is necessary for the system to adapt to the new style of development of recent years, a new engineering-BOM system (The New Engineering-BOM Worldwide System, referred to as NEWS hereafter) was constructed. It can manage vehicle product basic information in an integrated manner, is more efficient in drawing processing work, and can easily cooperate with other systems.

This BOM was developed by building unique Honda technology on the base of a commercially available software package, the first in the world as a mass production automobile supplier. Conventionally, this area of development has been "untouchable" and no technological evolution has been expected. However, with this NEWS it is much easier to introduce rapidly evolving technological innovations, in areas such as data communication or the IT field, into system development in this area. In addition, it is possible to communicate with other systems, without using copies of data. As for system configuration, conventional systems are built to work on a host computer, but this system utilizes a high speed PC in the business logic calculation domain, and so performance is improved. Even thinking about a stable system utilization rate, which can be a problem with this kind of system, by having multiple hardware configuration and development of independent control programs, stable utilization like that of a host computer was achieved.

* Tochigi R&D Center

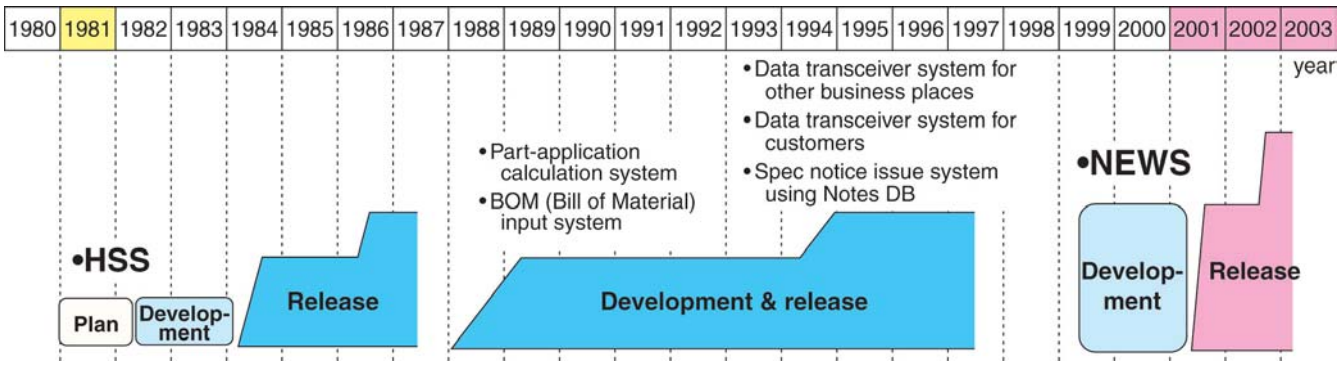


Fig. 1 The history of system development

2. Aims of Development

2.1. Concerns with the Conventional BOM System

2.1.1. Inefficient parts application method

With the conventional system, although there is the frame, engine, and transmission, data was managed in frame family units, and so when there was a spec change, it affected everything in the family. For example, when there was a change to a frame variation, it meant that engine and transmission family engineering change work had to be stopped simultaneously. In addition, associated data linked to engine or transmission data applied to a frame did not exist as BOM data.

2.1.2. Management of incomplete parts data

With the HSS, searches were made together for parts that are applied as standard parts and all parts that are applied as optional parts. Therefore, it was not possible to extract only parts data applied to a certain optional feature vehicle.

2.1.3. Data that was not shared

With the conventional system, data that was prepared by a design engineer prior to drawing issue (drawing release schedules, etc.) was not well managed. In addition, because there was no timely sharing of data between departments, parallel work in each process was dependent on personal communication, and this was an obstacle in truly shortening the development cycle.

2.1.4. Scattered system

The development history of the BOM and related systems is shown in Fig. 1. After the introduction of the HSS, a number of peripheral systems were developed to meet various needs. Because the direction of data flow in the system developed so far was one-way, there was no linking in the sense of mutual utilization of data. Therefore, in linking with other systems, the work of copying data between systems was generated. In addition, in the process of development, the design engineers had to call up many display screens, and manually input the same data into different formats. This meant a lot of duplicate work, and so an increase in design workload.

2.1.5. Low reliability in drawing delivery system

In the distribution of drawing data, the conventional system carried out only transmission management, and so reliability was low with a reception error rate of 10%. Furthermore, when passing data to the supplier, there was the work of investigating each time the situation surrounding customer receiving environment and processing it by hand.

2.1.6. Limits to system capacity

An increase in the number of variations, too, greatly affects system performance. At the start of system development, the number of model variations was about 400, and while the system was expanded to be able to process 3,000 variations, practical development was carried. However, the current variation count exceeds system processing capacity at 4,000, and processing takes time after system trouble occurs (Fig. 2).

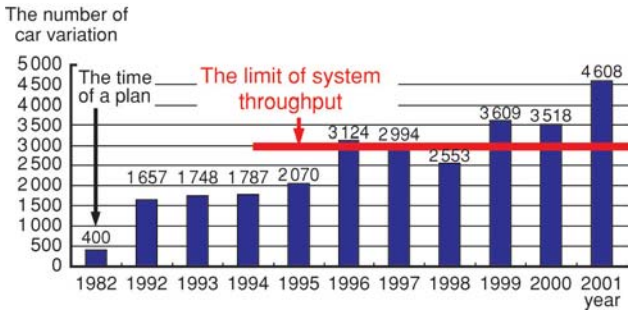


Fig. 2 Transition of the number of car variations

2.2. Aims of Development

The following aims were established in the construction of a new system, in order to resolve the issues set forth above.

(1) Complete data management of parts for one vehicle.
(2) Make possible simultaneous, parallel development through information sharing.
(3) Make possible centralized management of data flow through system integration.
(4) Contribute to shortening the development cycle by building the new system as a system that is unlimited in terms of processing data amounts.
(5) Actualize easy linking between various systems.

3. Details of Development

3.1. Functions Developed

With NEWS, function utilized by conventional multiple systems were improved in line with the development aims, and packaged. Explanations of the function developed are as follows.

3.1.1 Parts data management for a single whole vehicle

(1) Feature-application List (referred to as F-List hereafter)

Feature-applications are defined against variations in grade. Fig. 3 gives an example of this. In the table, an "0" means that it is applied, and a "-" means that it is not applied.

Family TNAEF

		Model	S02A							
		Destination	J							
Sec	Idx	Grade / Feature	EL	ML	ML-2	MI-A	MI-B	VI	VI-A	VI-B
Vertical Set										
A00		ABS								
	1	ABS	0	0	0	0	0	0	0	0
A00		DR SRS								
	1	DR SRS	0	0	0	0	0	0	0	0
A00		MISSION								
	1	MT	0	0	0	0	0	0	0	0
	2	AT	0	0	0	-	-	-	-	-
	3	CVT	-	-	-	0	0	0	0	0
A00		SUNROOF								

Fig. 3 F-List

(2) Part-application List (referred to as P-List hereafter)

By indicating part-application against feature combinations calculated automatically, part application against product can be automatically calculated. Fig. 4 gives an example. Rows having an "0" at the top right give the feature spec differences, and by inputting the part number at the bottom left, it is possible to indicate part-application for spec differences. In addition, the numbers on the bottom right express the number of parts applied.

An explanation of the part application indication process is as follows. First, the model development team and the spec management team establish feature specifications for a model, and the F-List is created. On the system side, when the spec has been decided, from the feature combinations the necessary product variations are calculated, and variation codes are created. The design engineer utilizes the F-List data, and creates the P-List. In creation of the P-List, first of all, the features that determine part spec differences are selected from the F-List data. Then the feature combinations are calculated, and the design engineer inputs part numbers for the resulting pattern. When it is saved, on the system side, the product variations that are integrated with the calculated feature combinations are automatically searched, and part-application determined. With this process, it is no longer necessary for the design engineers to manually indicate part-application for each and every variation (Fig. 5). This process was actualized in HFS, but its function was enhanced as part of NEWS functions.

2		3 DOOR				
3		4 DOOR				
	A00	SUNROOF				
1		NO SUNROOF	0	0	0	
2		SUNROOF				0
	F44	SPOT LIGHT				
1		NO SPOT LIGHT	0			0
2		SPOT LIGHT		0	0	
	F32	RR WASHER				
1		NO RR WASHER	0	0	0	0
2		RR WASHER				
1	62100-S02 -A000-H1		1			
2	62100-S02 -J100-H1			1		
3	62100-S02 -J100-H1				1	
4	62100-S02 -A100-H1					1
5	62100-S02 -A100-H1					
6	62100-S00 -A000-H1					

Fig. 4 P-List

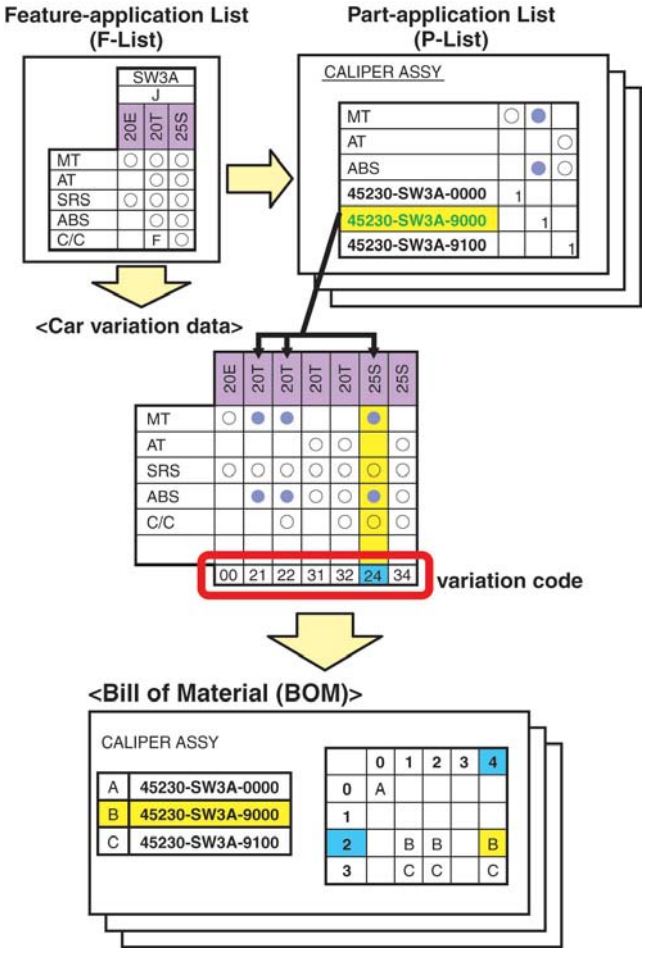


Fig. 5 Result of part-application calculation

(3) Joint List

Independently managing all variations in frame, engine, and transmission using the F-List, the various variation combinations are defined on the joint list, as data for one vehicle.

3.1.2 Simultaneous parallel development through information sharing

• PLUI (Parts List User Interface)

The PLUI makes it possible to input or reference the BOM using the same graphical user interface (GUI hereafter) from the memo state at the planning and concept stage through engineering changes after mass production. From the PLUI screen, it is possible to carry out operations such as referencing CAD drawings, displaying cost and mass, inputting drawing schedules, etc. (Fig. 6). At present, design engineers create and maintain the planning and concept stage parts lists on Microsoft Excel, etc., but data linking with the engineering-BOM created after drawing release is not possible in terms of the system. In addition, management of the data that accompanies the parts list depends on each individual. This is a cause of poor accuracy in cost and mass totals. With PLUI, at the planning and concept stage parts list and the engineering-BOM can be maintained with the same GUI on the same database, and an information sharing process is actualized. Through these measures, it is possible to have the following.

· Prevention of parts omissions in work by design engineer
· Provision of highly accurate BOM information to layout or cost and mass calculation systems, etc.

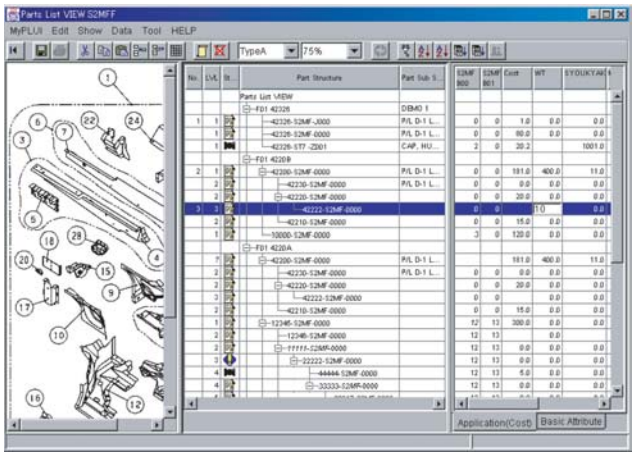


Fig. 6 PLUI display

3.1.3. Centralized management of data flow

In order to centrally manage drawing data flow from drawing release processing by designing engineer through distribution to plants and suppliers, the following processing functions were developed in NEWS.

(1) EC Data Reception

Check, using a bar code, to ensure uniformity between the CATIA data and the paper drawing with approval signatures.

(2) Total Check

Check feasibility of part application and drawing history, configuration.

(3) Obtaining Revision No.

Revision notification numbers are obtained in order of engineering change, so that there is no duplication.

(4) Calculation of EC Data Distribution Site

The worldwide facility distribution site for drawings or notifications is automatically calculated from part-application.

(5) Writing Revision No. on Drawings

The revision number is automatically written in the history column in CATIA drawing data.

(6) Scanning

Information drawn on paper is scanned, and stored in the database.

(7) English Translation

English translation of the notifications is carried out through data exchange with an outside translation company.

(8) Moving to Master Drawing File

CATIA drawing data is stored in the master drawing file.

(9) Distribution

Based on data distribution site calculation results, drawings and notification data are automatically distributed.

(10) Interface for manufacturing BOM

Engineering-BOM data is automatically distributed to the manufacturing-BOM, in notification order.

(11) BOM Search

BOM information, drawing and notification information, and CATIA data can be searched from a variety of angles. Fig. 7 shows the screen.

(12) Conversion to Mass Production

Prototype part numbers in CATIA drawing data are automatically converted to mass production part numbers, and moved to the manufacturing-BOM.

The above is a simple explanation of functions developed. These functions were developed as the basis for system application technology explained below.

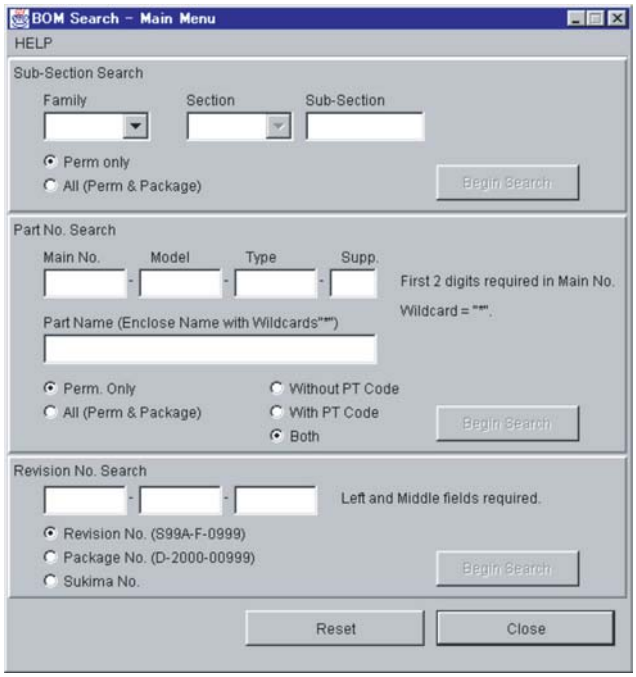


Fig. 7 BOM search screen

3.2. Detail of System Application Technology

In order to continue system evolution and to improve ease of system maintenance and application efficiency, this system is based on the data management software package eMatrix (MatrixOne, Ltd.), and with a three-tier system architecture (Fig. 8). On the client side, a GUI screen was developed in Java, so the users can easily input and reference parts information. In addition, an interface with CATIA was developed, strengthening data linking. The application servers are composed of UNIX and Windows NT, with the business logic created in TCL installed. In the database, Oracle was adopted from the point of view of performance and expandability.

The following technologies were adopted in a hierarchy.

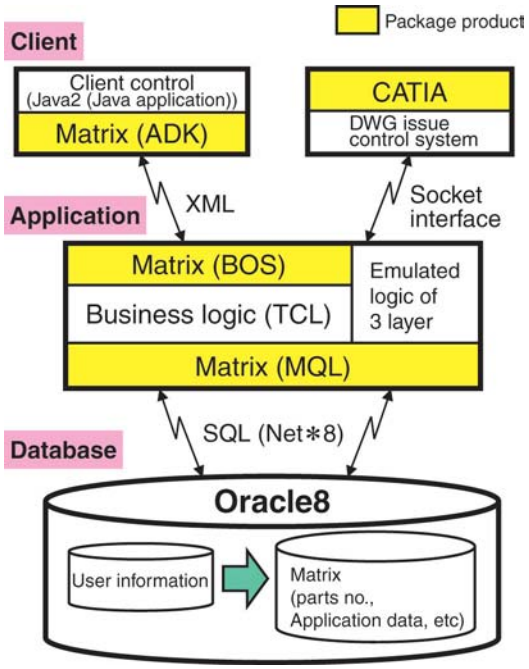


Fig. 8 3-tier architecture

3.2.1. Client layer

(1) Multi-Platform and Multilingual Measures

In order to maintain the same level of ease of operation among the workstations by IBM, SGI, and HP used as CAD terminals and Windows PCs used as OA stations, the same GUI was adopted. In addition, in order to ensure there is no effect due to differences in OS features, an integrated common function was created and adopted, relating to (1) automatic switching between similar fonts, (2) printing control, and (3) file path name control, etc.

Furthermore, the scheme outlined in Fig. 9 was adopted, to deal with other languages.

(2) A User-Friendly GUI

In order to improve ease of operation by the user, various GUI were actualized, including tree views, icons, pop-up menus, etc. Fig. 10 gives an example. With today's applications, it is ordinary technology, but conventionally, data is dispersed between the subsystems, and data storage formats were various, so it was difficult to actualize this flexible GUI.

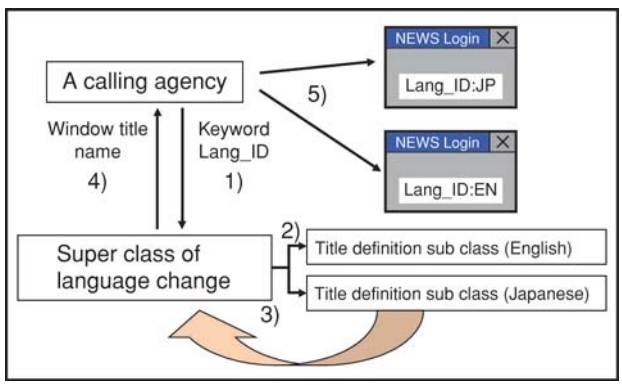


Fig. 9 Multi-language compatibility

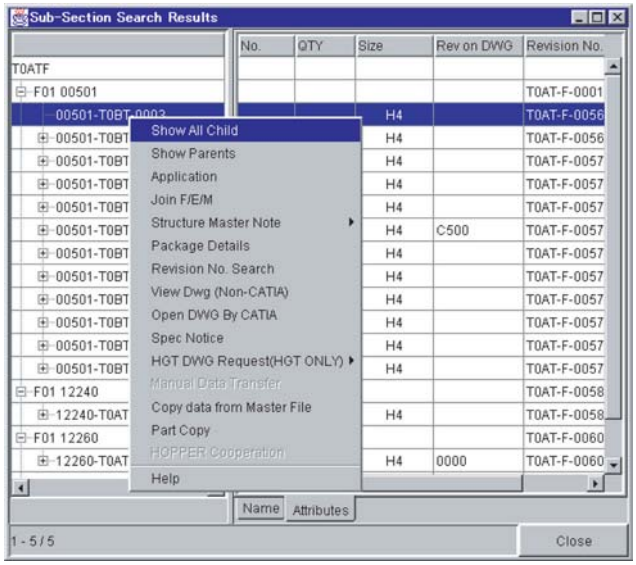


Fig. 10 Example of GUI

(3) Communication Method

With NEWS, the communication method adopted between clients and servers is the CORBA (Common Object Request Broker Architecture) IIOP (Internet Inter-ORB Protocol). In the future, studies will be made into a communication method that switches between communication within the application server using RMI (Remote Method Invocation) and external communication using XML (eXtensible Markup Language) (Fig. 11). With the communication method using XML, the elements handling communication are completely covered as a package, and without significant modifications to existing business applications, communication efficiency can be improved. Current testing confirms operation.

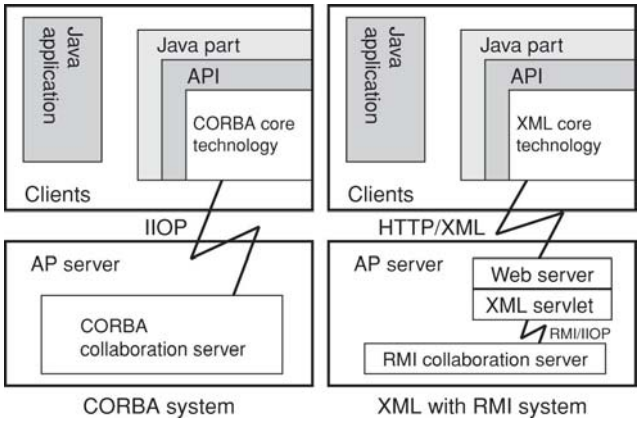


Fig. 11 Communication methods

3.2.2. Application server layers

With this system, as application servers, 2 UNIX servers and 36 Windows NT servers were introduced (Fig. 12). This gives the following benefits.

(1) High Speed

Because it is possible to use CPU so that each process can be independent, it is possible to introduce performance that exceeds that of a general-purpose computer. In addition, with future hardware evolution, it will be possible to actualize, at a low cost, even higher speeds.

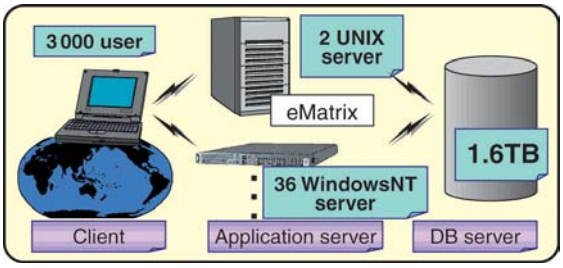


Fig. 12 System configuration

(2) Scalability

Even if the scope of business expands in the future and the number of users grows, it is easy to increase the number of servers, so ease of expansion as a system can be maintained.

(3) Reliability

Generally, the utilization rate for NT servers is 97%-99%, but by implementing (1) parallel devices and doubling (normal utilization backup device) and (2) utilization monitoring and automatic switching (threshold value monitoring) measures, the utilization rate reached 99.98%. An infrastructure was built that could maintain a utilization rate on a par with a mainframe system.

3.2.3. Database server layer

With this system, theoretically object-orientated data management is carried out. However, physically, Oracle has been adopted, which is a relational database. Therefore, both system design flexibility and maintenance of execution performance are achieved. Accordingly, in data definition design, there are no limits due to performance or resource economy. Because of this, it is possible to substantially and freely increase the amount of each type of data, such as number of product variations, thereby actualizing the development target of limitless processing data.

3.2.4. Data transmission and receiving system, utilizing MQ

In order to improve drawing data distribution accuracy, this system adopted a data transmission and receiving structure utilizing MQ (Message Queuing). Fig. 13 shows an outline of the structure. MQ is a transmission and receiving monitoring software, and it automatically compares information transmitted and information received. If the information is insufficient, data is automatically resent. This has made it possible to maintain transmission and receiving at almost 100%.

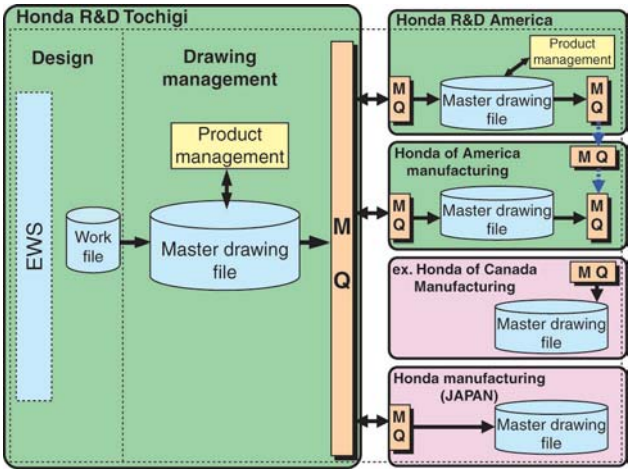


Fig. 13 Drawing transmission using MQ

4. Benefits

4.1. Benefits in Management of Parts Data for One Vehicle

With NEWS, it is possible to extract parts applied to option feature vehicles. That is to say, it is possible to manage all parts information from model to option. In addition, frame, engine and transmission data are managed in separate family F-Lists, and the combinations are defined in the joint list. This means that even when there is a change to a frame variation, there is no need to stop, at the same time, engine and transmission engineering change work, thereby improving efficiency.

4.2. Improved Work Efficiency with System Integration

By integrating the system, the design engineers drawing release work efficiency is improved. Fig. 14-(a) compares the workflow carried out by design engineers with the conventional system and with NEWS, and Fig. 14-(b) compares operation time. With work simplification, design drawing release work efficiency can be improved by approximately 30%. Concerning BOM accuracy, too, parent check error (error which occurs where there are parts which are not related to parent part or model application), which conventionally occurs frequently, now have an occurrence rate nearly 0.

It is also possible to centrally manage data flow from drawing release through distribution. In line with this, the engineering change process can be efficiently carried out as a re-configuration process. Fig. 15 compares EC data reception time for an engineering change, with the conventional system and with NEWS. In comparison with conventional system processing, with NEWS, work is simplified and at a faster speed, resulting in a 40% or more improvement in work time.

4.3. System Capacity Improvement

As explained in the previous section, with NEWS, a system was created that can handle an increase in the number of product variations.

In addition, with parallel devices, etc., system stability can be maintained.

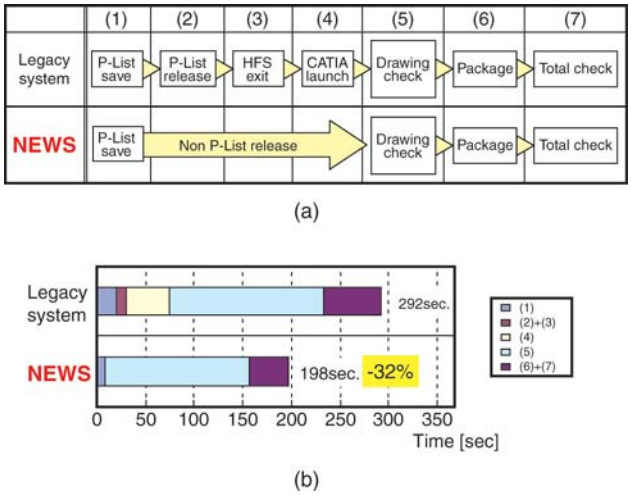


Fig. 14 Work flow on drawing release process

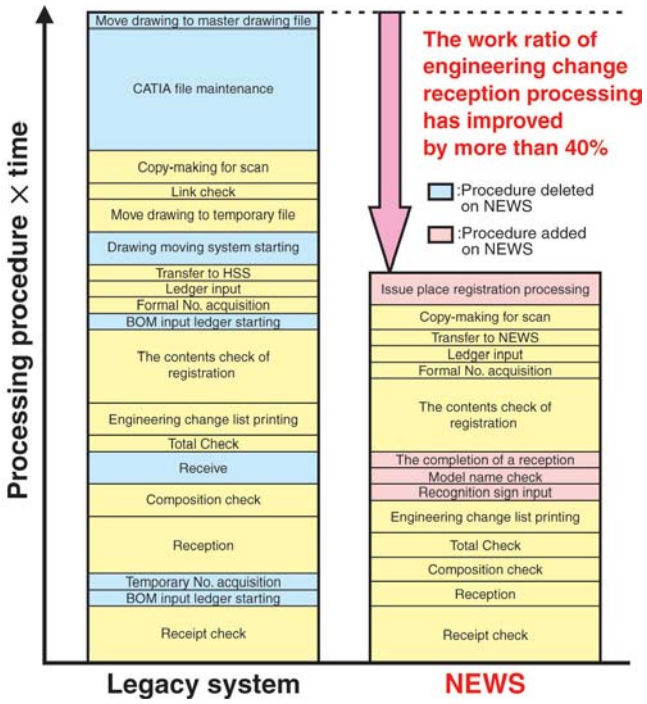


Fig. 15 Comparison of the throughput of NEWS and a legacy system

4.4. Ease of System Linking

In terms of linking with other systems, the NEWS part data is linked with the new cost system that automatically calculates, manages, and totals costs of parts for one vehicle. With this, it is possible to reduce the labor required for verification table input work.

5. Summary and Future Development

By creating NEWS that integrates the conventional BOM and related systems, and makes possible integrated management of vehicle parts basic information, improved drawing release processing efficiency, and links with other systems, the following results were achieved.

(1) The introduction of an option part-application search function and an joint list make it possible to completely manage basic product information such as frame, engine and emission associations, etc., in addition to information on all vehicle models and all variations.

(2) By integrating the drawing release and drawing distribution functions, drawing data can be centrally managed. In addition, by simplifying the work procedure, engineering change work efficiency is improved.

(3) Problems due to limitations in the number of variations that can be processed for one model or in the number of part numbers were eliminated, and the system was created that can handle an increase in data. In addition, by doubling up each domain in terms of hardware, the system will not completely stop even if there is a failure.

(4) As in the example of linking with the cost system, it is possible to see the benefits of easy linking with other systems and a reduction in processing labor.

In the future, with the adoption of XML, the communication method will evolve and system performance will improve. In addition, looking toward further integration of other development technological information, there will be strengthening of links with layout information management and application to verifications using DMU (Digital Mock Up). With these measures, it is possible to shorten the verification preparation period and reduce labor. In addition, by sharing, in real time, layout information before drawing release, it is possible to greatly contribute to completed vehicle quality enhancements and a short development cycle. Working towards expanded information sharing with manufacturing, studies will be made into system creation and data construction for data that is not yet handled by NEWS, such as color charts and mass production package style, etc.

6. Acknowledgements

The authors would like to express their sincere gratitude to the many people at Fujitsu, Ltd., and MatrixOne, Ltd., who generously gave technical support in the development of this system.

In addition, they would like to thank Mr. M. Kojima and Mr. S. Watanabe of Fujitsu, Ltd. for their cooperation in the writing of this report.

References

(1) Normile, D., Tyrka, K.: “Design anywhere, build anywhere,” Dos News, Vol. 56, No. 3, p. 77–78 (2001)

(2) Thilmany, J.: Beyond PDM, Mcch Eng., Vol. 123, No. 3, p.66–68 (2001)

(3) Oki, S., Masuda, M.: “Innovation of Manufacturing Information Technology”, MITSUBISHI MOTORS Technical Review, No. 13, p. 8–15 (2001)

(4) Kawano, S., Tsurumoto, T., Tsukihara, A.: “Speeding Up Design Release Information Flow”, Nissan Giho, No. 43, p. 78–81 (1998)

(5) Maruyama, N.: “A Winning Database Management Strategy”, Tokyo, NTT Publishing, p. 181 (1999)

(6) Miki, H., Tsuchiya, M.: “A Three-Tier Client/Server System Configuration”, Tokyo, Software Research Center, p. 216 (1996)

(7) Nakamura, M.: “Beyond the Limits of Utilization Rate”, Nikkei Computer, Nikkei BP, Ltd., p. 130–147 (2001-5)

■ Authors ■



Masataka YAMAMOTO



Hideyuki TANAKA



Wataru FUJITA

Technology for Applying Solid Lubricant to the Piston Skirt of Internal Combustion Engine and Its Effects

Hidemi OGIHARA*

ABSTRACT

A molybdenum disulfide piston coating technique was developed using the Wonder Process Craft (WPC) processing method to apply high-purity molybdenum disulfide onto the sliding surface of the piston skirt for an internal combustion engine. This technique is a world first, and the pistons manufactured using this process gained the full effect of durability while also achieving significant reduction in sliding resistance at a low cost because the coating process does not require use of a binder. The technique is also noteworthy for making manufacturing easier, since it does not alter the dimensions, shape, or surface roughness of the base material. In addition, this piston manufacturing process uses compressed air and molybdenum disulfide powder. The molybdenum disulfide discharged from the process can also be recycled. Thus the process realizes zero waste and addresses the current need for environmentally friendlier technology.

1. Introduction

Improving fuel efficiency in automobile engines is one effective way to pursue goals for more efficient energy resource usage, environmental preservation, and cleaner emissions. Reducing sliding resistance within internal combustion engines can offer significant improvements to fuel efficiency and the industry has seen many such developments, including the improvement of lubricating oil and the coating or plating of sliding surfaces with solid lubricants. On the other hand, methods that involve coating parts with a thin film of solid lubricant present certain difficulties, including the potential alteration of part dimensions and the diminishment of inherent lubricating performance due to binder materials added to the solid lubricant.

2. WPC Processing

The surface treatment method described in this report is based on the surface treatment method known as WPC (“Wonder Process Craft”), which is an application of shot peening technology. The WPC treatment uses a stream of compressed air to shoot fine particles (200 μm or smaller) of a material with desired qualities at high speeds (over 100 m/sec.) at the surface of the object being treated, thereby raising its surface temperature above the A3 transformation point (for ferrous metals) or above the recrystallization point (for nonferrous metals). This causes the outer surface layer of the treated object to melt momentarily and then recrystallize, resulting in modified surface properties. This type of surface heat-treat technology can be used to improve certain mechanical characteristics of the treated object, including sliding resistance.

* Tochigi R&D Center

3. Reducing Sliding Resistance Using Molybdenum Disulfide

As shown in Fig. 1, various types of surface treatment were experimentally applied to several piston skirts and these were then bench tested to compare the resulting levels of motoring friction among them. The results of this comparison suggested that a process to apply a layer of the solid lubricant molybdenum disulfide to the piston's sliding surface and its outermost layer would be the most effective way of modifying the surface to improve its sliding characteristics, and thus it was in this direction that we took our research and development efforts.

Our development of this new surface treatment technology focused on the following:

(1) Achieve a binderless treatment process (to take full advantage of reducing sliding resistance.)
(2) Suppress or prevent changes in the shape and/or dimensions of the objects treated
(3) Complete recyclability of wastes discharged from the process
(4) Sufficient repeatability
(5) Easy application to mass production
(6) Low cost

Further, pistons manufactured using this technology are named and described as "molybdenum disulfide shot pistons."

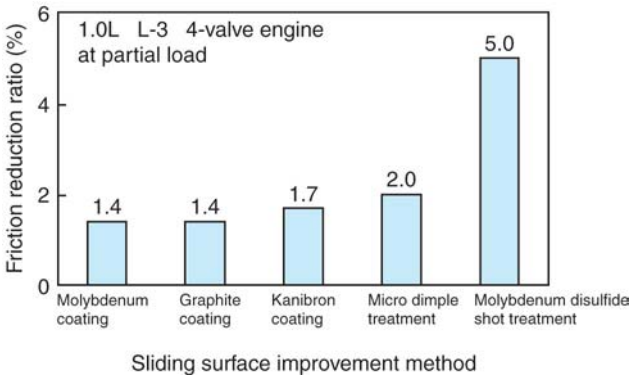


Fig. 1 Characteristics of surface treatment method and friction reduction ratio

4. Characteristics of Molybdenum Disulfide Shot Peening

Because the process used involves no added binder material, and relies instead on the formation of a high-purity solid lubricant layer embedded in the outermost layer of the treated object's surface, it is particularly effective toward reducing sliding resistance. Also, since WPC treatment involves thermal diffusion of a portion of the solid lubricant during application, the shape or dimensions of the treated object remain unchanged, ensuring that the process lends itself easily to mass production activities. Further, because the treated surface is very durable and highly resistant to peeling and frictional wear, the reduction of sliding resistance effects are long-lasting and sustained. Another advantage is that its only waste products are broken powder of molybdenum disulfide and air because the process uses only compressed air and molybdenum disulfide. Since the broken molybdenum disulfide grains are not altered except for being made smaller, they can be separated and sorted by size using a specially designed cyclone separator. Grains of uniform size can be collected, with no risk of introducing foreign matter, and either fed back into the process or reused in other applications. Therefore, the process is both environmentally friendly (since it generates no unusable waste) and useful toward reducing equipment cost (since no waste processing is required).

5. Measuring Molybdenum Disulfide Grain Size

An electrical sensing zone method particle size distribution analyzer (coulter counter) is used to measure the size of the scale-shaped or amorphous molybdenum disulfide grains. To summarize the measurement principle used by this analyzer, a particle passing through a fine pore causes a change in electrical resistance depending on its volume, and this change is converted into particle spherical diameter. Compared to laser Doppler and other two-dimensional techniques, this type of three-dimensional measurement technique yields values that are much closer to true values. The median diameter of the volume distribution determined by this method is used as the indicator of molybdenum disulfide grain size. (Molybdenum disulfide grain sizes listed hereafter are expressed using this volume distribution median diameter).

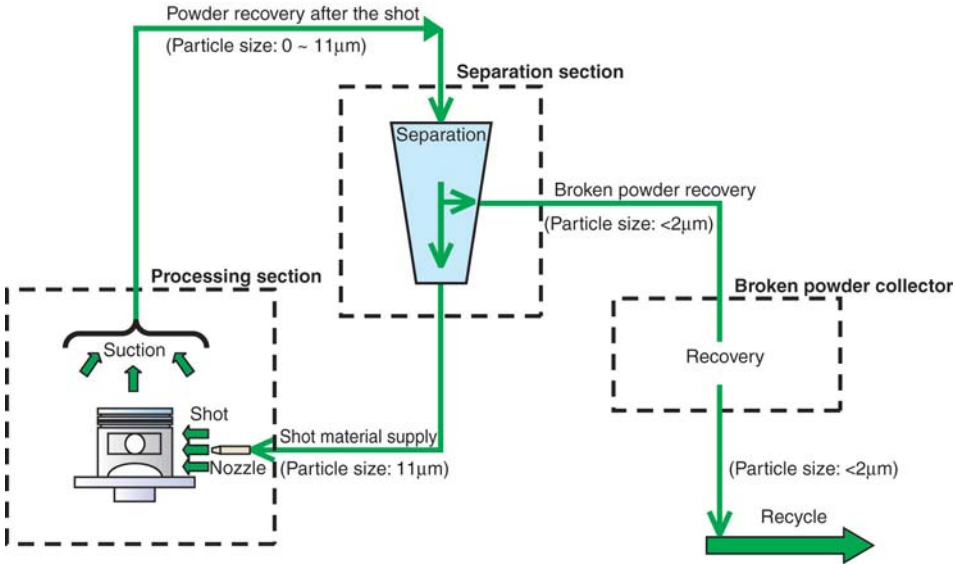


Fig. 2 Shot material supply process

6. Outline of Processing Facilities

As shown in Fig. 2, the processing facilities are comprised of three main sections: a separation section, a processing section, and a broken powder collection section. After being used for blasting in the processing section, the remaining molybdenum disulfide shot powder will be a mixture of grains that fractured after a single use and grains that did not fracture and remain whole. These are separated using a specially designed and built cyclone separator. Fractured molybdenum disulfide grains less than about 2 μm in size are sent to a collection device. Unfractured grains, or grains that have fractured but are still of a usable size, pass through the separator and are returned to the shot nozzle for re-use. Grains continue to be recycled in this way until they are finally fractured into an unusable size and are removed from the process by the separator.

Details of the process are shown in Fig. 3. Compressed air is used to shoot the molybdenum disulfide shot powder against the skirt of the piston. The piston itself is positioned on a turntable that rotates and the shot nozzle moves up and down, thereby ensuring that the spray of molybdenum disulfide powder is distributed evenly over the entire surface of the skirt.

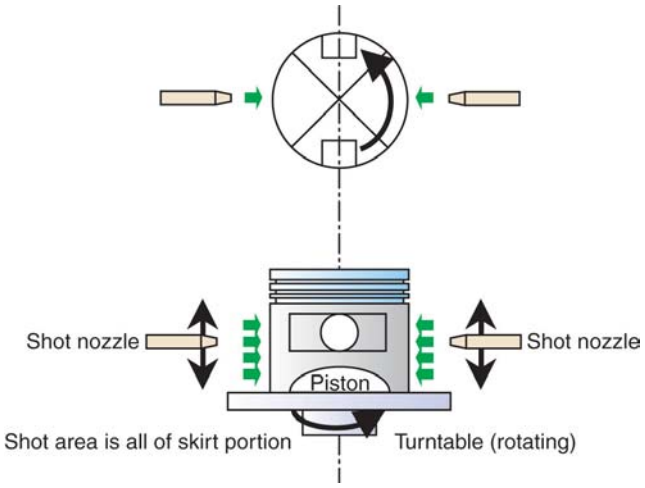


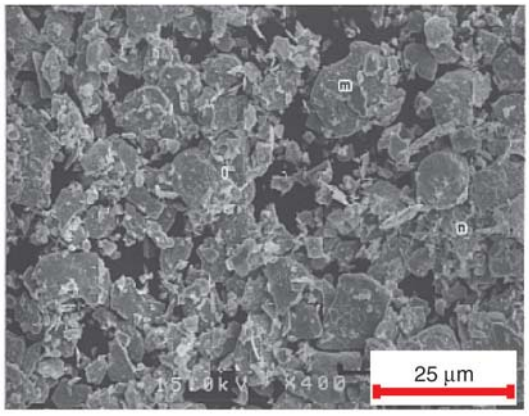
Fig. 3 Processing section outline

7. Establishing Optimum Blasting Conditions

Conditional parameters for air blasting include a variety of factors such as pressure, time, the quality, properties and grain size of the blasting medium, the mixture of blasting medium and compressed air, distance, and others. In some cases varying even one of these parameters can cause changes in the resulting surface properties, while in other cases varying even several parameters will result in no changes to the result. There are also opposite cases in which changing multiple parameters did link to changes in the resulting surface properties. In other words, determining optimum blasting conditions for such a process can be quite difficult under any circumstances. Our particular development attempted to use the WPC process to shoot molybdenum disulfide into a base metal material that was the first attempt of its kind, and the lack of precedent made it difficult to determine optimum blasting conditions. The parameters we eventually found to be particularly effective for use in molybdenum disulfide blasting are described below.

7.1 Optimum Blasting Medium Specifications

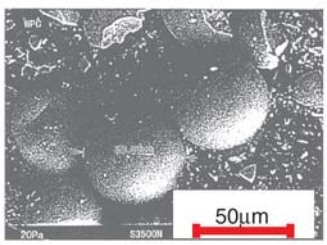
Figure 4 shows the fine molybdenum disulfide powder used in the air blasting process. In order to take sufficient advantage of molybdenum disulfide's inherent properties as a solid lubricant, we used powdered molybdenum disulfide of at least 98.5% purity, containing no binder additives, and of the largest available grain size (11 μm). This larger grain size was chosen to maximize the energy of the molybdenum disulfide for optimum penetration of the target surface. The results of experiments determined that smaller-sized particles could not penetrate deeply enough. Specially made larger-sized particles not generally available on the market also were found to be unsuitable since, with their larger size, they proved to fragment too quickly and completely under repeated use, also resulting in insufficient penetration. Eventually, considering various factors including molybdenum disulfide penetration depth and blast medium consumption rate due to grain fragmentation, it was determined that there exists an optimum size of 11 μm for the molybdenum disulfide shot grains, and this size was adopted for application in mass production.



Molybdenum disulfide powder SEM image

Purity	98.5% over
Particle size	11μm
Moisture	0.01%
Oil	0.03%

※ Particle size is mean of sensing zone method volume distribution



※ Reference: Ceramic beads for MD treatment

Fig. 4 Molybdenum disulfide powder for shot material

7.2 Optimum Blasting Pressure

To determine optimum blasting pressure, we referred to the parameters used in MD (micro-dimple) air blasting[1], which uses an air pressure of 0.34 MPa [3.5 kg/cm^2] to project roughly spherical ceramic beads having a hardness of HV 500–600 (Mohs 6–7), a specific gravity of 2.3–2.5, and an average grain diameter of ϕ 50 μm. To project scale-shaped molybdenum disulfide grains having a hardness of Mohs 1 and a specific gravity of 4.8 onto the target object, with considering such factors as units-per-hour requirements for piston production and shot material consumption through fragmentation, an optimum blasting pressure of 0.902 MPa [9.2 kg/cm^2] was established. This high pressure is generated using a special compressor. This blasting pressure is also closely linked to blasting time, and is a significant factor in determining the depth of molybdenum disulfide penetration.

7.3 Optimum Blasting Time

Experiments on optimum blasting pressure revealed that blasting time per unit area is closely linked to molybdenum disulfide penetration depth. Blasting time was established based on this and also such factors as production- and cost-related requirements. With blasting pressure set at a relatively moderate level, we thereafter were able to deepen the molybdenum disulfide penetration by setting longer continuous blasting times per unit area of the base metal. As shown in Fig. 5, intermittent blasting resulted in shallower penetration even when total blasting time was the same. We surmise that this happens because during intermittent blasting, the temperature of the heated base metal is allowed to drop again, while the process is momentarily stopped and waiting for the next blast, and that such repeated rises and falls in temperature result in a relatively lower temperature increase compared to that of continuous blasting. The temperature increase caused by continuous blasting is greater than that caused by intermittent blasting. It is thought that continuous blasting therefore produces deeper molybdenum disulfide penetration.

In reference to temperature increase, maximum increases of over 1,500 K have been reported based on the results of model calculations.[2]

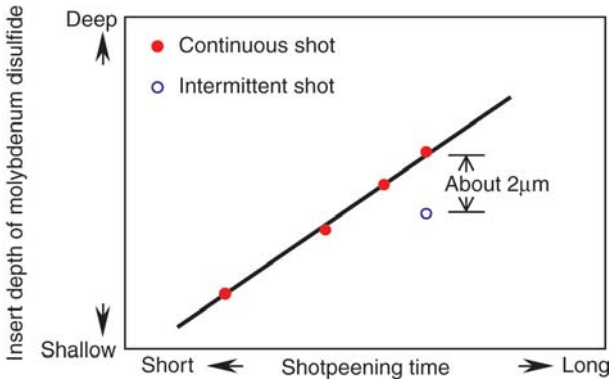


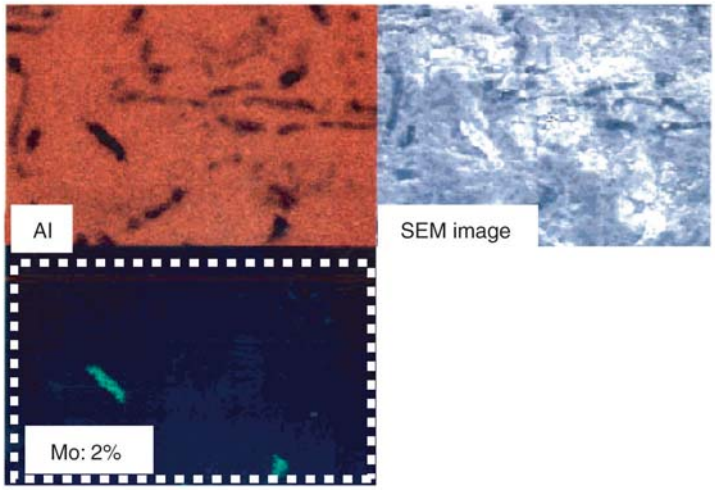
Fig. 5 Characteristics of insert depth of molybdenum disulfide and shotpeening time

7.4 Classification of Used Blasting Medium

The conditions mentioned above were established to minimize blasting medium grain fragmentation, as such fragmentation is unavoidable. Consequently, we developed a special cyclone separator component that ensures only grains about 11 μm in size are returned to the blasting process to be used again. This not only helps standardize penetration depth for more stable product quality, it also greatly reduces blasting medium consumption and contributes significantly to reduced production costs.

Depth	Surface	1μm	2μm	3μm
Molybdenum area ratio (%)	64	4	**2**	0

Color mapping results and molybdenum area ratio of each depth



FE-SEM/EDX surface analysis (Magnification: × 2 000 observation area: 60μm × 45μm)

Fig. 6 Measurement of molybdenum disulfide area ratio by image processing

8. Quantifying Molybdenum Disulfide Penetration Depth

Base metal penetration with molybdenum disulfide is a more complex structure than the uniformly thick membranes typical of coated or plated surfaces. In order to measure actual molybdenum disulfide penetration depth, we had to define what is meant by "penetration depth." First, we used ion milling (to avoid process-related heat effects, contamination and damage) to mill by 1 μm intervals into the sliding surface of a piston freshly treated with the molybdenum disulfide shot process. As shown in Fig. 6, each of the exposed surfaces was color-mapped using FE-SEM/EDX (Field Emission Scanning Electron Microscopy/Energy Dispersive X-ray Spectroscopy), indicating only the elemental molybdenum, followed then by segmentation image processing of the displayed surface and calculation of the molybdenum area ratio.

Based on the results of analysis using the method described above, and measurements of motoring friction, it became clear that if a surface with a molybdenum area ratio of greater than 2% exists at a depth of more than 2 μm from the initial sliding surface, then the sliding resistance reduction effect and the sustainability of this effect will be sufficient. Based on this we defined penetration depth as the deepest depth at which a molybdenum area ratio of 2% is found, and we set a depth of 2 μm or greater as the standard for molybdenum disulfide penetration.

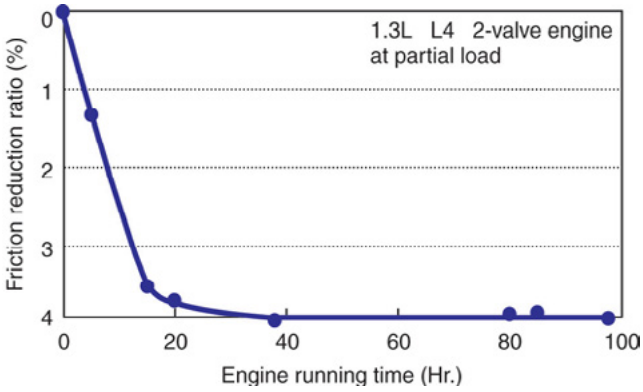


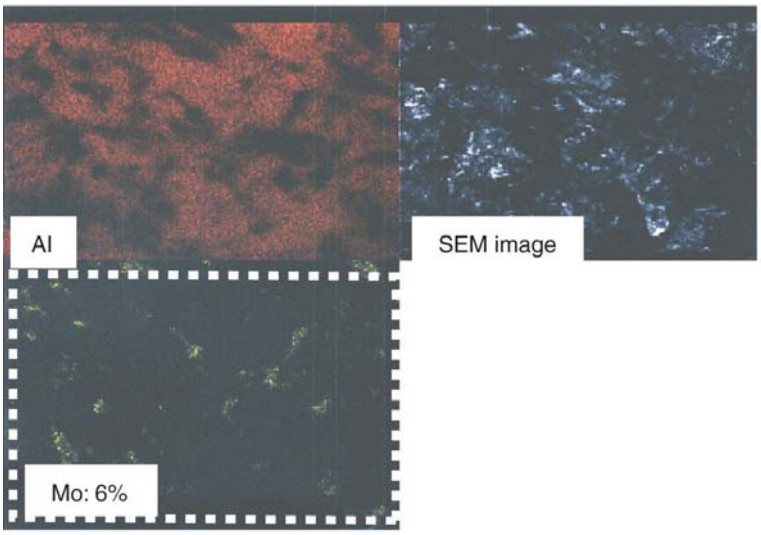
Fig. 7 Engine beak-in time and friction reduction ratio

9. Remaining Molybdenum Disulfide & Sustainability of Effect After Friction Wear of the Sliding Surface

As shown in Fig. 7, a piston treated with molybdenum disulfide to a depth of 2 μm was bench run for 100 hours. Partial-load motoring friction stabilized after 40 hours of operation, and the resulting level continued to remain stable even after 100 hours, with a 4% reduction in friction compared to that at starting time. Further, after the 100-hour mark, we examined the remaining presence of molybdenum disulfide on the friction-worn piston skirt striation tops (the

Depth	Surface	1μm	2μm	3μm	4μm
Molybdenum area ratio(%)	**6**	1	1	1	0.3

Color mapping results and molybdenum area ratio of each depth



FE-SEM/EDX surface analysis
(Magnification: × 2 000 observation area: 60μm × 45μm)

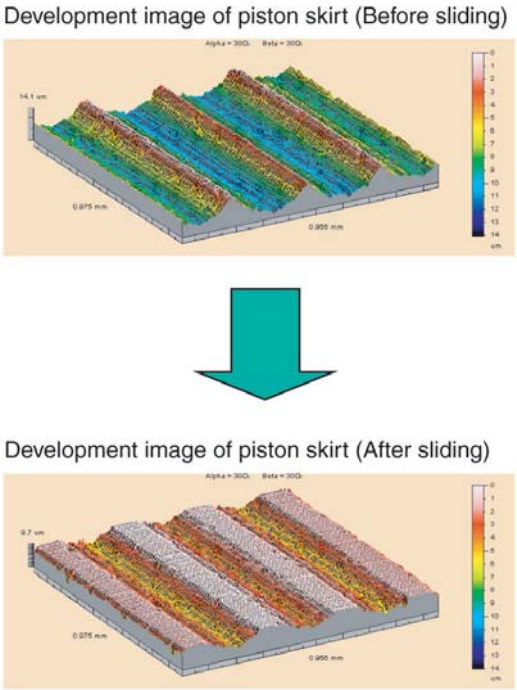


Fig. 8 Molybdenum disulfide residual on piston skirt surface after long period of running engine

actual sliding surface), using FE-SEM/EDX surface analysis color-mapping. As shown in Fig. 8, the results confirmed a molybdenum disulfide area ratio of 6%, as well as a 0.3–1% area ratio to a depth of 4 μm from the surface. The amount of reduction by friction to the striation tops after 100 hours was observed to be 2–4.9 μm in areas of high wear. The fact that we were able to confirm the remaining presence of molybdenum disulfide deeper than the initial penetration depth after longterm operation may be attributed to the transfer of molybdenum disulfide effected of high-purity molybdenum disulfide containing no binder material.

This is easy enough to imagine considering the crystalline structure of molybdenum disulfide. A molecule of molybdenum disulfide is comprised of one molybdenum atom and two sulfur atoms, with the molybdenum atom positioned diagonally below the sulphur atoms in a triagonal prism $2H_b$ formation (hexagonal laminate). The Mo-S bond within the layers is a covalent bond, including a fairly strong binding energy and an interatomic distance of only about 1.5 Å. In contrast, between the layers the only binding force is a van der Waals force binding the sulfur atoms at an interatomic distance of about 3 Å. This van der Waals force is inversely proportionate by a power of 7 to interatomic distance, meaning that the binding energy between the layers is considerably weaker than that within the layers. Consequently, because of the covalent bonds within its layers, molybdenum disulfide is relatively strong against perpendicularly oriented forces but, because the van der Waals forces between the layers are weak against forces acting horizontally, inter-layer sliding is exhibited. However, for this inter-layer sliding to occur, intervals between the layers must exist, and there exists a minimum laminal unit. Cross-sectional high-resolution electron microscope examination of the friction area of the molybdenum disulfide, from one time of the sliding portion, 4 layers of molybdenum disulfide have been observed.[3] In other words, it is hypothesized that if the molybdenum disulfide is in 4-molecule layers comprised of 3 nm-thick particles, self-cleavage will manifest and give rise to lubrication performance. Manifesting even greater friction reduction in the friction area requires orienting the layers parallel to the sliding direction (crystalline orientation) and perpendicular to the load orientation. It is thought this crystalline orientation is accomplished by adding load and sliding the particles, it is accompanied by crystal breakage and rotation that accelerates the transfer of the cleaved particles to separate areas.[4] The sliding experienced in an internal combustion engine piston is a sliding that receives the explosive force of the piston being pushed through the cylinder, and the surface pressure being received from this is clearly sufficient for such orientation. From the fact that stable friction reduction had appeared by the end of the continuous operation shakedown run, we surmise that the molybdenum disulfide completes its orientation through repeated crystal breakage and transfer early in the shakedown run, becoming one cause of a stabilized friction coefficient. These observations lead us to think that the friction reduction effects of molybdenum disulfide depend largely on its crystal structure. From this we can infer that the sliding resistance reduction properties of molybdenum disulfide do not necessarily increase with greater permeation depth, and that instead high sliding resistance reduction will still be achieved as long as permeation is below a certain specific depth. In bench tests measuring the motoring friction of actual pistons embedded with molybdenum disulfide to depths of 1, 2, 3, 4 and 12 μm, as shown in Fig. 9, all offered roughly similar sliding resistance reduction.

Insert depth of MoS_2	Friction reduction
1μm	2.1% (Results may be vary)
2μm	4.3%
3μm	3.9%
4μm	4.1%
12μm	4.3%

Fig. 9 Characteristics of insert depth of molybdenum disulfide and friction reduction ratio

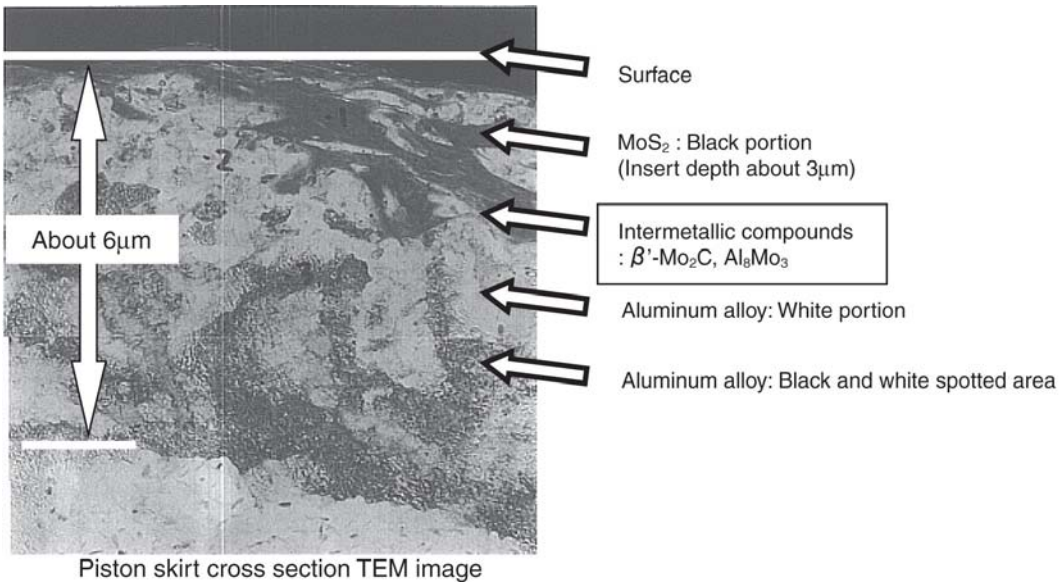


Fig. 10 Molybdenum disulfide insert condition

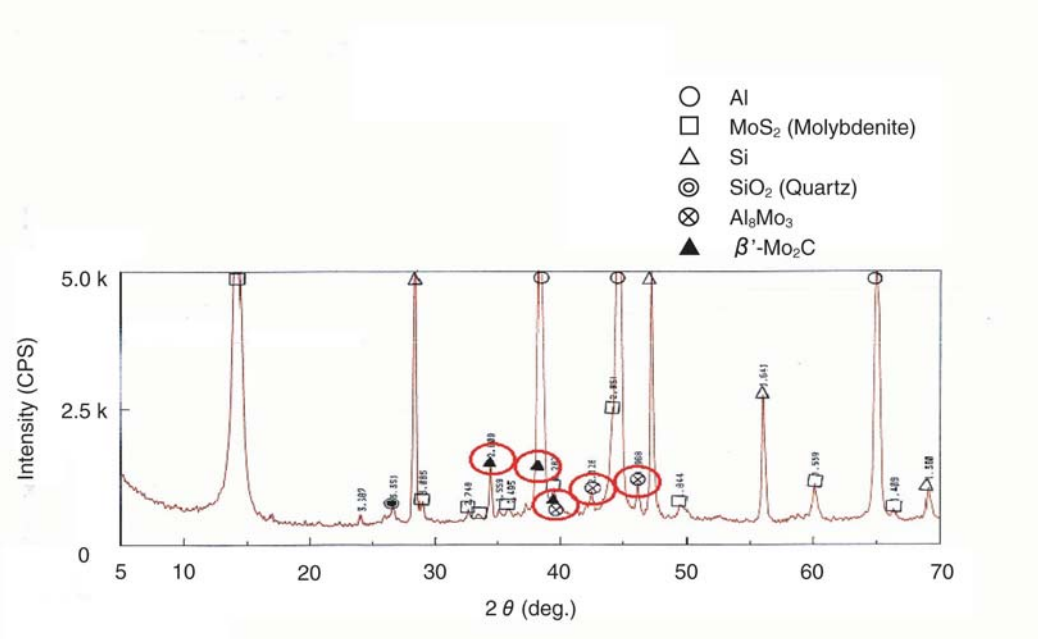


Fig. 11 X- ray diffraction measurement result

10. Observations of the Condition of Molybdenum Disulfide Penetration

Fig. 10 shows the results of TEM (Transmission Electron Microscope) examination of the penetration of molybdenum disulfide into the aluminum alloy base metal. Identification of those elements found by X-ray diffraction are shown in Fig. 11. These results give evidence that WPC treatment is in fact a surface improved heat treatment method, since two intermetallic compounds — β ’-Mo_2C and Al_8Mo_3, created only when aluminum alloys and molybdenum are present and subjected to temperature rises of at least several hundred degrees — are detected at the interface between the base metal and the embedded molybdenum disulfide. It has also been reported, in the model calculation results mentioned earlier, that the extreme temperature rises occurring over such tiny ranges in the course of this process is an extremely fast phenomenon on the order of μ secs.[(2)] Such temperature rises are thought to result from multiple continuously occurring phenomenon, including the conversion of the kinetic energy of the shot material into heat upon impact, as well as the shot particle size is on the micron order, most of it does not impact the surface of the base metal, but is instead carried by the pressurized air current to graze its surface, thereby generating heat by the friction of abrasion.

11. Intermetallic Compounds

The projected molybdenum disulfide becomes enmeshed in the upper layer of the aluminum alloy base metal, which has been melted by an extreme temperature increase, and at the same time, intermetallic compounds are formed in some areas, likely due to thermal diffusion. Since the two intermetallic compounds formed in this case, β ’-Mo_2C and Al_8Mo_3, are not corrosion-causing chlorides, fluorides or sulfides, we determined that their presence would not be problematic in terms of the required functioning in an internal combustion engine piston. Further, the aluminum alloy in the piston base metal and the molybdenum disulfide are not only simply in contact, they are actually adhered to one another by these intermetallic compounds, which may be viewed as a type of binder. Compared to cases in which such intermetallic compounds do not exist, we think that the presence of the bond actually helps to make the molybdenum disulfide more resistant to peeling and flaking.

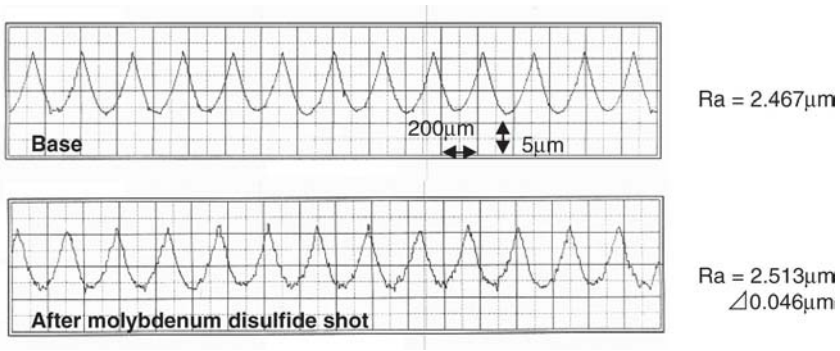


Fig. 12 Shot surface roughness

12. Surface Properties After Treatment

Examining the cross-sectional roughness curves for two different piston skirts, shown in Fig. 12, no significant difference can be seen between a piston without surface treatment and a piston that has been shot-treated with molybdenum disulfide. No change in piston diameter was observed after shot treatment. These results suggest there is no need to take factors such as dimension and shape into consideration when conducting molybdenum disulfide shot treatment, therefore manufacturing coated pistons is relatively easy.

13. Conclusions

- Using the WPC treatment process, molybdenum disulfide powder with a purity of at least 98.5% and containing no binder material is adhered to the skirt of an internal combustion engine piston by shooting it at high speed using compressed air, resulting in a 4% reduction in engine friction.
- The treatment causes a sliding resistance reduction effect that manifests immediately and remains sustained over a long period of time.
- The treatment does not cause any changes in the dimensions or shape of the piston.
- The treatment takes only a short time and is suitable for mass production.
- The only waste produced from process is completely recyclable molybdenum disulfide.

14. Afterword

We view this research as contributing to the development of new ways to utilize solid lubricants. In the future we will extend our study to the use of base metals other than aluminum alloy, with a view to finding fast application to various other kinds of sliding parts, contributing thereby to reduced resource usage and environmental preservation.

Pistons treated using the process described in this report are currently used in the 1.3-liter inline-4 two-plug engine newly developed for the Honda Fit car that was released in June 2001, and in the 1.3-liter inline-4 two-plug engine newly developed for the Honda Civic Hybrid car that was released in December 2001.

15. Acknowledgments

The author would like to thank Mr. Mase, Mr. Sugasawa, Mr. Kumagaya, and Mr. Ishiwata of Fuji Manufactory Co., Ltd., as well as Mr. Miyasaka of Fuji Kihan, for their kind support of this research from the beginning, and for the technical guidance and consulting they provided throughout.

Also, we thank Mr. Shimauchi and Mr. Kinoshita of Kawasaki Steel Techno-research Corporation for their ready and detailed advice and assistance regarding metallurgical structure analysis.

And finally, thanks to Mr. Kashiwaya of Sumico Lubricant Co., Ltd. for providing various information and instruction about molybdenum disulfide.

References

(1) Ogihara, H.: “Technology to Reduce Engine Sliding Resistance Through Surface Improvement,” Research Conference on Fine-Grain Impact Surface Treatments, “The latest surface improvement technology — Application of technology for surface improvement by fine particle bombarding”, 2nd Technical Lecture, pre-press edition, pp. 15–25, August 1999.

(2) Egami, N., Kagaya, T., et al: “Analysis of Particle Speed & Material Surface Temperature Distribution in Fine-Grain Peening,” Research Conference on Fine-Grain Impact Surface Treatments, “The latest surface improvement technology — Application of technology for surface improvement by fine particle bombarding”, 4th Technical Lecture, pre-press edition, pp. 18–24, October 2001.

(3) Takahashi, N., Kashiwaya, S.: High Resolution Transmission Wear 206, 8-14,1997

(4) Kashiwaya, S.: Junkatsu Keizai No. 385, 5-9, 1988.

■ Author ■



Hidemi OGIHARA

The Effect of Geometry on Stiffness and Deformation in Exhaust Manifold for In-line 4-Cylinder Engines

Masaru ENOMOTO*

ABSTRACT

Investigations were conducted on a quasi quantitative analysis method for exhaust manifold stiffness and deformation that is useful when designing exhaust manifolds for in-line 4 cylinder engines. This method analyzes the exhaust manifold as a combination of beams, making it possible to obtain the effects of the dimensions and shapes of major parts of exhaust manifold on stiffness and deformation. These results clarified the effects of various exhaust manifold shape characteristics (aspect ratio, branch ratio, offset ratio) on non-dimensional stiffness, and also the effects of aspect ratio on the non-dimensional warping quantity. In addition, the effects of each of the aspect ratio, collective part different angle, branch ratio and offset ratio on non-dimensional stiffness and deformation when the dimensions and shape of each exhaust manifold part are changed could also be clarified by obtaining the degree of effects of each factor. The proposed method is effective for determining and investigating the validity of major approximate dimensions, particularly when designing new exhaust manifolds with limited outer dimensions. Exhaust manifolds can be efficiently developed by performing CAE calculations on exhaust manifold shapes that have been determined using this method.

1. Introduction

The demand for automobile engines with cleaner exhaust emissions and lower fuel consumption is increasing throughout the world. As a consequence, conspicuous efforts are being made, for example, to reduce the heat capacity of engine exhaust systems (reducing wall thickness) in order to raise the temperature of the catalytic converter to the catalyst activation temperature as quickly as possible when starting the engine. Other efforts involve the use of lean burning to raise the exhaust gas temperature for the purpose of lowering fuel consumption, and so on. These approaches all impose

* Tochigi R&D Center

extremely harsh conditions on the exhaust manifold. Many problems arising during engine development can therefore be traced to the exhaust system, and the requirement for even further reduction of the development time means that there is strong demand for optimized design of the exhaust manifold in the initial stages of development.

It has recently become common to use CAE to estimate the stress, deformation, and other factors affecting each part of the exhaust manifold. When using CAE to design a new exhaust manifold, however, it becomes necessary to hypothesize a temperature for each of its parts in order to make the calculations. Those actual calculations cannot be performed unless the geometry of the exhaust manifold is determined in advance.

When designing a new exhaust manifold, therefore, it is crucial to understand beforehand the effects that the dimensions and shapes of the exhaust manifold parts will have on stiffness and deformation. Methods are being sought that will, in other words, make it possible to clearly grasp the major approximate dimensions of the exhaust manifold parts and to investigate their shapes in terms of stiffness and deformation, and to do these things in a short period of time at the designer's desk. In the interests of development efficiency, it is thought that the best method of designing a new exhaust manifold is first to use a quasi quantitative method to derive the approximate size. This then provides a basis for more precise calculations using CAE.

The authors formerly reported on a method for evaluating the reliability of an exhaust manifold using the restraint ratio.[1, 2] The present research deals with the stage prior to that by proposing a method for determining the effects of the dimensions of the various exhaust manifold parts on its stiffness and displacement ratio. In other words, this method can be used on the desktop to approximate the basic major dimensions and geometry when designing a new exhaust manifold for a 4-cylinder engine. Using a method of this kind to estimate the basic dimensions and geometry, for using those as a basis for CAE calculation of the restraint ratio and other factors, makes it possible to determine the final dimensions and geometry of an exhaust manifold within a short period of time.

The methods used previously for analysis relating to exhaust manifolds for in-line 2-cylinder engines served as the basis for the present analysis method.[3] These methods were extended for application to exhaust manifolds for 4-cylinder engines. The present approach also involved analysis and investigation in even greater detail.

Nomenclature

a_A Distance from the exhaust manifold center to the No. 2 port and No. 3 port entrances after deformation (see Fig. 3)

a_B Distance from the exhaust manifold center to the No. 1 port and No. 4 port entrances after deformation (see Fig. 3)

b Branch ratio (= U/y)

c Offset ratio (= L/y)

d_{A1} Deformation resulting from the moment generated in No. 2 port and No. 3 port

d_{A2} Deformation resulting from the load applied in No. 2 port and No. 3 port

d_{B1} Deformation resulting from the moment generated in No. 1 port and No. 4 port

d_{B2} Deformation resulting from the load applied in No. 1 port and No. 4 port

dx_A Amount of deformation in No. 2 port and No. 3 port (see Fig. 3)

dx_B Amount of deformation in No. 1 port and No. 4 port (see Fig. 3)

E Modulus of longitudinal elasticity

Gx_A Stiffness of collective part of No. 2 port and No. 3 port

Gx_B Stiffness of collective part of No. 1 port and No. 4 port

h_A Length of No. 2 port and No. 3 port after deformation (see Fig. 3)

h_B Length of No. 1 port and No. 4 port after deformation (see Fig. 3)

I Geometrical moment of inertia (geometrical moment of attachment flange + geometrical moment of port branch + geometrical moment of collective part)

L Distance from port entrance to port collective part (see Fig. 3)

M_0 Moment operating in each port (= WL)

m Aspect ratio (= L/U)

r Geometrical center of the opening of each port when the exhaust manifold is deformed (see Fig. 3)

$S_{A\theta}$ See Eq. (51)

S_{Am} See Eq. (52)

$S_{B\theta}$ See Eq. (56)

S_{Bm} See Eq. (57)

$T_{A\theta}$ See Eq. (37)

T_{Am} See Eq. (38)

T_{Ab} See Eq. (39)

T_{Ac} See Eq. (40)

$T_{B\theta}$ See Eq. (44)

T_{Bm} See Eq. (45)

T_{Bb} See Eq. (46)

T_{Bc} See Eq. (47)

U Length of exhaust manifold (see Fig. 3)

W Load acting upon each port

y Distance from port entrance to the port collective part (see Fig. 3)

ΔZ_A Quantity of warp in No. 2 port and No. 3 port (see Fig. 3)

$\Delta Z_A'$ Quantity of apparent warp in No. 2 port and No. 3 port

ΔZ_B Quantity of warp in No. 1 port and No. 4 port (see Fig. 3)

$\Delta Z_B'$ Quantity of apparent warp in No. 1 port and No. 4 port

θ Difference angle of collective part (see Fig. 3)

Ψ_A Opening angle of No. 2 port and No. 3 port when deformation occurs (see Fig. 3)

Ψ_B Opening angle of No. 1 port and No. 4 port when deformation occurs (see Fig. 3)

2. Analysis

The exhaust manifold is considered as a combination of beams to determine its stiffness. The method also seeks to identify the deformation caused by the moment generated in the various parts of the exhaust manifold, and the deformation caused by the load acted. These are combined to calculate the total deformation.

Fig. 1 shows an actual form and schematic model of the exhaust manifold for a 4-cylinder engine that is the object of this investigation. This exhaust manifold is considered to be left-right symmetrical. That is, the No. 1 port and No. 4 port parts are symmetrical with respect to the center line of the exhaust manifold, and the No. 2 port and No. 3 port parts likewise. Deformation is caused by *WL* and *W*.

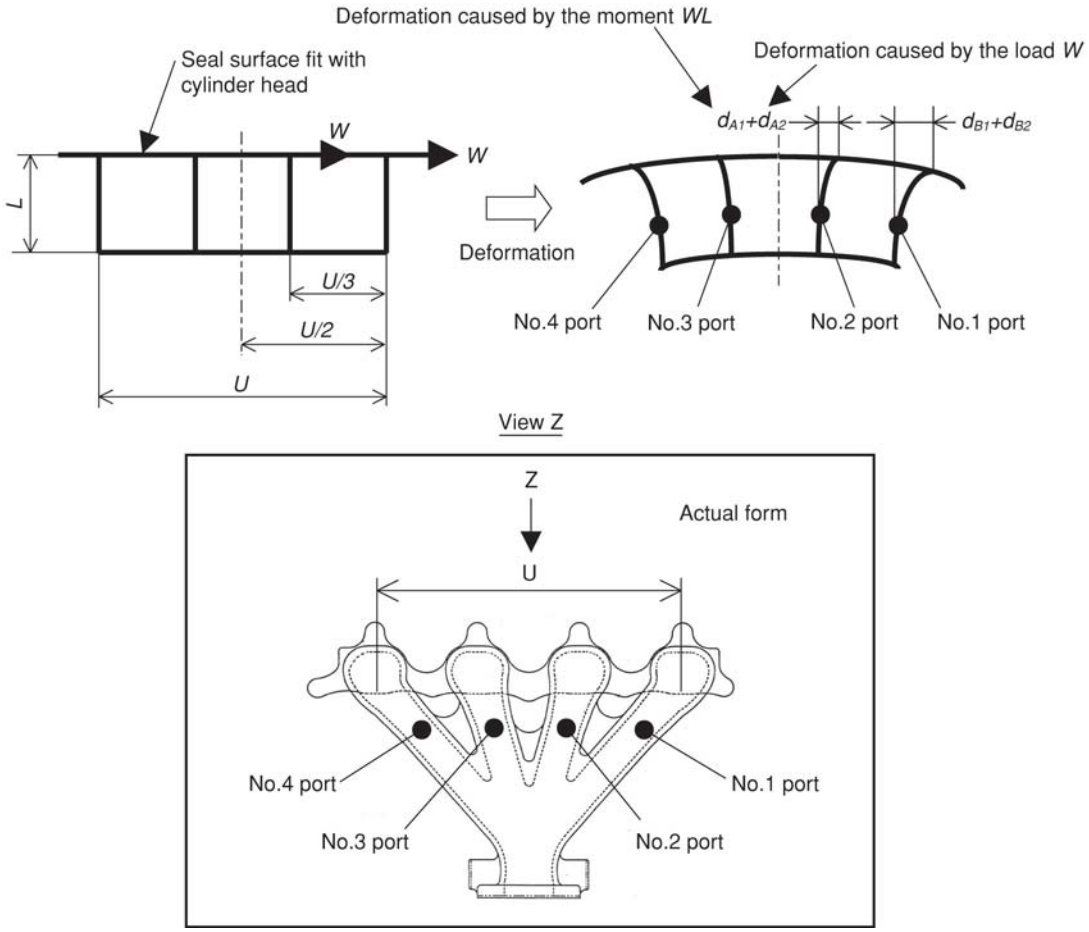


Fig. 1 Actual form and schematic model of exhaust manifold for in-line 4 cylinder engine. Deformation is caused by the moment *WL* and the load *W*.

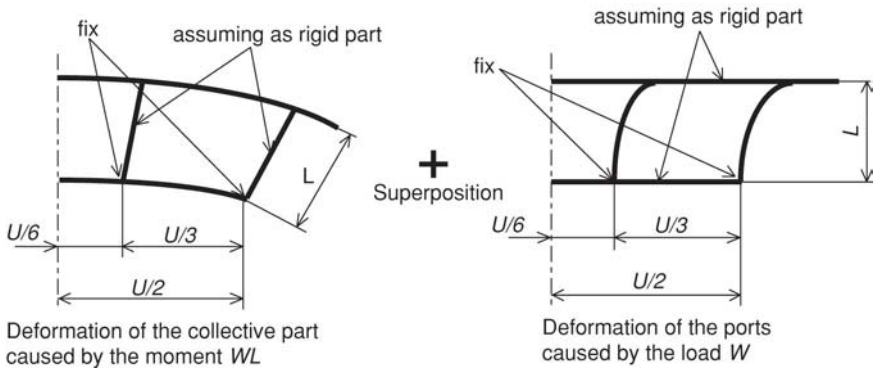


Fig. 2 Superposition of deformation of the collective part caused by the moment *WL* and deformation of the ports caused by the load *W*.

Fig. 2 is a schematic representation of the deformation caused by *WL* in the collective part and the deformation caused by *W* in the individual ports. The deformation of the collective part caused by the moment and the deformation of the individual ports caused by the load in this way are combined.

The section below introduces three non-dimensional numbers that represent geometrical properties of the exhaust manifold. These numbers are commonly applied in analysis and evaluation of the various dimensions and shapes of the exhaust manifold by a common index. They are the aspect ratio, branch ratio, and offset ratio.

The model used in this analysis is shown in Fig. 3.

2.1. Effect of Aspect Ratio and Collective Part Difference Angle on Stiffness

The case of the simplest geometry, where $\theta = 0°$, will be considered first.

d_{A1} is the deformation that occurs when the moment *WL* operates on the end of a beam of length *U/6*. This can be expressed by Eq. (1):

$$d_{A1} = M_0(U/6)^2/2EI = (WL/2EI)(U/6)^2 \quad (1)$$

Here *EI* is the flexural rigidity.

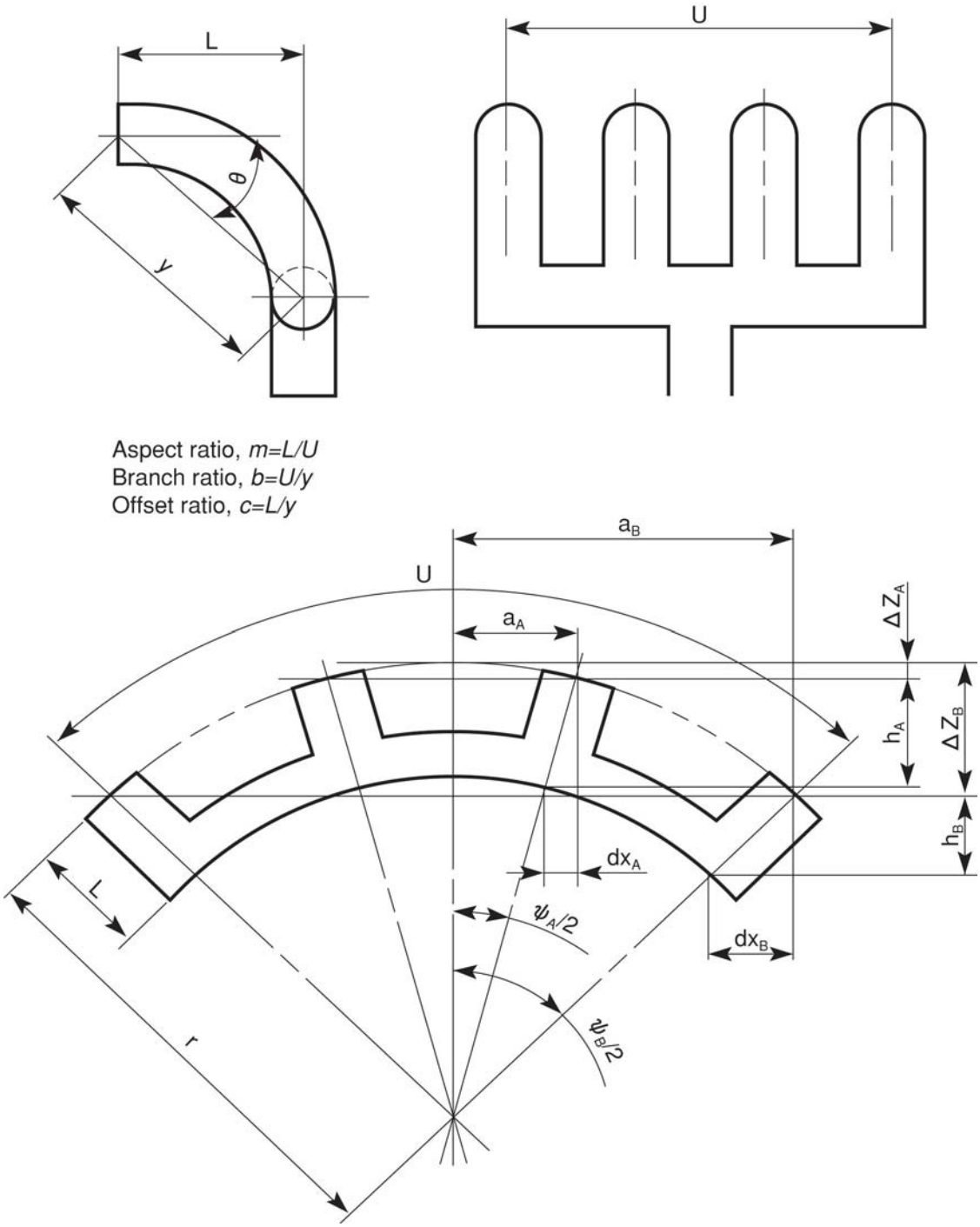


Fig. 3 Model of the exhaust manifold used for the analysis

Similarly, d_{B1} is the deformation that occurs when the moment WL operates on the end of a beam of length $U/2$. This can be expressed by Eq. (2):

$$\begin{aligned} d_{B1} &= M_0(U/2)^2/2EI \\ &= (WL/2EI)(U/2)^2 \end{aligned} \quad (2)$$

Consequently, the deformation $d_{A1}+d_{B1}$ of the ends of the collective part caused by the moments operating on each branch can be defined using Eqs. (1) and (2):

$$\begin{aligned} d_{A1}+d_{B1} &= (WL/2EI)(U/6)^2 \\ &\quad + (WL/2EI)(U/2)^2 \\ &= (5WLU^2)/(36EI) \end{aligned} \quad (3)$$

Next, d_{A2} and d_{B2} can represent the deformation that occurs when W operates on the end of beams of length L that have one end fixed, so that:

$$d_{A2} = d_{B2} = (WL^3)/(3EI) \quad (4)$$

Therefore, from Eqs. (1) and (4):

$$\begin{aligned} dx_A = d_{A1}+d_{A2} &= (WL)(U/6)^2/(2EI) \\ &\quad + (WL^3)/(3EI) \\ &= (WL)(U^2+24L^2)/(72EI) \end{aligned} \quad (5)$$

And from Eqs. (3) and (4):

$$\begin{aligned} dx_B = d_{A1}+d_{B1}+d_{B2} &= (5WLU^2)/(36EI) \\ &\quad +(WL^3)/(3EI) \\ &= (WL)(5U^2+12L^2)/(36EI) \end{aligned} \quad (6)$$

From Eqs. (5) and (6), the stiffness of the collective part will be:

$$\begin{aligned} Gx_A &= W/dx_A \\ &= (72EI)/[L(U^2+24L^2)] \end{aligned} \quad (7)$$

$$\begin{aligned} Gx_B &= W/dx_B \\ &= (36EI)/[L(5U^2+12L^2)] \end{aligned} \quad (8)$$

Since $m = L/U$, L can be eliminated from Eq. (7), leaving:

$$\begin{aligned} Gx_A &= (72EI)/[mU(U^2+24m^2U^2)] \\ &= (EI/U^3)\{72/[m(1+24m^2)]\} \end{aligned}$$

Therefore, the non-dimensional stiffness of No. 2 port and No. 3 port is:

$$Gx_AU^3/EI = 72/[m(1+24m^2)] \quad (9)$$

Similarly, L can be eliminated from Eq. (8), giving:

$$\begin{aligned} Gx_B &= (36EI)/[mU(5U^2+12m^2U^2)] \\ &= (EI/U^3)\{36/[m(5+12m^2)]\} \end{aligned}$$

Consequently, the non-dimensional stiffness of No. 1 port and No. 4 port is:

$$Gx_BU^3/EI = 36/[m(5+12m^2)] \quad (10)$$

Next the effect of θ will be considered.

Substituting $L/\cos\theta$ for L in Eqs. (1) through (8), these become:

$$d_{A1} = (WL/2EI)(U/6)^2\cos^{-1}\theta \quad (11)$$

$$d_{B1} = (WL/2EI)(U/2)^2\cos^{-1}\theta \quad (12)$$

$$\therefore d_{A1}+d_{B1} = (5WL/36EI)U^2\cos^{-1}\theta \quad (13)$$

$$d_{A2} = d_{B2} = (WL/3EI)\cos^3\theta \quad (14)$$

$$\begin{aligned} \therefore dx_A &= d_{A1}+d_{A2} \\ &= (WL/72EI)[(U^2/\cos\theta) \\ &\quad +(24L^2/\cos^3\theta)] \end{aligned} \quad (15)$$

$$\begin{aligned} dx_B &= d_{A1}+d_{B1}+d_{B2} \\ &= (WL/36EI)[(5U^2/\cos\theta) \\ &\quad +(12L^2/\cos^3\theta)] \end{aligned} \quad (16)$$

$$\begin{aligned} \therefore Gx_A &= W/dx_A \\ &= (72EI)/\{L[(U^2/\cos\theta) \\ &\quad +(24L^2/\cos^3\theta)]\} \end{aligned} \quad (17)$$

$$\begin{aligned} Gx_B &= W/dx_B \\ &= (36EI)/\{L[(5U^2/\cos\theta) \\ &\quad +(12L^2/\cos^3\theta)]\} \end{aligned} \quad (18)$$

Since $m = L/U$, L can be eliminated from Eqs. (17) and (18) and the non-dimensional stiffness derived by:

$$\begin{aligned} Gx_AU^3/EI &= 72/\{m[(1/\cos\theta) \\ &\quad +(24m^2/\cos^3\theta)]\} \end{aligned} \quad (19)$$

$$\begin{aligned} Gx_BU^3/EI &= 36/\{m[(5/\cos\theta) \\ &\quad +(12m^2/\cos^3\theta)]\} \end{aligned} \quad (20)$$

Eqs. (19) and (20) can be used with θ as a parameter to plot the non-dimensional stiffness Gx_AU^3/EI and Gx_BU^3/EI with respect to m. This yields Fig. 4 and Fig. 5, respectively. Plotting these again with respect to θ yields Fig. 6 and Fig. 7, respectively.

It can be seen in Fig. 4 through Fig. 7 that the stiffness increases as θ becomes smaller. As m becomes larger, however, the effect of θ becomes negligible. As m grows smaller, the stiffness increases exponentially. These observations can be made alike in No. 1 port and No. 4 port, and No. 2 port and No. 3 port. Comparison of the No. 1 and No. 4 ports with the No. 2 and No. 3 ports shows that, under identical conditions, the No. 2 and No. 3 ports have stiffness several times greater than the No. 1 and No. 4 ports (especially when m is small).

2.2. Changes in Non-dimensional Stiffness with Respect to the Branch Ratio

Substituting $m = \cos\theta/b$ in Eq. (9) yields:

$$Gx_AU^3/EI = 72b^3/(b^2\cos\theta+24\cos^3\theta) \quad (21)$$

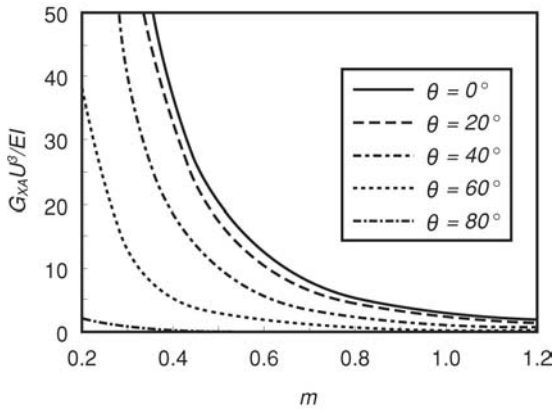


Fig. 4 Non-dimensional stiffness rigidity for No.2 and No.3 ports vs. aspect ratio "*m*".
Non-dimensional stiffness rigidity increases as "*m*" and θ become smaller.

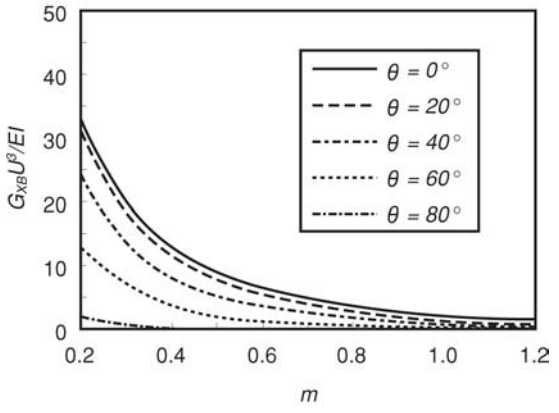


Fig. 5 Non-dimensional stiffness rigidity for No.1 and No.4 ports vs. aspect ratio "*m*".
Non-dimensional stiffness rigidity increases as "*m*" and θ become smaller.
In the case of a smaller "*m*", stiffness rigidity for the No.1 and No.4 ports is quite small compared with that of the No.2 and No.3 ports (Fig. 4).

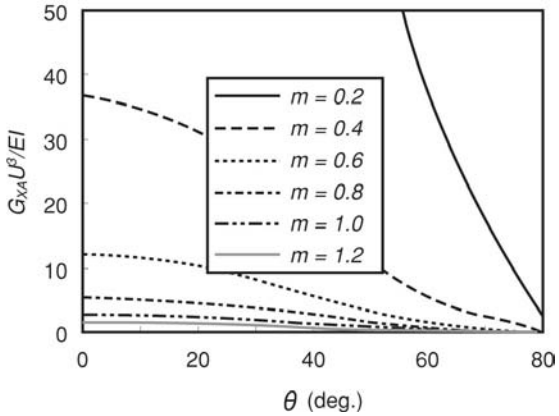


Fig. 6 Non-dimensional stiffness rigidity for No.2 and No.3 ports vs. deviation angle θ.

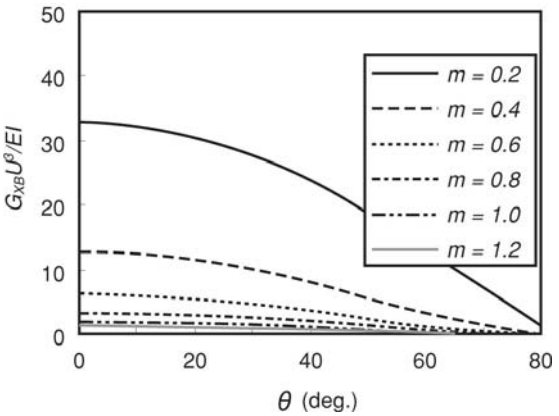


Fig. 7 Non-dimensional stiffness rigidity for No.1 and No.4 ports vs. deviation angle θ.

Similarly, in Eq. (10):

$$Gx_BU^3/EI = 36b^3/(5b^2\cos\theta+12\cos^3\theta) \quad (22)$$

Eqs. (21) and (22) can be used with θ as a parameter to plot the non-dimensional stiffness Gx_AU^3/EI and Gx_BU^3/EI with respect to *b*. This yields Fig. 8 and Fig. 9, respectively. Plotting these again with respect to θ yields Fig. 10 and Fig. 11, respectively.

It can be seen in Fig. 8 through Fig. 11 that the stiffness increases when θ becomes larger, if *b* remains the same. As *b* becomes smaller, however, that difference diminishes. As *b* grows larger, the stiffness increases exponentially. These observations can be made alike in No. 1 port and No. 4 port, and No. 2 port and No. 3 port. Comparison of the stiffness of the No. 1 and No. 4 ports with the No. 2 and No. 3 ports shows that, under identical conditions, the No. 2 and No. 3 ports have stiffness several times greater than the No. 1 and No. 4 ports (especially when *b* is small).

2.3. Changes in Non-dimensional Stiffness with Respect to the Offset Ratio

Eqs. (17) and (18) can be used with *m* as a parameter to plot the non-dimensional stiffness with respect to the offset ratio. The results are shown in Fig. 12 and Fig. 13, respectively.

The stiffness increases when *m* becomes smaller, if the offset ratio remains the same. When the offset ratio is smaller, however, that difference diminishes. As the offset ratio grows larger, the stiffness increases exponentially. These observations can be made alike in No. 1 port and No. 4 port, and No. 2 port and No. 3 port. Comparison of the stiffness of the No. 1 and No. 4 ports with the No. 2 and No. 3 ports shows that, under identical conditions, the No. 2 and No. 3 ports have stiffness several times greater than the No. 1 and No. 4 ports (especially when the offset ratio is small).

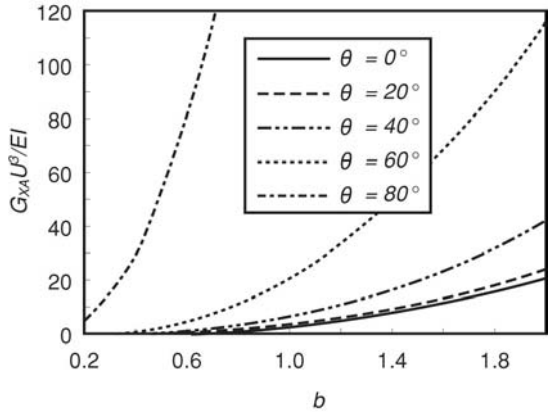


Fig. 8 Non-dimensional stiffness rigidity for No.2 and No.3 ports vs. branch ratio "*b*".
Non-dimensional stiffness rigidity increases as "*b*" and θ become larger.

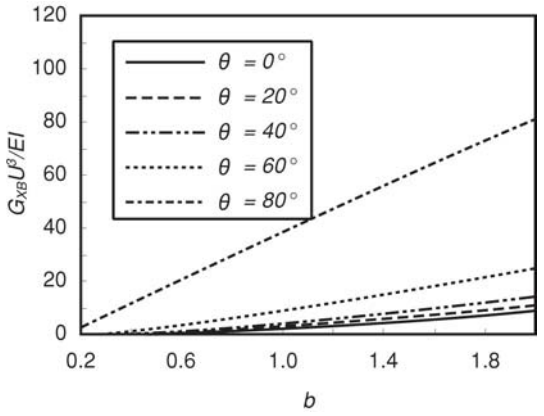


Fig. 9 Non-dimensional stiffness rigidity for No.1 and No.4 ports vs. branch ratio "*b*".
Non-dimensional stiffness rigidity increases as "*b*" and θ become larger.
Especially in the case of large "*b*", stiffness rigidity for the No.1 and No.4 port is smaller than that for the No.2 and No.3 ports.

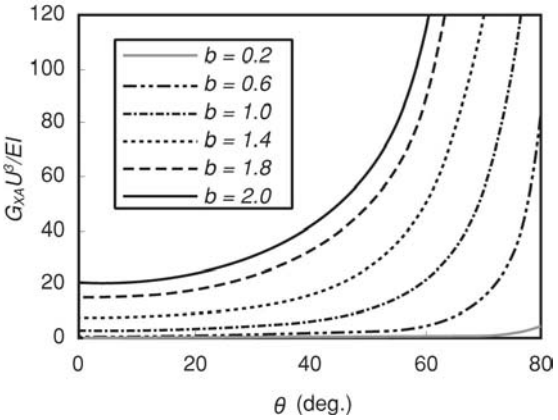


Fig. 10 Non-dimensional stiffness rigidity for No.2 and No.3 ports vs. deviation angle θ.

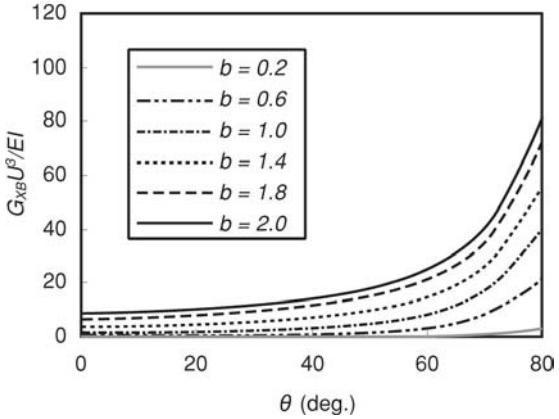


Fig. 11 Non-dimensional stiffness rigidity for No.1 and No.4 ports vs. deviation angle θ.

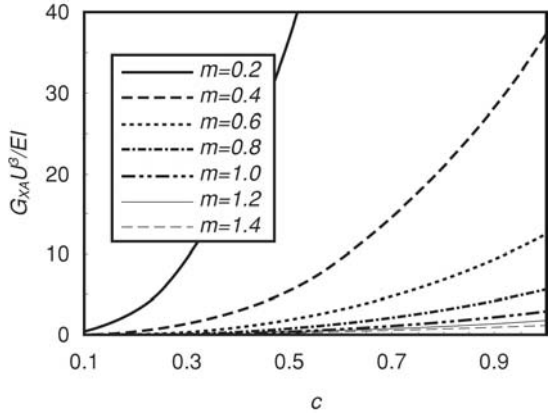


Fig. 12 Non-dimensional stiffness rigidity for No.2 and No.3 ports vs. offset ratio "*c*".
Non-dimensional stiffness rigidity increases as "*c*" becomes larger and "*m*" becomes smaller.

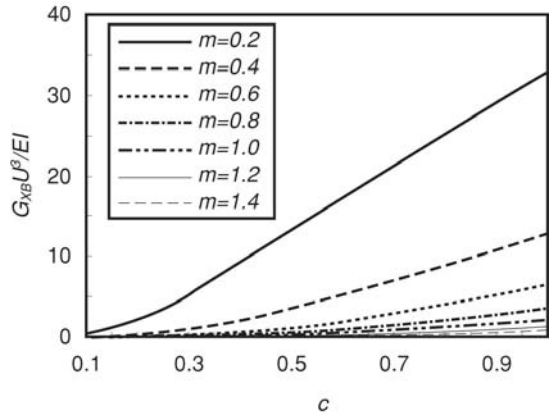


Fig. 13 Non-dimensional stiffness rigidity for No.1 and No.4 ports vs. offset ratio "*c*".
Non-dimensional stiffness rigidity increases as "*c*" becomes larger and "*m*" becomes smaller.
Non-dimensional stiffness rigidity for the No.1 and No.4 ports is smaller than that of the No.2 and No.3 ports.

2.4. Quantity of Warp

i) ΔZ_A

From Fig. 2 and Fig. 3:

$$r^2 = a_A^2+(r-\Delta Z_A)^2$$
$$= a_A^2+r^2-2r\Delta Z_A+\Delta Z_A^2$$

Here, since $\Delta Z_A << U$, it follows that:

$$r^2 = a_A^2+r^2-2r\Delta Z_A$$
$$\therefore 2r\Delta Z_A = a_A^2$$
$$a_A = [(U/6)^2-\Delta Z_A^2]^{1/2} \approx U/6$$

Consequently:

$$2r\Delta Z_A = (U/6)^2$$
$$\therefore r = (U/6)^2/(2\Delta Z_A) \quad (23)$$

When $\Psi_A << 1$:

$$dx_A/h_A = \tan(\Psi_A/2) \approx \Psi_A/2$$

Therefore:

$$\Psi_A/2 = dx_A/h_A = dx_A/L \quad (24)$$

Here, the length $U/6$ of the arc with radius r and angle $\Psi_A/2$ will be (see Fig. 3):

$$U/6 = r(\Psi_A/2) \quad (25)$$

Substituting Eqs. (23) and (24) in Eq. (25) yields:

$$U/6 = [(U/6)^2/(2\Delta Z_A)](dx_A/L)$$
$$= (U^2 dx_A)/(72L\Delta Z_A)$$
$$\therefore \Delta Z_A = (1/12)(U/L)dx_A$$
$$= [1/(12m)]dx_A \quad (26)$$

ii) ΔZ_B

Similarly:

$$r^2 = a_B^2+(r-\Delta Z_B)^2$$
$$= a_B^2+r^2-2r\Delta Z_B+\Delta Z_B^2$$

Here, since $\Delta Z_B << U$, it follows that:

$$r^2 = a_B^2+r^2-2r\Delta Z_B$$
$$\therefore 2r\Delta Z_B = a_B^2$$
$$a_B = [(U/2)^2-\Delta Z_B^2]^{1/2} \approx U/2$$

Consequently:

$$2r\Delta Z_B = (U/2)^2$$
$$\therefore r = (U/2)^2/(2\Delta Z_B) \quad (27)$$

When $\Psi_B << 1$:

$$dx_B/h_B = \tan(\Psi_B/2) \approx \Psi_B/2$$

Therefore:

$$\Psi_B/2 = dx_B/h_B = dx_B/L \quad (28)$$

Here, the length $U/2$ of the arc with radius r and angle $\Psi_B/2$ will be (see Fig. 3):

$$U/2 = r(\Psi_B/2) \quad (29)$$

Substituting Eqs. (27) and (28) in Eq. (29) yields:

$$U/2 = [(U/2)^2/(2\Delta Z_B)](dx_B/L)$$
$$= (U^2 dx_B)/(8L\Delta Z_B)$$
$$\therefore \Delta Z_B = (1/4)(U/L)dx_B$$
$$= [1/(4m)]dx_B \quad (30)$$

Considering the apparent warp quantity $\Delta Z_A'$ with respect to Eq. (26):

$$\Delta Z_A' = [1/(12m)](\cos\theta)dx_A$$
$$\therefore \Delta Z_A'/dx_A = [1/(12m)](\cos\theta) \quad (31)$$

Fig. 14 and Fig. 15 show the displacement ratios $\Delta Z_A'/dx_A$ derived from Eq. (31) for the No. 2 port and No. 3 port when m and θ are varied.

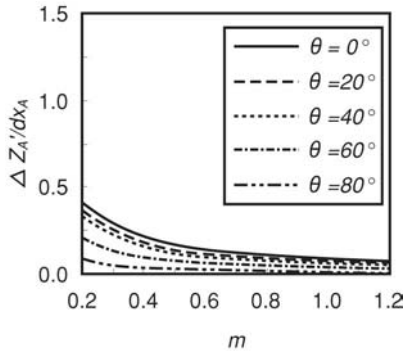


Fig. 14 Displacement ratio for No.2 and No.3 ports vs. aspect ratio "m".
Displacement ratio increases as "m" and θ become smaller.

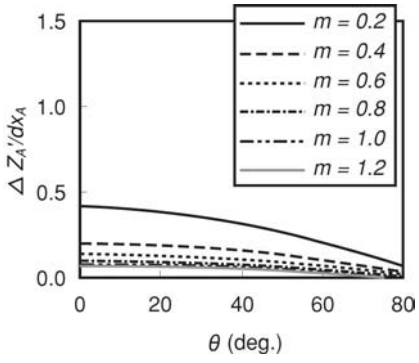


Fig. 15 Displacement ratio for No.2 and No.3 ports vs. deviation angle θ.

Similarly, from Eq. (30):

$$\Delta Z_B'/dx_B = [1/(4m)](\cos\theta) \quad (32)$$

Fig. 16 and Fig. 17 show the displacement ratios $\Delta Z_B'/dx_B$ derived from Eq. (32) for the No. 1 port and No. 4 port when m and θ are varied.

When θ remains the same, $\Delta Z_A'/dx_A$ and $\Delta Z_B'/dx_B$ diminish exponentially as the aspect ratio increases. When the aspect ratio remains the same, $\Delta Z_A'/dx_A$ and $\Delta Z_B'/dx_B$ increase as θ diminishes. When θ approaches 0°, however, this difference diminishes. The displacement ratio of No. 1 port and No. 4 port is several times larger than the displacement ratio of No. 2 port and No. 3 port.

2.5. The Branch Ratio with Respect to the Aspect Ratio

$$L/y = (L/U)(U/y) \quad (33)$$

Here, the offset ratio becomes $L/y = (y\cos\theta)/y$, so that, from Eq. (33):

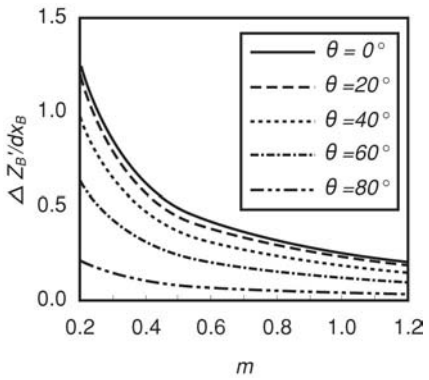


Fig. 16 Displacement ratio for No.1 and No.4 ports vs. aspect ratio "m".
Displacement ratio increases as "m" and θ become smaller.
The displacement ratio for the No.1 and No.4 ports is fairly large compared with that for the No.2 and No.3 ports.

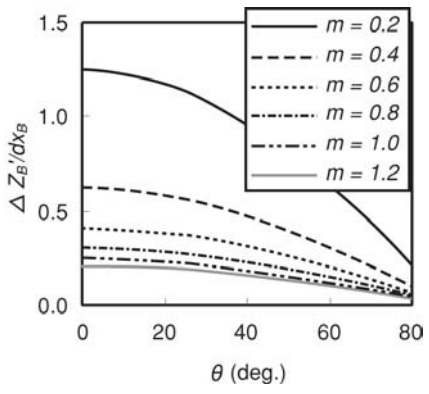


Fig. 17 Displacement ratio for No.1 and No.4 ports vs. deviation angle θ.

$$b = \cos\theta/m \quad (34)$$

The branch ratio derived from Eq. (34) when m and θ are varied is shown in Fig. 18.

When θ remains the same, the branch ratio diminishes nonlinearly as the aspect ratio increases. When the aspect ratio remains the same, the branch ratio is larger when θ is smaller.

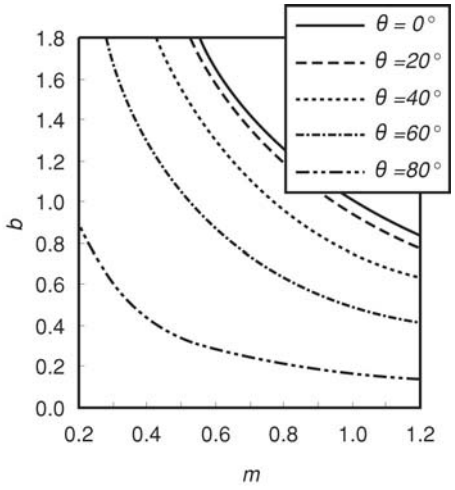


Fig. 18 Aspect ratio "m" vs. branch ratio "b".

3. Discussion

The results obtained through the analysis can be summarized as follows. The stiffness of the exhaust manifold can generally be increased by making m smaller (Fig. 4 and Fig. 5), making θ smaller (Fig. 6 and Fig. 7), making b larger (Fig. 8 and Fig. 9), and making c larger (Fig. 12 and Fig. 13).

In order to increase the stiffness in this way, y should be made smaller, while it is better for U to be larger. However, the effect of L is reciprocal with respect to m and c. The effect on stiffness of θ is also the reverse of both m and b. For example, when U is determined by the engine dimensions, making L smaller will generally also make y smaller. In such a case, therefore, m becomes smaller when L is small, even though c does not vary to any great extent. Meanwhile, b becomes larger (even if U is fixed because y is small).

Similarly, the deformation of the exhaust manifold can be reduced by increasing both θ and m (Fig. 14 to Fig. 17).

Designing an exhaust manifold requires attention to various constraints imposed by the engine and the engine compartment. This requires the selection of dimensions and geometry that achieve an optimum balance among these parameters, which can be done by identifying the best trade-off among the parameters.

Next, on the assumption that θ, m, b, and c can be varied independently, their respective proportionate effects on non-dimensional stiffness are sought. This allows determination of the non-dimensional stiffness varying rate when θ, m, b, and c are varied individually. Consequently, it becomes possible to identify the respective proportionate effects on non-dimensional stiffness both more clearly and quantitatively when the above θ, m, b, and c are varied individually for different dimensions assigned to the various exhaust manifold parts.

Non-dimensional stiffness is a function of the above four independent variables θ, m, b, and c. Therefore, if:

$$Gx_AU^3/EI = f_A(\theta, m, b, c) \quad (35)$$

Then Eq. (35) yields:

$$\begin{aligned} d(Gx_AU^3/EI) &= (\partial f_A/\partial\theta)d\theta \\ &+ (\partial f_A/\partial m)dm \\ &+ (\partial f_A/\partial b)db \\ &+ (\partial f_A/\partial c)dc \end{aligned} \quad (36)$$

Here, Eq. (21) is applied so that:

$$\begin{aligned} &\partial f_A/\partial\theta \\ &= \partial[72b^3/(b^2\cos\theta+24\cos^3\theta)]/\partial\theta \\ &= (72b^5\sin\theta+5184b^3\cos^2\theta\sin\theta) / \\ &\quad (b^2\cos\theta+24\cos^3\theta)^2 \\ &= T_{A\theta} \end{aligned} \quad (37)$$

Applying Eq. (19), then:

$$\begin{aligned} \partial f_A/\partial m &= \partial[72/\{m[(1/\cos\theta) \\ &\quad + (24m^2/\cos^3\theta)]\}]/\partial m \\ &= -72\cos^3\theta(\cos^2\theta+72m^2) / \\ &\quad (m\cos^2\theta+24m^3)^2 \\ &= T_{Am} \end{aligned} \quad (38)$$

Applying Eq. (21):

$$\begin{aligned} &\partial f_A/\partial b \\ &= \partial[72b^3/(b^2\cos\theta + 24\cos^3\theta)]/\partial b \\ &= (154b^4+5425b^2\cos^2\theta) / \\ &\quad (b^4\cos\theta+576\cos^5\theta+48b^2\cos^3\theta) \\ &= T_{Ab} \end{aligned} \quad (39)$$

Applying Eq. (19):

$$\begin{aligned} &\partial f_A/\partial c \\ &= \partial[72/\{m[(1/\cos\theta) \\ &\quad +(24m^2/\cos^3\theta)]\}]/\partial c \\ &= (82c^4+5424m^2c^2) / \\ &\quad (mc^4+576m^5+48m^3c^2) \\ &= T_{Ac} \end{aligned} \quad (40)$$

Therefore, when Eqs. (37) through (40) are substituted in Eq. (36), the following Eq. (41) is obtained:

$$\begin{aligned} d(Gx_AU^3/EI) &= T_{A\theta}d\theta+T_{Am}dm \\ &+ T_{Ab}db+T_{Ac}dc \end{aligned} \quad (41)$$

Similarly:

$$Gx_BU^3/EI = f_B(\theta, m, b, c) \quad (42)$$

In this case, Eq. (42) yields:

$$\begin{aligned} d(Gx_BU^3/EI) &= (\partial f_B/\partial\theta)d\theta + (\partial f_B/\partial m)dm \\ &+ (\partial f_B/\partial b)db + (\partial f_B/\partial c)dc \end{aligned} \quad (43)$$

Eq. (22) is applied here so that:

$$\begin{aligned} &\partial f_B/\partial\theta \\ &= (180b^5\sin\theta+1296b^3\cos^2\theta\sin\theta) / \\ &\quad (5b^2\cos\theta+12\cos^3\theta)^2 \\ &= T_{B\theta} \end{aligned} \quad (44)$$

Applying Eq. (20):

$$\begin{aligned} &\partial f_B/\partial m \\ &= -36\cos^3\theta(5\cos^2\theta+36m^2) / \\ &\quad (5m\cos^2\theta+12m^3)^2 \\ &= T_{Bm} \end{aligned} \quad (45)$$

Applying Eq. (22):

$$\begin{aligned} &\partial f_B/\partial b \\ &= (180b^4+1296b^2\cos^2\theta) / \\ &\quad (25b^4\cos\theta+144\cos^5\theta+120b^2\cos^3\theta) \\ &= T_{Bb} \end{aligned} \quad (46)$$

Applying Eq. (20):

$$\begin{aligned} &\partial f_B/\partial c \\ &= (180c^4+1296m^2c^2) / \\ &\quad (25mc^4+144m^5+120m^3c^2) \\ &= T_{Bc} \end{aligned} \quad (47)$$

Therefore, by substituting Eqs. (44) through (47) in Eq. (43), the following Eq. (48) is obtained:

$$\begin{aligned} &d(Gx_BU^3/EI) = \\ &\quad T_{B\theta}d\theta+T_{Bm}dm+T_{Bb}db+T_{Bc}dc \end{aligned} \quad (48)$$

The effects of θ and m on the displacement ratio is sought by a similar approach:

$$\Delta Z_A'/dx_A = g_A(\theta, m) \quad (49)$$

Then, from Eq. (49):

$$\begin{aligned} d(\Delta Z_A'/dx_A) &= (\partial g_A/\partial\theta)d\theta \\ &+(\partial g_A/\partial m)dm \end{aligned} \quad (50)$$

Eq. (31) is then applied here:

$$\partial g_A/\partial\theta = S_{A\theta} = -\sin\theta/12m \quad (51)$$

$$\partial g_A/\partial m = S_{Am} = -\cos\theta/12m^2 \quad (52)$$

Substituting Eqs. (51) and (52) in Eq. (50), therefore, the following Eq. (53) is obtained:

$$d(\Delta Z_A'/dx_A) = (-\sin\theta/12m)d\theta - (\cos\theta/12m^2)dm \quad (53)$$

Similarly:

$$\Delta Z_B'/dx_B = g_B(\theta, m) \quad (54)$$

Therefore, from Eq. (54):

$$d(\Delta Z_B'/dx_B) = (\partial g_B/\partial\theta)d\theta + (\partial g_B/\partial m)dm \quad (55)$$

Here Eq. (32) is applied:

$$\partial g_B/\partial\theta = S_{B\theta} = -\sin\theta/4m \quad (56)$$

$$\partial g_B/\partial m = S_{Bm} = -\cos\theta/4m^2 \quad (57)$$

Consequently, by substituting Eqs. (56) and (57) in Eq. (55), the following Eq. (58) is obtained:

$$d(\Delta Z_B'/dx_B) = (-\sin\theta/4m)d\theta - (\cos\theta/4m^2)dm \quad (58)$$

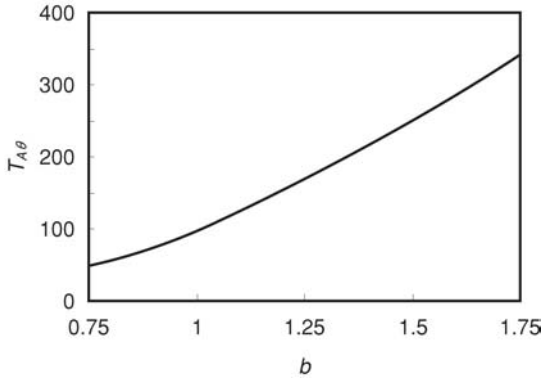


Fig. 19 "b" vs. "$T_{A\theta}$" in the case of θ=60deg.(constant) derived from Eq.(37).

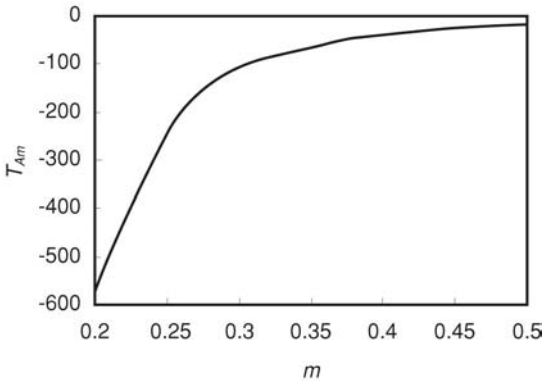


Fig. 20 "m" vs. "T_{Am}" in the case of θ=60deg.(constant) derived from Eq.(38).

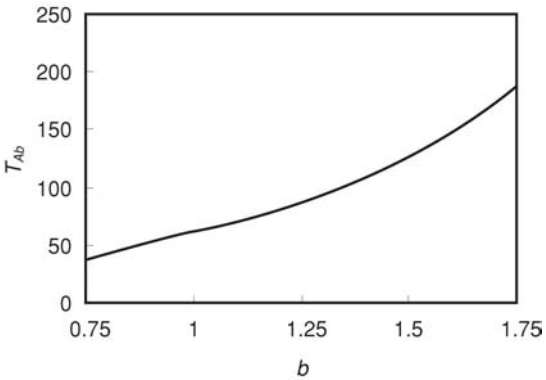


Fig. 21 "b" vs. "T_{Ab}" in the case of θ=60deg.(constant) derived from Eq.(39).

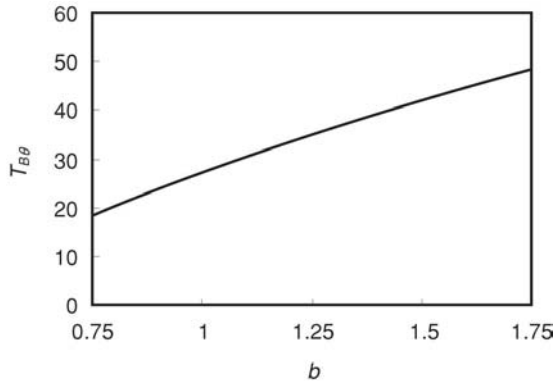


Fig. 22 "b" vs. "$T_{B\theta}$" in the case of θ=60deg.(constant) derived from Eq.(44).

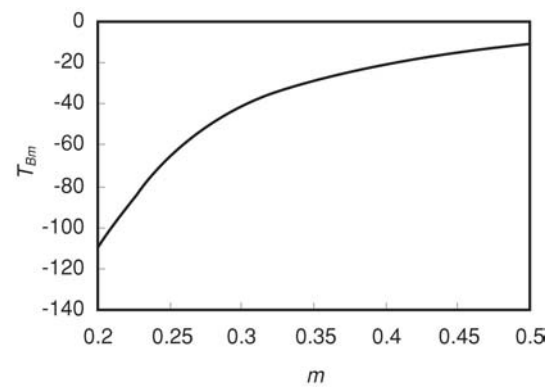


Fig. 23 "m" vs. "T_{Bm}" in the case of θ=60deg.(constant) derived from Eq.(45).

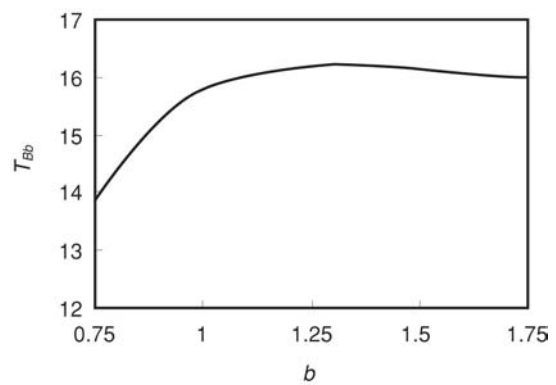


Fig. 24 "b" vs. "T_{Bb}" in the case of θ=60deg.(constant) derived from Eq.(46).

The above results make it possible to use Eqs. (37) to (40) and Eqs. (44) to (47) to obtain the several varying rate of stiffness $T_{A\theta}$, T_{Am}, T_{Ab}, T_{Ac}, $T_{B\theta}$, T_{Bm}, T_{Bb}, and T_{Bc}, which result from individual variations in θ, m, b, and c, respectively. The results in the case of $\theta = 60°$ (constant) are shown in Fig. 19 through Fig. 24. By this method, the effects on stiffness varying rate resulting from individual variations in θ, m, b, and c, respectively, can be identified clearly and quantitatively.

These figures indicate, for example, that under the same conditions, $T_{A\theta} > T_{B\theta}$, $|T_{Am}| > |T_{Bm}|$, and $T_{Ab} > T_{Bb}$. It is apparent that the varying rate for No. 2 port and No. 3 port is greater than that for No. 1 port and No. 4 port. Also, the absolute values of T_{Am} and T_{Bm} are smaller when m is larger for both paired No. 2 and No. 3 ports and No. 1 and No. 4 ports. Similarly, T_{Ab} and T_{Bb} are smaller when b is smaller. In addition, the absolute values of T_{Am} and T_{Bm} are smaller when θ is smaller, as are T_{Ab}, T_{Bb}, $T_{A\theta}$, and $T_{B\theta}$ likewise.

Next, the varying rates $S_{A\theta}$, S_{Am}, $S_{B\theta}$, and S_{Bm} for the displacement ratio of each cylinder occurring when θ and m are varied are sought from Eqs. (51) and (52) in the case of No. 2 port and No. 3 port, and from Eqs. (56) and (57) in the case of No. 1 port and No. 4 port. The respective results are shown in Fig. 25 and Fig. 26.

These figures indicate that the absolute values of $S_{A\theta}$, S_{Am}, $S_{B\theta}$, and S_{Bm} are greater when m is smaller. This shows, therefore, that the several varying rates with respect to changes in m become larger when m is smaller. Furthermore, the absolute values of $S_{A\theta}$ and $S_{B\theta}$ increase as θ increases, but the absolute values of S_{Am} and S_{Bm} conversely grow smaller as θ increases. This clearly shows, therefore, that the several varying rates with respect to changes in θ are small.

Now the relationships identified above will be used to demonstrate a calculation of the quantitative effects on the varying rate of the stiffness and the varying rate of the displacement ratio occurring due to variations in θ, m, b, and c. Typical dimensions of an exhaust manifold for use with an in-line 4-cylinder engine will be used as an example.

The following values will be used:

$\theta = 60°$
$m = 0.35$
$b = 1.25$
$c = 0.5$

Substituting the above values in Eqs. (37) through (40), the following results are obtained for No. 2 port and No. 3 port:

$T_{A\theta} = 166.7$
$T_{Am} = -65.5$
$T_{Ab} = 87.3$
$T_{Ac} = 48.1$

By similarly substituting values in Eqs. (44) through (47), the following results are obtained for No. 1 port and No. 4 port:

$T_{B\theta} = 35.0$
$T_{Bm} = -28.1$
$T_{Bb} = 16.2$
$T_{Bc} = 19.7$

This shows that when the variables for No. 2 port, No. 3 port, No. 1 port, and No. 4 port are varied the same amount, the factor that has the greatest effect on the stiffness varying rate is θ. This tendency is particularly marked in relation to No. 2 port and No. 3 port. The next largest effect is of m on No. 1 port and No. 4 port. Here, however, neither No. 2 port and No. 3 port, nor No. 1 port and No. 4 port, show any great difference between those effects and the effects of other factors b and c.

Eq. (51) and Eq. (52) yield the following warp quantities for No. 2 port and No. 3 port:

$S_{A\theta} = -(\sin 60°)/(12 \times 0.35) = -0.21$ (for θ)
$S_{Am} = -(\cos 60°)/(12 \times 0.35^2) = -0.34$ (for m)

Similarly, Eq. (56) and Eq. (57) yield the following for No. 1 port and No. 4 port:

$S_{B\theta} = -(\sin 60°)/(4 \times 0.35) = -0.62$ (for θ)
$S_{Bm} = -(\cos 60°)/(4 \times 0.35^2) = -1.02$ (for m)

For No. 2 port and No. 3 port, and No. 1 port and No. 4 port alike, the varying rate for m has a significant effect on the varying rate of the displacement ratio. The absolute values for both θ and m, which express the magnitude of that effect, are three times larger for No. 1 port and No. 4 port than they are for No. 2 port and No. 3 port.

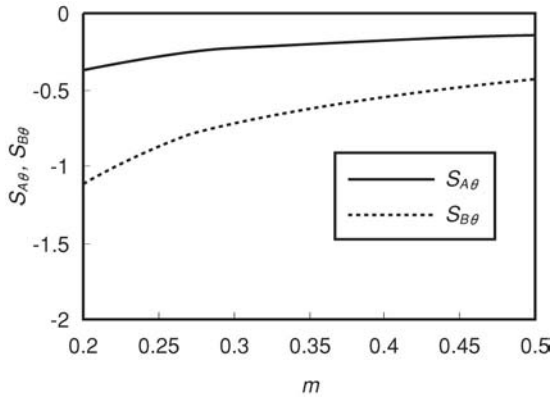


Fig. 25 "m" vs. "$S_{A\theta}$" and "$S_{B\theta}$" in the case of θ=60deg.(constant) derived from Eq.(51) and Eq.(56).

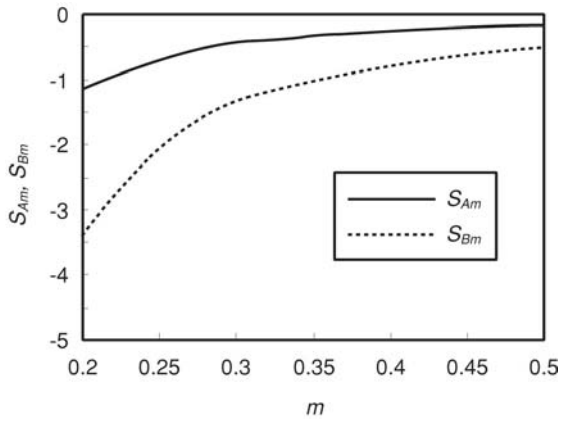


Fig. 26 "m" vs. "S_{Am}" and "S_{Bm}" in the case of θ=60deg.(constant) derived from Eq.(52) and Eq.(57).

A method of the kind described above can be used to determine the respective quantitative effects exerted on the varying rates of the exhaust manifold stiffness and of the displacement ratio by θ, m, b, and c when these factors are varied independently. In other words, it becomes possible to know in advance the values of the stiffness and displacement ratio for the dimensions and shapes of the various parts of an exhaust manifold while it is being designed, as well as the quantitative changes that take place in the varying rate of the stiffness and displacement ratio when the dimensions of various parts are changed. The approaches and methods described here, therefore, can provide effective guidance for deciding the approximate dimensions of the various parts when a new exhaust manifold is being designed.

4. Conclusion

This research examined a desktop method for determining the stiffness of exhaust manifolds for in-line 4-cylinder engines and the displacement ratio that obtains during the application of load and moment to the port areas of those manifolds. In conjunction with this, the project also undertook to determine the effects on the varying rates of the stiffness and the displacement ratio that result when the dimensions and shapes of the various parts are varied. The method described here treats the exhaust manifold as a structure of beams in combination, thus allowing it to identify what effects the difference angle of the collective part, the branch ratio, the offset ratio, the aspect ratio, and so on have on the stiffness and the displacement ratio.

As a result, it was possible to identify the quantitative relationship of the dimensions and shapes of the various parts of an exhaust manifold for an in-line 4-cylinder engine to the stiffness and the displacement ratio, and also to clarify the quantitative effects of those dimensions and shapes on the varying rate of the stiffness and the displacement ratio. This is a method that can be used when newly designing an exhaust manifold for an in-line 4-cylinder engine as a handy and effective technique for deciding the approximate dimensions of the various manifold parts.

Acknowledgements

The author wishes to thank many people inside and outside Honda for engaging in helpful discussion and providing useful suggestions during the course of this research project.

References

(1) Nakada, M., Ishii, K., Enomoto, M., Takahashi, S., Konishi, Y.: “Evaluation of Thermal Fatigue Life on the Exhaust Manifold by Analyzing Restraint Ratio” (in Japanese), JSAE Spring Papers, No. 20005229 (2000)

(2) Ishii, K., Nakada, M., Takahashi, S., Enomoto, M., Konishi, Y.: “Evaluation of Thermal Fatigue Life on the Exhaust Manifold by Analyzing Restraint Ratio,” FISITA World Automotive Congress 2000 (Seoul), No. F2000G295 (2000)

(3) Itoh, K., Ohtsuka, K., Akiyama, K., Yano, M., Doi, S.: “Thermal Deformation of an Exhaust Manifold” (in Japanese), JSAE Review, Vol. 24, No. 4, pp. 87–92 (October, 1993)

■ Author ■



Masaru ENOMOTO

Study of Simulation Technology for Limit Drivability

Takayuki TOYOSHIMA* Yasuhiro MIYATANI*
Yuji SATO* Shinta ARAI*

ABSTRACT

Using conventional technology, it used to be difficult to calculate vehicle behavior in a limit handling situation by mechanical system analysis and predict that behavior with a high degree of accuracy. A method using tire modeling based on Magic Formula has been developed, which has been optimized for limit behavior, and accounts for lateral tire deflection. From a vehicle standpoint, a method using car modeling based on conventional vehicle model has been developed for improvement of the suspension rate and traction torque control. These measures have made it possible to perform mechanical system analysis calculation of vehicle handling behavior up to the limit. As a result, it has become possible to attain a high degree of accuracy in predicting vehicle limit behavior in turns, which is one of the dynamic characteristics for limit drivability.

1. Introduction

Various indexes are used to indicate vehicle driving stability, and a number of techniques for predicting vehicle driving stability have been researched, developed and applied. However, limit handling stability is still difficult to predict, and constructing highly accurate prediction technology has been a pressing issue. Reproducing vehicle behavior in limit conditions in the virtual space of a simulation would allow desktop evaluation and make it possible to reduce the test load using actual vehicles. Furthermore, it is thought that prediction technology for limit conditions could provide a new opportunity for investigating characteristics, and contribute to more efficient vehicle development. This paper reports that technology was developed to more accurately predict cornering performance in limit conditions by improving the vehicle model based on conventional simulation technology for vehicle dynamics, and constructing a tire model for calculation of cornering performance in limit conditions.

* Tochigi R&D Center

2. Basic Approach

Vehicle dynamic characteristics in limit conditions include various items, but this study focused only on cornering performance in limit conditions. There are two main patterns for evaluating cornering performance in limit conditions. One is evaluation of limit performance in the steady state. The testing method is prescribed by the ISO steady state cornering test (ISO4138), which also prescribes basic methods for evaluating limit performance. The other is evaluation of limit performance in the transient state. This evaluation method is typified by the J-turn mode test. Thus far, the establishment of evaluation techniques has been an issue. Figure 1 shows typical evaluation methods for both patterns. The J-turn mode is prescribed by the ISO transient response test (ISO7401), but this is mainly for evaluation of characteristics for linear systems of transient response. Therefore, this study used the ISO test as a reference and set a different testing method in order to evaluate limit performance in the transient state. The J-turn described here

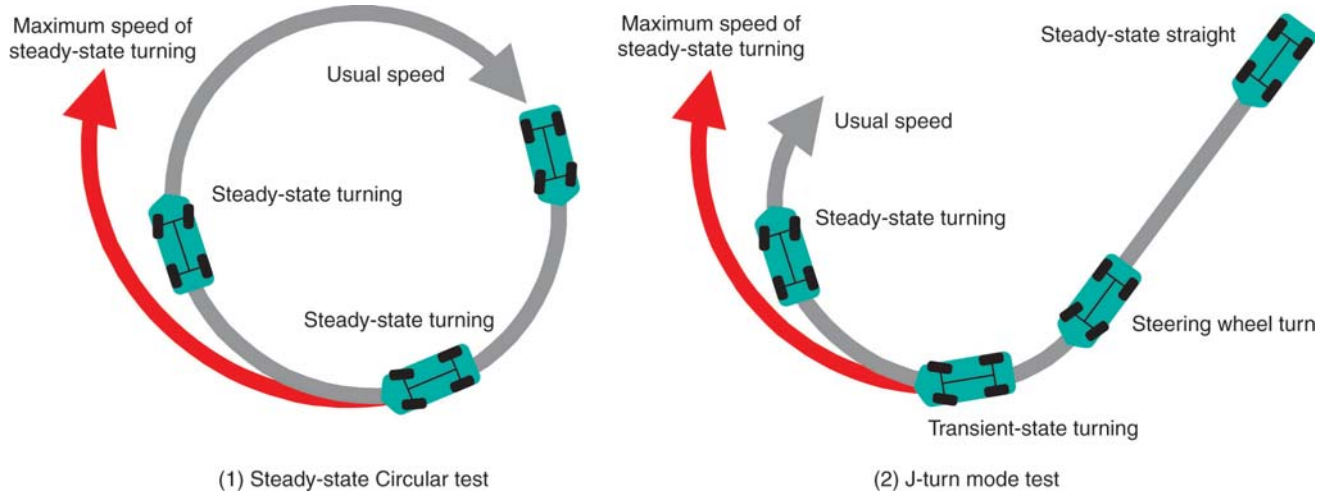


Fig. 1 Two patterns for evaluation of turning behavior

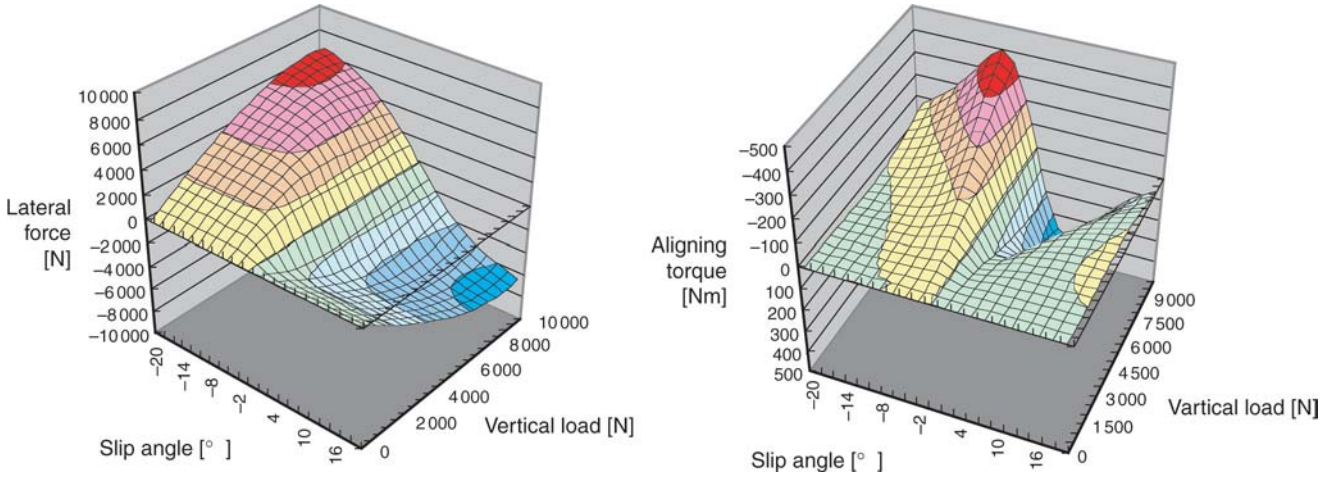


Fig. 2 Nonlinear characteristics of tire

indicates a driving pattern where the steering wheel is turned to a specific steering angle to transiently enter the turning state, then the vehicle cruises at a constant steering angle and speed until steady-state turning is reached. The vehicle behavior at the maximum speed ultimately reached is defined as the cornering performance at limit conditions, and the vehicle behavior at a sufficiently lower speed than the maximum speed is called the steady state cornering performance.

A number of tools for simulating and predicting vehicle behavior have been developed and applied thus far. However, none of these tools are capable of accurately expressing the strong nonlinear characteristics of the tires in limit conditions, or take into account the tire deflection characteristics, so application to investigations of cornering performance in limit conditions is difficult. In limit conditions, as shown in Fig. 2, the load, slip angle and other values become extremely large, and the generated force and torque exhibit strong nonlinear characteristics. In addition, Fig. 3 shows an image of tire deflection produced by lateral force on the tire, and the deflection amount in limit conditions is also a large value as shown here. Therefore, the results of calculations that ignore these factors will contain increasingly large errors, and the required accuracy cannot be obtained. Constructing a tire model that more accurately expresses tire cornering characteristics and deflection characteristics in limit conditions is a requirement for better predicting cornering performance in limit conditions.

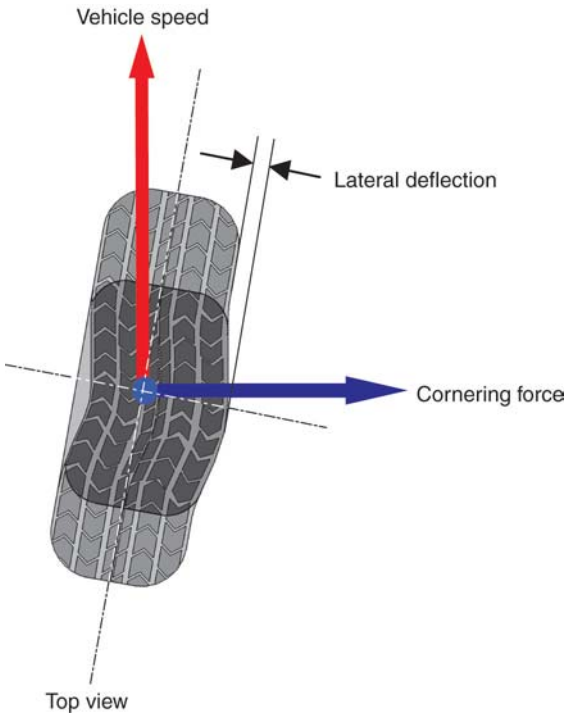


Fig. 3 Lateral deflection of tire

In addition, the state of areas other than the tire model is also quite different in limit conditions compared to normal conditions. Therefore, improvements must be made to the models to calculate the limit conditions. This includes improving characteristics settings in the large stroke range, stipulating the driving force and other conditions, etc.

Improving these models makes it possible to simulate vehicle behavior through mechanical analysis and better predict cornering performance in limit conditions.

3. Constructing a Tire Model

Construction of a tire model that can also be applied to better predict cornering performance in limit conditions can be broadly broken down into the following two elements.

(1) Expressing the cornering characteristics of tires in limit conditions
(2) Expressing the deflection of tires in limit conditions

3.1. Cornering Characteristics of Tires in Limit Conditions

Figure 4 shows the three main cornering characteristics of tires that are necessary to determine vehicle behavior. These three main characteristics are longitudinal force which is generated to the front and back of the tire, lateral force which is generated to the right and left of the tire, and self-aligning torque which is generated around the axis perpendicular to the tire contact surface. The absolute values of these three characteristics must be correctly understood and expressed by the model to more accurately express vehicle behavior in limit conditions.

There are many types of tire models with shapes suited to the application. Of these, three types of tire models were selected as candidates and judged for their appropriateness. These were a dynamic model typified by the Fiala[1] and Gim[2] theories, a mesh model using the finite element method, and a numerical model typified by Magic Formula.

The dynamic model calculates force dynamically by replacing the tire structure with a simple model. This allows significant investigations for determining the tire structure, but has the disadvantage of excessively large error with reality in limit conditions. This is thought to be because tires are made of complex, composite materials which exhibit complex changes that cannot be replaced with a simple structural model. Therefore, this model could not be applied to this simulation, which requires accuracy of absolute values.

The mesh model is capable of expressing tire characteristics that closely approximate reality. However, in order to obtain the required accuracy the model must have an extremely complex structure, and the complex calculations require an inordinate amount of time. This did not match the aims of this study, so this model also could not be applied.

Normally, the tire cornering characteristics change continuously relative to the four status levels of the load, slip rate, slip angle and camber angle acting on the tire. Therefore, if the tire model can be expressed by replacing these characteristics' values with the proper continuous functions having the status levels as the arguments, this numerical formula can be used as the tire model. A numerical model constructed based on actual measurement values offers the high accuracy of absolute values and also allows quick calculation, so this could be considered the most suitable tire model for this study.

Figure 5 shows the structure of the tire model used in this study. This is a Magic Formula, which is a typical tire numerical model.[3], [4]



Fig. 4 Three-component forces for tire performance

Longitudinal force

$$F_x = D_{xa}\cos\left[C_{xa}\tan^{-1}\{B_{xa}(\alpha + Sh_{xa})\}\right]$$

$$F_{x0} = D_x \sin\left[C_x \tan^{-1}\{B_x(\kappa + Sh_x) - E_x(B_x(\kappa + Sh_x) - \tan^{-1}(B_x(\ + Sh_x)))\}\right] + Sv_x$$

$B_{xa} = f(\kappa)$	$B_x = f(F_z)$
C_{xa} = Constant	C_x = Constant
$D_{xa} = f(F_{x0}, \gamma)$	$D_x = f(F_z)$
Sh_{xa} = Constant	$E_x = f(\kappa, F_z)$
$Sh_x = f(F_z)$	
$Sv_x = f(F_z)$	

Lateral force

$$F_y = D_{yk}\cos\left[C_{yk}\tan^{-1}\{B_{yk}(\kappa + Sh_{yk})\}\right] + Sv_{yk}$$

$$F_{y0} = D_y \sin\left[C_y \tan^{-1}\{B_y(\alpha + Sh_y) - E_y(B_y(\alpha + Sh_y) - \tan^{-1}(B_y(\alpha + Sh_y)))\}\right] + Sv_y$$

$B_{yk} = f(\alpha)$	$B_y = f(\gamma, F_z)$
C_{yk} = Constant	C_y = Constant
$D_{yk} = f(\alpha, F_{y0})$	$D_y = f(\gamma, F_z)$
Sh_{yk} = Constant	$E_y = f(\alpha, \gamma, F_z)$
$Sv_{yk} = f(\alpha, \gamma, F_z)$	$Sh_y = f(\gamma, F_z)$
$Sv_y = f(\gamma, F_z)$	

Aligning torque

$$M_z = -t\,F'_y + M_{zr} + s\,F_x$$

$$t = D_t\cos\left[C_t\tan^{-1}\{B_t\alpha_t - E_t(B_t\alpha_t - \tan^{-1}(B_t\alpha_t))\}\right]\cos(\alpha)$$

$$F'_y = F_y - Sv_{yk}$$

$$M_{zr} = D_r\cos\left[\tan^{-1}(B_r\alpha_r)\right]\cos(\alpha)$$

$$s = f(\gamma, F_z, F_y, R_0)$$

$\alpha_t = f(\alpha, \gamma, \kappa, F_z)$	$\alpha_r = f(\alpha, \gamma, \kappa, F_z)$
$B_t = f(\gamma, F_z)$	B_r = Constant
C_t = Constant	$D_r = f(\gamma, F_z, R_0)$
$D_t = f(\gamma, F_z, R_0)$	
$E_t = f(\alpha, \gamma, F_z)$	

Longitudinal Slip	: κ
Slip Angle	: α
Camber Angle	: γ
Normal Wheel Load	: F_z
Unloaded Tire Radius	: R_0

Fig. 5 Magic Formula model

The Magic Formula is a combination of trigonometric functions, and various curves can be expressed by setting the appropriate variables. The formula structure has a high degree of freedom for the slip angle α and slip rate κ, and can be expected to express nonlinear cornering characteristics up to limit conditions for general passenger car tires. However, the degree of freedom for the camber angle γ is relatively low, so it had been unclear thus far whether the cornering characteristics dependence on the camber angle can be accurately expressed up to limit conditions. The Magic Formula tire model conforms to the tire specific cornering characteristics as identified using a tire tester. Variables matching these characteristics are discovered using the optimization method, and used to construct the model. However, it is difficult for general tire testers to accurately test the tire status in limit conditions, and it is also difficult to accurately measure the forces generated by the tire in limit conditions. Therefore, a Magic Formula that also covered limit conditions could not be constructed with the normal optimization method. This study succeeded in more accurately identifying the tire forces generated in limit conditions through detailed analysis of the six-component forces for tire using actual vehicles and by improving the tire tester. These characteristic changes were investigated in detail, and it was found that they could be adequately expressed by a Magic Formula. In addition, a tire model applicable even in limit conditions could be constructed by utilizing a technique that offsets and optimizes the weighting for the cornering characteristics in limit conditions based on these facts. Figure 6 compares a tire model constructed by

the conventional method with a tire model constructed to calculate cornering performance in limit conditions using the technique set in this study. These figures confirm that the accuracy is better in limit conditions than in steady-state conditions.

3.2. Deflection Characteristics of Tires in Limit Conditions

Tires experience large deflection in the lateral direction in limit conditions, but Magic Formula cannot accurately express this lateral deflection. Figure 7 shows the phenomenon where lateral deflection of the tire in limit conditions causes the available tread width to become narrower due to the center of contact becoming displaced toward the inside of the vehicle. However, conventional simulations cannot express tire lateral deflection, so the effects of this narrowing of the available tread width cannot be reflected to the calculations.

This study allowed expression of these changes in the available tread width by inserting a spring element to the center of the hub that couples the tire model and the vehicle model. The Fig. 8 graph shows the deflection amount of the center of contact when various slip angles are applied. The deflection of the center of contact relative to the lateral force generated by the tire as determined from the slip angle and the vertical load is applied to the spring element in the center of the hub as the strain characteristic.

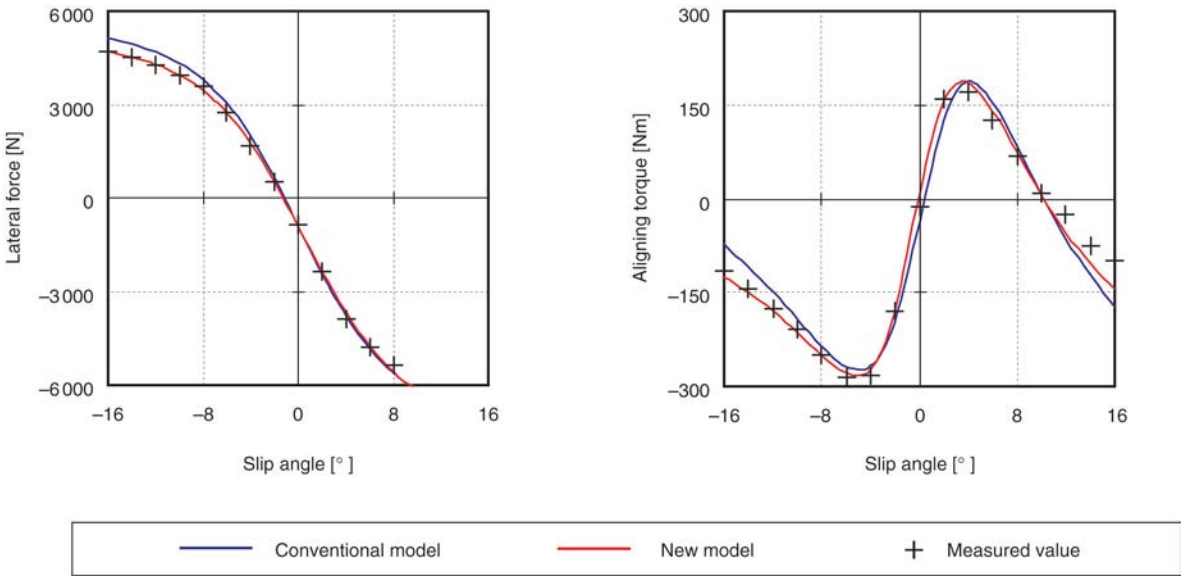


Fig. 6 Comparison between calculated value and measured value (Load 7,500 N, Camber angle 10°)

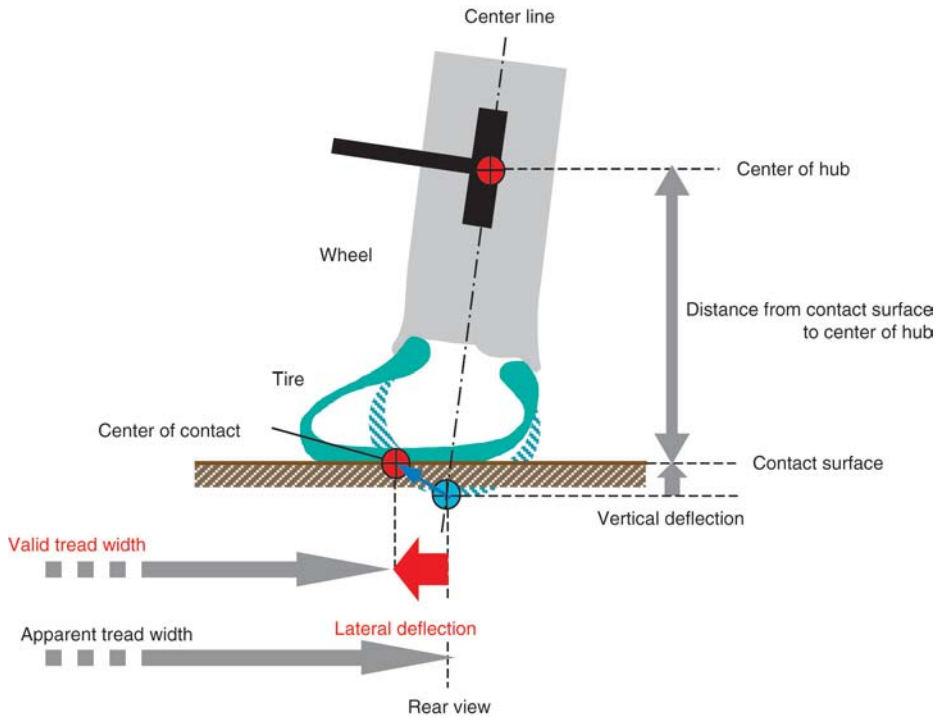


Fig. 7 Change of valid tread width

4. Vehicle Model Improvements

The main vehicle model items requiring improvement for better prediction of cornering performance in limit conditions are the following two elements.

(1) Improvement of the suspension rate
(2) Improvement of drive torque control

Note that in this study, all simulation models other than the tire model, such as the speed, steering and other stipulations generally called the driver model, are collectively referred to as the vehicle model.

4.1. Improvement of the Suspension Rate

In limit conditions the bump and rebound stroke reach ranges that are not used in normal conditions, so nonlinear characteristics equivalent to an actual vehicle must be set in the wide range from the full bump state to the full rebound state. Figure 9 shows an example comparison of the suspension rate used in the conventional simulation model and the suspension rate that takes into account limit conditions in this study. The former is not an issue for normal condition calculations, but the latter must be set for limit condition calculations.

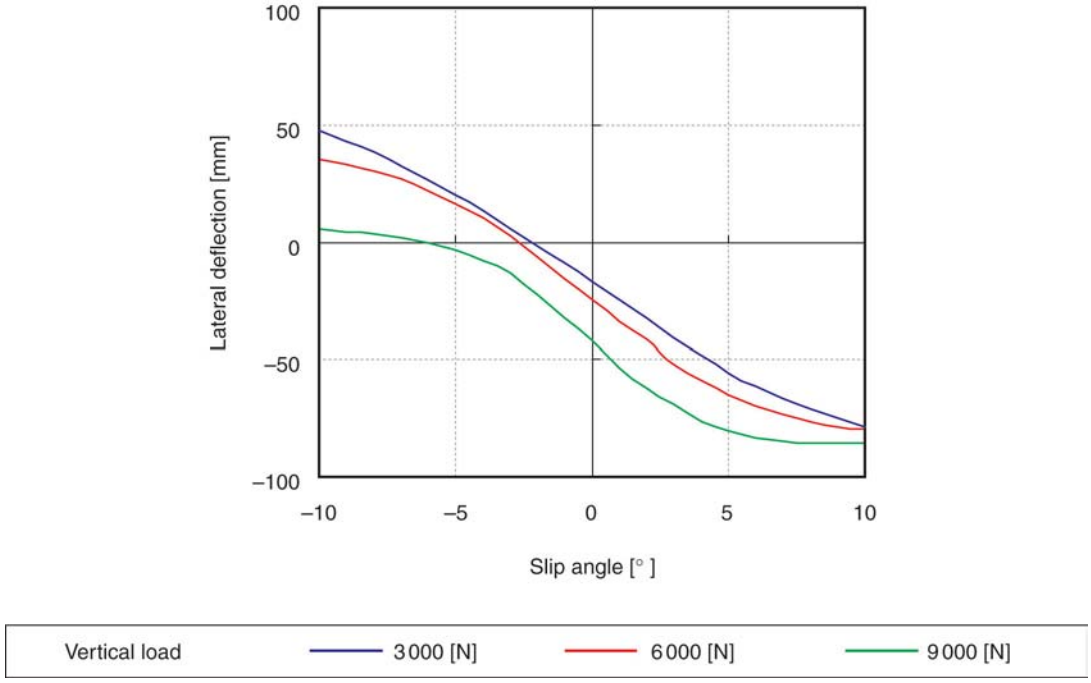


Fig. 8 Measurements of lateral deflection (Camber angle 5°)

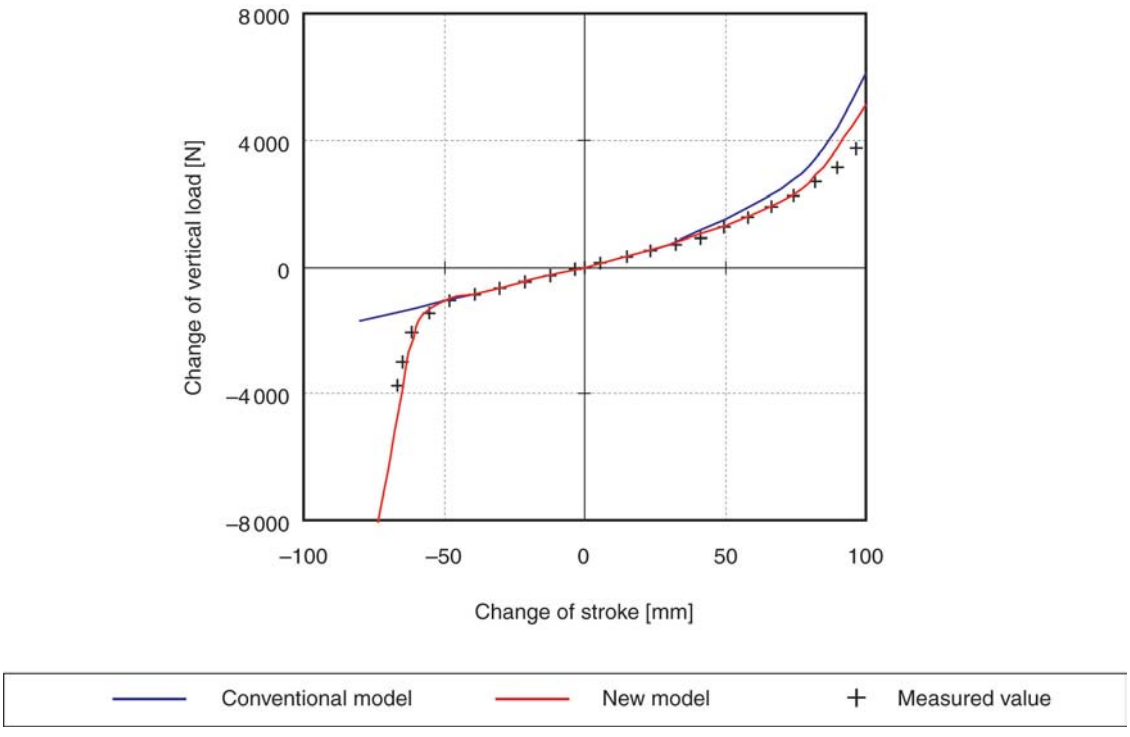


Fig. 9 Suspension rate

4.2. Improvement of Drive Torque Control

When the rapid turning state is entered from the high speed range, the longitudinal component of the side force of the tires relative to the vehicle acts as strong driving resistance. In tests using actual vehicles the speed is controlled by accelerator pedal operations to maintain a constant speed. However, the conventional simulation performs constant speed control by generating torque on the drive wheels. The driving resistance value is comparatively small when calculating normal conditions, so the drive torque value does not become extremely large and this is not a concern. However, the driving resistance value is large in limit conditions, so extremely large drive torque is generated suddenly. This creates the phenomenon where the effect of the tire friction circle causes a drastic drop in the tire lateral force compared to actual measurements, and produces a large offset in the calculation results. Therefore, when calculating the cornering performance in limit conditions, the drive torque control was adjusted to prevent sudden drops in the lateral force. As a result the speed approached the actual vehicle test values, and the drive torque and lateral force produced when transiting from straight to the turning state also approached the actual vehicle values. Figure 10 compares the drive force and lateral force calculated by the conventional simulation model, calculated by the newly constructed simulation model, and produced when driving an actual vehicle.

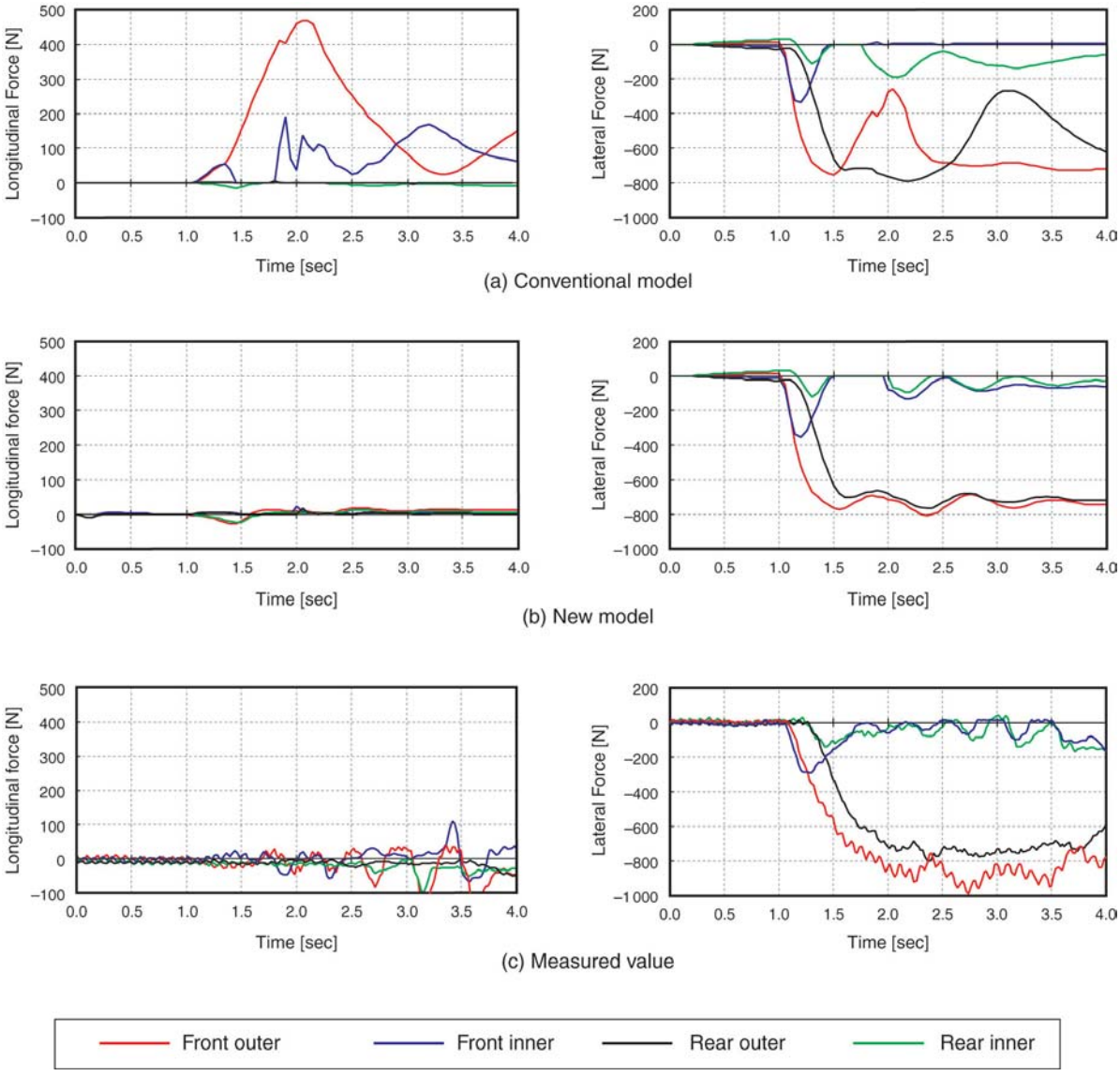


Fig. 10 Change of tire forces with torque control

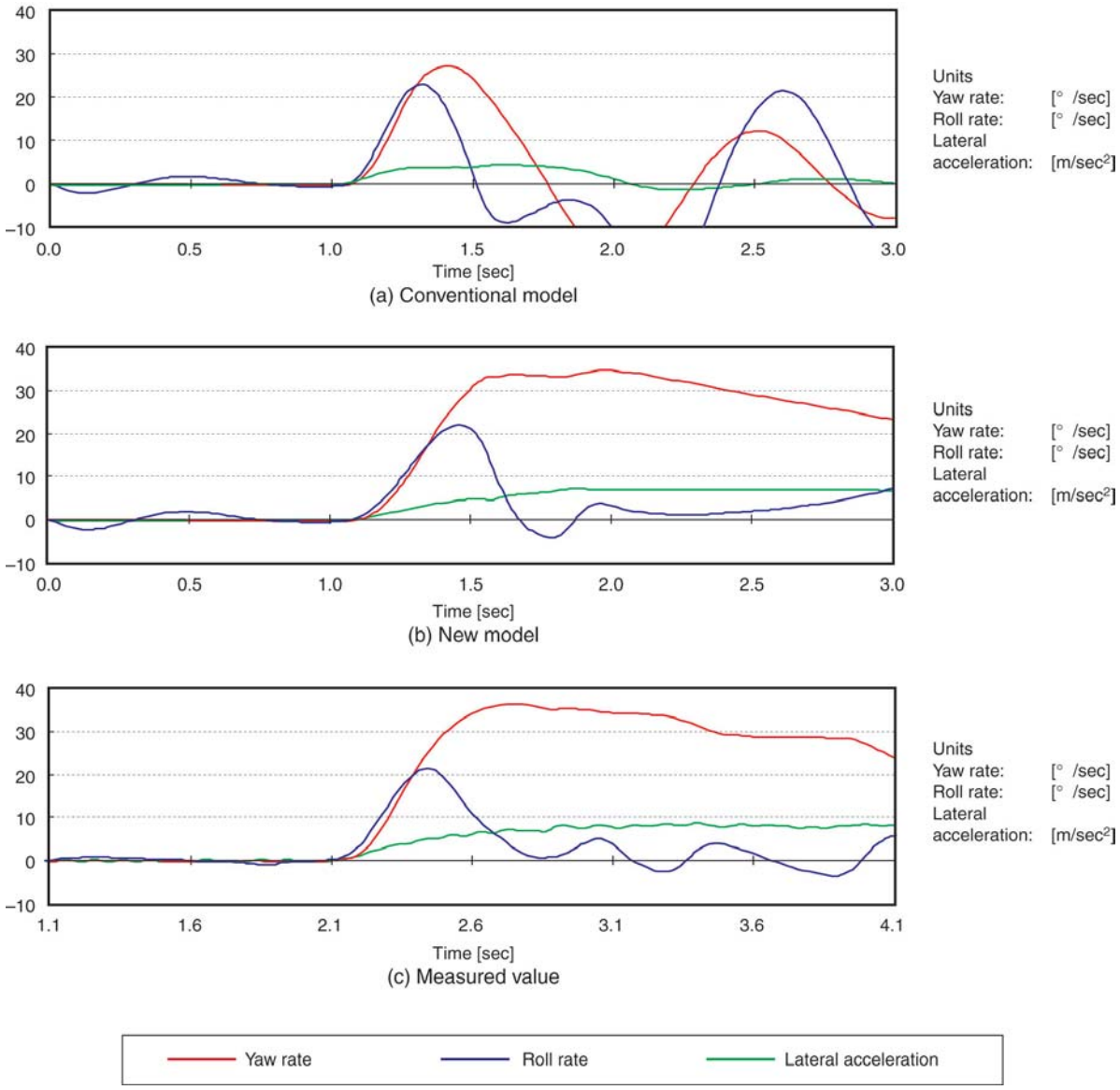


Fig. 11 Comparison between calculated value and measured value

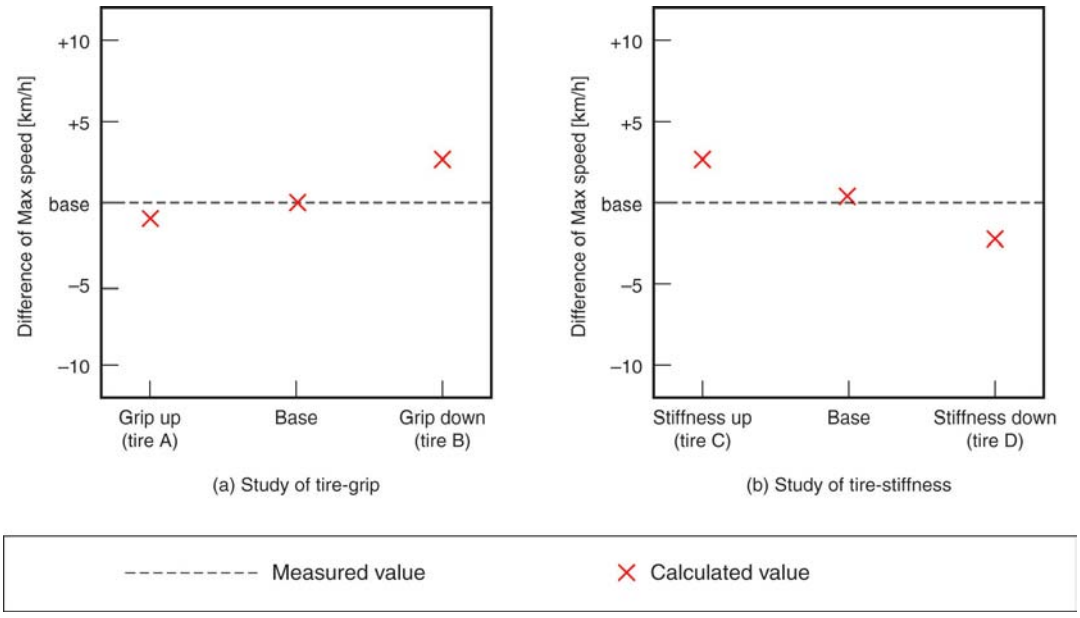


Fig. 12 Verification of simulation model

5. Calculation Results

Figure 11 shows the calculation results for J-turn mode driving obtained using the newly constructed tire and vehicle models. (a) shows the calculation results for the conventional simulation model, (b) shows the calculation results obtained by this study, and (c) shows the actual measurement values.

In limit conditions the vehicle behavior does not immediately shift to the steady state and the unstable state continues, so it is important to predict behavior during the several second interval following steering input. Compared with the actual measurement values, the simulated time series changes in the yaw rate, lateral acceleration, roll rate and other physical values during the approximately 2 seconds after steering input show a higher accuracy that is sufficient for predictive calculations in all cases.

In addition, Fig. 12 plots the relationships between the tire type and the maximum speed at which steady state turning becomes impossible for the two cases of different tire tread rubber (a) and different tire stiffness (b), using the constructed tire model as a reference. The calculation results match closely with the actual vehicle test results, thus confirming the validity of this simulation model.

6. Conclusion

This study aimed to construct technology for better predicting cornering performance in limit conditions with higher accuracy, and the following conclusions were obtained.

(1) The nonlinear characteristics of tires in limit conditions can be expressed using a Magic Formula tire model.
(2) Tire lateral deflection can be expressed by inserting a spring element to the center of the hub.
(3) A suspension rate with high accuracy over the maximum stroke width from the full bump to the full rebound state must be set by the vehicle model in order to calculate limit conditions.
(4) Extremely large drive torque generated to maintain a constant speed must be suppressed for limit condition calculations.
(5) Cornering performance in limit conditions can be reproduced with a high degree of accuracy in a virtual space by adding items (1) to (4) above to conventional technology.

The results of this study show that vehicle dynamic characteristics settings over a wide range including cornering performance in limit conditions can be observed through desktop simulations. In addition, the results also showed great potential for reducing evaluation using actual vehicles and for investigating a wide range of vehicle characteristics, etc.

References

(1) Fiala, E.: SeitenkrafteamRollenden Luftreifen, VDI, Vol. 96, No. 29 (1954)

(2) Gim, G., Nikravesh, P.E.: An Analytical Model of Pneumatic Tires for Vehicle Dynamic Simulations. Part 1: Pure Slips, International Journal of Vehicle Design, Vol. 11, No. 6, pp. 589–618 (1990)

(3) Pacejka, H.B.: The Tyre as a Vehicle Component, XXVI FISITA Congress, Prague, June, pp. 16–23 (1996)

(4) Maurice, J.P., Pacejka, H.B.: Dynamic Tyre Response to Yaw Angle Variations, AVEC 9836833

■ Authors ■


Takayuki TOYOSHIMA


Yasuhiro MIYATANI


Yuji SATO


Shinta ARAI

Establishment of a Development Method of a Water Jet Pump for 4-Stroke Personal Watercrafts

Masahiko TSUCHIYA* Tomohiro FUSE* Takashi WATANABE*

ABSTRACT

Honda's first Water Jet Pump for a Personal Watercraft with a 4-stroke engine has been developed. In the development, correlation of the calculation results with the actual test results was verified, and design tools such as an examination method of intake shape optimization, a characteristic calculation method for various aerofoil shapes, and a prediction method of Water Jet Pump performance were established. Using these tools, two Water Jet Pumps that matched each of the 4-stroke engines with different output power have been developed.

1. Introduction

At present, most personal watercraft (PWC) on the market utilize two-stroke engines. However, increasing awareness of environmental issues is causing restrictions on the operation of two-stroke PWC, and emissions regulations are also becoming increasingly stringent. Honda has therefore developed two cleaner, quieter and more comfortable four-stroke PWC, the AquaTrax F-12 and F-12X. Fig. 1 shows an external view of the AquaTrax F-12X.



Fig. 1 External view of AquaTrax F-12X

The AquaTrax F-12 engine is normally aspirated, and has a displacement of 1,235 cm^3. The F-12X engine has the same displacement, but the addition of a turbo-charger gives it the most powerful powerplant on the market. When developing the optimum water jet pumps for this PWC, in addition to matching pump performance, it was necessary to significantly control cavitation to achieve a match with the output characteristics of a turbo-charged four-stroke engine. Original 'design tools' were therefore developed in order to design new, high-efficiency pumps by analyzing the factors contributing to the characteristics of each section according to pump design theory.

2. Outline of Water Jet Pumps

PWC normally use axial flow or mixed flow water jet pump to provide propulsion. Because there is no necessity for any components to project from the bottom of the craft, these pumps are ideally suited to PWC. Another reason for the choice of these pumps is the fact that they function efficiently at high engine speeds, making them suited to the comparatively high-speed engines utilized in PWC. Fig. 2 shows the layout of the newly developed axial flow water jet pump, and the function of each section.

* Asaka R&D Center

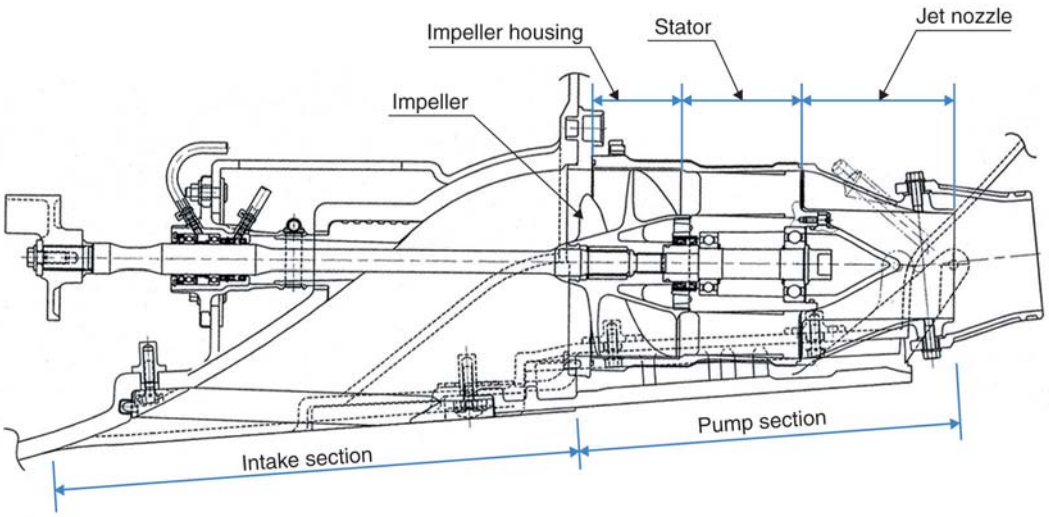


Fig. 2 Structure of developed water jet pump

2.1. Intake Section

The intake section, provided with curvilinear pipes to guide water from the flat bottom of the craft to the impeller, is one of the elements composing the water jet pump. The shape of the intake section has a tremendous influence on the performance of the craft. The shape of the comb-like intake grate positioned on the inlet, the shape of the inlet, the form of the pipes (in particular height), the cross-sectional area, and the rate of change of cross-sectional area, all affect intake efficiency.

2.2. Pump Section

The pump section of the axial flow water jet pump is composed of three parts: a cylindrical duct surrounding the impeller (impeller housing), a stator and a jet nozzle. For the sake of convenience, this paper will define the jet nozzle as part of the pump. The impeller is the most important component in the water jet pump, and transmits power by pressurization with water from the intake section. The stator efficiently converts the kinetic energy of the swirl from the impeller into propulsion, and is made of supporting materials to support the impeller shaft. The jet nozzle converts the amount of motion transmitted to the head by the water pressurized in the pump section into thrust. The diameter of the jet nozzle outlet affects the characteristics of the craft. Because dynamic pressure is high, a suction type bilge pump is also located in this section.

3. Aims of the Development

3.1. Intake Section

In deciding on the shape of the intake duct, it is necessary to give consideration to the minimization of cavitation and pressure loss within the intake section. The parameter which defines how much energy from ship velocity will be recovered as dynamic pressure in the intake duct is ε, the recovery ratio of dynamic pressure, and is found using equation (1):

$$\varepsilon = \frac{Pa+Po}{Pa+\frac{1}{2g}Vship^2} \quad (1)$$

Po: Total pressure directly in front of the impeller
Pa: Atmospheric pressure
Vship: Ship velocity
g: Acceleration of gravity

The magnitude of this value is known to affect propulsive efficiency, particularly at high speeds, but conducting tests with a completed craft to improve the shape of the intake is a complex and inefficient procedure.

Tests were therefore conducted on the performance of the intake section in isolation, using a scale model. By correlating the results of these tests with the results of computational fluid dynamics (CFD) calculations, a method of examining the shape of the intake duct was developed.

3.2. Shape of Impeller/Stator Aerofoils

The aerofoil shape is determined by the chord length, the camber and aerofoil thickness. The aerofoil shape is an important element which affects the aerofoil's lift coefficient (C_L) and drag coefficient (C_D). Furthermore, if the pressure distribution on the surface of the aerofoil causes negative pressure to exceed a certain limit and generates saturated vapor pressure, the phenomenon known as cavitation occurs. Excessive cavitation changes the characteristics of the aerofoils, which causes their efficiency to drop; in addition, the shock waves which occur when cavities collapse may cause erosion of the aerofoil surface, leading to serious damage to the aerofoils.

In the development of the pump section, the first necessary factor was understanding the characteristics generated by the shape of the aerofoils. A calculation program was optimized using the results of actual measurements of two-dimensional aerofoil characteristics, and a method was developed to allow calculation of these characteristics.

3.3. Pump Section

A calculation program for pump section performance was created using existing theory. This program was improved by correlation of calculation results with measurement results obtained from tests of the performance of the pump section in isolation, enabling the development of a method for calculating the performance of the pump section.

4. Development of the Intake Section

4.1. Performance Tests of Intake Section in Isolation

The loss coefficient ξs is defined using equation (2), where $\overline{a_s}$ is the mean value of static pressure in the intake duct.

$$\xi s = \frac{\frac{Vs^2}{2g} - \left(\overline{a_s} + \frac{Vi^2}{2g}\right)}{\frac{Vi^2}{2g}} \qquad (2)$$

Vi: Mean velocity directly in front of the impeller
Vs: Principal velocity in front of intake
g: Acceleration of gravity

A half-scale model of the intake section, as shown in Fig. 3, was used to conduct measurements of the pressure loss coefficient, to make flow visualization possible and to verify the velocity distribution in an isolated intake. The scale model was placed in the upper observation section of a cavitation tunnel. A new channel was created for the rear of the scale model, and flow velocity was varied using another pump. Pressure and flow velocity were measured at each section of the scale model, and the loss coefficient was measured for different intake and intake grate shapes. Pitot tubes distributed like a comb were set up at the position where leading edge of the impeller should be placed; by rotating the set of Pitot tubes, the distribution of flow velocity directly in front of the impeller could be measured. Fig. 4 shows details of the observed section, and Fig. 5 shows an example of velocity distribution directly in front of the impeller. The intake grate can be seen in the lower left of Fig. 4, and the Pitot tubes can be seen on both sides of the cone-shaped section just to the right of the center. This test verified the fact that variations in intake shape produced large differences in flow velocity directly in front of the impeller. By making the flow within the intake duct visible, the sections which made the greatest contribution to performance could be directly observed.



Fig. 3 1/2 scale model of intake

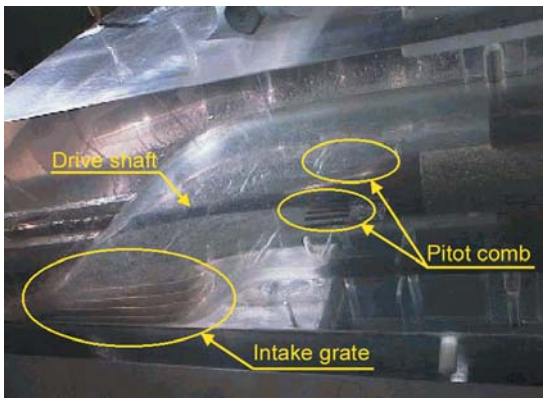


Fig. 4 Detail of intake 1/2 scale model

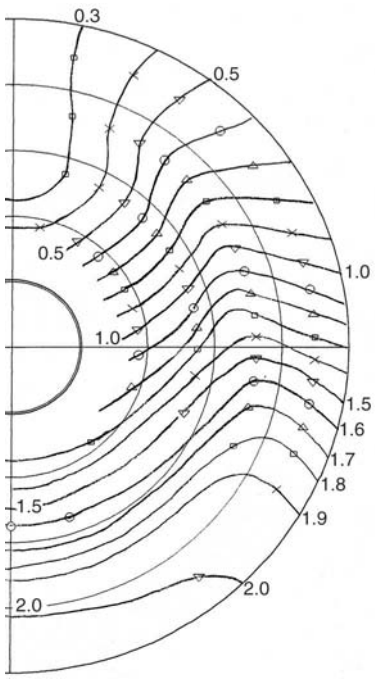


Fig. 5 Measurement result of velocity distribution inside intake duct

4.2. Intake Design Tools

A commercially available CFD solver was utilized to verify loss coefficient and internal flow conditions using the same intake shape as used in the tests of isolated intake performance. Calculation conditions were reset on the basis of correlation of intake performance test measurements and CFD calculation results.

Fig. 6 shows the flow in an axial cross-section, and Fig. 7 shows the velocity distribution in a duct section directly in front of the impeller. Figs. 6 and 7 show that the areas of highest flow velocity occur below the center. Intake velocity ratio, r, is defined using equation (3):

$$r = Vs / Vi \qquad (3)$$

Examples of examination of various intake shapes using CFD are shown by plan in Fig. 8. Restricting the size of the inlet, as Fig. 9 shows, reduces the loss coefficient at high speed (r = 2.5), but increases it at standstill (r = 0). In other words, in this example, there is a tradeoff between the performance at high speed and low speed.

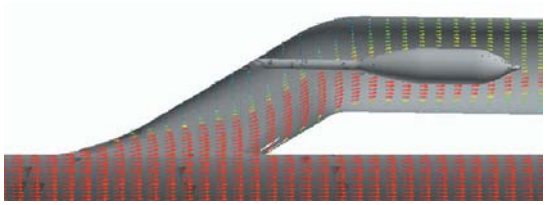


Fig. 6 Flow pattern inside intake duct by CFD (Side view)

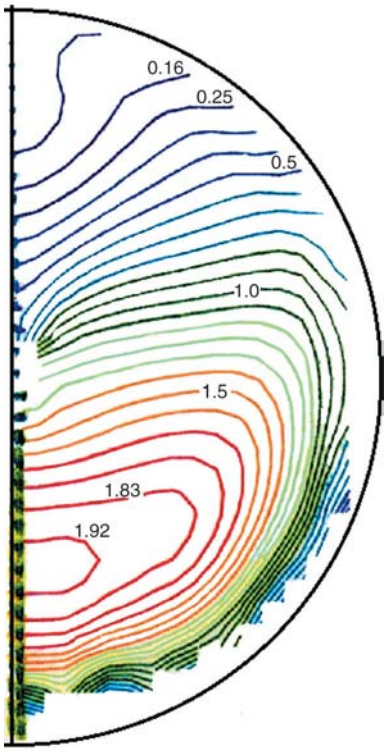


Fig. 7 Velocity distribution inside intake duct by CFD (Front view)

4.3. Correlation of Isolated Unit Test Results and Calculation Results

The velocity distribution directly in front of the impeller in Figs. 5 and 7 show the same qualitative tendencies. Fig. 10 shows a graph comparing intake loss coefficients found by CFD and measured in tests, and it is clear that there is a good correlation between the two sets of results. This method was used to establish target loss coefficient values to achieve a balance of flow velocities, and the intake shape was improved on this basis.

5. Aerofoil Development

5.1. Aerofoil Design Tools

Using existing theoretical formulas as a base, a program was formulated to calculate the characteristics of two-dimensional aerofoils.[(1)–(3)] Cavitation may be predicted to occur easily because of the harsh conditions under which PWC water jet pumps are operated. Both cavitation and non-cavitation states were therefore examined. To verify the accuracy of calculations, an NC1 foil[(4)] was used to correlate the calculated and the measured values. This aerofoil shape

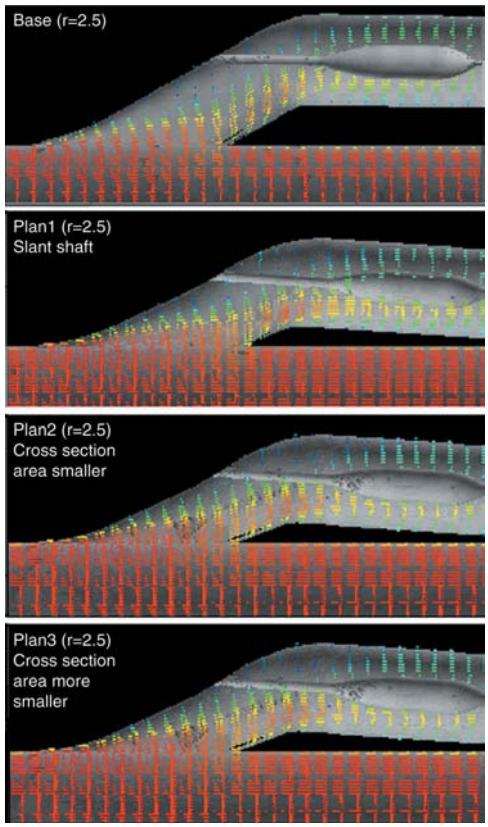


Fig. 8 Flow patterns obtained from CFD for intakes of different inlet shapes

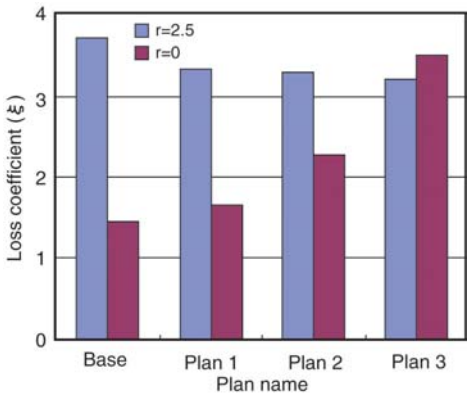


Fig. 9 Comparison of intake loss coefficient of various plans

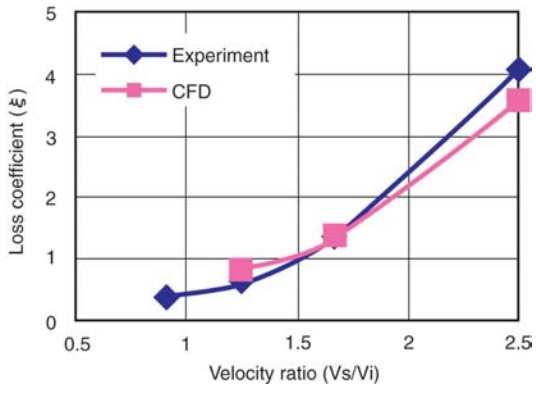


Fig. 10 Comparison of loss coefficients between experiment value and CFD value

was chosen because it is the model with the lowest thickness ratio (thickness ÷ chord length × 100) (ratio: 3.86) from which reliable test measurements can be obtained. Results showed an excellent correlation between the lift coefficients obtained from calculations and test measurements. A quantitative difference in drag coefficient was observed, but it was possible to verify that calculation results displayed the same general trend as test results. However, the thickness ratio which formed the target of this development was less than 3.0. Attempts were made to improve the accuracy of calculations, but given the necessity for data on thinner aerofoils, it was decided to obtain test data on the characteristics of super thin aerofoils.

5.2. Test for Two-dimensional Aerofoil Characteristics

Fig. 11 shows the test piece used to reproduce the characteristics of actual aerofoils with the same thickness ratio in cavitation tunnel tests. Two different aerofoil shapes were utilized in these tests to measure cavitation characteristics and the relationship between drag and lift and cavitation and non-cavitation states, and to provide data on the characteristics of super-thin aerofoils. The cavitation number, σ, is found using equation (4). These figures are used as a scale to express the ease of occurrence of cavitation. Fig. 12 shows representative cavitation states occurring during testing. These are model cavitation states obtained by measuring lift and drag and adjusting the cavitation number by varying the pressure within the cavitation tunnel (depressurization), the angle of attack and the flow velocity. From the left, these forms of cavitation are known as bubble cavitation, sheet cavitation and cloud cavitation.

$$\sigma = \frac{P - Pv}{\frac{1}{2}\rho V^2} \tag{4}$$

P: Static pressure of flow medium
Pv: Saturated vapor pressure of flow medium
ρ: Density of flow medium
V: Velocity of flow medium

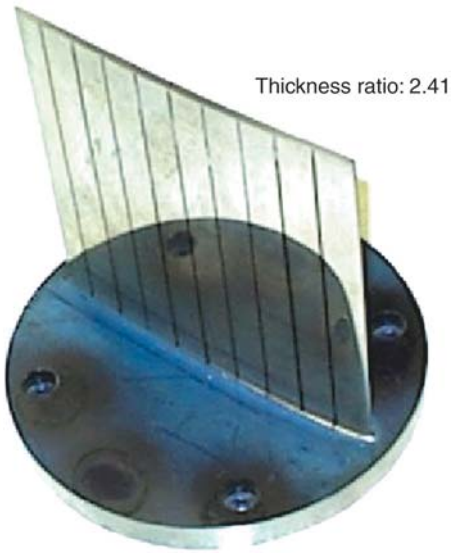


Fig. 11 Test piece of 2-dimentional aerofoil

5.3. Correlation of Calculation Results and Results of Tests of Characteristics

The calculation program for aerofoil characteristics described in 5.1 was optimized using the results of the tests described in 5.2, enabling the formulation of a “calculation program for the prediction of aerofoil characteristics”. This program makes it possible to predict the characteristics of unknown super-thin aerofoils. Figs. 13 and 14 show examples of comparisons between calculated values and measured values. Fig. 13 shows lift and drag coefficients and lift-drag ratio when angle of attack is varied. Fig. 14 shows lift and drag coefficients when cavitation number is varied for a particular angle of attack. These results verify an acceptable level of accuracy in the program’s predictions.

6. Development of Pump Section

6.1. Non-cavitation state

6.1.1. Pump section design tools

The calculation program for the prediction of two-

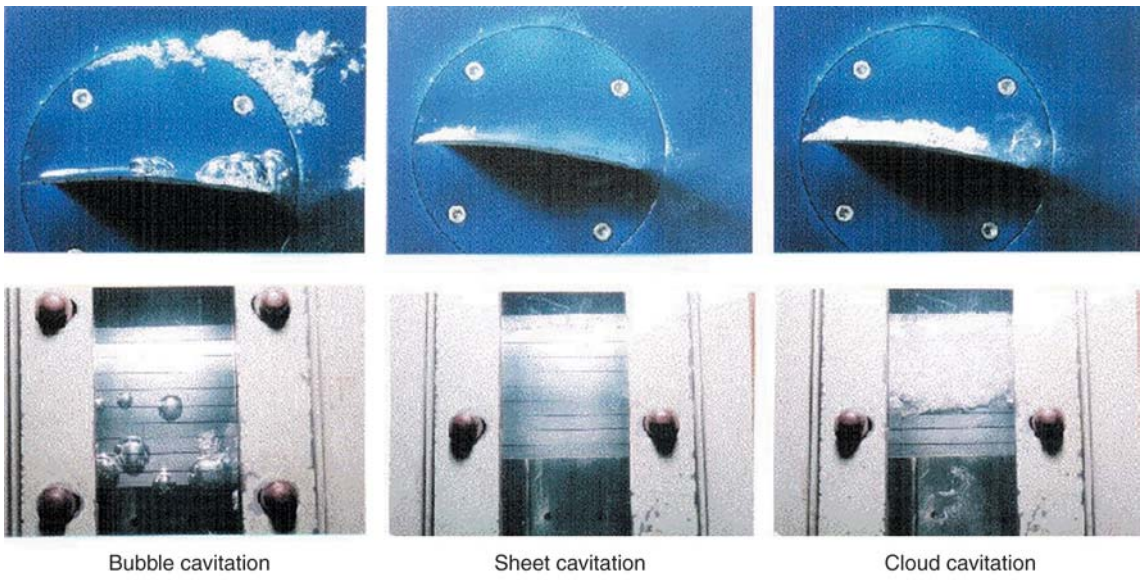


Fig. 12 Cavitations on 2-dimensional aerofoil

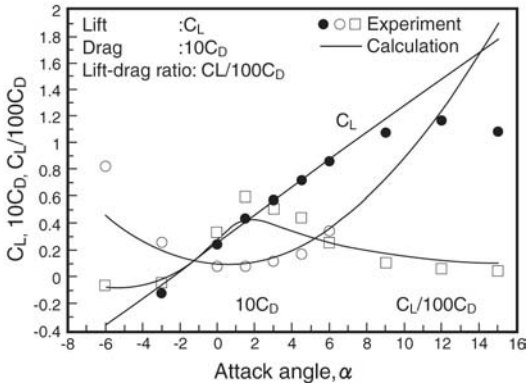


Fig. 13 Comparison of measurement results and calculation results in difference of attack angle

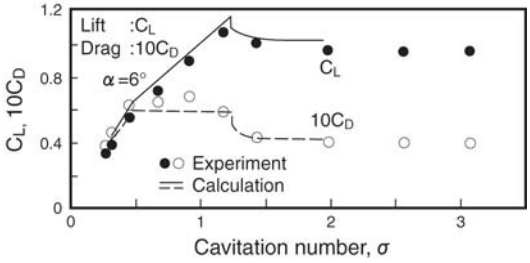


Fig. 14 Comparison of measurement results and calculation results in difference of cavitation number

dimensional aerofoil characteristics described in 5.3 was developed into a calculation program for the prediction of three-dimensional pump performance. This program uses three-dimensional lifting surface theory to calculate the performance of a pump section given the geometric shape of an impeller and stator when operating in a non-cavitation state with uniform flow.

6.1.2. Tests of pump performance in isolation

Tests were conducted on the performance of an actual pump section in isolation in a non-cavitation state. Figs. 15 and 16 show test equipment. These tests enabled the following improvements:

- By making stream lines observable using the oil film method, it was possible to verify differences between the actual stream lines on the surface of the impeller aerofoil and the hypothetical stream lines obtained by calculation. These results were used to optimize the calculation algorithm.
- Bilge pump efficiency (the bilge pump removes water from inside the craft using negative pressure generated by the dynamic pressure of the jet nozzle) and improvements were made to performance.
- The intense swirl flow arriving at the nozzle from inside the stator was studied, and a method for its efficient recovery was developed.

Fig. 15 shows the pump section installed in the test equipment. Inlet flow volume and velocity, pump section pressure and impeller torque and speed were measured, and pump performance data (head coefficient, load coefficient, pump efficiency) were obtained. Fig. 16 shows the test equipment in operation.

6.1.3. Correlation of calculation results and isolated unit test results

Coefficients for the calculation program for pump performance described in 6.1.1 were adjusted on the basis of the results of the tests described in 6.1.2, to create a program capable of predicting the performance of the newly designed pump. Fig. 17 shows an example of a comparison between calculation and test results. This plot charts pump performance results obtained from running tests in addition to isolation test results and calculation program results, with a high degree of correlation demonstrated between the three sets of results.



Fig. 15 Test equipment for water jet pump



Fig. 16 Test equipment for water jet pump in operating

6.2. Cavitation States

6.2.1. Performance tests of the pump section in isolation

Water jet pumps used in normal watercraft require optimization of performance and efficiency for a certain fixed range of operating conditions. However, an extremely broad range of operating conditions must be taken into consideration in the case of PWC: it is necessary to achieve performance not only at maximum speed, but across the range from standstill to fully open throttle and at sudden

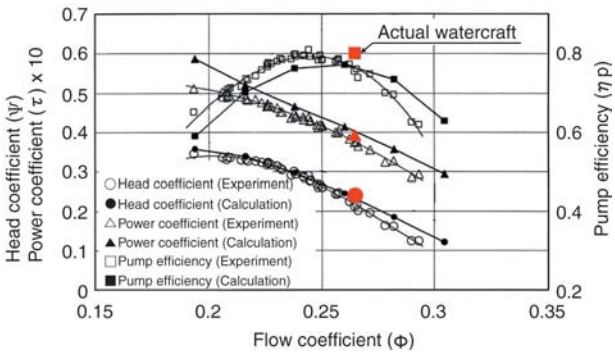


Fig. 17 Comparison of pump performance between measurement results and calculation results

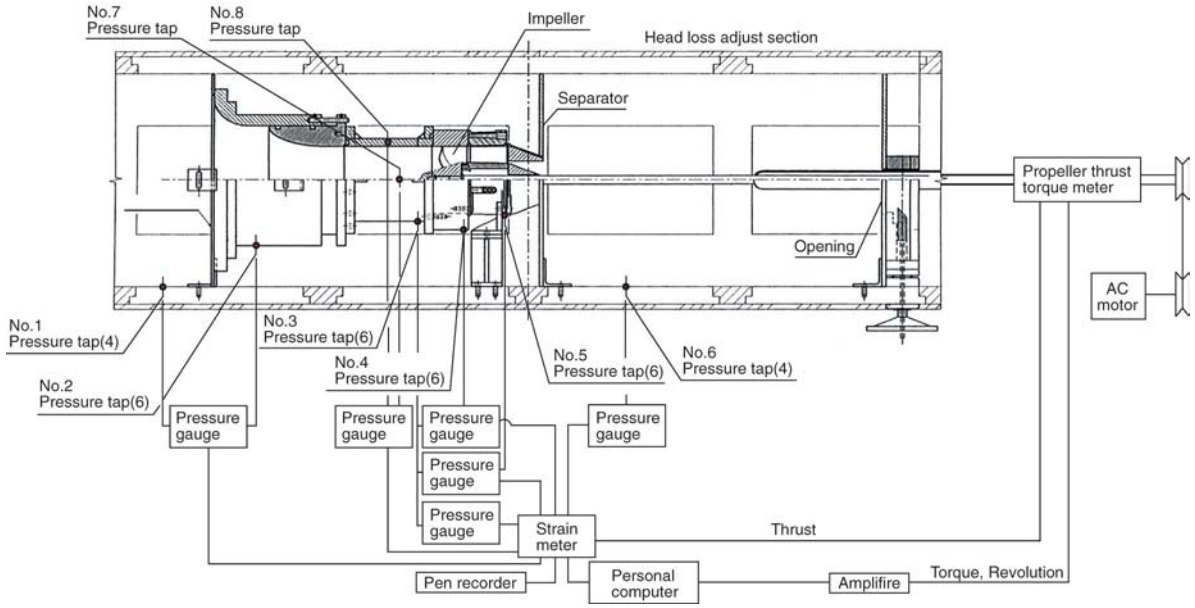


Fig. 18 Design of cavitation test equipment

acceleration and deceleration. The impellers in these craft turn at high speeds, making the possibility of cavitation extremely high, but for the reasons discussed above, the pumps cannot only be optimized for high speeds, but must achieve a balanced cavitation performance.

In addition, in the newly developed PWC, rapid pickup from the four-stroke engine's characteristic idling to high engine speeds and sudden changes in power characteristics due to increased supercharging from the turbo-charger cause cavitation to occur easily, leading to engine revolution overshoot and a feeling of insufficient acceleration when sudden acceleration is applied. To prevent this, it was necessary to develop a water jet pump in which cavitation was reduced as much as possible.

The cavitation test equipment shown in Figs. 18 and 19 was designed to enable quantification of this phenomenon, to render it observable, and allow improvement of cavitation performance under a wide range of operating conditions. Tests were conducted on a pump placed in the flow channel of this cavitation tunnel.

This equipment was designed to make impeller torque and thrust measurable by positioning the pump in the observation window of the cavitation tunnel. The volume of flow was regulated by a throttle valve downstream from the pump to adjust the loss head. This equipment not only rendered cavitation observable through depressurization, but enabled values to be obtained for thrust, which was impossible using the test equipment for the water jet pump in isolation shown in Fig. 15.

By making cavitation states in an actual pump observable, it was possible to verify that the shape of the impeller aerofoil tips contributes significantly to the occurrence of cavitation. The results made it possible to understand the general outline of optimum shapes.

Fig. 20 is a bucket chart for initial generation of cavitation for different impeller shapes. The results demonstrate that the impeller type termed C12 is the shape which suppresses cavitation to the greatest extent. Figs. 21 and 22 show the results of actual observations of cavitation. Fig. 21 shows the base impeller, and Fig. 22 shows the C12 type. Both types were tested simulating the same high-speed conditions, and the results make it clear that the improved type has significantly reduced cavitation.

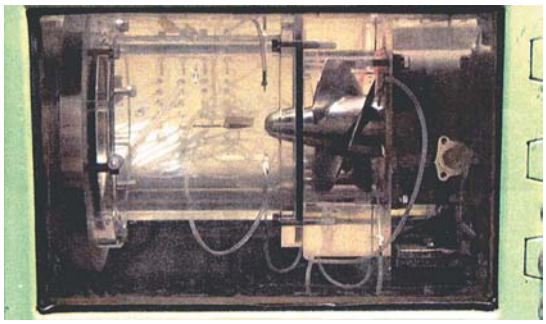


Fig. 19 Observation window of cavitation test equipment

7. Tests on the Completed Craft

7.1 Water Jet Pump Performance Required in PWC

In the normal development flow of water jet pumps, the first prerequisite is estimating the drag of the completed craft. The flow continues with the establishment of the power consumption of a pump matched to the engine's maximum power, the choice of housing diameter and the design of the impeller and stator, examination of the intake shape, the selection of nozzle diameter, etc. In tests of the completed craft, performance in the following points used to evaluate PWC water jet pumps must match target performance:

- Sufficient propulsion at running start and re-acceleration, and efficient use of that propulsion for acceleration.
- Accurate response of propulsion in line with rider's intention (throttle control).
- Thrust reengages smoothly at a dead start when over-revving after a spin, etc.
- Sufficient level of hook-up performance.

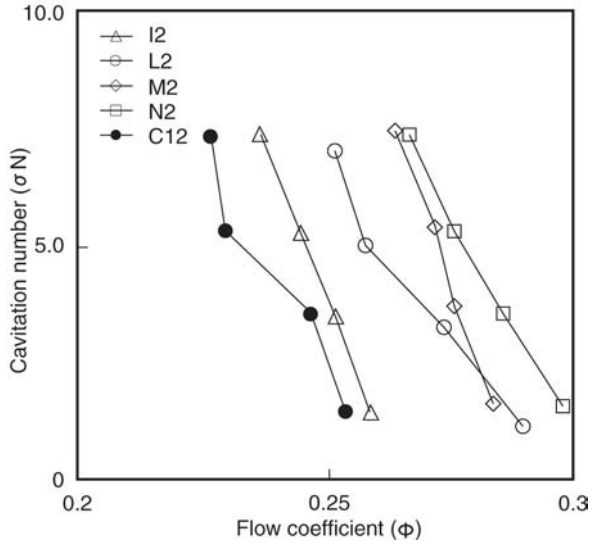


Fig. 20 Initial generation of cavitation by flow coefficient

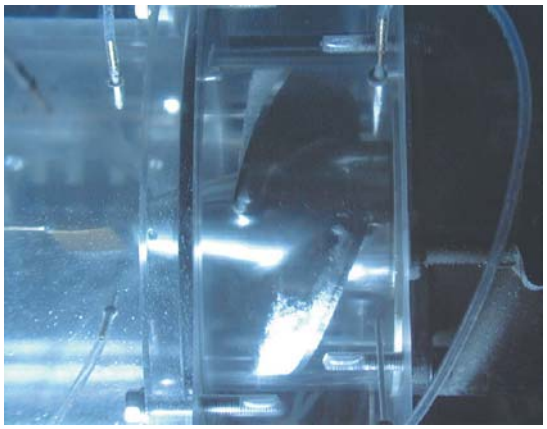


Fig. 21 Cavitation test result before improvement

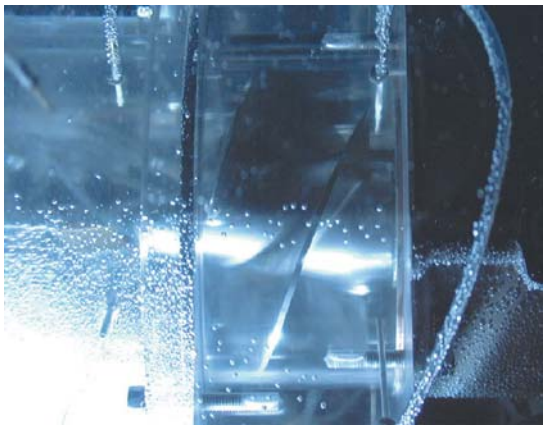


Fig. 22 Cavitation test result after improvement

7.2. Results of Tests on Completed Craft

The water jet pump which was designed on the basis of the results of the studies previously described was tested in the completed craft to evaluate matching and feeling. No difficulties in basic performance were observed. Improvements were made using data obtained in isolated unit tests and cavitation tests, and the pump was tuned to increase power consumption of a pump in the transients. Adjustment of engine power characteristics improved the sense of continuity of acceleration and the feeling of initial acceleration.

8. Conclusion

Honda has developed water jet pumps matched to two different four-stroke engines with different power outputs. An original method of development of water jet pumps was created, using the following design methods:

(1) Results from isolated unit tests utilizing a scale model were correlated with CFD calculation results. The calculation guidelines established in this way enabled the creation of a method for prediction of intake loss coefficient.

(2) Data obtained from measurements of the characteristics of super thin aerofoils were correlated with the results of calculations of aerofoil characteristics, enabling the creation of a method for predicting the characteristics of unknown aerofoil shapes.

(3) Results of tests on pump performance in isolation and results of the newly formulated calculations for prediction of pump performance were correlated, enabling the creation of a method for the prediction of water jet pump performance.

Reference

(1) Kato, Y.: Cavitation, Maki Shoten, p. 96 (1979)

(2) Kinnas, S.A., Fine, N.E.: “A Nemerical Nonlinear Analysis of the Flow around Two- and Three-Dimentional Partially Cavitating Hydrofoils,” Journal of Fluid Mechanics, Vol. 254, pp. 151–181 (1993)

(3) Nakatake, K., Ando, J., Kataoka, K., Yoshitake, A.: “A Simple Method for Planar Aerofoils,” Journal of the West-Japan Society of Naval Architects, Vol. 88, pp. 151–181 (1993)

(4) Yamaguchi, H., Kato, Y., Tanimura, S., Toyota, M.: “Research on Aerofoil Shapes for Trans-Cavitation Propellers,” Journal of the Society of Naval Architects of Japan, Vol. 182, pp. 49–57 (1997)

■ Authors ■


Masahiko TSUCHIYA


Tomohiro FUSE


Takashi WATANABE

Development of an Off-Throttle-Steer System for Personal Watercraft

Takao KOCHI* Goro YAMASAKI*
Mamoru URAKI* Hajime SHOGASE*

ABSTRACT

Personal Watercrafts (PWC) are vehicles propelled by a water jet and steered by changing the direction of the water jet. Because of the decreasing of the thrust when the throttle is fully closed during running, the steering force also decreases. This phenomenon is different from that of land vehicles. To minimize this, the Off-Throttle-Steer (OTS) System has been developed Basically, the system controls engine speeds using the signal of full steering, and also uses a throttle opening, a running speed of PWC predicted by engine speed, and a timer for determining the control timing as other control signals. Thus, a natural steering characteristic was obtained by balancing a turning characteristic at high speed and controllability at low speed.

1. Introduction

Personal watercraft (PWC below) have become popular with large numbers of users as a means of enjoying leisure time on the water, with the US being the major market. PWC are propelled by a water jet and steered by changing the direction of the water jet. This system causes thrust to decrease when the throttle is fully closed (off throttle) during normal running, and in some cases the rider may be unable to turn in the intended direction. This paper introduces the Off-Throttle-Steer system (OTS), developed to resolve this issue The Honda AquaTrax F-12 and F-12X have been provided with this system.

2. Outline of the OTS System

There are two types of OTS systems: rudder type OTS and OTS which increases engine speed. The present system enables turning by increasing engine speed. Fig. 1 shows a structural diagram of the throttle body used in this system.

In this system, full steering of the steering handle with the throttle off activates a switch positioned on the steering shaft. This engages a solenoid valve, which causes a diaphragm to release the negative pressure built up in the surge tank, opening the throttle valve. This increases engine speed, ensuring turnability. Because paddle speed sensors are unstable and easily affected by waves, in this system calculation of the craft speed, a necessary element of control information, is calculated in the ECU on the basis of engine speed and the level of openness of the throttle.

* Asaka R&D Center

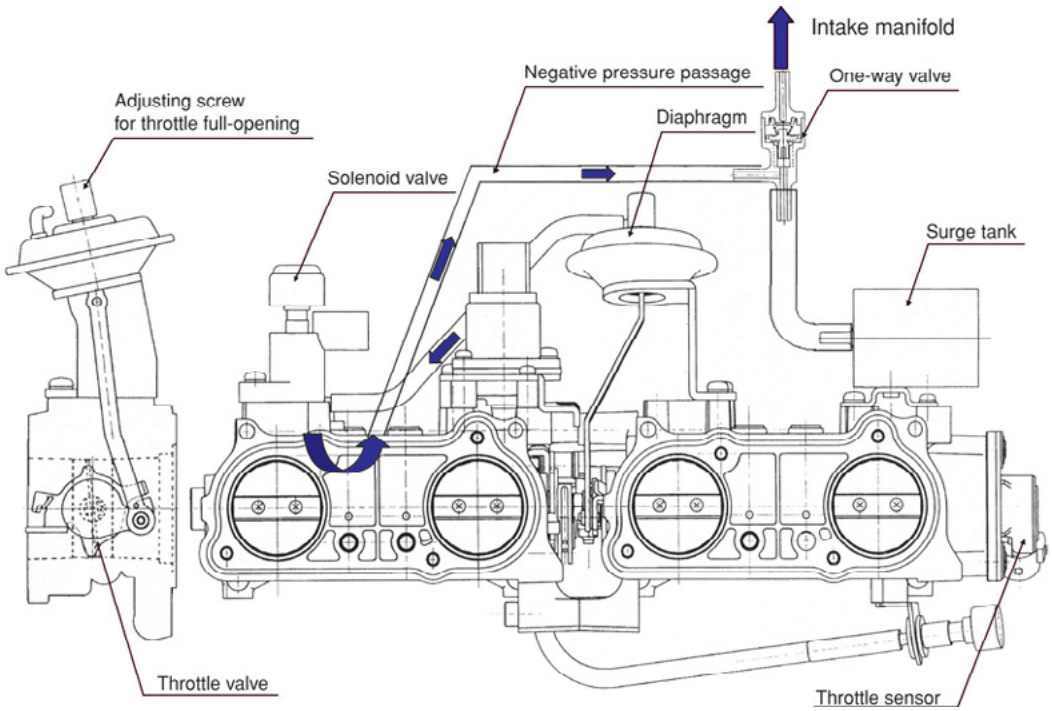


Fig. 1 Construction of OTS system

3. Evaluation of OTS System Performance

3.1 Running Test Method

The PWC's performance was evaluated by measuring running locus and yaw rate when turning with the throttle off and with full steering from low speed to high speed, with and without operation of the OTS system. As running conditions, engine speed was maintained between 1,400 and 2,000 r/min, and the craft was run at 50, 70, and 90 km/h. Evaluation of unnatural feelings in turning response and acceleration were conducted with multiple riders. Fig. 2 shows the scale used for this subjective evaluation.

3.2 Measurement System

Evaluation of running locus is important in evaluating turnability. However, it is difficult to accurately measure running locus in the case of watercraft. When a craft is run over a course marked out by buoys, etc., the effect of waves and wind do not allow the achievement of sufficient accuracy, and it is difficult to obtain measurement results enabling appropriate evaluations. In these tests, a running locus measurement system (Dual RTK system) using GPS was employed to resolve these difficulties. Two high-accuracy GPS antennas and an A/D converter were fitted to the craft. Running locus data at an accuracy of ±5 cm for every 200 ms were obtained by measuring the position, direction and speed of the test craft and calculating its relative position with a land-based GPS ground station. By positioning GPS antennas at the front and rear of the PWC, it was possible to measure the craft's drift angle, etc. Craft behavior was measured using a gyroscope, and these data were later used in analysis. Fig. 3 shows the test craft.

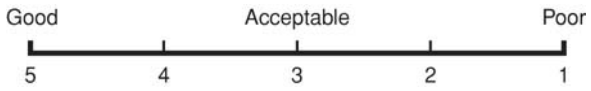


Fig. 2 Subjective evaluation rating scale

3.3 Performance Targets

To establish performance targets for the OTS system, PWC steering characteristics with the throttle disengaged were first measured without the OTS system. Fig. 4 shows a time history data for yaw rate at full steering with the throttle fully closed. The time history data for the yaw rate of a motorcycle (MC below) performing a J-turn from the same starting speed as the PWC is shown for comparison with land vehicle characteristics. MC resemble PWC in their on-saddle riding position, and exhibit similar banking



Fig. 3 Prototype PWC

behavior during turning. It can be seen that the MC yaw rate tends to maintain a constant value. By contrast, the PWC demonstrates a positive yaw rate at the beginning of its turn, but this then decreases, to reach a negative value inverse turning direction. Fig. 5 shows the PWC running locus at this time. The PWC demonstrates turning behavior at the beginning of the steering operation, but as the area of Fig. 5 circled in red shows, in the second half of the time period represented, it tends to move in a straight line, despite the continuation of the steering operation. Running locus data obtained from the front and rear GPS equipment on the test craft also indicate that the PWC is not turning. It was conjectured that this phenomenon was the origin of the unnatural feeling in turning response experienced by PWC riders. These results established the performance target for the OTS system as the maintenance of yaw rate above a negative level while steering continues.

In addition, to realize a natural feeling of control in line with the intentions of the rider, the following targets were established:

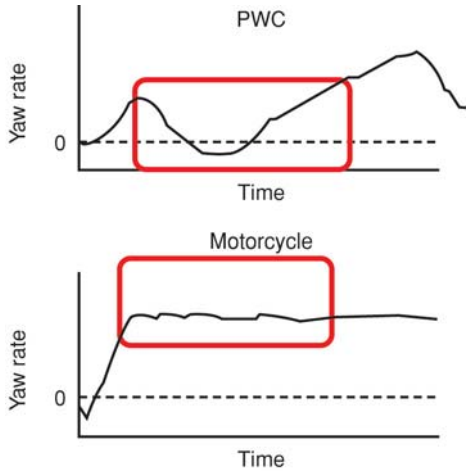


Fig. 4 Comparison of yaw rate characteristic between PWC and motorcycle

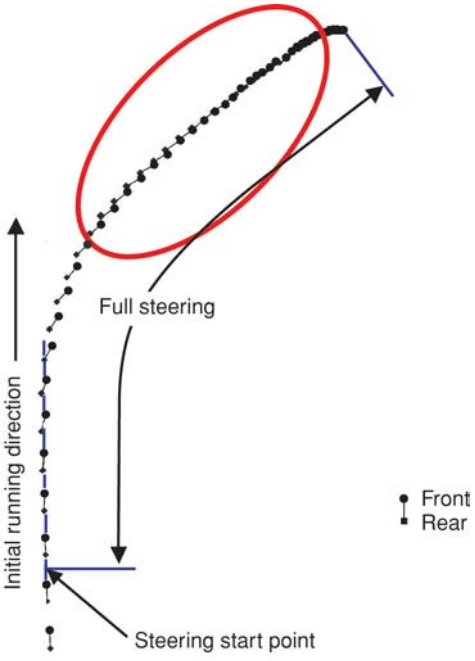


Fig. 5 Running locus without OTS system

(1) Reduction of the unnatural feeling of increase in engine speed when the throttle is closed.
(2) Operation of the OTS system at low speed only when the necessary conditions are met.
(3) Stable turning behavior when the OTS system operates at high speed.

3.3.1 OTS operating conditions

Fig. 6 shows the results of subjective evaluations of turning feeling at various speeds without the OTS system. Because the engine and pump are directly linked, the pump provides thrust at low speeds, including when idling, and turning response was therefore rated acceptable at these speeds even without the OTS system. On the basis of these results, the speed for operation of the OTS system was established at 40 km/h and above, at which the turning feeling had been rated at 3 and below (acceptable range).

It is difficult to estimate craft speed from engine speed when the craft is decelerating with the throttle off. Taking into account the deceleration characteristics shown in Fig. 7, time to deceleration to 40 km/h was taken as standby time, and used to estimate craft speed directly before the point at which the throttle was turned off. Fig. 8 shows the relationship between craft speed and standby time. If the time from turning off the throttle to operation of the steering switch is within standby time, craft speed is judged to be 40 km/h or over, and the OTS system operates.

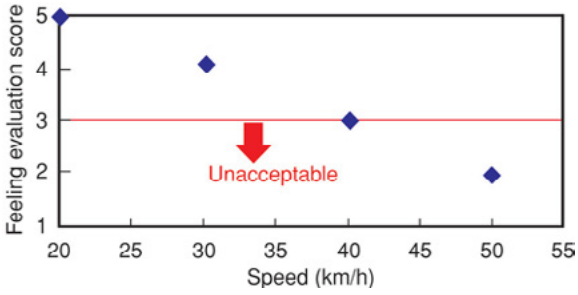


Fig. 6 Subjective evaluation result of turning feel without OTS

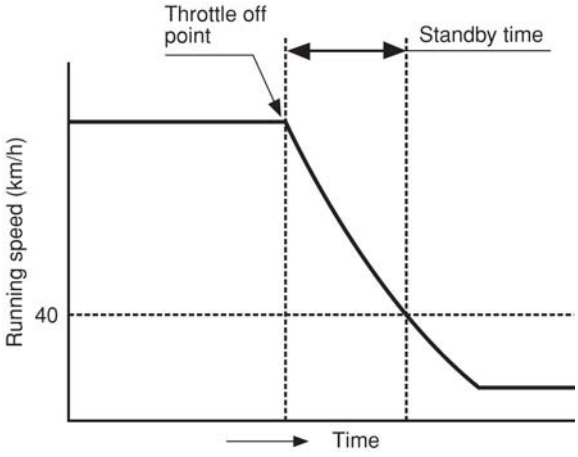


Fig. 7 Prediction of deceleration characteristic

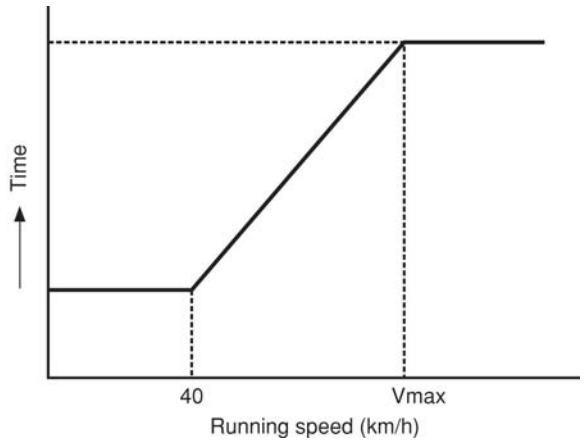


Fig. 8 Relation between PWC running speed and standby time

The following were established as conditions for stopping operation of the OTS system when the rider is turning the craft in the direction he or she desires:

- · When the steering switch turns off at full steering
- · When the rider opens the throttle
- · When 7 seconds have elapsed since the system commenced operation

3.3.2 Engine speed for OTS operation

Fig. 9 shows the results of subjective evaluation of turning and acceleration feeling with the OTS system operating at various engine speeds. The broken line indicates that as the set engine speed gets higher, evaluation of turning response tends to increase, but when it gets too high, the craft's behavior becomes unstable and the evaluation drops. The evaluation of acceleration feeling is also observed to decline as engine speed increases. To minimize an unnatural feeling of acceleration, engine speeds of 2,000 r/min and below were established. Table 1 shows the tendency of minimum yaw rate values. Yaw rates are considered positive when they occur in the same direction as the direction of steering. The yaw rates tend to reach negative values at high craft speed. However, at 1,800 r/min and above, yaw rate remains positive even at 90 km/h. From subjective feeling and yaw rate results, target engine speed was established as 1,800–2,000 r/min.

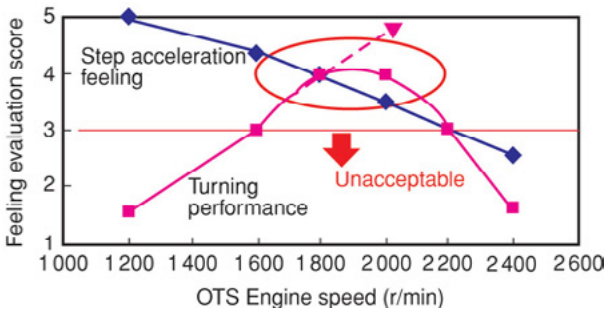


Fig. 9 Subjective evaluation results of acceleration and turning feeling by different engine speeds

3.3.3 Control at high speed

Fig. 10 shows the relation between craft speed and yaw rate with OTS in operation for a variety of initial craft speeds. With only simple control of increase of engine speed, yaw rate tends to increase rather than decrease during high-speed turns, giving rise to an excess yaw rate. This is because at high speed, directly after the throttle is fully closed, engine speed does not fall to idle level, and turning is executed at a higher engine speed than that established for OTS. Delay times for operation of the OTS system after the throttle is closed were therefore established. Fig. 11 shows test results for various delay times. If a delay time of 0.9 sec or above is set, it is possible to control the excess yaw rate.

Table 1 Observed direction of minimum yaw rate

	OTS Engine speed (r/min)		
Speed (km/h)	1 200	1 600	1 800
40	Positive	Positive	Positive
50	Negative	Positive	Positive
70	Negative	Positive	Positive
90	Negative	Negative	Positive

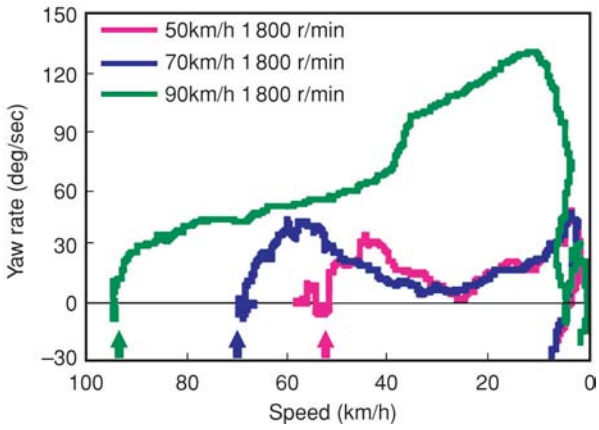


Fig. 10 Yaw rate during decelerating by different initial running speeds

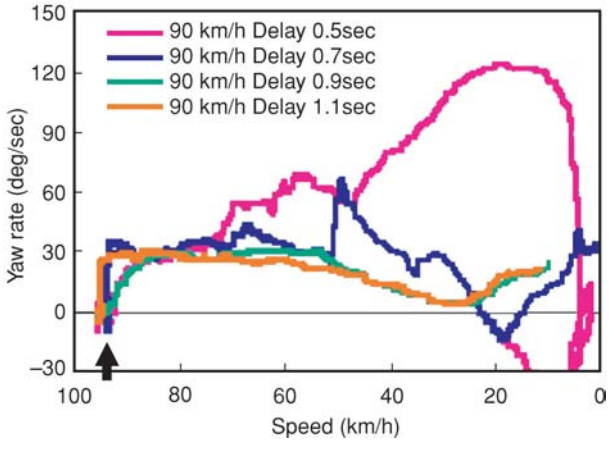


Fig. 11 Yaw rate during decelerating by different delay times

3.3.4 Overall evaluation of OTS system control

Fig. 12 shows a chart of OTS system operation for the various points at which the system operates. Fig. 13 shows the running locus of a PWC with the throttle off using this configuration of the OTS system, compared with the running locus without the OTS system. It is clear that with the OTS system the craft continues to turn while steering is maintained. This system has been utilized in the AquaTrax F12 and F12X, which feature different engine characteristics, and has achieved the same evaluation with changes only to set engine speed and delay time required to respond to craft characteristics.

4. Conclusion

An OTS system for PWC which exerts control which the rider experiences as natural has been constructed. The following findings were obtained:

(1) Subjective evaluation of turning feeling established that the craft speed for which OTS was required was 40 km/h and over.
(2) Appropriate engine speed for operation of the OTS system was 1,800–2,000 r/min.
(3) Delaying the timing of operation of the OTS system was effective in preventing excess yaw rate at high speed.

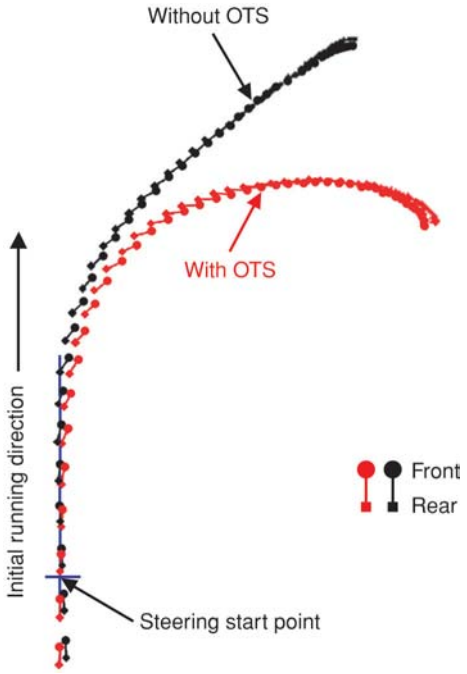


Fig. 13 Comparison of running locus between without and with OTS

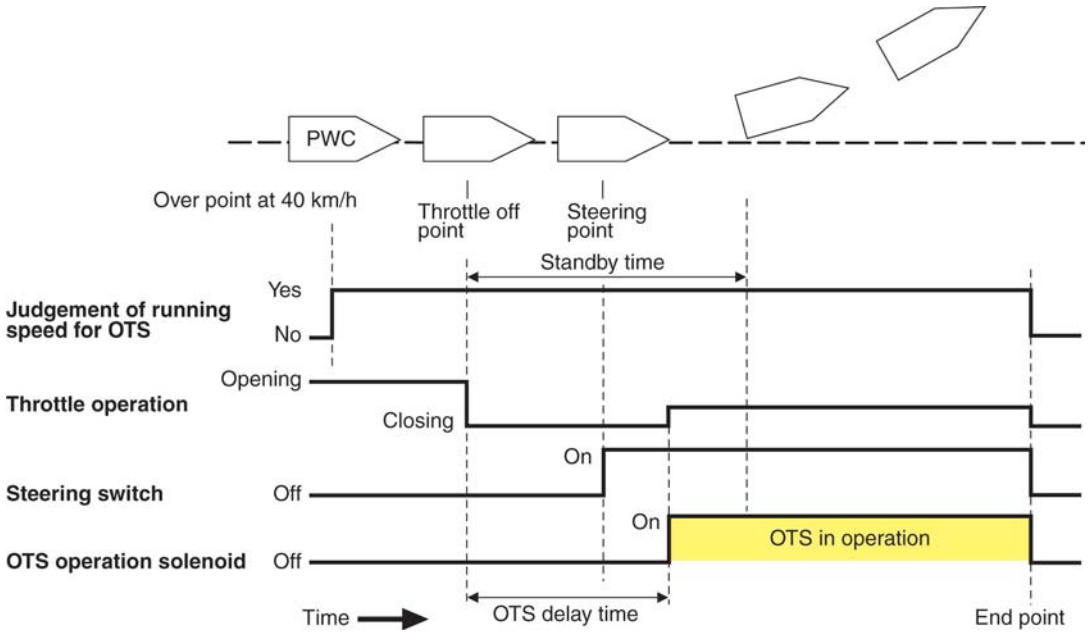


Fig. 12 OTS system operation

■ Authors ■


Takao KOCHI


Goro YAMASAKI


Mamoru URAKI


Hajime SHOGASE

Reliability of Lead-free solder for Automotive Electronic Devices and Its Applications

Tsunehisa HATA* Junichi OHMURA*
Masato MORIYAMA* Tomoo WATANABE*

ABSTRACT

Although an Sn-Pb alloy is generally used for solder at present, environmental considerations have occasioned a search for lead-free solder alloys. The present research evaluated lead-free solder to determine whether it could replace Sn-Pb solder, beginning with the evaluation of the reliability of the solder joint. The evaluation examined reliability under five degradation modes: thermal fatigue, intermetallic compound layer, creep, vibration fatigue, and ionic migration. Lead-free Sn-Ag-Cu solder showed the longest life under thermal fatigue, which is the most crucial element in reliability, and it was confirmed to have reliability superior to Sn-Pb solder in the thermal environments encountered in ordinary use. The Sn-Ag-Cu solder was then put into use as a product in a keyless entry transmitter, where it was demonstrated to satisfy product quality and endurance quality requirements.

1. Introduction

As the global movement for environmental protection continues, restrictions on hazardous substances in vehicles have also been strengthened in recent years. The EU has adopted the WEEE (’08) hazardous substance standards for household electrical appliances and an EU directive (’03) regulating hazardous substances in vehicles and the processing of end-of-life vehicles. In Japan, a household electrical appliance recycling law went into effect in 2001, and a proposed law on vehicle recycling is also presently being studied. The reduction or total elimination of lead and other hazardous substances has come to be unavoidable. Meanwhile, there is resistance to changing the composition of solder in electrical components installed in vehicles because safety considerations demand high reliability in such components. Even if reliability could be assured, however, cost considerations would still be an issue because of anticipated increases in the costs of processing and peripheral materials. At present, therefore, the movement to adopt lead-free materials in automobiles is sluggish compared to the corresponding movement for household electrical appliances.

The present research evaluated the reliability of lead-free solder using reliability evaluation techniques[1] for examination of joints made with Sn-Pb solder. With the support of those results, the application of lead-free solder to products was studied. This article reports on the resolution of the issues of reliability and cost, and the successful mass production of an electronic device with lead-free solder in the form of a keyless entry transmitter.

2. Reliability of Solder

Electrical components installed in vehicles are subjected to the environmental factors of humidity, vibration, and temperature, as shown in Fig. 1, which cause degradation. There are also internal factors that cause degradation of the components, such as electrolytic dissociation and strain. These factors are summarized in terms of solder characteristics in the diagram of solder joint reliability factors shown in Fig. 2.[1]

* Tochigi R&D Center

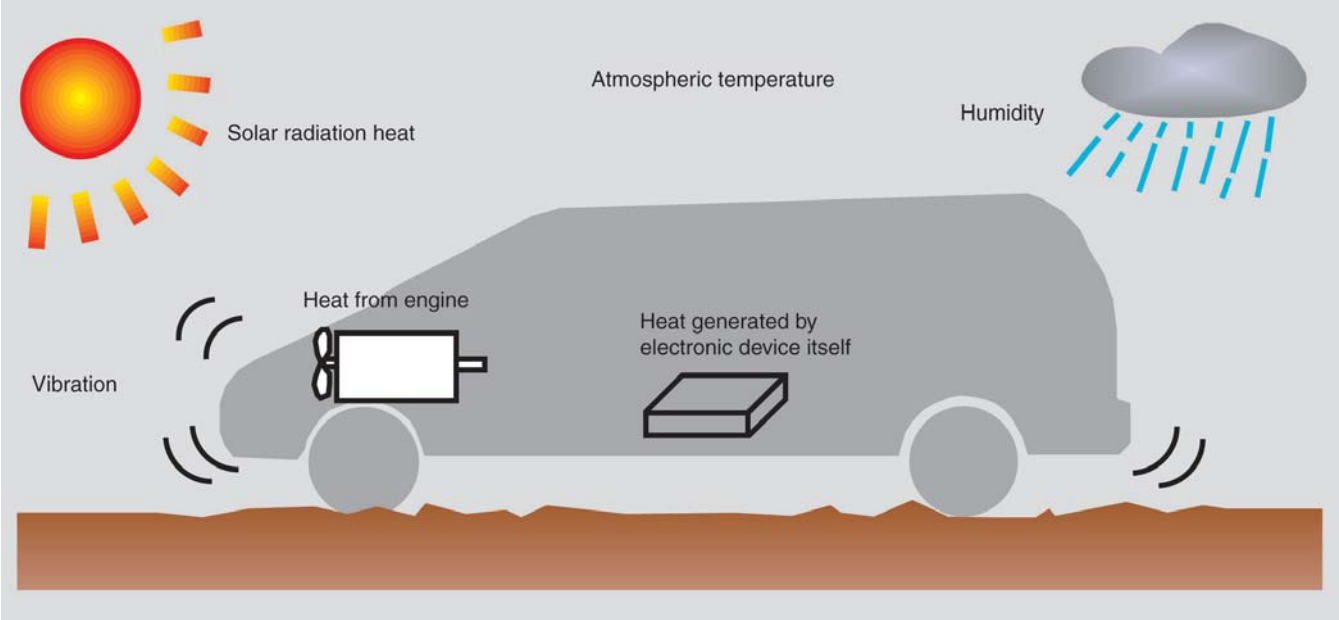


Fig. 1 Stress factors in the automotive environment

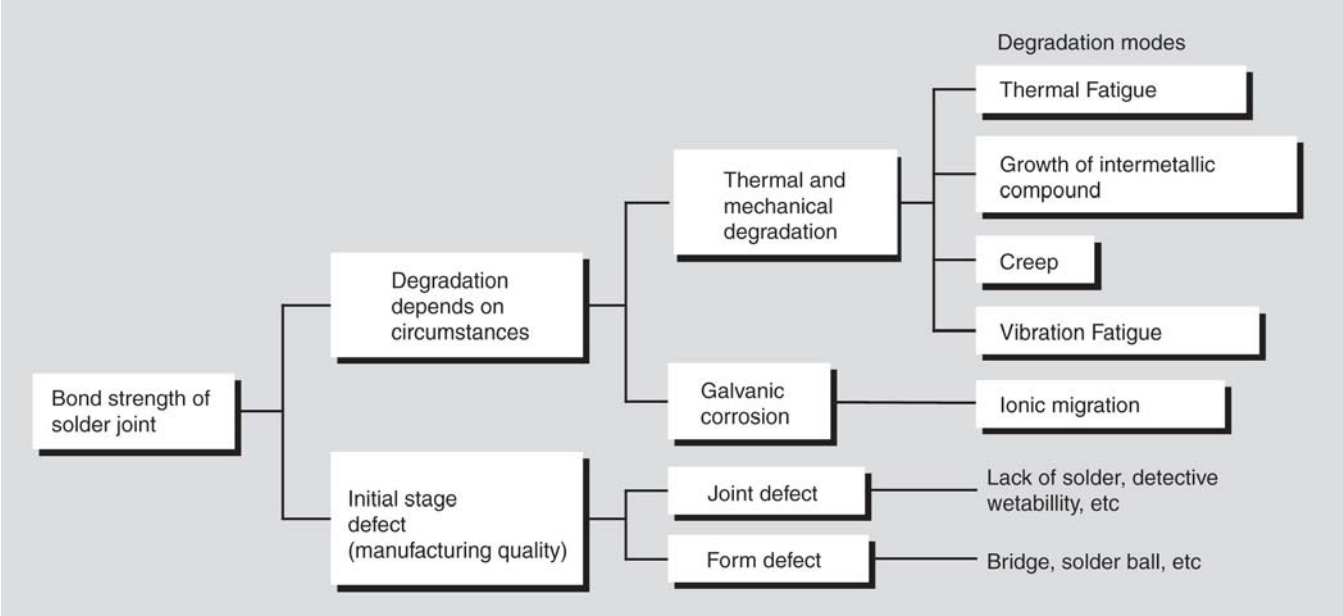


Fig. 2 Solder joint reliability factors

The environmental degradation modes that were considered were: (1) thermal fatigue, (2) growth of intermetallic compounds, (3) creep, (4) vibration fatigue, and (5) ionic migration. Reliability evaluation is the operation of determining whether or not the specified functions can be maintained under given conditions and for a given period of time. In specific terms, this is proving that environmental degradation-type malfunctions will not occur within the period of guaranteed use.[3] [4]

Given these considerations, a reliability evaluation of lead-free solder was conducted by comparing lead-free solder in the form of various types of low melting point Sn-based eutectic alloy with Sn-Pb solder. This will be explained below with reference to the five degradation modes.

2.1. Thermal Fatigue

Fig. 3 shows the mechanism of the occurrence of thermal fatigue.[1] [2]

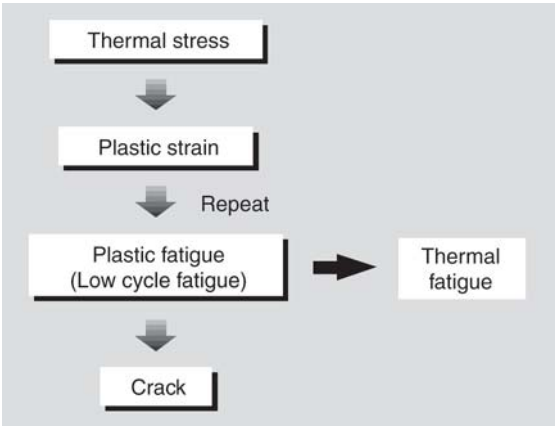


Fig. 3 Mechanism of the occurrence of thermal fatigue

Since the degradation factor is temperature change (ΔT), the most appropriate accelerated test is thermal cycle testing, in which a load is applied by alternating high and low temperatures. Evaluation was conducted using different solder compositions.

Four types of solder were used: (1) Sn-37Pb, (2) Sn-3.5Ag-0.75Cu, (3) Sn-7.5Bi-2Ag-0.5Cu, and (4) Sn-8Zn-3Bi. A ceramic chip resistor (size 2125), which has a coefficient of thermal expansion significantly different from that of the substrate, was mounted on a glass-epoxy substrate using those types of solder. The thermal cycle conditions were temperatures of –40 °C – 120 °C at 30 minutes each. The results are shown in Fig. 4, Table 1, and Fig. 5. It was determined from the failure mode and internal soundness that Sn-Bi types and Sn-Zn types would be difficult to guarantee, and subsequent evaluation was focused on the Sn-Ag-Cu solder.

Sn-Ag-Cu solder was subjected to thermal cycle testing at three levels of ΔT, between the different temperatures (1) –40 °C – 125 °C, (2) –40 °C – 100 °C, and (3) –40 °C – 80 °C. The results are shown in Fig. 6 and Fig. 7. It is apparent that the Sn-Ag-Cu solder shows longer life than Sn-Pb solder in the low ΔT region (165 °C and below) that corresponds with the region of ordinary use.

Next, the electrode surface treatment specifications of the chip part were examined for reference purposes. Sn-3.5Ag solder was used together with test pieces mounted with chip resistors with four different types of surface treatment: (1) Sn-10Pb, (2) Sn 100%, (3) Sn-3.5Ag, and (4) Sn-10Bi. These were subjected to thermal cycle testing at –40 °C – 125 °C for 30 minutes each. The results are shown in Fig. 8. With Sn-10Bi, the crack growth rate was higher on the low cycle, and, as shown in Fig. 9, there were problems such as peeling at the boundary between the component and the solder, and this was judged unacceptable for use.

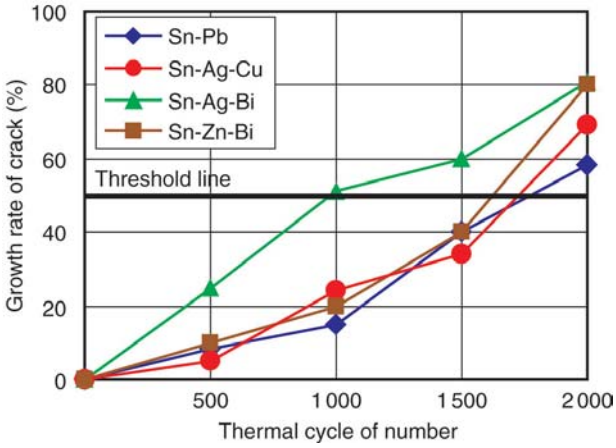


Fig. 4 Tendency of chip resistor degradation classified by solder material

Table 1 Results of thermal cycle test

Solder composition	Mean life-cycle (50% crack)	Internal soundness
Sn-Pb	1 800	OK
Sn-Ag-Cu	1 750	OK
Sn-Bi	1 000	OK
Sn-Zn	1 650	OK

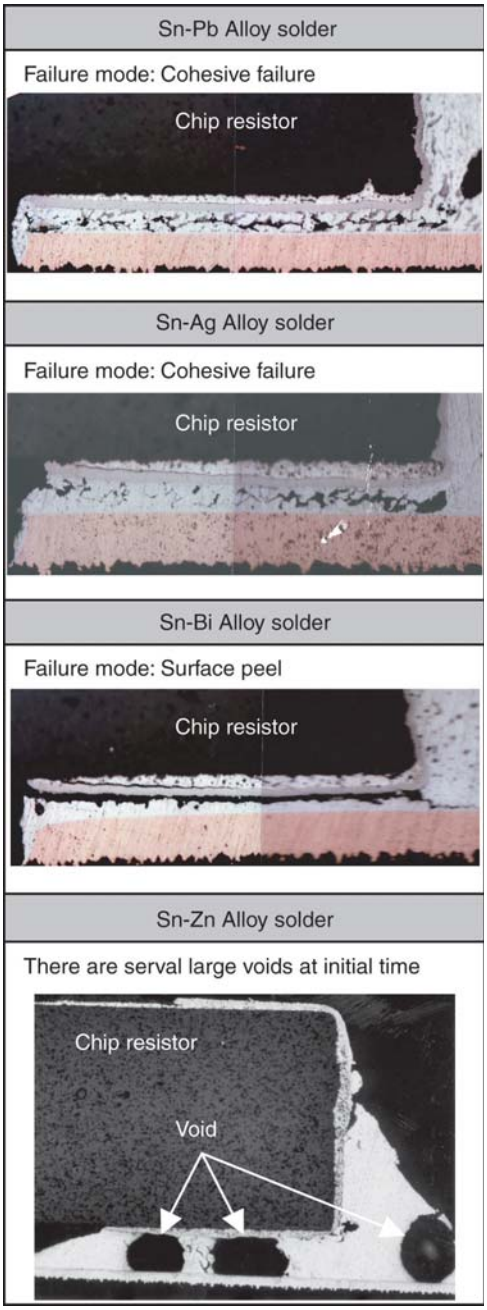


Fig. 5 Cross cut section of solder joint

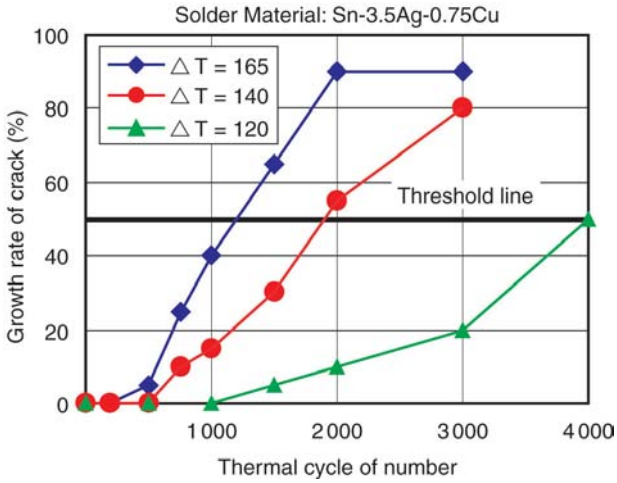


Fig. 6 Tendency of chip resistor degradation classified by ΔT

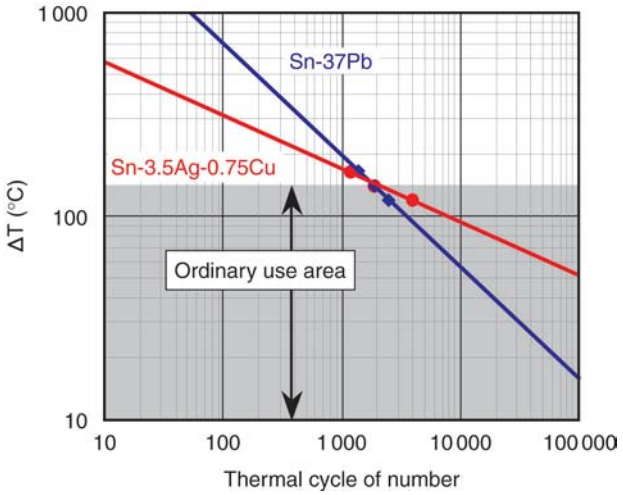


Fig. 7 Limit line of durability of thermal fatigue (chip resistor)

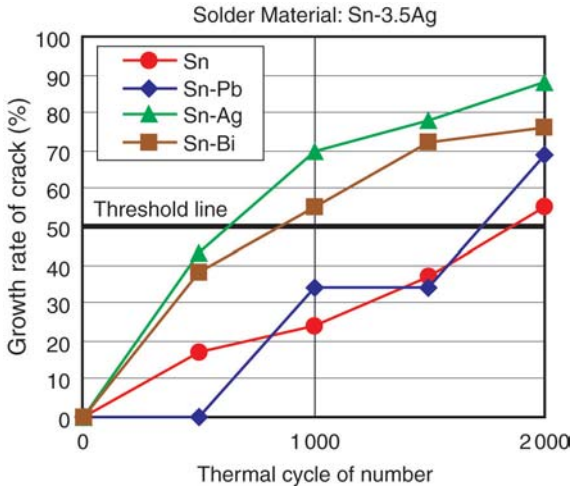


Fig. 8 Tendency of chip resistor degradation classified by electrode material (chip resistor)

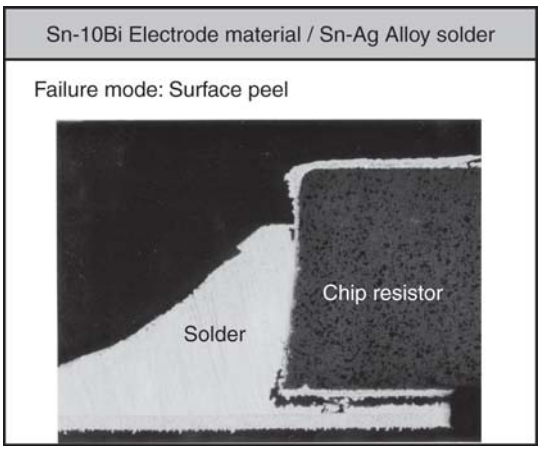


Fig. 9 Cross cut section of solder joint

2.2. Growth of Intermetallic Compounds

When the solder forms a fused junction, the Sn in the solder and the metal (here it is Cu) that forms the substrate pattern form an intermetallic compound layer, as shown in Fig. 10, by interdiffusion. Upon initial use, the solder and the Cu on the substrate exhibit a strong bond. In the usage environment, however, an intermetallic compound layer grows and enters a stable compound phase. This conversely becomes fragile, causing concern that it will have an influence on the life of the joint.[1]

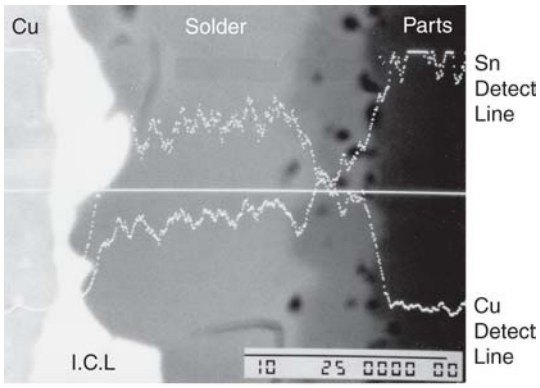


Fig. 10 Micrograph of intermetallic compound layer (I.C.L)

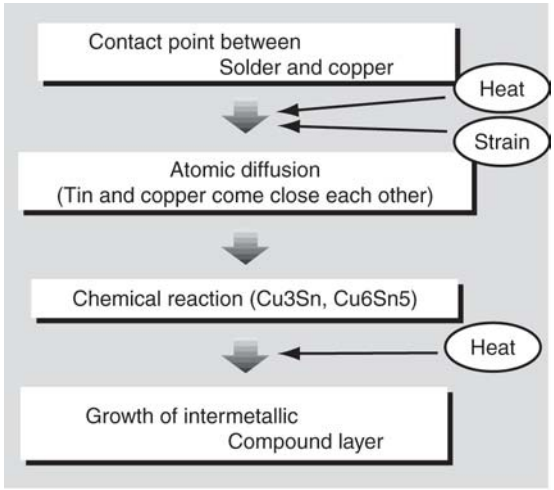


Fig. 11 Mechanism of the growth of an intermetallic compound layer

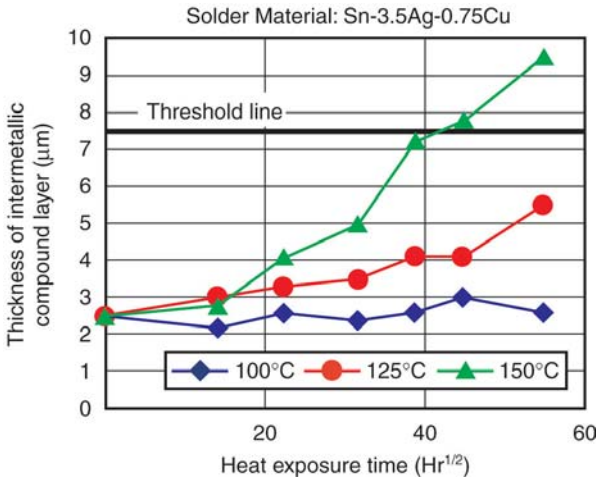


Fig. 12 Growth pattern of the intermetallic compound layer

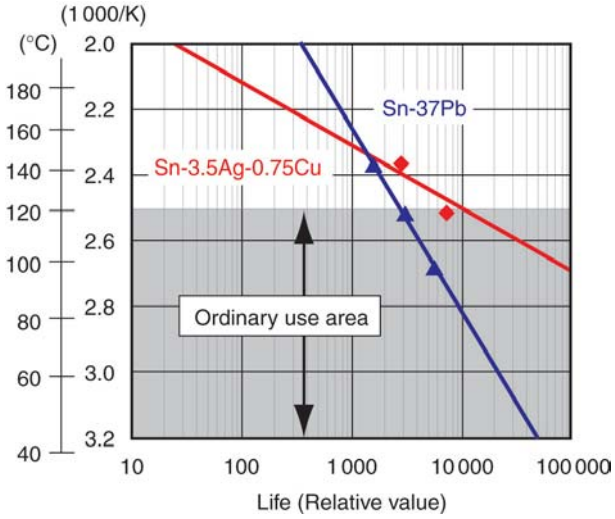


Fig. 13 Limit line of durability of the intermetallic compound layer fracture

Fig. 11 shows the mechanism of the growth of an intermetallic compound layer. It is apparent from this that heat is a factor in degradation, and an isothermal soak test is optimal for the acceleration test. Chip resistors (size 3216) were mounted on a glass-epoxy substrate and allowed to soak under isothermal conditions at the three levels of (1) 150 °C, (2) 125 °C, and (3) 100 °C. The results of this testing are shown in Fig. 12. Fig. 13 is a life chart that has plotted the lifeline point at 7.5 μm. It is apparent from this that Sn-Ag-Cu solder has reliability equal to or better than that of Sn-Pb solder in the ordinary use temperature region.

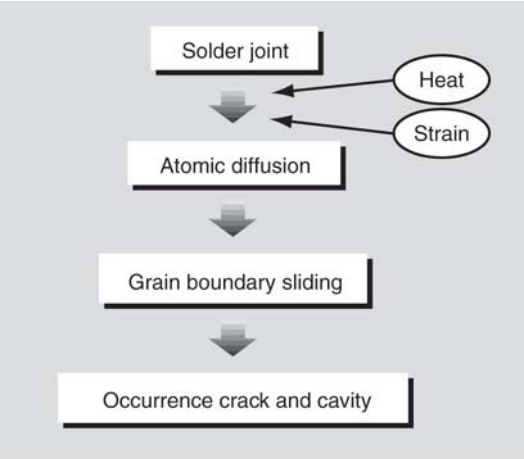


Fig. 14 The creep fracture mechanism

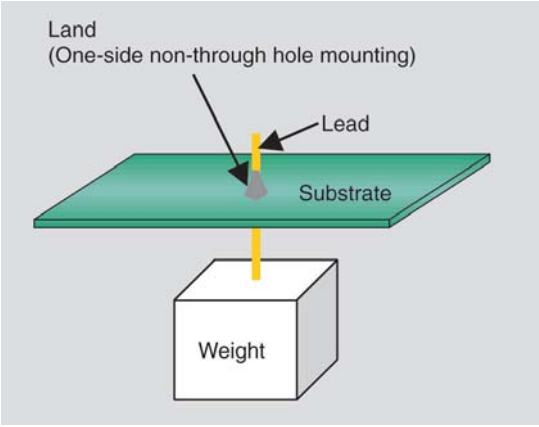


Fig. 15 Creep test method

2.3. Creep

The low melting point of solder means that care must be taken against creep damage even at ordinary temperatures, just as with resin and rubber.[1] Fig. 14 shows the mechanism of creep occurrence, for which the degradation factors are heat and strain. The test piece shown in Fig. 15 was subjected to an isothermal soak test at 125 °C. The results are shown in Fig. 16. It is apparent that the fracture time is superior to that of Sn-Pb solder by two digits of magnitude or more.

2.4. Vibration Damage

A Plastic Leaded Chip Carrier (PLCC), which is capable of high load settings, was used as the test piece and subjected to vibration testing by the method shown in Fig. 17. The environmental temperature was kept at 125 °C, the frequency of the base of the vibrator at 100 Hz, and the acceleration at 25 G, and the weight of the load attached to the back of the PLCC was varied at several levels. Acceleration sensors were attached to the base of the vibrator and to the PLCC to verify that they were vibrating at the same amplitude and phase. The results are shown in Fig. 18.[1] [2]

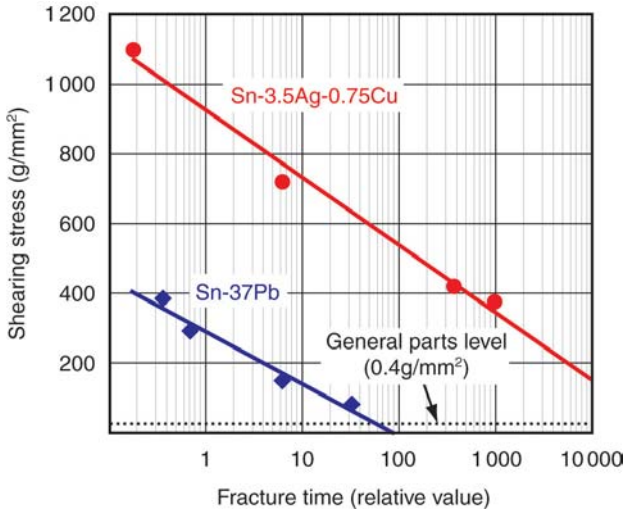


Fig. 16 Creep fracture life chart

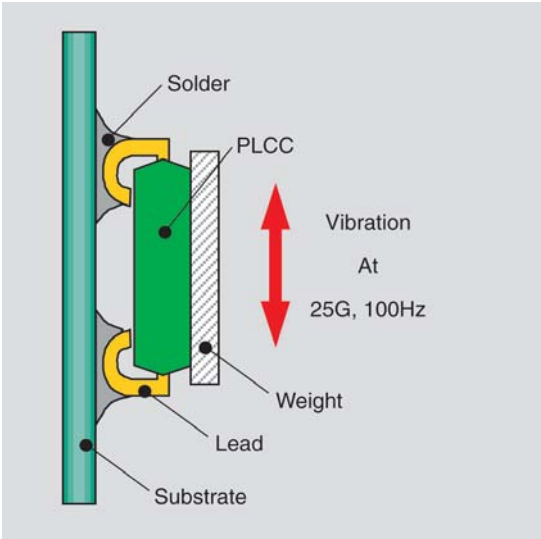


Fig. 17 Vibration test method

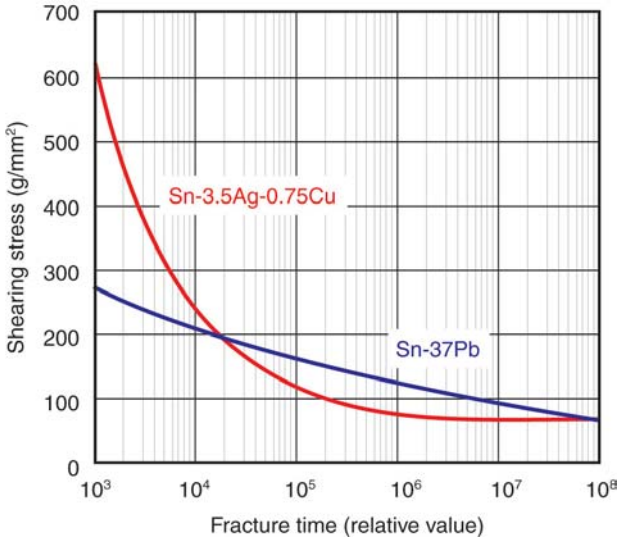


Fig. 18 Breakage probability life curve

The S-N diagram (10% breakage probability life curve) shows the shearing stress applied to the joint on the vertical axis, and the number of cycles to fracture (the life) on the horizontal axis. The shearing stress values converge where the number of cycles is greater. This is the phenomenon of the so-called fatigue limit. It can be determined that, although the Sn-Ag-Cu solder exhibits a different pattern than the Sn-Pb solder, their fatigue limits are at the same level.

2.5. Ionic Migration

Ionic migration is the phenomenon that occurs when voltage applied in an environment of heat and humidity results in the metal between the electrodes on the printed wiring board solving out onto the insulation layer and forming dendrites (also known as whiskers). Repeated occurrence of this phenomenon can lead to a short circuit. The three degradation factors in ionic migration are humidity (environmental), electrolytic strength (voltage), and temperature. The interaction of these three factors determines the short circuit durability.

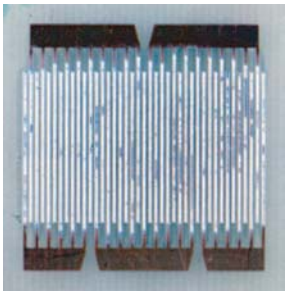


Fig. 19 Sample for ionic migration test

The JIS II comb-shaped electrode shown in Fig. 19 was first pre-fluxed, and then cleaned. The soldered specimen was then tested under the following conditions: (1) High-temperature and high-humidity: 85 °C, 85% RH, bias voltage of 50 V applied for 1,000 hours, and then (2) dew cycle: 5 °C – 25 °C, 20 minutes each, bias voltage of 50 V applied for 1,000 cycles. These test conditions are harsher than the conditions of the actual usage environment, and the results showed that no ionic migration occurred in either the Sn-Pb solder and the Sn-Ag-Cu solder.

The reliability of the Sn-Ag-Cu solder was evaluated from the reliability engineering perspective, under the five solder degradation modes: (1) thermal fatigue, (2) growth of intermetallic compounds, (3) creep, (4) vibration fatigue, and (5) ionic migration. Miner's law and other methods were also applied to evaluate market life for all the degradation modes. The results verified that Sn-Ag-Cu solder has reliability equal to or better than Sn-Pb solder.

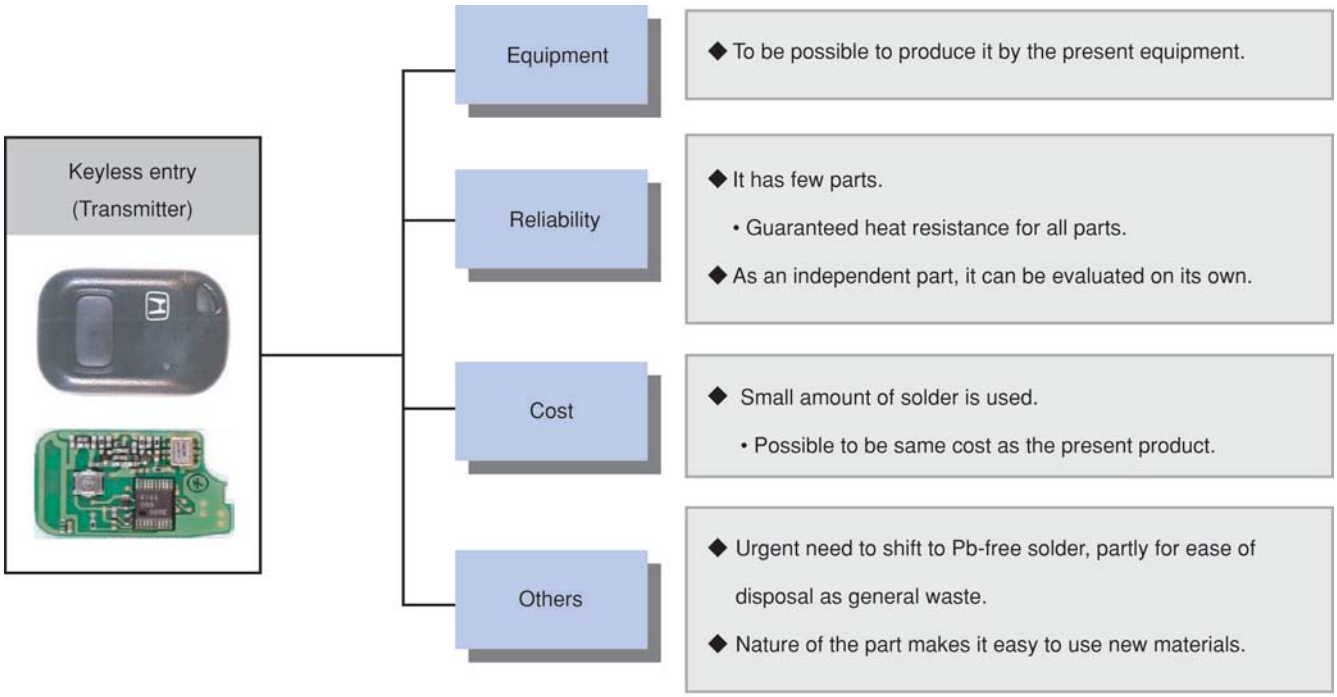


Fig. 20 Reasons for selection of keyless entry (transmitter)

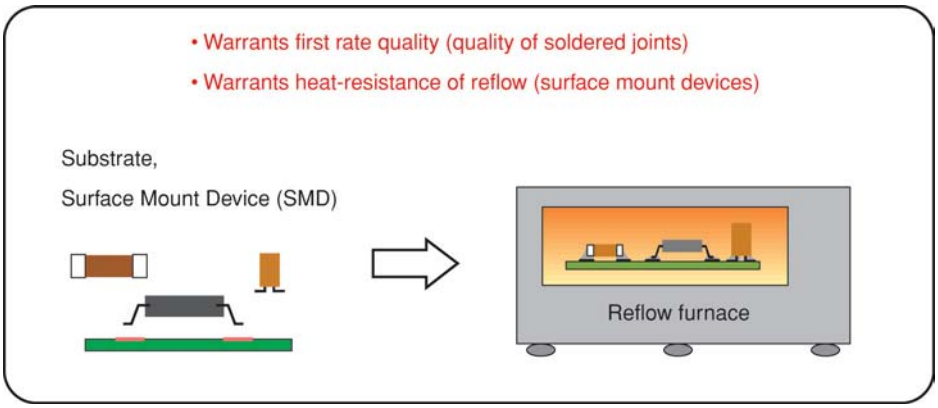


Fig. 21 Reflow soldering process

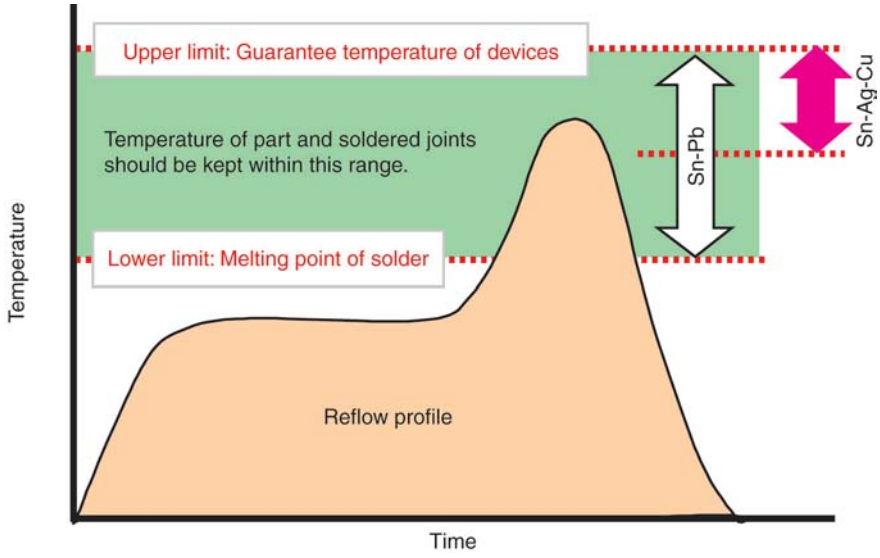


Fig. 22 Temperature profile of reflow soldering

3. Application in Products

Having verified that Sn-Ag-Cu solder has reliability equal to or better than the current mass-produced Sn-Pb solder, the use of lead-free solder applied to products was investigated. The product selected for application was the keyless entry transmitter, for the reasons shown in Fig. 20.

Fig. 21 shows a conceptual view of the reflow soldering process involved.

3.1. Solution of Solder Mounting Issues

The most difficult issue in applying Sn-Ag-Cu solder to a product is that it has a significantly higher melting point (219 °C as opposed to 183 °C) than Sn-Pb solder. In other words, the product must be manufactured within a narrower reflow temperature control range than is required with Sn-Pb solder in order to maintain the quality of the solder joint within the guaranteed heat resistance temperature of the product components. Fig. 22 shows the reflow soldering conditions that resolved this issue for Sn-Ag-Cu solder.

There is only slight variation in component temperatures when reflow soldering on the keyless entry transmitter because of the small number of component parts and the minor differences in the size of those parts. Consequently, it was possible to identify the conditions that would assure solder quality and component parts quality without making any alteration to the existing reflow equipment used with Sn-Pb solder.

3.2. Results of Product Performance Evaluation

In order to judge whether Sn-Ag-Cu solder provides satisfactory product performance, reliability evaluations were conducted on all specifications of the keyless entry transmitter that require reliability. The results verified that Sn-Ag-Cu solder provides the reliability required for the keyless entry transmitter, and also that it has reliability equal

Table 2 Results of model spec test

Test Item	Result
Thermal cycle	OK
Heat resistance	OK
Switch endurance	OK
Transmission performance	OK
General performance	OK

to or better than the conventional Sn-Pb solder and is suitable for use with the keyless entry transmitter. Table 2 shows selected results from the product performance evaluation. Thermal fatigue is crucial to the reliability of solder, and the evaluation results on this item will be explained in further detail in section 3.2.1.

3.2.1. Thermal fatigue

Thermal fatigue, which is considered to be the most severely demanding criterion in solder reliability evaluation, was evaluated at the lower limit of the solder joint quality obtained under manufacturing conditions that allow mass production. This was also done to predict thermal fatigue life of the joints. The results verified that no cracking occurred due to thermal fatigue in the Sn-Ag-Cu solder joint, and that the thermal fatigue life was sufficient.

Fig. 23 and Fig. 24 show the results of the observation of solder joint cross-cut sections after thermal fatigue testing. Fig. 25 shows a graph of the predicted thermal fatigue life.

4. Conclusion

(1) The reliability of lead-free soldering was evaluated from the perspective of reliability engineering for the five solder degradation modes of (1) thermal fatigue, (2) growth of intermetallic compounds, (3) creep, (4) vibration fatigue, and (5) ionic migration. The results verified that Sn-Ag-Cu solder has reliability equal to or greater than Sn-Pb solder.

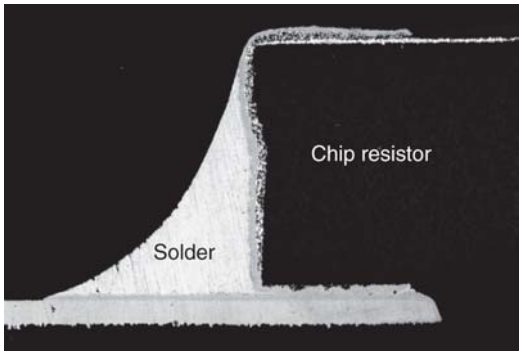


Fig. 23 Sn-Ag-Cu alloy solder cross-cut section (After the thermal cycle test)

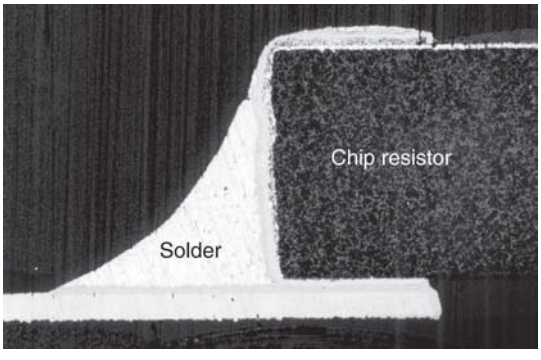


Fig. 24 Sn-Pb alloy solder cross-cut section (After the thermal cycle test)

(2) With its high reliability verified, Sn-Ag-Cu solder was applied to a keyless entry transmitter. In order to hold down costs when using this solder on a product, it was decided not to alter the equipment or the component designs, and regardless, the results obtained were satisfactory in terms of product quality, product performance, and durability.

5. Postscript

The reliability of lead-free solder has previously been reported in the Technical Review (Vol. 12, No. 1).[5] Where that research performed evaluation of test pieces with bare-chip die bonding, the present research was conducted on the assumption that ordinary mounting substrate would be used, and reliability evaluation was also conducted. The two research projects yielded wide-ranging information on the reliability of lead-free solder.

At present, the adoption of lead-free household electrical appliances is spreading, and the lead-free movement not only for solder materials but also for treatment of electrode surfaces in component parts is making progress.

The solder material being used is converging on the same Sn-Ag-Cu solder used in the present research. For treatment of the electrode surfaces of component parts, however, there is growing use of Sn-Bi plating with a low Bi concentration (4% or less) for semiconductors and aluminum electrolytic capacitors as a measure to improve the solder wettability and prevent whisker formation between the leads. The present research verified that items plated with Sn-Bi10% showed reduced reliability in thermal fatigue testing. Therefore, care is required when mixing in parts that have Sn-Bi plating.

The change to lead-free automotive electronic devices has progressed with the gradual introduction of lead-free mass-production products starting in August 2000. Meanwhile, Honda has used lead-free solder for the first time in keyless transmitters for models such as the Odyssey and Avancia. Mass production of these products was initiated in August 2001 by Honda Lock MFG. Co., Ltd. With these keyless transmitters having opened the way, the adoption of lead-free automotive electronic devices can be expected to expand steadily.

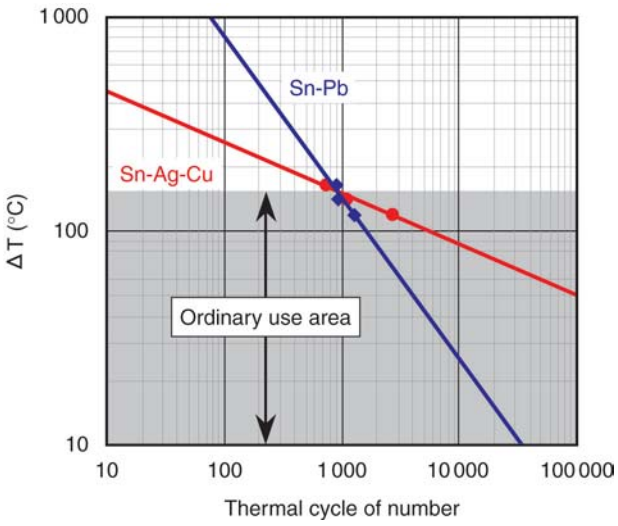


Fig. 25 Limit line of durability of thermal fatigue (chip resistor)

6. Acknowledgements

The authors gratefully acknowledge the cooperation extended by Mr. Shimano and Mr. Sato of KEHIN CORPORATION and by Mr. Miyasaka of NESTEC INC. in the fabrication of test specimens and testing, the assistance provided by Mr. Suyama of HONDA LOCK MFG. CO., LTD. with product development, and the support given by all the others involved in the present research.

References

(1) Masato MORIYAMA, et al., “Reliability of Solder Joints in Automotive Electronic Devices,” Honda R&D Technical Review, Vol. 9, pp. 156 – 166 (1997).

(2) Junichi OHMURA, et al., “Research in Lead-free Solder Mounting of Automotive Electronic Devices,” Japan Welding Society Mate ’2000, pp. 307 – 312 (2000).

(3) Japan Standards Association, ed., *Microelectronics Test Methods and Procedures*, Japan Standards Association, Tokyo (1987).

(4) Jennie S. HWANG, “Solder Paste for Electronics Packaging,” pp. 283 – 309, Kogyo Chosakai, Tokyo (1991)

(5) Toshihiro OOKAMA, et al., “Reliability Evaluation of Lead-free Solder Joints in the Automotive Environment,” Honda R&D Technical Review, Vol. 12, No. 1, pp. 137 – 144

■ Authors ■


Tsunehisa HATA


Junichi OHMURA


Masato MORIYAMA


Tomoo WATANABE

Development of Pb-free Free-cutting Steel Enabled to Omit Normalizing for Crankshafts

Atsushi AMATAKA* Satoru SUWA*

ABSTRACT

A Pb-free free-cutting steel for crankshafts was developed which resulted in the omission of the normalizing process. In order to omit the normalizing process, adequate hardness and fine microstructures, as obtained in normalized steel, must be achieved in the free-cutting steel after forging and air-cooling. These requirements were met by adjusting chemical composition of steel. A target was to achieve productivity of the developed steel based on Ca-S free-cutting steel, equal to that of the conventional Pb-S free-cutting steel. As a result of examining non-metallic inclusion's composition, volume, shape and dispersion in the steel, it was found that the shape and dispersion contributed to an improvement in machinability. By manufacturing a crankshaft with this steel, the cost of the normalizing process was eliminated and the reduction of Pb by 13 g became possible for a motorcycle equipped with a 954 cm^3 engine.

1. Introduction

The normal method used to manufacture crankshafts for large motorcycles has involved hot forging and nitrocarburizing. S48CL1S1 Pb-S free-cutting steel has typically been used to achieve satisfactory strength and productivity.

This present work investigates a steel composition that enables omission of the normalizing process, which is usually required in the production process for automobile components, and the application of an optimized form of this steel material to a motorcycle engine. A study was also undertaken to make this steel Pb-free. The crankshaft production procedure is shown in Fig. 1. The machining process involves the four steps of lathe turning, drilling, grinding, and gear cutting. Depending on the machines and tools used, and on the machining conditions, 120 or more different machining operations may be necessary; consequently, it is extremely difficult to determine the machinability of a crankshaft material by means of simplified cutting tests alone.

This project, therefore, used material forged from sulfur free-cutting steel made from conventional Pb-S free-cutting steel (hereafter referred to as conventional steel) which had been processed to be Pb-free. This forged material was then subjected to the crankshaft mass production process, and the problems involved were identified. Although there were no problems with drilling, grinding, or gear cutting, in which this material was equal to the conventional steel, it is apparent from the chips shown in Fig. 2 that this material had inferior frangibility when lathe turned, and the machining equipment was unable to eject it automatically.

The study was accordingly focused on ways of improving chip frangibility in order to produce a Pb-free free-cutting steel.

* Asaka R&D Center

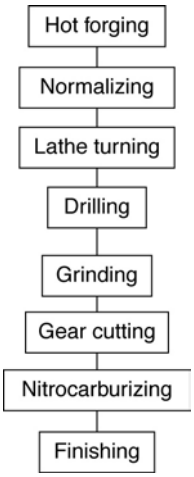


Fig. 1 Production process for crankshaft



Fig. 2 Chips of sulfur free-cutting steel generated by lathe turning

2. Alloy Design

2.1. Study on the Omission of Normalizing

The purpose of normalizing is to improve the coarse microstructure resulting from the effects of heating, forging, and cooling that occur during hot forging.

Figure 3 shows the microstructure of steel that had been heated to 1,200 °C, forged and then cooled, and of steel that had been normalized after similar processing. The effect of normalizing was to change the coarse ferrite-pearlite grains into fine ferrite-pearlite grains.

On the other hand, reducing the amount of carbon (C) and manganese (Mn) increases the ferrite area fraction, while the addition of nitrogen (N) increases the number of nucleation sites for ferrite. This is known to have the effect of yielding a fine microstructure, even when normalizing is omitted after a forging operation.[1]

The target ferrite area fraction for the required steel, therefore, was set to 40%, which is equivalent to normalized S48C. The gears, splines, timing sprockets, etc. on a motorcycle crankshaft are frequently machined directly, and the timing sprockets are induction hardened to increase their wear resistance, giving them an induction hardened hardness of HRC50 or better. Consequently, the lower limit for the C content was set at 0.40%.

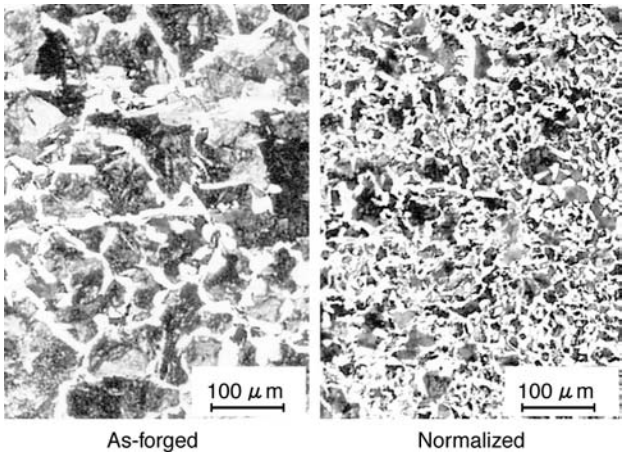


Fig. 3 Microstructure of conventional steels

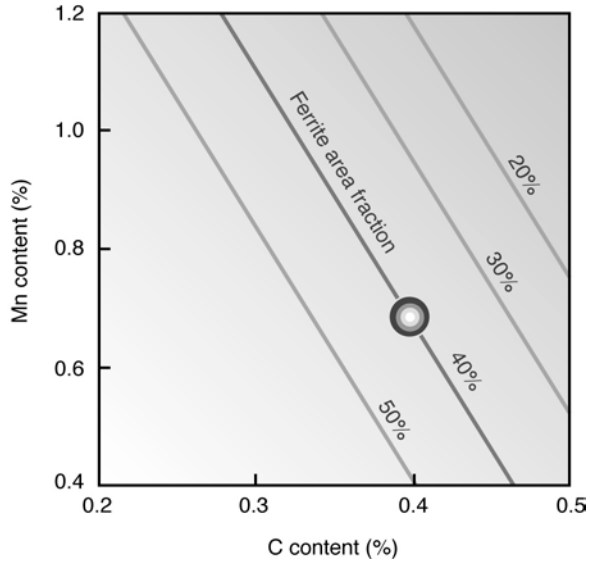


Fig. 4 Influence of carbon and manganese on ferrite area fraction

The C content, Mn content, and ferrite area fraction are related as shown in Fig. 4. Reducing the C content results in a significant increase in the ferrite area fraction. With the reduced C content set at 0.40%, the Mn content could be set at 0.70% in order to achieve the ferrite area fraction target. The hardness increased markedly when the N content was 0.020% or greater, so 0.020% N was set as the upper limit.

2.2. Study of Methods for Making Steel Pb-Free

Methods for making Pb-free steel have been addressed in reports[2, 3] on regulatory trends and machining effects, as well as in proposals for Pb-free free-cutting steel made by steel manufacturers.[4–12] These methods can be broadly classified under the two following types:

- The addition of previously unused substances such as Bi or BN as a lead substitute[4–6]
- The improvement of conventional free-cutting steel[7–10]

Table 1 Target of chemical composition of developed steel

mass (%)

	C	Si	Mn	P	S	Cr	N	Pb	Ca
Developed steel	0.40	0.20	0.70	0.017	0.050	0.06	0.017	—	0.0020

Table 2 Chemical composition of developed and conventional steels

mass (%)

	C	Si	Mn	P	S	Cr	N	Pb	Ca
Developed steel	0.40	0.19	0.72	0.017	0.049	0.06	0.017	—	0.0022
Conventional steel S48CL1LS1 *	0.47	0.18	0.78	0.025	0.047	0.17	0.010	0.07	—
Comparison steel S40CS1U *	0.40	0.18	0.70	0.010	0.049	0.07	0.016	—	0.0017

* JASO M 106-92

The former method leaves many questions unanswered regarding regulatory trends for previously unused substances, the future availability of such substances and so on. The latter method takes the approach of adding elements that have a proven history of effectiveness for free cutting. This study proceeded on the basis of adding S and Ca.

Machinability is commonly evaluated by the criteria of chip frangibility, tool life, cutting force, and hardening cracks. The main effect of adding lead to free-cutting steel is improved chip frangibility resulting from embrittlement during machining and stress concentration.[4]

Crankshaft cutting tests conducted with conventional steel and sulfur free-cutting steel processed to be Pb-free also confirmed this within the effective region of embrittlement for the lead in chips that had been discolored blue. At that point, the target chip frangibility for the developed steel in the lathe turning process was set to be equal to that for the conventional steel, and the type, quantity, shape, and dispersion of non-metallic inclusions were determined on the basis of added S and Ca.

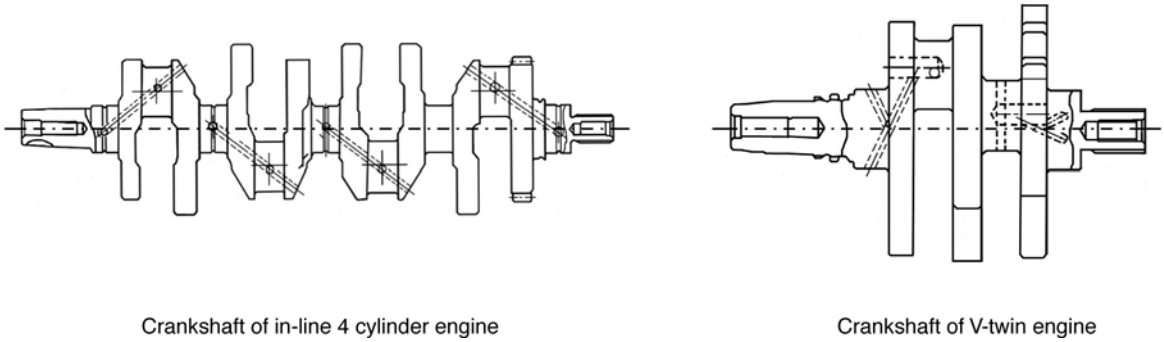
The non-metallic inclusions were mainly of the sulfide type (MnS) and low-melting-point oxides (CaO-Al_2O_3-SiO_2, etc.). Improved machinability was apparent with increasing MnS content, although quenching cracks sometimes occurred during induction hardening. Consequently, the S content was set to 0.050%, which is equal to the JASO S1 level. The constitution and shape of CaO inclusions changed according to the amount of Ca added, the amount of oxygen in the molten steel, and so on. [12] The Ca content was therefore set to 0.0020%, and the oxygen content was optimized to adjust the low-melting-point oxide inclusions.

The plan was to make the non-metallic inclusions finer in size and more evenly dispersed. The target values for the basic chemical composition of the developed steel are shown in Table 1.

3. Testing Methods and Results

3.1. Testing the Steel Properties

Samples were prepared of the developed steel, conventional steel, and a comparative steel, the latter being a calcium-sulfur free-cutting S40CS1U steel with non-metallic inclusions dispersed differently from those in the developed steel. The chemical compositions of the test materials are shown in Table 2. The developed steel and comparative steel were melted in a 70-ton steel converter, continuously cast, and then hot rolled into round bars of 80 mm in diameter. The conventional steel was melted in a 90-ton electric furnace, continuously cast, and then hot rolled into round bars of 78 mm in diameter in order to easily differentiate it from the other samples to the extent that it would not affect the properties of the steel. Each of these steel materials was heated to 1,200 °C, the temperature envisaged for hot forging, and air cooled. The conventional material was then maintained at a temperature of 880 °C for four hours, after which it was normalized by air cooling.



Crankshaft of in-line 4 cylinder engine

Crankshaft of V-twin engine

Fig. 5 Geometry of crankshafts for motorcycle

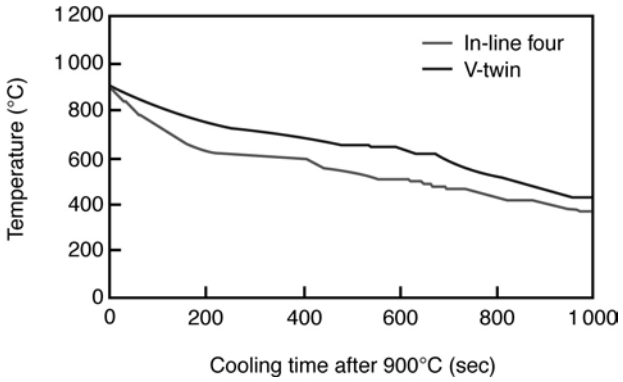


Fig. 6 Cooling curve of air-cooled crankshafts after hot forging

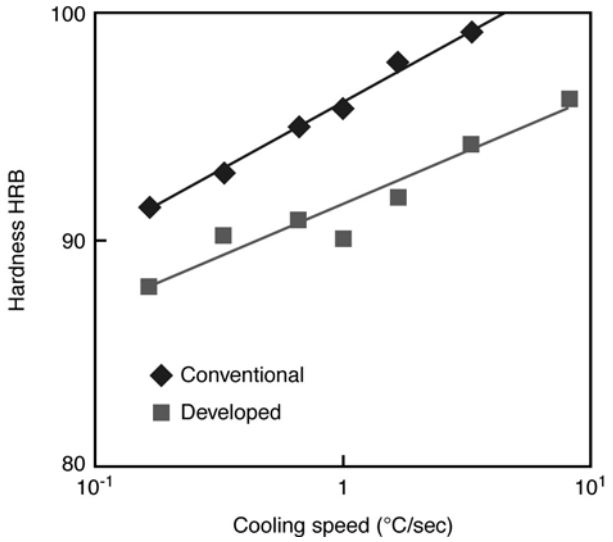


Fig. 7 Influence of cooling speed on hardness after hot forging

3.1.1. Microstructure and hardness of the air-cooled materials after hot forging

If normalizing is to be omitted, it is necessary to use air cooling alone to obtain the required microstructure and hardness after hot forging. Accordingly, an investigation was made of the cooling rate by air cooling after hot forging typical crankshafts. Figure 5 shows the geometry of crankshafts for in-line 4-cylinder and V-twin engines, and Fig. 6 shows the cooling curve. The average rate of cooling from 900 °C to 700 °C after hot forging the crankshafts was 0.56–1.56 °C/sec.

Each material was next heated to 1,250 °C in a hot-deformation simulator (Thermecmastor), subjected to 50% forming by compression at a process temperature of 1,100 °C, and then cooled at 0.17–8.33 °C/sec, after which the hardness was measured. Figure 7 shows the relationship between the cooling rate and hardness. The developed steel achieved a hardness approximately 3–6 points lower than the conventional steel. When cooled at a rate of 1 °C/sec, which is equivalent to the usual air cooling rate for a crankshaft after forging, the developed material achieved a hardness of HRB90, this being equal to that for the normalized conventional steel sample.

3.1.2. Non-metallic inclusions

The dispersion and types of non-metallic inclusion in the developed steel and comparative steel were verified in longitudinal sections. The upper photographs in Fig. 8 show the dispersion of non-metallic inclusions. It is apparent that the sulfide type of non-metallic inclusion in the developed steel was more finely dispersed than that in the comparative steel.

A qualitative analysis of the oxide type of non-metallic inclusion by an electron probe X-ray micro-analyzer (EPMA) is shown at the bottom of Fig. 8. The oxide type of non-metallic inclusions in the developed steel are of the low melting point variety containing Ca, Al, and Si.

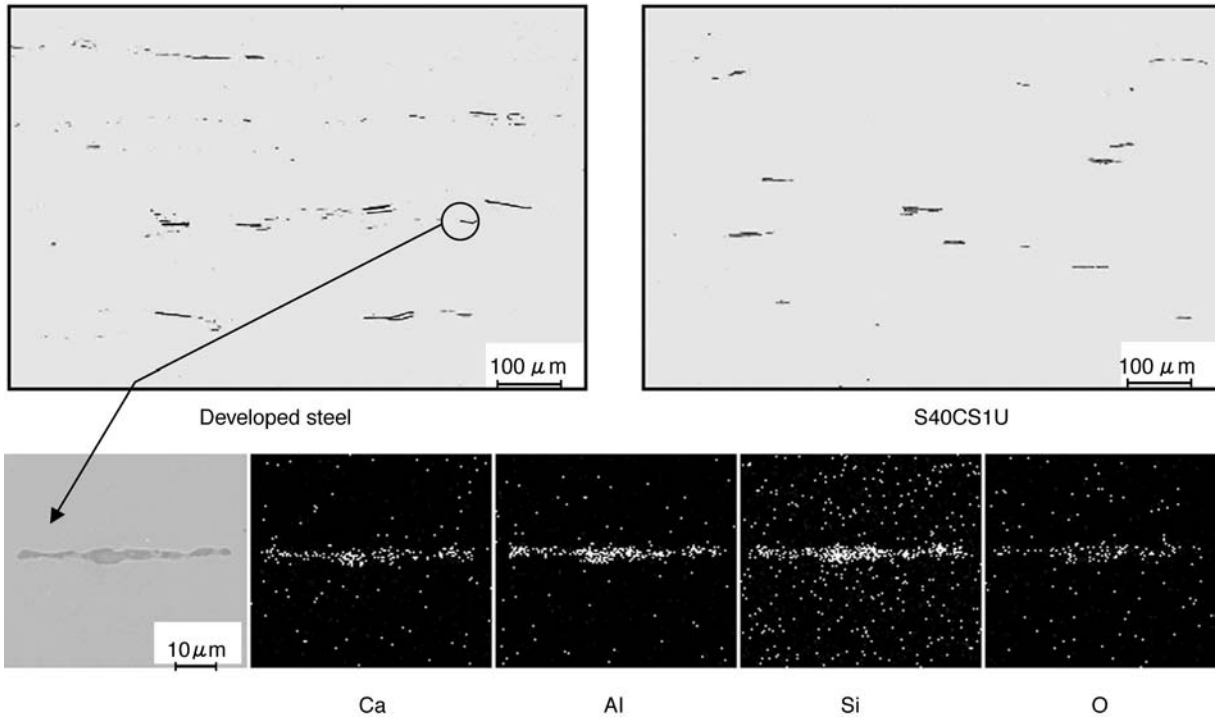


Fig. 8 Distribution of non-metallic inclusions and oxide inclusion image by EPMA

3.1.3. Chip frangibility

The effect of the shape and dispersion of non-metallic inclusions on chip frangibility for the developed steel and comparative steel were compared. The crankshaft machining operation with the least favorable conditions for chip frangibility was used for the evaluation, Fig. 9 showing the machining geometry and conditions.

In order to evaluate the chip frangibility, ten of the larger chips generated by cutting to a total depth of 6 mm were recovered and their weight was measured. Photographs were taken of longitudinal sections with a 100-power microscope and measurements were made of the number of non-metallic inclusions in eight visual fields in order to evaluate the shape and dispersion of the non-metallic inclusions. Figure 10 shows the relationship between the chip weight and number of non-metallic inclusions. An index was generated for the number of non-metallic inclusions, whereby a level of 1 represents a chip that can be ejected automatically. It is apparent that the chip weight decreased as the number of non-metallic inclusions increased, thus improving the chip frangibility. The chemical compositions of the developed steel and comparative steel were similar to those of S40CS1U, Fig. 8 showing the only major difference to be in the distribution of sulfide- type non-metallic inclusions. It can be concluded that the fine dispersion of sulfide-type non-metallic inclusions made the main contribution to favorable chip frangibility for the developed steel.

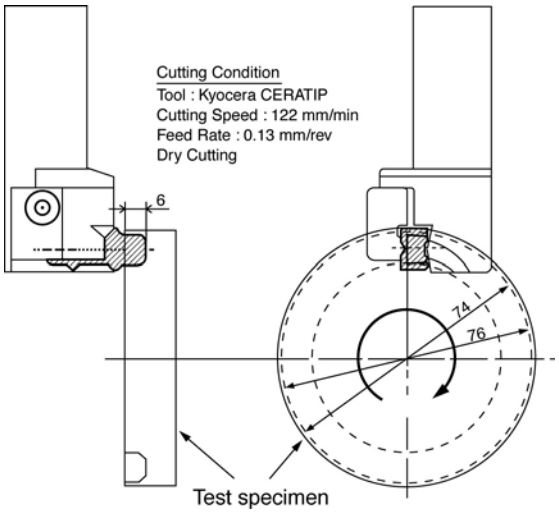


Fig. 9 Geometry of cutting test specimen and cutting condition

3.1.4. Mechanical properties

The mechanical properties of the developed steel and conventional steel are shown in Table 3. The developed steel has a tensile strength (TS) equal to that of the conventional steel, while the yield strength (YP), elongation (EL), and Charpy impact strength of the developed steel are approximately 20–30% lower than the figures for the conventional steel. Nevertheless, the Charpy impact strength ratio (C/L) in the cross-sectional direction (C) and longitudinal direction (L), which is an index used for Pb-free free-cutting steel, is 0.35 for the developed steel and 0.31 for the conventional steel. The anisotropy of the developed steel is thus equal to that of the conventional steel.

Table 3 Mechanical properties of developed and conventional steels

	Direction	TS (MPa)	YP (MPa)	EL (%)	Impact value (J/cm²)	Impact value Ratio C/L
Developed steel	L	660	311	23.8	52.0	0.35
	C	638	303	10.9	18.4	
Conventional steel	L	699	455	28.6	76.0	0.31
	C	704	448	14.6	23.6	

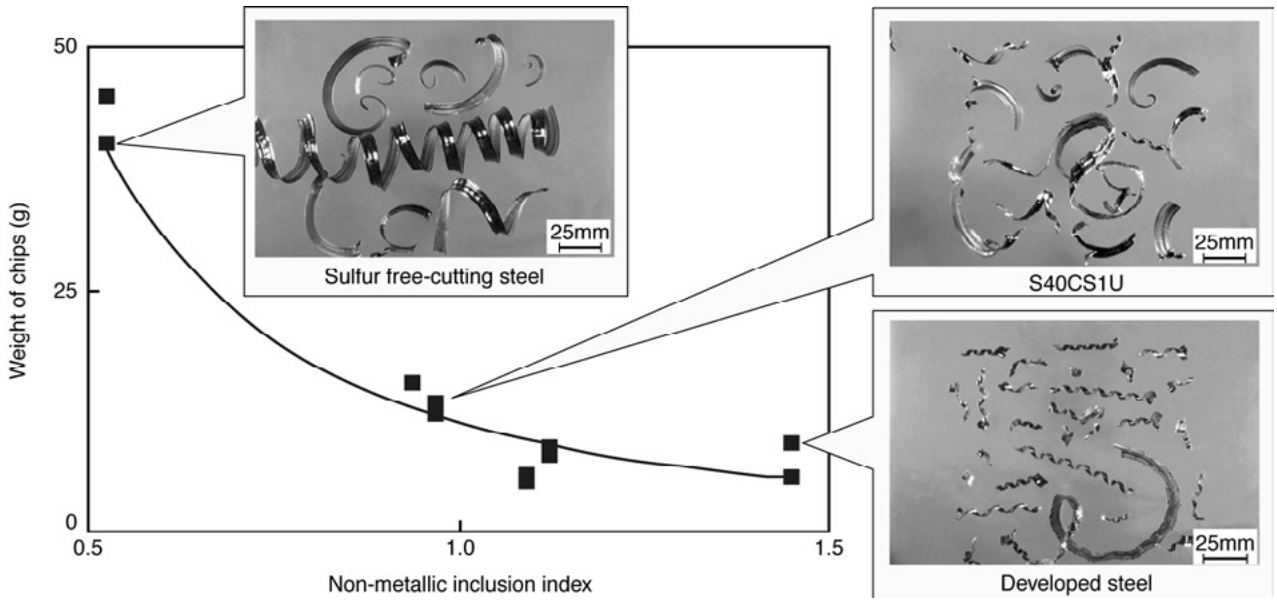


Fig. 10 Influence of non-metallic inclusion index on weight of chips generated by lathe turning

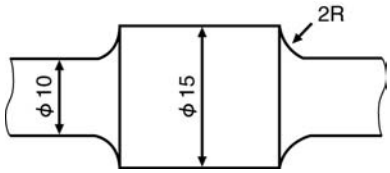


Fig. 11 Geometry of rotating-bending fatigue test specimen

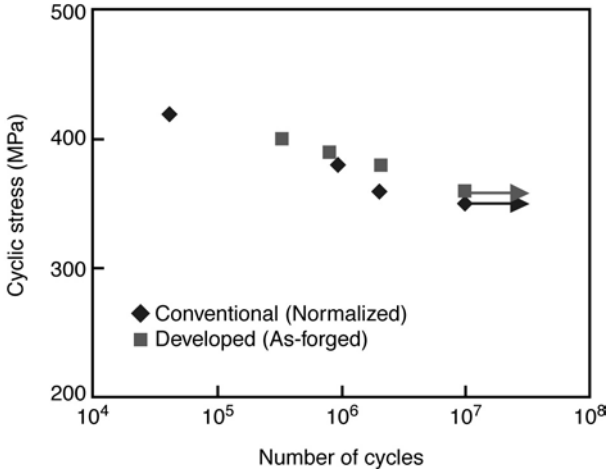


Fig. 12 Result of rotating-bending fatigue test

3.1.5. Rotating-bending fatigue strength

The developed steel and conventional steel were subjected to a rotating-bending fatigue test, each test specimen first being salt-bath nitrocarburized at 580 °C for 70 minutes. The test specimen geometry is shown in Fig. 11, and the test results are shown in Fig. 12. It is apparent that the developed steel has the same fatigue strength as the conventional steel.

3.2. Crankshaft Testing

The developed steel and conventional steel were subjected to comparative tests of their properties. The crankshaft for an in-line 4-cylinder engine shown on the left in Fig. 5 was used as the specimen, the developed and conventional steel materials being produced as described in section 3.1. The machining processes shown in Fig. 1 were used on both materials, except that the normalizing process was omitted for the developed steel.

3.2.1. Microstructure and hardness of materials air-cooled after hot forging

Figure 13 shows the microstructure of the crankshaft air-cooled after hot forging. The target hardness of HRB89 and the desired fine microstructure were obtained with hot forging and air cooling alone.

3.2.2. Machinability

A comparison was made of the frangibility of chips from each of these materials generated by lathe turning during the mass production process. The chips from the developed steel and conventional steel are shown in Fig. 14. The chip weight, measured by the method described in section 3.1.3, was 5.5 g for the developed steel and 8.2 g for the

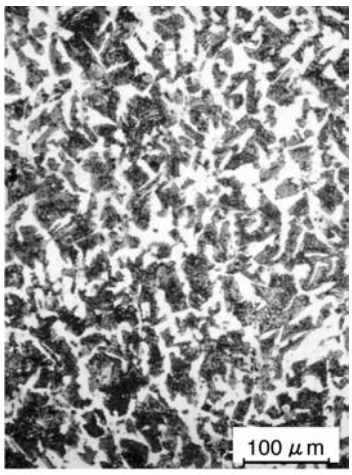


Fig. 13 Microstructure of developed steel after hot forging

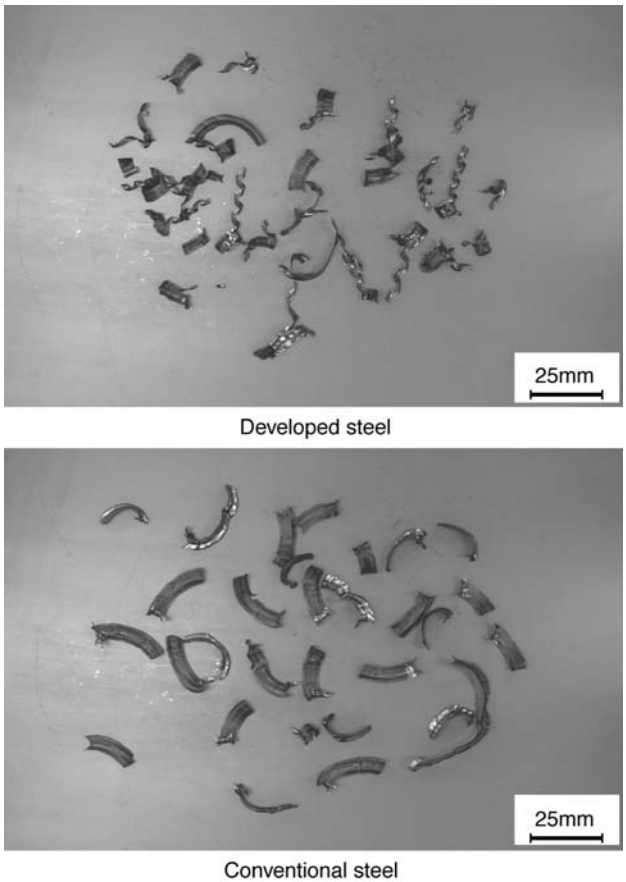


Fig. 14 Chips of developed and conventional steels generated by lathe turning

conventional steel. The developed steel therefore achieved more favorable chip frangibility than the conventional steel, as well as machinability equal to that of the conventional steel in the drilling, grinding, and gear-cutting processes. In addition, the developed steel allowed lathe turning under the same conditions and tool change criteria the same as those for the conventional steel.

3.2.3. Nitrocarburized properties

Each crankshaft sample was salt-bath nitrocarburized at 580 °C for 70 minutes, and the resulting properties are shown in Table 4. The surface hardness, practical nitrocarburized case depth, and compound layer depth of nitrocarburizing were similar for both the developed steel and conventional steel samples.

Table 4 Comparison of nitrocarburized properties between developed and conventional crankshafts

		Developed steel	Normalized conventional steel
Compound layer depth after lapping	mm	0.008	0.008
Surface hardness	Hmv	630	639
Practical case depth	mm	0.35	0.26

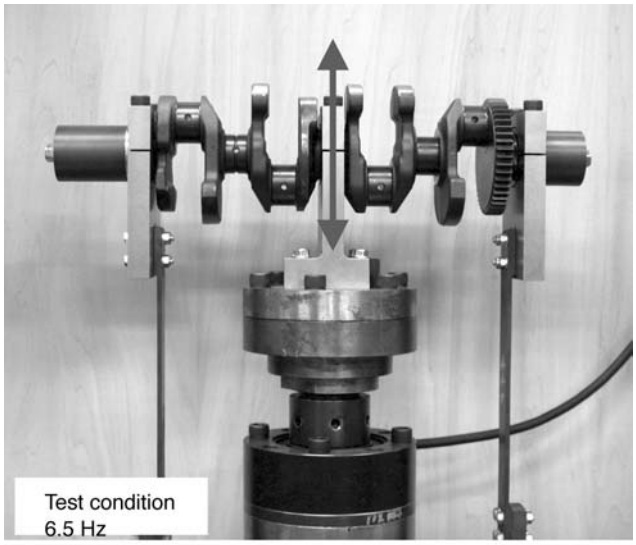


Fig. 15 Bending fatigue test method for crankshaft

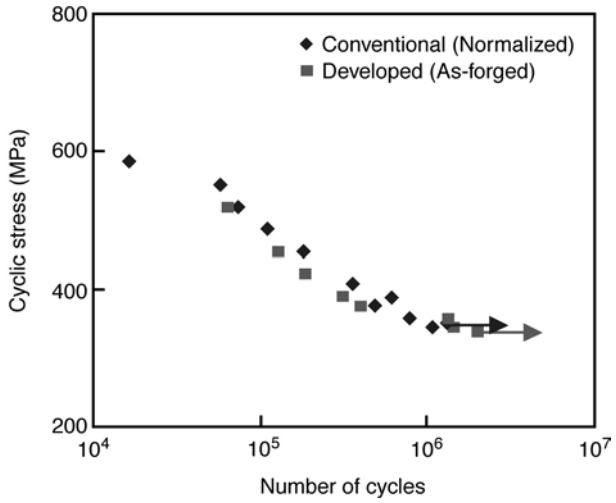


Fig. 16 Result of bending test for crankshafts

3.2.4. Bending fatigue strength

A comparison between the bending fatigue strength of the developed steel and conventional steel crankshafts was performed by the method shown in Fig. 15. The journals at both ends of the crankshaft were held in place, and the center journal was subjected to completely reversed bending stress. A strain gauge mounted on the fillet portion of the center journal was used to measure the resulting stress. As shown in Fig. 16, the bending fatigue strength of the developed steel was equal to that of the conventional steel.

4. Conclusion

The technique of omitting normalizing after forging, which has already been applied to the mass production of automobile crankshafts, was optimized for application to motorcycle crankshaft steel. This steel was at the same time treated to provide Pb-free free-cutting steel. The distinctive features of this steel are summarized below.

(1) Omission of normalizing after forging was enabled by adjusting the carbon, manganese, and nitrogen contents of the steel.

(2) Adjustment of the type, quantity, shape, and dispersion of non-metallic inclusions in calcium-sulfur free-cutting steel to appropriate values made it possible to achieve a chip frangibility equal to that of conventional Pb-sulfur free-cutting steel. It also made it possible to maintain the same machining conditions and tool change criteria as those used conventionally after making the steel Pb-free.

(3) The developed steel also has nitrocarburized properties and fatigue strength equal to those of conventional Pb-sulfur free-cutting steel when used to produce a crankshaft.

This project sought to optimize the composition of steel for crankshaft use in motorcycles and automobiles. A Pb-free composition was attained without detriment to the various properties of the steel, and this steel has been adopted for mass production in the 2002 model year CBR954RR motorcycle and the lightweight That's automobile.

5. Acknowledgements

Grateful thanks are given to the parties involved at Sumitomo Metals (Kokura) Ltd. for their significant cooperation during the course of this development project.

References

(1) Matsumura, Y., Kurebayashi, Y.: “Development of Nitrocarburizing Steel for Crankshafts,” DENKI-SEIKO [ELECTRIC FURNACE STEEL], Vol. 71, No. 1, pp. 73–80 (2000)

(2) Katayama, S.: “Lead Regulation Effects on Machinability and Measures in Response,” KIKAI GIJUTSU [MECHANICAL ENGINEERING], Vol. 48, No. 6, pp. 18–23 (2000)

(3) Nishi, K.: “Making Improved Machinability Steel Pb-free is Unavoidable,” KIKAI GIJUTSU [MECHANICAL ENGINEERING], Vol. 48, No. 6, pp. 24–28 (2000)

(4) Somekawa, M., Kaiso, M., Matsushima, Y., Yaguchi,

H.: “Free Cutting Steels without Lead Addition,” KOBE STEEL ENGINEERING REPORTS, Vol. 51, No. 1, pp. 13–16 (2001)

(5) Iwama, N.: “Development of Bi Free Cutting Steel & Super Free Cutting Steel with Controlled Shape Sulfides,” KIKAI GIJUTSU [MECHANICAL ENGINEERING], Vol. 48, No. 6, pp. 37–40 (2000)

(6) Shiraga, T.: “Pb-free BN Free Cutting Steel,” KIKAI GIJUTSU [MECHANICAL ENGINEERING], Vol. 48, No. 6, pp. 44–45 (2000)

(7) Abeyama, S., Kimura, A., Nakamura, S.: “Development of Free-Machining Steel with Controlled Shape Sulfides—SSS Free-Machining Steel,” JOURNAL OF THE JAPAN INSTITUTE OF METALS, Vol. 24, No. 6, pp. 518–520 (1985)

(8) Kano, T., Tsugui, K., Nakamura, S.: “New Free-machining Steel with Calcium Sulphides Surrounding Calcium Aluminate Inclusion,” DENKI-SEIKO [ELECTRIC FURNACE STEEL], Vol. 71, No. 1, pp. 89–94 (2000)

(9) Kano, T.: “Free-machining Steel with Calcium Sulphides Surrounding Calcium Aluminate Inclusion,” KIKAI GIJUTSU [MECHANICAL ENGINEERING], Vol. 48, No. 6, pp. 46–48 (2000)

(10) Tsunekage, N.: “Development of S-Ca Free-machining Steel,” KIKAI GIJUTSU [MECHANICAL ENGINEERING], Vol. 48, No. 6, pp. 41–43 (2000)

(11) Ono, T.: “A Review of Recent Studies for Machinability of Steel,” Technical Report of Sumitomo Metals Industries, Ltd., Vol. 48, No. 1, pp. 4–21 (1996)

(12) Araki, T., et al.: “Development of Free-machining Steel Production Technology and Quality Improvement,” 96th and 97th Nishiyama Memorial Technology Lecture Meetings, Tokyo, the Iron and Steel Institute of Japan, p. 215 (1984)

■ Authors ■



Atsushi AMATAKA



Satoru SUWA

Development of a Titanium Material by Utilizing Off-Grade Titanium Sponge

Yuji MARUI* Toyotaka KINOSHITA* Kyo TAKAHASHI*

ABSTRACT

A titanium alloy for forging and a pure titanium material for exhaust systems have been developed for the purpose of reducing the weight of a motorcycle frame and improving the engine performance. A feature of the material is the use of off-grade titanium sponge that includes many impurities for production of titanium ingot. Stable characteristics have been obtained by controlling oxygen equivalent after setting the volume of tolerable impurities by considering mechanical properties and productivity. In spite of low-cost, this material design provided the same design strength compared to the conventional material, and enabled production with existing equipment. Using this new material and changing the manufacturing and surface treatment process enabled us to provide titanium parts at a lower cost. This technology is a fundamental one for producing titanium raw material for motorcycles and automobile applications, and it is expected to apply to other titanium alloys.

1. Introduction

In recent years, strict environmental regulations have been enacted around the world. These regulations are applied to motorcycles as well as automobiles. There is a growing demand for low emission technologies and technologies for improving fuel economy.[1] [2] Therefore, the use of titanium in components has become essential in order to improve motorcycle maneuverability and to improve fuel economy. The high cost of materials has proven to be a major obstacle in the adoption of titanium components in motorcycles. For large motorcycles, there is strong demand to adopt titanium for exhaust system components, such as the exhaust pipe and muffler, which have a major effect on engine output and running stability. However, a large amount of titanium is used in the structural components of the vehicle, the cost of these components must be reduced relative to the cost of the engine components. In previous research conducted on the use of titanium in engine components, a titanium alloy was developed for automobiles by recycling scrap material in a plasma progressive casting furnace (PPCF). This method proved less expensive than earlier methods. Resulting from this work, the world's first titanium connecting rod for a mass-production motorcycle was developed.[3] [4] In order to reduce the cost of titanium and expand its use, attention turned towards titanium sponge, a raw material which accounts for 1/3 or more of the total cost of producing titanium materials. This effort resulted in the development of less expensive pure titanium and titanium alloys. These materials were later used in an exhaust pipe, a variable control valve device (H-TEV: Honda Titanium Exhaust Valve), mufflers for the 2002 Fire Blade (for Europe), the CBR954RR (for North America and Japan), and exhaust pipe and inlet valves for the CRF450R. Figs. 1 and 2 show external views of some of these components.

2. Development Aims

2.1 Production Process for Wrought Titanium Products

In 1999, almost all of 11,662 tons of wrought titanium products were produced by the Kroll method.[5] In this method, chlorine and carbon are added to rutile ore, producing titanium tetrachloride ($TiCl_4$), an intermediate material. After distillation and refining, the material is reduced with magnesium, producing a titanium sponge which is at least 99.995% pure. Next, the titanium sponge is pressed

* Asaka R&D Center



Fig. 1 CBR954RR and titanium parts (Muffler, Exhaust pipes, H-TEV)



Fig. 2 CRF450R and titanium parts (Exhaust pipe, Inlet valves)

and shaped into a melting electrode, which is then used to produce a titanium ingot. Subsequently, the ingot is put through the forging and rolling process to produce the final wrought product (sheet, rod, wire, etc.). This long and complicated production process is one reason why wrought titanium is expensive. Fig. 3 shows a comparison of the production process for conventional material and the production process for the newly developed material.

2.2 Current Situation for Off-grade Titanium Sponge

Approximately 27,000 tons of titanium sponge is produced in Japan each year.[5] However, because there are only a few producers and suppliers of titanium sponge worldwide, the cost is affected greatly by the level of demand for aircraft. Given that titanium sponge of a high level of purity is required for aircraft production, it was necessary to reconsider the titanium sponge specifications for automobiles in order to obtain titanium at a lower, stable cost. Only the

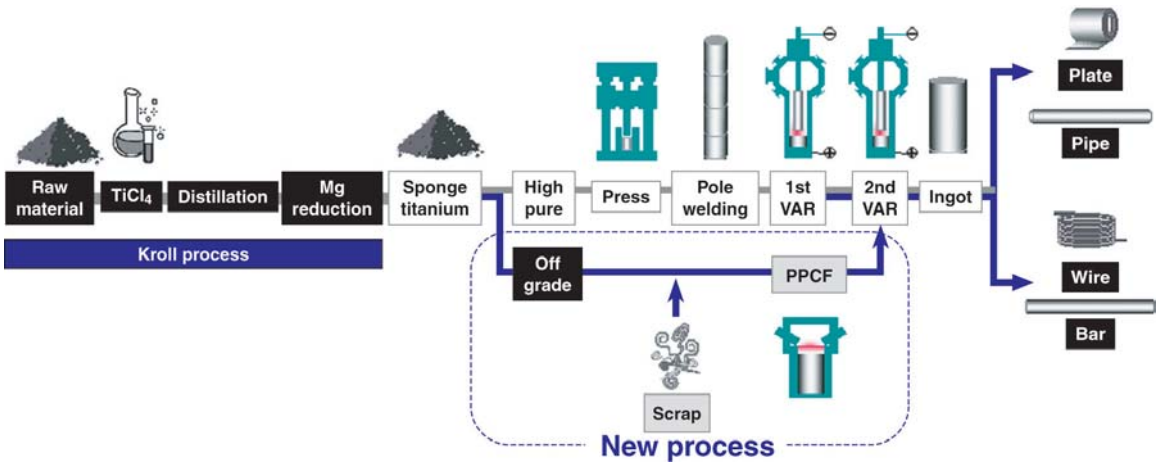


Fig. 3 Manufacturing process of titanium

center of a lump of titanium sponge is pure enough for forging. This pure center accounts for about 80 to 90% of the sponge's weight. The external layer of the sponge lump is known as "off-grade titanium sponge". The sides of the sponge contain Fe, Ni, and Cr impurities that enter the sponge from the stainless steel reaction vessel that is used in the magnesium reducing process, while the bottom of the sponge contains N, Cl, Mg, and other impurities from the chloride reducing process. The off-grade portion is primarily added to steel. When a chemical analysis of off-grade titanium sponge was conducted per JIS H-1610, approximately 60 to 80% of the sponge did not meet MIL or ASTM standards because the iron was too high, otherwise it was of comparatively high purity, as shown in Fig. 4. It was decided to study the possibility of using off-grade titanium sponge for forging.

3. Material Design

3.1 Composition Design of Pure Titanium

The pure titanium that is currently used in motorcycles is primarily used in the exhaust system, namely, the exhaust pipe and the muffler. JIS grade 2 was used, based on strength and processibility. These components are primarily shaped by cold pressing and bending. When off-grade titanium sponge is used for shaping, the impurities tend to produce a higher tensile strength and reduced stretchability. Because processing demands strict mechanical properties, impurities can be allowed only to the extent that the material still retains the level of stretchability that is needed for processing.

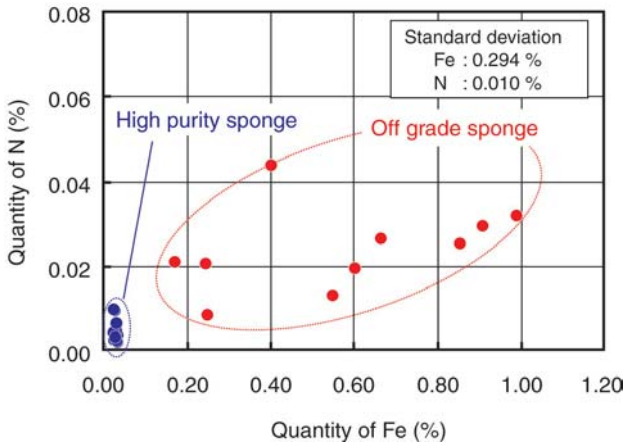


Fig. 4 Distribution of impurities constituent

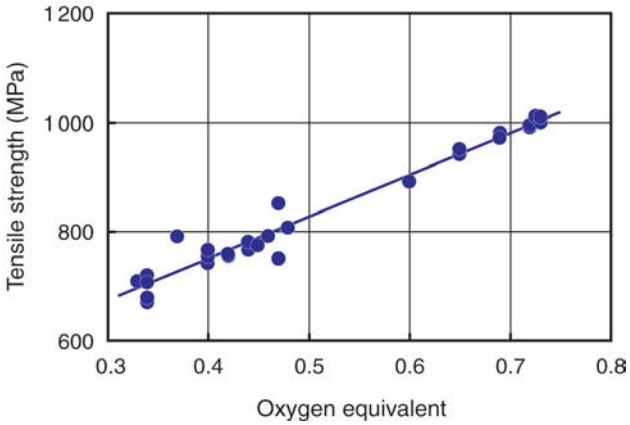


Fig. 5 Relationship between oxygen equivalent and tensile strength

After studying the stretchability needed in various types of shaping processes, 30% was established as the minimum target for stretchability. In addition, while there are many elements that can be found as impurities in off-grade titanium sponge, attention was focused primarily on the elements Fe, O, and N, which have an effect on the mechanical properties. These impurities can be represented in terms of allowable oxygen equivalent as determined by experimental equation (1). The oxygen equivalent is derived by multiplying the amount of each element by a coefficient that reflects that element's effect on mechanical properties relative to oxygen, and then summing the results. The oxygen equivalent is proportional to the mechanical properties. This relationship is illustrated in Fig. 5. Equation (1) shows that the impact of Fe on the mechanical properties is extremely small.

$$\text{Oxygen equivalent } Oeq = [O] + 2.77[N] + 0.086[Fe] \quad (1)$$

The allowed amount for each element is decided on the basis of the target oxygen equivalent and the actual distribution of the constituent elements in the titanium sponge. Table 1 shows the stipulated values for the chemical composition of pure titanium developed according to these allowances. Plates produced with this composition are designated as HTPR (Honda pure Titanium Plate Refine), while tubes produced with this composition are designated as HTTR (Honda pure Titanium Tube Refine).

3.2 Composition Design of Titanium Alloys

For reasons concerning strength and availability, the titanium alloy Ti-6Al-4V is frequently used in engine components. Because the mechanical strength of the base alloy is high and the effect from impurities on mechanical strength is low, the service limits for these components compared with pure titanium, could be relaxed. In addition, a high level of stretchability for these components is not required, as they are produced by hot forging.

However, in addition to altering the mechanical properties as described above, the amount of impurities also alters the β transformation temperature, as shown in Equation (2).

Table 1 Chemical composition of HTPR

wt %

	H	O	N	Fe
HTPR	0.013 max	0.10 max	0.020 max	0.52 max
JIS TP340-C	0.013 max	0.20 max	0.050 max	0.25 max

Ti: Bal

Table 2 Chemical composition of Ti-64FE

wt %

	Al	V	Fe	O	N
Ti-64FE	5.50 ~ 6.75	3.50 ~ 4.50	1.0 max	0.21 max	0.05 max
ASTM Ti - 6Al-4V	5.50 ~ 6.75	3.50 ~ 4.50	0.4 max	0.20 max	0.05 max

Ti: Bal

$$T\beta = 886.0 + 147.7[O] + 294.3[N] + 20.4[Al] - 13.1[V] - 19.8[Fe] + K \quad (2)$$

K: Effect of all other components (C, Mn, etc.)

In order to produce components while maintaining the $\alpha + \beta$ phase, it was necessary to lower the forging temperature below that required for conventional forging. After considering productivity and yield of the forging material, it was decided to reduce the titanium forging temperature by as much as 30 °C compared with the conventional forging temperature. The distribution of constituents in titanium sponge was also taken into consideration when establishing the allowable levels of impurities that would satisfy the forging temperature reduction. Table 2 shows the chemical composition of the developed titanium alloy (Ti-64FE).

4. Results

4.1 Composition

4.1.1 Correlation of composition

In order to obtain the prescribed pure titanium or titanium alloy, titanium sponge and additives containing each alloying element were melted together to form a heat of casting metal. Unlike other metals, it is not possible to control the composition during melting. Instead, a uniform composition is obtained by performing vacuum arc remelt (VAR) twice. In addition, it is not possible to remove impurities other than hydrogen during melting. Therefore, changes in the composition of ingots versus the set composition of off-grade titanium sponge were verified across a number of lots by melting in a mass-production blast furnace. The composition was measured at the top, middle, and bottom of each ingot. The results are shown in Fig. 6. According to these results, the intended composition of the titanium sponge was accurately reflected in the ingots, with no clear segregation of constituents by location.

4.1.2 Low density inclusion

A low density inclusion (LDI) is a localized concentration of an α stabilizing element such as O or N in an ingot, with the characteristic of being extremely hard and brittle. This defect is usually caused by nitrides mixed in the titanium sponge. Titanium nitrides such as TiN have a high melting point, which poses a concern since they are not completely melted by the VAR process. If using off-grade titanium sponge, it is especially important to verify LDIs in the titanium alloy. This is because they have a large effect on the fatigue strength when the material is used for engine components. In order to check for the occurrence of LDIs resulting from the use of off-grade titanium sponge as a raw material, 800 g ingots produced by prototype melting was evaluated. The three types of titanium sponge indicated below were melted for comparison, and a chemical analysis of the sponge surface was also conducted.

(1) Titanium sponge suitable for actual use, but at the upper limit of impurities
(2) Titanium sponge not suitable for actual use due to a high level of impurities
(3) Titanium sponge of a high level of purity that had been forcibly nitrided.

The results indicated the presence of only two LDIs, both found in sponge (3). No other abnormalities were found. The impurities in the sponge surface consisted almost entirely of iron, with traces of Mg and Cl found adhering to the surface in the case of sponge (2). TiN, the most damaging LDI, was not found.

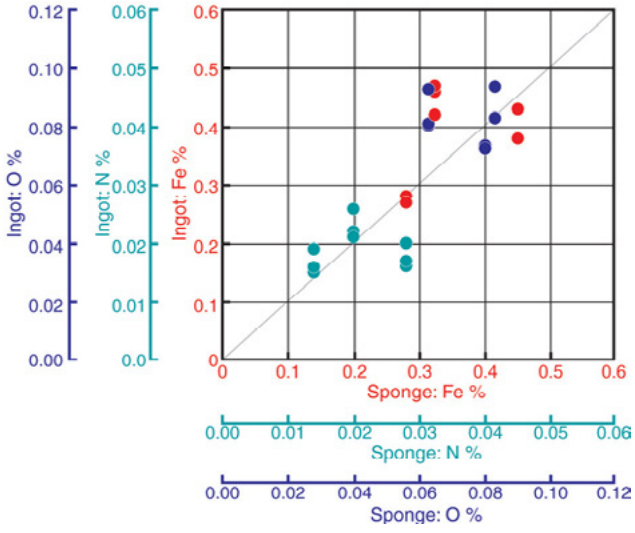


Fig. 6 Comparison with impurities constituent

4.2 Mechanical Properties

4.2.1 Static strength

Table 3 shows the results of tension tests performed on HTPR and Ti-64FE. These tests confirmed the tendency towards increased tensile strength and proof stress and decreased stretchability due to the high oxygen equivalent level compared with conventional materials. The stretchability of HTPR was particularly noted, successfully maintaining at least 30% stretchability at the oxygen equivalent upper limit targeted in the composition design.

4.2.2 Dynamic strength

Pure titanium is generally applied to exhaust system components produced from sheet metal by welding. It is important to evaluate the fatigue strength not only in the base metal, but also in the weld beads and parts exposed to heat. The HTPR fatigue strength evaluation was conducted by means of the Shenk completely reversed plane bending fatigue test. The test was conducted with different flat samples each having different types of TIG welding distinguished by the presence or absence of grooves and filler material. The test results for all samples showed them to be equivalent to JIS grade 2 or better. Fig. 7 shows a comparison of the results for a butt joint which was TIG welded on one side.

Table 3 Mechanical properties

			σ B (MPa)	σ Y (MPa)	EL (%)
Ti alloys	Ti-64FE		1 099～1 102	1 035	15.0～15.6
	Ti-6Al-4V (ASTM SPEC)		895 min	825 min	10 min
CP Ti	HTPR[1)]	L direction	500～510	333～343	29～30
		C direction	510～519	402～412	33～35
	JIS Grade 2	L direction	353～363	206～216	37～40
		C direction	372～382	235～245	39～40

HTPR[1)]: Oeq Max condition
L: Rolled direction
C: Rolled perpendicular direction

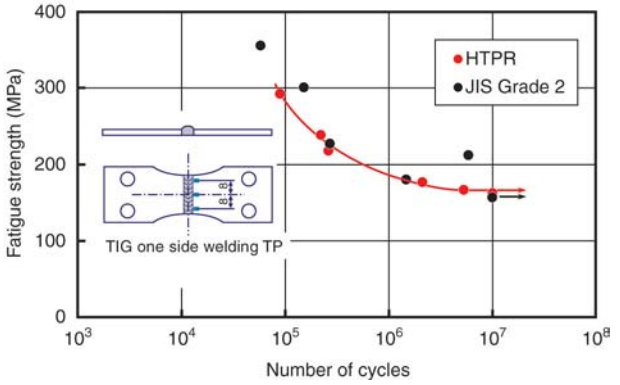


Fig. 7 Fatigue strength of TIG one side welding

Titanium alloys that are used for strength components exhibit a large decline in fatigue strength when notched. As described in section 4.2.1, relaxing the allowable impurity levels tends towards increased strength. This tendency can be enhanced through the oxygen diffusion treatment described in section 4.4. A comparison of the fatigue strength characteristics of Ti-64FE was conducted using the rotating-bending fatigue test. In this test, oxygen was diffused through the air by heating, and the test samples were both plain and notched, with hardened surfaces (OD treatment). The results are shown in Fig. 8. As shown in Table 4, all test samples exhibited fatigue strength that was equivalent to or better than conventional materials. These results indicate that the same strength design criteria that are used for conventional materials can also be used for both of the titanium alloys.

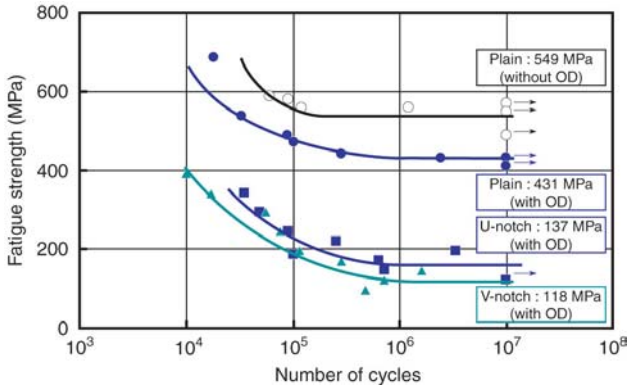


Fig. 8 Fatigue strength of Ti-64FE

Table 4 Comparison of fatigue strength

	Ti-64FE		Ti-6Al-4V	
	with OD	without OD	with OD	without OD
Plain	431	549	323	431
U-Notch	137	314	147	314
V-Notch	118	108	88	118

(MPa)

4.3 Weldability

The test samples created for section 4.2.2 were used to study the cross-sectional structure of the TIG weld and the segregation of impurities. The results are shown in Fig. 9. Cross-sectional observations indicated a tendency towards fineness in the base metal structure in the original HTPR material and also the weld. This is likely due to the effect of Fe, one of the constituent impurities. When constituent segregation of the weld was studied by EDS, no clear segregation of any of the constituents was found. In addition, the weldability of the material was equivalent to that of conventional material under identical welding conditions, with no differences in the amount of material melted or in the extent of the area affected by heat.

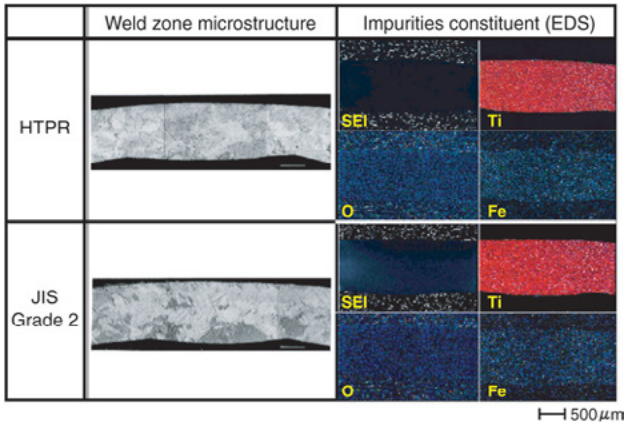


Fig. 9 Weld zone microstructure and impurities constituent

4.4 Durability and Seizure Resistance

Bare titanium metal surfaces exhibit very strong seizure properties. Therefore, the ground surfaces of titanium components must be treated to prevent seizure. Previously, the OD treatment was used to ensure seizure resistance.[6] In order to check the effect of this treatment on the oxygen diffusion of impurities, a comparison was conducted between the current material and Ti-64FE that had been subjected to the OD treatment. The comparison looked at structure and hardness, and used a faville type adhesive wear test to check the seizure limit load. Fig. 10 shows the results of the faville type adhesive wear test. These results show no difference in the OD treatment structure or hardness, and show a seizure limit load greater than that of the current material. This can be attributed to the original material being harder than the conventional material.

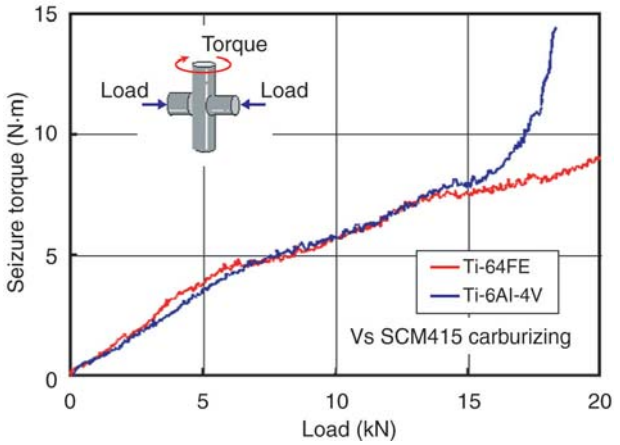


Fig. 10 Seizure property

4.5 Press Formability

In general, titanium cold press formability exhibits different properties from those of steel, as shown in Table 5, due to the small n value (work hardening) and the large r value (anisotropy).[7] Furthermore, in order to know the limits when using HTPR, test pieces were used to verify the effects on the formability that is necessary in the course of component fabrication. These were tested through a bending test (bending formability), an Erichsen test (punch stretch formability), and an expansion test (stretch flanging). Table 6 shows the results of these tests. HTPR exhibited properties that were roughly midway between those of JIS grade 2 and grade 3, and offered slightly inferior formability (especially bendability) when compared to conventional material. This is related most closely to the stretching value of the mechanical properties. This is due to the fact that although the stretching value of HTPR is set to be equal to JIS grade 2, the effective stretching value of conventional material is higher. When creating components, it is essential that shape design take the actual differences in these properties into consideration.

4.6 Mechanical Formability

In order to use titanium alloys in engine components, it is important to verify differences in mechanical formability in order to consider productivity and costs. In the case of Ti-64FE, as described earlier, increased impurities tend to result in a harder original material. Therefore, a comparison of mechanical formability was conducted on the basis of differences in the time needed to form Ti-64FE under the titanium component forming conditions that have been previously applied in mass production. The machining processes that were checked were milling, drilling, fine boring, and grinding. Data was obtained for each process under the same conditions and for the same processing time as for conventional material, and the results indicated no differences in mechanical formability. In addition, when these conditions were re-examined under changed conditions, such as replacing cemented carbide tools with throw away inserts, optimizing the processing conditions (cutting speed and feed), and adding coatings to tools, it was found that the processing time could be reduced by half compared to conventional materials.

Table 5 Property of the formability of titanium

1) Small $\sigma 0.2$ / E	Poor	Large spring back
2) Hard to carry out work hardening. (n Value)	Good	Easy sharp forming
	Poor	Low limit of forming
		Easy to come out of sectional deformation
3) Large anisotropic (r Value)	Good	Excels as compared with steel sheets (deep drawing)
	Poor	Large radius of bend

5. Component Production Technologies

5.1 Muffler

Regarding independent forming factor evaluation during cold press forming described in section 4.5, each factor is a composite during actual production. When establishing a component press plan, independent forming factor evaluation is inadequate. Therefore, an FLD (Forming Limit Diagram) was established as a map of forming limits.[8] An FLD is created by scribing a circle on a sheet and then plotting the maximum (piercing) distortion when various mutually perpendicular distortions are applied to the sheet. Based on the growth pattern of the distortion that accompanies progressive forming in locations that are subjected to strong processes, it is possible to predict the risk of fractures occurring, or the degree of safety in avoiding fractures. Fig. 11 shows the FLD for HTPR. These results indicated that, compared with conventional materials, careful planning is essential in the punch stretch forming region.

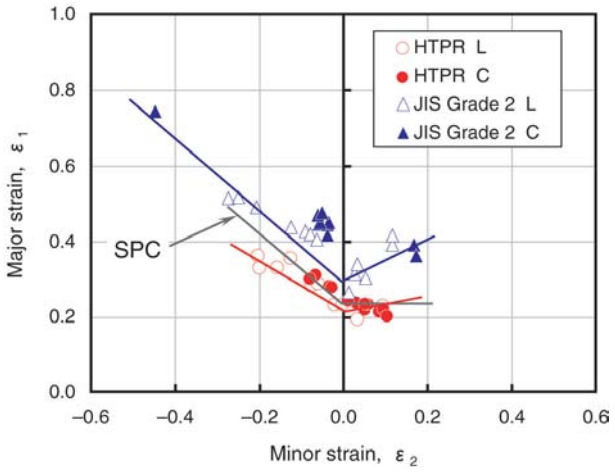


Fig. 11 Forming limit diagram of HTPR

Table 6 Formability of HTPR

	n Value		r Value		Erichsen cupping test	Guided bend test	Punch stretch test
	L direction	C direction	L direction	C direction	Erichsen Number	Radius of bend	ϕ12 Hole expansion
HTPR	0.131	0.085	2.3	5.6	8.5	1.5t	83%
JIS Grade 1	0.141	0.074	1.9	9.9	13.0	Close contact	165%
JIS Grade 2	0.135	0.089	2.5	6.3	10.5	Close contact	140%
JIS Grade 4	0.100	0.083	1.0	5.5	5.7	2.5t	64%
SUS304	0.470	0.511	1.0	1.0	–	–	–

L: Rolled direction
C: Rolled perpendicular direction

One of the features of the muffler's appearance is the color of the external pipe. Typically, the color of titanium is obtained by some sort of surface treatment such as plating, or by using oxidation interference color obtained by heating in a furnace or by anodizing. By using shot peening on the external pipe, this muffler features a new appearance not found with any other surface treatment.

5.2 Exhaust Pipe

Primarily bending and welding produces exhaust pipes. In the case of the exhaust pipe for the CRF450R where bending a ϕ41-t1.0 pipe into a U shape with R60 (1.5D) was required, the processing was extremely difficult. Application of a mandrel on a drawing and bending bender was necessary. A copper alloy was used for the mandrel material, and the optimal bending conditions were determined, such as the amount to be pushed out, and the force to be used in the rear to push the tube out. In addition to maintaining a flat ratio of 95% or more, the bent shape described previously could be obtained consistently. In addition, it was possible to keep the reduction in the thickness of the sheet on the outer R portion of the bend to less than 10%.

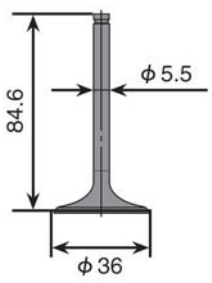
TIG welding was primarily used to join the exhaust pipe components. In light of productivity and cost considerations, however, seam welding was used for the mouth collar joint at the base of the exhaust pipe. In seam welding, the electric current, the weld time, and the pressurization force are important factors. With HTTR, an excellent nugget could be obtained under the same conditions as JIS grade 2.

5.3 Inlet Valve

Table 7 shows the specifications for the inlet valve. In order to reduce product costs, Ti-64FE was adopted as the material and the production method for the plain form was altered significantly. Generally, because the valve head is produced by upset forging, wire that has the same diameter as the stem is used for the valve forging material. However, because the production of titanium wire requires a repeating cycle of rolling, wire drawing, annealing, and the removal of the oxidized surface layer, the production yield is poor and the cost is higher than that of rod material. Therefore, extrusion was adopted for the valve material production method, since that method provides valve forging material from inexpensive rod material. Extrusion requires that careful attention be paid to temperature conditions in particular. At low temperatures, the stem may be bent or the head may not be fully formed. In the vicinity of the β transformation temperature, the stem may fracture. Therefore, the setting for impurity levels and the temperature range in which forming will be stabilized under the forming conditions were discovered. The specifications for the wear resistance treatment called for an inexpensive OD treatment to be applied to the entire surface. In conjunction with this, the pretreatment process was simplified. These changes made it possible to produce less expensive components.

Table 7 Specification of titanium inlet valve

Material	Ti-64FE
Stem end	Oxygen diffusion
Stem	Oxygen diffusion
Face	Oxygen diffusion



6. Effects on Actual Equipment

Compared with conventional stainless steel equipment, a weight reduction of 400 g for the CRF450R exhaust pipe and of 1.3 kg and 1.2 kg for the CBR954RR exhaust pipe and muffler, respectively, were obtained. These weight reductions contribute to enhanced power characteristics and controllability and stability characteristics. In the inlet valves, the heads are large diameter but at 25 g, the weight of the inlet valves has been reduced by over 40% compared to conventional heat-resistant steel. As a result, it became possible to ensure the stability of the behavior of the valve system in the required range of rpms. It was also deemed possible to reduce the valve spring storage space to the minimum size, and to lower the cam shaft as far as possible. As a result, the increase in the height of the cylinder head was minimized and a lightweight, compact cylinder head was realized. In addition to the effects brought about by these performance improvements, the equipment is also made more attractive by virtue of featuring “titanium-made components.”

7. Conclusions

Pure titanium and titanium alloys that are less expensive and not readily affected by fluctuations in market prices since they use off-grade titanium sponge as a raw material, were developed for forged parts.

(1) Verification of the characteristics required by the component production process and management of impurities through oxygen equivalents made the use of off-grade titanium sponge possible.
(2) The characteristics of this material are equivalent to or better than those of current materials, making it possible to use the same conventional design standards to study components. In addition, because existing facilities can be used for production, no new investments are required.
(3) By reviewing current component production processes along with the materials, it was possible to supply less expensive titanium components for mass-production vehicles.

This technology is basic to raw materials used for titanium in automobiles. It is expected that it can be widely applied to produce titanium alloys used in other industrial fields.

Acknowledgements

Deep gratitude is expressed to all involved in the joint development of the material at Nippon Steel Corporation, Kobe Steel, Ltd., Daido Steel Co., Ltd., and in component production at Sankei Giken Kougyou Co., Ltd. and Nittan Valve Co., Ltd.

References

(1) Horiike, T. et al, Introduction to Exhaust Emission Reduction Technologies of VFR800FI, HONDA R&D Technical Review Vol. 10, pp. 42–48 (1998)

(2) Tsukui, T. et al: Development of the directory Activated Variable Valve Control System, SAE Paper 1999-01-3319

(3) Kato, T.: PPC Furnace Development and Equipment, Titanium and Zirconium, Vol. 32, No. 2, p. 96 (1984)

(4) Yamada, H.: Electric Steelmaking, Vol. 54, No. 1, p. 53 (1983)

(5) Japan Titanium Association Journal, World of Titanium, p. 27

(6) Hagiwara, Y. et al: Lightweight Titanium Connecting Rods for Motorcycles, HONDA R&D Technical Review, Vol. 2, pp. 229–237 (1990)

(7) Titanium Association Journal: Titanium Processing Technologies, p. 71

(8) Nippon Society of Plastic Manufacturing Journal, Press Manufacturing Process Design and Die Design, Corona Publishing Co., Ltd., p. 16

■ Authors ■


Yuji MARUI


Toyotaka KINOSHITA


Kyo TAKAHASHI

Weight Reduction with Plastic Foam for Structural Components of Vehicle

Yasushi TOSHIMITSU* Akifumi SONODA**

ABSTRACT

Focusing on absorbing energy in the side frames of a vehicle as compressive deformation occurs during a frontal impact, increased energy absorptance and weight reduction of the structural components of a body do occur by filling them with urethane foam. It was found that it is possible to achieve approximately 30% weight reduction by filling urethane foam and modifying cross-section structures while insuring flexural rigidity and absorbed energy equal to that of body frames. At the same time efforts were also made to construct CAE technology that enables investigation into a lightweight body frame structure filled with plastic foam. The difference in absorbed energy between CAE simulations and tests with an actual hybrid frame unit consisting of aluminum piping (shell element) filled with urethane foam (solid element) was approximately 10% while under 50% compressive deformation or more.

1. Introduction

While automobile crash safety performance continues to get better, vehicle body weights are increasing. On the other hand, CAFE target values are being established and improvements in fuel economy mandated in order to reduce greenhouse gas emissions. Amidst these circumstances, demands are increasing for the conflicting goal of lighter vehicle body weights.

Thus far the main use of plastic foam in vehicle bodies has been for soundproofing. However, there is potential for enhancing crash performance through the use of foam in structural components. One example of this application focused on the increase in energy absorption and reduction in vehicle deformation distance during bending deformation of structural components of the vehicle that were filled with plastic foam.(1) This case mainly used epoxy foam.

This paper reports on research performed on vehicle structural components filled with plastic foam that enable reductions in weight while maintaining crash safety performance.

* Tochigi R&D Center
** PSG Inc.

2. Concept of Weight Reduction

First, the concept of reducing weight using plastic foam is described below. When a metal pipe structure with the enclosed section in the lengthwise direction such as the side frame of a vehicle undergoes compressive deformation, it generally exhibits the deformed state shown in Fig. 1. Fig. 2-a shows the relationship between the force and the deformation distance at that time, and Fig. 3-a shows the relationship between energy absorption and the deformation distance at that time. On the other hand, when the same metal pipe is filled with plastic foam, the relationships between the deformation distance and the force and between the deformation distance and the energy absorption are as shown in Fig. 2-b and Fig. 3-b. When the main structural components (for example the side frame) of a vehicle undergo compressive deformation during a crash, they exhibit the performance shown in Fig. 2 and Fig. 3. Looking at the energy absorption (Fig. 3) which is particularly important, the plastic foam filled component shows a higher energy absorption even for the same deformation distance.

This is an effect of filling with plastic foam. Conversely, when the energy absorption is the same, the radial thickness of the metal pipe can be reduced as shown in Fig. 4. At this time, the filled plastic foam increases the weight, but an even greater weight reduction is achieved by reducing the radial thickness of the metal pipe, which leads to an overall reduction in the weight.

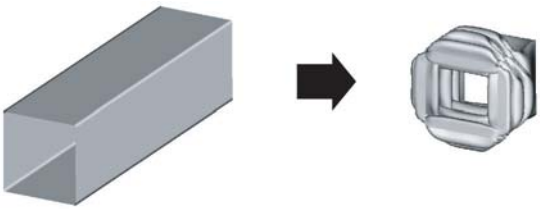


Fig. 1 Compressed deformation shape of metal frame

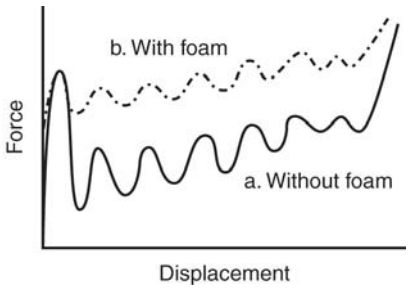


Fig. 2 Force vs. axial displacement

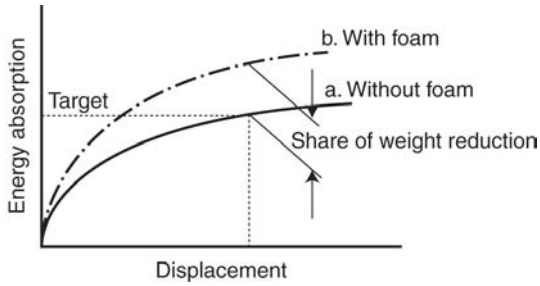


Fig. 3 Energy absorption

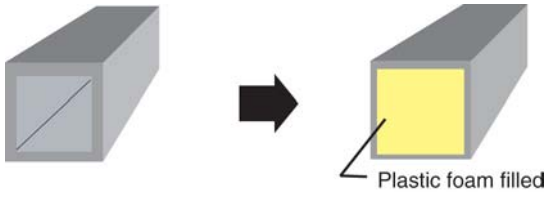


Fig. 4 Concept of weight reduction by means of plastic foam

3. Research Approach

This research was approached from the following three viewpoints.

3.1. Selection of Plastic Foam

There are various types of plastic foam including urethane, epoxy resin, rubber and PET. However, the aim was to select a type that allows for the large deformation of a compressibility of 50% or more, and which generates a large force during the compression process.

3.2. Verification of the Effects of Filling with Plastic Foam

The energy absorption and bending stiffness properties of plastic foam filled frames (hereafter “hybrid frames”) were investigated by varying the radial thickness, section size and structure, and comparing it to existing lightweight energy absorptive structures (for example, a “crash box” which is a type of frame structural component attached to the tip of the side frame).

3.3. Construction of CAE Technology for Investigating Lightweight Structures

In order to allow CAE-based prediction of performance for different hybrid frame structure, the initial theme was to construct performance prediction technology for the foam and metal portions. Following that, technology for predicting hybrid frame performance was constructed.

4. Setting Targets

This research took the following approaches toward setting targets.

(1) The new structure should result in a larger reduction in weight compared to existing energy absorptive structures. And, the vehicle structural component properties (compressive energy absorption, bending stiffness) should be equivalent to crash boxes with a 30% reduction in weight.

(2) Construction of CAE technology that predicts hybrid frame crash performance should be possible.

5. Course of the Investigations

5.1. Selection of Plastic Foam

Various types of plastic foam were molded into test pieces of the shape shown in Fig. 5, and compression tests were performed using Amsler’s universal testing machine. Fig. 6 shows the force and displacement measurements. The foaming rate was set at 3 times for all cases. The results showed that rigid urethane foam[(2)] most satisfied the plastic foam selection aims, so rigid urethane was selected as the plastic foam. In addition, Fig. 7 shows that the relationship between energy absorption and weight is roughly linear, and that deformation of 50% or more, that is to say compression of 2 times or more is possible. Therefore, the foaming rate was set at 3 times due to demands for greater energy absorption.

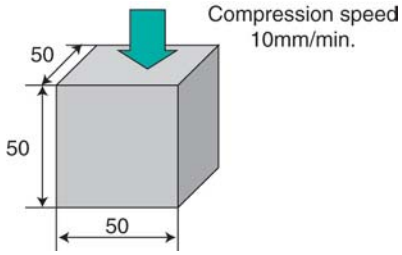


Fig. 5 Plastic foam test piece and compression test

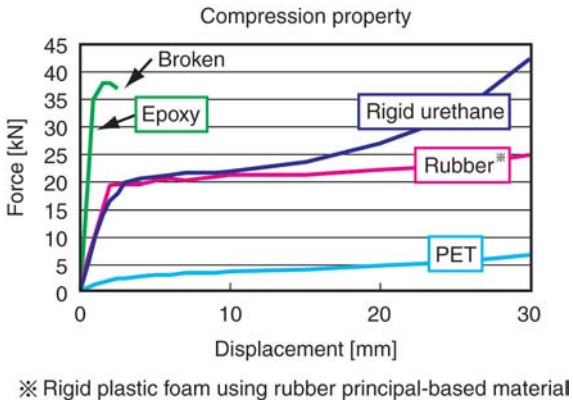


Fig. 6 Compression test result of plastic foam

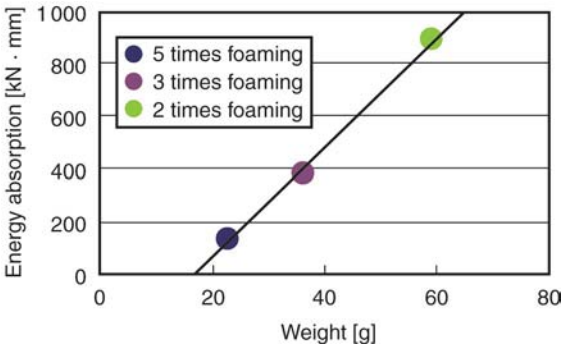


Fig. 7 Axial compression test result

5.2. Verification of the Weight Reduction Effects of Hybrid Foam

Test parts were manufactured, and compression and bending tests were performed to quantitatively clarify the weight reduction effects. Test pieces having various sectional sizes and radial thickness were manufactured as shown in Table 1. The metal pipes corresponding to the side frame used the same aluminum materials as those used for crash boxes. The compression test parts were all 240 mm long, and the bending test parts were all 800 mm long. The test method used Amsler's universal testing machine to measure the force and the deformation distance. Fig. 8 shows an outline of the compression test apparatus, and Fig. 9 shows an outline of the bending test apparatus.

Fig. 10 shows the compression test results for the parts illustrated in Table 1 in terms of weight and energy absorption. The arrows in the figure indicate the change when urethane foam is added. This indicates that the type (4)-a specifications in Table 1 provided energy absorption equal or greater than the crash box while allowing a 30%

Table 1 Section form for supplied test pipes

1. Aluminum pipe

(1)-a	(1)-b	(2)-a	(2)-b	(3)-a	(3)-b
ϕ60-t2 Foam filled	ϕ60-t2	ϕ50-t2 Foam filled	ϕ50-t2	ϕ50-t3 Foam filled	ϕ50-t3

2. Aluminum dual pipe

(4)-a	(4)-b	(5)-a	(5)-b
ϕ60-t2/ϕ40-t1 Foam filled	ϕ60-t2/ϕ40-t1	ϕ55-t2/ϕ40-t2 Foam filled	ϕ55-t2/ϕ40-t2

3. Aluminum hexagon pipe

(6)-a	(6)-b	(7)
Width50 All holes filled	Width50	Width90 (Crash box)

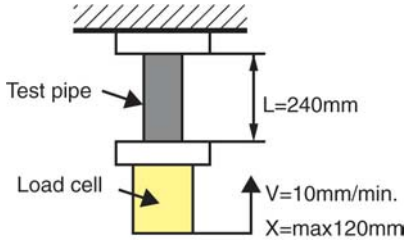


Fig. 8 Axial compression test setup

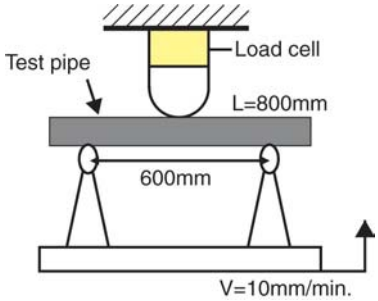


Fig. 9 Bending test setup

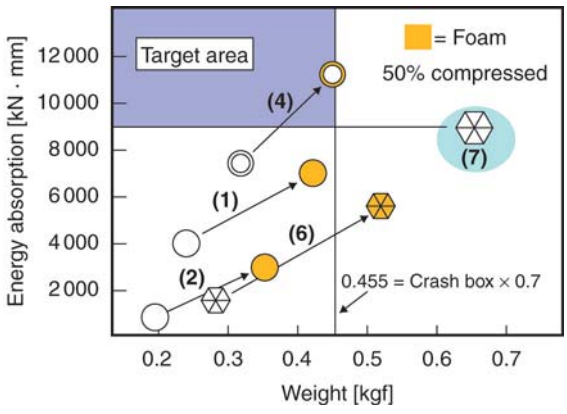


Fig. 10 Axial compression test result

weight reduction. Furthermore, Fig. 11 compares the compressive properties, energy absorption and bending stiffness of this specification, with the crash box, and shows that even the bending stiffness of this specification is equal or greater than the crash box. This clarified that of the aforementioned test parts, the hybrid frame that provided results most satisfying the targets was the aluminum dual pipe filled with urethane foam (specification (4)-a) shown in Table 1.

5.3. Construction of CAE Technology for Investigating Lightweight Structures

Among the few cases that have simulated large deformation of a hybrid frame using plastic foam[3], it cannot be said that the CAE results have always accurately reproduced the actual test results. This study aimed to reproduce the force waveform and energy absorption amount relative to the displacement distance. The investigation used the explicit method software RADIOSS.

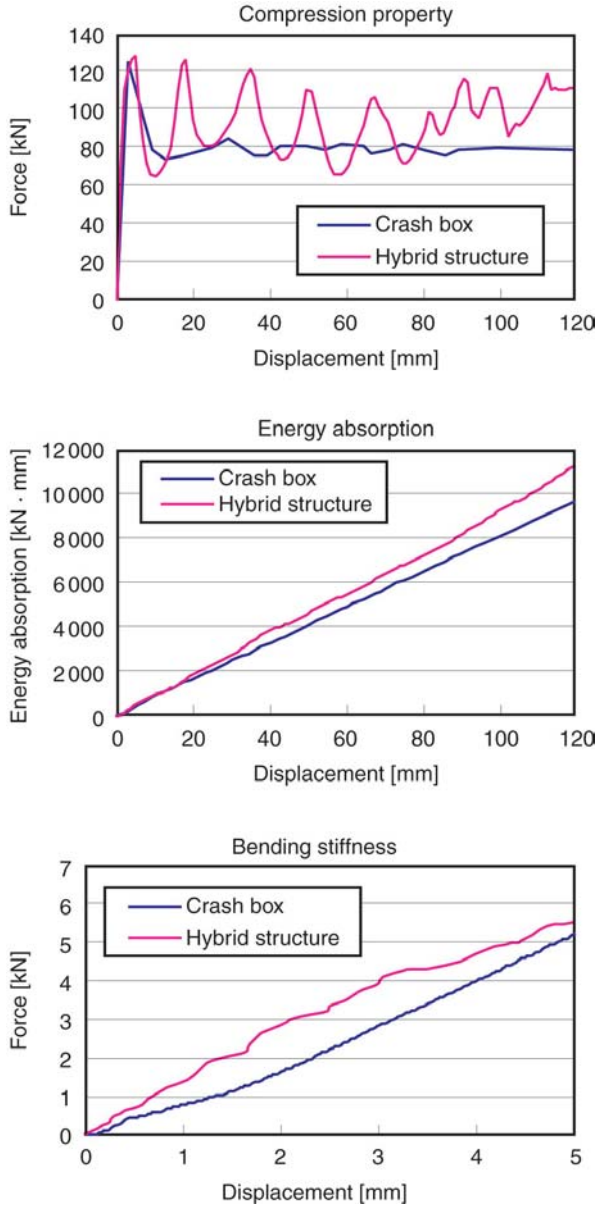


Fig. 11 Test result of compression and bending test

5.3.1. Simulation of the foam portion

The material model that provides the simulation results closest to the urethane foam curve was selected from among the plastic foam relationships between the compression force and deformation distance shown in Fig. 6. Like the tests, the simulation model was comprised of cubes having 50 mm per side, and was modeled with solid elements as shown in Fig. 12.

Fig. 13 shows the compressed deformation shapes obtained from actual tests and a simulation using the material model selected above. The simulation fairly reproduces the test results with compressive deformation appearing as barrel-shaped bulging. In addition, Fig. 14 shows the force and energy absorption curves relative to the deformation distance, and accuracy was excellent with a difference of only 2 to 3% from the test results in both cases.

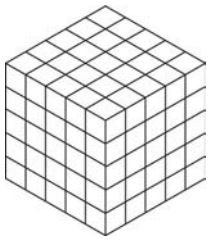


Fig. 12 CAE model for plastic foam

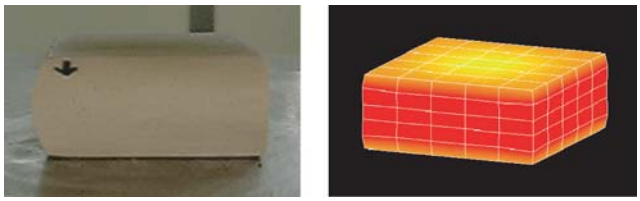


Fig. 13 Compressed deformation shape of plastic foam

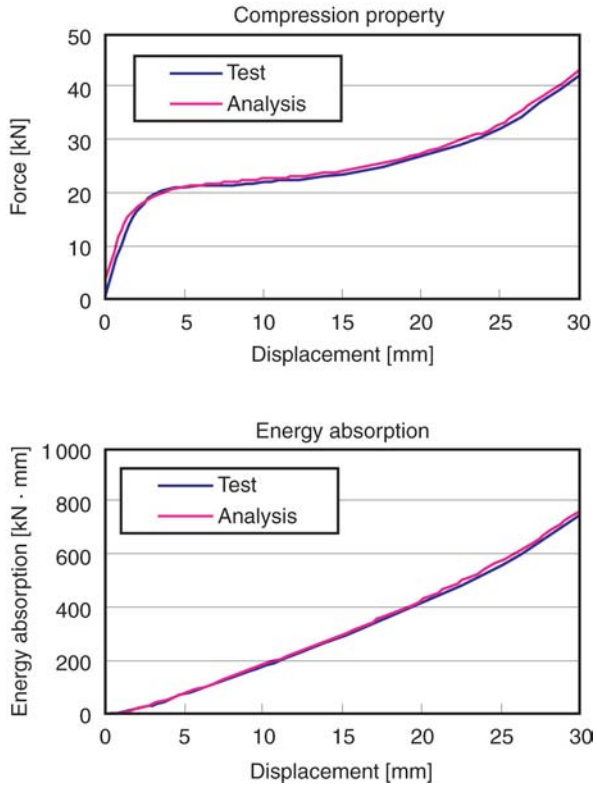


Fig. 14 Comparison of compression quality for plastic foam

5.3.2. Simulation of the metal portion

The metal portion was investigated by creating a model of the aluminum pipe (1)-b in Table 1 with a length of 240 mm and 1/4 the section in the diameter direction as shown in Fig. 15 as the simulation model. The mesh pitch was created in consideration of achieving a balance between accurately reproducing portions with bellows-shaped deformation and the calculation time. At this time material property data corresponding to the crash box was used.

Fig. 16 shows the test and simulated compressive deformation states of the aluminum pipe, and shows that the bellows-shaped deformation was also fairly accurately reproduced. In addition, although the test results for the components of force movement were not accurately reproduced as shown in Fig. 17, the energy absorption was reproduced with a difference of approximately 10%.



Fig. 15 CAE model for metal pipe

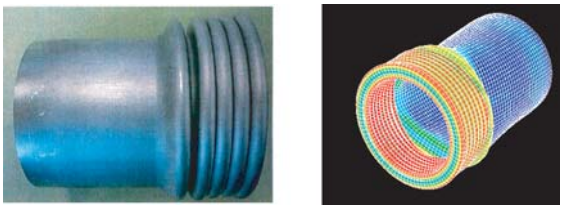


Fig. 16 Compressed deformation shape of aluminum pipe

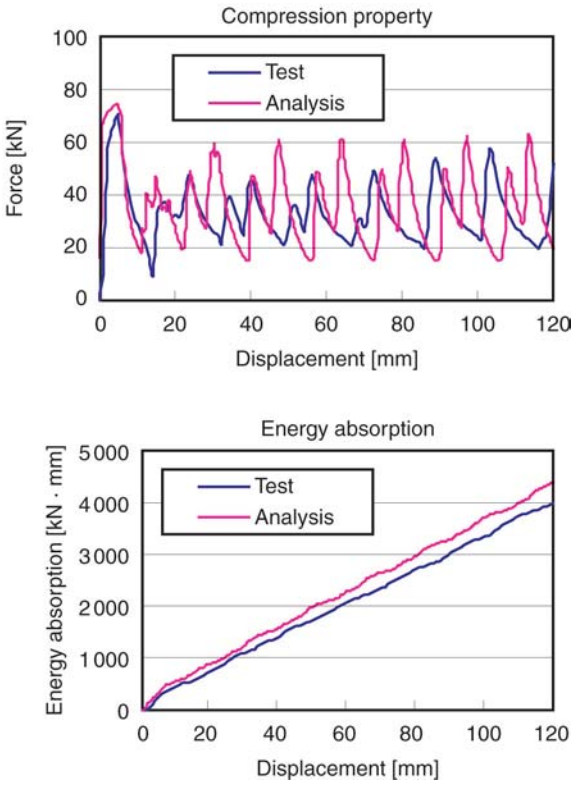


Fig. 17 Comparison of compression quality for aluminum pipe

5.3.3. Simulation of hybrid frame

A hybrid frame model was created that reflected the simulated foam and metal portion contents. A 240 mm long 1/4 section model of the urethane foam filled aluminum pipe specifications (1)-a in Table 1 was created as shown in Fig. 18. The calculation time was reduced by using a detailed solid element mesh pitch for portions experiencing complex deformation, and a rough solid element mesh pitch for other portions.

Fig. 19 shows the test and simulated compressive deformation states of the hybrid frame, and Fig. 20 shows the relationship between the force and displacement distance and the energy absorption curve. Although the bellows-shaped crushing on both ends was reproduced, the movement

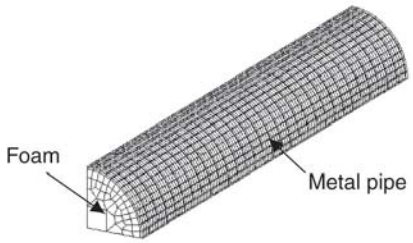


Fig. 18 CAE model for hybrid structure



Fig. 19 Compressed deformation shape of hybrid structure

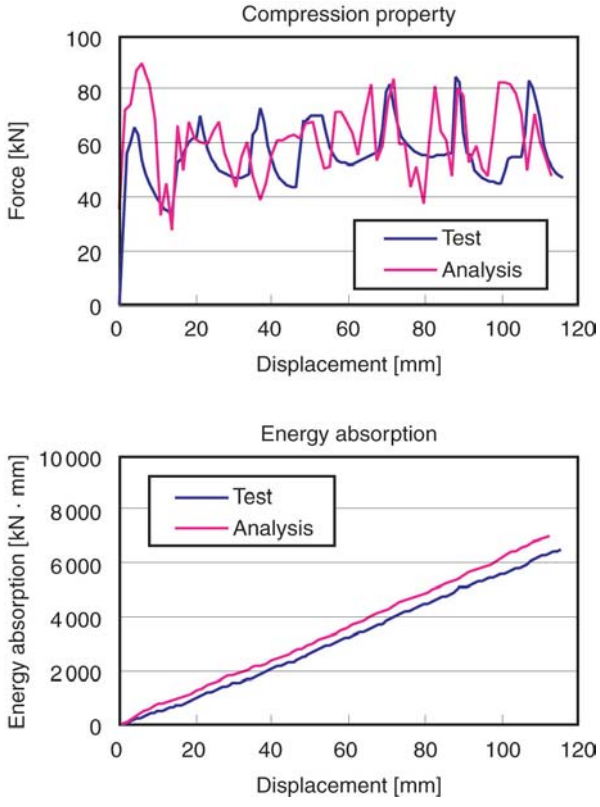


Fig. 20 Comparison of compression quality for hybrid structure

of force was not accurately reproduced. However, the energy absorption was reproduced with a difference of approximately 10%.

6. Conclusion

(1) The foam filled aluminum dual pipe structure (4)-a was proven to allow weight reduction while maintaining compressive energy absorption and bending stiffness properties compared to the crash box (7) shown in Table 1.
(2) The hybrid frame (1)-a shown in Table 1 was investigated using RADIOSS. The results showed that while energy absorption could be predicted within a difference of approximately 10% compared to the test results, the waveforms including the movement of force component relative to the deformation distance showed insufficient correlation, so this remains a future issue.

Acknowledgements

The authors wish to express their deepest thanks to related parties in the Antivibration Rubber Development Division and R&D Division of Tokai Rubber Industries, Ltd. for their enormous cooperation in promoting this research.

References

(1) Ishida, K., Fukahori, M., Hanakawa, K., Tanaka, H., Matsuda, K.: Development of a Technique to Strengthen Body Frame with Structural Foam, Society of Automotive Engineers of Japan, Inc., Proceedings of the Spring Convention, No. 7, p. 21–24 (2000)

(2) Imai, Y.: Polyurethane Foam, Chapter 8 Rigid Polyurethane Foam, Kyoto, Koubunshikankoukai Corp, p. 79–91 (1987)

(3) Jamil M.Alwan, Chi-Chin Wu, Clifford C.Chou: Effect of Polyurethane Foam on the Energy Management of Structural Components, SAE Paper 2000-01-0052

■ Authors ■



Yasushi TOSHIMITSU



Akifumi SONODA

Development of New Pre-processor for Car Body Analysis

Fumio NAKANO* Atsushi IWAMOTO*
Kenji TAKADA* Norikazu MATSUURA*

ABSTRACT

A new pre-processor was developed to shorten the finite element modeling process while improving calculation accuracy for car body analysis. The new pre-processor made it possible to create high quality models efficiently in a short time regardless of the skills and experience of the modeler. This was achieved by automatically identifying and correcting penetration and intersection between elements after division of a body in white into shell elements, automatically analyzing and converting spotwelds and other connection data into finite element data, assigning accurate material properties, automatically adding mass and incorporating dummies and barriers by compiling a material property, parts and mass database. In addition, the pre-processor was also given simple shape modification functions allowing model changes to be made in a short time when investigating specifications.

1. Introduction

Recent demands on product development have intensified for the development of high performance and high quality products in a short time. As one means for achieving this, designs can now be verified using detailed digital mockups created from three-dimensional CAD data. The development of automatic finite element generation algorithms[(1)–(3)] from these digital mockups has also made it possible to construct car body finite elements models in a short time without simplifying the CAD data or increasing the accuracy for finite element generation. However, demands for improved calculation accuracy and improvements in computer performance have also resulted in increasing model size and detail[(4)], so calculation model quality as typified by the following items that have a large effect on calculation accuracy has become an issue.

(1) Initial penetration between elements (components)
(2) Element shape quality around spot connections

Therefore, even if finite element generation is speeded up by automation, the man hours required for model correction increase, so models with a high calculation accuracy still take a long time to complete.

The modeling period must be shortened to respond to the need for shorter development periods. In addition, in order to minimize differences in calculation results between individual modelers, it has also become necessary to automate or simplify correction work, the addition of finite element data other than the body in white, mass distribution, and other tasks. This paper reports on the development of a new pre-processor for car body analysis that deals with these issues.

2. Analysis Flow

Finite element analysis divides data into elements often called a mesh. The body in white mesh for performing car body analysis is currently created from three-dimensional CAD data using an in-house automatic mesh generator. The mesh data for a single car body is generated by this automatic mesh generator software in the same format as the parts structure tree. This data is managed together with the connection data (for example, spot welding, metal inert gas welding and other connection methods, connection positions) (Fig. 1), and a different model is automatically created for each crash analysis, vibration analysis or other analysis type.

* Tochigi R&D Center

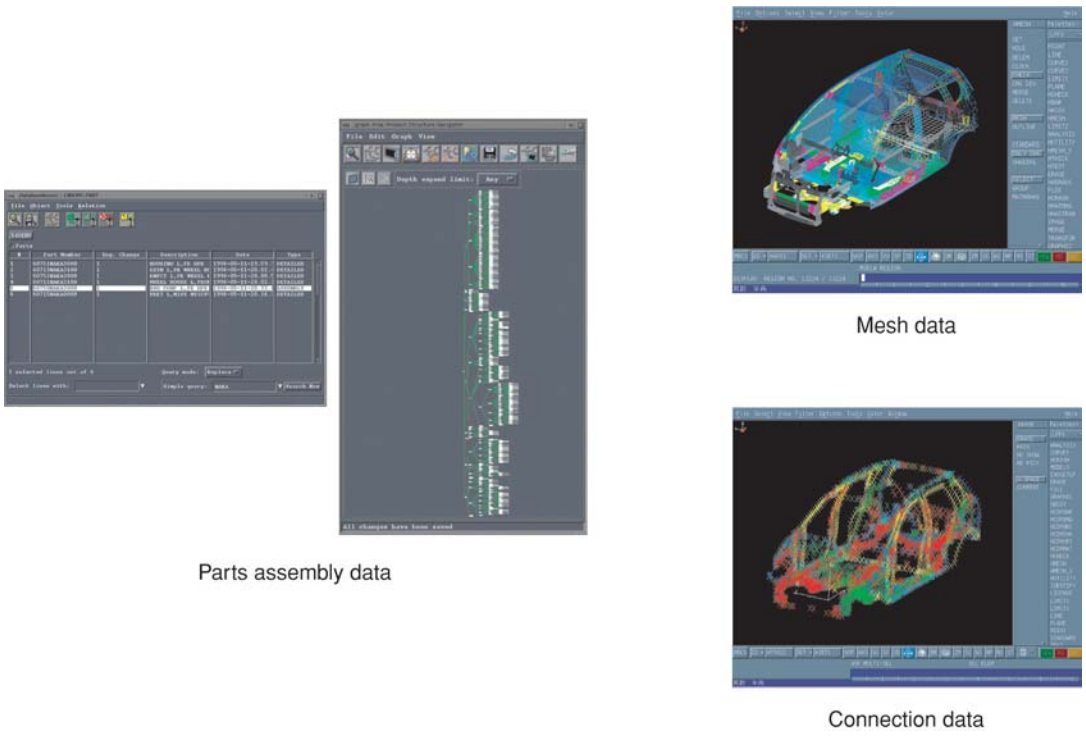


Fig. 1 In-house mesh generator

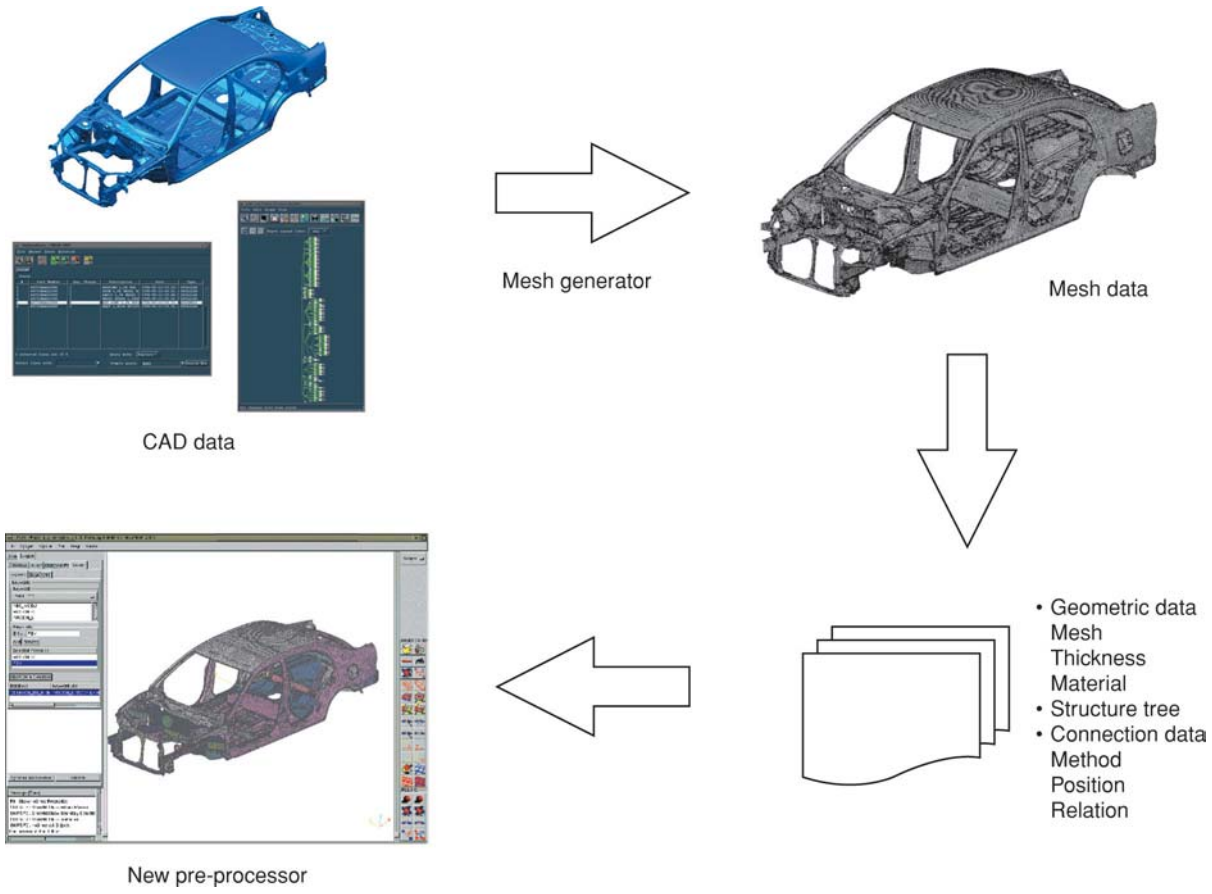


Fig. 2 Mesh data flow

Functions were developed for the new pre-processor to allow the following series of car body analysis modeling operations to be performed on models created by the automatic mesh generator in an extremely short time.

(1) Loading of finite element data and connection data
(2) Correction of initial penetration between elements
(3) Automatic generation and correction of connection elements
(4) Material property settings
(5) Component connections other than the body in white
(6) Mass setting
(7) Boundary conditions

This paper introduces items (1) to (6) which help to greatly reduce the model creation period, and the shape modification functions that are needed when investigating specifications.

3. New Pre-processor Functions

3.1. Loading of Finite Element Data and Connection Data

First, the mesh data (nodes, elements, plate thickness, materials) for each body in white component created by the automatic mesh generator, the connection data (connection method, position, connected component names) and the parts configuration are loaded. (Fig. 2)

3.2 Correction of Initial Penetration

When performing crash analysis, if elements penetrate or intersect in the initial state before deformation, reaction force is generated at that point and affects the calculation accuracy, so this must be eliminated as much as possible. However, even if there is no penetration in the three-dimensional CAD data that is the basis for finite element generation, penetration may occur in the mesh data due to the problems of the curvature of curved surfaces and the element size. (Fig. 3) Therefore, the new pre-processor simplifies correction of initial penetration by performing the following four steps in order. (Fig. 4)

(1) Automatic correction of intersection
(2) Displaying the direction of correction for intersecting nodes, and automatic correction after confirmation by the modeler
(3) Direct movement of intersecting nodes by mouse operations
(4) Automatic correction of interference

Case studies have shown that approximately 50% of intersecting portions are corrected by step (1), approximately 20% by step (2), and the remaining approximately 30% by step (3).

Using these functions makes it possible to perform work that formerly took approximately ten days in a single day or less.

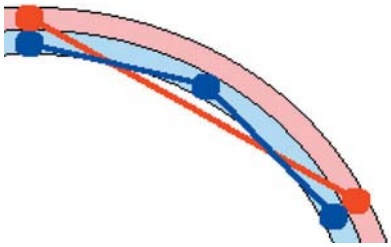


Fig. 3 Initial penetration by difference of mesh size

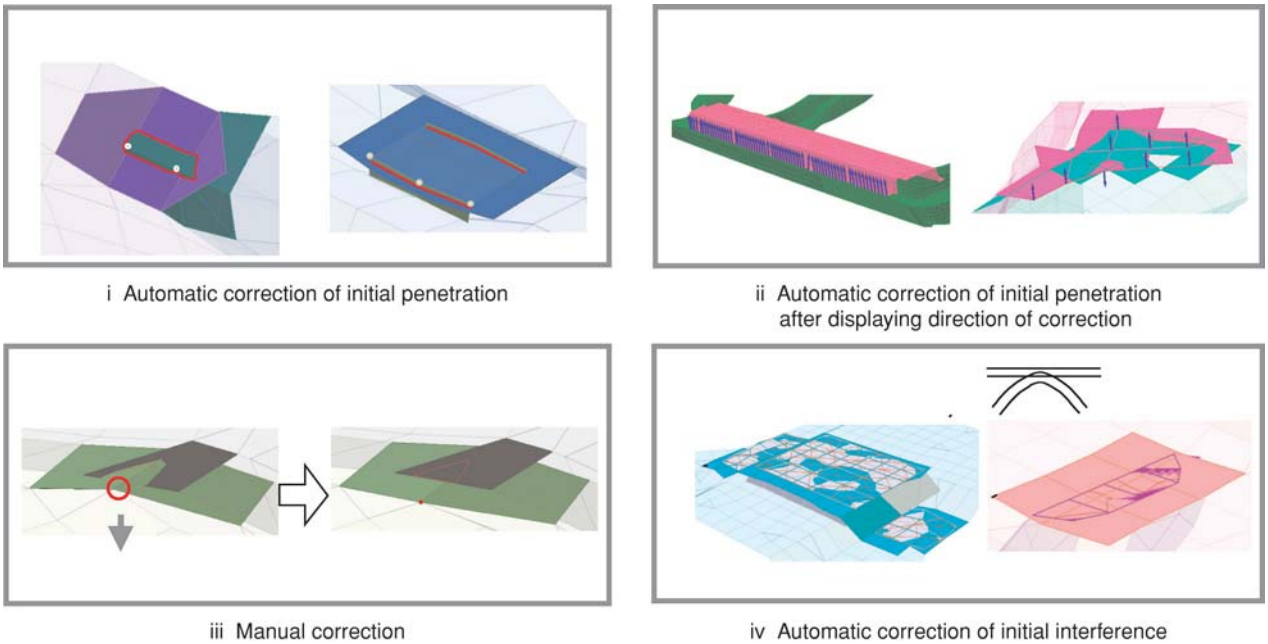


Fig. 4 Correction of initial penetration and interference

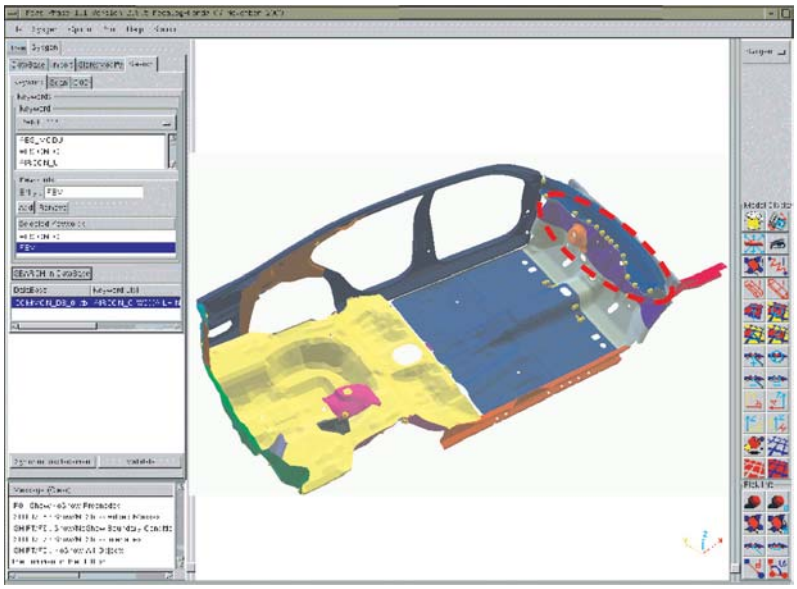


Fig. 5 Display of bad geometric data spots

3.3. Definition of Connection Elements

The spot welding, metal inert gas welding, bolt connection, hemming and glue elements are automatically defined using the connection data loaded in section 3.1. Current crash analysis programs use a spot data definition method like that of RADIOSS contact type 2 (INTERFACE TYPE2)[5), (6)] which does not use nodes to configure elements in spot positions. However, in this case the calculations sometimes end in error when projection cannot be performed normally from the spot position to neighboring elements. The new pre-processor was given functions to display these spot data (Fig. 5), modify the data (Fig. 6), and create simple spot data (Fig. 7). In addition, functions for creating other spot models such as spot models for strength and stiffness analysis (Fig. 8) were also added to support applications other than crash analysis.

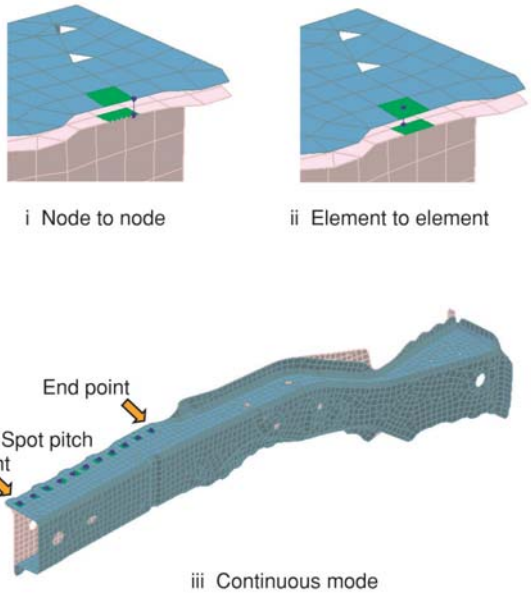


Fig. 7 Function of spot data creation

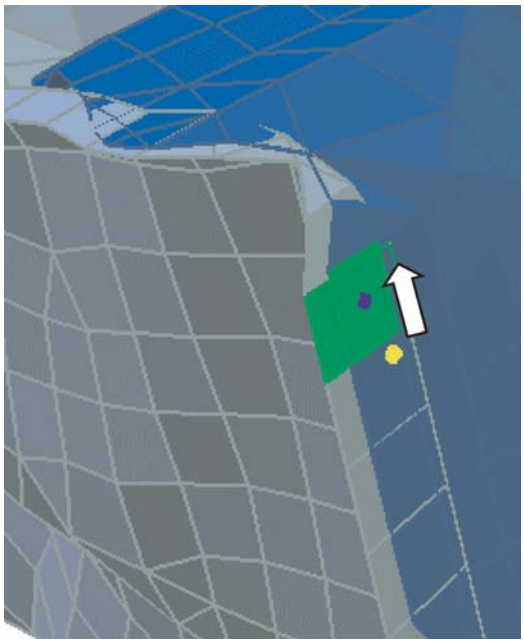


Fig. 6 Modification of spot data

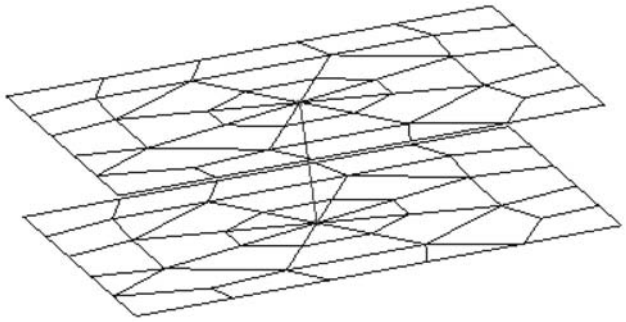


Fig. 8 Spot data for strength analysis

3.4. Material Property, Parts and Mass Databases

Improving the reproducibility of finite element models is an extremely important item for improving the accuracy of finite element analysis and detailed investigation of results in the future. The key points for this are thought to be as follows.

(1) Accurately setting material properties
(2) Modeling and setting parts
(3) Setting mass data

3.4.1. Material property database

When analyzing nonlinear problems, the stress-strain curve of the materials must of course be set as accurately as possible. Furthermore, when performing crash analysis the dependence of the yield stress on the strain rate must also be taken into consideration.

Automobiles are comprised of an extremely large number of different materials. Thus far it had been extremely difficult to set these values accurately, and this had adversely affected the calculation accuracy. Therefore, a material property database was compiled, and the new pre-processor first loads the material property names noted in the mesh data, and then automatically sets the correct stress-strain curve.

In addition, a function was also provided to allow modelers to access the database and select the optimum values when changing the material property specifications.

3.4.2. Parts and mass databases

The handling of parts other than the body in white will be an extremely important factor for finite element analysis in the future. For example, the parts reproducibility affects both improvement in the calculation accuracy for the high frequency regions during vibration analysis, and also improvement in the deformation amount and acceleration accuracy during crash analysis.

The current issue is that creating the finite element models for the necessary parts requires approximately the same number of elements and creation time as for the body in white.

However, the body in white creation time has been shortened by the automatic mesh generator. Therefore, the parts models must also be created by the time the body in white is completed. In addition, when connecting the parts, if the connection methods and correction of intersection are not also automated, the analysis period cannot be shortened.

On the other hand, when the desire to change the specifications arises after the required parts have been set in the body in white and analysis has been performed, work to replace parts is necessary. When parts that have been set are removed and the setting work is performed again using a general-purpose pre-processor, errors often occur in the original finite element data. In particular, models targeted by the new pre-processor are comprised of numerous parts and connection data, and replacing even a single part makes it necessary to accurately delete all the connection data, mass data, boundary conditions and other data related to that part.

Therefore, parts and mass databases that include data managing functions were developed for the new pre-processor in order to solve the above issues. (Fig. 9)

Parts other than the body in white are registered as parts modeled with finite elements or other models and parts not so modeled. However, the part name, part number, destination, analysis type and other key words are added during registration so that anyone can reliably search for the target part. This has also proven effective when searching for common parts for other models.

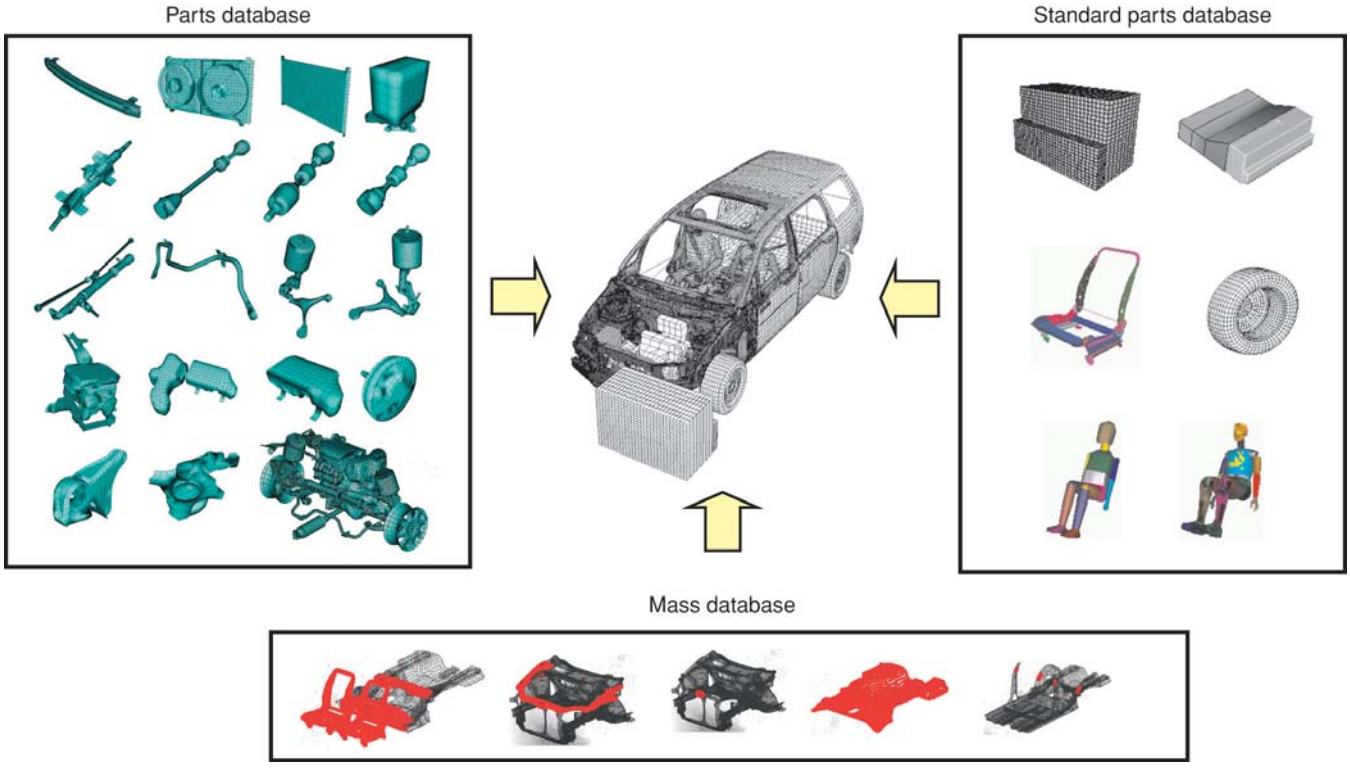


Fig. 9 Parts and mass databases

When attaching parts stored in the parts database to the body in white, the necessary template is set for each analysis type. This makes it possible for even beginners to accurately attach parts by following the steps below, and also prevents parts omissions. (Fig. 10)

(1) Setting the position
(2) Checking for and correcting penetration
(3) Connection to the body in white

There is also a function that searches for and displays parts near the connection position. This allows connection work to be performed even if the name or other information regarding the other part to be connected is not known. Also, connected and unconnected locations are indicated with different colors for each connection type, allowing easy checking of connection omissions.

The registered mass data can be automatically distributed to parts requiring added mass using a template similar to that of the parts database. (Fig. 11)

In addition, normally the mass and longitudinal balance of the completed finite element model and the actual vehicle do not match, so a function was also developed for automatically adding mass to achieve the target mass and longitudinal balance. (Fig. 12)

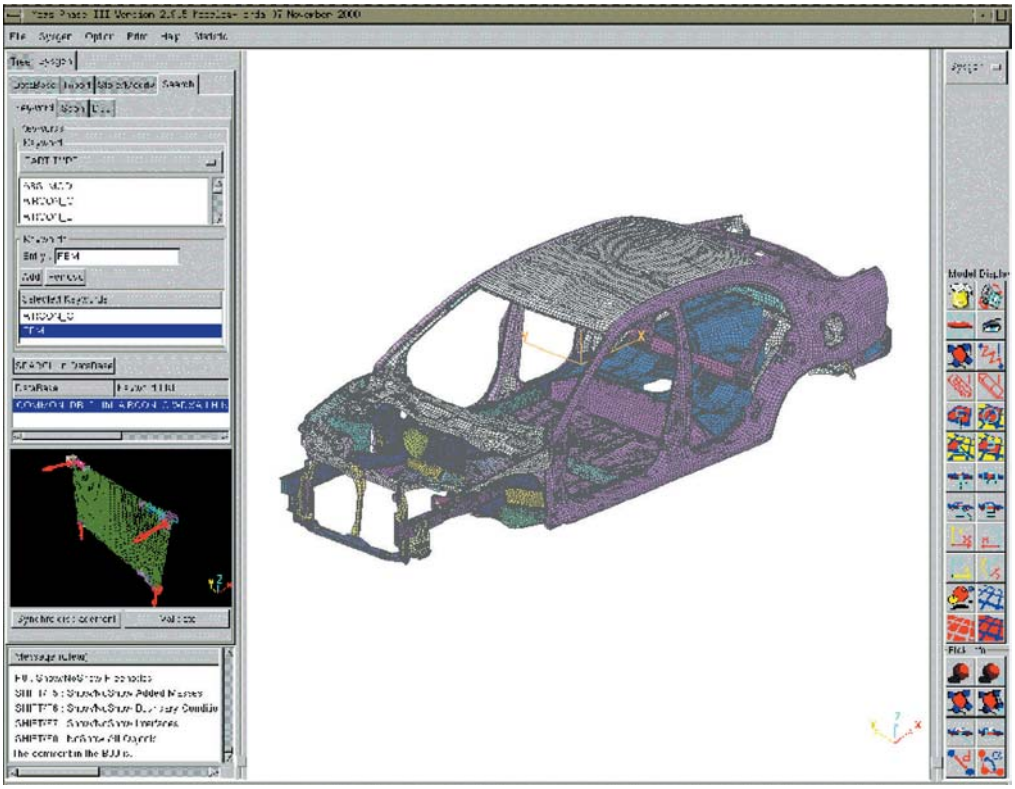


Fig. 10 Menu for automatic connection from parts database

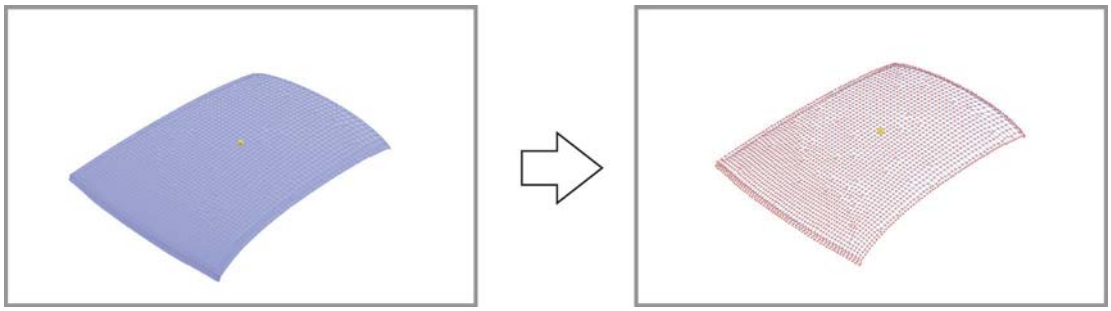


Fig. 11 Automatic mass distribution

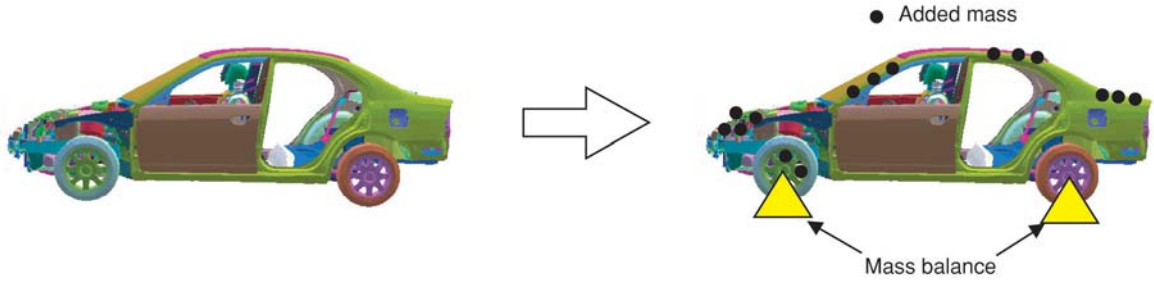


Fig. 12 Automatic mass distribution

3.5. Simple Shape Modification Function

When modifying the finite element model shape, the ideal method is to modify the shape at the CAD data and then generate the mesh again. However, in this case work to correct initial intersection, set conditions for connection, and set parts must be repeated each time the shape is changed. Therefore, the following functions were developed to allow simple shape modification using the created finite element model in order to reduce the analysis man hours when investigating different proposals. (Fig. 13)

(1) Section shape modification
(2) Extension
(3) Section scaling
(4) Rotation and translation
(5) Symmetrical copy
(6) Mesh creation by node offset

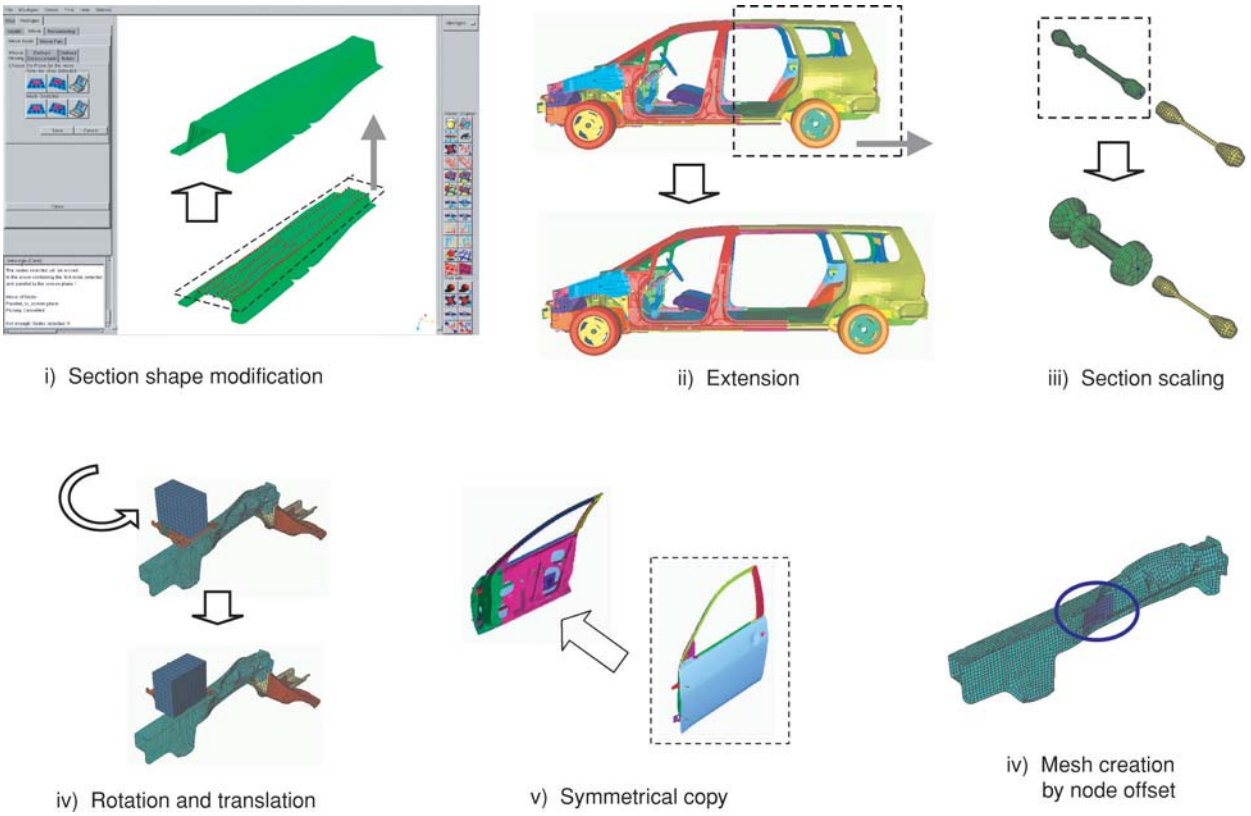


Fig. 13 Mesh data modification

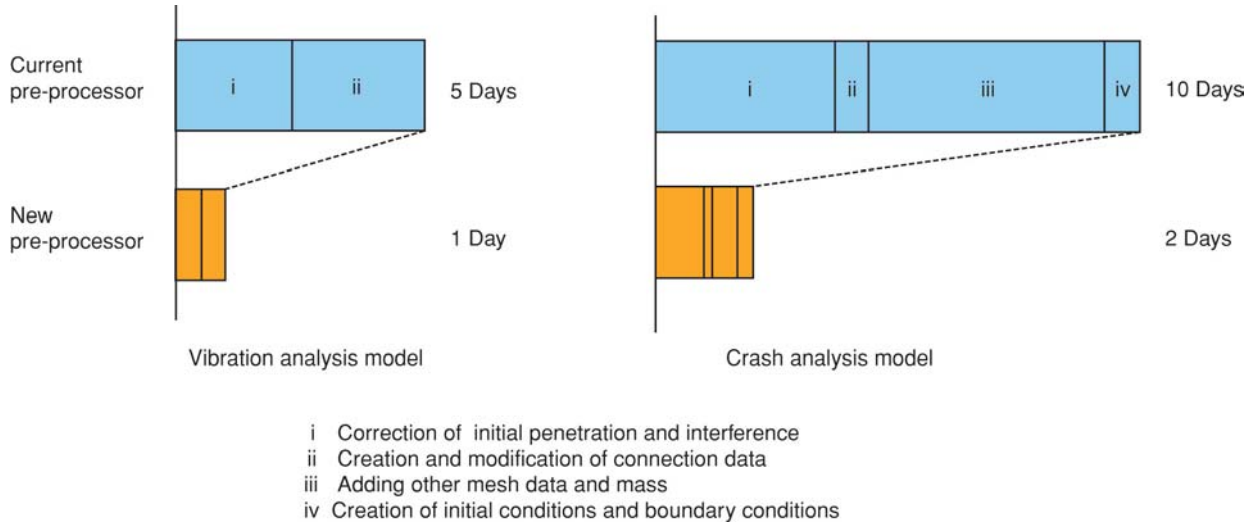


Fig. 14 Modeling period

4. Application Examples

Actual examples of models created using the new pre-processor are introduced below.

Fig. 14 compares the modeling periods with the current method, and Fig. 15 compares the calculation results with test results. These examples show that the modeling period is reduced compared to the current modeling method, and the calculation accuracy is also excellent.

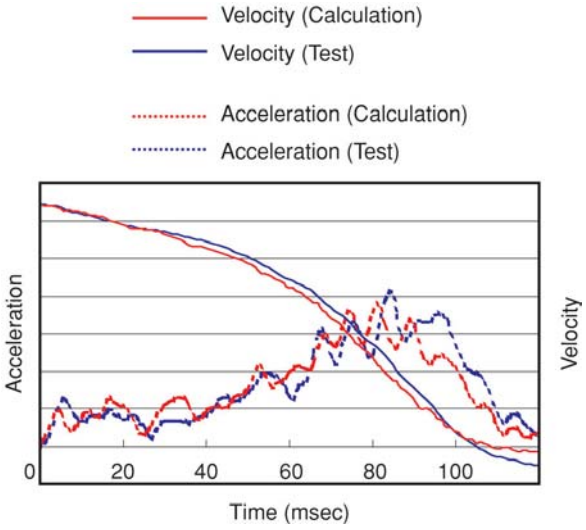


Fig. 15 Acceleration and velocity of floor in frontal offset crash

5. Conclusion

Use of the aforementioned initial penetration automatic correction function, analysis-specific connection model automatic creation function, and material property, parts and mass databases enabled the following.

(1) Calculation conditions could be added in two days after completion of the body in white model by the automatic mesh generator.
(2) Even less experienced engineers could perform the analysis operations that are currently performed by specialists.
(3) Specifications could be changed easily and swiftly.

References

(1) Shimada K.: Physically-based mesh generation: automated triangulation of surfaces and volumes, Ph.D. Thesis, Massachusetts Institute of Technology, USA (1993)

(2) Shimada K., Liad JH., Itoh T.: Quadrilateral meshing with directionality control through the packing of square cells, Proceedings of the 7th International Meshing Roundtable, p. 61–75 (1998)

(3) Inoue K., Itoh T., Yamada A., Furuhata T., Shimada K.: Face clustering of a large-scale CAD model for surface mesh generation, Computer-Aided Design 22, p. 251–261 (2001)

(4) Fujitani K., Present Status and Future Scope for Simulation in Car Development, JOURNAL OF SOCIETY OF AUTOMOTIVE ENGINEERS OF JAPAN, Vol. 55, No. 6, p. 4–8 (2001)

(5) RADIOSS-CRASH VERSION 4.2 MANUAL (2000), MECALOG JAPAN K. K.

(6) RADIOSS ENVIRONMENT EXAMPLE GUIDELINE VERSION 4.1 (1999), MECALOG JAPAN K. K.

■ Authors ■


Fumio NAKANO


Atsushi IWAMOTO


Kenji TAKADA


Norikazu MATSUURA

Research for Vibration Analysis with Full-Vehicle Model

Toshiya YOKOI* Kengo OKAMURA*
Jiro NINOMIYA* Masaki NAGAHISA*

ABSTRACT

Techniques of full vehicle analysis directed at all suspension and body-related parts were combined with test-based engineering and simulation techniques in a two-sided approach intended to develop a technology for reduction of floor and steering vibration. The test-based engineering clarified the mechanism of vibration initiation by means of full vehicle modal analysis, operational deflection shape analysis, and transfer path analysis implemented by excitation of the suspension. Modifications were then made to an actual car based on the results obtained from analysis. The simulation techniques involved modeling of all the subject parts, and the creation of a finite element model (160,000 nodes) that matched the actual car with a high degree of accuracy. Sensitivity analysis was then applied to analyze the weak points, and calculations were made to implement modifications in the finite element model. Both the test-based engineering and the simulation techniques were confirmed to reduce vibration levels in the actual car, thus substantiating the validity of these analytical techniques.

1. Introduction

In new model development, there continues to be requirements to make the body lighter, as a measure for environmental protection. In addition, for collision safety performance, a variety of collision test methods continues to be established, with many requirements for body construction and body rigidity.

However, there are many times where the floor and steering vibration during driving does not match the measures being taken to reduce vehicle weight and to enhance collision safety. The quality required for floor and steering vibration is higher than it was before, and in order to balance this quality with other performance items, it has become necessary to have effective vibration solutions that fully make clear the causes of the vibration. However, causes of vibration lie not simply in the tires and suspension; and because many parts, including the body and steering structures, are involved, it is often difficult to understand the vibration generating mechanisms. Highly accurate analysis technology is therefore required.

This research project has dealt with full vehicle analysis technology that looks at all parts contributing to floor and steering vibration. The methods of approach were test-based engineering using an actual car, and simulation technology using the finite element method. A reduction in vibration was realized by implementing countermeasures to the basic causes of vibration after analyzing the generating mechanisms. This paper reports on the details of the project.

* Tochigi R&D Center

2. Vehicle Analysis

2.1. Target Area Setting

After selecting, in an actual running test, the road surface and speed conditions where is it easy to feel the difference in vibration levels against a comparison vehicle, evaluation point vibrations levels were measured for the steering wheel and floor evaluation points. The selected conditions were a slightly rough road, at a vehicle speed of 45 km/h. The measurement results for the test vehicle and the comparison vehicle are shown in Fig. 1.

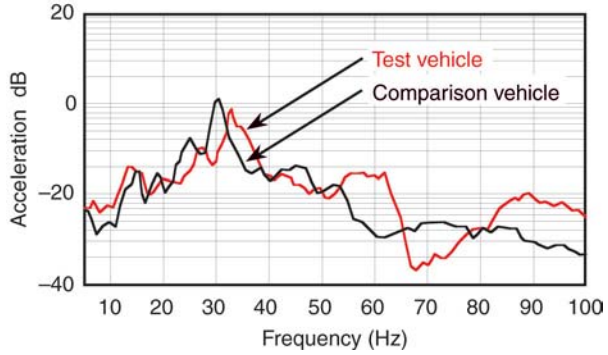


Fig. 1 Steering wheel vertical acceleration

In this way, measuring 3-direction translational acceleration of two evaluation points, the frequency range where the test vehicle is not as good as the comparison vehicle is brought out. Then, using operational deflection shapes and principal component analysis, as explained below, the ranges are categorized according to those having the same causes, from the vehicle's dynamic behavior and input force contributions. An outline explanation of the analysis method is given below.

2.2. Operational Deflection Shapes

This is a method for analyzing vehicle behavior in an actual running test. In this project, actual running test measurements were made of 3-axis acceleration at a total of 341 points on the suspension and body, and deflection shapes were specified in the relevant frequency ranges from animation observation.

2.3. Principal Component Analysis

Conventionally, front and rear wheels are excited separately, and input force contribution is determined against evaluation point response. However, this time the contribution of each input force was specified for each evaluation point vibration direction, applying multivariate analysis and using operational deflection shapes of actual running test data. As a result, it is possible to understand, by frequency range, the input contribution against evaluation point vibration in an actual running test. Figure 2 gives an example of principal component analysis calculation results vs. steering vertical vibration.

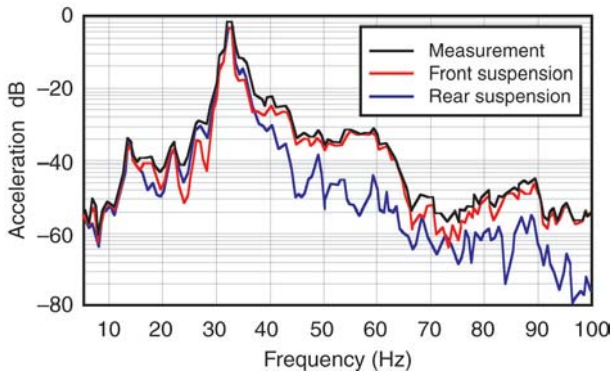


Fig. 2 Contribution of input force for steering wheel vertical acceleration

2.4. Full Vehicle Modal Analysis

The analysis method used in target area setting was introduced above, and other methods are introduced below, used in order to more fully understand the details of this phenomenon. The first is experimental modal analysis. In this project, using an actual car in a laboratory test, the unsprung mass (lower arm) had random burst excitation applied, for the front and rear wheels separately. Through this excitation of the input force points when driving, it was possible to discover the excitation mode in an actual running test. In addition, by simultaneously carrying out constant vertical excitation of the body of 2.5 Hz, it was possible to eliminate the high frequency friction component. Using this method, 8-100 Hz frequency vibrations can be analyzed.

2.5. Transfer Path Analysis

Unsprung mass is connected to the body through multiple suspension arms, etc., and if contributions for each transfer path are known, it is also possible to take countermeasures using suspension bushes. The second analysis method is one used to determine the contributions of each path, and for this, two types of measurements are necessary. The first is measurements of suspension attachment point response when exciting the evaluation point (body transfer function measurements). The second is measurements to determine bush transfer force (input force measurements) by calculating suspension bush displacement during an actual running test from relative acceleration and by multiplying it with bush dynamic elasticity modulus. By carrying this out in all three directions for each suspension attachment point, it is possible to calculate evaluation point response as the total of input force × body transfer function. Highly rigid bushes have small displacement, and with this method it is difficult to maintain calculation accuracy, but an example of transfer path analysis calculation results against steering fore-aft vibration is given in Fig. 3.

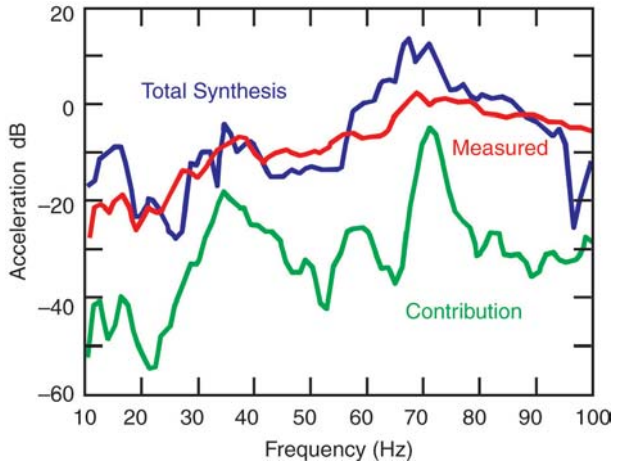


Fig. 3 Result of transfer path analysis for steering fore-aft vibration

In the chart, the red line represents steering fore-aft acceleration measurement values that are the evaluation points, and the blue line represents the calculated values. They are similar in inclination. A transfer path example, among the calculated values, is shown with the green line. It is possible to confirm that around 35 Hz and 70 Hz peaks, the contribution of the transfer path represented by the green line is large.

2.6. Weakness Analysis Results

An outline introduction of analysis methods was made above. Now two examples will be given, including the results of the analysis using both of these methods, and the various major causes in the areas where the test vehicle is worse than the comparison vehicle.

The first example is the area where vertical direction is worse for both the floor and steering wheel, around 26 Hz. Using full vehicle modal analysis in this area, (1) 25.43 Hz rear suspension vertical mode, (2) 27.89 Hz body 2nd bending mode, and (3) 32.07 Hz rear suspension fore-aft mode were discovered. From the mode shape, it is assumed that those contributing greatly to steering wheel vertical vibration are (2) and (3). The mode shapes are shown in Figs. 4–6.

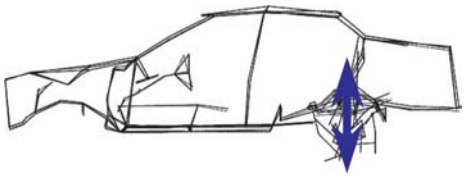


Fig. 4 Rear suspension vertical modal shape (Experimental modal analysis)

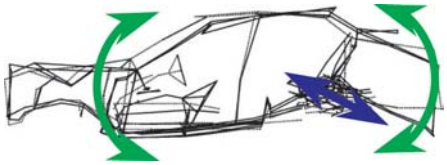


Fig. 5 Body 2nd bending modal shape (Experimental modal analysis)

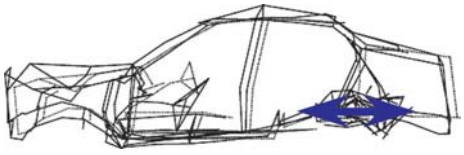


Fig. 6 Rear suspension fore-aft modal shape (Experimental modal analysis)

Checking these with operational deflection shape results, body 2nd bending was discovered at 26.86 Hz, and it was learned that rear suspension movement at that time was closer to vertical than fore-aft. (Fig. 7)

Using only experimental modal analysis, the focus is on suspension fore-aft vibration, but in this case the countermeasure must be applied for vertical vibration. It was learned that it is very important to fully and accurately understand the phenomena, using a number of methods.

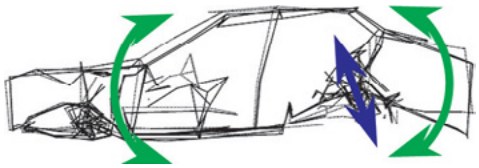


Fig. 7 Body 2nd bending shape (Operational deflection shapes)

The second example concerns the steering wheel lateral vibration at 75–100 Hz. From the results of the experimental modal analysis, it was confirmed that, at 92.18 Hz, front sub-frame turning and fore-aft motion stimulate steering shaft lateral bend, and the steering wheel lateral vibration becomes larger (Fig. 8). This is a curve fitting of a high frequency range that is normally thought to be difficult, but by taking measurements fully confirming linearity, reciprocity, etc., and by repeatedly checking curve fitting, it is possible to have highly accurate curve fitting.

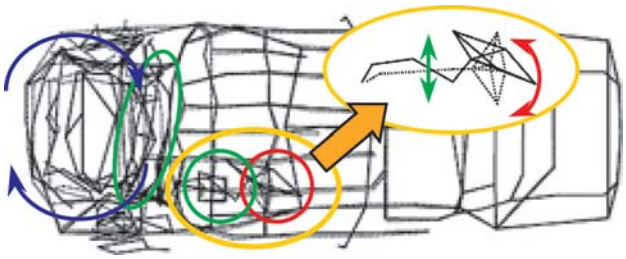


Fig. 8 Front sub frame yaw rotation modal shape (Experimental modal analysis)

3. The Effect of Vehicle Modification

3.1. Modal Sensitivity and Modal Design

Using the methods above, the major causes of each weak area were discovered, but in order to specify effective countermeasure locations and methods, it is necessary to identify a highly sensitive area.

In this point in the project, attempts were made to specify areas where countermeasures were required, using modal sensitivity analysis. An example of sensitivity analysis is given in Fig. 9.

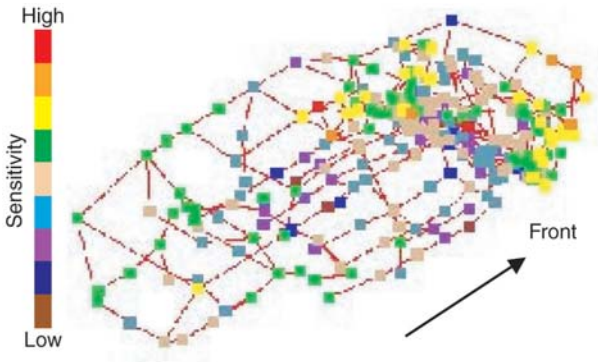


Fig. 9 Modal sensitivity

Modal sensitivity analysis is a method of calculating how much modal natural frequency and amplitude levels will change when the mass and rigidity of the part concerned changes. It is effective in identifying the areas for highly effective countermeasures.

In addition, because it is possible to add an imaginary stiffener regardless of the actual construction, it is also possible to study new constructions.

Next, use was made of a modal-modified calculation method for simulating the effects of changes to mass and rigidity. With modal-modified calculations, mass and rigidity changes are made to the modal model, and the modified model created. From natural frequency analysis of this model, it is possible to compare mode natural frequency value and amplitude levels before and after the mass and rigidity changes. Simulations of the level of effect of the countermeasures can be made, as shown in Fig. 10.

Furthermore, through synthesis of the transfer function after mass and rigidity changes, it is also possible to check characteristic changes in frequency areas far from the target mode. An example of synthesis is shown in Fig. 11.

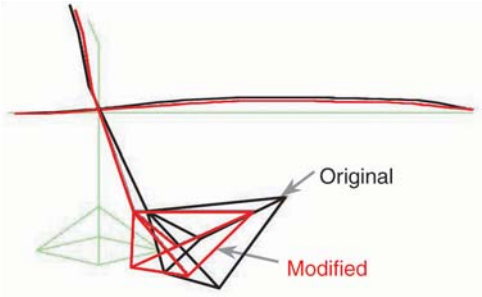


Fig. 10 Modal sensitivity
(Steering wheel lateral acceleration)

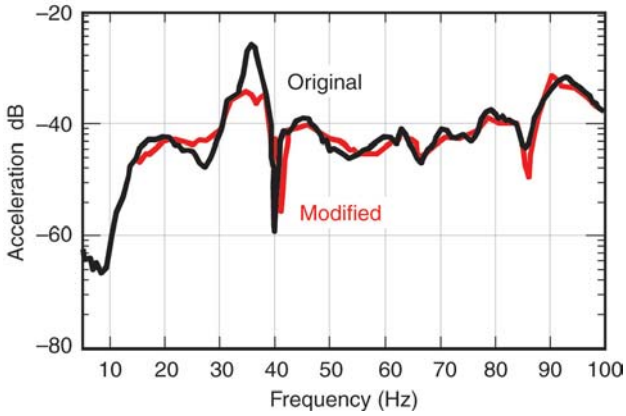


Fig. 11 FRF's synthesis

3.2. Implemented Modifications

Through the aforementioned modal sensitivity analysis and modal modification, effective modification proposals to reduce vibration came to light.

Therefore, an actual car was modified, and a vibration-countermeasure car built. Table 1 gives examples of the modifications made.

Table 1 Example of modification

Target modes	Details of modification
Local modes steering wheel, shaft hanger	· Increase stiffness for steering shaft bending · Reinforce steering hanger right connection to A-pillar
Local modes of rear sub-frame	· Front part of rear sub-frame reinforce + additional beam to body · Rear suspension lower arm connecting point reinforce
2nd body bending mode	· Increase stiffness of rear side frame · Front body (lateral and vertical) reinforce

3.3. Confirmation of Effect of Modifications

Using actual running test measurements of vibrations from the countermeasure car a study was made of the level of achievement against the target level.

The effectiveness of these countermeasures is shown in Fig. 12. There is a reduction in steering vibration level in many frequency bands, and it was confirmed that a dramatic reduction was achieved at 25–40 Hz.

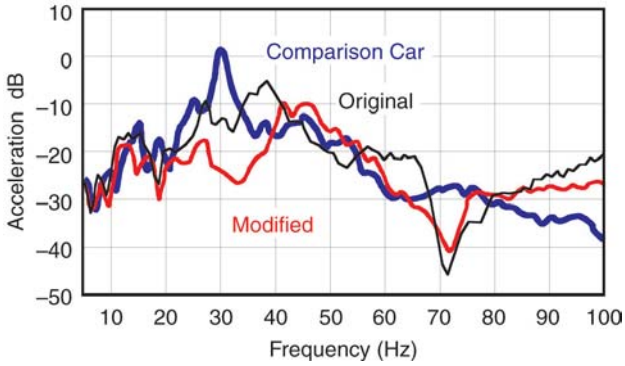


Fig. 12 Result of modification
(Steering wheel vertical acceleration)

4. Simulation Model Creation

For the analysis methods mentioned so far, a test vehicle is necessary. In making the new model development cycle shorter, however, there are cases where it is necessary to simulate vibration levels without a test vehicle.

Therefore, the next step was to create a full vehicle finite element model for simulation technology. In order to obtain a correlation with experimental modal test data, the objective was to create a model with which it was possible to calculate frequency response function (referred to as FRF hereafter) between the unsprung mass (lower arm) and floor or steering wheel. Multiplying this by the road surface input force determined from an actual running test, it was possible to make a simulation calculation of actual car floor and steering vibrations.

4.1. Flow of Model Creation

The subject parts were suspension, engine, exhaust, trimmed body, and steering system (gear box, hanger, column, wheel). The trimmed body mentioned here is the actual car, excluding suspension, engine and exhaust, and steering system (wheel, column, and gear box).

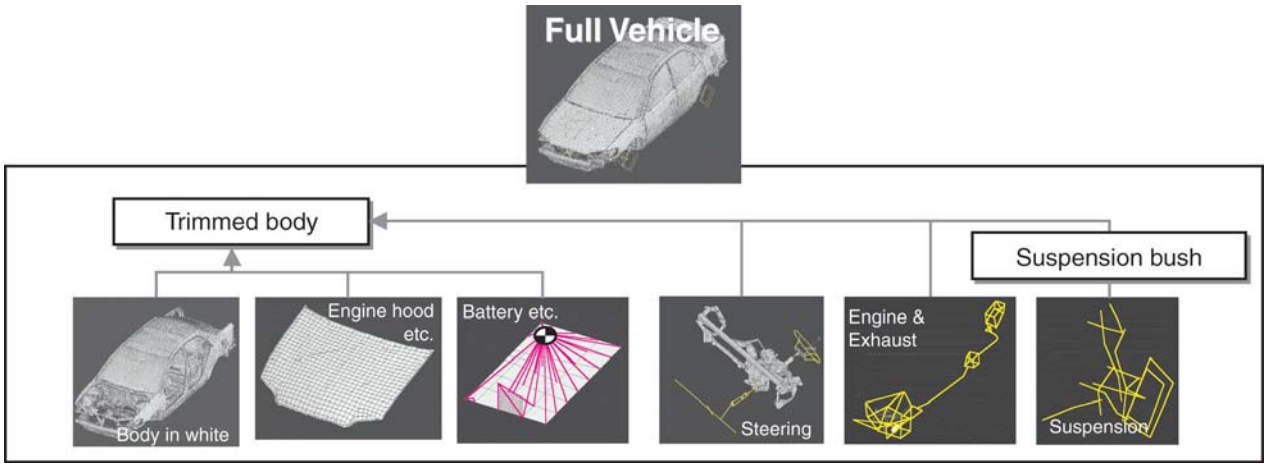


Fig. 13 Flow of full vehicle modeling

First, a finite element model was created for each component, and according to the results of component jig tests, a correlation study was carried out. The modeling method varied for each part, considering the part's level of effect on vibration. Next, the parts were connected, creating a full vehicle finite element model.

The method was to have 3 or 4 people working on model creation simultaneously, and to study the causes of problems in the finite element model so it could be carried out at an early stage. The flow of model creation is shown in Fig. 13.

4.2. Trimmed Body

The trimmed body finite element model used was the one created for acoustic analysis. This trimmed body model was created from the model of the body-in-white, and among the trimmed parts, parts that affect accuracy, such as the engine hood, are modeled in detail. Parts such as the battery which are considered to have little effect on accuracy are modeled as concentrate masses. The sub-frame is also modeled in detail. The final model is compared with the body-in-white and trimmed body test models, making a correlation study. Suspension attaching point local rigidity is very important here, so a correlation study is carried out between attaching point inertance and the index.

4.3. Engine and Exhaust

Because the engine has no resonance points at 200 Hz or less according to the excitation results, it is shown as a concentrated mass, given mass and inertia moment (6 direction) applied.

As for the exhaust, modeling is necessary because of the large number of modes at 100 Hz and less. However, the exhaust pipe is expressed as a BAR element, while the catalyst unit and muffler are a concentrated mass. From the results of a correlation study with experimental modal analysis results, it was learned that it is necessary to have detailed modeling of the flexible joint, and it was expressed as a SHELL element. The model created is shown in Fig. 14.

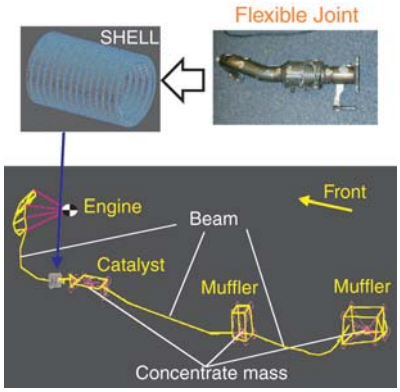


Fig. 14 Engine and Exhaust model

4.4. Suspension

For the suspension, component experimental modal analysis tests were carried out, and the modal parameters obtained were converted into a direct matrix input force format (DMIG format), thereby creating the finite element model. The advantage of this method is that the suspension, which is strongly non-linear making finite element modeling difficult, can be expressed as a very small model of 74 nodes. Furthermore, data obtained from the experimental modal analysis is input directly, making it highly accurate. On the other hand, the disadvantage is that once the model is created, it is not possible to have a design change. In order to carry out component testing, at this time, the suspension was attached to a sub-frame firmly fixed to a concrete jig, and excitation testing carried out. The created model is connected to the sub-frame through a suspension bush. The dynamic elasticity modulus measured on the component was used as a bush characteristic. The model created is shown in Fig. 15.

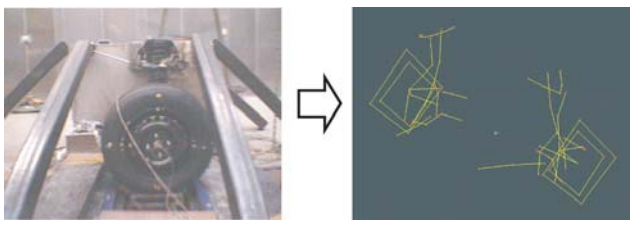


Fig. 15 Testing of suspension and FE-model

4.5. Steering System

In order to reproduce steering vibration accurately, detailed modeling of the hanger and column was carried out, as SHELL elements. However, the gear box and wheel were simply modeled as BAR elements. A correlation study was carried out between them and the results of the excitation test. The model created is shown in Fig. 16.

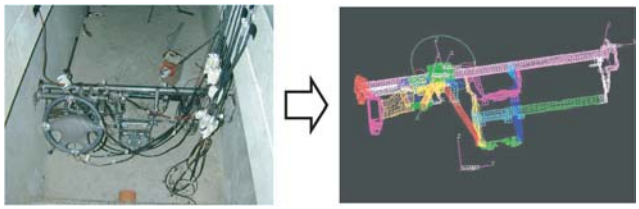


Fig. 16 Steering system

4.6. Full Vehicle Modeling

By linking together all the sub-models, a full vehicle model was created, as shown in Fig. 17.

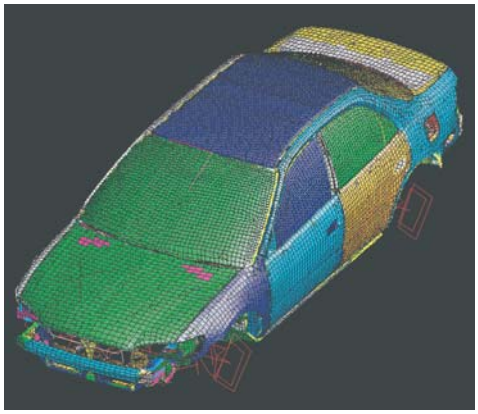


Fig. 17 Full vehicle FE-model

The floor and steering responses (3 directional) against suspension input force using the prepared model were compared with actual car measurement results, and a correlation study made. Here, accuracy was improved mainly by changing the rigidity of connections between sub-models.

The accuracy of the final finished model appears in the FRF between unsprung mass and steering or floor, as shown in Figs. 18 and 19.

In the 10–90 Hz frequency band, the results of a comparison with actual car measurement data showed that the accuracy of the finite element model created in this project was sufficient to be used in simulating vibration levels.

5. Study of Construction using a Modification Simulation

5.1. Outline

Using the full vehicle model for vibration analysis as explained in Section 4, studies were made of proposals for modifications to reduce vibration to the target levels, and the effectiveness of the proposals were reviewed. First, areas that should be modified were identified using sensitivity analysis. Next, simple modifications were made, and the benefits simulated.

Through these studies, it was possible to carry out modifications that effectively reduce vibration levels.

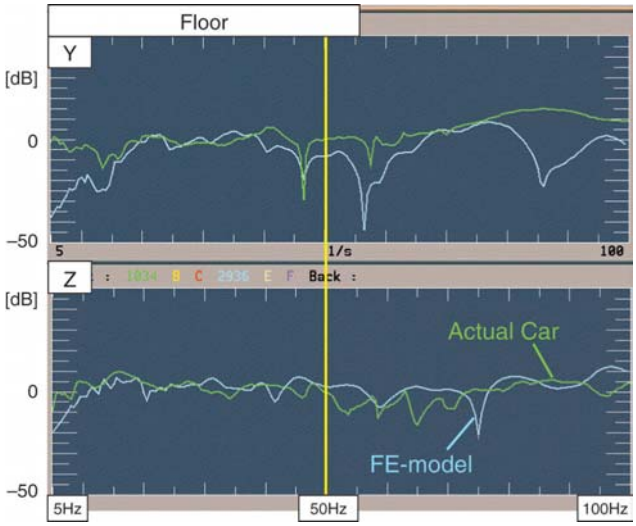


Fig. 18 Final synthesis with full vehicle model

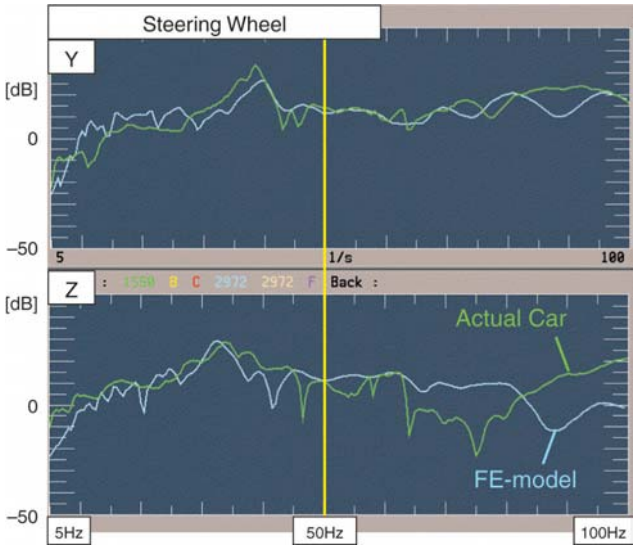


Fig. 19 Final synthesis with full vehicle model

5.2. Specification of Areas for Modification

In order to make effective modification, the following three methods were used.

(1) Finding the Dominant Modes

This is a method that discovers the dominant modes that greatly affect the evaluation index, and can be used to determine the areas that must be qualitatively strengthened. Figure 20 shows the steering wheel lateral bending mode shape, which greatly affects one evaluation index.

(2) Strain Energy

This method is used in order to determine the areas that should be quantitatively modified. The strain energy density of all the dominant modes selected in (1) is totaled, and modification areas specified. Figure 21 shows distribution of strain energy density totals for each group. Here, strain

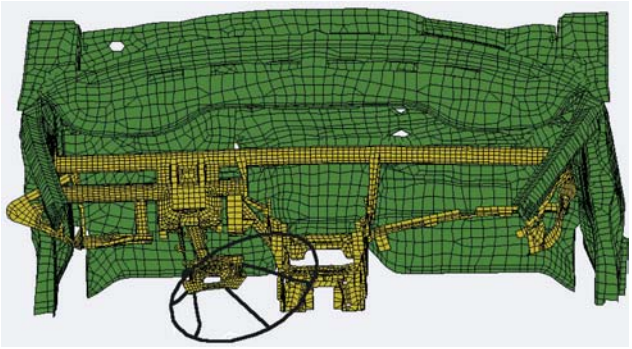


Fig. 20 Steering wheel lateral bending mode

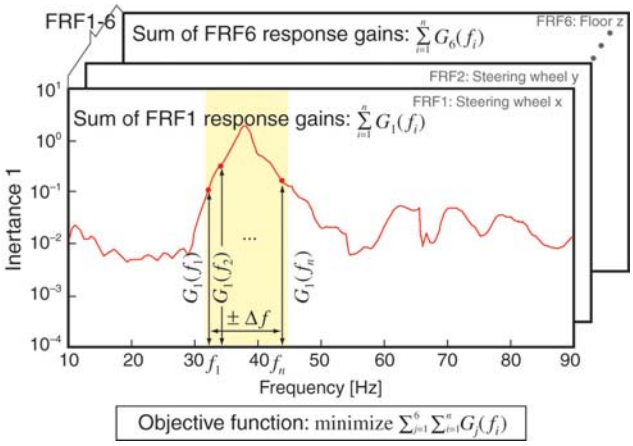


Fig. 22 Objective function of sensitivity analysis



Fig. 21 Strain energy density of body shells

energy density was calculated with each part comprising the body-in-white as one group. With this method, groups, that is parts, that would give a high modification benefit were specified, according to the magnitude of the strain.

(3) Frequency Response Function (FRF) Sensitivity

What follows is an explanation of the method using FRF sensitivity as an actual evaluation function. In sensitivity calculations, the normal finite element method is used. Table 2 gives the objective function, constraint conditions, and design variance for sensitivity analysis. In objective function, the FRF level of a total of the 6 directions — floor 3 directions and steering 3 directions — according to suspension input force is used. As shown in Fig. 22, at each FRF, the focus frequency $\pm \bullet f$ [Hz] response gain sum is determined, and minimizing the sum of FRF for floor and steering three directions is the objective function.

Table 2 Calculation conditions of sensitivity analysis

Objective function	minimize	$\sum_{j=1}^{6} \sum_{i=1}^{n} G_j(f_i)$
Constraint condition	subject to	$W_{opt} \leq W_{init}$
Design variance	shell thickness	

$G_j(f_i)$: FRFj Response gain at f_i (i = 1, 2, ..., n; j = 1, 2, ..., 6)
n: Number of evaluation frequencies
W_{opt}: Optimized weight
W_{init}: Initial weight

The FRF sensitivity obtained through these calculations is shown in Fig. 23. Here, as well as in (2), sensitivity was calculated with each part comprising the body-in-white as one group. With this method, sensitivity concerning direct FRF is calculated, and areas that can be very effectively modified are effectively specified, even more than when using strain energy.

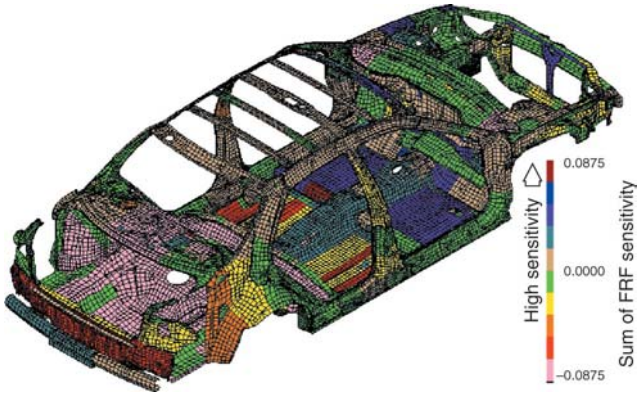


Fig. 23 FRF sensitivities of body shells

5.3. Results of Simulating the Effect of Modification Proposals

The results of simulated effects from the modifications carried out using the methods described in the previous paragraphs are given below. Figure 24 shows examples of body modifications and Fig. 25 shows examples of steering system modifications, with their effects on the evaluation index. From these diagrams, it can be seen that it is possible to reduce vibration by about 10–30% with each modification. Figures 26 and 27 shows the floor 2-direction and steering wheel 2-direction actual running test vibration level simulation results when theses modifications are carried out. From these results, by making these modifications, it is possible to simulate a reduction in the 70–90 Hz range and 35–40 Hz steering vibration level.

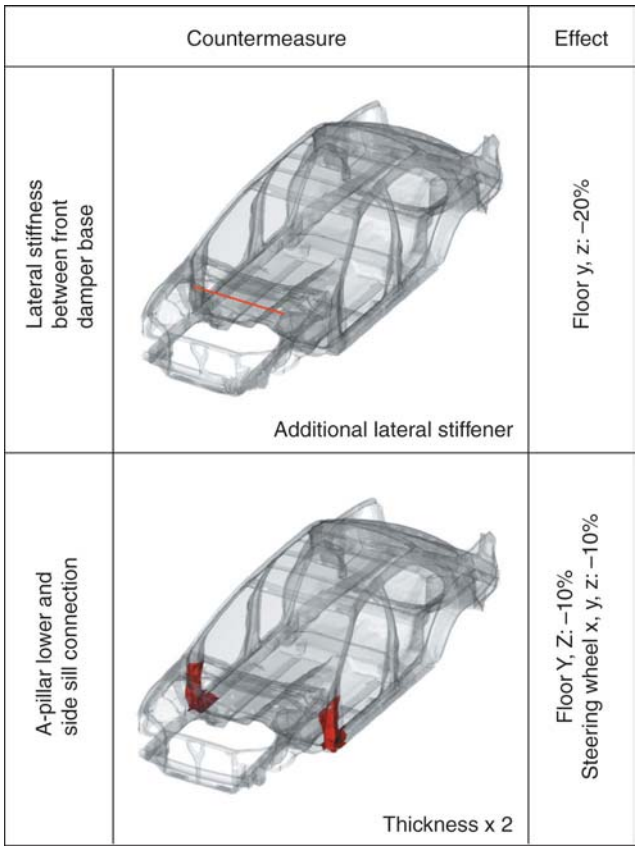


Fig. 24 Examples of body refinement for floor and steering wheel response

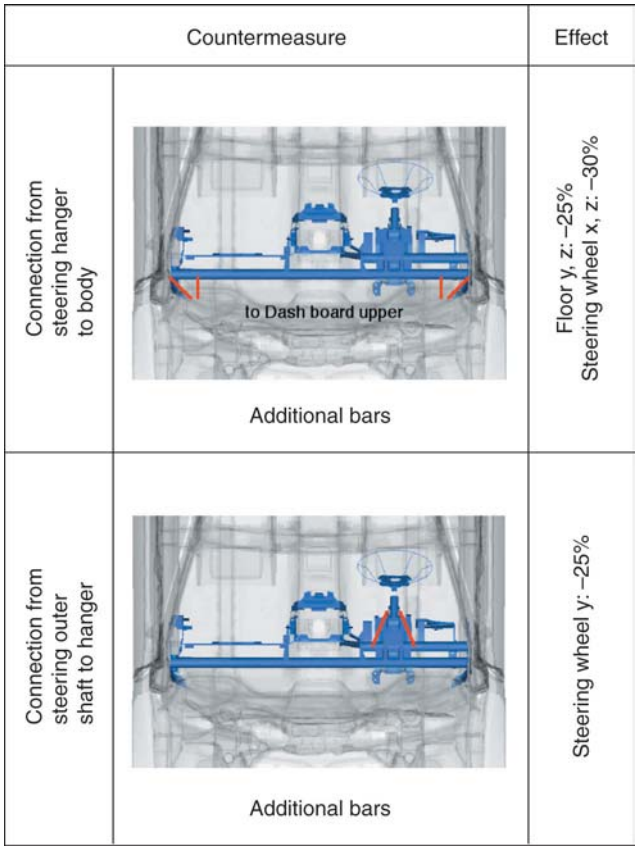


Fig. 25 Examples of steering refinement for floor and steering wheel response

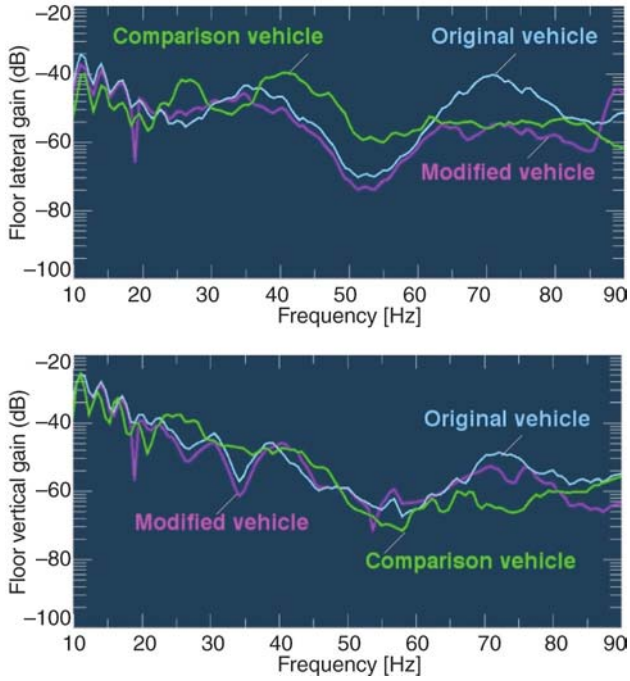


Fig. 26 Floor response gain of comparison, original and modified vehicles

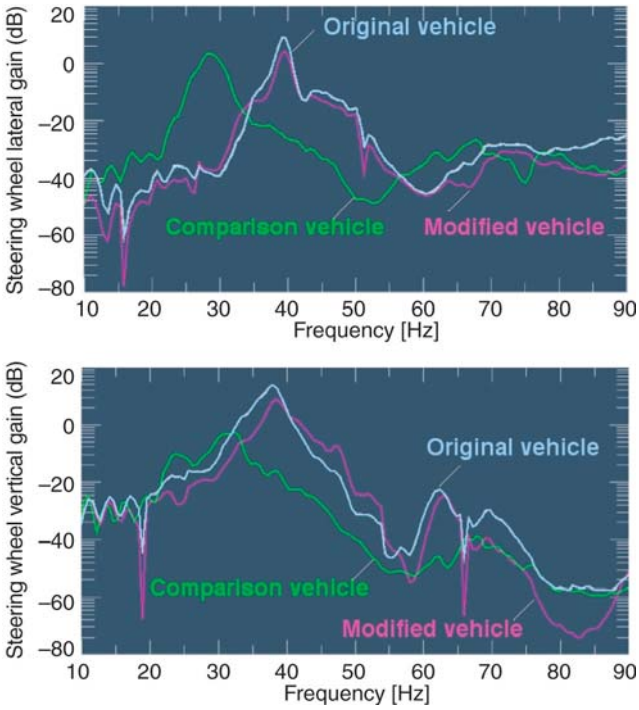


Fig. 27 Steering wheel response gain of comparison, original and modified vehicles

5.4. Results of Measuring the Effect of Modification Proposals

Based on the countermeasures obtained from the calculation results, actual car modifications were carried out, and the effects checked. The floor vertical vibration level is shown in Fig. 28, and steering wheel vertical vibration level in Fig. 29.

The improvement effect in the 70–90 Hz range and in the 35–40 Hz steering response are the same as the calculation results, and there was a reduction in vibration level.

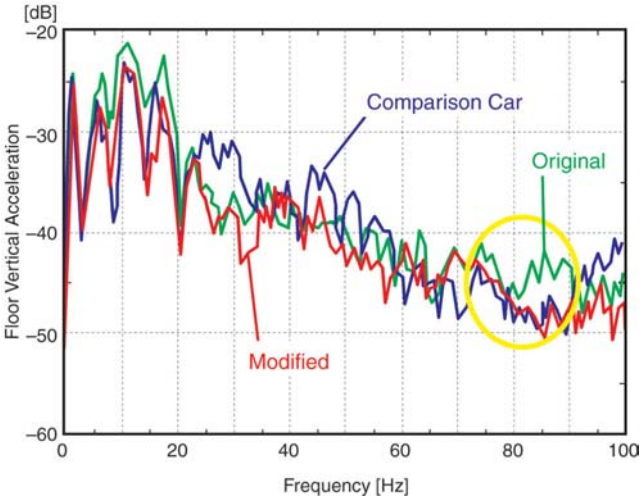


Fig. 28 Floor vertical acceleration

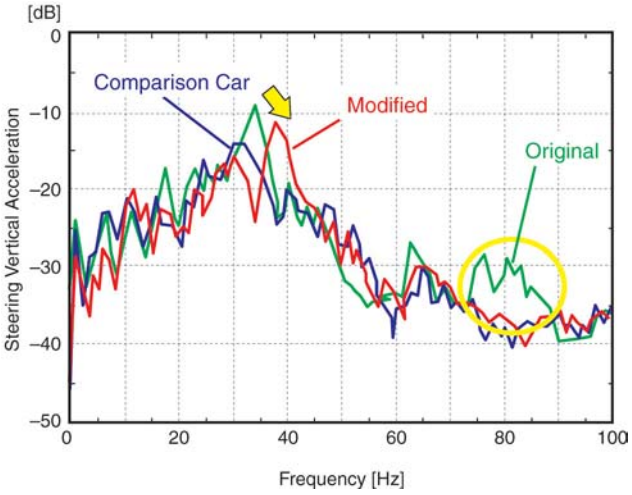


Fig. 29 Steering vertical acceleration

6. Summary

Through this research project, the following achievements were made, in the analysis of floor and steering vibration.

(1) Full vehicle analysis was tackled, using both experimental methods and simulation technology. It was possible to simulate modifications that address the major causes of vibration.

(2) Modifications were made according to the simulation results, and it was confirmed that the vibration reduction benefit tendency was the same as the simulations.

In addition, in this full vehicle analysis, experimental methods and simulation technology were used, and once again the advantages of each were brought to light.

· Advantages of experimental methods

It is possible to accurately check vibration levels.

It is possible to accurately understand the actual vibration generating mechanisms.

· Advantages of simulation technology

Vibration level simulations and mechanism analysis can be carried out without an actual car.

It is possible to study constructions that are impossible with an actual car.

In reality, a full understanding of the actual phenomenon was gained through experimental methods; mechanism analysis and study of modification proposals was carried out through both experimental methods and simulation technology. Then, the effects of the modifications where checked through experimental means. This type of development — a fusion of experimental methods and simulation technologies (hybrid development) — is very advanced in terms of the amount of time needed for analysis, analysis accuracy, and effective countermeasures.

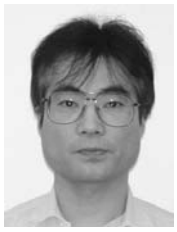
7. Acknowledgements

The authors would like to take this opportunity to offer their heartfelt gratitude to all those at LMS International who generously gave their support and cooperation in this research project.

■ Authors ■


Toshiya YOKOI


Kengo OKAMURA


Jiro NINOMIYA


Masaki NAGAHISA

Development of Metal Pushing V-Belt for Continuously Variable Transmission

Tooru YAGASAKI* Hideaki AOYAMA* Toshihiro SAITO*
Kazuo ISHII* Yoshinari OKADA* Mamoru ARIKAWA*

ABSTRACT

Metal pushing V-belt is the core technology of CVT. Up to the present, only Van Doorne's Transmissie b. v. has engaged in the mass production of this component. As a result of knowledge obtained from ongoing analysis of the power transmission mechanism, newly conducted measurements of block compression force for slack string and numerical analysis, Honda is the first automotive manufacturer to have independently developed the metal pushing V-belt for mass production. This newly developed metal pushing V-belt features reduced pitch diameter and increased power transmission, to achieve compactness of the CVT and a wider ratio range.

1. Introduction

Numerous companies have spent years in research on metal pushing V-belts, but to date Van Doorne's Transmissie, b.v., is the only company to have engaged in the mass production of this component. Several factors lie behind this: despite the fact that CVT has received attention as an ideal automotive transmission technology, numerous issues in the transmission capacity and efficiency, start-up performance and mass producability of metal pushing V-belt CVT have retarded the spread of the technology[(1)]; in addition, the almost complete absence of papers on metal pushing V-belt development has meant that no clear overview of all aspects of the technology is available[(2)], and VDT's strong patent rights[(3)] have discouraged other contenders in the field. Honda has successfully applied the knowledge accumulated over years of analysis of transmissions (joint research with Doshisha University)[(4)–(6)] and newly conducted measurements of clearance between elements and numerical analysis[(7)] to the development of an original metal pushing V-belt. This paper discusses the specifications of this belt, and gives an outline of the development process.

* Tochigi R&D Center

2. Development Concept

To achieve compactness, ensure start-up drive power, and improve fuel economy in CVT, the ratio range must be enlarged. For compactness, it is necessary to decrease the distance between shafts; when doing this, the minimum pitch radius must be decreased to maintain or increase the ratio range. However, decreasing the minimum pitch radius while transmitting the same amount of torque increases the necessary pressure of the pulley on the metal belt, increasing the average tension of the rings in operation and the amplitude of ring stress caused by bending when the belt winds around the pulley. These factors make a high degree of strength essential. The development concept for this project was therefore established as follows:

The metal belt would be configured so as to make it possible to decrease the minimum pitch radius, and at the same time to reduce the load on the rings and increase durability.

3. Structure of the Metal Belt / Component Specifications / Outline of Improvements

3.1. Structure of the Metal Belt

The metal belt is composed of several hundred elements and two rows of multiple rings (see Fig. 1).



Fig. 1 Metal pushing v-belt

3.2. Elements

The elements are movable blocks that run between the pulleys and support thrust. The elements transmit torque from the drive pulley to the driven pulley by pushing against each other along with the right and left rows of rings. Fig. 2 shows the structure of the elements and the names of each section.

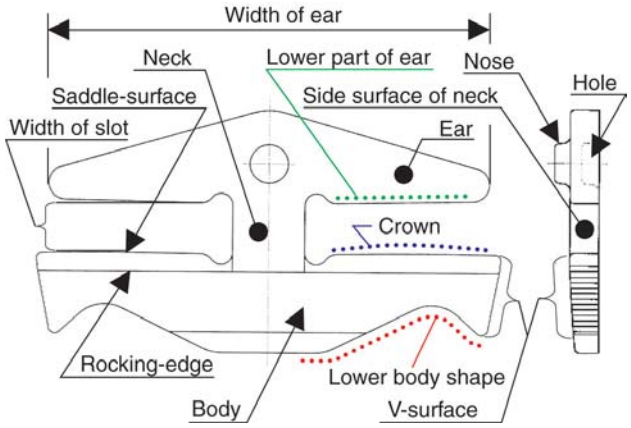


Fig. 2 Configuration of elements

3.2.1. V-surface length

When pulleys of the same shaft diameter are at minimum pitch, the lower sections of the V-surfaces of the elements of the former metal belt manufactured by other companies (termed “former elements” below) are brought into a position in which interference with the pulley shaft can easily occur. The V-surface in the newly developed elements is shorter than the lower section of the body, preventing interference between the V-surface and the pulley shaft, and enabling a reduction of diameter at minimum pitch. As a result, ratio range is 10% wider for the same distance between shafts and the same pulleys. Fig. 3 shows the relationship between pulley and element position at minimum pitch in the formerly used metal belt manufactured by other companies (termed “former belt” below) and the newly developed belt.

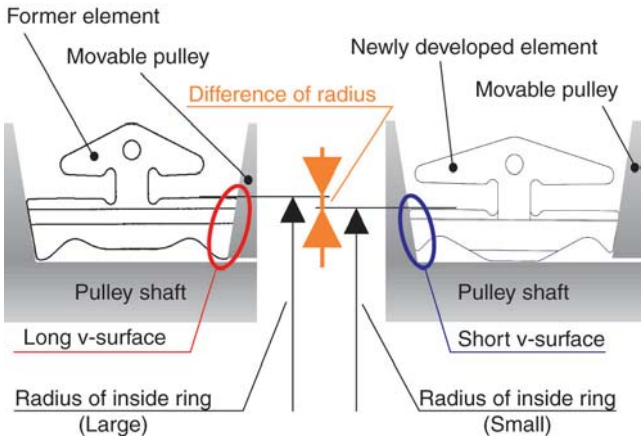


Fig. 3 Achievement of wider ratio

3.2.2. V-surface rigidity

The lower body shape was determined by element strength and V-surface friction characteristics, to ensure good friction characteristics by parallel displacement of the element V-surface and the pulley V-surface.

3.2.3. Groove on element V-surface (channel width/pitch)

To maintain actual contact length while shortening the V-surface length in the newly developed belt, the ratio of the channel on the V-surface was changed from 75% in the former belt to 45%, while maintaining the friction coefficient, lubrication performance, and wear resistance of the former belt.

3.2.4. Ear width

The ear width has been increased against the former element, to allow contact of the lower section of the ear from the ring crowning center to the pulley in order to reduce ring stress caused by contact with the outermost ring.

3.2.5. Slot width

Clearance between the lower section of the ear and the saddle surface has been increased in comparison to the former elements. In this configuration, the nose and hole of the element always make contact before the contact between the ring and the lower section of the ear, reducing contact stress with the ring.

3.2.6. Nose height

To prevent the nose leaving the hole and maintain alignment despite increases in total clearance between the elements (see 3.4.1) due to declining durability, the nose is higher and the hole is deeper in the newly developed belt than in the former elements.

3.2.7. Position and diameter of nose and hole

The center of the ear has been positioned to facilitate ease of formation creating a structure in which element nose and hole contact occurs before contact between the lower section of the ear and the rings. The diameter of the nose and hole has been increased and their fillet profile (radius and taper angle) at the base has been changed, increasing their strength.

3.2.8. Element contact surface

When power is transmitted by the elements aligned in strings, the points at which any element is in contact with the element in front and behind are limited to both sides of the ears and from the lower section of the neck to the center of the rocking edge. This configuration makes it possible to maintain good alignment of the elements in strings, and to stabilize belt behavior. Furthermore, press processing has made it easy to control thickness and die quality.

3.2.9. Element thickness used to regulate clearance

Elements of 1.6 mm thickness are used to regulate clearance, as against the 1.4 mm elements used in the former belt. This has increased element strength while maintaining the ability to adjust clearance between elements (see 3.4.1) found in the former belt.

3.3. Rings

The ring assembly features two rows of multiple rings in layers. In the section of the belt wrapped around the pulley, these rings push the elements against the pulleys, and control the element path between the two pulleys (strings). Fig. 4 shows the structure of the rings and the ring assembly, and gives the names of the various parts.

3.3.1. Width

It is well known that when pulleys are rendered movable, misalignment generally occurs.[(2)] The ring width has therefore been reduced to absorb the increased misalignment between the pulleys generated by increasing the speed ratio range. The amount of overhang with the element saddle has been set within a range that prevents a negative effect on durability.

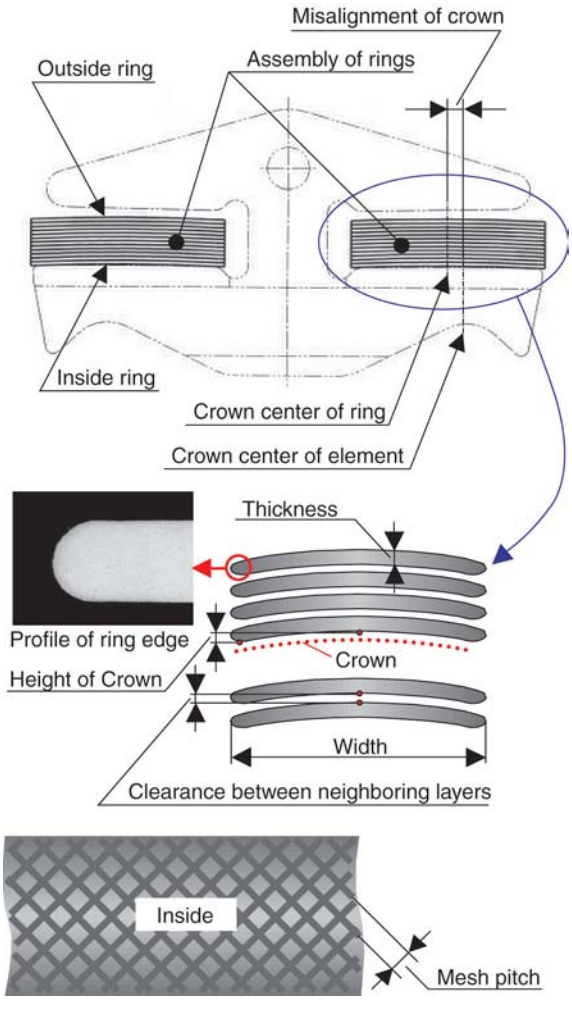


Fig. 4 Structure of rings and ring assembly

3.3.2. Edge shape

To reduce the load on the rings when the ring edge is in contact with the side surface of the element neck or the pulley V-surface, the ring edges have been given a fully rounded shape.

3.3.3. Mesh shape

The mesh shape has been set at an even pitch to maintain the oil film between the rings, ensure centering and ease of manufacture of assembly.

3.3.4. Crowning shape

Offsetting the ring and element crowning centers has achieved stable behavior of the power directed towards the pulley V-surface by the layers of rings when the metal pushing V-belt is in operation. This means that the rings always approach the pulley V-surface, which is smoother than the element necks. Because of this, the frequency of ring edge contact with the element neck (a non-continuous surface) has been minimized, preventing ring edge wear and damage.

3.3.5. Curvature

When the rings are set up in the assembly after curving and shaping in the production process, sections of the ring edges contact the pulley V-surface and the edge of the element neck, affecting the durability of the belt. Because the crowning center of a ring in the assembly does not correspond with those of other rings above and below, centering becomes unsuitable, and abnormal wear can easily occur to inner and outer surfaces, or ring edges. To prevent this, a new ring curvature measurement method was developed, and the bending of the ring in production is controlled within a specified range.

3.3.6. Layer clearance

To increase ring durability and maintain lubrication, an optimum range was set for clearance between rings.

3.4. Belt Assembly

The metal pushing V-belt is composed of several hundred elements and two rows of rings, and the accuracy of the total assembly is considered to be the sum of the accuracy of each element and ring assembled.

3.4.1. Total clearance between elements

If the total clearance between elements is large, the range of slip and the slip velocity of the elements in the drive-side pulley increase, causing wear of the pulley V-surface (see 4.1.2, Fig. 7).

On the other hand, if the clearance is too small it exerts a negative effect on efficiency, and therefore the optimum range was set. The space in which the thickness gauge is inserted in Fig. 5 is the total clearance between elements.

3.4.2. Difference between left and right total clearance between elements

When there is a large difference between left and right total clearance between elements, it causes abnormal contact between the pulley V-surface and the element V-surface, leading to wear. To prevent this, the difference has been controlled within a specified value.



Fig. 5 Total clearance of elements

3.4.3. Difference between inner length of left and right rings

If the inner circumferences of the left and right rings differ, one side of the ring is put under excessive tension, with a negative effect on durability. Differences in circumference have been controlled within a specified limit to prevent this phenomenon.

3.4.4. Average difference of thickness between elements

When vertical variations occur in the thickness of elements, the saddle surface pushes the rings up, placing an excessive strain on them. This causes the outermost ring and the lower section of the ear to come into contact and their behavior to become unstable, which negatively affects the life cycle of the belt. Horizontal variations cause the side surface of the element neck and the ring edge to come into contact, leading to the possibility that high surface pressure will be exerted on sections of the ring edge. To prevent these occurrences, the average difference of thickness has been controlled within a specified range.

4. Kinematic Analysis of Element

Measurements of clearances between elements in slack strings were taken to analyze the structure of the metal pushing V-belt, and an appropriate total clearance between elements was established on this basis.

4.1. Establishing Total Clearance Between Elements

4.1.1. Changes in clearance between elements in operation

Fig. 6 shows a graph representing changes in behavior with different settings for total clearance between elements. The vertical axis represents clearance between elements during operation, and the horizontal axis represents time. The clearance between elements during operation achieves its maximum value in the string running from the driven pulley to the drive pulley, and then suddenly decreases at the entrance to the drive pulley. It increases over the drive pulley again, and then suddenly decreases and reaches zero in the middle of the drive pulley. Element clearance during operation shows a tendency to increase with increases in total element clearance.

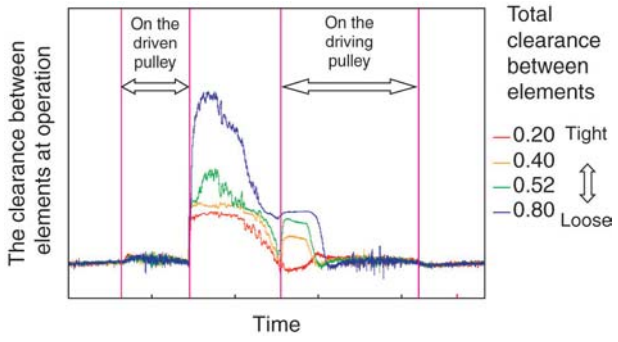


Fig. 6 Clearance between elements at operation

4.1.2. Relative slip velocity between belt and pulley

Fig. 7 is a graph showing calculation results for relative slip velocity of the belt and the pulley when the clearance between elements suddenly reaches zero in the middle of the drive pulley during operation.

The vertical axis shows the relative slip velocity between belt and pulley, and the horizontal axis shows total clearance between elements. The relative slip velocity between belt and pulley is around zero until point p for total clearance between elements, then increases after point q, with the distance between points p and q representing the border for slip velocity increase. In the newly designed belt, after point q the slip velocity of the belt relative to the pulley increases, causing wear of the element and pulley V-surfaces to occur more easily. To take this into account, an appropriate range was established for the total clearance between elements in the belt assembly.

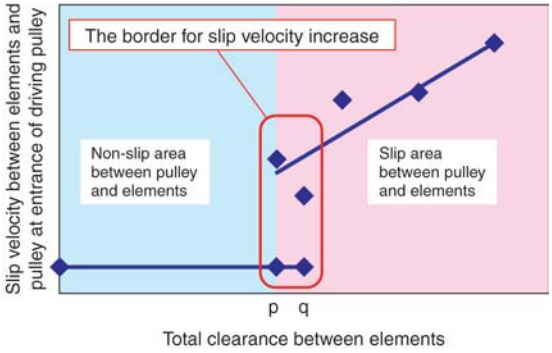


Fig. 7 Slip velocity between elements and pulley on driving pulley

5. Durability and Reliability

To enable belt strength to be increased, various durability tests were conducted, followed by stress simulations using the same conditions. In addition, a new method for evaluation of inclusions in materials was developed.

5.1. Belt Behavior/Stress Simulations

The simulation method has been described in a previous paper[7], and details will therefore be omitted here.

5.1.1. Belt strength and durability

Fig. 8 shows an S-N diagram for the metal pushing V-belt. The vertical axis represents the amplitude of stress on the innermost ring, and the horizontal axis represents the number of bending cycles for the belt. Stress in the newly designed belt was analyzed against the former belt under two standard loads. Results show lower stress in the newly designed belt.

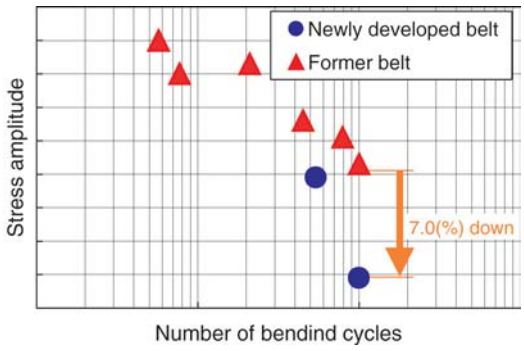


Fig. 8 S-N diagram of CVT belt

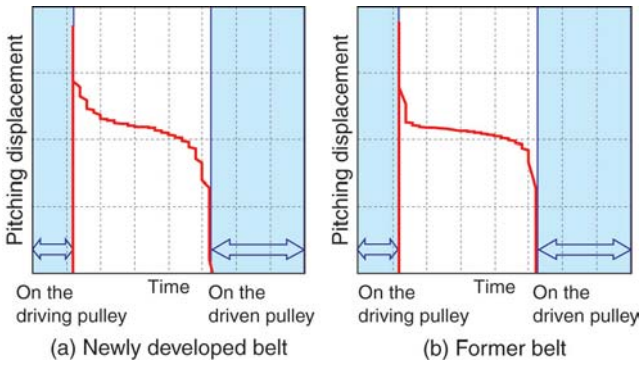


Fig. 10 Element pitching behavior

5.1.2. Causes of difference in ring stress

Fig. 9 compares ring stress waveforms for the innermost rings of the former and the newly designed belt under identical conditions. The difference in the stress waveforms at points e and f is conspicuous, which represent the change in stress in the section wrapped around the driven pulley. The waveform for the newly designed belt changes smoothly at the entrance and exit of the pulley. If we compare the rate of change of element pitching behavior, we see that the change in the angle of pitching displacement around the entrance and exit of the pulley is smaller in the newly designed belt (points g and h in Fig. 9). Fig. 10 shows change in the angle of pitching displacement in the section running between the exit of the drive pulley and the entrance of the driven pulley.

The rings receive a reactive force from the change in the angle of pitching displacement, and because of this the operating load of the rings is smaller in the newly developed belt, and ring stress is therefore reduced. This is because the shorter V-surface length has brought the distance between the rocking edge and the middle point on V-surface closer.

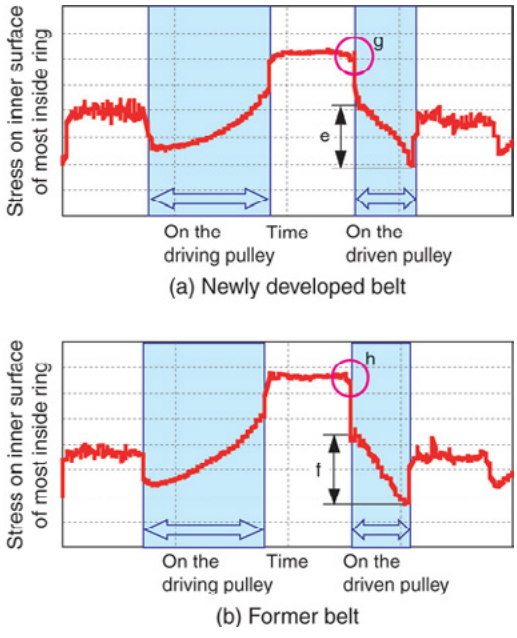


Fig. 9 Ring stresses

5.1.3. Element nose strength

The role of the nose is to maintain good alignment during operation, but excess load can cause damage to this section. The limit loads which produced damage had already been clarified in the element tests to be described below. Because of this, it was known that estimation of the nose load during operation was an important factor in judging belt durability. This load is affected by the clearance between nose and hole, and by the width of the slot. Fig. 11 shows operating loads on the nose and hole during belt operation. Nose-hole contact was observed in the string on the side on which pushing force between the elements was not generated. The maximum load on the nose occurs around the pulley entrance and exit.

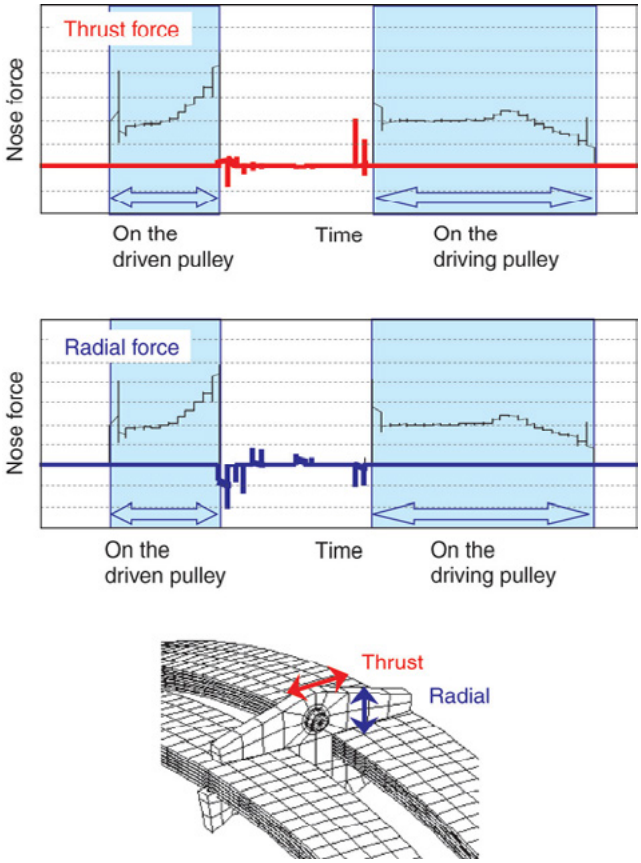


Fig. 11 Nose-hole contact

Fig. 12 shows the maximum load on the nose when the clearance between nose and hole is varied. These results show that when clearance exceeds a specific value, the load on the nose suddenly increases. This demonstrates that increasing clearance has a negative effect on belt alignment. The influence of slot width on nose load is shown in Fig. 13. These results show that when slot width exceeds a specific figure, nose load increases, but ring stress decreases.

The results described above made it possible to reduce ring stress by setting optimum values for clearance between the nose and hole and the slot width.

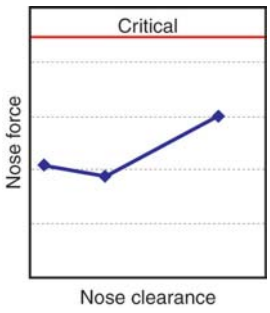


Fig. 12 Nose-Hole reaction forces by the clearance

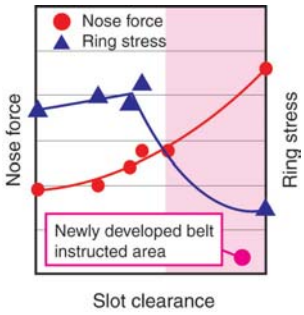


Fig. 13 Nose-hole reaction force and ring stress by element slot clearance

5.2. Element Strength

The hyper-eutected steel used for the elements is quenched and tempered to obtain the required tenacity and fatigue strength, but the heat treatment conditions necessary to obtaining these characteristics had been insufficiently studied. The test model shown in Fig. 14 was therefore used to conduct strength and fatigue tests on the nose in isolation, enabling evaluation of effects of heat treatment and molding accuracy on fatigue strength.

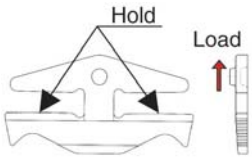


Fig. 14 Test mode

Fig. 15 shows the effect of varying quench time, and demonstrates that fatigue strength drops with increased quench time.

The cause of this is thought to be the growth of crystal grains and the precipitation pieces shown in Fig. 16. These precipitation pieces were assayed as cementite (Fe_3C). Fig. 17 shows a photograph of the fracture surface after fatigue tests, demonstrating that a long quench time causes a grain fracture surface. Fig. 18 demonstrates the effect of nose shaping accuracy and fatigue strength.

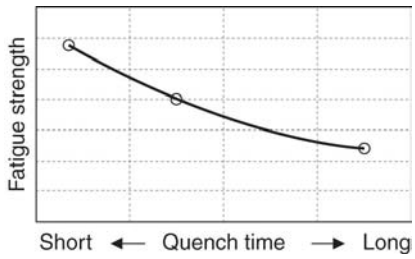


Fig. 15 Relationship between quench time and fatigue strength

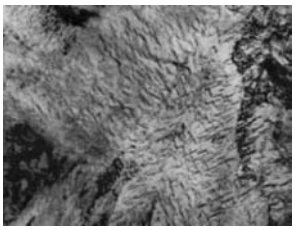


Fig. 16 Precipitation pieces in a phase

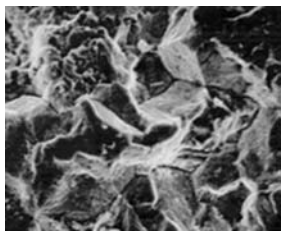


Fig. 17 Fatigue fracture surface for long quench time

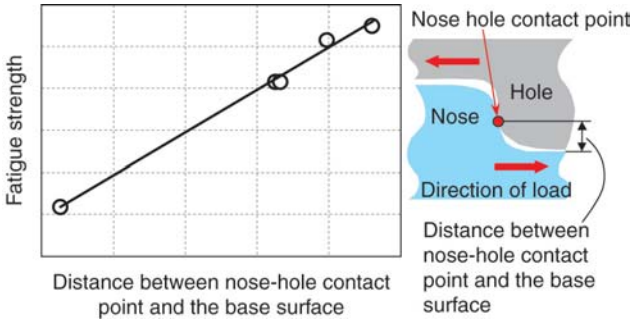


Fig. 18 Relationship between distance between nose-hole contact point and the base surface and fatigue strength

Strength is mainly affected by the position of contact between nose and hole, and when target accuracy is not achieved, fatigue strength drops. These results enabled designers to establish the optimum heat treatment conditions and the required level of accuracy in forming the nose, and assisted in deciding on the final specifications of the elements. Fig. 19 shows the results of durability tests on the belt assembly, and these show a good correlation with the results of tests of element fatigue strength. The final specifications necessary to ensuring fatigue strength in the nose were established on the basis of these results.

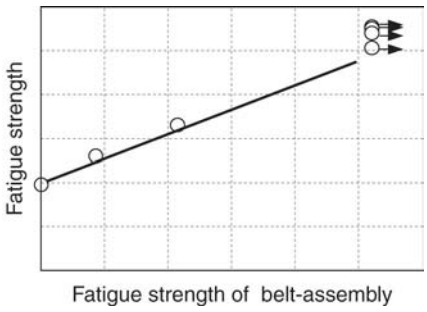


Fig. 19 Relationship between fatigue strength of belt-assembly and fatigue strength of elements

5.3. Ring Strength

The rings in the newly developed belt are 0.18 mm thick. This is to ensure pliable bending in the rings so that there will be no resistance when the belt wraps around the pulleys, or put another way, to minimize the bending stress when the belt wraps around the pulley. High strength to prevent failure under tension and high fatigue strength to resist continuous bending is required from these extremely thin rings. Taking these requirements into consideration, 18Ni maraging steel was selected as the material for manufacture of the rings because it is one of the highest strength materials available. To further increase the superior characteristics of 18Ni maraging steel in the newly developed belt, the non-metallic inclusions in the material were reduced in size, and the heat treatment conditions were improved. This has significantly increased fatigue strength.

5.3.1. Inclusions

The rings in metal pushing V-belts require strength at ultra-high cycles. Research to the present has demonstrated that at high cycles below 10^7, the surface is the initiation point of fractures in high-strength steel, while at ultra-high cycles above 10^7, inclusions in the material are the sources of fatigue fractures[8]–[10]. In maraging steel, Ti (C, N) inclusions are the point of origin of fractures, and fatigue fractures at 10^6 have been reported[10]. However, the fatigue behavior of maraging steel at ultra-high cycles has not been sufficiently clarified. For this reason it was judged necessary first to test the fatigue behavior of the material at ultra-high cycles. The upper limit for conventional fatigue tests using rotational bending and stretching pressure is approximately 50 Hz. For this reason, twenty days is required to reach 10^8 cycles, and time restrictions make evaluations in this ultra-long longevity area extremely difficult. However, it has recently become possible to evaluate ultra-high cycle fatigue using ultrasonic fatigue tests[11], [12]. This method was used in the development of the new belt to clarify the fatigue behavior of maraging steel at ultra-high cycles. The results of these tests established a limit value for the diameter of inclusions, below which they would not negatively affect fatigue at ultra-high cycles. Because the bending stress on the ring is dispersed around the entire circumference, as stated above there is a possibility of fractures originating in the inclusions, and therefore evaluation of the inclusions adds another level of reliability. Inclusions are normally evaluated by optic microscopy of the fracture surface[13], [14], but this method is limited in its powers of resolution. Ability to detect inclusions was therefore increased using the dissolution method. The solvent used was a 10% methanol bromide solution. 5 g of the material for evaluation was dissolved, and the inclusions trapped in the mesh after filtering were observed with an Scanning Electric Microscope (SEM). Fig. 20 shows an SEM photograph of an inclusion.

Depending on the size of the inclusion, the area of the projection surface affects fatigue, and the square root of the surface is generally utilized as a parameter in evaluating inclusions[10]. This development utilized the following equation to find d*, the diameter of a circle with the same projection surface area, and used this as a parameter.

$$d^* = 2\sqrt{\frac{ab}{\pi}} \quad (1)$$

Where a and b are the lengths of the long side and the short side of the inclusion respectively.

The filtered inclusions were all subjected to image processing and d* was found for each. Fig. 21 is an extreme value statistical graph with plots of inclusion diameter d* found through the dissolution-filtration method described above for steel K (the ring material used in the former belt) and steel L (the ring material used in the newly developed belt).

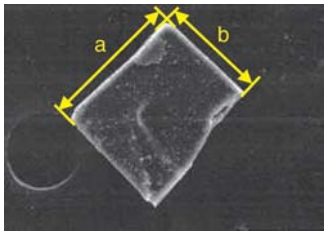


Fig. 20 SEM photograph of Ti (C, N) inclusion

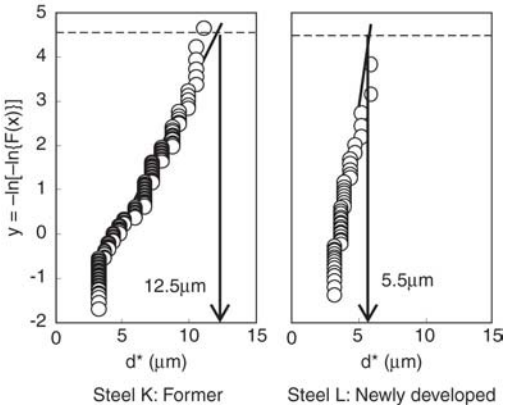


Fig. 21 Diameter distribution of non-metallic inclusions

As this graph shows, it is possible to predict the maximum diameter of the inclusions occurring in steel K and steel L using the bilateral exponential distribution[15]. To predict the maximum diameters it is necessary to establish the recurring section for the extreme value statistics, and given that the aim here was 99% certainty, the recurring section was set at y = 4.6. Reading the values at y = 4.6 from the graph, we find predictions of 12.5 μm and 5.5 μm for maximum diameter of inclusions in steel K and steel L respectively. By means of this sequential processing, it is possible to predict the maximum diameter of inclusions to a high degree of accuracy. Fatigue tests for these steels were conducted using ultrasonic fatigue test equipment. Stress during the tests was calculated using the results of measurements of displacement of one edge of the test piece using a whirlpool-type displacement meter[11]. Fig. 22 shows an S-N diagram of test results. High-strength steels normally generate S-N diagrams with no fatigue limit in the ultra-high longevity area[9]–[11], and these test results demonstrate the same tendency. The results show that steel L has superior fatigue strength to steel K at 10^9 cycles. Furthermore, the results of SEM observation of the fatigue fracture surfaces show that all fractures in steel K are initiated at inclusions. Fig. 23 shows representative photographs.

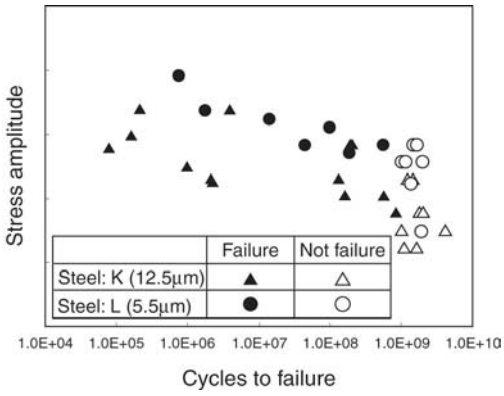
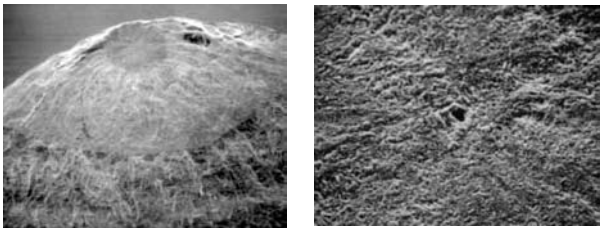


Fig. 22 S-N diagram by ultrasonic fatigue test



(a) Fracture face (b) Ti (C,N) at crack initiate point

Fig. 23 SEM photograph of fracture face

Analysis has confirmed the presence of Ti, and it has been demonstrated that the crystals are rectangular, so it is clear that Ti (N, C) inclusions initiate fractures. Observing the fatigue fracture surfaces for steel L with an SEM indicates that fractures originating on the surface and fractures initiated by inclusions both occur in this material. Whichever the initiate point, the S-N diagram shows the same longevity. It is clear, therefore, that if predictions of maximum inclusion diameter using extreme value statistics are 5.5 μm or less, as for steel L, it does not negatively affect fatigue longevity. Production process control was therefore initiated to control the diameter of inclusions in ring materials.

5.3.2. Heat treatment

After the ring materials have been welded into cylindrical shapes, they are cut and rolled into rings. The materials then go through solution heat treatment to achieve homogeneity of structure when rolled, correction processing (to supplement the circumference), and finally aging and nitriding to produce the finished ring. Conditions for solution heat treatment and aging have been considered optimum to produce the maximum hardness and stretching strength after final processing. However, because the most important characteristic for the rings used in metal pushing V-belts is fatigue strength under constant bending, it is necessary to optimize processing conditions from this perspective. High hardness is an important factor in fatigue characteristics, but the residual compression stress produced on the surface of the material by nitriding is more effective. Therefore conditions were optimized on the basis of the results of tests on the relationship between the residual surface stress produced by nitriding and heat treatment conditions. Residual surface stress was measured using X-ray analysis. The relationship between the temperature for solution treatment directly after rolling and the residual stress on the surface of the material was investigated, and Charpy V-notch testing were used to determine the effect of solution temperature on tenacity. The results are shown in Fig. 24.

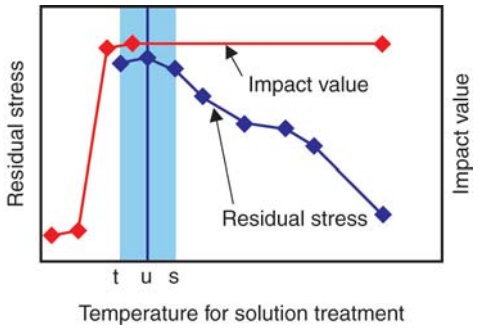


Fig. 24 Relationship between solution treatment condition and residual stress or Charpy impact value

It is clear from these results that residual stress varies with solution conditions, and that the maximum value of residual compression stress occurs below the temperature represented by point s on the diagram. The results of Charpy V-notch testing show that when solution temperature is low, residual work hardening causes tenacity to drop, with impact value dropping suddenly below the temperature represented by point t on the diagram. These results led to the temperature shown at point u in the diagram being selected as the solution heat treatment temperature allowing residual surface stress and tenacity to be balanced.

The newly developed rings and the former rings were put through fatigue tests using the rotational bending fatigue test apparatus shown in Fig. 25. Results are shown in Fig. 26, with tension as the load parameter for the vertical axis.

An example of a former ring which fractured at 10^4–10^5 cycles is shown in Fig. 27. As the Figure shows, a Ti (C, N) inclusion was the initiate point of the fracture. The newly developed rings, by contrast, did not fracture from inclusions, and demonstrated a 30% improvement in fatigue strength over the former rings in the 10^8 cycle ultra-high longevity area.

The results discussed above demonstrate that controlling the diameter of inclusions below the point at which they begin to affect fatigue longevity and optimizing heat treatment conditions has significantly increased fatigue strength.

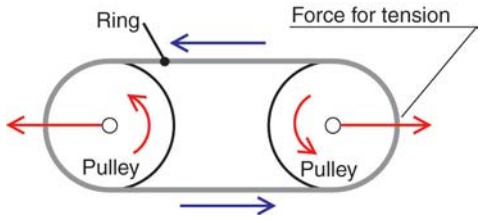


Fig. 25 Illustration of the ring fatigue test

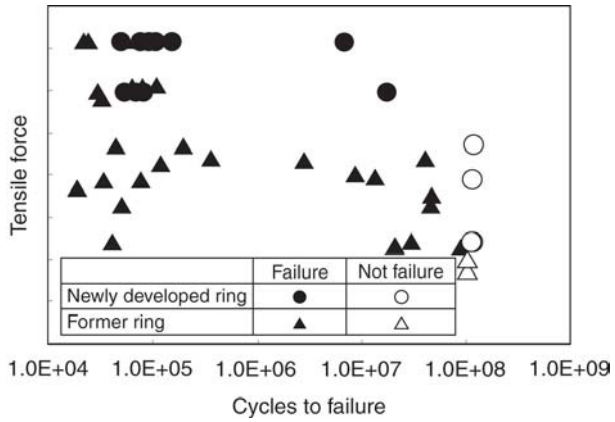


Fig. 26 Comparison of fatigue behavior in former and newly developed rings

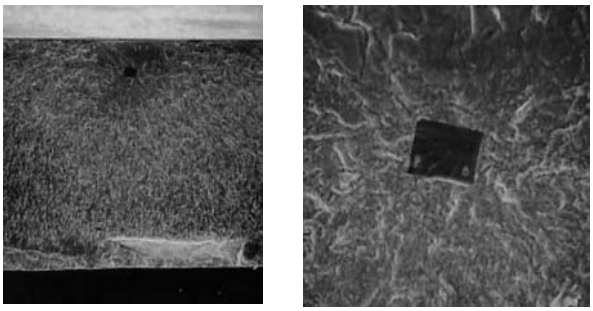


Fig. 27 SEM photograph of fracture face

6. Conclusion

Honda has developed and successfully mass-produced an original metal pushing V-belt for CVT. This development has made possible the reduction of minimum pitch radius for pulleys, reduced the load on the rings and increased fatigue strength. The newly developed metal pushing V-belt has the following characteristics:

(1) Total clearance between elements has been fixed below a specified value. If total clearance between elements is too large, element and pulley slip velocity in the drive-side pulley suddenly increases, causing wear to the pulley V-surface.

(2) The element V-surface has been shortened to increase the speed ratio range. The shorter V-surface has resulted in a reduction in pitching moment and stress on the rings in the pulley contact area.

(3) Increased slot width and the establishment of an optimum range for nose-hole clearance has ensured that the nose and hole will make contact before the lower section of the ear and the ring, resulting in a reduction of stress operating on the ring.

(4) Taking into account the significant effect of heat treatment of the elements (mainly quench time) and accuracy in formation of the nose and hole (mainly nose-hole contact position) on the fatigue strength of the nose and hole, treatment and formation have been optimized.

(5) Dissolution in solution and extreme value statistical analysis were combined as a method of evaluating inclusions in ring materials, enabling high-accuracy prediction of the maximum diameter of inclusions. Fatigue strength in the newly developed rings has been significantly increased by controlling the maximum diameter of inclusions to a size at which they do not affect fatigue strength.

(6) The finding that residual compression stress on the surface of the ring changes with variations in solution conditions enabled the establishment of heat treatment conditions balanced with tenacity, leading to increased fatigue strength in the rings.

7. Afterword

The success of this development was based on research guidelines obtained from studying the existing belt mass-produced by Van Doorne's Transmissie, b.v. Theoretical studies of shape and further research in production technologies will be important factors in future evolution.

In conclusion, the authors would like to express their deep debt of gratitude to the many people who provided assistance in the course of this project, and to Van Doorne's Transmissie, b.v., for their understanding of Honda's intention to mass produce its own metal pushing V-belt.

References

(1) Osono, K., Aoki, T.: "Development of a Metal Pushing V-belt for an All-electronically-controlled CVT," HONDA R&D Technical Review, Vol. 8, pp. 21–33 (1996)

(2) Hendriks, E., et al.: Aspects of a Metal Pushing V-Belt for Automotive Cut Application

(3) Van Doorne's Transmissie, b.v.: Catalog

(4) Kanehara, S., et al.: "Research on Pushing Block-type Metal Belt Transmission Mechanisms," HONDA R&D Technical Review, Vol. 7, pp. 49–67 (1995)

(5) Yoshida, H.: "A Study of Forces Acting on Rings for Metal Pushing V-Belt Type CVT," SAE Paper 970686

(6) Fujii, T., et al.: "Research on CVT Utilizing Metal Pushing V-Belt," JSAE Pre-publication Collection, No. 975, pp. 269–272 (October, 1997)

(7) Saito, T., et al.: "Development of Stress Simulation Techniques for CVT Metal Pushing V-Belts," HONDA R&D Technical Review, Vol. 13, No. 1, pp. 125–130 (2001)

(8) Emura, H., et al.: "Fatigue Strength Characteristics of High-strength Steel", Transactions of Japan Society of Mechanical Engineers, Vol. 55, No. 509, A, pp. 45–50 (1989)

(9) Abe, T., et al, "Surface and Internal Fatigue Fractures in High-strength Steel," Spring Technology Association, 1998 Spring Lecture Series Collection, pp. 17–20 (1998)

(10) Murakami, Y., et al.: "The Effect of Minute Defects and Inclusions on the Fatigue Strength of Maraging Steel," Transactions of Japan Society of Mechanical Engineers, Vol. 53, No. 492, A, pp. 1482–1491 (1987)

(11) Ishii, H., et al.: “Evaluation of Longevity and Fatigue Strength of Steel Alloys Used in Mechanical Structures Using Ultrasonic Fatigue Testing,” Transactions of Japan Society of Mechanical Engineers,. Materials Division Lecture Series, pp. 591–592 (1999)

(12) Ishii, H., Yagasaki, T., Akagi, H.: “Evaluation of giga-cycle fatigue properties of some maraging steels by intermittent ultrasonic fatigue testing,” Proceedings of the International Conference on Fatigue in the Very High Cycle Regime, pp. 89–96 (2001)

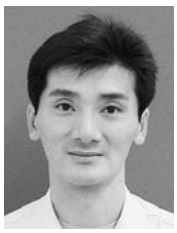
(13) Microscopic Testing Method for the Non-metallic Inclusions in Steel, JIS G 0555

(14) Standard Practice for Determining the Inclusion Content of Steel, ASTM E 45

(15) Shibata, T.: “Development of Extreme Value Statistics and Application to Materials Problems,” Sanyo Technical Report, Vol. 3, No. 1, pp. 8–16 (1996)

■ Authors ■


Tooru YAGASAKI


Hideaki AOYAMA


Toshihiro SAITO


Kazuo ISHII


Yoshinari OKADA


Mamoru ARIKAWA

Application of Metal Pushing V-Belt Stress Simulation with CVT Pulley Stiffness

Toshihiro SAITO* Takemasa OKANO*

ABSTRACT

A simulation method was developed allowing simultaneous evaluation of dynamic behavior and ring stress for the estimation of the durability of metal pushing V-belts for CVT's. The high rotational speed range of the CVT is simulated utilizing the finite element method used in crash analysis. This paper focuses on dynamic behavior of the pulley, and the simulation method, which was modified to allow the pulley stiffness to be reflected. The pulley stiffness values are found by applying static loading to the three-dimensional FEM model. As a result, it is found that the flexional stiffness affects the ring impact stress at the pulley entrance and exit. Furthermore, the mechanism of contact between the ring edge and pulley surface or the element due to the ring misalignment caused by the pulley flexion is clarified. For the first time, these results make it possible to obtain design guidelines for the pulley stiffness that includes consideration of belt durability.

1. Introduction

The increasing demands for additional environmental compliance by automobiles have caused manufacturers to turn their attention to the continuously variable transmission (CVT) as a transmission technology that simultaneously achieves improvement in both performance and fuel economy. CVT performance is characterized by quietness and smooth acceleration without shift shocks, while it achieves fuel economy superior to that of other automatic transmissions by using integrated control with the engine to maintain a rotational speed range with high combustion efficiency. As the need to increase the transmission capacity of the CVT continues to rise, however, it has also become essential to realize the contradictory goal of reducing the weight of the CVT. As the belt and pulley assembly accounts for a major proportion of CVT weight, the issue will be how to assure durability of this assembly while making it lighter in weight. This paper describes the modification of our previously reported technique for simulation of metal belt behavior and stress[1] to give it the capability to account for pulley flexional stiffness. This has made it possible for the first time to define the influence of pulley flexional stiffness on belt strength, and this result is also reported here.

2. Development Aims

Fig. 1 shows the main section of the CVT used in this project. The driving torque is shifted and transmitted from the drive pulley to the driven pulley by a metal belt.[2), (3)]

* Tochigi R&D Center

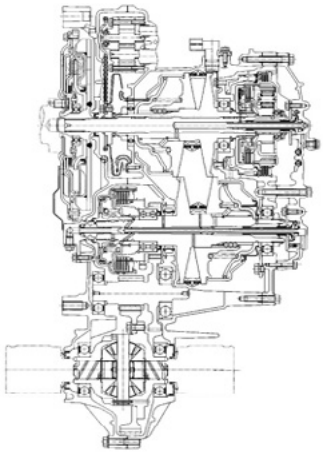


Fig. 1 CVT main section

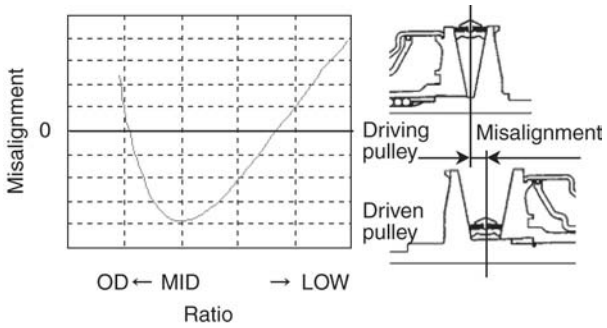


Fig. 2 Belt misalignment variation by ratio

When the metal belt wrapped around the drive pulley and driven pulley is in operation, its center does not move within a single plane, but rather displays a slight out-of-plane movement. This out-of-plane displacement of the metal belt is termed misalignment. Durability tests have shown that greater misalignment reduces the life of the metal belt. This misalignment is not reduced to zero even when the pulleys are defined as rigid bodies (Fig. 2), and the amount of misalignment is determined by the distance between the pulley axles and the transmission ratio.

Furthermore, the rigidity of the actual pulleys is limited, so it is crucial to take their deformation into account when considering misalignment.[4] As things presently stand, however, the relationship between the amount of misalignment during CVT operation and the strength of the metal belt is not sufficiently established.

Given the above, the development aims were defined as follows:

(1) To clarify misalignment during CVT operation and
(2) To explain the influence of pulley rigidity on belt strength.

3. Misalignment

3.1. Misalignment during CVT Operation

Due to the difficulty of measuring belt alignment during operation, the first step taken was to use previously reported simulation methods to study this behavior.[1] Fig. 3 shows the analysis model used for the simulation. The model was simplified to use 280 elements and three rings in each layer in order to reduce the computation time, as the objective in this case was to determine the influence of pulley rigidity.

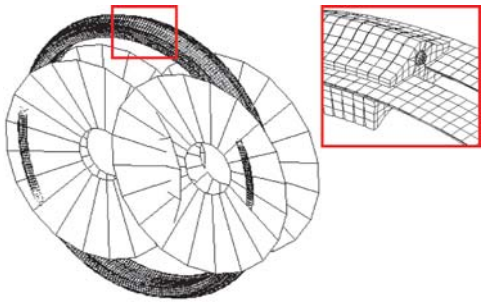


Fig. 3 Metal pushing V-belt Model

Both the drive pulley and the driven pulley were defined here as rigid bodies, and the pulley deflection was not taken into account. The initial condition was set for only a specified amount of misalignment. Points a, b, c, and d in Fig. 4 represent boundary points on the belt track, while DR is the section b-c wrapped around the drive pulley and DN is the section d-a wrapped around the driven pulley. With this arrangement, the misalignment of an element is a fixed value in the sections wrapped around the drive pulley and the driven pulley, and the element displays a sudden change in behavior immediately before the drive pulley entrance. The alignment reference value of zero designates the center of the belt around the opposing side of the pulley on the driven side.

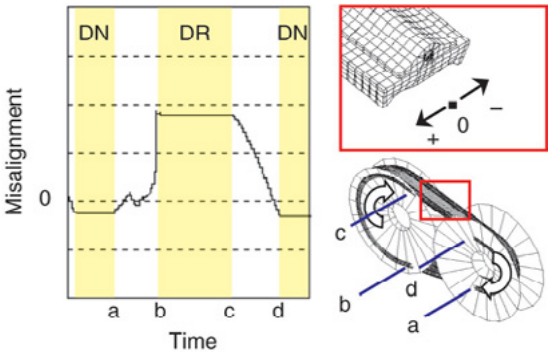


Fig. 4 Misalignment of element

Meanwhile, as shown in Fig. 5, misalignment of the left and right rings differs from misalignment of the elements. The ring moves smoothly over the saddle surface while maintaining a constant relative speed differential.

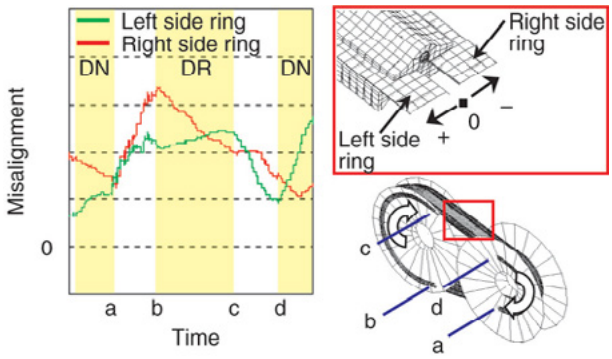


Fig. 5 Misalignment of rings

3.2. The Influence of Ring Stress

Fig. 6 shows the stress waveform for the left and right side ring edges at this time. It is apparent that the rings are influenced by the misalignment of the elements, so that the left and right side rings display different stress conditions. The ring edges show even greater stress.

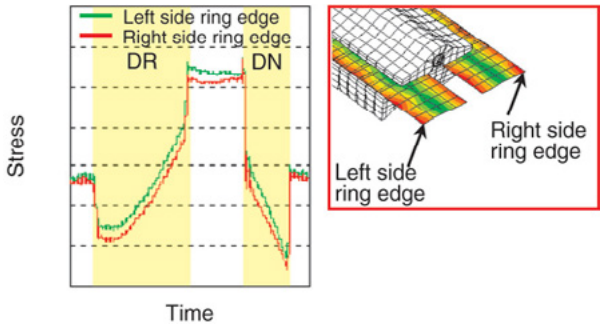


Fig. 6 Ring stress distribution

4. Pulley Flexional Stiffness

4.1. Pulley Rigidity and Misalignment

In order to investigate the influence of pulley rigidity, the next step was to insert rotational springs (Fig. 7) representing pulley flexional stiffness as an addition to the previously-reported simulation model.[1] The flexional stiffness was calculated by creating a three-dimensional finite element (FEM) model of the pulley and applying a belt load statically. The pulley displayed deformation in both radial and circumferential directions according to its rigidity. The greatest flexional deformation, however, was in the radial direction. Consequently, attention was focused solely on pulley deflection.

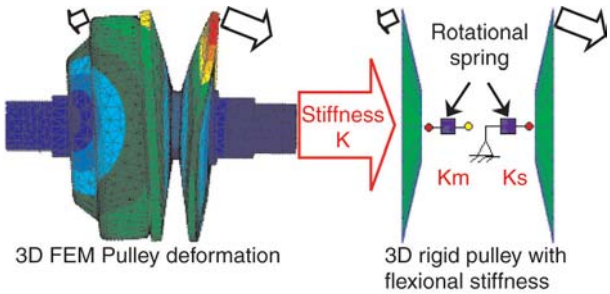


Fig. 7 Analysis model

Fig. 8 shows element misalignment with reference to flexional stiffness. The pulley rigidity here only takes into account the drive side, where deflection is greatest. Different values are set for the left and right sides of the pulley, since the left and right of the pulley section ordinarily differ in shape. It is apparent that, as a result, the amount of misalignment when the belt is wrapped around the drive pulley is greater than it was with the rigid pulley above.

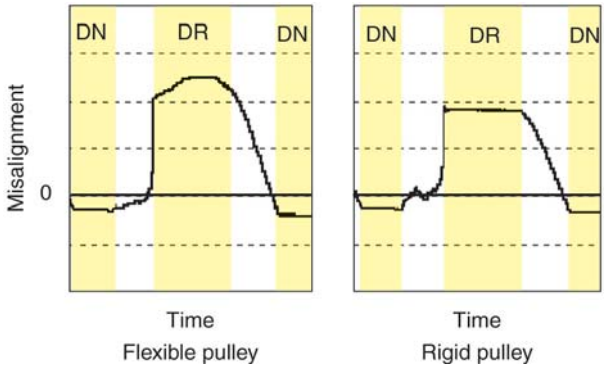


Fig. 8 Influence of flexibility on misalignment

4.2. Parameter Study of Pulley Rigidity

The next step was to examine how ring stress changes under the effect of pulley rigidity. Fig. 9 shows the combinations of left and right pulley rigidity values in p through u as used in the parameter study.

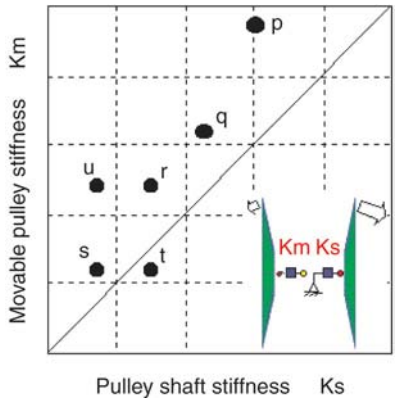


Fig. 9 Pulley stiffness used in parameter study

4.2.1. Absolute value of pulley rigidity

When only the absolute value is changed and the ratio of left and right pulley rigidity is kept the same, then the stress amplitude in the ring increases as the rigidity is raised. Points A, B, C, and D in Fig. 10 represent locations in the lateral direction on the ring. The maximum values for stress in the circumferential direction are plotted.

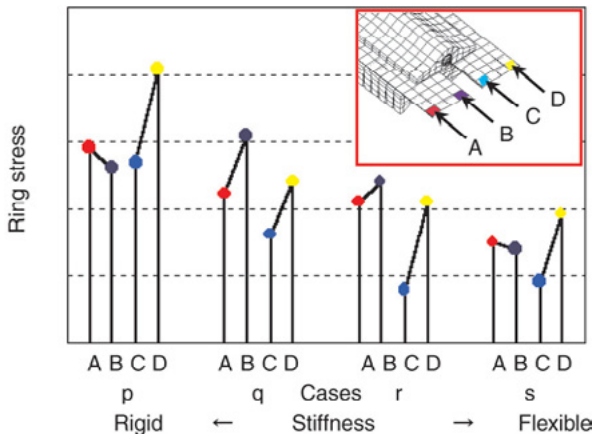


Fig. 10 Ring stress distribution by absolute values for stiffness

Fig. 11 shows the ring stress waveform for the rigidity combinations p and s. The rigidity value is higher in p than in s, and it is apparent the stress amplitude increases at the pulley entrance and exit.

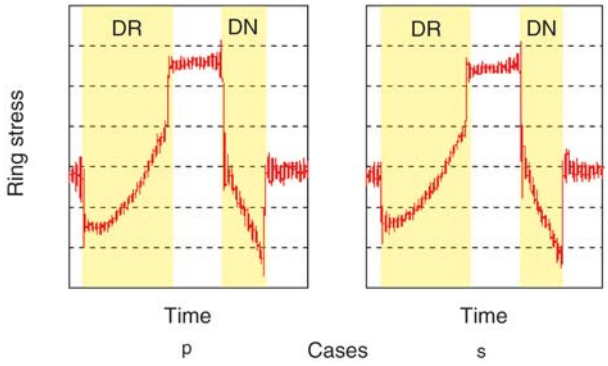


Fig. 11 Ring stresses difference

It is conceivable that this is the result of ring stress caused by the increased impact load on the V-surface of the element at the pulley entrance when the flexional stiffness is high (Fig. 12).

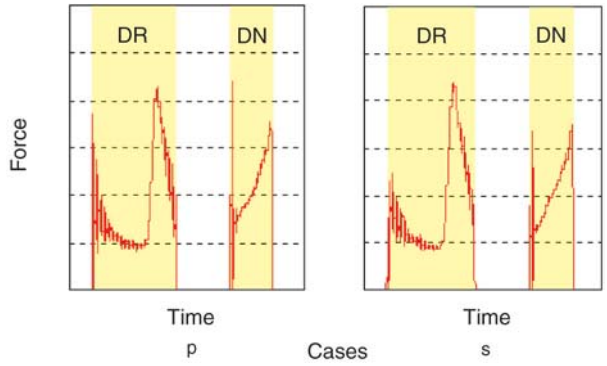


Fig. 12 Element normal force on V-surface

4.2.2. Pulley rigidity ratio

For the next step, Fig. 13 shows the stress amplitude in the rings when the ratio of rigidity on the left and right sides of the pulley is changed.

It is apparent that, although some change occurs in the stress amplitude, the extent of its influence is slight.

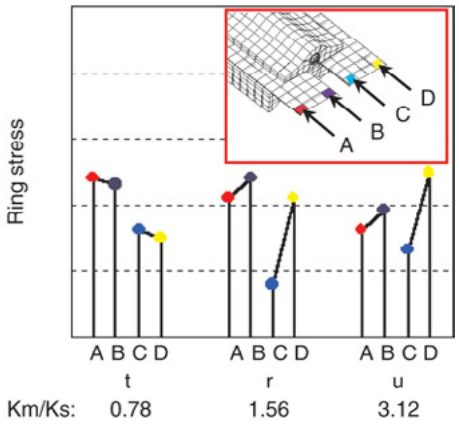


Fig. 13 Ring stress distribution by stiffness

However, the pulley rigidity ratio does have a direct effect on the relative alignment location of elements and rings. In the case of pulley rigidity t, for example, the difference in clearance between the element and ring edge during a single belt cycle is shown in Fig. 14.

The relative clearance between the element and ring inside the drive pulley has decreased, and there is reason for concern about edge contact.

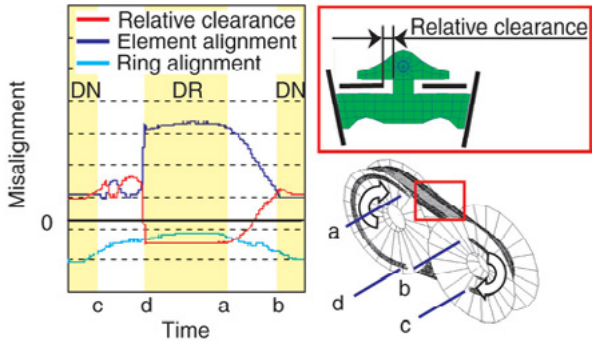


Fig. 14 Relative clearance between element and ring

Similarly, Fig. 15 shows the ring edge clearance with a different left-right pulley rigidity ratio. E and H are the clearances between the left and right ring edges and the pulley, while F and G are the clearances between the left and right ring edges and the element neck.

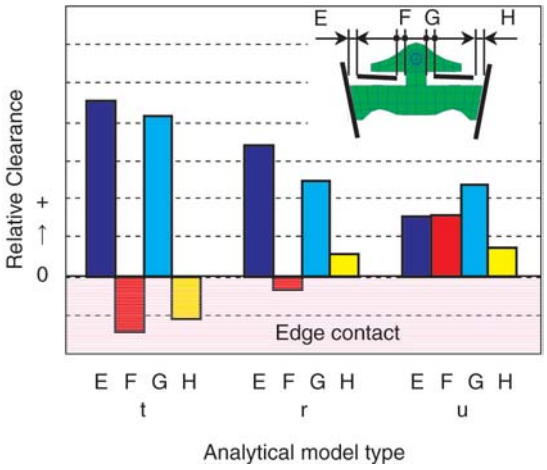


Fig. 15 Ring edge contact by stiffness

This means, in other words, that the clearance between the ring edge and the pulley or the element neck is decreased by the rigidity ratio, and as a result, ring edge contact occurs more frequently during CVT operation. When such contact occurs, there is reason for concern about damage from ring edge wear and other such factors due to the relative speed differential between the ring and the pulley, or the ring and the element. Consequently, it is important to pay careful attention to the amount of misalignment when deciding the pulley rigidity ratio.

5. Conclusion

Analysis of the influence of pulley rigidity on belt misalignment and on the ring stress that occurs with misalignment yielded the following information.

(1) Raising the pulley flexional stiffness contributes to ring impact stress at the pulley entrance and exit, which increases the stress amplitude.
(2) The ratio of left and right pulley rigidity has little influence on ring stress amplitude. There are cases, however, when changes in misalignment due to the rigidity ratio cause ring edge contact to occur.
(3) Given the above, it is necessary to pay careful attention to ring impact stress and edge contact when determining pulley specifications that allow for belt durability.

6. Acknowledgements

As the belt and pulley assembly accounts for a major proportion of CVT weight, the demand for weight reduction will be never-ending. When determining the basic CVT framework, therefore, it is a matter of great significance if pulley rigidity, which is needed for drive power transmission, can be clarified in terms of belt durability.

In conclusion, the authors would like to express their deepest appreciation to the parties concerned at Hibbitt, Karlsson & Sorensen, Inc. for their great cooperation in improving solvers during the course of development of this simulation.

References

(1) Saito, T. et al.: “Development of Metal Pushing V-Belt Stress Simulation for Continuously Variable Transmission,” Honda R&D Technical Review, Vol. 13, No. 1, pp. 125–130 (2001)

(2) Kanehara, S. et al.: “A Study on the Transmitting Mechanism of Pushing Block Type Metal Belts,” Honda R&D Technical Review, Vol. 7, pp. 49–67 (1995)

(3) Asama, H. et al.: “Drive Mechanism of Metal Pushing Type Belts, Automotive Technology,” Vol. 26, No. 2, pp. 78–81 (1972)

(4) Sauer, G.: Grundlagen und Betriebsverhalten eines Zugketten Umschlingungsgetriebes, Nr. 293, Duesseldorf: VDI-Verlag (1996)

■ Authors ■



Toshihiro SAITO



Takemasa OKANO

Development of a Spin Forming Procedure for CVT Pulley Covers

Akihito OHASHI* Toshihiro SAITO* Toyoji HISATSUNE*

ABSTRACT

The metal pushing V-belt type continuously variable speed transmission (CVT) commonly has a hydraulic chamber that is formed by fastening together the movable pulley and pulley cover parts. The mechanism by which damage occurred to the pulley cover in the spin-formed fastening portion during development was clarified. In order to understand the damage mechanism, the area of the pulley cover subjected to spin forming was examined with a scanning electronic microscope. This revealed that voids had formed inside the examined area, as expected under the theory of ductile fracture, and it was confirmed that durability varied with the form of the voids. Quantitative treatment of the damage was made possible by numerical analysis of the mechanism of void formation using McClintock's equation for damage evaluation. It was further confirmed that the results of this numerical analysis agreed with the results of durability tests of the pulley, verifying the validity of the analytical values.

1. Introduction

At present, many four-wheeled vehicles use metal pushing V-belt type continuously variable speed transmissions (CVT), and various new technologies are being developed for each functional element of the CVT. There is a high demand for measures concerning manufacturing method, cost, weight, etc., related to the pulley, which forms the core of the metal pushing V-belt type CVT.

The CVT pulley system is composed of the movable side and the fixed side. The movable side pulley transmits torque by clamping the belt in the space between it and the fixed side, hydraulically. The force holding the belt is generated by applying hydraulic pressure to the hydraulic chamber formed by the back of the movable pulley. In order to form this hydraulic chamber, it is necessary to connect the pulley and the cover. Connection methods include press fit, spin forming, and tightening by screws, and there are many types where the pulley and cover are an integrated shape. Among these methods, spin forming is a process whereby the press formed cover is connected to the pulley through plastic forming. It is also an advanced method that has a low production cost. However, research results published concerning connection strength of spin forming are insufficient. In particular, there are almost no quantitative evaluation results concerning the groove shape of the pulley's connecting part and connection strength of the pulley cover.

This research project analyzed the mechanism that was generating cracking in the pulley cover connection part that occurred in the pulley prototype parts, from the material point of view, and at the same time, the generation mechanism was quantified, through numerical analysis. Through this, spin forming connection strength technology was created, making for CVT pulley strength and reliability. This paper reports on the above.

* Tochigi R&D Center

2. The Aims of Development

Fig. 1 is the main section of a CVT incorporating these results. As shown in the diagram, the pulley cover that forms the hydraulic chamber with both the drive pulley and the driven pulley is connected to the pulleys with spin forming. The spin forming referred to here means the process of pushing in, along the perimeter and using a roller, the cover that turns together with the pulley, as shown in Fig. 2, after the cup-shaped cover is engaged in the movable pulley. In this instance, there is no turning force on the roller doing the machining, but rather while it moves along the cover, there is translation motion in the direction of the cover radius.

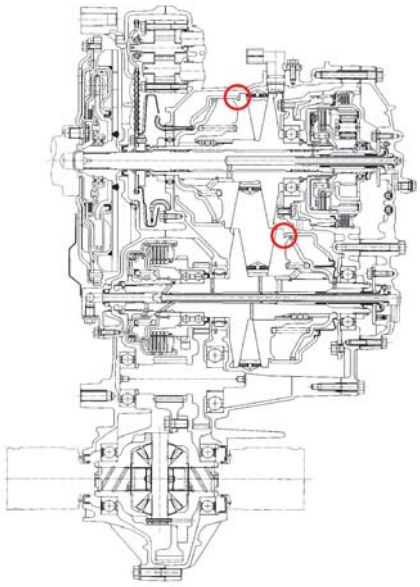


Fig. 1 CVT main section

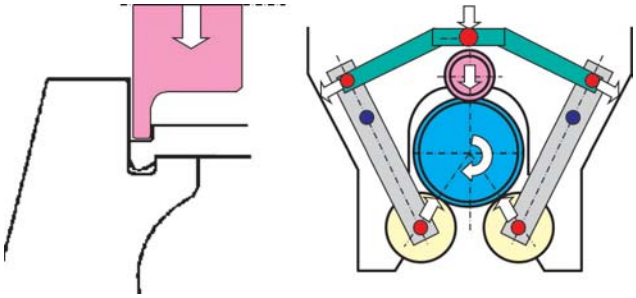


Fig. 2 CVT pulley cover forming

Connection strength in pulley spin forming is determined by surface pressure of the area where the pushed in cover material is clamped with surfaces of the pulley groove. Accordingly, factors affecting connection strength include, as shown in Fig. 3, the indentation depth, indentation position, shape of the pulley groove edge, etc.[(1)] It has been confirmed, through testing, that groove edge shape in particular contributes highly. In vehicle durability tests, when the pulley edge shape is maintained as a sharp corner, there is cracking in the direction shown in Fig. 4. In contrast, when the edge is given an arc shape with certain amount of radius, the cracking does not occur. With this shape, no matter what the spin form process, the cover side shape that corresponds to the pulley part after forming follows the pulley shape and creates a tightly connected shape. Results of durability tests in a vehicle show a relationship between the force with which the pulley clamps the belt and the product lifespan. These results are shown in Fig. 5. From these results it was learned that a small rounding of the pulley edge leads to the fatigue life growing by tens of times.

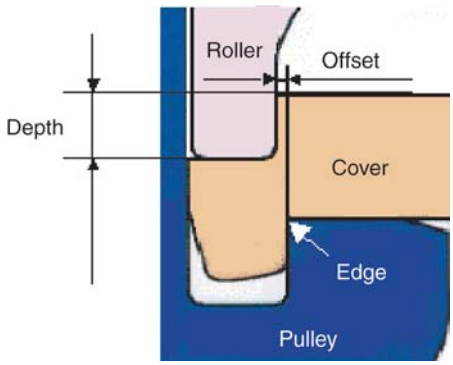


Fig. 3 CVT pulley cover forming



Fig. 4 Section of pulley crack

By showing that this small difference in shape is a major direct contributor to spin forming strength, it is possible to secure spin form strength beyond the constant level, and achieve a stable connection.

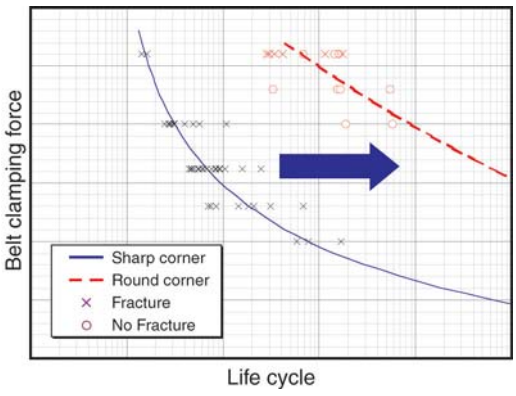


Fig. 5 Loading condition

3. Analysis of Damage Mechanism

3.1. The Effect of Stress Concentration Factor

At the cover edge part, which is the point of origin of pulley cover damage, there is a stress load from the metal belt to the pulley V surface, which causes repetitive bend stress to occur. The difference in sharp corner and slightly rounded shapes in the pulley cover edge that received this sort of repetitive bending is the major factor affecting connection strength. It is thought to be due to differences in stress concentration in the edge area.

In order to clarify the effect of the small arc shape on material fatigue, test pieces made of rolled steel plate, the same material as the cover, were created by grinding, with different radius edges on a V-shaped notch groove, and the fatigue limit of plane bending was measured, under constant minimum stress. The shape of the test pieces is shown in Fig. 6, and the test results are given in Fig. 7.

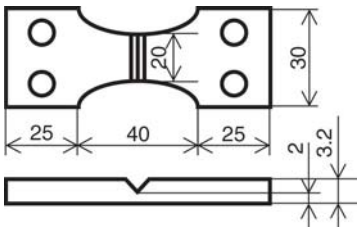


Fig. 6 Fatigue test specimen

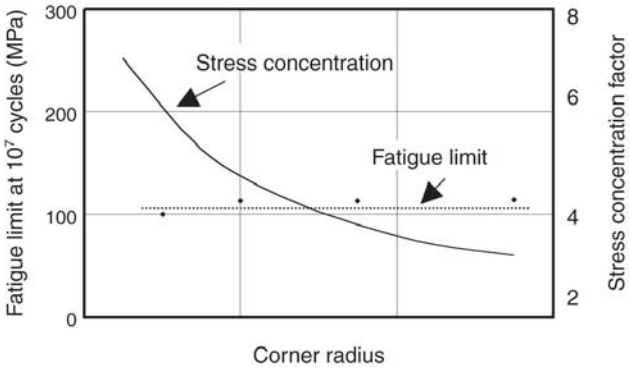


Fig. 7 Relationship between fatigue limit stress and stress concentration factor

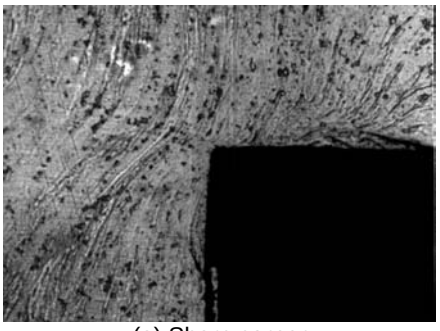
From these results, the stress concentration factor of the cover material increases as the arc's radius dimension decreases in the small notched groove, and the material fatigue strength does not change but remains a constant value.

That is to say, the difference in pulley cover durability when the pulley cover edge has a sharp corner and when it is slightly rounded cannot be explained by the stress concentration factor on the edge part.

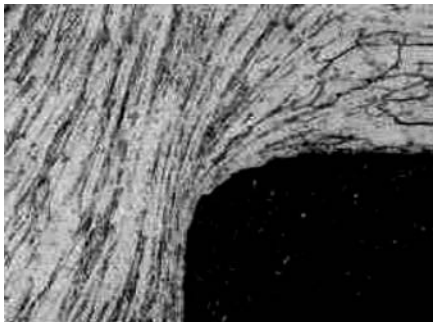
3.2. The Effect of Plastic Forming Damage on the Spin Forming Part

The pulley cover spin forming part is subject to large shear plastic forming in a particular area. At this time, the plastic forming damage to the cover material is thought to differ according to the edge part's sharp corner shape or small arc shape. An investigation of this forming damage difference was carried out by observing the microstructure of a spin formed part's cross-section. Fig. 8 shows the results of observation at a magnification of 400 times, using an optical microscope.

From these results, it was learned that with a sharp-corner pulley, as shown in Fig. 8-(a), the cover material's fiber flow does not follow the sharp corner shape, and is cut by the edge. In comparison, in the pulley having a rounded shape, as shown in Fig. 8-(b), the fiber flow follows the arc shape. This difference can be clearly seen. When a metal microstructure is pulled in a deformation direction, fiber flow leads to a plant fiber state.



(a) Sharp corner



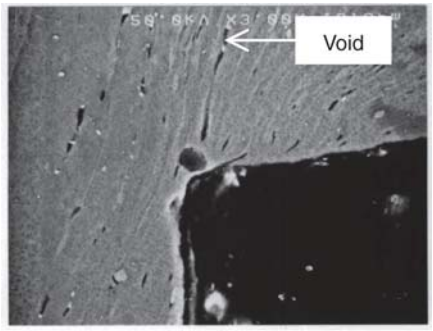
(b) Round corner

Fig. 8 Microstructure of pulley cover

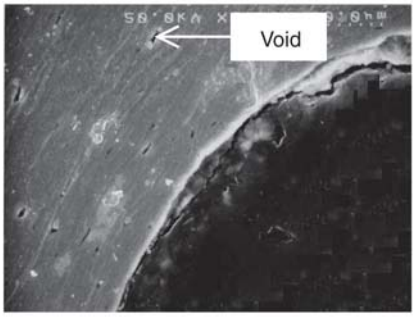
Although it was learned that there are differences in fiber flow when the edge has a sharp corner and when it is rounded, the effect that fiber flow has on material strength, etc., was not clear.

Therefore, the cover material microstructure was further magnified by 3,000 times, using an SEM (scanning electron microscope). The results are shown in Fig. 9.

From the SEM microstructure observation, as shown in Fig. 9-(a) and (b), both with a sharp corner and a rounded corner, voids can be seen in the shear forming part. It is well known that inclusions occur in plastic forming of the base material, and there is an accumulation of dislocation in the base material's boundary face, and that it grows in the direction of microstructure deformation, that is, the fiber flow direction. Accordingly, as shown in Fig. 9-(a), when the pulley edge part is a sharp corner, fiber flow is cut, and voids appear in the material surface. These voids in the material surface can easily become the point of origin of fatigue failure, just as with micro-cracks.



(a) Sharp corner



(b) Round corner

Fig. 9 SEM image microstructure of pulley cover

From this we know the reason why that the connection strength drops for pulley covers having sharp pulley edge corners is because voids generated in spin plastic forming appear in the material surface by the fiber flow cutting. Giving the edge part a rounded shape limits voids in the material surface, and it is possible to improve pulley cover connection strength.

4. Quantitative Evaluation of Forming Damage

The generation of voids around the pulley cover edge is now clear, and it is assumed that the number of voids and their size would affect spin forming durability. Next, quantitative evaluation of this as forming damage was considered.

4.1. The Rupture Theory of Ductile Materials

Generally, ductile fracture has material inclusions, etc, as its point of origin, whereby tiny voids occur, and they gradually grow, finally coming together and causing fracture. In particular, it is important to quantify voids near the surface layer. In this, McClintock's[2] equation (1) has been adopted, among the various parts of the theory of rupture.

$$\int^{\varepsilon} \left[\frac{2}{\sqrt{3(1-n)}} \sinh \left\{ \frac{\sqrt{3(1-n)}}{2} \frac{(\sigma_1+\sigma_3)}{\sigma} \right\} + \frac{(\sigma_3-\sigma_1)}{\sigma} \right] d\varepsilon = C_3 \quad (1)$$

McClintock's equation expresses damage caused by the generation of voids as stress and plastic strain history, and its special feature is that it can quantify the damage in frequent response to material shear displacement.

4.2. Development of a Forming Simulation Method

The calculation model used to simulate the actual spin forming process, and the deformation diagram, is shown in Fig. 10. Here, the model shows the spin forming stroke applied to the forming roller, and while the work is turned, two support rollers support it. The results of this simulation showed that the forming roller reaction force was the same as that actually measured, so it was judged that the forming process was reproduced. However, because it is a simulation that adopts a finite element method that categorizes, as a solver, according to crash analysis code, or uses a 3D model, to investigate more closely around the pulley cover edge would take a lot of calculation time, and in practical terms is not a good method.

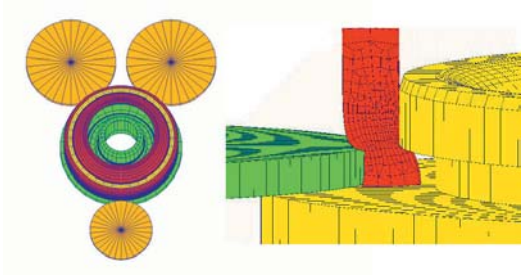


Fig. 10 Forming simulation in 3D

Next, a new forming damage comparison was made between a new 3D model section and a 2D model (Fig. 11) having the same mesh density. Because the results showed that both were quantitatively equal, a detailed analysis of the area around the pulley edge was carried out, using the 2D model.

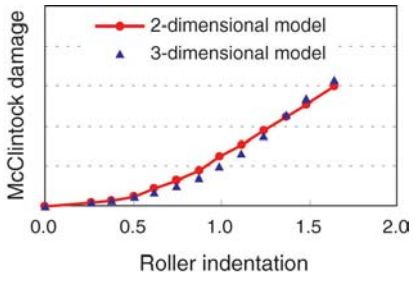


Fig. 11 Comparison of analyses

4.3. The Benefits of Rounding the Pulley Edge

The 2D model deformation diagram used in the investigation into the benefits of rounding the pulley edge, and McClintock damage contour diagram are shown in Fig. 12. The deformation diagram showed good correlation with the section shape of actual spin forming, and so was judged an appropriate result.

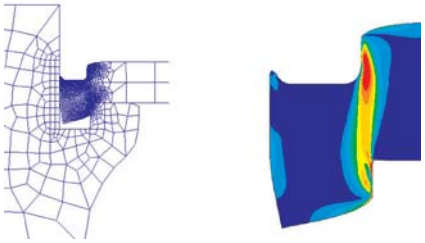


Fig. 12 McClintock damage distribution

Because the damage maximum value was in the same location as the cover cracking point of origin around the edge, the next step was to calculate, in the same way, the damage generated with a number of rounded edge shape radiuses. At that time, indentation depth was taken as a constant value. The results, as shown in Fig. 13, made it clear that there is a sudden increase in damage if the edge rounding radius becomes less than value b. That is to say, pulley cover connection strength in spin forming can be greatly enhanced by rounding the pulley edge.

Furthermore, the relationship between pulley edge rounding dimension and indentation depth is shown in Fig. 14. If the rounding dimension is greater than the value shown as c, even if the indentation depth is great, there is no dramatic increase in the amount of damage.

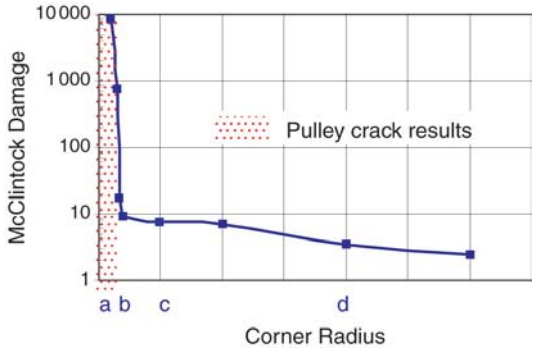


Fig. 13 Damage versus edge radius

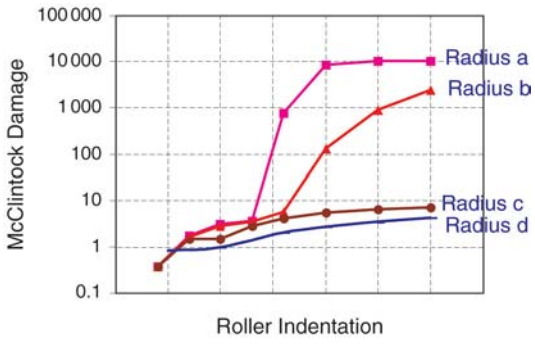


Fig. 14 Damage versus indentation

5. Verification of Durability and Reliability of Connection Strength

Because a drop in pulley cover connection strength actually occurred in a belt reaction force durability test, an investigation was made into how forming damage and stress change while driving.

5.1. Durability Simulation

In the durability test, the metal belt is wrapped around the spin formed pulley, and the vehicle is driven by a fixed speed ratio, belt clamping force, and revolution speed. At this time, belt reaction force is applied to roughly half of the pulley, so it is necessary to carry out analysis with a 3D model. As previously determined, 2D forming simulation results can be developed as 3D results, and so belt reaction force was applied statically. For the belt reaction force, results from a previously reported[3] metal belt behavior and stress simulation were used.

Fig. 15 shows the pulley stress contour diagram of the forming process obtained in this way.

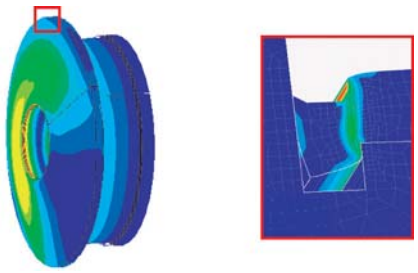


Fig. 15 Pulley stress with belt loading

5.2. Amount of Increase in Damage when Driving

The amount of increase in damage during driving is shown in Fig. 16. From this diagram it can be seen that the amount of damage increase is between 0.1% and 1% at time of forming. This shows that the pulley when driving is used within the material's elastic range, and from the damage point of view, the forming process is dominant.

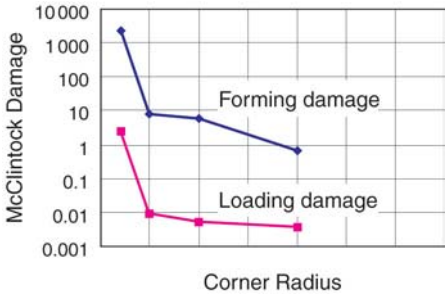


Fig. 16 Damage increment under loading

5.3. The Amount of Increase in Stress when Driving

In verification of connection strength durability and reliability, it is important to know the stress state generated when driving. To this end, as shown in Fig. 17, the simulation was applied under the 3 different belt clamping forces A, B, and C, and the spin forming area's stress increase amount was determined.

As shown in Fig. 18, the shorter the lifespan becomes, the more the stress increases. However, the amount of increase is extremely small – 0.004 to 0.009. This is because the residual stress is maintained as it is, in the plastic range when the spin forming area was formed. Therefore, it is assumed that it is difficult to affect belt reaction force.

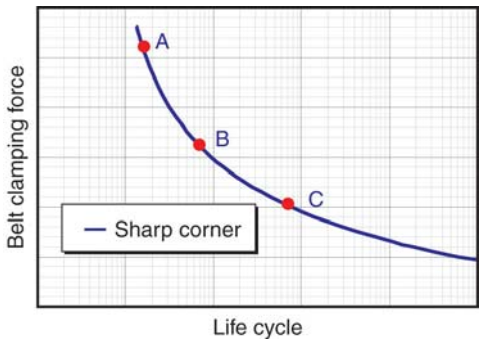


Fig. 17 Three loading conditions

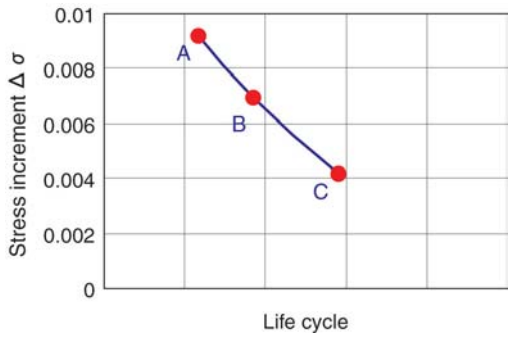


Fig. 18 Stress increment with belt loading

6. Summary

In order to secure a metal belt type CVT pulley cover spin forming connection strength at a constant level or better, the following technologies have been established.

(1) In fatigue tests of the pulley cover material, using V notched test pieces with small radius, even if the notch edge arc radius falls below the pulley edge radius which leads to critical damage, there is no difference seen in fatigue strength drop.

(2) In the areas around the pulley cover edge where pulley cover spin forming is carried out, in a state where the material cannot escape, that is to say, in a state nearing hydrostatic pressure, voids are generated.

(3) When making spin forming connections, if the radius dimension of the rounded pulley edge is below a fixed value, cover side material plastic flow is prevented, void appear in the surface layer, and there is a drop in material strength.

(4) Through the use of a damage simulation that utilizes the McClintock equation, a technology was developed to quantify state changes of the pulley cover material originating around the pulley edge.

The cause of pulley connection part cracking is not simple stress concentration, but rather is understood to be due to the fact that material fluidity during machining was not guaranteed to the extent of considering the void generating state. In the future, when carrying out plastic forming that involves large deformation, such as spin forming, it is vital that decisions be made on strength after processing, from the points of view of material, and the damage inflicted.

References

(1) Japanese Patent Kokai No. (1996) 8-210454: Actuator Case Spin Forming Structure, for a Pulley for Variable Speed Transmission

(2) McClintock, F.A.: A criterion for ductile fracture by the growth of holes, J. Applied Mechanics, P.363–371 (1968)

(3) Saito, T., et al: Development of a CVT Metal Belt Stress Simulation Technology, Honda R&D Technical Review, Vol. 13, No. 1, p.125–130 (2001)

■ Authors ■


Akihito OHASHI


Toshihiro SAITO


Toyoji HISATSUNE

Optimisation of Transonic Gas Turbine Blades with Evolution Strategies

Markus OLHOFER* Toshiyuki ARIMA** Yaochu JIN*
Toyotaka SONODA** Bernhard SENDHOFF*

ABSTRACT

Evolution strategies belong to the class of evolutionary algorithms which are direct pseudo-stochastic search methods which mimic the principles of Neo-Darwinian evolution. They are known to be powerful optimisation techniques in particular for the solution of multi-modal, noisy and non-differentiable complex problems. For problems where a continuous representation is "natural", like the geometry of gas turbine blades, evolution strategies are particularly suitable. Besides the choice of the search operators, the representation is one of the most crucial elements in optimisation. The advantages and disadvantages of different approaches are discussed in this work. Furthermore, to evaluate different geometric alternatives the fluid-dynamical properties of the blades have to be estimated. We propose a framework in which a Navier-Stokes solver and a neural network approximation model are combined. In this way, the computationally expensive evaluation of the fluid dynamics can be reduced while guaranteeing correct convergence of the optimisation algorithm. Finally, the optimisation results are discussed and the performance of the optimised and the original blades are compared both for the simulation method and for the transonic windtunnel experiment. In both results it can be seen, that a high performance increase is achieved.

1. Introduction

The application of optimisation methods to complex systems in control, manufacturing and design has significantly increased in recent years. This increase is due to the development of new powerful optimisation methods which can handle nonlinear, multi-modal, non differentiable, dynamic, noisy and mixed combinatorial/continuous optimisation problems. Furthermore, the sharp increase of the available computing power makes extensive simulations like in computational fluid-dynamics feasible even in an optimisation framework.

* Honda R&D Europe (Germany) GmbH
** Wako Research Center

Evolutionary algorithms and the evolution strategy, which is employed in this work for the problem of design optimisation, are among the most powerful and most versatile of these new optimisation methods.

Examples for the application of evolutionary algorithms can be found in very different areas ranging from chip design[1-3] and the optimisation of mechanical structures[4, 5] to the generation of neural structures[6, 7] and even to the optimisation of the aesthetic of a design[8]. Applications for the optimisation of aerodynamic properties can be found in different areas of the aircraft design. Whereas Obayashi et al.[9] and Sobieszanski-Sobieski et al.[10] focus on the optimisation of the plane body, Vicini et al.[11], Doorly[12] and Jones et al.[13] target the optimisation of the inner air flow in gas turbines.

Although a solid theoretical basis of this type of optimisation algorithms is available, still constructive methods on how the algorithm has to be adapted to a particular problem and how the overall system has to be designed are sparse. Particular attention has to be paid to the representation of the optimisation problem, e.g. the geometry of a gas turbine blade and the way in which changes are inflicted on the representation in order to obtain alternative solutions. Since the computational cost of the fluid-dynamics simulations is very high, measures have to be taken to reduce the number of evaluations of alternative solutions. We approach this problem by employing a specific strategy which exploits information from past optimisation steps to minimise the necessary number of calculations. Furthermore, another recently developed method from computational intelligence, the neural network is used as an approximation tool to *learn* the fluid-dynamical properties of certain geometries. Some geometries can then be evaluated without the use of the computational fluid dynamics (CFD) solver.

In this paper, we will outline the set-up of a successful optimisation project consisting of several modules which address the questions raised in the previous paragraph. The core modules are the optimisation method and the CFD solver. The problem of representation is discussed in the context of the design of gas turbine blades and a framework for the integration of neural networks as approximation tools into the overall optimisation approach is described. In the last sections, we discuss the results of the optimisation both with regard to the results of the CFD calculations, as well as, to physical measurements in a transonic windtunnel.

2. Evolutionary Algorithms

2.1. Principles

Evolutionary algorithms are direct pseudo-stoch-astic search methods which mimic the principles of Neo-Darwinian evolution, see e.g. by Fogel[14]. A population of possible solutions (e.g. a vector of continuous parameters, the objective variables, describing a blade geometry) is adapted to solve a given problem (e.g. minimisation of pressure loss) over several generations. The adaptation occurs by variation of solutions contained in a population and by selection of the best solutions for the next generation. The variations can be classified as purely stochastic (usually called mutation) and combinatoric/stochastic (usually called recombination or in the context of genetic algorithms crossover). Formally, an evolutionary algorithm can be described as follows, schematically the evolution cycle is shown in Fig. 1:

ALGORITHM

$t := 0;$

initialise $P_g(0) := \{g_1(0), ..., g_\mu(0)\}$

decode and evaluate $P_g(0) : \Psi(c_{\Theta_c}^{-1}(P_g(0)))$

do

recombine	$P'_g(t) := r_{\Theta_r}(P_g(t))$
mutate	$P''_g(t) := m_{\Theta_m}(P'_g(t))$
decode	$P''_p(t) := c_{\Theta_c}^{-1}(P''_g(t))$
evaluate	$P''_p(t) := \Psi(P''_p(t))$
slect	$P_p(t+1) := s_{\Theta_s}(P''_p(t) \cup Q)$
code	$P_g(t+1) := c_{\Theta_c}(P_p(t+1))$

$t := t + 1$

until stop

NOMENCLATURE

$P_g(t)$	genotype population, generation t
$P_p(t)$	phenotype po;ulation, generation t
Q	additional set of individuals, e.g. $P_p(t)$
$g_1(t)$	genotype of the first individual
Ψ	fitness function
μ, λ	population size (parents, offspring)
r_{Θ_r}	recombination operator
m_{Θ_m}	mutation operator
c_{Θ_c}, s_{Θ_s}	coding and selection operator

In the formal description, the coding and decoding processes have been explicitly included. They describe the transition from the genotype, which is also called the representation or the blueprint, to the phenotype, which is evaluated. The representation is one of the most important factors in the design of evolutionary algorithms. Together with the search operators most of the current algorithms can be classified with respect to the representation they use, e.g. genetic algorithms, evolution strategies, genetic programming and evolutionary programming.

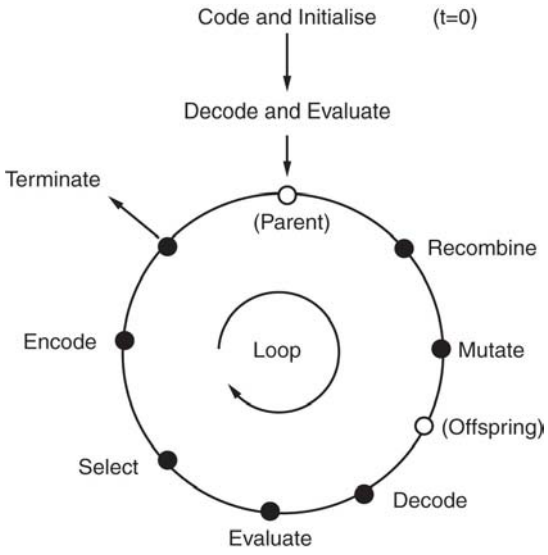


Fig. 1 The evolution cycle.

2.2. Evolution Strategy

In the evolution strategy (ES) the essential variations during the evolutionary search are mutations which are realized by adding normal distributed random numbers to the objective variables. In Fig. 2 different normal distributions are shown; they determine the distribution of the offspring around the parent. The variances σ^2 of the normal distribution are called the strategy parameters of the search process and their values determine the width of the search. The variances have to adapt during the process to the local topology of the search space. This process of *self-adaptation* is one of the key principles of ES. It relies on a "second-order" or indirect selection of the strategy parameters which are part of each individual. In Fig. 3 a bird's eye view of different normal distributions $N(\boldsymbol{a}_1, (\sigma_1^1, \sigma_1^1))$, $N(\boldsymbol{a}_2, (\sigma_2^1, \sigma_2^1))$ and $N(\boldsymbol{a}_3, (\sigma_3^1, \sigma_3^2))$ is shown for a two dimensional representation space. The "probability axis" would be perpendicular to the paper and the circles (ellipse) correspond to lines of equal probability (due to the symmetry of the normal distribution). These lines are also called iso-density lines. Thus, if the parent vector is given by $\boldsymbol{a}_1$, ca. 46% of all offspring will lie within the shown circle with radius σ_1^1 (91% for radius $2\sigma_1^1$).

In the standard evolution strategy only a diagonal covariance matrix is used, i.e. the mutation of the objective x is carried out by adding $N(0, \sigma_i^2)$ distributed random numbers z_i to each component x_i. The "step-sizes" σ_i are also subject to mutations (log-normal distributed) both for each component separately (parameterised by τ) and overall (parameterised by τ'). Thus, the individual consists of both the objective and the step-size vector. Formally, the standard evolution strategy with self-adaptation can be expressed as follows: (see e.g. Schwefel[15])

$$\sigma_i(t) = \sigma_i(t-1)\exp(\tau' z)\exp(\tau z_i) \quad (1)$$

$$\boldsymbol{x}(t) = \boldsymbol{x}(t-1) + \tilde{z} \quad (2)$$

$$z_i, z \sim N(\mathbf{0}, 1), \tilde{z} \sim N(\mathbf{0}, \tilde{\sigma}(t)^2)\,.$$

The selection in ES is typically deterministic, i.e. from μ parent individuals, λ offsprings are produced and from these the best μ individuals are selected to form the parent population of the next generation. This method is usually abbreviated to (μ, λ)-selection.

Evolution strategies are often used with some kind of recombination operator (discrete or intermediate), which is basically the same as the crossover operator in genetic algorithms, however, it usually plays a minor role for the search process and is completely omitted in this work.

2.2.1. Covariance matrix adaptation

The derandomized Covariance Matrix Adaptation (CMA)[16] differs from the standard ES mainly in three respects:

- Instead of the variances (σ_i^2), the full covariance matrix of the probability density function

$$f(z) = \frac{\sqrt{\det(C^{-1})}}{(2\pi)^{n/2}} \exp\left(-\frac{1}{2}(z^T C^{-1} z)\right). \quad (3)$$

  is adapted for the mutation of the objective parameter vector. The (σ_i^2) can only describe probability distributions with the main axes parallel to the coordinate axes. Using the full covariance matrix $\boldsymbol{C}^{-1}$, rotated distributions, like the blue ellipse in Fig. 3, can be represented. Since $\boldsymbol{C}^{-1}$ has to be positive definite with $\det(\boldsymbol{C}^{-1})>0$, the different matrix entries cannot be determined independently and the detailed adaptation algorithm is a little more involved.
- In order to reduce the stochastic influence on the self-adaptation, one stochastic source for both the adaptation of the objective and of the strategy parameters is used. Note, that in eqs. (1) and (2), the stochastic elements (z, z_i) and $\tilde{z}$ are independent. In the derandomized approach, the *actual* step length in the objective parameter space is used to adapt the strategy parameter.

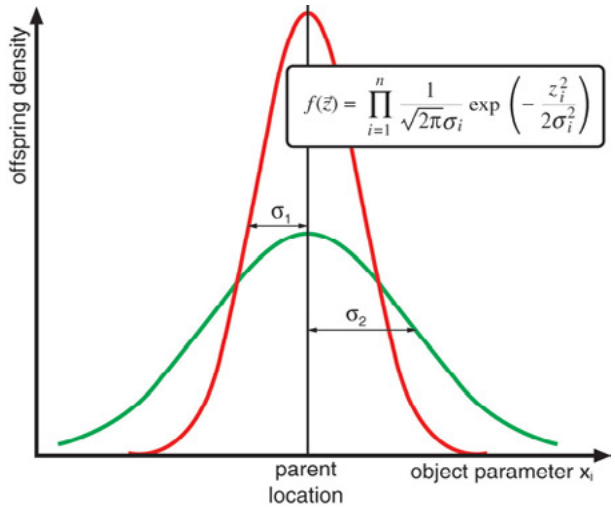


Fig. 2 The normal distribution $N(0, \sigma^2)$ for different variances σ^2. For the n-dimensional case, $f(z) \sim N(0, \sigma^2)$ is given.

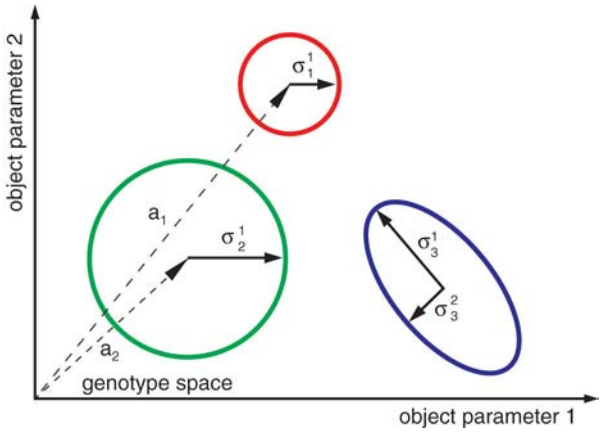


Fig. 3 Iso-density lines for three different two dimensional normal distributions.

- The second method is the introduction of the cumulative step size adaptation. Whereas the standard evolution strategy extracts the necessary information for the adaptation of the strategy parameters from the population, the cumulative step size adaptation additionally relies on information collected during successive generations. This leads to a reduction of the necessary population size.

3. Overview of the Gas Turbine Engine

3.1. A Single Gas Turbine Engine

The simplest gas turbine engine for an aircraft is a turbojet. As shown in Fig. 4, the turbojet engine is essentially designed for the purpose of producing high-velocity gas at the jet nozzle. An axial flow compressor is located in the forward section of the engine. The compressor is followed by a combustion chamber. Behind which is an axial flow turbine that produces the power needed to drive the compressor. Lastly, there is the jet nozzle. The compressor raises the pressure of the incoming air before it enters the combustion chamber. Fuel is sprayed through nozzles into the front of the chamber. The resulting mixture of fuel and air is burned and the expanding gas rushes into the turbine section, causing the turbine rotors to rotate. On leaving the turbine section, the gas is expelled to the outside air through the jet nozzle. The power that the turbine rotors extract from the gas is used to drive the compressor. The turbine must produce sufficient power to turn the compressor and yet leave enough energy in the exhaust gas to generate a worthwhile amount of forward thrust. Superior compressor and turbine combinations eventually led to successful engines.

3.2. Axial Flow Compressor Blades

The axial flow compressor consists of a multi-stage unit comprising of a row of rotor blades followed by a row of stator blades. As shown in Fig. 5 (a), the absolute velocity is initially accelerated by the rotor blades, and then decelerated in the stator blade passages wherein the kinetic energy transferred in the rotor is converted to the static pressure. The process is repeated until the required pressure rise is achieved. The rotor and stator blades consist of airfoil sections with the passage between adjacent blades forming a divergent duct. Therefore, the flow velocity relative to the rotor and stator is decreased. The stage is usually designed to give a pressure gradient along its length to ensure that the fluid maintains a reasonably uniform axial velocity as the density increases toward the downstream. That is why there is a gradual reduction of the air annulus area in the compressor meridional passage, see Fig. 4.

3.3. Axial Flow Turbine Blades

As mentioned earlier, the turbine has the function of providing the power to drive the compressor. To produce the driving power, the turbine consists of fewer stages, each stage comprising of a row of stator blades followed by a row of rotor blades, as shown in Fig. 5 (b). However, the passage between adjacent blades forms a convergent duct. The flow is relatively stable due to a negative pressure gradient, as compared with the positive pressure gradient for the compressor blades. This is why a single stage turbine can drive a large number of compressor stages. When the gas expands in the combustion process, it forces its way onto the turbine stator blades where it is accelerated to about the speed of sound due to the convergent shape of the blade. At the same time the gas is swirled by the stator blades in the direction of the rotation of the rotor blades. Due to the impact of the gas on the rotor blades and due to the subsequent flow of the gas through the rotor blades, energy is absorbed which causes the rotor blades to rotate at high speed and in turn provides the power for driving the compressor.

3.4. Seeking a New Design Principle

In order to reduce the engine weight and the manufacturing cost, it is very attractive to reduce considerably the number of stages needed in the compressor

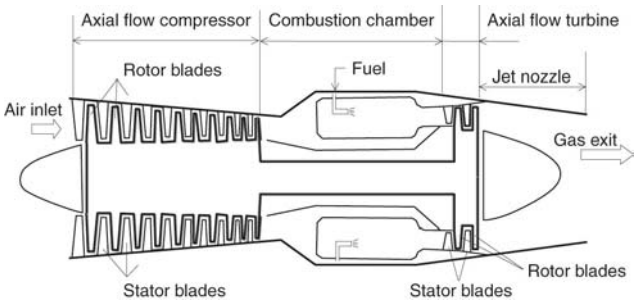


Fig. 4 Schematic view of a typical single gas turbine engine.

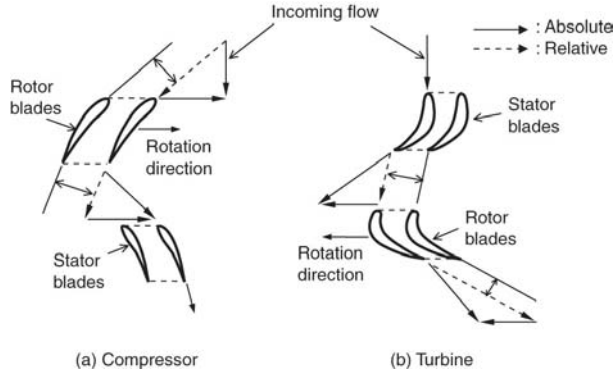


Fig. 5 Comparison of typical forms of (a) the compressor and (b) the turbine blades.

and/or turbine part of the engine while maintaining the same level of efficiency. However, in order to realize such a reduction, the aerodynamic engineer has to uncover new design principles for very highly loaded gas turbine blades. Many aerodynamic properties have to be taken into account for the design of very high loaded blades. The designer has to pay attention to the steady pressure loss due to *shock waves themselves*, due to *an interaction of the shock waves with boundary layers*, due to *the secondary flow* and due to *the tip clearance flow*. Furthermore, the designer has to consider the effect of the Reynolds number on the compressor and on the turbine. The Reynolds effect will be a critical problem especially for a low-pressure turbine in a twin-spool small turbofan engine. Other potential sources of pressure losses are *unsteady phenomena*, like an interaction of stator blades with rotor blades.

By concentrating on conventional designs, the "expert's way of thinking" can be too restricted. In these cases, stochastic optimisation methods like evolution strategies can uncover new principles due to their "inherently unbiased" approach.

4. Optimisation of Gas Turbine Blades

In order to apply evolution strategies to the optimisation of blade geometries, we have to define a suitable representation. This set of objective variables describes a blueprint for the construction of a blade and is stored in the individual, see Fig. 10. Of course different blueprints or blade models are possible, all with specific drawbacks and merits. Examples of models which have been used previously for the optimisation of gas turbine blades are described in Section 4.1.

In order to evaluate the quality of a geometry, computational fluid dynamic (CFD) calculations are used which are described in more detail in Section 4.2 and which allow an accurate prediction of the streaming conditions around the blade for realistic transonic constraints.

Due to the high computational demand of CFD calculations, additionally an approximation model has been used to speed up the estimation of the blade quality, see Section 4.3. Finally, in Section 4.4. the overall system architecture is described and in Section 4.5 some results of the optimisation are given.

4.1. Representation of the Blade Geometry

In Figs. 6, 7 & 8, three blade models are described. The main difference is the degree of freedom which they allow in order to modify the geometry. A representation, which allows a detailed description of the geometry, tends to need a large number of parameters. On the other hand, the number of parameters determines the dimension of the search space and significantly influences the number of iterations which the optimisation methods need to find an optimal or near optimal solution. In general, an optimal representation of a geometry is flexible enough to describe any geometrical property, using only a minimal number of parameters, i.e. it is compact and flexible. Compactness of a blade model can be achieved by using expert knowledge about the problem and about known solutions.

An example for such a kind of model defined for subsonic stationary blades is given in Fig. 6. Only parameters which are assumed to be very important for both the flow conditions and the stability of the design are included in the

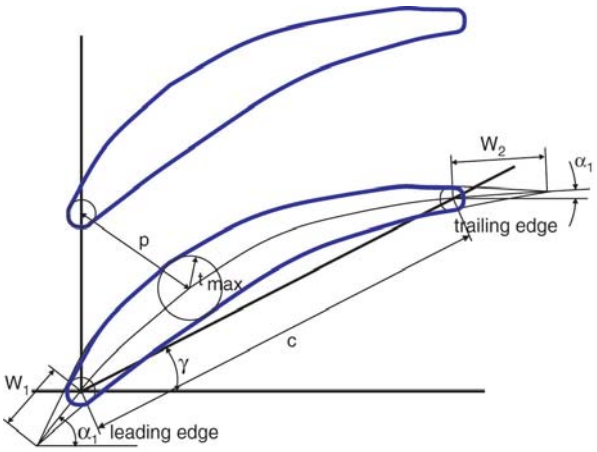


Fig. 6 Encoding of a compressor stator blade which is strongly based on a priori knowledge.

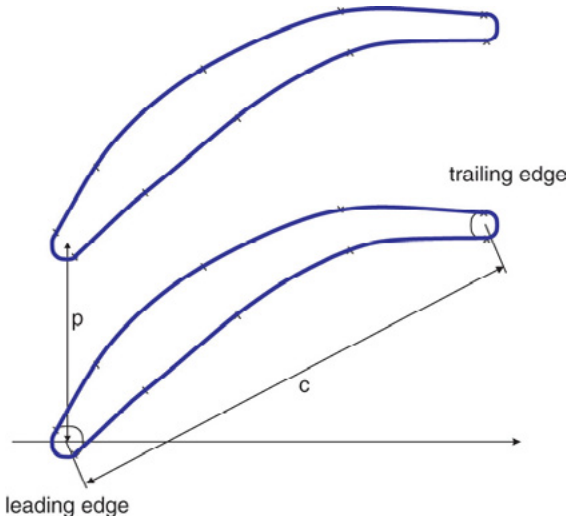


Fig. 7 Extended encoding for the suction and pressure side of the blade.

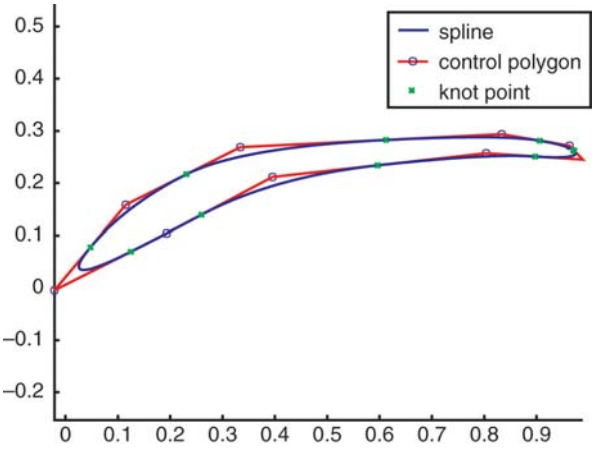


Fig. 8 Spline encoding of the compressor stator blade with increased degree of freedom at the cost of a higher dimensional search space.

model. The curves describing the suction and pressure side of the blade are defined by 3rd order Bézier splines. The splines are fixed by angles and radii at the leading and trailing edge and by a defined radius in the middle section of the blade which defines for example the thicknesses and wedge angles. This model allows a highly compact representation of the design, however, the freedom for modifications of the geometry is restricted. In turn this restricts the possible outcome of the optimisation.

A more detailed description of the curves can be achieved by increasing the degree of freedom at the middle part of the blade. Such an extended model is shown in Fig. 7 where the curves at the suction and pressure side are defined by higher order polynomials which are tangential to the circles at the leading and trailing edge. In this case, a more detailed description of the blade is realised at the cost of a higher dimensional search space. This representation has been successfully employed for the optimisation of gas turbine blades with evolution strategies by Olhofer et al.[17].

An even more flexible model describing the cross section of a blade is shown in Fig. 8. The description is based on a cyclic Non-uniform Rational B-spline (NURBS). Besides elementary constraints like closeness, continuity and differentiability only the number of control points is predetermined, which influences the smoothness of the spline and at the same time the degree of details which can be represented. The degree of freedom of this model can be increased or decreased by inserting or removing control points in the spline description. A priori knowledge can still be represented by defining a suitable initialisation of the blade geometry. This can be seen in Fig. 9, where the same model is used to describe a rotating turbine blade. In particular due to the changeable degree of freedom this model is used in the optimisation discussed in the remainder of this paper. In Fig. 10 the complete representation of the blade and the strategy parameters, which are contained in each individual, are shown.

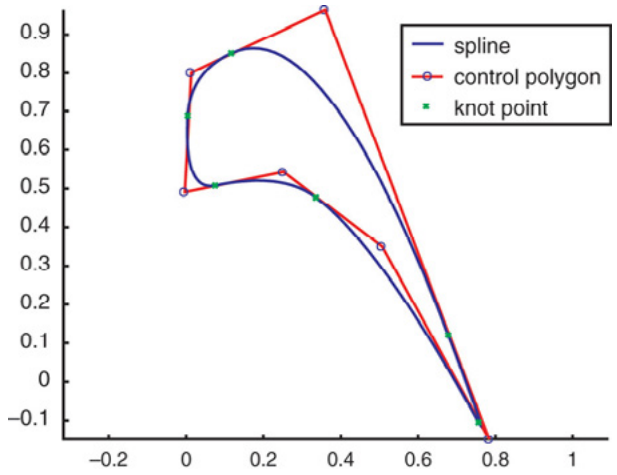


Fig. 9 Spline encoding of a turbine rotor blade using the same model as in figure 8.

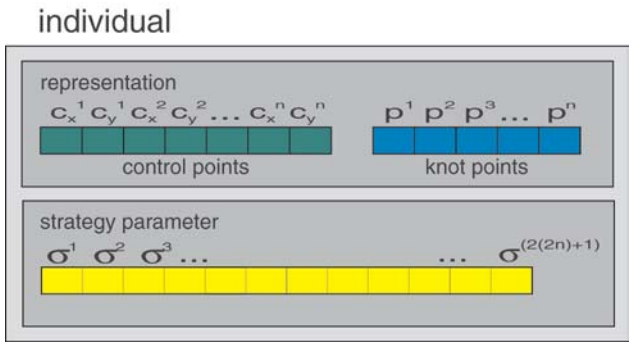


Fig. 10 Set-up of each individual, consisting of the representation of the blade, which are the control and knot vectors of the splines, and the strategy parameters of the CMA evolution strategy.

4.2. Notes on the CFD Calculations

In this section the flow solver used in this work and its most important features will be described. The performance of the solver was investigated in detail and demonstrated by Arima et al.[18]

The basic equations governing the viscous flow through blade rows are the three-dimensional, Reynolds-averaged, Navier-Stokes equations. To complete the system of governing equations, the Reynolds stress tensor, which results from the Reynolds-average for the Navier-Stokes equations, is evaluated using a low Reynolds number (κ–ε) equation proposed by Chien et al.[19].

The governing equations are solved using an implicit time-marching finite-difference scheme to obtain a steady-state solution. The implicit approximate factored (IAF) scheme based on the diagonal alternating-direction-implicit (ADI) scheme developed by Pulliam and Chaussee[20] has been applied for the time integration. The high-accuracy total-variation-diminishing (TVD) formulation proposed by Chakravarthy and Osher[21] has been used for the inviscid terms. The viscous terms have been evaluated using standard second-order, central-difference formulae. The turbulence quantities are obtained by lagging, once the mean flow equations have been updated.

The boundary conditions are needed to calculate the flow field in blade rows. Along the blade surfaces, the no-slip condition is imposed on the velocities. The pressure is extrapolated from the adjacent grid points and the density is computed using the adiabatic wall condition. The turbulent kinetic energy, κ and the isotropic dissipation rate, ε are set to zero along the solid boundaries.

At the inflow boundaries, the total pressure and temperature profiles and two inlet-flow angles are specified; and the static pressure is extrapolated from the interior flow field domain. The turbulent kinetic energy and dissipation

rate imposed at the inflow boundary are derived from the specified free-stream turbulence intensity and the unit eddy viscosity at the inflow boundary. At the outflow boundaries, the static pressure is specified. The density and velocity components, *k* and *e* are extrapolated from those at interior points. At the periodic boundaries upstream of the leading edge and downstream of the trailing edge, the values at two corresponding points should be equal. The detailed numerical procedures have been previously reported by Arima et al.[18].

4.3. Neural Network Models and Evolution Control

Since the computational cost of numerically solving the Navier-Stokes equations is very high, it is important in aerodynamic optimisation to reduce the number of CFD simulations. One way to achieve this is to build an approximate model with a priori knowledge from both design engineers and previous design optimisation. To this end, artificial neural network models, described for example in Bishop[22], can be used.

Artificial neural networks are parallel computational systems consisting of a large number of simple nonlinear processing elements (known as neurons) connected by weights. One of the most important features of neural networks is their ability to learn from human knowledge and experimental data like described e.g. by Jin et al.[23] by adjusting the structure of networks and the strength of the weights. After the learning (also called training) process has been completed, the neural network model can be used to predict an unseen value for a given input. In this work, neural networks are used to approximate the task of a Navier-Stokes solver. Although the applicability of the neural network will be restricted to geometries which are similar to the ones it has learned before, it can evaluate the different designs at a much faster speed than the CFD method. In other words, given the parametric description of the blade geometry, the neural network is able to predict the performance of the blade at a much lower computational cost than a Navier-Stokes solver. Of course, it is assumed that the neural network has been successfully trained.

Feedforword multi-layer perceptron (MLP) neural network models are employed in this work. As discussed in Section 4.1, Non-uniform Rational B-Splines (NURBS) have been used to represent the blade geometry. Therefore, the input-output relationship of the neural network model can be described as

$$\boldsymbol{P} = NN(\boldsymbol{CP}), \tag{4}$$

where $\boldsymbol{P}$ is a vector of performance, such as pressure loss and deviation angle, and $\boldsymbol{CP}$ is a vector of control points of the NURBS. The structure of the neural network model used in this work is illustrated in Fig. 11, where

$$\boldsymbol{CP} = (x_1, y_1, ..., x_n, y_n) \tag{5}$$

are the x and y coordinates of the control points of the B-splines; $\boldsymbol{P} = (\omega, \alpha_2)$ are the pressure loss and the deviation angle.

It is unlikely that the neural network model will show the same performance as the CFD solver. This is mainly due to the limited a priori knowledge, sparse data available for training, and the high dimensionality of the input space, i.e. large n in eq. (5). For example, in our work, 26 control points have been used to describe the blade geometry. For a two-dimensional description of a blade, the input space of the network is therefore 52 dimensional. On the other hand, the

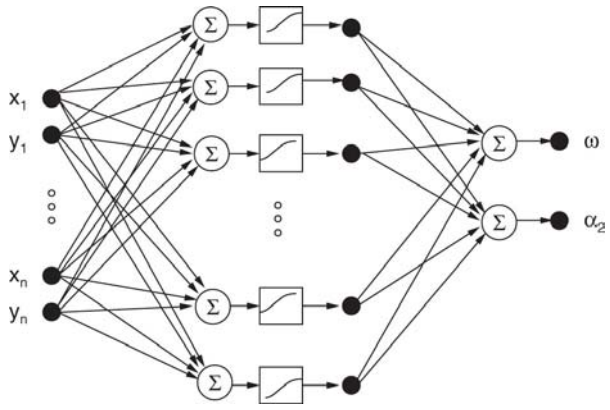


Fig. 11 The neural network model.

data is usually limited because of the high computational cost for their generation. As found by Jin et al.[24], the evolutionary algorithm may converge incorrectly when false minima are present in the neural network model. This problem can be addressed in two respects. Instead of a global model, a local model should be used which approximates only a part of the search space. In this way, it is much easier to get a high quality model with limited training data. Furthermore, the network model should not be used to replace the CFD method, but to supplement it. This approach has been called “evolution control” [24] and will be introduced in the following.

Individual-based and generation-based evolution control schemes have been suggested by Jin et al.[24]. A key issue in evolution control is how often the approximate model should be used, which is usually called model management in optimisation. So far, this has not received much attention in evolutionary optimisation with approximate models. Either the approximate model is assumed to be correct and no evolution control is considered like in the work of Redmond et al.[25], or the approximate model is used at a fixed frequency like by Ratle et al.[26]. To use the neural network model more effectively, a framework for model management in evolutionary optimisation has been used here, see Fig. 12 and by Jin et al.[27]. The main idea behind the framework is that the better the fidelity of the neural network model is, the more frequently the model should be used. In other words, the evolution control frequency is adjusted adaptively during optimisation based on the model quality, which can be estimated using the past data both from the Navier-Stokes solver and from the neural network model.

From Fig. 12, it can be seen that in an evolution cycle, there are ξ generations in total, among which η generations use the CFD solver, and $(\xi - \eta)$ generations use the neural network model for fitness evaluation. Once the CFD solver is used, new data become available. The training data will be used both for the estimation of the model quality and during on-line learning (model update). Three steps are implemented

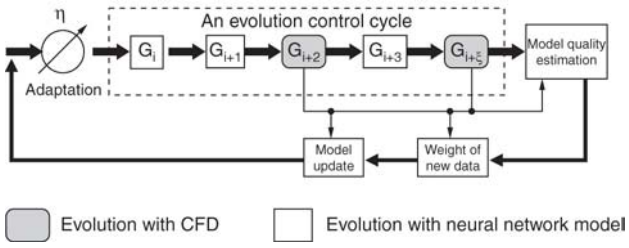


Fig. 12 A framework for evolution control. In an evolution cycle, there are ξ generations, among which h generations use the CFD solver, and (ξ - η) generations use the neural network model for fitness evaluation.

after each evolution control cycle. Firstly, the model quality is estimated, which is achieved by comparing the results from the CFD solver with the ones from the neural network model. Secondly, the covariance matrix of the CMA evolution strategy is exploited to assign a weight to the new data samples for on-line learning. This is useful because the covariance matrix contains information on the search direction of the evolution strategy. The more likely it is that the evolution strategy will visit a particular region in search space in the next steps, the larger the weights will be that are assigned to the samples from this region. The larger the weight of a sample the more important this sample will be during on-line learning. Thirdly, the neural network model will be updated using the new samples collected within the last evolution control cycle. Suppose that in an evolution control cycle, N new samples have been collected, then the cost function for on-line neural network learning with weighting is described as follows:

$$E = \frac{1}{E}\sum_{i=1}^{N} w(i)\,(\omega(i) - (\hat{\omega}(i))^2, \tag{6}$$

where ω(i) is the i-th new sample calculated from the CFD solver and $\hat{\omega}(i)$ is the one predicted by the neural network model for the same blade geometry; $w(i)$ is the weight for the i-th sample obtained in the following way:

$$w(i) = \exp\left(-\frac{1}{2}(\boldsymbol{P}_\Delta(i))^T C^{-1}\boldsymbol{P}_\Delta(i)\right)$$
$$\boldsymbol{P}_\Delta(i) = \boldsymbol{CP}(i) - \boldsymbol{CP}_R(i), \tag{7}$$

where $\boldsymbol{CP}(i)$ is the input vector to the neural network (the geometry) for the i-th sample, $\boldsymbol{CP}_R(i)$ is a reference vector, usually the best geometry in the last generation in which the CFD solver has been used for fitness evaluation, and $\boldsymbol{C}^{-1}$ is the covariance matrix of the evolution strategy discussed in Section 2.

4.4. Overall System Architecture

The overall system architecture is shown in Figure 13. All parts of the program including the optimisation algorithm, as well as, the quality evaluation are realised as modules which can easily be modified or exchanged according to the needs of the optimisation task.

The algorithm is initialised with a known geometry, which is the starting point for the optimisation. This assures that basic properties and constraints are fulfilled so that the flow can be calculated using the CFD method described in Section 3. In particular for the optimisation of the blade geometry in this work, a proper initialisation is important, since non-stationary flow fields cannot be evaluated.

After the initialisation of the algorithm the iteration process – over different generations – starts with the reproduction of the initial parent population.

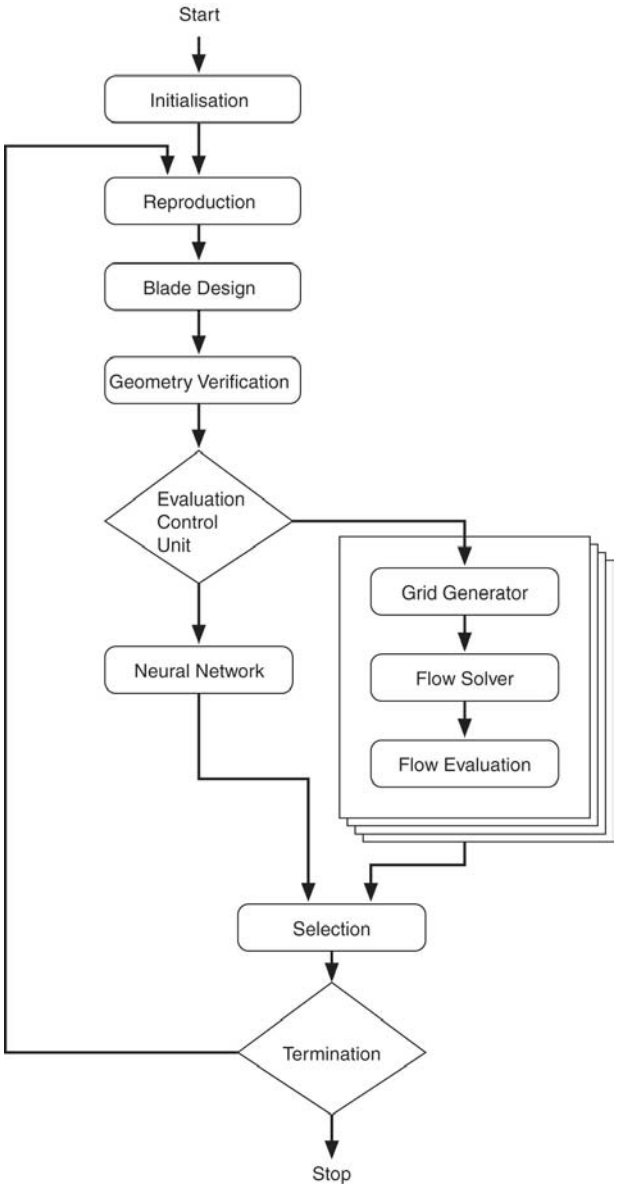


Fig. 13 The overall, modular system architecture.

The representations of the geometries – the blueprints, which are generated in the reproduction step, are mutated according to the used method, see Section 2. Next, in the "design module" the blade models are generated from the representations. In order to determine the quality, different criteria have to be taken into account. In addition to the flow conditions, constraints concerning the mechanical and thermal stability have to be evaluated in the "geometry verification" module.

Thereafter, two different modules are used to estimate the fluid-dynamics properties of the blade. On the one hand, the Navier-Stokes flow solver is used. The results are in very good agreement with physical measurements, however, at the drawback of a high calculation time. Therefore, this part of the system is parallelised: the quality of different geometries is evaluated in parallel on different machines of a computing cluster which was built for this purpose. In this work, the communication between different processes has been organised with the message passing library PVM described by Geist et al.[28]. On the other hand, a neural network model is used to further increase the calculation speed. The frequency with which the neural network model is used is determined by the evolution control method, which was outlined in the previous section.

After the evaluation of all geometries within the actual population the best ones are selected and used as parents in the next reproduction step – the next generation. The algorithm is terminated after it has converged to an optimised geometry or after a given time limit has been reached.

4.5. Optimisation Results

Firstly, we will present the results from optimisation runs using the CMA evolution strategy, see Section 2, without using the neural network module.

In a second part, the speed up due to the use of a neural network is demonstrated by an example of an optimisation of a transonic turbine blade.

In the last part, the comparison of the performance of an optimised turbine blade with the previously available blade geometry is shown. Additionally, results from a physical measurement in the transonic wind tunnel for plane cascades of the DLR (Deutsches Zentrum für Luft und Raumfahrt e.V / German Aerospace Centre) Göttingen are presented in the figure in order to allow a comparison of the simulation results and the physical measurements both of the optimised and the initial geometry.

4.5.1. Evolution strategy

The presented results were obtained with a $(\mu, \lambda)=(1,12)$ evolution strategy. The population was initialised with an existing blade geometry. In Fig. 14 the history of the overall quality during the optimisation process is shown. The number of quality evaluations (calculations) rather than generations is shown on the *x*-axis of all plots. Figures 15 (a) & (b) show the development of the pressure loss ω and the deviation angle α_2 during the optimisation, which are the main criteria for the optimisation. The outliers in Fig. 15 correspond to simulations which did not converge mainly due to unstable non-stationary flow conditions. These geometries were removed from the population.

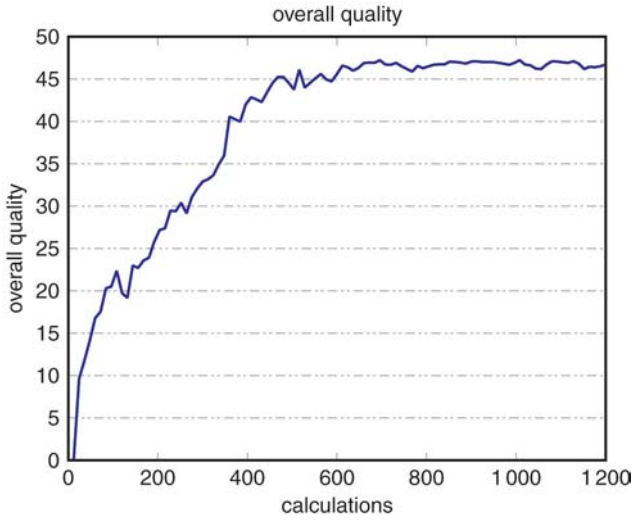
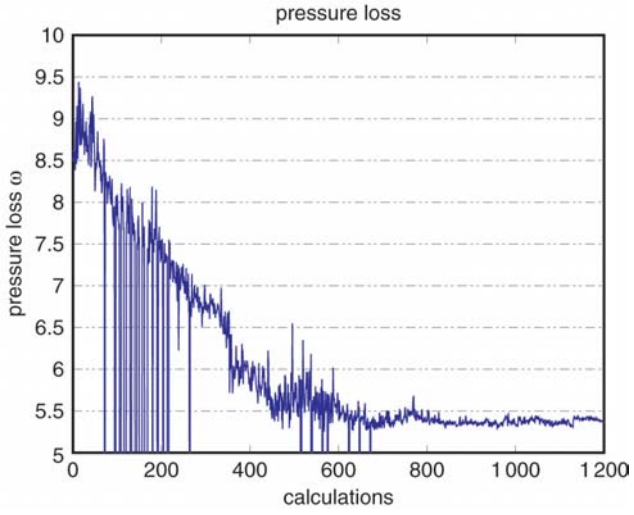
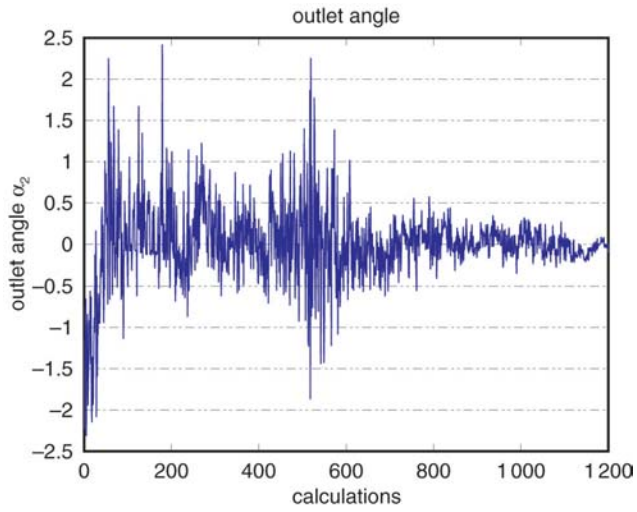


Fig. 14 Blade Quality.



(a)

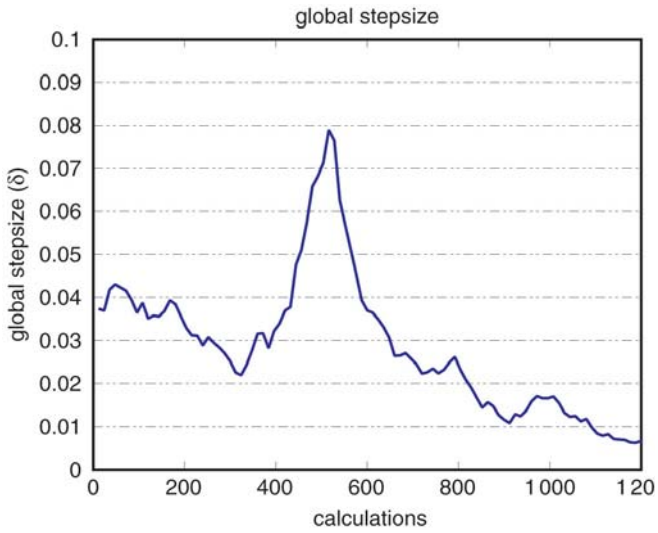


(b)

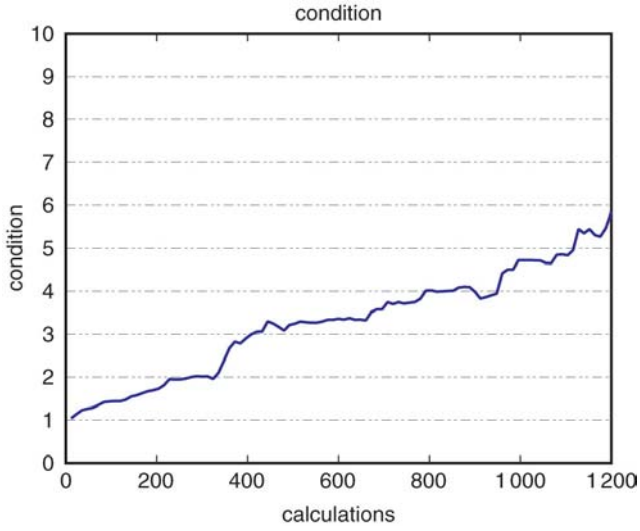
Fig. 15 (a) Total pressure loss and (b) outlet angle.

In order to generate valid geometries, we introduced in the quality function a strong bias towards geometries which fulfil all constraints. Therefore, during the first generations mainly the deviation angle is adapted to the desired value. Thereafter, the deviation angles of the individuals fluctuate within the given tolerance range and the optimisation focuses on the pressure loss.

In order to observe the self-adaptation of the strategy parameters, the global step size δ and the condition of the covariance matrix during the optimisation are shown in Figs. 16 (a) & (b). The condition of a matrix is the relation between its largest and smallest eigenvalue. If all eigenvalues are equal, i.e. the condition of the matrix is one, the iso-density lines of the probability density function for the mutation of the parameters are circles and no adaptation of the strategy parameters has taken place. The larger the difference between the eigenvalues the more pronounced is the "cigar-shape" of the iso-density lines and the more distinct is the preference to one direction. The magnitude of the mutation is controlled by the global step size. In these figures it can be seen, that the global step size as well as the preferred search direction, given by the covariance matrix of the normal distribution, are adapted very early and continuously during the optimisation to the local structure of the quality function. To draw general conclusions, e.g. on the nature of the search space, from these observations which only rely on one particular optimisation run is difficult. However, we can conclude that a self-adaptation of the strategy parameters indeed occurs and that it is guiding the process of evolution to regions of the search space where high quality geometries can be identified.

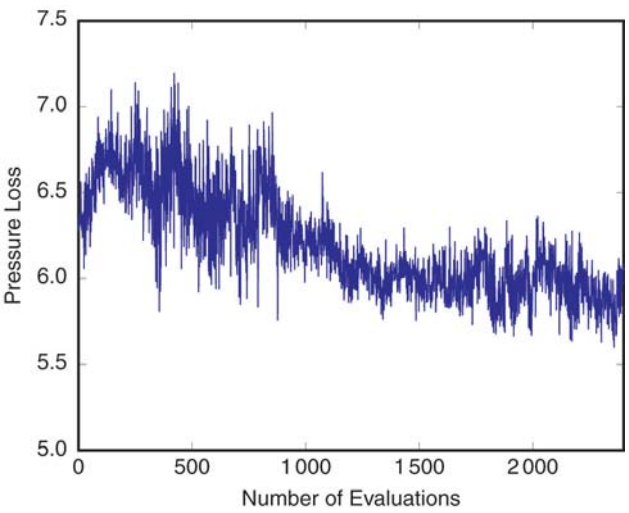


(a)

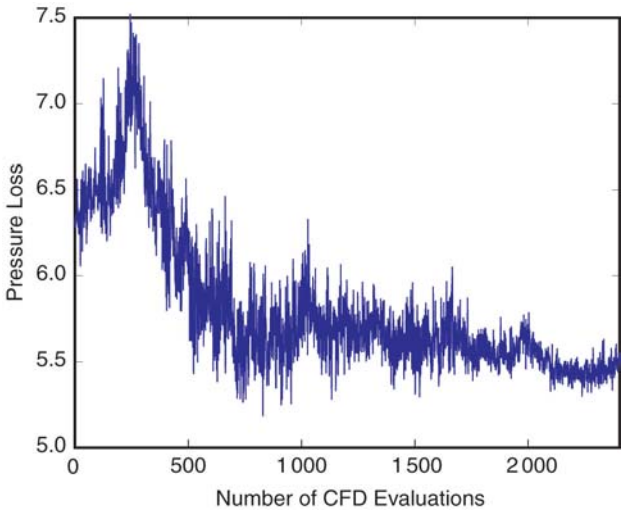


(b)

Fig. 16 (a) Global step size of the CMA algorithm and (b) condition of the covariance matrix.



(a)



(b)

Fig. 17 Optimisation without (a) and with (b) the neural network.

4.5.2. Neural network approximation

Due to the extremely high computational cost of CFD simulations it is beneficial to use approximation models for the estimation of the quality of geometries. Besides being universal approximators, neural networks are particularly suitable for this application because they can be adapted online to new search regions during the optimisation.

Even in case of a lower accuracy of the estimated quality compared to CFD simulations the overall calculation time for optimisations can be reduced often by a factor of two. In Fig. 17 (a) the pressure loss of generated geometries during an optimisation run is shown without using a neural network. In Fig. 17 (b) the result of the same optimisation is shown, but with additional use of the approximation model. On the *x*-axis of both figures the number of CFD evaluations is plotted. Since this is the time consuming part in the optimisation, this number is proportional to the overall computation time. Therefore, using the approximation model, we can increase the total number of evaluations while maintaining a constant overall computation time. In the example the quality which is reached after about 2000 CFD simulations can be reached with the help of an approximation model after some hundred CFD evaluations.

4.5.3. Physical measurement

Besides high performance at the design point, another aim of the optimisation of turbine parts is good performance under variations of the working conditions. In Fig. 18 the total pressure loss ω for the optimised blade is plotted for different outlet velocities m_2. The variations of m_2 are a result of the variations of the thrust in turbines used for the propulsion of aircrafts. The design point which was the target for the optimisation is at ca. m_2 = 1.136 *mach* which is marked by the black vertical line in the figure. The green line shows the pressure loss for the initially available, original turbine blade whereas the red line shows the pressure loss for the optimised design.

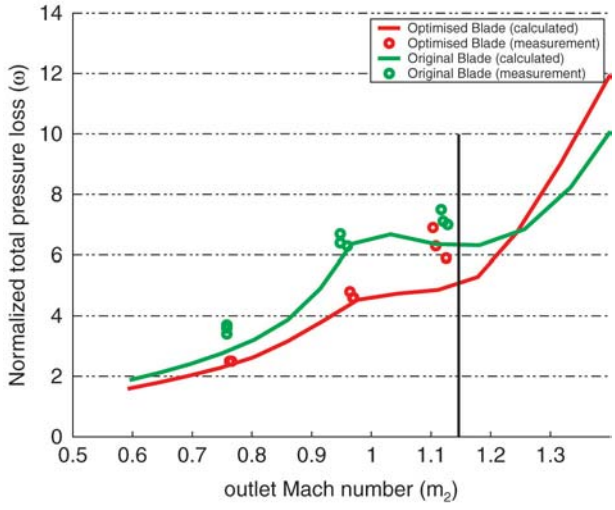


Fig. 18 CFD simulation and physical measurement results for the initial and the optimised blade geometry.

In the simulation the total pressure loss at the design point of the optimised blade geometry is ca. 20% less compared to the original blade. The performance for larger and smaller velocities around the design point is also considerably improved, for smaller m_2 even to a larger degree than at the design point. This tendency is supported by the physical measurement at the DLR transonic wind tunnel for plane cascades in Göttingen, Germany; the data is shown as circles. Both the measurements, as well as, the simulations are very complicated and error-prone, therefore, slight variations like at the design point are to be expected. In addition to the substantial reduction in the pressure loss, the optimised blades did also show unique and previously unknown geometric properties, which exploited some nonlinearities in the flow around the blade to minimise the loss. The turbine experts were able to understand and interpret the flow physics induced by these geometric peculiarities and therefore, new design principles were formulated as a result of the optimisation.

5. Discussion and Summary

In this paper, we outlined the optimisation of transonic turbine blades, starting with the description of the evolution strategy, the optimisation algorithm, which we employed. When we choose the representation, we usually have to face a trade-off between compactness and flexibility. A compact representation allows us to operate in a lower dimensional search space, however, we might not be able to describe all geometrical variations. A higher degree of flexibility gives us a higher degree of freedom for the design, however, the optimisation task will be harder. In order to overcome this problem, recently, adaptive representations have been suggested which aim at combining the best of both worlds, i.e. starting with a compact representation and increasing the flexibility only at specific parts of the geometry during the optimisation, see Olhofer et al.[29].

CFD simulations are computationally expensive, therefore, we proposed a framework in which approximate models, in our case neural networks, can be efficiently combined with the Navier-Stokes solver. The framework takes the actual model fidelity into account and thus, guarantees correct convergence while minimising the number of necessary evaluations using the CFD solver.

The results of the optimisation show that the evolution strategy is able to adapt to the specific topology of the search space. The pressure loss of the optimised blade geometry is reduced by 20% compared to the original, standard blade. Furthermore, it was possible to associate properties of the optimised flow field to geometric changes of the blade. Thus, new design *principles* have been extracted besides of generating one singular optimisation result.

The high quality of the simulation method was finally demonstrated by comparing the physical measurement in a transonic windtunnel to the numerical results both for the original and the optimised blade.

New, “intelligent” optimisation methods together with the latest developments in numerical simulations of system properties, e.g. fluid-dynamics, and processes, e.g. controllers, are likely to play an increasing role in the future of system engineering. Although much remains to be learned from the biological principles of evolution, the optimisation set-up outlined in this work already provides a powerful framework for the solution of complex problems.

6. Acknowledgements

The authors would like to thank E. Körner and M. Hasenjäger for stimulating discussions and their support and advice.

References

(1) T. Arslan, E. Ozdemir, M. S. Bright, and D. H. Horrocks. Genetic synthesis techniques for low-power digital signal processing circuits. In *Proceedings of the IEE Colloquium On Digital Synthesis*, pages 7/1-7/5. IEE, London, UK, Feburuary 1996.

(2) R. S. Zebulum, M. A. Pacheco, and M. Vellasco. Synthesis of CMOS operational amplifiers through Genetic Algorithms. In *Proceedings of the Brazilian Symposium on Integrated Circuits, SBCCI'98*, pages 125-128, Rio de Janeiro, Brazil, September 1998. IEEE.

(3) M. S. Bright and T. Arslan. Multi-objective design strategies for high-level low-power design of DSP systems. *IEEE International Symposium on Circuits and Systems, ISCAS 99*, 1:80-83, May-June 1999.

(4) G.M. Robinson. Load cell shape optimisation using genetic algorithms and finite elements analysis. In *Proceedings of the 14th IMEKO TC3 Conference*, pages 167-172, Warsaw, Poland, 1995.

(5) A.J. Keane and S.M. Brown. The design of a satelite boom with enhanced vibration performance using genetic algorithm techniques. In I.C. Parmee, editor, *Proceedings of the Conference on Adaptive Computing in Engineering Design and Control 96*, pages 107-113, University of Plymouth, Plymouth, 1996.

(6) Xin Yao. Evolving artificial neural networks. *Proceedings of the IEEE*, 87(9):1423-1447, 1999.

(7) B. Sendhoff and M. Kreutz. Variable encoding of modular neural networks for time series prediction. In V.W. Porto, editor, *Congress on Evolutionary Computation CEC*, pages 259-266. IEEE Press, 1999.

(8) H. Furuta, K. Maeda, and W. Watanabe. Application of genetic algorithm to aestetic design of bridge structures. *In Microcomputers in Civil Engineering*, 10/6:415-421, 1995.

(9) S. Obayashi, Y. Yamaguchi, and T. Nakamura. Multiobjective genetic algorithm for multidisplinary design of transonic wing planform. *Journal of Aircraft*, 34(5):690-693, 1997.

(10) J Sobieszanski-Sobieski and R. T. Haftka. Multidisciplinary aerospace design optimization: Survery of recent development. In *34th AIAA Aerospace Sciences Meeting and Exhibit*, Reno, Nevada, 1996. AIAA Paper 96-0711.

(11) A. Vicini and D. Quagliarella. Airfoil and wing design through hybrid optimization strategies. In *16th Applied Aerodynamics Conference*. American Institute of Aeronautics and Astronautics, 1998. AIAA Paper 98-2729.

(12) D.J. Doorly. Parallel genetic algorithms for optimization in cfd. In J. Périaux and G. Winter, editors, *Genetic Algorithms in Engineering and Computer Science*. Wiley, 1995.

(13) Brian R. Jones, William A. Crossley, and Anastasios S. Lyrintzis. Aerodynamic and aeroacoustic optimization of airfoils via a parallel genetic algorithm. In *Proceedings of the 7th AIAA/USAF/NASA/ISSMO Symposium on Multidisciplinary Analysis and Optimization*, 1998. AIAA Paper 98-4811.

(14) D.B. Fogel. *Evolutionary Computation*. IEEE Press, 1995.

(15) H.-P. Schwefel. *Evolution and Optimum Seeking*. John Wiley & sons, New York, 1995.

(16) N. Hansen and A. Ostermeier. Completely derandomized self-adaptation in evolution strategies. *Evolutionary Computation*, 9(2):159-196, 2001.

(17) M. Olhofer, T. Arima, T. Sonoda, and B. Sendhoff. Optimization of a stator blade used in a transonic compressor cascade with evolution strategies. In I. Parmee, editor, *Adaptive Computation in Design and Manufacture (ACDM)*, pages 45-54. Springer Verlag, 2000.

(18) T. Arima, T. Sonoda, M. Shirotori, A. Tamura, and K. Kikuchi. A numerical investigation of transonic axial compressor rotor flow using a low-Reynolds number k-e turbulence model. *Journal of Turbomachinery*, 121:44-58, 1999. Transactions of the ASME.

(19) K. Y. Chien. Predictions of channel and boundary-layer flows with a low reynolds number turbulence model. *AIAA Journal*, 20:33-38, 1982.

(20) T. H. Pulliam and D. S. Chaussee. A diagonal form of an implicit approximate factorization algorithm. *Journal of Computational Physics*, 39:347-363, 1981.

(21) S. R. Chakravarthy and S. Osher. A new class of high accuracy tvd schemes for hyperbolic conservation laws. In *AIAA 23rd Aerospace Scinces Meeting*. American Institute of Aeronautics and Astronautics, 1985. AIAA Paper 85-0363.

(22) C. M. Bishop. *Neural Networks for Pattern Recognition*. Oxford University Press, Oxford, UK, 1995.

(23) Y. Jin and B. Sendhoff. Knowledge incorporation into neural networks from fuzzy rules. *Neural Processing Letters*, 10(3):231-242, 1999.

(24) Y. Jin, M. Olhofer, and B. Sendhoff. On evolutionary optimization with approximate fitness functions. In *Proceedings of the Genetic and Evolutionary Computation Conference*, pages 786-792. Morgan Kaufmann, 2000.

(25) J. Redmond and G. Parker. Actuator placement based on reachable set optimization for expected disturbance. *Journal Optimization Theory and Applications*, 90(2):279-300, August 1996.

(26) A. Ratle. Optimal sampling strategies for learning a fitness model. In *Proceedings of 1999 Congress on Evolutionary Computation*, volume 3, pages 2078-2085, Washington D.C., July 1999.

(27) Y. Jin, M. Olhofer, and B. Sendhoff. Managing approximate models in evolutionary aerodynamic design optimization. In *Congress on Evolutionary*

Computation (CEC), volume 2, pages 592-599, Seoul, Korea, May 2001.

(28) A. Geist, A. Beguellin, J. Dongarra, W. Jiang, R. Manchek, and V. Sunderam. *Parallel Virtual Machine: A Guide to Networked and Parallel Computing*. The MIT Press, 1994.

(29) M. Olhofer, Y. Jin, and B. Sendhoff. Adaptive encoding for aerodynamic shape optimization using evolution strategies. In *Congress on Evolutionary Computation (CEC)*, volume 2, pages 576-583, Seoul, Korea, May 2001.

■ Authors ■


Markus Olhofer


Toshiyuki Arima


Yaochu Jin


Toyotaka Sonoda


Bernhard Sendhoff

Development of a Simple Model for Simulation of Engine Gas Flow

Hiroshi KOBAYASHI* Satoshi YAMAGUCHI* Fumitomo KATAKURA*

ABSTRACT

An engine model allowing real-time computation and having a high degree of reusability was developed for application as a system design tool and as hardware in the loop system (HILS) for electronic control unit (ECU) development.

A distinctive feature of this model is that it is composed of simple models of engine parts. These parts are units in which the gases flow through the engine, they are modeled by applying the law of energy and mass conservation.

The model was installed in a rapid prototype system and used to conduct a comparison with an actual vehicle while it was in operation. The results of the comparison confirmed that the engine air inlet mass rate, the pressure, and temperature in the inlet and exhaust pipes could be predicted with acceptable accuracy.

1. Introduction

In order to provide the customer with high-quality, timely, low-cost products, it is vital that automotive manufacturers raise the level of development efficiency.

To make this happen, the number of trials should be reduced, and the most common approach is, at the design stage, to predict performance, and fix important details of part models by using simulations. In recent years, there has been a movement towards even higher design quality, through integration of CAD and CAE, reduction in labor for model data creation, and inclusion of simulations in the design flow.(1) On the one hand, CAE utilization for single parts has become common, on the other hand, there is an ever-stronger demand for performance predictions for systems which consist of any number of parts.

In ECU development, a virtual system called HILS has been created, and systems that develop control programs and carry out verifications have also been completed.

It has also been generally true that in the design of this system and development of the ECU, simulations have been implemented with different models and in different environments. However, if it were possible to pass over the system built at the development stage, to the ECU development center, as a virtual system, without having to wait for completion of a prototype vehicle, then it would be possible to improve development efficiency through parallel development.

This research project focuses on gas flow in the engine system, and proposes a simulation model that can be applied to both performance predictions, such as turbocharger matching, and HILS for ECU development. This paper reports on the concept of the proposed model, the results of a study of the algorithms used, and the results of a verification comparison between the model and an actual vehicle.

* Tochigi R&D Center

2. Concept of the Model

For the purposes of system performance predictions and application to HILS, the model should meet the following requirements.

(1) Real-time computation
(2) A high degree of reusability

For the application to HILS, real-time computation is an essential condition. Even though computer performance has been improved, modeling a finely discretized system requires significant computing resources, the time taken for calculations is not practical, so generally it is handled as a coarse model using a lumped constant system. In examining the engine gas flow handled in this research project, while there are some phenomena such as pulsation or interference that can only be expressed by spatially finely resolved models, it became clear that even with a coarse model using a lumped constant system, adequate results can be obtained.[2] In this research project, use of the lumped constant system model, giving priority to calculation speed, was assumed, and phenomena expressed with a distributed constant system were expressed as a compensation value.

Because the created model has a high degree of reusability, the time to create new models can be reduced when studying other systems. Therefore, development efficiency is improved. In order to have a desired high degree of reusability, it was very important to fully consider input and output parameters that do not limit single part modeling and connections between models. In this research project, the law of energy and mass conservation was applied to the flow of gas between parts, and as the input/output parameters common between models used to calculate energy, gas mass flow, gas composition ratio, and gas pressure relating to temperature and mass flow were selected.

As explained by Takahashi[3], gas composition needs to be calculated in order to account for the effect of EGR gas on combustion. In particular, with lean-burn combustion that is applied in direct injection gasoline engines and diesel engines, exhaust gases, including excess air, is once again sucked into the cylinder via the EGR valve, and so its effect is even higher. In this research project, flow in each component is calculated, and at the same time, changes in gas specific heat according to component mass proportions are consecutively calculated. The result of the calculation is reflected in calculations of pressure and temperature affected by the specific heat.

In the sections below, details of the model and results of a verification comparison with an actual vehicle are explained.

3. Model Calculation Algorithms

3.1. Overall Outline

A model was created, focusing on gas flow, for the engine component parts of the turbocharger, intercooler, exhaust and inlet pipes, EGR valve, throttle valve, and cylinders. That is to say, no consideration was given to the EGR mechanical parts of the EGR valve, etc., at this time. Because, in terms of gas flow function, inlet and exhaust pipes are equivalent, and EGR valve, throttle valve, and turbocharger nozzle functions are equivalent, basically the same model was used. In order to reduce the amount of data and the calculation load, physical formulae were used as much as possible, and calculation steps were based on time.

An explanation of each model follows.

3.2. Gas Model

3.2.1. Application of the law of energy and mass conservation

Gas pressure, temperature, and composition in the system vary due to compression and expansion due to the turbocharger, cooling in the intercooler, combustion in the cylinder, and gas mixing in the EGR. These thermodynamic parameter changes are governed by the equation of state for ideal gas (Equation 1).

$$pv = mRT \tag{1}$$

p: pressure
v: volume
m: mass
R: gas constant
T: temperature

In this way, the various states of gas, changing according to engine part function, can be modeled by applying the law of energy and mass conservation — for example cooling in the intercooler cannot be converted physically, so it can be captured as thermal energy reduction; and gas mixing in the EGR is a physical conversion, so it can be modeled as addition of the energy and mass of the air and the EGR gas. In this way, the various phenomena in gas flow can be expressed in simple arithmetic calculations of energy and mass, and measurable parameters such as temperature and pressure can be easily calculated.

3.2.2. Gas components

Specific heat, which changes according to gas components, is determined by the components and their mass proportions. In particular, because exhaust gas recirculation amount is continually adjusted by the EGR valve, the air and exhaust gas mix proportion continually changes, so does specific heat. Therefore, in model calculations, too, it is necessary to continually calculate gas specific heat inside the inlet pipe.

Among the exhaust gases generated by combustion, only CO_2 (carbon dioxide) and H_2O (water) are considered, while NO_x (nitrous oxide), CO (carbon oxide) and HC (hydrocarbon) are in such small quantities in normal combustion that they have been excluded. In addition, the CO_2, N_2 (nitrogen) and H_2O, which are generated by reaction of air (N_2, O_2) and fuel (C_nH_m) at the stoichiometric air-fuel ratio, are together defined as combustion gases, and the gases handled by the model are of two types — combustion gas and air. Combustion gas components are assumed to be fixed, and that specific heat is calculated as follows (Equation 2).

$$C_{cmb} = K_{CO_2} \cdot CO_2 + K_{H_2O} \cdot H_2O + K_{N_2} \cdot N_2 \tag{2}$$

C_{cmb}: combustion gas specific heat
CO_2: Carbon dioxide's molecular weight
H_2O: Water's molecular weight
N_2: Nitrogen's molecular weight
K_{CO_2}, K_{H_2O}, K_{N_2}: constants

In this way, by handling the gases flowing in the engine as the two components of air and combustion gas, it is possible to reduce the load of computing load. The specific heat in any part of the system can be calculated in Equation 3.

$$c_{mix} = c_{air} \cdot (1-\lambda) + c_{cmb} \cdot \lambda \quad (3)$$

c_{mix}: Specific heat of mixture of air and combustion gases
c_{air}: Specific heat of air
c_{cmb}: Specific heat of combustion gases
λ: gas component ratio

3.3. Turbocharger

The turbocharger consists of two parts – the compressor that compresses the air, and the turbine that recovers the exhaust gas energy and converts it into rotation energy. In addition, the turbocharger revs are determined from the balance of turbine shaft torque received from the compressor's and turbine's expansion and compression work.

3.3.1. Compressor model

The compressor model calculates compressor upstream and downstream gas flows, component ratio, as well as downstream gas temperature and shaft torque necessary for compression, from the compressor upstream and downstream pressures, upstream gas temperature, and shaft rev can be calculated. Upstream gas flow rate is calculated from a 3D Characteristics Table according to the upstream and downstream compression ratio, as shown in Fig. 1-(a), and turbine revolution speed. Because the gas flow calculated from the characteristics table is volume flow rate on the upstream side, it is converted to mass flow rate according to upstream gas temperature and pressure. Leak is negligible for the compressor, thus gas flow both upstream and downstream, and component ratios, are the same (Equations 4, 5).

$$G_{C_in} = G_{C_out} = f\,(N_{tb}^*, \lambda_{C_in}, T_{C_in}, P_{C_in}, P_{C_out}) \quad (4)$$
$$\lambda_{C_out} = \lambda_{C_in} \quad (5)$$

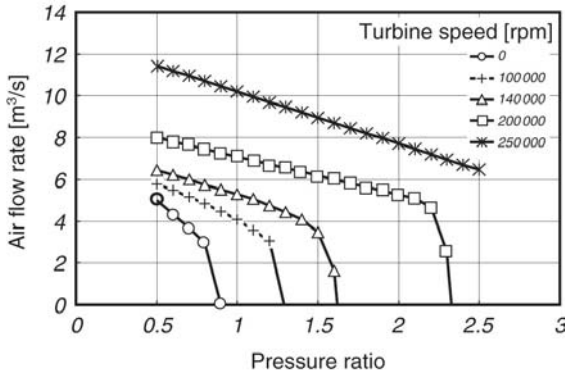
G_{C_in}: compressor upstream gas flow
G_{C_out}: compressor downstream gas flow
N_{tb}^*: turbine revs
λ_{C_in}: compressor upstream gas component ratio
λ_{C_out}: compressor downstream gas component ratio
T_{C_in}: compressor upstream gas temperature
P_{C_in}: compressor upstream pressure
P_{C_out}: compressor downstream pressure

The asterisk (*) shown in Equation 4 indicates a parameter handled inside the model, and is used separately from the externally input and output parameters.

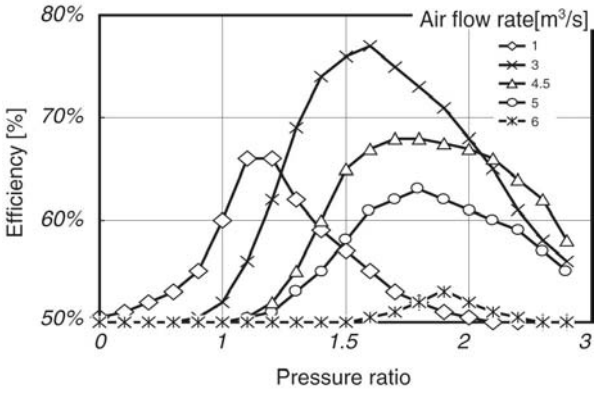
Downstream gas temperature rises due to compression, in reality there is a tendency for the temperature to be higher than of ideal adiabatic compression. As a non-dimensional value expressing this, the compressor adiabatic efficiency characteristics determined, as shown in Fig. 1-(b), by upstream and downstream compression ratio and gas flow calculated in (a) is used, and compressor downstream temperature is calculated (Equation 6).

$$T_{c_out} = f\,(\eta_{tb}^*, \lambda_{C_in}, T_{C_in}, P_{C_in}, P_{C_out}) \quad (6)$$

T_{c_out}: compressor downstream gas temperature
η_{tb}^*: compressor adiabatic efficiency
λ_{C_in}: compressor in-flow gas component ratio



(a) Air flow rate



(b) Efficiency

Fig. 1 Turbine Characteristic 3D Table

Considering mechanical energy used to compress the gas, based on the law of energy conservation to be equivalent to the difference of gas energy between compressor upstream and downstream, the shaft torque necessary for future compression is calculated (Equation 7). The upstream and downstream energies are determined from temperature, gas components, and the amount of gas passing through, used in Equations 4, 5, and 6.

$$M_C^* = f\,(N_{tb}^*, h_C^*) \quad (7)$$

M_C^*: shaft torque necessary for compression
h_C^*: compressor upstream and downstream gas energy difference

3.3.2. Turbine

It was assumed that the turbine is fitted with a variable nozzle, and calculates shaft torque obtained through turbine upstream gas flow, downstream gas temperature and expansion, from turbine upstream and downstream pressures, upstream gas temperature, shaft revs and nozzle opening.

Turbine upstream and downstream gas flow can be calculated according to the same characteristics table method used for the compressor, but as a consideration to reduce the amount of data, a physical formula was applied, based on Bernoulli's principle. In addition, in the same way as with the compressor, upstream and downstream gas flow and component ratios are assumed to be the same (Equations 7, 8).

$$G_{tb_in} = G_{tb_out} = f(A_{tb}, \lambda_{tb_in}, T_{tb_in}, P_{tb_in}, P_{tb_out}) \quad (7)$$
$$\lambda_{tb_in} = \lambda_{tb_out} \quad (8)$$

G_{tb_in} : turbine upstream gas flow
G_{tb_out} : turbine downstream gas flow
A_{tb} : turbine nozzle opening surface area
λ_{tb_in} : turbine upstream gas component ratio
λ_{tb_out} : turbine downstream gas component ratio
T_{tb_in} : turbine upstream gas temperature
P_{tb_in} : turbine upstream pressure
P_{tb_out} : turbine downstream pressure

In the same way as with the compressor, downstream gas temperature is calculated using the turbine adiabatic efficiency (Equation 9).

$$T_{tb_out} = f(\eta_{tb}^*, \lambda_{tb_in}, T_{tb_in}, P_{tb_in}, P_{tb_out}) \quad (9)$$

T_{tb_out} : turbine downstream gas temperature
η_{tb}^* : turbine adiabatic efficiency

Considering mechanical energy used to turn the turbine to be equivalent to the turbine upstream and downstream gas energy difference, the shaft torque necessary to turn the turbine is calculated (Equation 10).

$$M_{tb}^* = f(N_{tb}^*, h_{tb}^*) \quad (10)$$

M_{tb}^* : shaft torque obtained according to expansion
h_{tb}^* : turbine upstream and downstream gas energy difference

3.3.3. Rev calculation

Turbine revs are calculated from shaft torque difference determined by compressor and turbine, and from friction torque of the rotating shaft (Equation 11).

$$N_{tb}^* = K_N^* \cdot \int (M_{tb}^* - M_c^* - M_f^*) dt \quad (11)$$

M_f^*: turbine shaft friction torque
K_N^*: constant

3.4. Intercooler

As for the intercooler, downstream gas temperature is calculated from cooling efficiency, upstream gas flow, upstream gas temperature and external temperature (Equation 12).

$$T_{IC_out} = f(\eta_{IC}^*(G_{IC_in}), T_{IC_in}, T_a) \quad (12)$$

T_{IC_out} : intercooler downstream gas temperature
η_{IC}^* : cooling efficiency
G_{IC_in} : intercooler upstream gas flow
T_{IC_in} : intercooler upstream gas temperature
T_a : external temperature

Because there is no mass conversion in the intercooler, downstream gas flow and component ratio is equal to that upstream. In addition, ignoring pressure loss, there is no change between upstream and downstream pressures.

3.5. Throttle Valve, EGR

For both the throttle valve and EGR models, in the same way as the turbocharger's variable nozzle, upstream and downstream gas flows are calculated using Bernoulli's principle.

3.6. Inlet and Exhaust Pipes

Both the inlet pipe and the exhaust pipe can be considered as constant volume chambers where gases flow in and out. Temperature and pressure inside the pipes are calculated from gas energy in and out, and from mass balance (Equations 13-1 and 13-2).

$$P_{ch} = f(V_{ch}, \lambda_{ch_in}, \lambda_{ch_out}, G_{ch_in}, G_{ch_out}, T_{ch_in}, T_{ch}) \quad (13\text{-}1)$$
$$\mathrm{T_{ch}} = f(V_{ch}, \lambda_{ch_in}, \lambda_{ch_out}, G_{ch_in}, G_{ch_out}, P_{ch}) \quad (13\text{-}2)$$

P_{ch} : pressure inside pipes
V_{ch} : volume inside pipes
λ_{ch_in} : component ratio of gas flowing into the pipe
λ_{ch_out} : component ratio of gas flowing out of the pipe
G_{ch_in} : gas flow into the pipe
G_{ch_out} : gas flow out of the pipe
T_{ch_in} : temperature of gas flowing into the pipe
T_{ch} : temperature in the pipes

Component ratio of gas flowing out of pipes is a complete mixture of air and combustion gas held in the constant volume chamber.

3.7. Cylinder

The cylinder model calculates cylinder in-flow gas flow, exhaust gas flow, temperature and component ratio, from cylinder in-flow gas pressure, temperature, and component ratio, and from fuel flow, and engine speed.

3.7.1. In-flow gas

Cylinder model is expressed as time-averaged constant flow without considering intermittent gas flow due to number of cylinders and piston reciprocating motion. In-flow gas flow is calculated from intake volume efficiency, intake gas pressure, temperature, and cylinder exhaust amount (Equation 14).

$$G_{cyl_in} = f(V_{cyl}^*, \eta_{v_cyl}^*, Ne, \lambda_{cyl_in}, T_{cyl_in}, P_{cyl_in}) \quad (14)$$

G_{cyl_in} : cylinder intake gas flow
V_{cyl}^* : engine displacement
$\eta_{v_cyl}^*$: intake volumetric efficiency
Ne : engine speed
λ_{cyl_in} : cylinder in-flow gas component ratio
T_{cyl_in} : cylinder in-flow gas temperature
P_{cyl_in} : cylinder in-flow gas pressure

3.7.2. Exhaust gas

Exhaust gas is calculated as the total of cylinder in-flow gas and fuel flow amount (Equation 15).

$$G_{cyl_out} = G_{cyl_in} + G_{fuel} \quad (15)$$

G_{cyl_out} : mass flow rate of exhaust gas
G_{fuel} : mass flow rate of injected fuel

Exhaust gas energy consists of intake gas energy and fuel energy being exhausted. Concerning thermal energy due to combustion, assuming that the water generated remains as vapor, a lower heat of combustion is used as the fuel generated energy for each unit weight. The exhaust temperature is calculated from the proportion of flow-in energy and exhaust gas energy, which is defined as the rate of exhaust loss (Equation 16).

$$T_{cyl_out} = f(\eta_{ex_cyl}^*, \lambda_{cyl_in}, G_{cyl_in}, G_{fuel}, T_{cyl_in}) \qquad (16)$$

T_{cyl_out} : exhaust gas temperature
$\eta_{ex_cyl}^*$: exhaust loss rate
λ_{cyl_in} : cylinder in-flow gas component ratio
G_{cyl_in} : cylinder intake gas flow
G_{fuel} : fuel flow
T_{cyl_in} : cylinder in-flow gas temperature

If the amount of air in the intake gas is less than the minimum amount of required air for complete combustion, which is determined from fuel flow and ideal air-fuel ratio, excessive fuel is discharged as unburned fuel.

4. Verification Comparison with Actual Vehicle

4.1. Vehicle Engine System used for the Comparison

The vehicle engine system used at this time was one fitted with a turbocharger and EGR. Fig. 2 connects the models created as part units, and is a block diagram comprising the same system as the actual engine.

4.2. Environment for Verification Comparison with the Actual Vehicle

The verification comparison with an actual vehicle used a real-time method that compared the model calculations and the vehicle measurements, while the vehicle with the model installed is driven. Verification while driving has the advantage of carrying out an on-the-spot comparison under a variety of driving conditions.

Fig. 3 introduces the system used in the verification. The engine model described in the block diagram is created in a personal computer (PC hereafter), and after converting it to a rapid prototyping system (RPS hereafter) executable file, it is downloaded to the RPS and executed. From the engine ECU, model input information such as the engine revs, EGR valve opening, etc., and data for actual vehicle comparison such as the intake air amount, etc., is given to the RPS. Furthermore, data that is not measured by the ECU, such as exhaust pressure and temperature, is input into the AD converter in the RPS, via the signal-processing device. The vehicle comparison data handled by the RPS can be monitored on the PC, along with the calculated model values.

Motorola's Power PC (100 MHz) was fitted to the RPS used, and it is possible to make calculations with floating point. The model's calculation load with the above system was such that model calculation time was approximately 2 msec, and calculation cycle 10 msec.

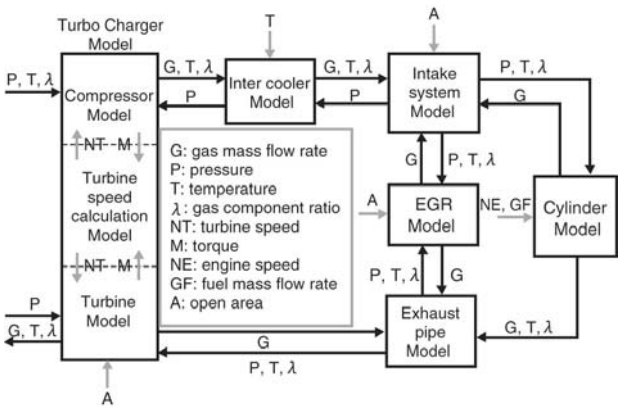


Fig. 2 Engine model block diagram

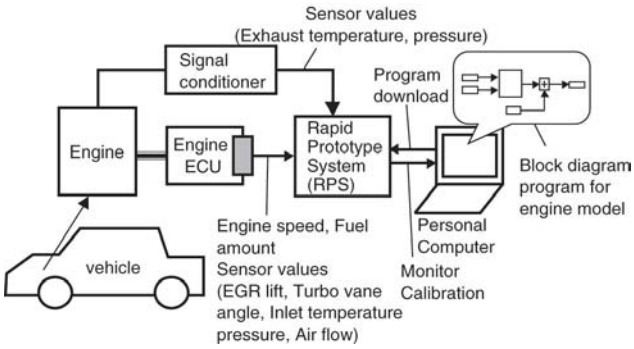


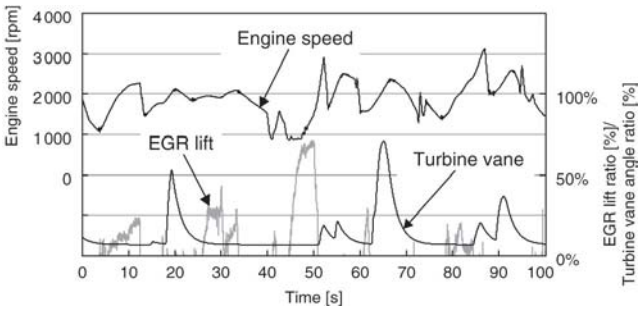
Fig. 3 Model verification system

4.3. Results of Comparison Verification

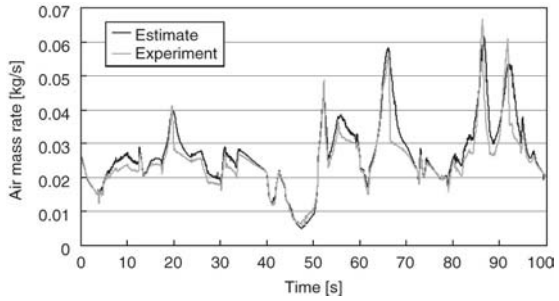
Fig. 4 shows an example of verification results. Vehicle driving was repetitions of arbitrary acceleration and deceleration. For model accuracy verification, a comparison was made of intake air amount, as well as pressure behavior inside inlet and exhaust pipes and temperature behavior.

Fig. 4-(a) shows the behavior of engine revs, EGR valve opening, and turbocharger nozzle opening. These values are measured by the ECU, and become model calculation inputs. Fig. 4-(b) is on the same time axis as Fig. 4-(a), and concerning intake air amount, a comparison is made of actual vehicle and model-calculated behaviors. In addition, Fig. 4-(c) shows a comparison of pressures in the inlet and exhaust pipes, and Fig. 4-(d) the temperatures.

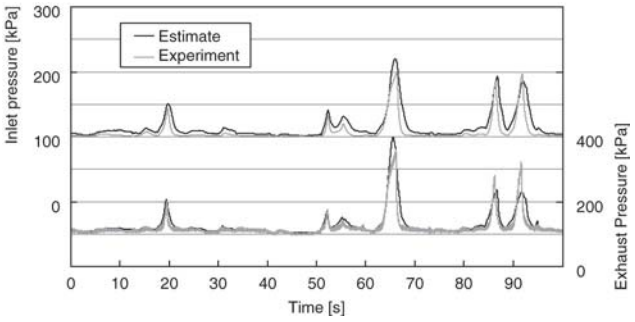
As shown in the comparison results, although when the load drops from a high load, the discrepancy of exhaust temperature is noticeable, as a simple model, gas behavior in various engine components can be roughly simulated. One cause of the discrepancy may be the fact that turbocharger characteristics accuracy, inlet and exhaust pipe radiation heat and their dynamic characteristics are not considered. Another potential cause of the discrepancy may result from measurement accuracy. Future improvements are planned.



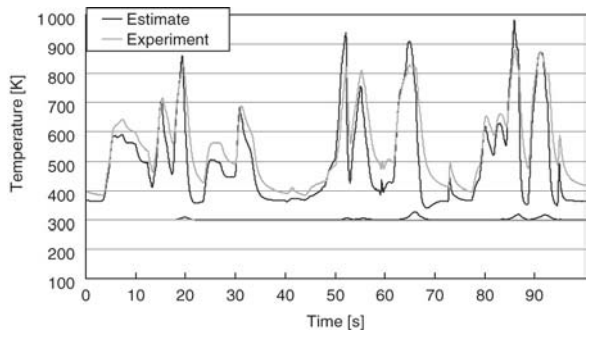
(a) Dynamic behavior of actual engine and actuator



(b) Air mass rate of engine intake



(c) Dynamic behavior of inlet and exhaust pressure



(d) Dynamic behavior of inlet and exhaust temperature

Fig. 4 Test comparison

5. Summary

A model was created concerning gas flow in the engine, with the following main considerations: real-time calculation, a high degree of reusability, system performance predictions, and application to HILS. As for real-time calculation, the model was created on the assumption of lumped constant system modeling. For a high degree of reusability, in addition to part unit modeling, common input and output parameters were established for each part model, thereby eliminating the constraints in connections between models, and heightening the degree of reusability of the model for other systems. This was achieved through the application of the law of energy and mass conservation.

Model accuracy based on these concepts was verified through a real-time comparison between vehicle measurement and model calculation. The results showed that although there is still room for improvement in vehicle and calculation methods and accuracy, as a simple model it is possible to roughly simulate gas behavior in each part. The outlook is good for its use in outline system studies that do not require high precision, and for its application to HILS.

In order to apply this model as a study tool for a system requiring high accuracy, further model accuracy improvements are required. At the same time, it is possible to develop this model beyond gas flow and engine parts, therefore to include more parts for development work.

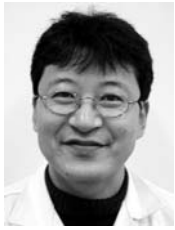
References

(1) Sawada, R.: Simulation Technology and CAD System Fusion, Automotive Technology, Vol. 55, No. 6, p. 14-18 (2001)

(2) Itoyama, H. et al: A Study of an EGR Control System for Diesel Engines Based on an Intake/Exhaust System Model, SAE Technical Paper Series, 970621

(3) Takahashi, S. et al: Exhaust Gas Recirculation Model for Design and Evaluation of Engine Control Systems, The Society of Instrument and Control Engineers Transactions, Vol. 35, No.2, p. 230–237 (1999)

■ Authors ■


Hiroshi KOBAYASHI


Satoshi YAMAGUCHI


Fumitomo KATAKURA

Prediction of Chain Load in Timing Chain System

Hiroshi TAKAGISHI* Hitoshi SUGAWARA*

ABSTRACT

A chain load prediction technique was established to investigate timing chain durability under conditions of a variable valve lift timing mechanism and a continuously variable valve timing mechanism. Modeling a tensioner with a relief valve and valve train made it possible to predict the chain load at different relief pressures and valve timings. Furthermore, telemeter techniques were also developed enabling direct measurement of the chain load at high engine speeds, which was formerly impossible. The validity of the simulation was also verified using an actual engine. These developments made it possible to predict the chain load up to high engine speeds at different relief pressures and valve timings.

1. Introduction

Cases of engine cam drive using chains are increasing in recent years in order to improve durability and reduce size. This makes it necessary to predict the load produced on the timing chain from the design stage. For this reason, techniques for predicting timing chain loads have been actively researched by various companies for the past ten or so years. A wide range of efforts have been reported from simple analysis[(1)–(3)] that performs calculations by adding the valve train torque to a simple model which views the cam and chain as a mass-spring system, to large-scale analysis[(4)-(6)] that performs calculations by replacing each link plate of the chain with a particle. However, simple analysis cannot adequately take into account the effects of hydraulic tensioners which are the most important for development, and large-scale analysis also has problems such as the extensive calculation time that makes timely analysis impossible. Therefore, this paper reports the development of simulation technology capable of accurately predicting the chain load in a short time from the design stage.

2. Focus and Themes

Timing chain system behavior is governed by the inertia of the cams, sprockets and other parts, and by the attenuation of the spring comprised by the chain and subcomponents. The hydraulic tensioner in particular is a hydraulic mechanism with a built-in relief valve, and has a large effect on the chain load.

Also, in the case of gasoline engines, the valve train drive torque is the dominant force that excites the chain system, and the valve train parts have a large effect on the chain drive torque.

Therefore, a simulation technique was established focusing on the following points.

Focus 1: Modeling the characteristics of a tensioner with a relief valve
Theme: Assuring the accuracy of tensioner frequency dependent behavior due to relief valve flow channel resistance

Focus 2: Creating a model that includes the valve train which is the main exciting force on the chain
Theme: Assuring the accuracy of changes in the chain load due to differences in the valve train specifications

* Tochigi R&D Center

3. Modeling the Characteristics of a Tensioner with a Relief Valve

3.1. Simulation Model

Fig. 1 shows the tensioner used in this study. The force applied to the tensioner plunger is maintained by the main spring and the oil taken into the high-pressure chamber. If the input load is high at this time, the oil leaks from the relief valve and the gap between the plunger and the housing opens to reduce the load.

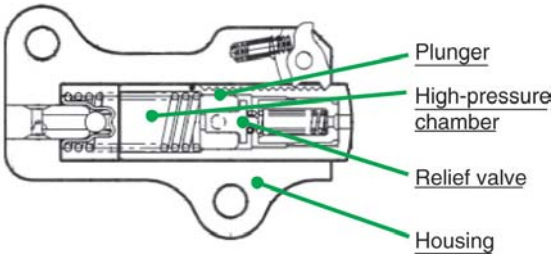


Fig. 1 Chain tensioner cross section

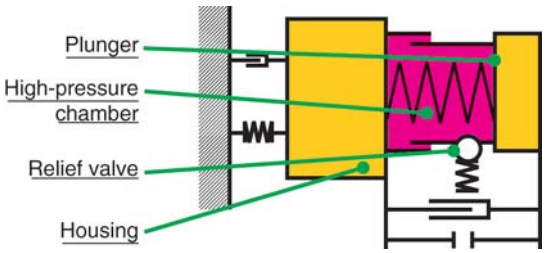


Fig. 2 Tensioner simulation model

This tensioner is replaced with the coupled vibration model of the plunger, spring, high-pressure oil chamber and housing shown in Fig. 2. The main spring and high-pressure chamber models are located between the piston and the housing, and the pressure-dependent nonlinear stiffness of the oil due to the influx of air is also taken into account. An oil intake check valve is also incorporated into the high-pressure chamber model. In addition to leakage from the gap between the piston and the housing, oil discharge from the relief valve was also modeled. Taking into account the pressure loss due to the viscous resistance of the oil during discharge, the flow rate of the oil passing through the relief valve at this time was approximated using the following equation.

$$Q = \pi \cdot d \cdot l \cdot \sqrt{\frac{2 \cdot P_h}{\rho \cdot (1 + \xi)}}$$

Q: Flow rate
d: Valve sheet diameter
l: Valve lift
Ph: High-pressure chamber oil pressure
ξ: Coefficient of loss
ρ: Oil density

3.2. Verification Test

Discrete vibration tests were conducted using a hydraulic exciter to understand the dynamic characteristics of the discrete tensioner. Fig. 3 shows an outline of the test apparatus. The tensioner is fixed on the plunger and excited by pressing the plunger against a load detector. Excitation was performed by feeding hydraulic fluid from an external pump to the tensioner. Measurement assumed crank second order resonance up to 6,000 rpm, and was performed in the three steps of 30 Hz, 100 Hz and 200 Hz. Excitation consisted of displacement control, and was performed with a sine wave having a double amplitude of 0.4 mm. The validity of the simulation was verified by creating a Lissajous' waveform from the load generated and the tensioner displacement.

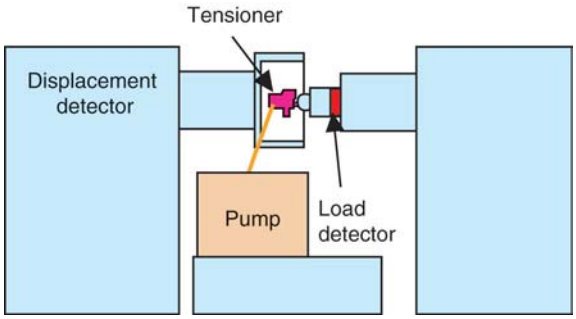


Fig. 3 Hydraulic excitation test apparatus

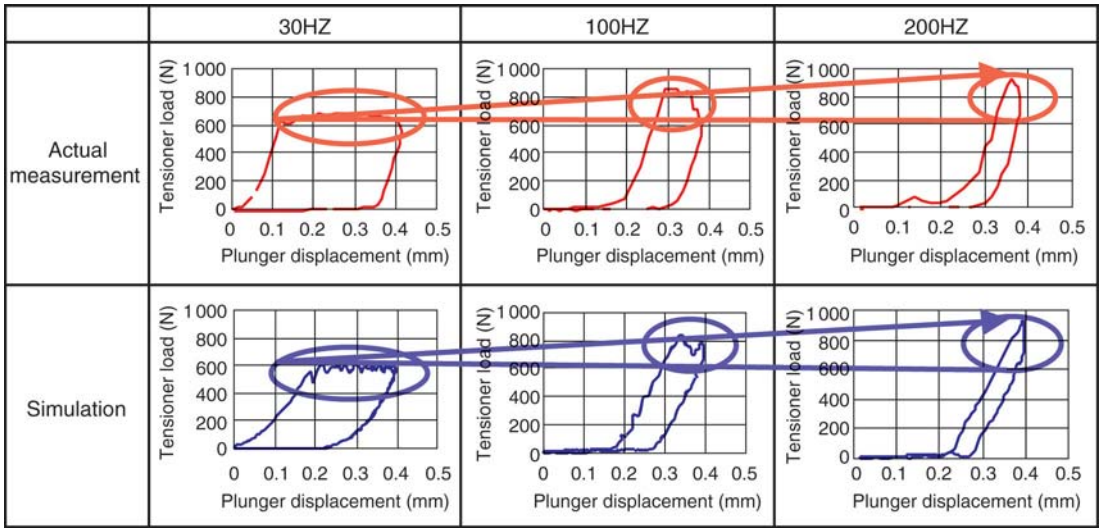


Fig. 4 Result of tensioner discrete excitation

3.3. Verification Results

Fig. 4 shows that the load and displacement could be accurately reproduced at 30 Hz, 100 Hz and 200 Hz. In particular, the reduction hysteresis and increase in the load at high frequencies could be accurately reproduced. This established that the simulation possessed sufficient practical accuracy for the discrete tensioner.

4. Creation of a Model Including the Valve Train which is the Main Exciting Force on the Chain

4.1. Simulation Model

The validity of the chain load simulation was verified using the engine shown in Fig. 5. This engine combined a variable valve timing lift mechanism and continuous variable valve timing mechanism, and featured high fuel economy, high output and reduced exhaust gas levels.

To perform the simulation, a calculation model was created of the chain system and the valve train in order to predict the timing chain load. Each valve system part was divided into particles, and a multi-body system approach that links each particle with stiffness and attenuation was adopted. Calculation used the second order Predictor/Corrector method[7], and calculations were performed in the steady operation state in 200 rpm intervals.

Fig. 6 shows the overall model. The valve, rocker arm and cam shaft drive train model is driven by the chain model. Also, the chain model tension is maintained by the model of the tensioner with a relief valve described in section 3.1.

The details of each part are described below.

Fig. 7 shows the variable valve timing lift mechanism valve train, and Fig. 8 shows its model. Model creation focused on the case when using a high-speed cam with a large chain load. At high speeds the three rocker arms are coupled by pins. Therefore, the simulation also modeled the rocker arms in the same manner with the high-speed rocker arm in the center driving the left and right rocker arms.

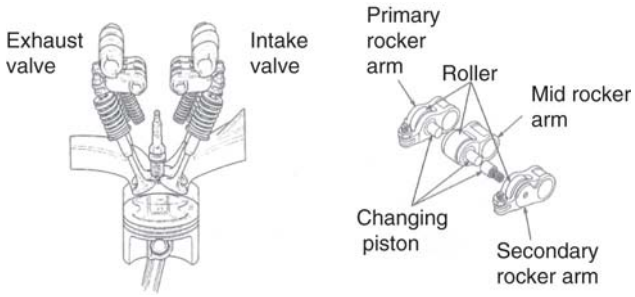


Fig. 7 Valve train

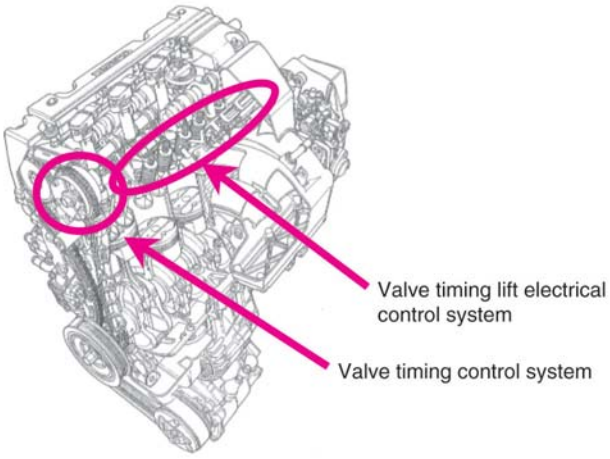


Fig. 5 Engine used for validation

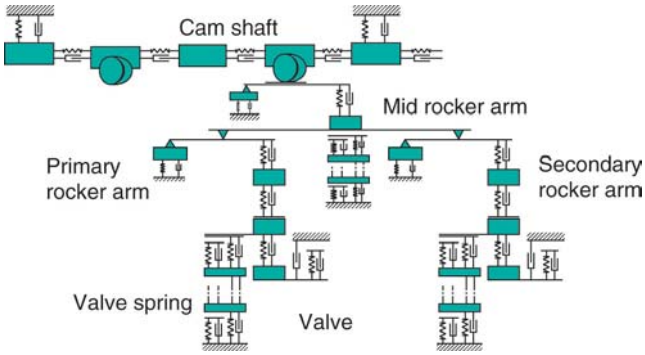


Fig. 8 Valve train simulation model



Fig. 6 Overall simulation model for timing chain load

Fig. 9 shows the structure of the continuously variable valve timing mechanism. This mechanism is a vane type actuator, and transmits driving force via oil filling its four chambers. This makes it possible to reduce the stiffness in comparison to steel parts.

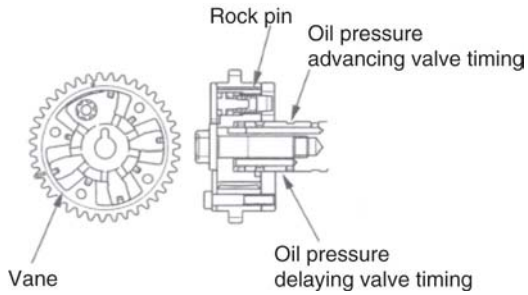


Fig. 9 Valve timing control actuator

Therefore, the stiffness was estimated and modeled using the following equation.

$$C = 4 * K * \frac{A^2}{V} * r^2$$

C: Stiffness
K: Bulk modulus of the oil (oil air content 10%)
A: Pressure receiving area
V: Oil volume per chamber
r: Effective radius

Fig. 10 shows the chain arrangement. The chain is a 6.35 mm pitch silent chain that drives both the intake and exhaust sprockets simultaneously.

Guides are provided to prevent lateral chain vibration on the tension side between the intake cam and the crank and between the intake and exhaust cams. The tensioner maintains the chain load on the slack side between the exhaust cam and the crank using an arm.

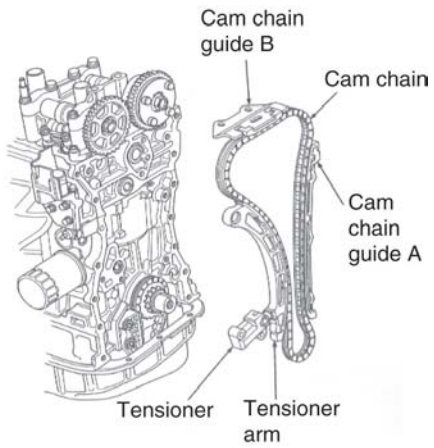


Fig. 10 Timing chain system

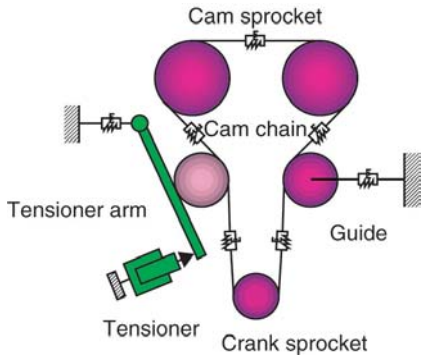


Fig. 11 Timing chain simulation model

The timing chain load is maintained in the direction perpendicular to the chain advance by guides and a tensioner in this manner. Thus, during normal operation, the tensioner plunger displacement is approximately 0.1 to 0.2 mm, and the lateral chain vibration can be ignored. Therefore, a one-dimensional model was created in the longitudinal vibration direction which is the main direction of chain tension.

Fig. 11 shows the chain model. The inertia of each part is coupled by the chain stiffness and attenuation, and an arm and tensioner are provided between the exhaust cam and the crank as in an actual engine. The model was created so that the tensioner maintains the chain load via this arm.

4.2. Tests to Verify the Validity of the Chain Load Simulation

Verification used an engine under development, and the simulation results were compared with the measurement results of firing tests.

4.2.1. Verification by torque measurement

First, the validity of the chain load simulation was verified by a relatively simple torque measurement.

The chain drive torque was measured by affixing a strain gauge to a thin tube attached to the crank sprocket. The simulation created a similar axle model and calculated the drive torque. This drive torque was divided by the pitch radius of the sprocket and used as the chain load for verifying the validity of the simulation. Comparison was performed in the high speed range using the high-speed cam at 6,000 rpm or more when the chain load is high. In addition the inlet valve timing advance was varied in the three steps of 0, 30 and 50 degrees as shown in Fig. 12 to check the tracking performance of the simulation. Fig. 13 shows the results of comparing the maximum chain load values.

The simulation accurately reproduced the maximum chain load over the wide range from 6,000 to 8,600 rpm. The simulation also accurately followed changes in the valve timing advance. Fig. 14 compares the time series data at a valve timing advance of 30 degrees at each speed of 6,000, 7,000 and 8,600 rpm. The waveforms match at each speed, thus confirming that the chain load can be reproduced with high accuracy.

Next, the tracking performance of the simulation at different tensioner relief valve pressures was verified. Fig. 15 shows the results when the relief pressure was lowered from 2.2 MPa to 1 MPa. These results verified that the developed simulation has excellent tracking performance even with respect to changes in the relief pressure.

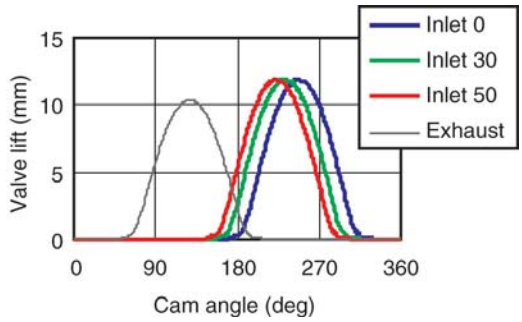


Fig. 12 Valve lift timing

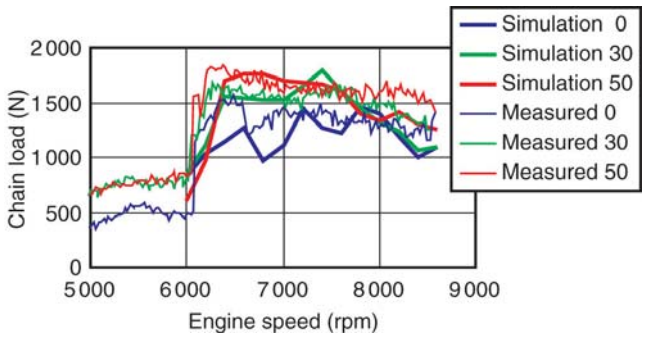


Fig. 13 Maximum value of timing chain load

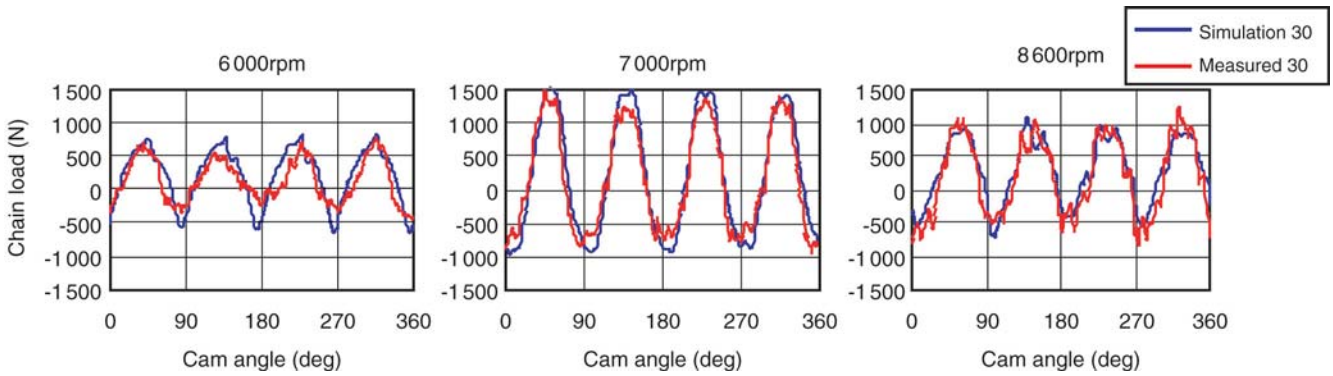


Fig. 14 Timing chain load fluctuation

4.2.2. Verification by chain load measurement

Estimating the chain load from the torque generated in the crank portion is a simple technique. However, this technique is unable to measure not only the pre-load applied to the chain, but also the chain load generated between the cams. Therefore, the signal from the strain gauge affixed to the chain must be extracted in order to directly measure the chain load. There have also been cases in the past where measurement was performed by connecting a piano wire or other auxiliary cable. However, this technique requires that the chain cover be removed for measurement, which not only causes lubricating oil to splatter, but the piano wire also flies about when the piano wire mount comes off due to centrifugal force, which is extremely dangerous. Therefore, these problems were solved by using a telemeter.[8] Fig. 16 shows a chain with the telemeter attached. The chain load is detected from a strain gauge affixed over the guide plate. The holder weight was reduced to allow measurement up to the

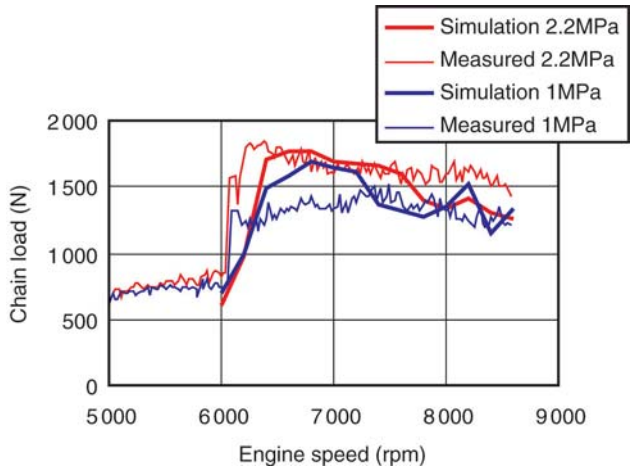


Fig. 15 Maximum value of timing chain load (Relief pressure 2.2 Mpa, 1 Mpa)

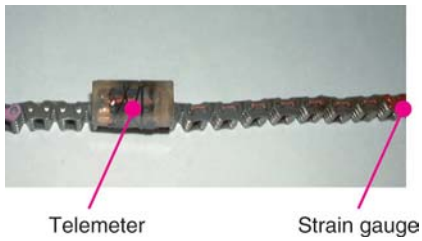


Fig. 16 Chain with telemeter

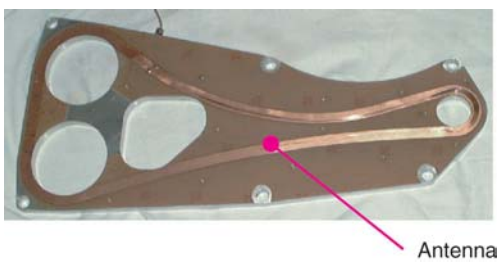


Fig. 17 Antenna for telemeter

high rpm range, and the strain gauge and holder were separated by an appropriate distance to prevent the strain gauge from being affected by centrifugal and inertial forces. Current was supplied from the antenna shown in Fig. 17 through the telemeter to the strain gauge, and the signal detected at the same time was extracted externally from the telemeter through the antenna.

Fig. 18 shows an example of the output signal. Changes in the chain load could be measured continuously as the chain passed through the tension side and slack side spans and the span between the cams. Using this telemeter system made it possible to directly measure the chain load up to the high rpm range of 8,000 rpm or more.

The load generated on the chain was also taken from the simulation and compared with these results.

Fig. 19 compares the chain load measurement results obtained using the telemeter and the simulation results for each span up to 7,000 rpm. These results confirmed that changes in the chain load can be accurately reproduced in each span.

5. Example of Application

The established simulation was applied to investigate measures for reducing the chain load. Fig. 20 shows the sprocket shapes before and after optimization, and Fig. 21 shows the chain load for each shape. The moment of inertia of the exhaust cam sprocket was increased from 0.00029 kgm^2 to 0.0007 kgm^2, and the chain second order resonance rotations were adjusted to minimize the cam second order excitation force. This reduced the chain load by approximately 15%, and these effects were also confirmed using an actual engine.

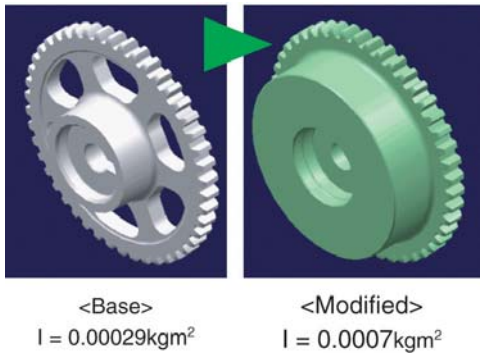


Fig. 20 Cam sprocket shapes

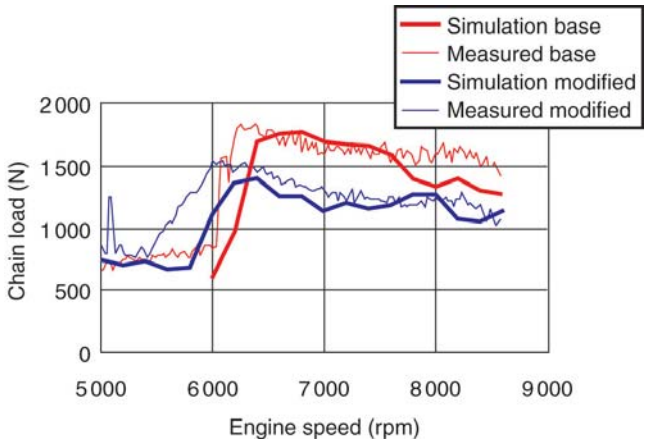


Fig. 21 Example of application

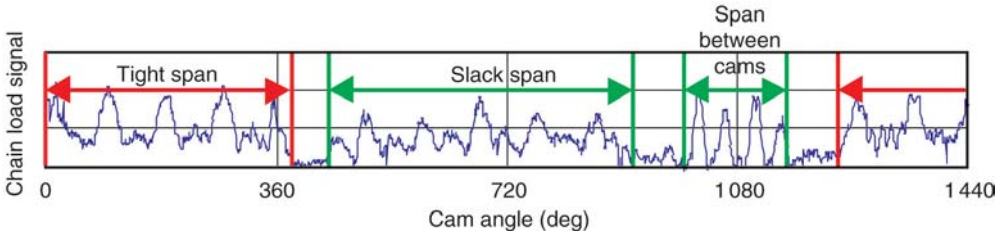


Fig. 18 Example output signal

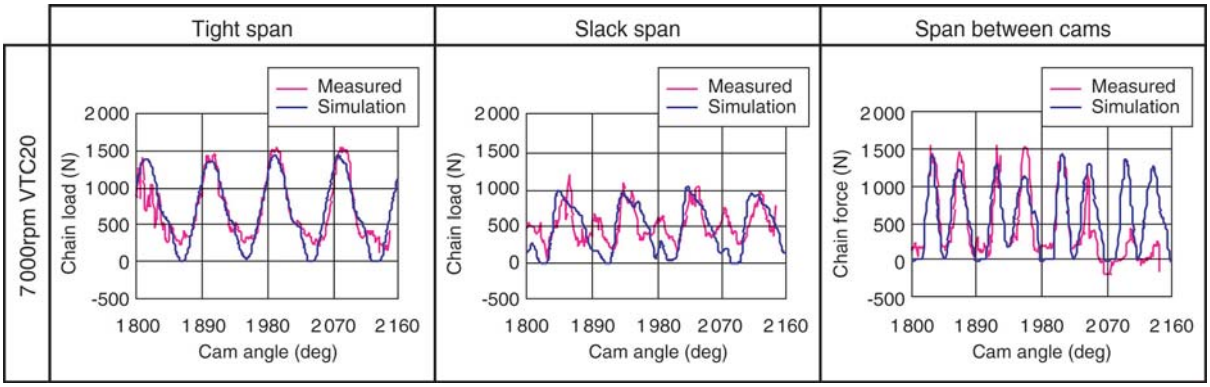


Fig. 19 Chain load comparison between simulation and telemeter measured data

6. Conclusion

This research yielded the following results.

(1) A timing chain load prediction technique was established which takes into account tensioner frequency dependent behavior due to relief valve flow channel resistance and has sufficient accuracy for practical application to different valve timings.

(2) This simulation was applied to an actual development, and confirmed to be effective for reducing the chain load.

7. Acknowledgements

The authors wish to express their deepest thanks to all parties for their immense cooperation in developing this simulation.

References

(1) Wang, K. W.: Vibration Analysis of Engine Timing Chain Drives with Camshaft Torsional Excitation, SAE Paper 911063

(2) Reinicke-Murmann, J.: Analysis and Development of Camshaft Drive Systems Using a Computer Simulation, SAE Paper 9400448

(3) Hwang, Shng-Jiaw: Torsional Response of Automotive Timing Chain Systems, SAE Paper 940689

(4) Gregori, H.: Simulation der dynamischen Effekte im Steuerkettentrieb mit Hilfe der FE-Method, Konstruktion 45 p. 358–364 (1993)

(5) Rosse, J.: Simulating the Dynamic Behaviour of Chain Drive Systems by Advanced CAE Programs, SAE Paper 960298

(6) Ishimoto, E., Suzuki, K.: Vibration of Roller Chain Drive System, TSUBAKI TECHNICAL REVIEW Vol. 5, No. 1, p. 41–48 (1995)

(7) Hellinger, W. Priebsch, H. H, Rainer, G.Ph: Auslegung von Ventiltrieben für Hochleistungsmotoren — Rechnerische und Experimentelle Verfahren. 16. Internationales Wiener Motorensymposium 1995

(8) Weber, C.: Experimental Investigation into the Dynamic Engine Timing Chain Behavior, SAE Paper 980840

■ Authors ■



Hiroshi TAKAGISHI



Hitoshi SUGAWARA

Development of Gear Train Behavioral Analysis Technologies Considered Nonlinear Elements

Shingo UEDA* Tatsuo SUZUKI*
Mitsuyoshi KAMIYA* Tadashi NIINO*

ABSTRACT

It has been identified that the rotation behavior of gears is influenced by housing deformation, radial clearance, tooth elastic deformation, etc., in the modeling process of the behavior calculation model of a gear train in motorcycle engines. To maintain a high level of accuracy, influence factors were converted to the stiffness components in the rotational direction, and were built in the rotational transfer model of the gear train. Furthermore, a behavior calculation model of a crankshaft was combined as a drive excitation source of the behavior calculation model of gear train. Time domain numerical integration method was used for calculation of the transient response that changes widely by engine speed change. A jump phenomenon of response behavior of the driven gear was predicted that is a characteristic of a non-linear response. The calculation result accuracy was confirmed through correlation with an actual test engine. It was understood that this behavior calculation of gear trains could be used as a technological tool for engine development.

1. Introduction

There are various mechanisms used for revolution transfer in an engine such as gears, chains, CVT, and fluid couplings.

A small engine such as a typical general motorcycle engine shown in Fig. 1, contains a transmission mechanism. The requirements for low weight and miniaturization of motorcycle engines, are higher than those for passenger car engines as is the requirement for high engine r/min and high load factor. In order to meet the requirement, many gear train mechanisms are adopted for the valve train and accessory power train systems.

Incorrect behavior of the gear train system reduces durability and becomes a source of noise that can make a product less attractive. Undesirable gear train behavior includes an unstable revolution speed leading to a rattling noise in the gears, thrust movement of helical gear, and inclination due to a lack of bearing rigidity. The prediction of gear train behavior becomes difficult when considering these unnecessary behaviors for rotation transfer.

When resonance occurs in a motorcycle engine gear train system consisting of small parts, the usual countermeasure is to increase the natural frequency of the system and to set the resonant frequency outside normal engine speed range. An alternative way is the use of springs and dampers that have a buffer function in the rotational direction. However, many prototype tests were required to decide the final specifications as there were no tools available for predicting gear train behavior even for the rotational transfer direction.

This paper reports the development of a simulation method for the rotational behavior of the gear train system, and its calculated results were agreed with experimental results including non-linear response.

* Asaka R&D Center

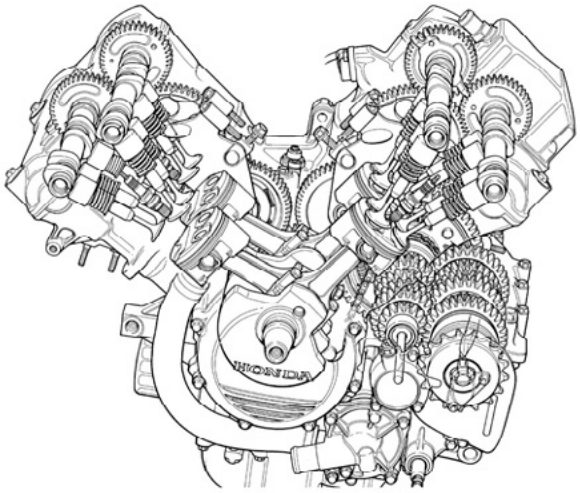


Fig. 1 Example of gear train system for a motorcycle engine

2. Modeling of Revolution Transfer Mechanism

2.1. Modeling of Revolution Transfer Mechanism

Generally, the driven gear is forced to oscillate by the angular velocity fluctuation of the crankshaft.

The basic model of the gear train system was made as a single degree of freedom model and forced vibration considered with backlash and friction. Composition of the basic model is shown in Fig. 2. A one-dimensional model produced by connecting basic models in-line or parallel was made as a model of gear train. Each basic model is combined in-line or parallel, and the one-dimensional gear train model was constructed by these combined systems. The number of the degrees of freedom is decided only by the number of transfer elements. The modeling approach for spring characteristics is explained in Subsection 2.2. Damping coefficient C is determined as a unique function of K by the parameter study.

The damper frictional resistance was dealt with as a continuous slide. The frictional force was supposed to be an almost constant value when the speed difference is above a certain fixed slight speed difference, and to be zero at no speed difference the discontinuous area has been interpolated as shown in Fig. 3. When angular velocity fluctuation is given to gear train, it shows the phenomenon that the driven gear drives the drive gear. This phenomenon is produced by the release of rotational inertia energy saved in a driven gear. When the backlash and angular velocity fluctuations are considered simultaneously, it is understood that the gear tooth flank repeatedly comes in contact and separates. Therefore, we used time domain numerical integration method according to Newton-Ruphson Method for the behavior calculation of a gear train model.

2.2. Modeling of Spring Characteristics

The gear stiffness in the rotational direction of the simulation model is an important parameter that influences the accuracy of analysis. This gear rigidity consists of a composition of rigidities of each part, for example, shafts to support rotating units, bearings, housings, hub-tip twist, tooth flank slant, etc. Each gear has the radial clearance and can move within it. Such drive gear movement in the radial

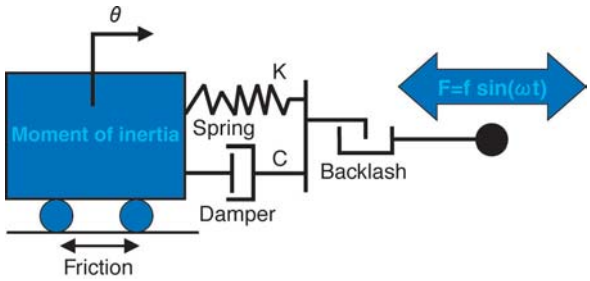


Fig. 2 Forced torsional vibration model of single degree of freedom system with clearance and friction

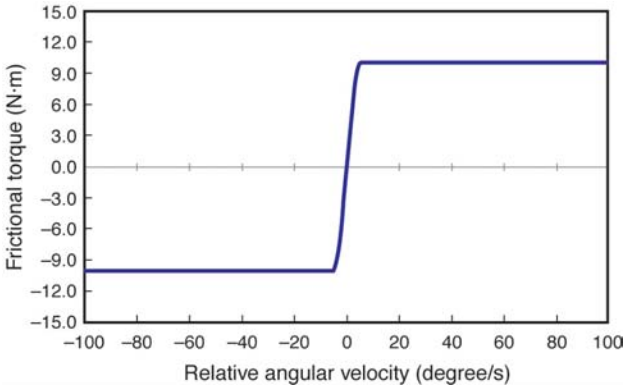


Fig. 3 Continuous friction torque

direction influences the rotational displacement of the driven gear. In the gear train, rotational displacement of the end driven gear could be integrated one by one. Therefore, it is very difficult to predict the rigidity in the rotational direction by simulation, the same as it is difficult to physically measure it.

Under the circumstances, we devised a method to obtain the rigidity of the rotation direction of each gear by combining a calculation result with a measurement result. Following is the explanation of this method as it applies to a cam gear train of a motorcycle engine used in a simulation model as shown in Fig. 4.

At first, we obtained load-displacement characteristics of the total gear train system by FEM static analysis. Next, we listed the configuration factors that influence displacement in the rotational direction. We carried out contribution ratio analysis of each listed factor for displacement of the rotation direction of the total gear train system. In addition, we obtained volume of deformation of each gear from a result of FEM static analysis beforehand.

We performed the actual measurement. It was carried out by stopping the revolution of the crankshaft. We measured the displacement of the cam gear tooth flank from when the backlash is zero. That tooth flank was caused by applying a known torque to the camshaft. The gear movement in the radial directions is also measured at normal and reverse rotation of gears. Finally, the simulated rigidity of the whole gear train system in the rotational direction was correlated with the measured rigidity, and the FEM analysis was verified with high accuracy. For the actual statical FEM analysis model, the gear holder, cylinder block and even the measurement equipment are modeled precisely. The influence of equipment was removed from the rigidity of the gear train system using the contribution ratio analysis.

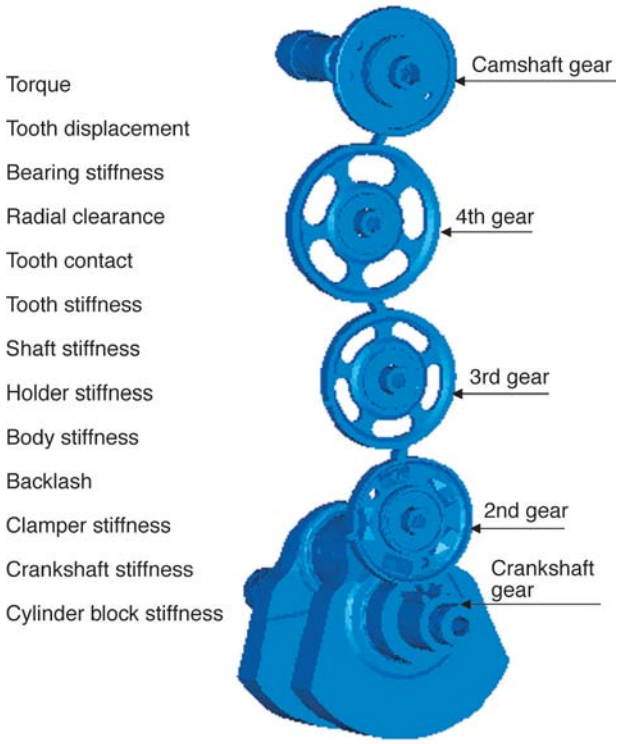


Fig. 4 Structure of gear stiffness calculation model

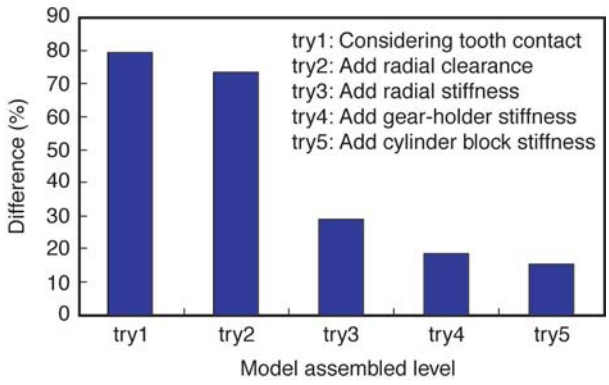


Fig. 5 Difference of gear train total stiffness between simulation results and physically measured values

Figure 5 is an example of data used for contribution ratio analysis of the factor that influenced displacement in the rotational direction. From this data, it was found that the difference between the physically measured value and the calculated one became smaller by adding factors that influence the rigidity in the rotational direction to the static FEM analysis model one by one. The rigidity data of an individual gear in the rotational direction were obtained from correlated FEM static analysis by the rigidity of the total gear train system, and inputted for the behavioral analysis model.

2.3. Modeling of Structure of Non Linear Damper

A gear train characteristic is that there is no phase difference between the drive side and the driven side when transformation and clearance are ignored. Deformation of parts and clearances in the actual gear train generate impact loads to the tooth flank. Therefore, we often use a damper which reduces the shock using the damper stroke operated by the deformation of springs, rubbers and frictional force occurring simultaneously. This operation angle of the damper generates a phase difference in the gear train. Generally, the phase difference due to the damper stroke is larger than the gear deformation and clearance.

When applied to the simulation model, we used the physically measured value instead of the design value for damper characteristic. A typical damper characteristic has a hysteresis as shown in Fig. 6. As for the non-linear spring characteristics of the damper, we adopted the median value of the hysteresis curve as an input value, and made interpolation with the spline function of damper stroke angle - torque. The hysteresis was also adopted for the damper spring characteristic that was decided by the relative angular velocity vector occurring between parts of the drive side and the driven side of the damper.

3. Gear Train of Actual Machine and Model

In the case of the power train system of an actual machine, behavior in the rotational direction of each gear is complicated because they have the backlash of each part, the bumper mechanism acting like a damper, and stoppers to limit the stroke angle. Vibration within the backlash in the rotational direction causes the tooth flank impact load. In addition, if the engine speed is close to it's natural frequency, rotational behavior becomes more complicated because the increase in damper stroke amplitude is forcefully limited by a stopper accompanied by shock.

There are some parameters in this analysis model, such as the amount of backlashes, non linear spring characteristics of each part, rigidity of damper stoppers, and each damping characteristic. These parameters were obtained by the method of combining calculated results with measured results. Fig. 7 shows the verification of correlation results between the physically measured value and calculated value for rigidity of the total gear train system in the rotational direction, when we decided each parameter.

In addition, Fig. 8 shows rigidity of each gear in the rotational direction obtained from the FEM static analysis model having correlation of rigidity of the total gear train system in the rotational direction. The gradient of each graph shows the rigidity in the rotational direction of the each gear. The rigidity was calculated from the rotational angle of each gear that includes the displacement caused by deformation. The small gradient in the graph means that not only the rigidity of the gear is high but also the rigidity of the bearing is high as well, which is the supporting part of the gear. Each backlash value was obtained from the graph. The cross points of the vertical axis, where torque equals zero, and the extension line of each gear stiffness indicates the movable range caused by the backlash and radial clearance.

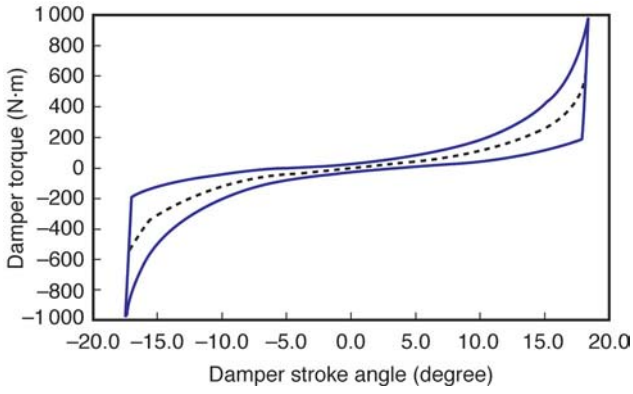


Fig. 6 Spring and friction damper characteristics

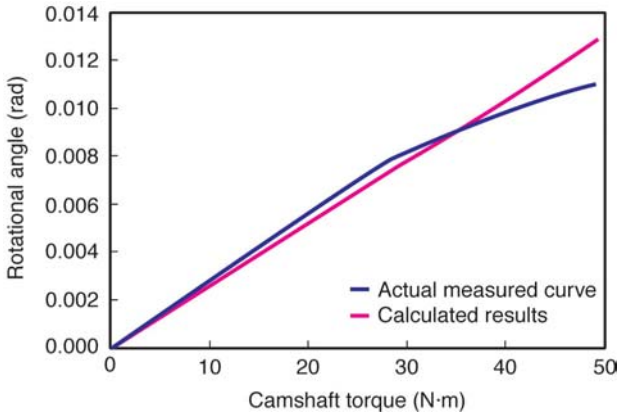


Fig. 7 Correlation between simulation and test about the gear train system torsional stiffness

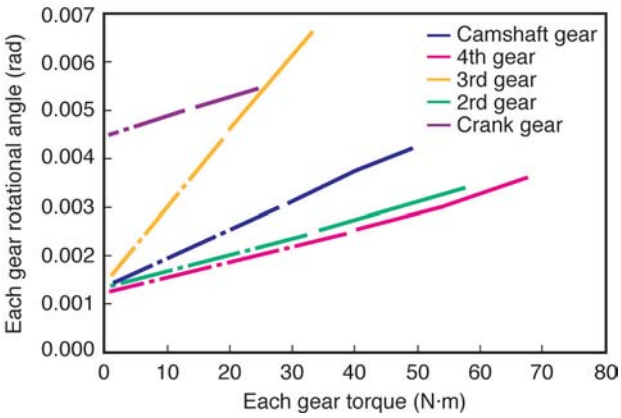


Fig. 8 Torsional stiffness of each gear

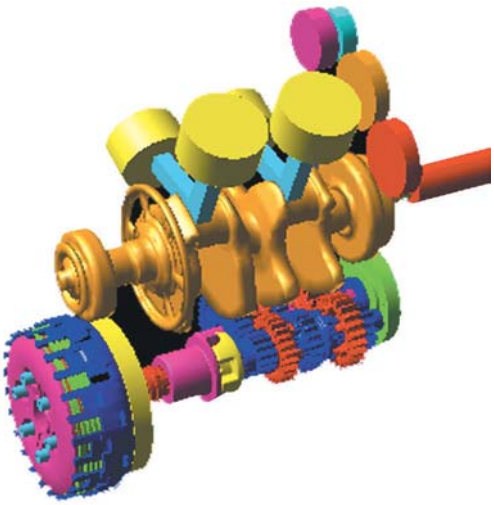


Fig. 9 Model of V4-type crankshaft behavior simulation

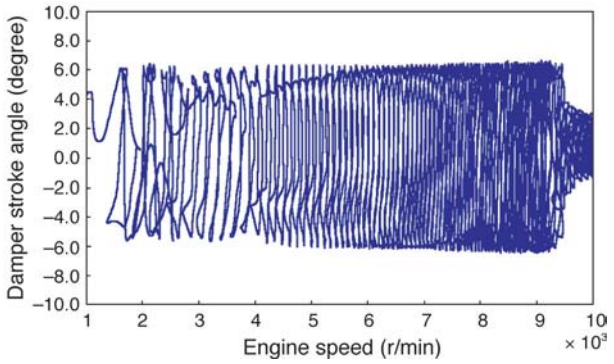


Fig. 10 Calculated damper stroke angle operating by WOT scanning mode

4. Application Example

4.1. An Application to Generator Power Train System

To adopt a gear train for the accessory drive train of the 90 degree V-type 4-cylinder engine, as shown in Fig. 9, we produced a simulation model (2) for behavior calculation of the crankshaft. The cylinder pressure value is determined as a function of the crankshaft angle, and is loaded on the piston. Therefore the piston drives the crankshaft and the fluctuation of the angular velocity provides the rotational vibration for the gear train. We carried out a response behavior analysis of the drive gear train system of a generator using this model simulating a firing operating condition. The operating condition was set to full load acceleration, at an engine speed range of 3,000-10,000 r/min referring to a physical engine test on a test bench. Figure 10 shows the calculation result that is the behavior response amplitude of the damper stroke angle. The graph shows that the stroke angle amplitude is limited by a stopper in the area of low and middle engine speeds. A jump phenomenon that the amplitude converges in discontinuity occurred when the engine speed was 300 r/min slower than the resonance engine speed (9,864 r/min) that was theoretically calculated using moments of inertia and spring characteristics in the current model.

The transfer torque fluctuation that is absorbed by the damper is shown in Fig. 11. It was observed from the calculation result that the amplitude of the damper torque increases with engine speed, but, suddenly converges in discontinuity at high engine speed. It was also found that the timing of the jump phenomenon was synchronized between the stroke angle and damper torque amplitudes. Therefore, we made an experimental damper having the same non-linear specifications as the current simulation model and installed it on an actual test engine. As a result, we could confirm that the jump phenomenon occurred at 8,500 r/min as shown in Fig. 12 and the calculation was verified.

From the result, we could simulate the jump phenomenon non-linear response behavior using the behavior calculation model of the gear train operated over a wide range of engine speeds that are specific to motorcycle engines.

4.2. Trial of Aggressive Practical Use of Jump Phenomenon

As a result of simulation and measurements, we understood that the amplitude of the damper stroke angle and the torque was reduced after the jump phenomenon occurred.

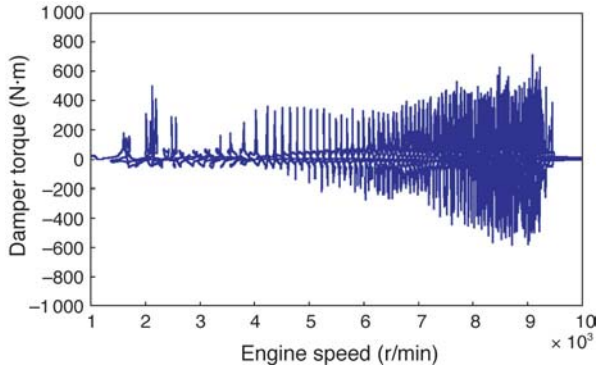


Fig. 11 Calculated results of damper torque operation by WOT, scanning mode

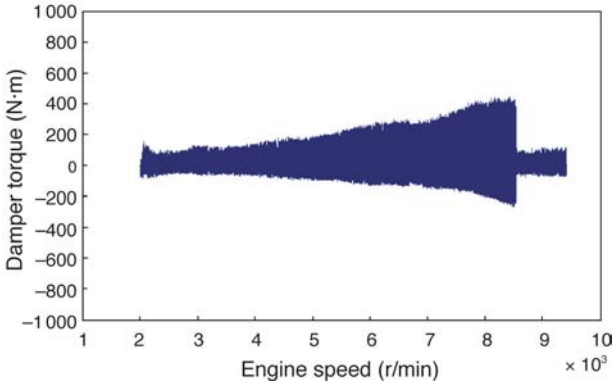


Fig. 12 Measured results of damper torque operation by WOT, scanning mode

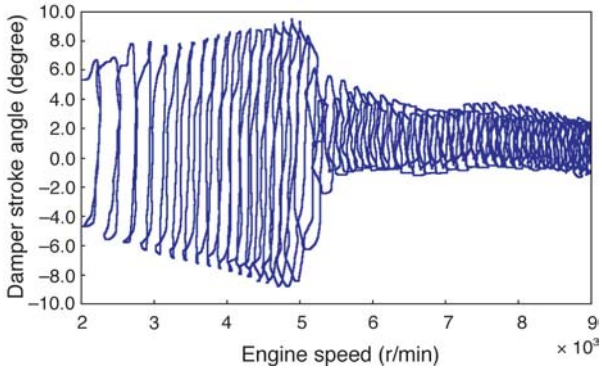


Fig. 13 Calculated damper response, in case of V4-type engine operating WOT, scanning mode

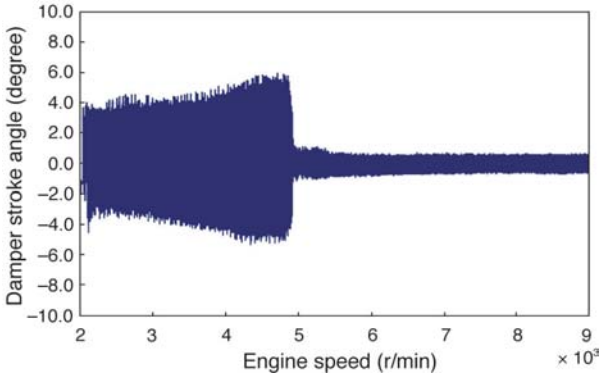


Fig. 14 Physically measured damper response, in case of V4-type engine operating WOT, scanning mode

We tried to effectively generate the jump phenomenon at engine speeds less than 3,000 r/min where the time of engine usage is very short, and at the normal engine speed range of 3,000-10,000 r/min where the damper behavior is stable.

Through the parameter studies, to generate the jump phenomenon at a low engine speed, we found that a big enough moment of driven part inertia and small enough spring rate are the requirements.

In order to improve the accuracy of predicting the engine speed at which a jump phenomenon occurs, we used the measured values of the damper characteristics and the in-cylinder pressure. Figure 13 shows the simulated transient response of the damper stroke angle amplitude and Fig. 14 shows measured result with an actual test engine. Although there is a difference in the absolute amplitude value, we could improve the accuracy of the motion simulation since the engine speed where the jump phenomenon occurred was 4,800 r/min in both cases. However, we also found that the structure to generate a jump phenomenon at engine speeds lower than 3,000 r/min requires a larger inertia of moment and smaller spring rate, which makes the engine layout too large.

4.3. An Example of Jump Phenomenon Practical Usage

Through extended parameter study, we found the important factor required to generate the jump phenomenon is not a faster engine speed but a larger application of the vibration frequency. We selected a horizontal opposed 6-cylinder engine, as shown in Fig. 15, having a combustion stroke at every 120 degrees of crank angle for the study of multi-cylinder engines since the torque fluctuation frequency becomes high. The gear train system is installed as the generator drive line, and the damper was mounted on the drive side of the generator in this engine. This generator's equivalent inertia moment is equal to the crankshaft and offsets the moment of rolling direction that occurs when the motorcycle engine speed is changed. The stroke angle of the damper is large and the spring rate is small. The operation mode was set to full load acceleration of 1,000-5,000 r/min and the damper torque was calculated as shown in Fig. 16.

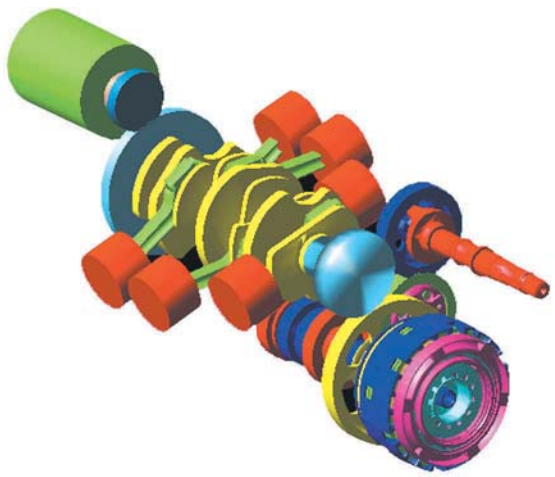


Fig. 15 Model of F6-type crankshaft behavior simulation

This graph shows the torque amplitude is already small enough at a low engine idling speed and the gear train is insulated from resonance through the range of calculation. This contributes to the creation of a motorcycle with low vibration.

4.4. Application Example of the Cam Gear Train

In the case of the engine running at a high speed, the gear train is adopted for the valve train system. It is understood that one advantage of the cam gear train is more precise dynamic valve timing at high engine speeds compared with a cam chain drive. However, there is a backlash in this cam gear train as well and output performance deteriorates when valve timing is lost in the case when rotational behavior becomes unstable. In addition, it gives a bad influence to the valve motion and greatly deteriorates the durability of the valve.

Therefore, by applying this calculation method to the experimental engine, we tried to correlate between the calculated and measured results for the cam gear train behavior. We used the crankshaft motion simulation model results as described in 4.1 and input it into the cam gear train model. Figure 17 shows the results of both the calculation and measurement of cam gear angular velocity fluctuation. The calculation has good correlation with the measurement for angular velocity fluctuation in amplitude and phase. As described above, this calculation method enables us to examine the gear train specifications before building a physical prototype. The flexibility of determining specification was by clarifying the factors that contribute to the rigidity along rotational direction, as described in 2.2, although it was thought the rigidity of each gear should be higher in order to set the resonant frequency outside the normal engine speed range.

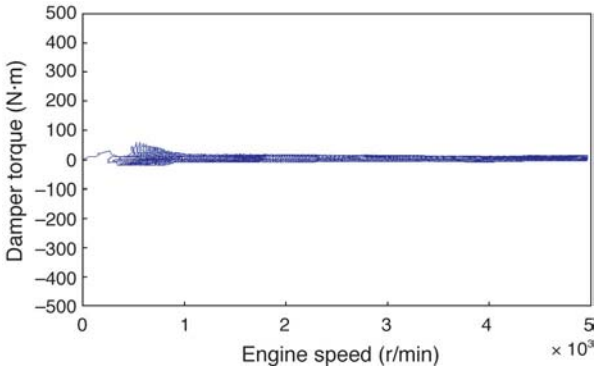


Fig. 16 Calculated damper response, in case of F6-type engine operating WOT, scanning mode

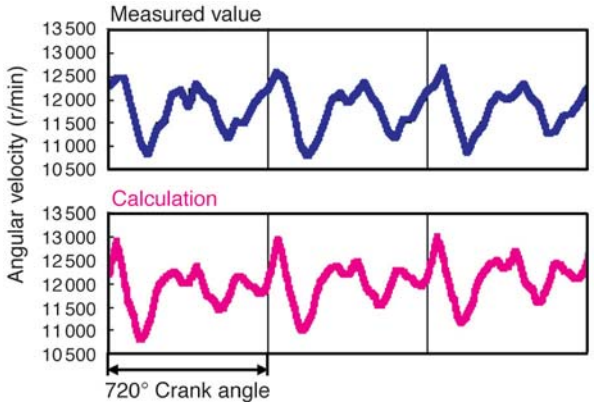


Fig. 17 Correlation between phisically test and simulation about camshaft angular velocity

5. Conclusion

We established the behavior simulation method of rotational transfer mechanism including non-linear elements and the following was found:

(1) The behavior of response calculation for a gear train has been completed over a wide range of engine speeds and the jump phenomenon that is the characteristic of a non-linear response was simulated. This technology has enough accuracy and is applicable to commercial engine development.

(2) Analysis accuracy has been improved for performing behavior simulation of a gear train by adding elements such as deformation of bearing, radial clearance, and slant rigidity of the tooth flank.

References

(1) Masumi KATAOKA, Shinichi ONO, Tsuneo SUZUKI: Study on forced torsion vibration of 2 degrees of freedom series having excessive play and friction. The University of Tokyo, Process Technology R&D Laboratories, Report Vol. 35 No. 3. March, 1989.

(2) Tadashi NIINO, Tatsuya IWAMOTO, Shingo UEDA: Establishment of Dynamic Motion Simulation Technologies of Crankshaft used in Motorcycle Engine. Society of Automotive Engineers of Japan, Inc., Arts and Sciences Lecture, Proceedings, No. 146 (2000)

■ Authors ■


Shingo UEDA


Tatsuo SUZUKI


Mitsuyoshi KAMIYA


Tadashi NIINO

Quantification of Luxury and Sporty Car Interior Sounds Perceived by the General Public in Different Markets

Kousuke NOUMURA* Junji YOSHIDA*

ABSTRACT

Sensory evaluation tests were conducted to clarify differences in Japanese, German, and American perception of car interior sounds. The results of statistical analysis indicate that perceptions can be classified under two major categories: Luxury and Sporty, and that car interior sounds can be represented by these two axes. Further analysis of the sensory evaluation tests showed that sound preferences could also be described by these same categories. It is seen that even people with different preferences could have the same perception of luxury and sporty sounds. By country, a sporty acceleration sound was most preferred by Japanese, American, and German subjects, respectively. An application was developed that is capable of computing objective values for luxury and sporty sounds.

1. Introduction

To guarantee overall automobile marketability, improvements to sound quality are essential. In order to achieve these improvements, many psychoacoustic metrics have developed to quantify human hearing as an objective index. There have been a number of proposals for psychoacoustic metrics around the world, ranging from attributes that express simple auditory stimulus levels, such as loudness or roughness, to complex attributes, such as annoyance or sportiness[(1)]. However, as an index, these are usually multiple choice, so giving due consideration to market differences and driving condition differences, it is difficult to incorporate everything. Therefore, a rational, easy-to-use index is desirable.

In this research project, sensory inspections were implemented, with the subjects being ordinary Japanese, German, and American people. An ordinary person's perceptions about sounds inside cars were clarified through statistical analysis. Objective evaluation attributes were then determined, that can be applied universally, under different driving conditions including acceleration, cruising, and idling, etc. The goal was to develop a sound evaluation system that realizes this calculation algorithm. In addition, mention is also made of which sound qualities are preferred by the people in each country, by making clear the links between the various attributes and sound preferences.

* Tochigi R&D Center

2. Sensory Evaluations

2.1. Subjects

The people involved in the evaluation were men and women from each of the countries involved, ordinary people in their 20s through their 50s. Table 1 shows the number of people involved in the actual testing under the various driving conditions.

Table 1 Number of subjects

Driving condition	Japanese		German		American	
	Male	Female	Male	Female	Male	Female
Acceleration	23	7	25	5	18	12
Cruise	16	8	15	5	5	3
Idle	16	8	16	4	17	10

2.2 Sounds Presented in the Evaluations

Sixteen sounds were selected for each of the following driving conditions: under acceleration, cruising and at idle. Binaural measurements were taken on 21 vehicles using an artificial head microphone located in the front passenger seat. In order to determine universal objective evaluation attributes, the focus of attention was to have as many different vehicle models and driving conditions as possible. The composition of models ran from small 3-cylinder through large 8-cylinder powered vehicles. Moderate acceleration, fast acceleration and cruising at speeds between 40 km/h and 150 km/h were used. These presentation sounds were edited to be 2 seconds in length, and in order to limit non-continuous sound generation, an exponential function weighting process was carried out for 0.2 sec at each beginning and end of the signal.

When listening to the sounds, headphones were used, but compensation was made to frequency characteristics and sound level considering headphone characteristics. The sound reproduced was faithful to the original sound.

Table 2 Kinds of attribute for subjective testing

	Japanese	German	American
1	大きさ	laut	Loud
2	こもり感	dröhnend	Booming
3	滑らか感	glatt	Smooth
4	鋭さ感	scharf	Sharp
5	重厚感	klingt solide	Solid
6	迫力感	kraftvoll	Powerful
7	軽快感	lebendig	Alive
8	高級感	Exklusivität	Luxury
9	ファントゥドライブ	Spaß am fahren	Fun to drive
10	スポーティ感	sportlich	Sporty
11	好み	bevorzugen Sie	Preference
12	のび感	durchzugsstark	Engine extensibility

2.3 Evaluation Attributes

To describe vehicle interior sound attributes, terms such as those shown in Table 2 are often used. Comparing these 12 attributes from the different countries, while there may be differences in feelings, and the impression given by the sound might not be exactly the same, those terms that were roughly equivalent were selected.

In this report, in order to relate the meaning of the words with the sensory feelings, and in order to avoid changing the meaning of the words through translation, we have included the terms in their original languages — Japanese, German, and English.

2.4 Test Method

In carrying out the test while giving weight to judgment accuracy by the subjects, the method of paired comparison[(2)] — where the sounds are listened to and compared with each other — would be the most appropriate. However, with 16 types of presentation sounds, 120 pairs comparing 12 attributes, and furthermore, with 3 types of driving conditions, the test scope was impractical. Therefore, a new test method, a tournament type of paired comparison, was used. With this method, the 16 types of sound were randomly made into 8 pairs, and a comparison judgment made according to evaluation scores, as shown in Table 3. The selected sound was treated as a “winner”, and comparisons continued as a tournament. The subjective difference of each sound in this tournament is calculated by focusing on the losers. In each comparison, the winner’s scores are subtracted from the loser’s score, creating negative scores, and then totaling the scores along each sound’s branches on the elimination tree from the winner. The winner would have 0 points (nothing subtracted). At this time, it is very important for the comparison combinations to be randomly changed, to eliminate the effect of combinations.

A personal computer and a playback system are used for the test, as shown in Fig. 1. The subjects are asked to operate an original application. There is 1 second of silence before each of the two presentation sounds, making a total of 6 seconds. This sequence is repeatedly played until the subject makes a judgment. When the subject makes a judgment, the sound with the higher score wins and so

Table 3 Standard of judgment for subjective testing

Score	Japanese	German	American
0	判断できない	keine von beiden	Undecidable
1	ややそうである	trifft etwas zu	Applicable to some extent
2	そうである	trifft zu	Applicable
3	非常にそうである	trifft voll zu	Applicable to the greatest degree



Fig. 1 System for subjective testing

remains, and the program moves to the next presentation sound. The software program automatically operates this series of events and calculates the difference.

3. Analysis of Sound Perception

3.1 Extracting the main evaluation attributes (comprehensive attributes) perceived inside a car

Based on the order data from each evaluation attribute obtained from the sensory evaluation test, statistical analyses were made. First, with the purpose of quantifying the average perception of ordinary people, an analysis of variance[3] was carried out for each of the 12 types of evaluation attributes. Attributes that differed between subjects were eliminated. Table 4 gives the analysis results for the three subject markets. At this time, attributes with a significant probability of 0.05 or more were eliminated from analysis.

Next, principal component analysis[4] was carried out, to extract the main perceived evaluation attributes for sounds inside a car.

The results of this principal component analysis showed that for Japanese people, during acceleration the factor load weightings for “sporty”, “engine extensibility” and “powerful” were 0.981, 0.952, and 0.877 respectively, as shown in Table 5, so the first major component is defined as the sporty series attributes.

In the same way, when an analysis was made of each country’s driving conditions, although the number one and number two components differed according to driving conditions, they were the sporty series or the luxury series, or even a combination of the two, and it was obtained that the sporty series and the luxury series can mainly be expressed in 2 axes. Therefore, the sporty series and the luxury series resulted in comprehensive evaluation attributes — for Japanese “supo-ti kan” and “koukyuu kan”, for Germans “sportlich” and “Exklusivität”, and for Americans “Sporty” and “Luxury”.

The words of the comprehensive evaluation attributes, “sporty” and “luxury”, are not words that originally describe sounds. However, the reason they were taken up at this time is assumed to be a result of ordinary people passively learning automotive sounds in the market, and these attributes are ordinarily identified as the product characteristics of automobiles. In addition, these attributes indicate concepts for automobile development.

3.2 Selection of Evaluation Attributes that are Vital Elements (Elemental Attributes) in Comprehensive attributes

As previously noted, the words for comprehensive attributes do not, in themselves, describe sound, resulting in a tendency toward vagueness. If it is made clear what sort of elemental attributes comprise the comprehensive attributes, then the information will be more detailed and will be easier to link to physical properties. Therefore, multiple regression analyses[4] were carried out in order to extract the elemental attributes comprising the comprehensive attributes.

Table 4 Result of analysis of variance

(1) Japanese

Attribute	Acceleration	Cruise	Idle
大きさ	0.000	0.000	0.000
こもり感	0.000	0.000	0.000
滑らか感	0.000	0.000	0.000
鋭さ感	0.000	0.000	0.000
重厚感	0.000	0.001	0.000
迫力感	0.000	0.000	0.000
軽快感	0.000	0.612	0.000
高級感	0.002	0.000	0.000
ファントゥドライブ	0.000	0.000	0.000
スポーティ感	0.000	0.000	0.004
好み	0.000	0.000	0.000
のび感	0.000		

(2) German

Attribute	Acceleration	Cruise	Idle
laut	0.000	0.000	0.000
dröhnend	0.000	0.000	0.000
glatt	0.000	0.000	0.000
scharf	0.000	0.000	0.000
klingt solide	0.000	0.000	0.000
kraftvoll	0.000	0.000	0.000
lebendig	0.000	0.000	0.000
Exklusivität	0.000	0.000	0.000
Spaß an fahren	0.000	0.660	0.149
sportlich	0.000	0.000	0.006
bevorzugen Sie	0.000	0.000	0.000
durchzugsstark	0.000		

(3) American

Attribute	Acceleration	Cruise	Idle
Loud	0.000	0.000	0.000
Booming	0.000	0.005	0.000
Smooth	0.000	0.000	0.000
Sharp	0.000	0.105	0.049
Solid	0.261	0.830	0.006
Powerful	0.000	0.033	0.185
Alive	0.000	0.003	0.000
Luxury	0.000	0.000	0.000
Fun to drive	0.000	0.350	0.069
Sporty	0.000	0.341	0.360
Preference	0.000	0.000	0.000
Engine extensibility	0.000		

Table 5 Result of principle component analysis

(1) Japanese

Driving condition	Acceleration			Cruise		Idle		
Attribute	Factor loading 1	Factor loading 2	Factor loading 3	Factor loading 1	Factor loading 2	Factor loading 1	Factor loading 2	Factor loading 3
大きさ	0.740	–0.522	–0.228	0.942	–0.250	0.928	–0.149	0.256
こもり感	–0.611	0.484	0.529	–0.591	0.782	–0.072	0.936	0.037
滑らか感	0.055	0.944	0.037	–0.778	0.498	–0.891	–0.006	–0.307
鋭さ感	0.881	–0.256	–0.297	0.947	–0.253	0.531	–0.597	–0.212
重厚感	–0.063	0.081	0.979	–0.100	0.976	0.465	0.753	0.357
迫力感	0.877	–0.398	0.151	0.958	–0.143	0.909	0.253	0.269
軽快感	0.779	0.330	–0.460			–0.786	–0.490	–0.033
高級感	–0.325	0.865	0.079	–0.767	0.605	–0.905	0.196	0.133
スポーティ感	0.981	–0.088	–0.138	0.856	–0.306	0.174	0.194	0.952
のび感	0.952	–0.032	–0.006					
Eigenvalue	5.057	2.494	1.640	4.987	2.419	4.455	2.202	1.332
Variance %	50.566	24.941	16.395	62.338	30.240	49.497	24.466	14.800
Cumulative %	50.566	75.506	91.902	62.338	92.577	49.497	73.962	88.763

(2) German

Driving condition	Acceleration		Cruise		Idle	
Attribute	Factor loading 1	Factor loading 2	Factor loading 1	Factor loading 2	Factor loading 1	Factor loading 2
laut	0.688	0.651	0.828	0.467	0.675	0.709
dröhnend	0.428	0.611	0.773	0.531	0.458	0.81
glatt	–0.476	–0.803	–0.553	–0.814	–0.832	–0.484
scharf	0.578	0.651	0.812	0.464	0.85	0.26
klingt solide	–0.476	–0.802	–0.506	–0.857	–0.947	–0.042
kraftvoll	0.853	0.424	0.791	0.526	–0.215	0.946
lebendig	0.883	0.426	0.809	0.54	0.667	0.605
Exklusivität	–0.172	–0.974	–0.501	–0.85	–0.965	–0.122
sportlich	0.889	0.389	0.805	0.49	0.521	0.74
durchzugsstark	0.941	0.26				
Eigenvalue	4.657	4.037	4.684	3.645	4.671	3.285
Variance %	46.565	40.374	52.04	40.5	51.902	36.495
Cumulative %	46.565	86.939	52.04	92.54	51.902	88.397

(3) American

Driving condition	Acceleration		Cruise		Idle	
Attribute	Factor loading 1	Factor loading 2	Factor loading 1	Factor loading 2	Factor loading 1	Factor loading 2
Loud	0.673	0.665	0.885	0.142	–0.724	0.648
Booming	0.622	0.664	0.136	0.976	–0.688	0.58
Smooth	–0.314	–0.875	–0.903	–0.3	0.892	–0.284
Sharp	0.83	0.457			–0.053	0.92
Solid					0.882	0.122
Powerful	0.901	0.334	0.789	0.462		
Alive	0.842	0.472	0.928	–0.047	–0.823	0.348
Luxury	–0.204	–0.93	–0.862	–0.252	0.829	–0.528
Sporty	0.904	0.371				
Engine extensibility	0.919	0.136				
Eigenvalue	4.851	3.211	3.843	1.342	3.936	2.098
Variance %	53.901	35.681	64.045	22.363	56.236	29.972
Cumulative %	53.901	89.582	64.045	86.408	56.236	86.207

As shown in Table 6, Japanese people in particular felt a sound was “supo-ti kan”(sporty) the more it was “hakuryoku kan”(powerful) and “keikai kan”(alive), and felt it as “koukyuu kan”(luxury) the less it was “ookisa kan”(loud) and the more it was “nameraka kan”(smooth). The Germans felt a sound was “sportlich”(sporty) the more it was “lebendig”(alive), and that it was “Exklusivität”(luxury) the more it was “klingt solide”(solid) and “glatt”(smooth). In addition, Americans found a sound “sporty” the more it was powerful and alive, while as “luxury” the less it was loud and the more it was smooth.

The sensory evaluation tests carried out in this report were divided according to driving conditions, in order to improve the evaluation accuracy of the subjects. The partial regression coefficients in the multiple regression equation, obtained through analysis, are different. It was thought that the cause of the difference in partial regression coefficients was due to changes in sound perception due to differences in driving conditions, or that the partial regression coefficient, which is a probability factor, differs due to the presentation sound being different without change in perception. Structural equation modeling was used to make this clear.[5]

Structural equation modeling is a statistical method that can analyze, in a single group, models having multiple cause and effect relationships. It is also called 2nd generation multivariate analysis. Thinking about different driving conditions, Table 7 gives the results of analysis into conditions in which the cause and effect factors of elemental attributes corresponding to comprehensive attributes are the same, and conditions in which the cause and effect factors are different. That is to say, conditions when perceptions were the same under different driving conditions, and conditions when the perceptions were different. Whether it was Japanese people, Germans, or Americans, following Akaike Information Criteria AIC[5] (a model where the smaller the value the better), the model with the same perceptions had smaller values. Therefore, it was considered that sound perceptions do not change, even if driving conditions are different. Equations were found that express the links with the elemental attributes, as shown in Table 8.

In addition, using an analysis of variance by country eliminated sporty feeling during idling. The multiple regression correlation factor was low, and structural equation modeling a common cause and effect coefficient could not be found. Therefore, it was not possible to comprehensively quantify driving conditions. It was difficult for the presentation sounds during idling to give the impression of being sporty, and it was thought to be due to large variation between the subjects.

4. Relating Subjective Evaluation Attributes with Psychoacoustic Metrics

4.1 A Revision to Conventional Psychological Evaluation Attributes

Through conventional research, the authors previously reported the attribute expressing the amount of auditory stimulus[6] as “loudness”, and expressing the level of fluctuation as “level of sound fluctuation unpleasantness”, etc. However, in further study, “level of sound fluctuation unpleasantness” was revised, becoming “strength of fluctuation”. The “unpleasantness” associated with the words “level of unpleasantness” is something subjective that varies by individual and depends on values. It was judged inappropriate as an expression of the amount of stimulation.

Table 7 Result of sound perception as same or different depends on different driving conditions

Country	Comprehensive attribute	Sound perception	AIC	Result
Japanese	高級感	Same	–15.97	Better
		Different	–12	–
	スポーティ感	Same	– 6.745	Better
		Different	– 6	–
German	Exklusivität	Same	–16.126	Better
		Different	–12	–
	sportlich	Same	– 1.998	Better
		Different	0	–
American	Luxury	Same	–16.076	Better
		Different	–12	–

Table 6 Result of multiple regression analysis

Country	Comprehensive attribute	Driving condition	Multiple regression formula
Japanese	高級感	Acceleration	= –0.40 × 大きさ感 +0.55 ×滑らか感
		Cruise	= –0.22 × 大きさ感 +0.78 ×滑らか感
		Idle	= –0.65 × 大きさ感 +0.21 ×滑らか感
	スポーティ感	Acceleration	= 0.62 × 迫力感 +0.53 ×軽快感
		Cruise	= 0.80 × 迫力感
		Idle	= 1.31 × 迫力感 +0.80 ×軽快感 –0.55 × 鋭さ感
German	Exklusivität	Acceleration	= 0.41 × klingt solide +0.51 × glatt
		Cruise	= 0.98 × klingt solide
		Idle	= 0.77 × klingt solide +0.22 × glatt
	sportlich	Acceleration	= 0.77 × lebendig +0.23 × scharf
		Cruise	= 0.95 × lebendig
		Idle	= 0.41 × lebendig +0.51 × klingt solide –0.92 × glatt
American	Luxury	Acceleration	= –0.33 × Loud +0.55 × Smooth
		Cruise	= –0.14 × Loud +0.82 × Smooth
		Idle	= –0.51 × Loud +0.49 × Smooth
	Sporty	Acceleration	= 0.30 × Powerful +0.66 × Alive

Table 8 Result of structural equation modeling (Equation)

Country	Comprehensive attribute	Driving condition	Multiple regression formula
Japanese	高級感	Acceleration	= −0.32 × 大きさ +0.65 ×滑らか感
		Cruise	
		Idle	
	スポーティ感	Acceleration	
		Cruise	= 0.64 × 迫力感 +0.52 ×軽快感
		Idle	
German	Exklusivität	Acceleration	
		Cruise	= 0.77 × klingt solide +0.21 ×glatt
		Idle	
	sportlich	Acceleration	
		Cruise	= 0.82 × lebendig +0.17 ×scharf
		Idle	
American	Luxury	Acceleration	
		Cruise	= −0.34 × Loud +0.63 ×Smooth
		Idle	
	Sporty	Acceleration	= 0.30 × Powerful +0.66 ×Alive

4.2 The Introduction of New Psychoacoustic Metrics

At this time, in addition to conventional attributes, a “loudness of pure tone” calculation algorithm was conceived because it is thought to be important as an element that is part of a sporty sound. “Loudness of pure tone” is an attribute that becomes larger as a single pure component becomes dominant, among the complex sounds in a critical band (band, hereafter). Conceptually, there is a reciprocal relationship between “strength of fluctuation” and “loudness of pure tone”.

In addition, “percent of loudness” was introduced to express the proportion of “loudness” in each band, against the total band addition value. “Percent of fluctuation intensity” was another attribute introduced, expressing the amount of protrusion of “fluctuation intensity” in a band that is caught between two bands.

4.3 Relating Elemental Attributes with Psychoacoustic Metrics

In order to relate the elemental attributes comprising the comprehensive attributes with the psychoacoustic metrics that indicate auditory stimulus calculated from physical properties, the same methods described in Section 3 were utilized. The psychoacoustic metrics necessary to develop relationships were extracted using multiple regression analysis. Through structural equation modeling, the applicability of driving conditions was verified; and the cause and effect factor was calculated. As a result, shown in Fig. 2, it was possible to quantify the attributes by country — psychoacoustic metrics calculated from physical properties, elemental attributes, and comprehensive attributes, in that order, including their relationships. For example, in explaining the Japanese “luxury” in Fig. 2-(1), the smaller the total band “loudness” and the smaller the “fluctuation intensity”, the more it felt like “luxury”. In particular, “fluctuation intensity” was a factor in the loss of luxury feeling the higher the frequency component. For the Japanese “sporty” in Fig. 2-(2), there is a strong relationship between the 2–9 Bark “loudness of pure tone”, the 2 Bark “percent of loudness”, and the total band “loudness”. The larger these values, the higher the “sport feeling”. Looking at it this way, in general, although there are differences in the level of effect in each band, in all countries there were the commonalities that the smaller the “loudness” and “fluctuation intensity”, the more it is “luxury” and the larger the “loudness” and “loudness of pure tone” the more sporty it felt.

The Japanese “sporty” changes especially when 1 Bark “loudness” increases or decreases as shown in Fig. 2-(2). For example, when 1 Bark “loudness” becomes large, “hakuryoku kan”(powerful) increases and “keikai kan”(alive) drops, and even if the main element of sporty changes from “keikai kan”(alive) to “hakuryoku kan”(powerful), there is the feeling that the “supo-ti kan”(sporty) has not changed. This is because the symbol for the cause and effect factor for the 1 Bark “percent of loudness” that is an element of “hakuryoku kan”(powerful), and the symbol for the cause and effect factor for the 1 Bark “loudness” that is an element of “keikai kan”(alive) were reversed.

5. Analysis of Preferences

The previous sections have been concerned with comprehensive attributes for sounds inside a car. This section analyzes the preferences of the subjects.

Assuming that there are patterns in subject preferences, a cluster analysis was carried out for classification. Also, by evaluating sounds that are rich in sound varieties, the differences in each subject’s preferences are evident, and the categories are made clear. Therefore, the subject of the analysis was sound during acceleration, which showed a low correlation (Table 9) between “sporty” and “luxury” in the comprehensive attributes.

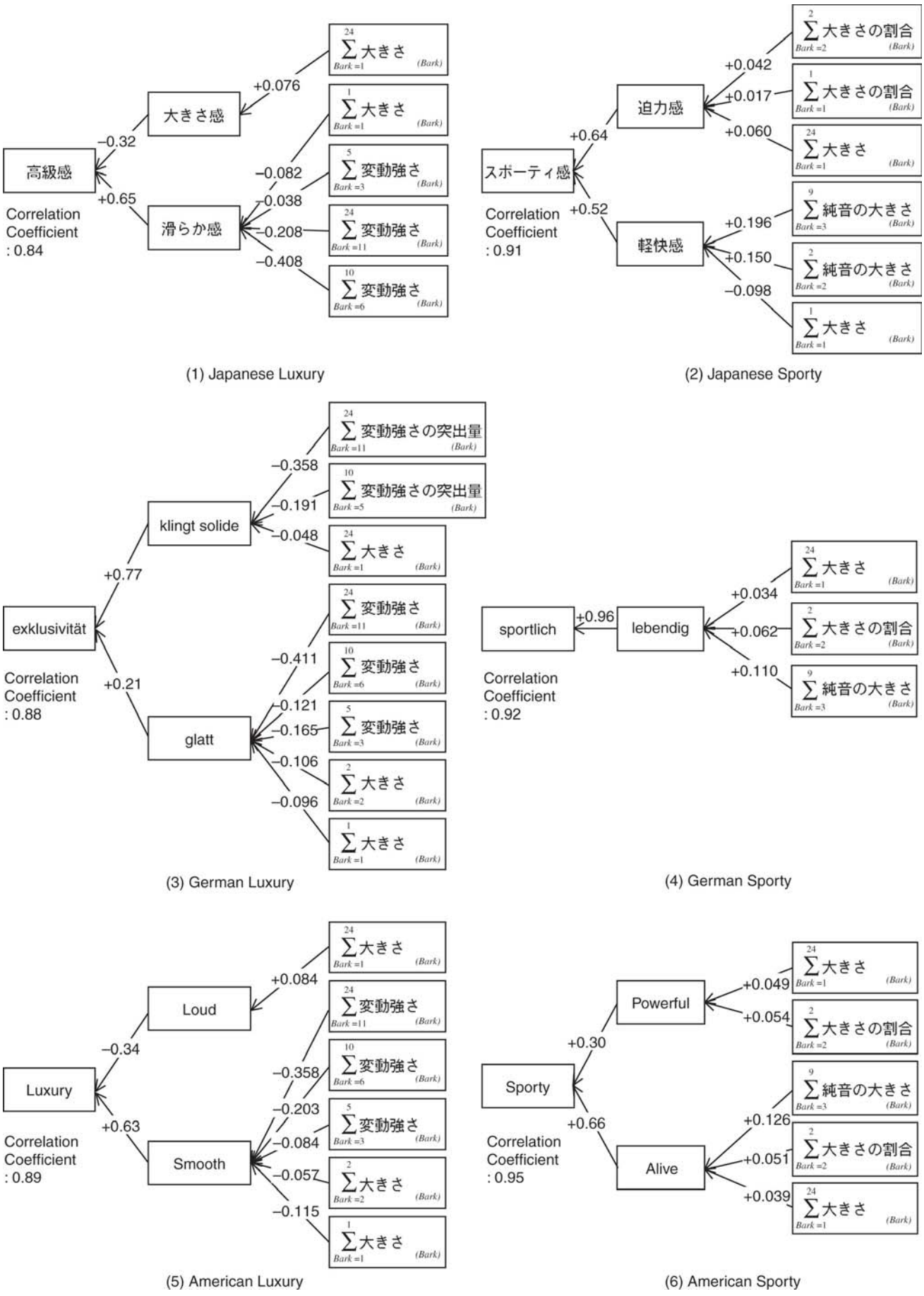


Fig. 2 Sound quality feeling model

Table 9 Correlation of luxury and sporty

Country	Acceleration	Cruise
Japanese	–0.41	–0.81
German	–0.53	–0.82
American	–0.54	

As shown in Table 10, the Japanese subjects were divided into two clusters — the subject group that preferred a sporty sound, having a correlation of 0.89 between sporty and prefer; and the subject group that preferred luxury, having a correlation of 0.95 between luxury and prefer. The subject group that preferred a sporty feel was 59% of all subjects, while those in the group that preferred luxury were 41% (Fig. 3). In addition, examining whether or not people with different preferences had the same perceptions of the

Table 10 Correlation of preference and each attribute (Japanese)

	高級感	スポーティ感	大きさ	こもり感	滑らか感	鋭さ感	重厚感	迫力感	軽快感
All subjects	0.36	0.50	0.15	–0.04	0.65	0.31	–0.22	0.24	0.68
Cluster 1	0.95	–0.66	–0.76	0.74	0.90	–0.72	0.21	–0.72	0.24
Cluster 2	0.11	0.89	0.68	–0.65	0.57	0.80	0.02	0.79	0.79

Table 11 Correlation of comprehensive attributes depends on preference (Japanese)

	Luxury favorite subjects “好み”	Sporty favorite subjects “好み”
All subjects “好み”	0.15	0.73

	Luxury favorite subjects “高級感”	Sporty favorite subjects “高級感”
All subjects “高級感”	0.93	0.86

	Luxury favorite subjects “スポーティ感”	Sporty favorite subjects “スポーティ感”
All subjects “スポーティ感”	0.92	0.98

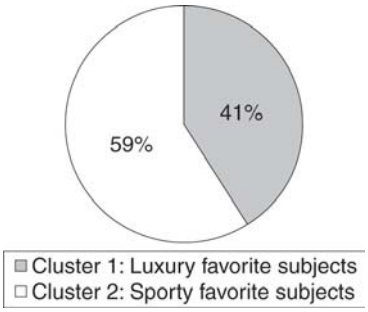


Fig. 3 Cluster of preference (Japanese)

Table 12 Correlation of preference and each attribute (American)

	Luxury	Sporty	Loud	Boom	Smooth	Sharp	Solid	Powerful	Alive
All subjects	0.51	0.27	–0.10	–0.11	0.42	0.21	0.36	0.25	0.22
Cluster 1	0.77	–0.49	–0.66	–0.63	0.79	–0.53	0.11	–0.44	–0.48
Cluster 2	–0.17	0.86	0.61	0.57	–0.52	0.78	0.60	0.80	0.85

Table 13 Correlation of comprehensive attributes depends on preference (American)

	Luxury favorite subjects “Preference”	Sporty favorite subjects “Preference”
All subjects “Preference”	0.63	0.55

	Luxury favorite subjects “Luxury”	Sporty favorite subjects “Luxury”
All subjects “Luxury”	0.93	0.93

	Luxury favorite subjects “Sporty”	Sporty favorite subjects “Sporty”
All subjects “Sporty”	0.96	0.96

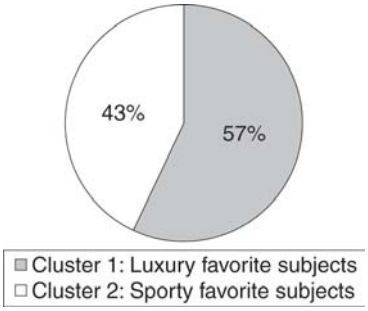


Fig. 4 Cluster of preference (American)

comprehensive attributes or not, it was considered that there is no difference in comprehensive attributes, from the results of correlation functions for each cluster, as shown in Table 11. For the Americans, too, the same analysis was carried out, and the results (Tables 12, 13 and Fig. 4) showed that 43% liked the sporty feeling, and 57% preferred a luxury feel. In the same way as with the Japanese, concerning comprehensive attributes, there is the same in perception due to preferences. On the other hand, almost all the German subjects — 86% (Table 14, Fig. 5) — preferred luxury, and there were almost none that preferred the sporty sound like the Japanese and Americans.

From these results, it is important to consider preferences according to the market when controlling sound quality.

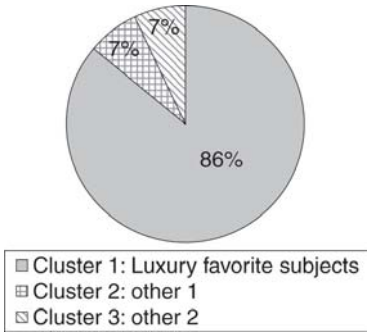


Fig. 5 Cluster of preference (German)

6. Sound Quality Evaluation System

Until now, we have used an original application that can calculate psychoacoustic metrics corresponding to a signal that was binaurally recorded using an artificial head microphone. An algorithm that calculates comprehensive attributes was added to this, and as shown in Fig. 6, software was developed. Furthermore, it has become a rational system that is integrated from analysis through trial sounds, by adding functions such as a general analysis function that can carry out conventional frequency analysis, etc., and a function that can carry out sound filtering and compare trial sounds before and after filtering in real time, among others.

7. Examples of Application

Fig. 7 shows an application of this method for interior sound to a Japanese vehicle of about 2,000 cc of engine displacement. This example is Japanese perceptions of luxury and sporty feeling when the vehicle was driven in 2nd gear in a fully loaded state. As revs rise, “loudness” and “fluctuation intensity”, main psychoacoustic metrics for luxury sound, grow larger, and luxury sound drops. Also, as revs rise, “loudness of pure tone”, a main psychoacoustic metric for sporty, grows larger, and the sporty sound increases.

8. Summary

Through sensory evaluation tests by ordinary Japanese, Germans, and Americans, the following facts were obtained.

Table 14 Correlation of preference and each attribute (German)

	Exklusivität	sportlich	laut	dröhnend	glatt	scharf	klingt solide	kraftvoll	lebendig
All subjects	0.92	–0.45	–0.72	–0.65	0.75	–0.66	0.73	–0.53	–0.49
Cluster 1	0.95	–0.55	–0.76	–0.71	0.80	–0.69	0.76	–0.59	–0.56
Cluster 2	0.06	0.24	–0.25	0.13	–0.18	0.13	0.29	0.49	–0.01
Cluster 3	0.53	–0.08	–0.46	–0.06	–0.15	–0.58	0.15	0.32	0.44

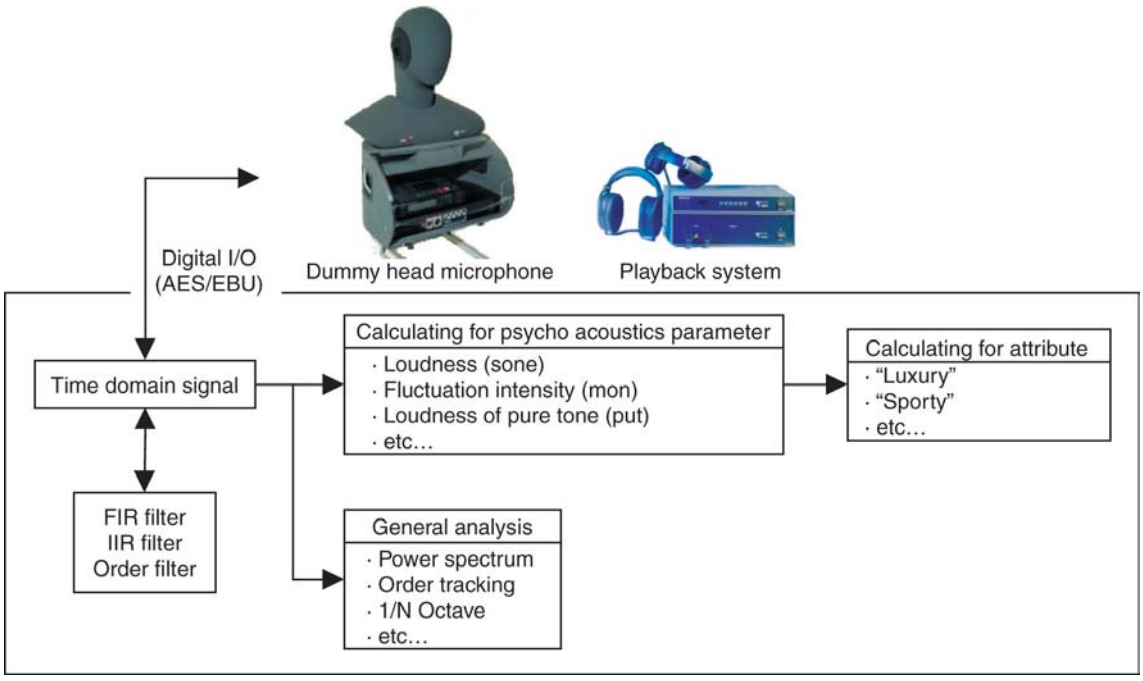


Fig. 6 Sound quality evaluation system

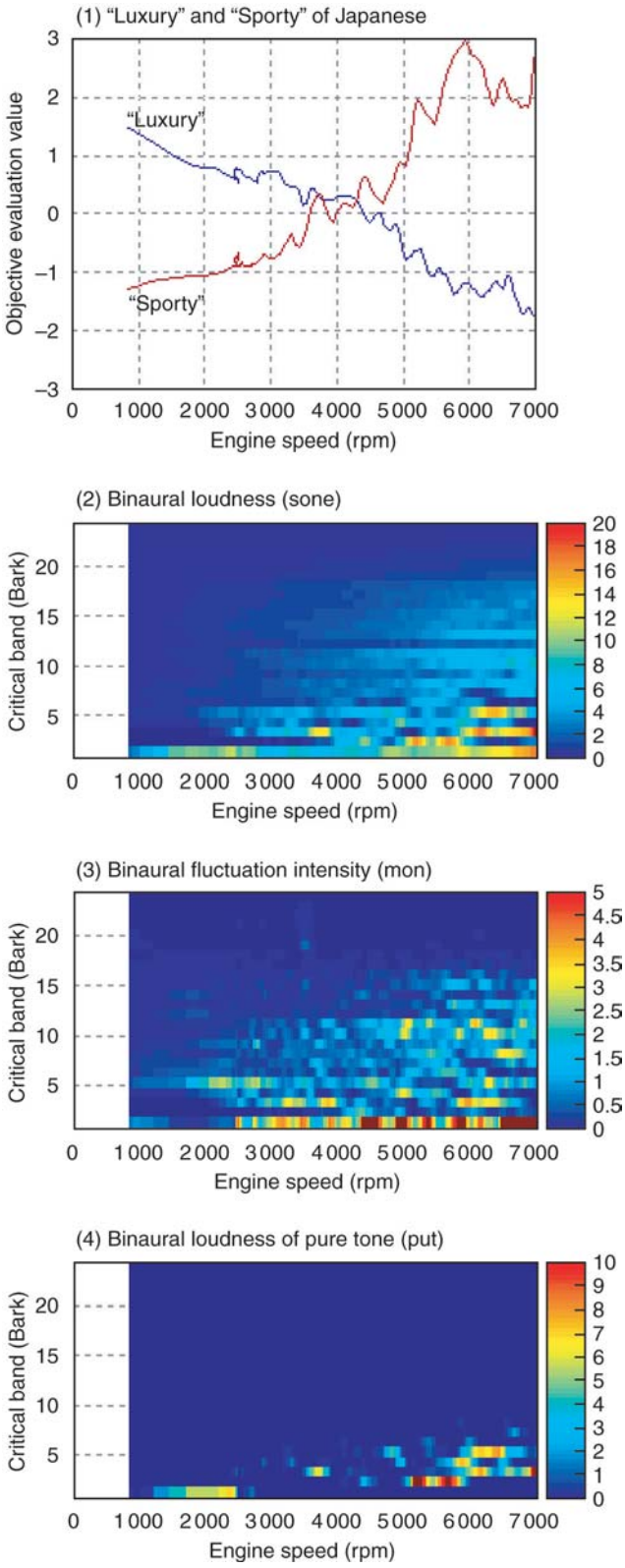


Fig. 7 Objective evaluation value of sound in cabin

(1) Regarding sounds perceived in a car cabin, although there are differences of degrees in people of different countries, it was learned that, in the main, perceptions can be expressed on the 2 axes of whether or not it gives a luxury feel, and whether or not it is sporty. It was also possible to quantify these perceptions, using objective numbers.

(2) Even if driving conditions were different, there was no difference in perceptions of luxury components and sporty components. However, at this time it is not possible to quantify sporty feeling when idling.

(3) Making a comparison between countries concerning the luxury component and the sporty component, each attribute comprising the psychoacoustic metrics were roughly the same, but the Japanese sporty component ("supo-ti kan") had a special feature. When there was a 1 Bark loudness increase or decrease, there was a tendency towards reciprocation between "hakuryoku kan" (powerful) and "keikai kan" (alive). These cancel each other out, and are not really seen as a change to "supo-ti kan"(sporty).

(4) As for preference regarding sound during acceleration, approximately 60% of the Japanese subject group preferred the "supo-ti kan" (sporty) feel, while 40% preferred the "koukyuu kan" (luxury). Approximately 40% of the American subject group preferred "sporty" while 60% preferred "luxury". Almost 90% of the German subject group preferred "Exklusivität" (luxury). Therefore, it is not possible to determine an unambiguously good sound, and it is necessary to make sound quality improvements giving consideration to each market's preferences.

(5) Modifying the conventional sound quality evaluation system, psychoacoustic metrics were added, a system was developed that can also calculate comprehensive attributes.

Acknowledgments

The authors would like to express their deep appreciation for the support and cooperation extended to them by the people at Toyo Corp., and at Müller-BBM GmbH (Germany), and Müller-BBM VibroAkustik Systeme GmbH (Germany).

References

(1) Ishii, Y., et al: "Development of Software to Objectively Evaluate Sound inside a Sports Car," Honda R&D Technical Review, Vol 13, No. 1, pp.131–138 (2001)

(2) Namba, S., Kuwano, S. : Method for Psychoacoustic Measurement for Sound Evaluation, Tokyo, Corona, 1998, p. 238.

(3) Ishimura, S.: Easy-to-understand Statistical Analysis, Tokyo, Tokyo Tosho, 1993, p. 216.

(4) Ishimura, S.: Easy-to-understand Multivariate Analysis, Tokyo, Tokyo Tosho, 1992, p. 216.

(5) Toyoda, H.: Structural Equation Modeling (An Introduction), Tokyo, Asakura Shoten, 1998, p. 336.

(6) Noumura, K., Okada, Y.: "Automotive Sound Evaluation Method considering Hearing Characteristics," Honda R&D Technical Review, Vol. 9, pp. 131–139 (1997)

■ Authors ■



Kosuke NOUMURA



Junji YOSHIDA

Research of Semi Solid Casting of Iron

Masayuki TSUCHIYA* Hiroaki UENO* Isamu TAKAGI*

ABSTRACT

One result of the research on semi solid casting of iron is the development of parts having qualities that combine the superior material properties of iron with the dimensional accuracy of aluminum die-cast parts. In addition, this manufacturing method also improves the factory environment by eliminating the need for sand molds, and it utilizes the same equipment and facilities in an Al-thixo casting plant. To establish this technology, research was conducted on iron material (composition iron-carbon-silicon), molding methods using optimal billet heating speeds and copper die materials, and methods for the continuous casting of raw material billets for Fe-thixo casting. This manufacturing method was studied with an oil pump cover, in which the oil pump is directly driven by the engine crankshaft, and the same dimensional accuracy was obtained as the conventional aluminum die-cast product. Furthermore, an improvement in the volume efficiency of the oil pump was also confirmed due to the stiffness improvement and clearance reduction effects.

1. Introduction

Ferrous alloy die-casting has been researched in the U.S. and Japan[(1)], but there were issues with composition variance and handling of the high temperature molten iron and also with die life, so this particular research did not lead to practical applications. On the other hand, the semi solid casting method (hereafter “thixo casting”) uses semi solid billets with stable compositions, so the heated billets are easy to handle and the casting temperature can be set lower than normal die-casting temperatures, which results in less solidification latent heat. For these reasons, thixo casting is being researched as a method with relatively little thermal shock on the die for the pressurized casting of iron and copper alloys with high melting points, which result in a short die life that makes die-casting uneconomical. In addition, compared to conventional iron part casting methods, the thixo casting method also allows casting of thin and complex shapes similar to aluminum die-casting, making it suitable for parts requiring the strength of iron and the high degree of shape freedom (characteristic of aluminum die-casting). This research established Fe-thixo casting technology based on thixo casting method knowledge obtained with aluminum[(2)], and evaluated the manufactured parts.

The research was conducted in four areas: material composition, casting methods, raw material manufacturing methods, and applied parts.

2. Fe-thixo Casting Principle and Casting Method

2.1. Casting Principle

The Fe-thixo casting method heats an iron alloy to the semi solid state, and then performs pressurized casting into a die. Thixo casting combines the solid and liquid phases, so the following points are required to improve the material characteristics of the product.

- Laminar flow filling having liquid characteristics in the semi solid state and with few defects must be established.
- The composition must have a eutectic quantity (quantity of eutectic components present during final solidification) that provides superior molten iron feed characteristics during solidification.[(2)(3)]

* Tochigi R&D Center

Fig. 1 shows a two-element status diagram for Fe-carbon (Fe-C). Semi solid regions exist around 1,500 °C (δ + Liquid) at carbon = approximately 0.2%, and around 1,200 °C (γ + Liquid) at carbon = approximately 2.0%.

The semi solid temperature range is wide and even heating of the billet is easy, so the thermal shock on the casting equipment and the die can be reduced. Therefore, the composition was evaluated by selecting the γ + L semi solid region, measuring the viscosity in the high temperature semi solid state, and measuring the solidification latent heat by the cooling method. The results indicated the following, and established that semi solid casting can be performed for Fe-carbon (Fe-C) in the same manner as Al-thixo casting.

- The solid phase forms globules in the semi solid state as shown in Fig. 2 and Fig. 3, so the relationship between the shear velocity and viscosity has linear characteristics. This allows handling as a liquid in the same manner as an Al-Si semi solid composition even in the Fe-C semi solid region.

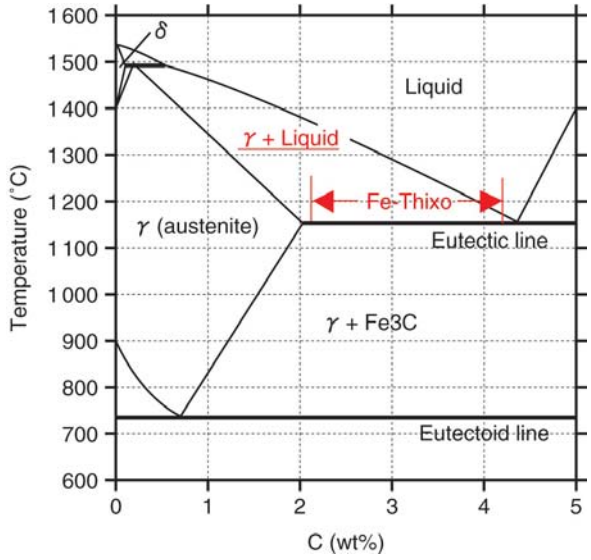


Fig. 1 Fe-Carbon

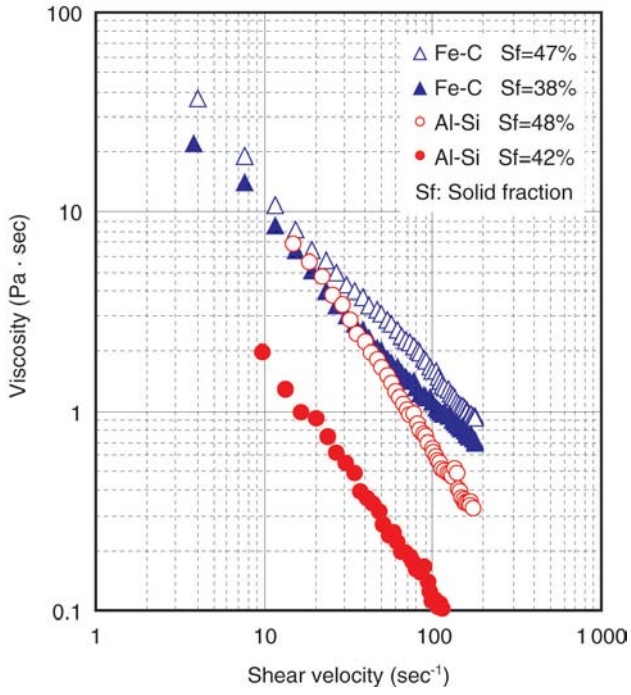


Fig. 2 Relationship between velocity and viscosity

- As shown in Fig. 4, the latent heat distribution has two steps in the same manner as Al-Si, and eutectic components are present during final solidification.

2.2. Casting Overview

Fig. 5 shows an overview of casting with the test apparatus. Fe-thixo casting was possible by following the procedure and using the facilities described below.

- a) When Fe-C materials are heated, the graphite in the structure forms a solid solution and the volume shrinks, causing deformation and making it difficult for the billet to stand on its own. Therefore, the billet is inserted into a SUS pallet and heated horizontally.
- b) The billet is heated inside an induction heating coil to a temperature of 1,180 to 1,220 °C.
- c) The pallet is transported using a fork and inserted to the injection port. An oxide film forms on the surface of the heated iron billet, so handling is easy.
- d) Casting is performed using a 200-ton horizontal injection die-cast machine for aluminum die-casting. Fe-thixo casting assumes heat treatment, so laminar flow filling is basically used to prevent blistering during heat treatment due to the inclusion of air. The injection system was improved to allow low-speed injection for laminar flow filling.
- e) Gates and distributors are established on the die to eliminate the oxide film that forms on the billet surface, and the product is removed from the die with a curing time of 5 s or less to prevent product cracking inside the die.

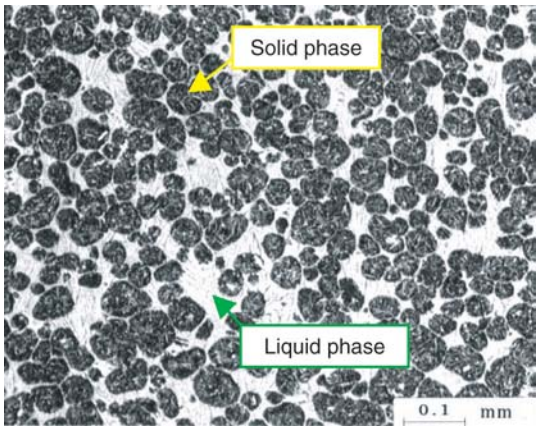


Fig. 3 Microstructure of Fe-thixo casting (etching)

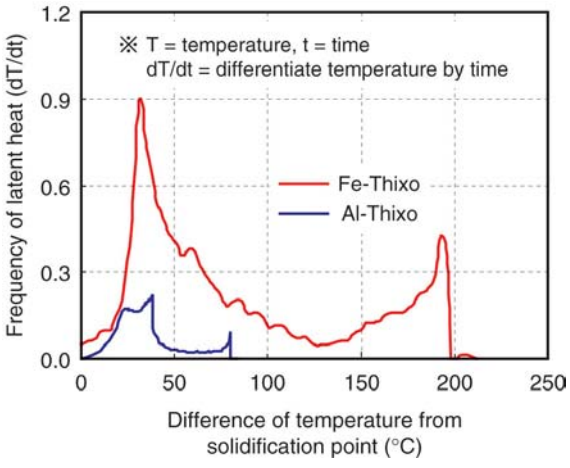


Fig. 4 Latent heat distribution

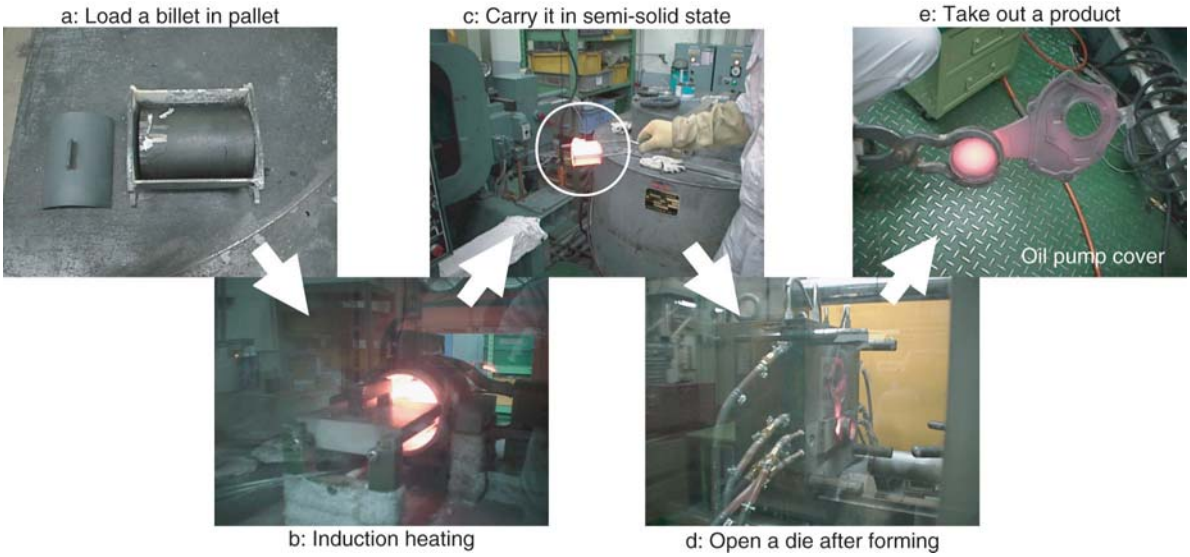


Fig. 5 Fe-thixo casting

3. Material Characteristics

3.1. Setting the Components

As mentioned above, the Fe-thixo casting method feeds molten iron during solidification by selecting a composition that has eutectic components present during final solidification, and this is effective for filling in the solidification shrinkage portions. The optimal eutectic component quantity (hereafter "eutectic quantity") during final solidification for Fe-thixo casting was obtained, and the composition was set.

3.1.1. Setting the carbon and silicon quantities

The tension compression fatigue strength is sensitive to defects, and was evaluated to set the eutectic quantity. Bar-shaped test pieces with the eutectic quantity adjusted to 10 to 45% were cast, heat treated and cut to the test piece shape, then the tension compression fatigue strength (breakage probability 10% value at 10^7 times) was measured. Fig. 6 shows these measurement results plotted by fatigue/tensile-strength rate (value obtained by dividing the tension compression fatigue strength by the tensile strength). The results are divided into two areas with a boundary at a eutectic level of 30%, and the region with an eutectic quantity of 30% or more shows a fatigue/tensile-strength rate (0.45 to 0.60) equal to that of steel without internal defects. This indicates that molten iron feed during solidification is ensured by setting a eutectic quantity of 30% or more.

On the other hand, when the eutectic quantity increases, the heated material is in a near-liquid state, so the thixo casting merit of easy handling during heating and transport is lost. Also, when the eutectic quantity exceeds 50%, the amount of solidification shrinkage during final solidification increases, and surface splitting and cracking were observed. Therefore, the optimum eutectic quantity for Fe-thixo casting is from 30% to less than 50%.

Fig. 7 shows that the eutectic quantity varies according to the carbon and silicon quantities. First the eutectic quantity was set to 30% to 50% as noted above, then the carbon and silicon quantities were set with targets of a Young's modulus of 180 GPa which exceeds globular graphite cast iron that is competitive as an iron-based material, and an impact strength of 10 J/cm^2 (Charpy U notch, JIS3 test piece) which is equal or greater than FCD450 required of parts.

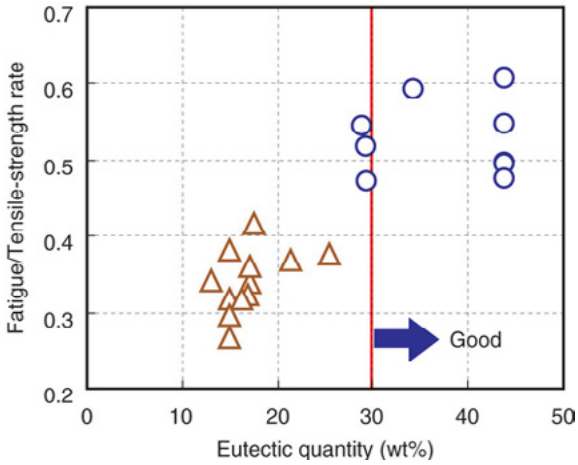


Fig. 6 Relationship between eutectic and fatigue/tensile-strength rate

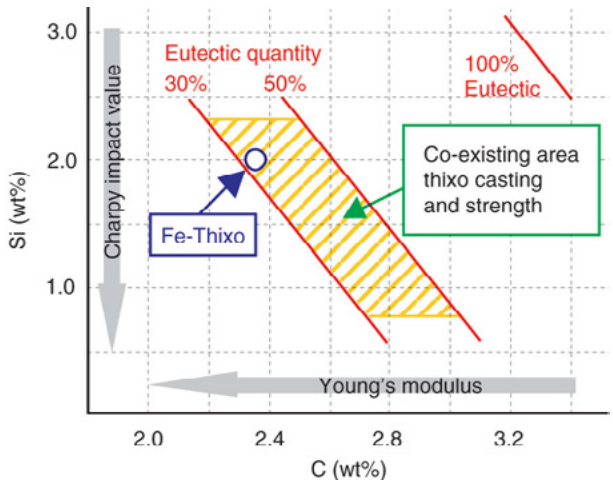


Fig. 7 Relationship between C-Si and eutectic quantity

When setting the carbon quantity, the composition of this casting method is such that a drop in the Young's modulus due to graphite precipitation after heat treatment of the cast product is unavoidable. Furthermore, the Young's modulus of Fe-thixo materials drops as the precipitated graphite area increases. Therefore, the added carbon quantity must be as low as possible.

In addition, increasing the added silicon amount generally produces hard and brittle silico-ferrite, and produces drops in both stretch and impact strength. The Charpy impact values of prototype materials having the silicon quantity adjusted between 1.5 to 6.5% were evaluated, and the results showed that the impact strength dropped markedly at an added silicon quantity of 3.0% or more.

Based on the above relationship between eutectic quantity and the carbon and silicon quantities, the applicable Fe-thixo casting range is the shaded region shown in Fig. 7. Taking into account component tolerance ranges when manufacturing raw material billets, the basic composition was set at carbon = 2.35% and silicon = 2.0%.

3.1.2. Setting the chromium and nickel quantities

Table 1 shows the final composition with chromium and nickel added to prevent the surface cracking that occurs when casting thin parts with complex shapes. Chromium strengthens the chilled structure during casting, and nickel prevents surface cracking by transforming the solid phase into a tenacious γ structure. These added chromium and nickel quantities are also adjusted according to the mechanical characteristics required of the cast product. Chromium is not added and only nickel is added when emphasizing impact strength, and both chromium and nickel are added when emphasizing tensile strength.

Table 1 Chemical compositions of Fe-thixo casting (wt%)

C	Si	Mn	P	S	Ni	Cr
2.30/2.40	1.95/2.05	0.60/0.70	<0.035	<0.04	0.50/1.00	0.00/0.50

3.2. Heat Treatment and Mechanical Characteristics

With the Fe-thixo casting method, rapid cooling in the die causes the liquid phase portions to form a hard and brittle chilled structure with the carbon in solid solution, so annealing heat treatment is essential for ensuring the required impact strength. This research aimed to obtain a wide range of material characteristics by setting the optimum heat treatment conditions.

That is to say, i) the tensile strength σ_B = 400 to 600 MPa range as a replacement for globular graphite cast iron, ii) the σ_B = 600 to 800 MPa range as a replacement for unrefined steel, and iii) the σ_B = 600 to 1,000 MPa range as a replacement for high strength parts.

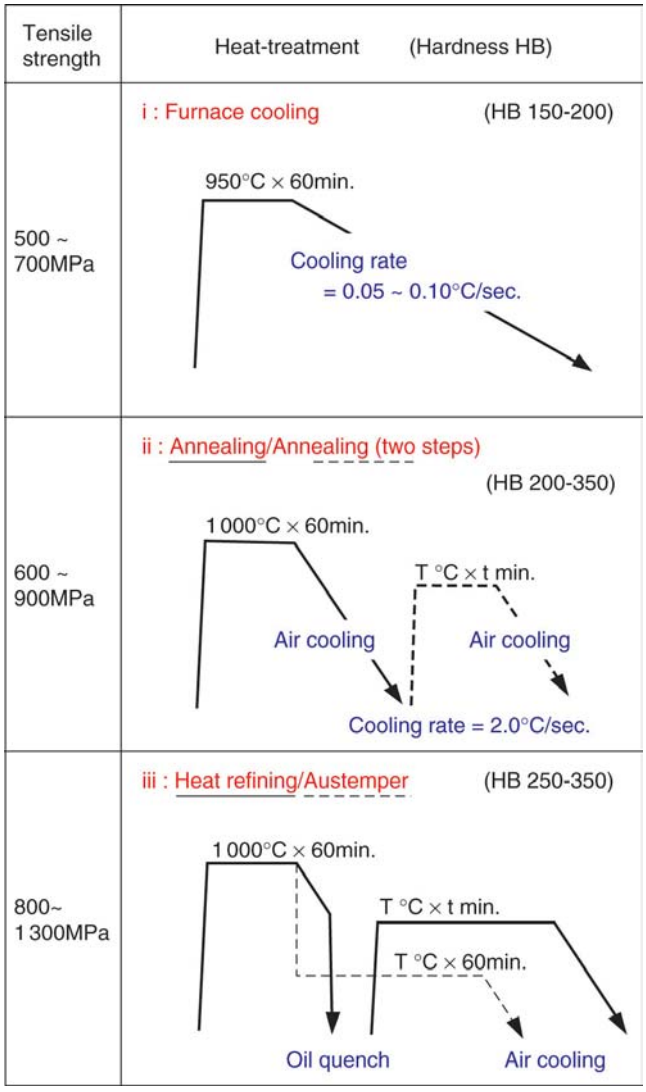
Table 2 shows the set heat treatment conditions, and Fig. 8a shows the tensile strength for each heat treatment performed on cast rod-shaped test pieces. (i) and (ii) can be separated by adjusting the cooling speed after annealing. (i) used furnace cooling with a cooling speed of 0.05 to 0.10 °C/s, and achieved a tensile strength of 500 to 700 MPa. (ii) used air cooling with a cooling speed of approximately 2 °C/s and two-step annealing, and achieved the target tensile strength of 600 to 900 MPa. In addition, (iii) performed heat refining as a high strength material, and a tensile strength of σ_B = 800 to 1,300 MPa was obtained by heat refining to increase the strength and impact strength, or by austemper heat treatment to induce isothermal transformation at a temperature of 300 to 450 °C immediately after annealing. The results showed that Fe-thixo materials can be applied to a wide strength range. A Young's modulus of 180 GPa or more was also achieved as shown in Fig. 8-d.

Fatigue strength tests and Charpy impact tests were also conducted. As shown in the Fig. 8-b graph, the wide fatigue strength range of σ_B = 200 to 500 MPa was obtained. In addition, the Charpy impact values in Fig. 8-c show that the furnace cooled materials achieved Charpy impact values of 10 J/cm^2 or more, which is equivalent to FCD450.

Malleable iron must generally be cured at around 900 °C for 5 to 15 hours to anneal the chilled structure.[4] In comparison, Fe-thixo can break down the chill with a curing time of 1 hour or less. The reason that chill breakdown is possible in a short time is thought to be that the graphite precipitation sites increase due to the following mechanisms, thus shortening the carbon diffusion distance.

- During heat casting, the solid phase portions transform into a martensite (M) + austenite (γ) structure with the carbon in a supersaturated solid solution. This increases the graphite precipitation sites during annealing, which shortens the diffusion distance and thus shortens the precipitation time.

Table 2 Heat treatment



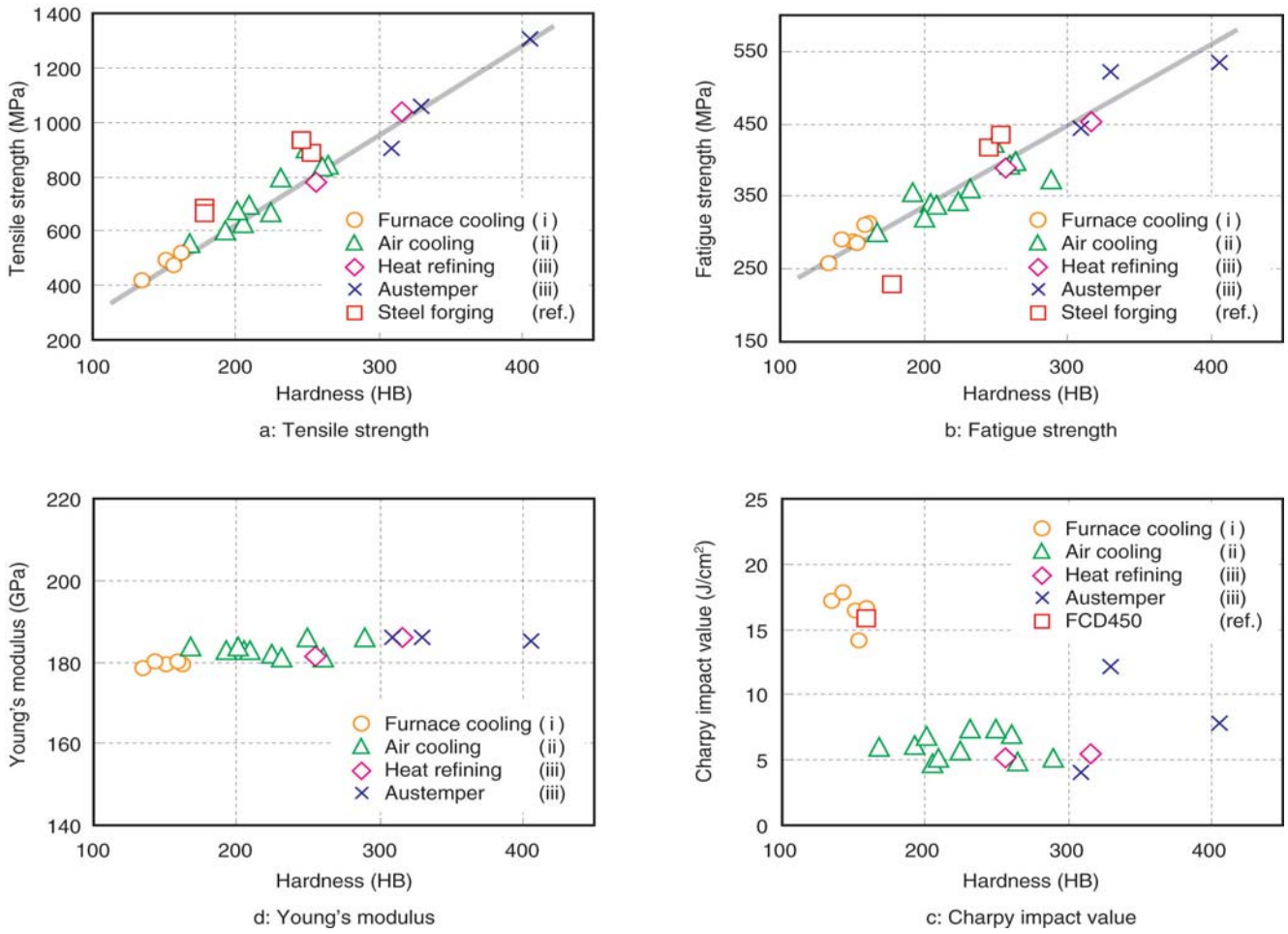


Fig. 8 Mechanical properties vs heat treatment

- The chilled portions that were liquid phase have wide boundaries with the solid phase, so strain is produced by the differences in thermal expansion between the solid and chilled portions during heat treatment, and these portions contribute as sites where the graphite can precipitate in an energetic and stable manner.

Horie et al. reported that the annealing time can also be shortened using atomized cast iron powder with surfaces having short diffusion distances that allow energetic and stable precipitation.[5] However, the same principle is thought to be operating in this case as well.

4. Casting Methods

4.1. Formation of Solid Phase Globules by Heating

For the material to have fluid characteristics in the semi solid state, the solid phase must form globules. In aluminum semi solid casting, the dendrites in the material billet structure are severed during the material manufacturing process and form globules. This research established a method for dividing a normal dendrite structure material billet such as shown in Fig. 9-a into globules by controlling the heating rate.

Figs. 9-b and 9-c show the structures obtained by heating the billet to 1,200 °C at different heating rates in the temperature range of the austenite transformation point or higher, and then water cooling the billet. When the billet is heated at high speed (80 °C/min), the dendrites are severed and the structure is suitable for thixo casting. However, when the heating rate is slower (44 °C/min), the solid phase portions join and form larger, coarser structures. Fe-C material dendrites are thought to form globules because the carbon solid solution is wide at 2.1%, so differences in the carbon concentration occur within the dendrites during rapid heating. The high concentration portions are thought to transform into the liquid phase, and the low concentration portions remain in the solid phase, causing the dendrites to divide. Further, as shown in Fig. 10 it was also determined that the heating rate at which division is possible depends on the dendrite arm spacing (DAS II, see Fig. 9-a). When the DAS II is small, the carbon diffusion distance becomes shorter, so division is possible even at a slower heating rate.

4.2. Die Materials

In Fe-thixo casting, 1,200 °C semi solid molten iron flows into the die, so the die is subject to thermal shock. However, copper materials were used for the die as a countermeasure to suppress the die temperature rise and thermal stress. The thermal stress produced by die thermal shock under two-dimensional constraint conditions is expressed by equation (1) below.[6]

$$\sigma = \frac{\alpha E (Tm - Td)}{1 - \nu} \qquad (1)$$

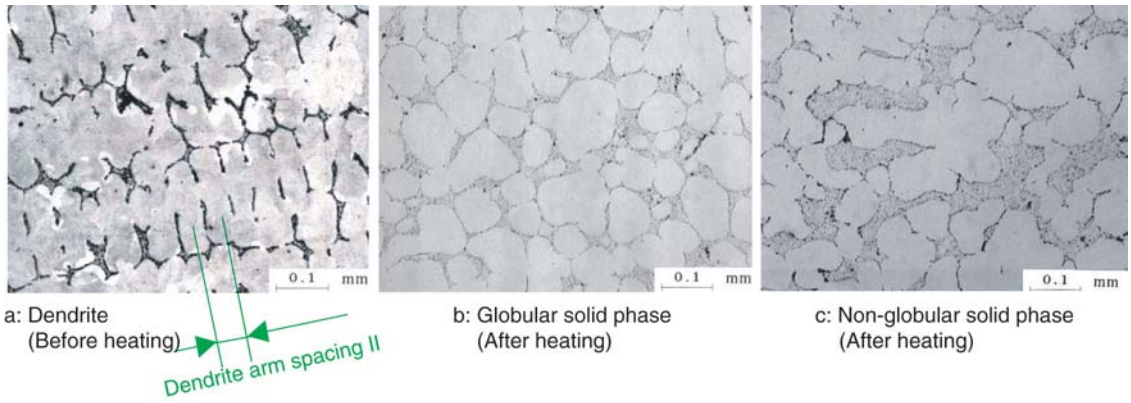


Fig. 9 Microstructure of Fe-thixo casting

Here, σ is the thermal stress, α is the thermal expansion rate, E is the Young's modulus, Tm is the maximum measured temperature value, Td is the die preheating temperature, and ν is the Poisson's ratio of the die materials. If the thermal stress when the molten iron flows into the die exceeds the compressive yield stress of the die materials, tensile stress remains in the die when the temperature drops after the product is removed, and this stress accumulates and leads to cracking. Therefore, in contrast to the ferrite dies used for aluminum die-casting, copper (NGK INSULATORS, LTD. MC-9) dies were used for Fe-thixo casting. Copper materials have a high density and thermal conductivity, so the temperature rise during molten iron inflow is small and little thermal stress is produced. Fig. 11 shows the compressive thermal stress produced by thermal shock in each part as calculated from measurements made using thermocouples located at a depth of 1 mm from the surface that contacts the molten iron. The only portions exceeding the compressive yield stress of the copper mold were the gates for removing the oxide film. The stress produced on the runner and the product portion was below the compressive yield stress of the copper mold. This indicated that copper dies can be used for the runner and the product portion by making the gates periodic replacement parts. Test pieces were cast using a copper die for 1,200 shots, and there was no heat cracking.

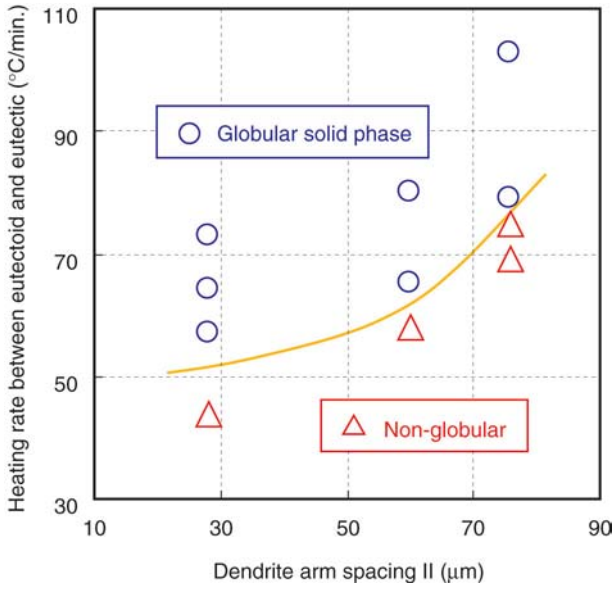


Fig. 10 Relationship between dendrite arm spacing II and heating rate

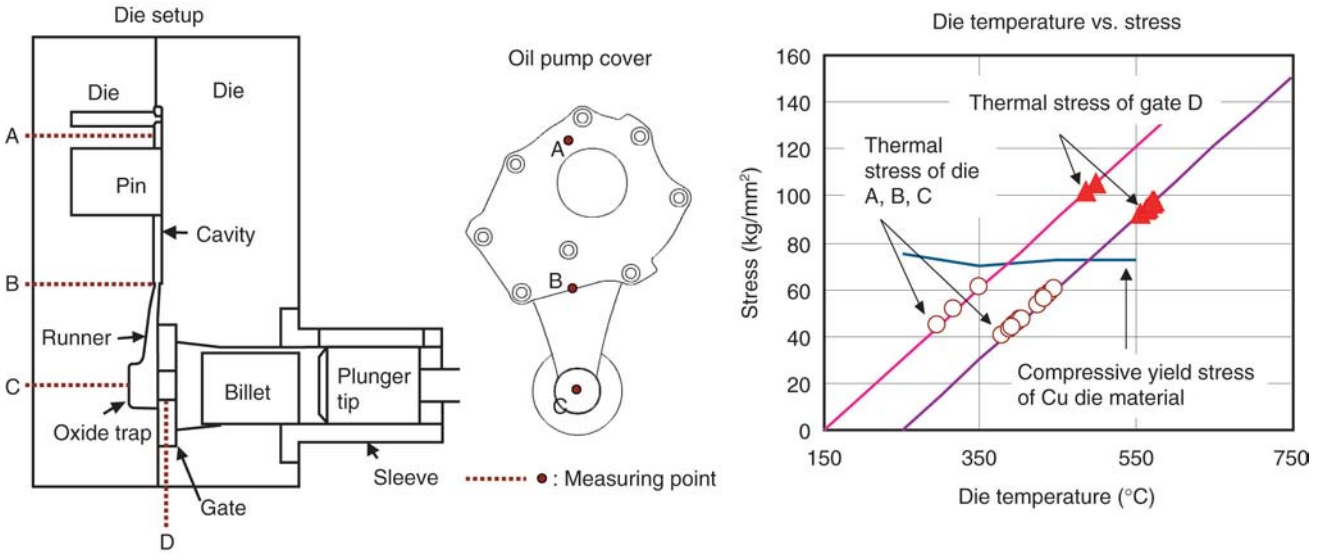


Fig. 11 Measuring points of die temperature and calculated thermal stress

4.3. Casting Size and Flow Length

The Pokorny equations for the product flow length (2) and the maximum filling time (3) in the die-casting method are expressed by the following equations.[7]

$$\text{Flow length } L = \text{Flow velocity } V \times \text{Maximum filling time } Tf \quad (2)$$

$$Tf = \frac{0.5px2\{qa + c(tm - ts)\}}{k\{tm - (td \times 1.15)\}} \quad (3)$$

K: thermal conductivity of the molten iron,
qa: molten iron latent heat,
c: specific heat,
p: molten iron density,
tm: molten iron temperature,
ts: solid phase line temperature,
td: die temperature,
x: thickness × 1/2

Compared to aluminum die-casting, Fe-thixo casting has a greater temperature difference between the molten iron temperature and the die temperature, so there were concerns that the maximum filling time would become shorter. However, as shown in Table 3 the molten iron has a high density and low thermal conductivity, so a filling time equal or greater than that for aluminum die-casting was obtained.

Table 3 Calculated maximum filling time

		Fe-thixo	ADC12
K	cal/s · cm · °C	0.099	0.23
qa	cal/g	55	94
c	cal/g · °C	0.166	0.26
p	g/cm^3	7.1	2.4
tm	°C	1 200	650
ts	°C	1 150	520
td	°C	200	200
x	cm	0.3	0.3
Filling time	**sec**	**0.21**	**0.14**

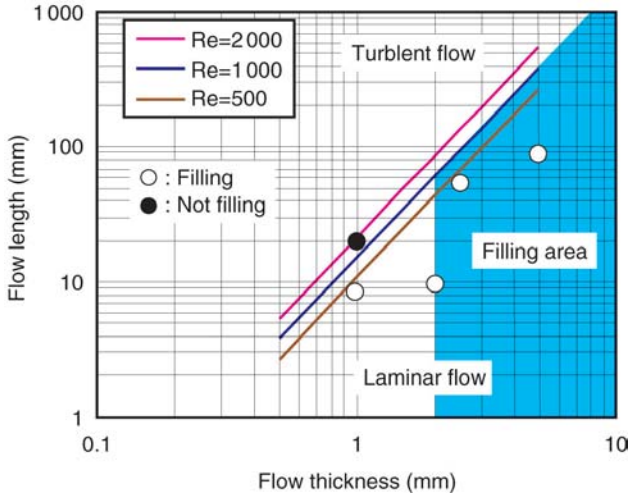


Fig. 12 Filling area of Fe-thixo

Controlling the filling rate to achieve laminar flow filling is essential to prevent the inclusion of air during Fe-thixo casting. The flow rate upper limit is determined for thixo casting which assumes laminar flow filling, so there is a theoretical correlation between the product thickness and the flow length. Therefore, the area below the Reynold's number lines shown in Fig. 12 is presumed to be the range over which sound products can be cast. Filling was verified by casting thin plate step-shaped test pieces, and the results were plotted in Fig. 12. These results confirmed that while 5.0 mm and 2.5 mm thick parts were filled, the flow length for 1 mm thick parts was approximately 10 mm.

5. Continuous Casting of Raw Materials

Low-cost mass production of uniformly shaped materials with stable composition and internal quality is required for the billets used in Fe-thixo casting. Developed materials having a semi solid range at 200 °C were unstable and broke easily inside the mold in places where solidification cores occurred. Thus, manufacturing is not possible with current continuous casting technology, which selects compositions with a narrow semi solid range. Therefore, it was necessary to establish new continuous casting technology. This research optimized the mold materials, drawing conditions, and molten iron temperature control to allow horizontal continuous casting of developed materials using a structure such as that shown in Fig. 13.

Issues for continuous casting raw materials (hereafter "continuous casting materials") are thought to be the black skin on the surface and solidification shrinkage defects in the core areas. However, these issues were resolved by casting rod-shaped test pieces and evaluating the fatigue strength which is susceptible to defects. A black skin approximately 0.5 mm thick is present on the surface (Fig. 14), and when this film mixes to the inside of the product, it can act as a defect and lower the fatigue strength. However, the fatigue strength of test pieces cast using continuous casting materials with this black film was evaluated, and it was confirmed that the black skin had no effect on the fatigue strength.

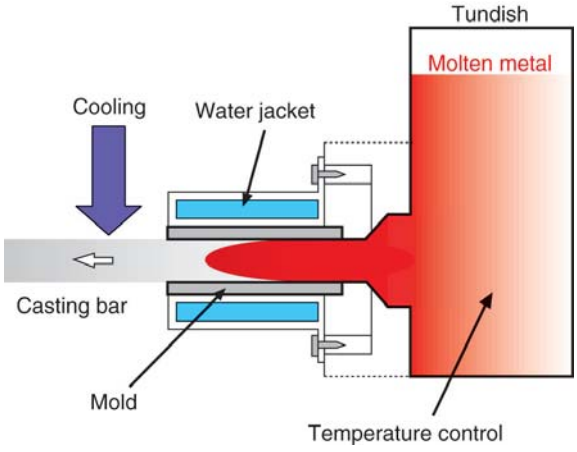


Fig. 13 Horizontal continuous casting

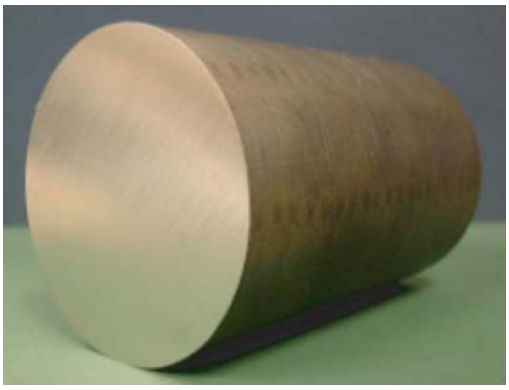


Fig. 14 Continuous casting bar

In addition, the effect of internal defects was evaluated using a billet having a cavity with a diameter of approximately 5 mm intentionally created in the center. This defect was crushed during the heating and casting process so that the defect did not remain in the cast product, and there was found to be no effect on the fatigue strength.

6. An Example of an Automotive Parts Study

A prototype engine oil pump cover directly driven by the crankshaft was manufactured using the Fe-thixo casting method. Fig. 15 shows the cast product, and Fig. 16 shows the pump structure. This part is currently manufactured by conventional aluminum die-casting, but Fe-thixo casting increases the stiffness and makes it possible to reduce the clearance with the iron rotor while heated, thus improving the pump volume efficiency. In addition, if the cover stiffness can be maintained at the same level as the aluminum die-cast part, the cover thickness can be reduced and the pump rotor thickness can be increased by the same amount, making it possible to increase the pump capacity without changing the crank shaft length. Some other companies manufacture the oil pump cover using the steel plate fine blanking method. However, in this case most surfaces require machining such as the convex portions after press molding the ports or the flat countersunk screw joining surface, and this machining increases the cost. Therefore, this oil pump cover is a part that can benefit from the material characteristics of steel and the degree of shape freedom of aluminum die-casting which are features of the Fe-thixo casting method.



Fig. 15 As-cast oil pump cover

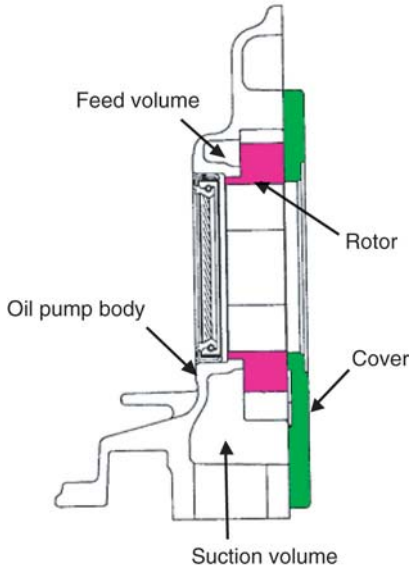


Fig. 16 Structure of engine oil pump directly driven by crank shaft

Improvements in volume efficiency and pump efficiency were confirmed in specific characteristics tests on the oil pump as shown in Fig. 17. In addition, specific durability tests also showed that the flow degradation rate, flat countersunk screw tightening torque degradation, and wear all cleared the standard values, and confirmed sufficient performance as an operational part.

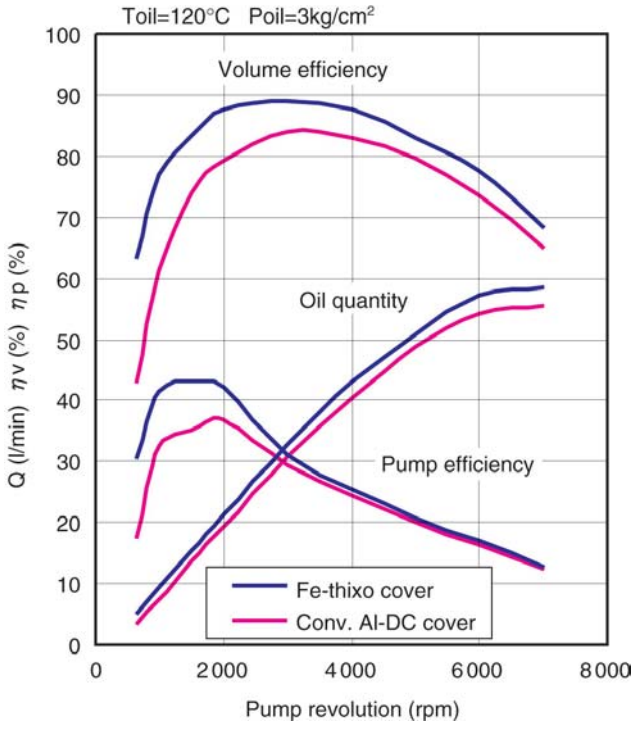


Fig. 17 Difference in oil pump efficiency between Fe-thixo and Al-DC cover

Table 4 Accuracy of Fe-thixo cover (mm)

	Size range	~30 (mm)	50-80(mm)
Fe-thixo cover	Deviation 3σ	0.16	0.31
General tolerance 1st class of JIS	Al die-cast	±0.25	±0.35
	Steel forging	±0.4	±0.6

Table 4 shows the dimensional accuracy evaluated by the dimension between the pump cover screw holes. The dimensional variance for a deviation of 3 σ was within ±0.25 and ±0.35 for the dimension setting values of 30 mm or less and 50 to 80 mm, respectively, which satisfies the general tolerance 1st class of JIS for aluminum die-casting. In addition, a surface roughness of 25S or less was confirmed to be possible by performing heat treatment in a nitrogen atmosphere.

7. Conclusion

Fe-thixo casting technology was established which offers excellent casting performance and allows manufacture of parts combining the material characteristics of iron with a degree of shape freedom and dimensional accuracy equivalent to aluminum die-casting. The following knowledge was obtained.

(1) Fe-thixo casting exhibits excellent casting performance with a composition having a eutectic quantity of 30 to 50%. Materials having a wide strength range from σ_B = 400 MPa to 1,000 MPa could be obtained by selecting the heat treatment for the cast product.

(2) Fe-thixo casting allows rapid heating of the billet in the austenite region by using copper die materials and lowering the injection system speed. Also, a maximum filling time equal or greater than that for aluminum was obtained, and casting with a partial thickness of 1 mm was possible.

(3) A continuous casting method for Fe-thixo compositions was established by optimizing the die materials, drawing conditions and molten iron temperature.

(4) A prototype oil pump cover was manufactured, and the Fe-thixo casting method was confirmed to have a degree of shape freedom and dimensional accuracy equivalent to aluminum die-casting. Applying Fe-thixo casting to the cover of an engine oil pump directly driven by the crankshaft made it possible to both increase the pump volume efficiency and reduce the size.

References

(1) Miyata, Hamanaka, Komatsu, Suzuki: Manufacture of Prototype Automotive Parts by the Iron Die-cast Method and Observations, Casting 50, p. 629–635 (1978)

(2) Saito, Nakamura et al.: Development of Car Body Joint Parts by Thixo Casting, HONDA R&D Technical Review Vol. 11, No. 2, p. 149–158 (1999)

(3) Saito, Shiina et al.: Patent No. 2794539, Thixo Casting Method

(4) Japan Casting Association publication: Casting Science Handbook, Revised 4th Edition, p. 688 (1986)

(5) Horie, Hiratsuka, Konishiki et al.: Annealing Behavior of Atomized Cast Iron Powder, Casting Science 73, p. 662–667 (2001)

(6) Japan Society of Mechanical Engineers publication: Heat Transfer Engineering Materials, Revised 4th Edition, Tokyo, Maruzen, p. 32 (1994)

(7) National Federation of Die-cast Industry Unions publication: Die-cast Technicians Handbook, Tokyo, Keikinzoku Tsushin Aru Co., Ltd., p. 169 (1988)

■ Authors ■


Masayuki TSUCHIYA


Hiroaki UENO


Isamu TAKAGI

Development of Sinter Diffusion Bonding for Rotor Core of Hybrid Car

Toshiyasu KOMATSU* Satoru SHINZAKI*
Youichi NAKAHARA* Kazuo ASAKA**

ABSTRACT

This research focused on composite technology to bond materials for rotor cores, which require both magnetic properties and mechanical properties at once, and analyzed diffusion bonding of sintered material and the bonding area as a factor affecting it. As a result, it was determined that the strength of the bonding zone depends on the bonding area, and diffusion bonding was verified as an applicable technique for bonding magnetic material and structural material, which are different materials. This report describes the establishment of a sinter diffusion bonding technique that provides satisfactory bonding strength. This was accomplished by improving the bonding area through application of pressure by press fitting of the inner and outer components, which was in addition to the difference in thermal expansion of the sintered material. Application of the developed material to rotor cores for use in hybrid cars has made it possible to achieve both functionality and strength, to significantly improve productivity, and to reduce costs by 50%.

1. Introduction

Decreasing automobile fuel consumption has become an issue that must be taken into consideration due to concerns about global environmental conservation and the depletion of petroleum resources. One measure for resolving this issue is the adoption of hybrid powerplants that combine combustion engines with electric motors. Given this context, Honda has also placed a hybrid car, the Insight, on the market. It will be necessary to further develop this approach and extend it to Honda's major product models. The issues of improving motor efficiency and lowering costs are crucial for realizing that purpose. The target here was cost reduction techniques for motor rotors, and the aim was to establish moderately-priced manufacturing techniques that would yield both the required magnetic properties and the mechanical properties, as shown in Fig. 1. The fabrication of ordinary motor rotors so that they will possess both magnetic and mechanical properties tends to involve cost increases because machining

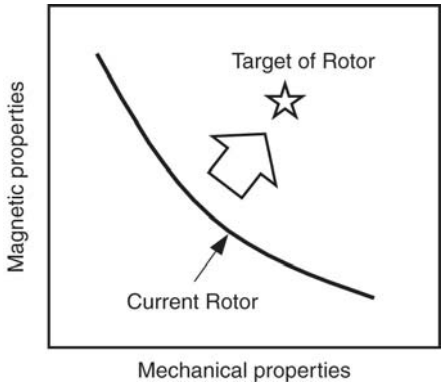


Fig. 1 Relationship between mechanical properties and magnetic properties

* Tochigi R&D Center
** Hitachi Powdered Metals Co., Ltd.

is required after mechanical bonding or press fitting of the two kinds of material. Here, instead, near-net shape forming using powder metallurgy methods was explored as a way to reduce the machining process and lower the cost, and the possibilities for diffusion bonding of different materials were studied.

The diversification of uses for sintered machine parts has been accompanied by new demands for parts with complicated, undercut shapes, such as notched shapes and laterally undercut shapes, as shown in Fig. 2. Various different bonding methods have consequently been developed. Fig. 3 shows the kinds of bonding method for sintered machine parts.[1] In terms of bonding strength and cost, it is difficult to apply any of these methods to rotors except diffusion bonding, which makes use of the phenomenon whereby ions and atoms permeate another substance and are diffused through it. Liquid phase sintering (a method for causing shrinkage and diffusion bonding by generating a large amount of liquid phase in the sintering process) requires special chemical compositions. It also generates a large amount of liquid phase, so that dimensional accuracy becomes difficult to control. Solid diffusion bonding was used, therefore, as a bonding method that yields bonding strength sufficient for the rotor to function. This method makes use of the different thermal expansion in the combined materials during the sintering process to cause the materials to contact each other on their bonding surfaces and bond them by diffusion in their solid phase. This method is adopted with automobile engine sprockets and other such parts that have two sets of teeth.[2]

The shapes of the inner and outer components of motor rotors, however, are different from automobile engine sprockets in that the outer component, in particular, is so thin that adequate bonding strength cannot be achieved by the difference in thermal expansion alone. This article reports on the consequent development of sinter diffusion bonding techniques that improve the bonding area and bonding strength. This was achieved by focusing on the properties of the sintering materials and on the initial inner part diameter over sized in order to clarify the primary factors that influence the diffusion bonding of different materials.

2. Bonding Mechanism and Technical Issues

In general, the factors that influence sinter diffusion bonding include sintering temperature, sintering time, and bonding area. Of these factors, sintering temperature and sintering time are under the constraints imposed by the manufacturing process. For the present development, therefore, it was decided to seek improvement of bonding strength by expanding the bonding area. The mechanism of bonding caused in particular by the factor of pressure was applied for this purpose. This mechanism is shown in Fig. 4.[3] When pressure is applied to the bonding surfaces of two metals, the metal atoms approach each other to a distance as close as the Å level. When the atomic distance approaches the lattice constants (point a in Fig. 4), the atomic force reaches equilibrium so that electrons are shared and bonding takes place. Consequently, applying pressure effectively and increasing the bonding area are issues of great importance in diffusion bonding.

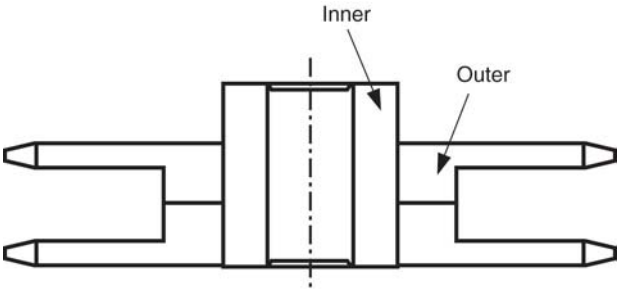


Fig. 2 Shape of undercut

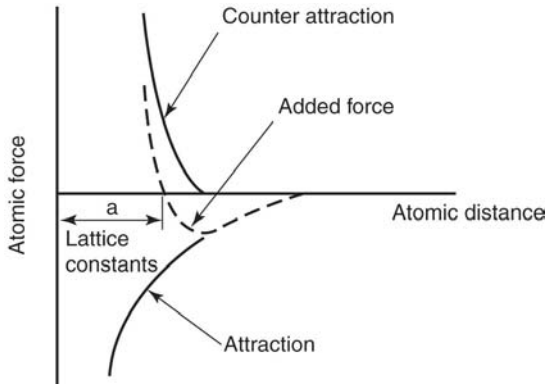


Fig. 4 Relationship between atomic force and atomic distance

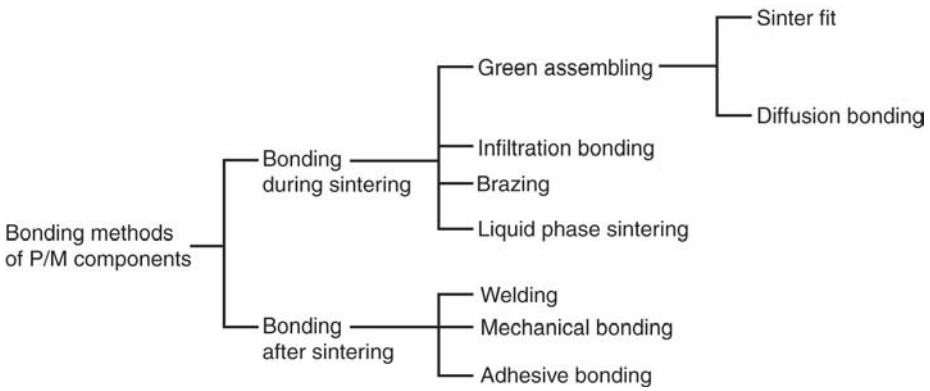


Fig. 3 Bonding methods of P/M components

3. Testing and Evaluation Methods

3.1. Rotor Material Specifications

Materials with mechanical properties and magnetic properties such as shown in Table 1 were used for the rotor materials. Fe-Cu-Ni-C material was used for the inner part for its mechanical properties, and Fe material was used for the outer part for its magnetic properties. Table 2 shows the chemical composition of each part.

The raw powder used in the inner part was based on pure iron powder with the addition of mixed powder containing copper, nickel, and carbon. Water atomized iron powder was used as the raw powder for the outer part.

Table 1 Mechanical and magnetic properties

Item	Inner	Outer
Tensile strength (MPa)	318	200
Yield strength (MPa) (0.2% Yield point)	260	–
Rotating bending strength (MPa)	190	–
Magnetic flux density (T)	–	1.04
Coercive force (A/m)	–	350
Resistivity ($\mu\Omega \cdot$ cm)	–	16.4
Density (g/cc)	6.4 min	6.9 min
Apparent hardness	HRB 50 min	HRF 50 min

Table 2 Chemical composition

Chemical Composition (wt%)				
	Fe	C	Cu	Ni
Inner	Bal.	0.6	1.5	2.7
Outer	100.0	–	–	–

3.2. Measurement of the Thermal Expansion Curve

Fig. 5 shows the shape of the specimens used to measure the thermal expansion curves for the inner and outer parts. A Dilatometer 1,570 made by Tokyo Industry Co. was used as the test device. Measurement was conducted by raising the temperature from the ambient temperature to 1,130 °C in an atmosphere of endothermic gas, maintaining that temperature for 20 minutes, and then lowering the temperature back to the ambient temperature.

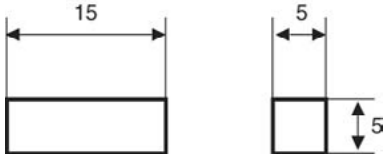
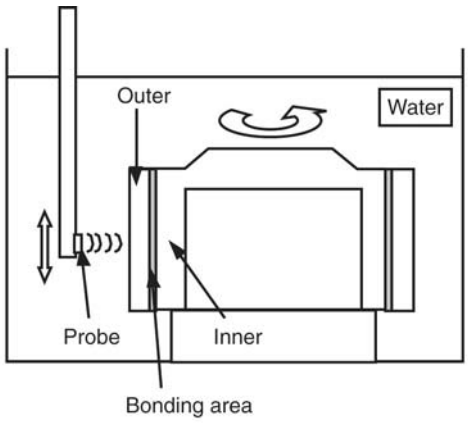


Fig. 5 Heat expansion test specimen

3.3. Bonding Area Measurement Method

Supersonic flaw detecting was used as the method for non-destructive examination of the condition of the bond formed by sinter diffusion bonding of the inner and outer parts. Fig. 6 shows the measurement device. A rotor impregnated with oil was placed in water and rotated. As supersonic waves were directed vertically against the bonding surface, a probe was moved up and down that surface to measure the reflected wave. A smaller reflected wave indicates a better bond. Based on the results of this measurement, the rate of diffusion bonding area (*Rs*) was determined as the proportion of the diffusion bonding area that is actually sound in relation to the designed total bonding surface.



Device for supersonic flaw detecting: Canon M-500A

Fig. 6 Device for supersonic flaw detecting

3.4. Bonding Strength Test

The strength of the bonding surface was measured using specimens as shown in Fig. 7 and the method shown in Fig. 8 to measure the force of rupture of the bonded portion. The method used to derive the rotor bonding strength is shown below. The force of rupture per square millimeter (*Ps*) was calculated using formula (1), and the bonding area (*S*) was calculated using formula (2). These two were then substituted in formula (3) to obtain the bonding strength (*P*).

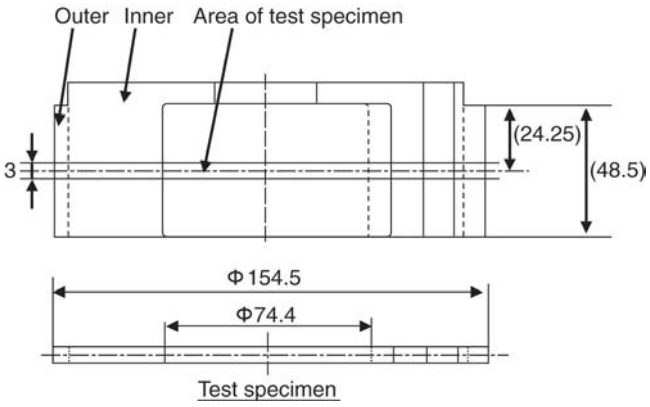


Fig. 7 Diffusion bonding test specimen

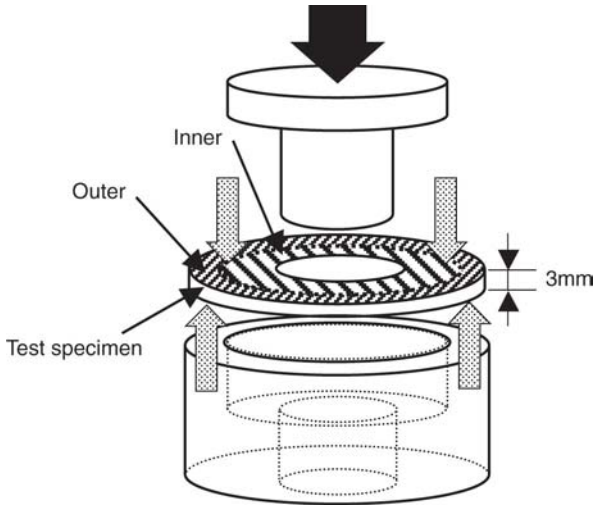


Fig. 8 Measurement method of diffusion bonding strength

$$Ps = Pt / St \quad (1)$$
$$S = A_0 \cdot (Rs/100) \quad (2)$$
$$P = Ps \cdot S \quad (3)$$

S: Diffusion bonding area of rotor (mm^2)
A_0: Calculated diffusion bonding area (mm^2)
Rs: Rate of diffusion bonding area (%)
Ps: Force of rupture per square millimeter (N/mm^2)
Pt: Force of rupturing specimen (N)
St: Diffusion bonding area of specimen (mm^2)
P: Diffusion bonding strength of rotor (N)

4. Results

4.1. Thermal Expansion Characteristics

Fig. 9 shows the thermal expansion curves for the Fe material (EO material) and Fe-Cu-Ni-C material (ENK material) during the sintering process. These curves show similar tendencies up to 800 °C. Past that temperature, however, the quantity of thermal expansion in the Fe-Cu-Ni-C material begins to change, and at 1,083 °C, which is the melting point of Cu, the expansion of the copper causes the quantity of thermal expansion to be greater in the Fe-Cu-Ni-C material than the Fe material. Study was then done of combinations of the Fe material, which has superior magnetic properties, as the outer part, with the Fe-Cu-Ni-C material, which has strong mechanical properties, as the inner part, using the pressure resulting from the difference in the quantity of thermal expansion.

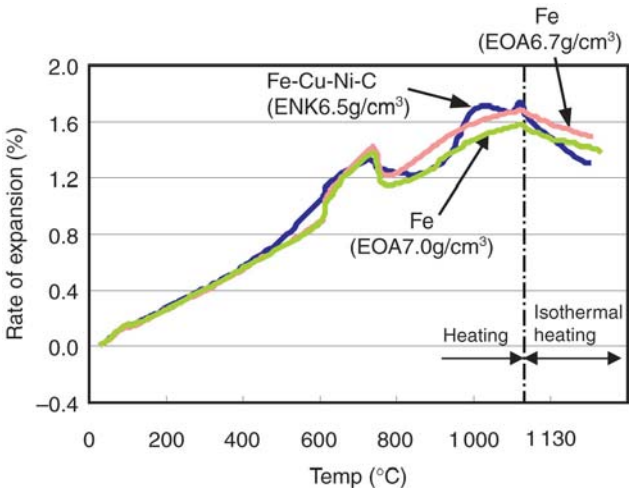


Fig. 9 Characteristic of expansion

4.2. Factors Influencing the Bonding Area

The factors affecting the bonding area were identified in order to select the optimum conditions for diffusion bonding of the outer Fe material and the inner Fe-Cu-Ni-C material.

4.2.1. Influence of density

The relationship between the density of the inner and outer parts and the rate of diffusion bonding area was investigated. Fig. 10 shows the relationship between the inner part density and the rate of diffusion bonding area. It was determined that the rate of diffusion bonding area did not change even when the density of the inner part was varied as much as 6.4–6.6 g/cm^3, with the density of the outer part kept constant. Fig. 11 shows the relationship between the outer

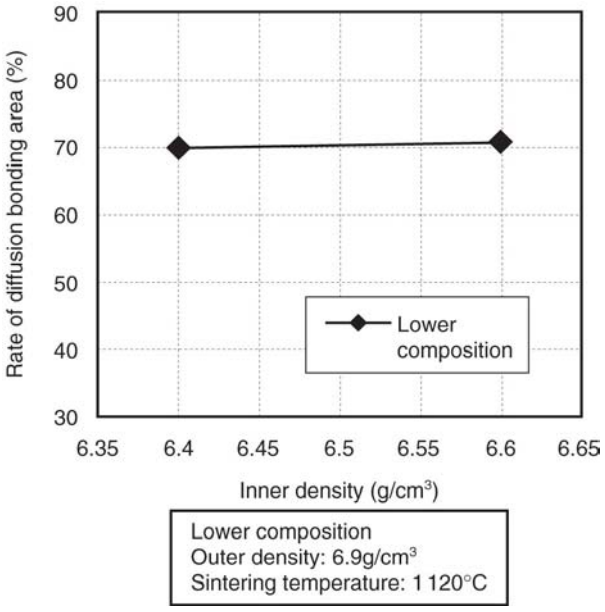


Fig. 10 Relationship between inner density and rate of diffusion bonding area

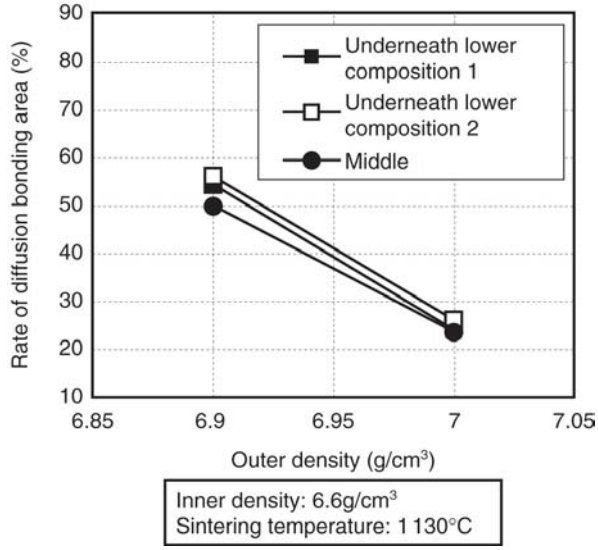


Fig. 11 Relationship between outer density and rate of diffusion bonding area

part density and the rate of diffusion bonding area. This shows that the rate of diffusion bonding area tends to decrease when the outer part density is high.

This finding is the opposite of what would be expected from the thermal expansion curves of these parts. That is, higher density of the outer part would ordinarily result in smaller thermal expansion. A larger quantity of thermal expansion in the inner part would lead to higher pressure, so that the bonding area would tend to increase. With this rotor bonding, however, more than just the difference in the thermal expansion of the parts was involved. Some strain in the outer part ascribable to the shape of the rotor was a factor, so that the bonding area could not be defined from the thermal expansion curves alone.

4.2.2. Influence of sintering temperature

Fig. 12 show the relationship between sintering temperature and rate of diffusion bonding area. It is apparent that the rate of diffusion bonding area decreases as the sintering temperature rises higher. According to the thermal expansion properties, the outer part continues to expand up to the vicinity of 1,150 °C, so that higher sintering temperatures result in lower pressure between the outer and inner parts, and diffusion bonding is impeded as a result.

4.2.3. Influence of chemical composition

The findings up to this point suggested that the reason diffusion bonding did not progress even when the thermal expansion of the two parts was significantly different was that the pressure on the outer part from the inner part was too high and resulted in strain in the outer part. Therefore, studies were done to alter the chemical composition of the parts in order to decrease the quantity of thermal expansion and determine the influence of the weakened pressure that would result. Table 3 shows the chemical composition of the inner part as decreasing amounts of Cu are added, and Fig. 13 shows the results from measurement of the rate of diffusion bonding area for those chemical compositions. The results clearly show little effect on the rate of diffusion bonding area even when the quantity of thermal expansion is decreased to lower the pressure. This showed that the conventional method of diffusion bonding that makes use of differences in thermal expansion would not work with the rotor shape.

It is known that the magnetic properties of a rotor are

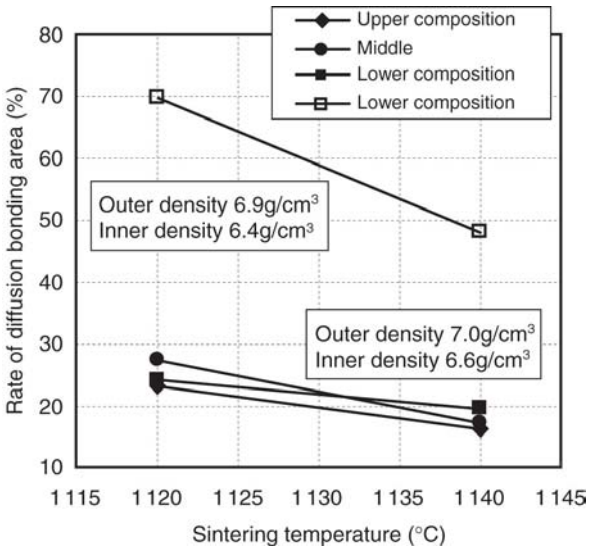


Fig. 12 Relationship between sintering temperature and rate of diffusion bonding area

Table 3 Inner chemical composition of decreasing Cu

(wt%)	Cu	Ni	C
Underneath lower composition 1	1.470	2.940	0.686
Underneath lower composition 2	1.455	2.910	0.679

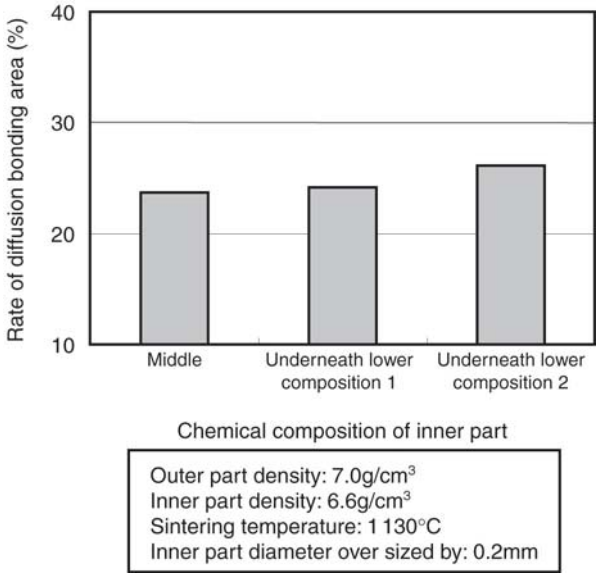


Fig. 13 Influence of chemical composition

generally improved by increasing the density of the outer part, and that the strength can be increased by using higher sintering temperatures. Under these conditions, however, the bonding area tends to decrease. Even changing the chemical composition of the inner part to reduce the quantity of thermal expansion of the copper in it had little effect on the bonding area. Means of applying pressure to the bonding surfaces other than by differences in thermal expansion were therefore investigated.

4.2.4. Influence of initial inner part diameter over sized

After fabrication of the various green compacts, a press fitting process is required in order to achieve diffusion bonding of the inner and outer parts. Fig. 14 shows the

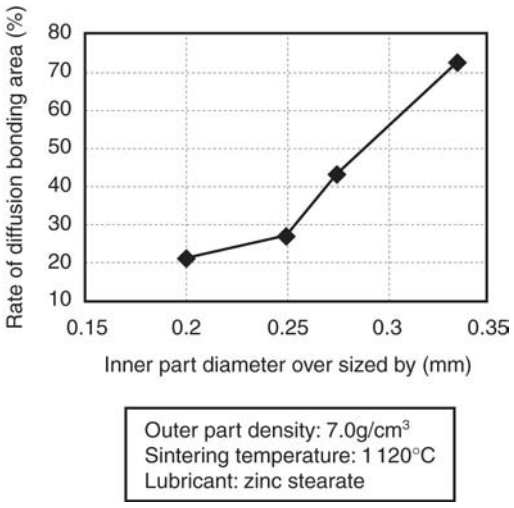
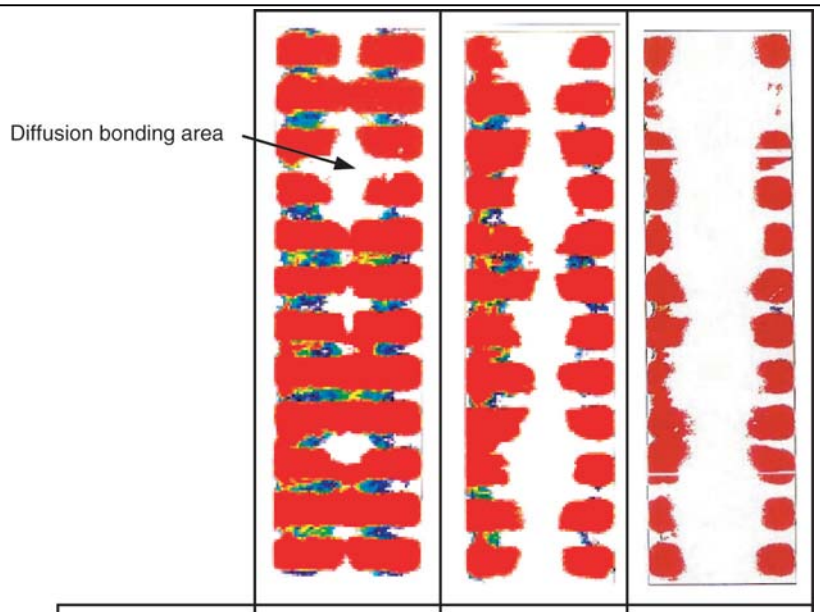


Fig. 14 Relationship between interference and rate of diffusion bonding area



Rate of diffusion bonding area (%)	18%	48%	69%
Inner part diameter over sized by (mm)	0.200	0.275	0.335

Fig. 15 Rate of diffusion bonding area measured by supersonic flaw detecting

relationship between the initial inner part diameter over sized and the rate of diffusion bonding area. The initial inner part diameter over sized refers to the difference between the internal diameter of the outer part and the external diameter of the inner part. It is apparent that as this inner part diameter over sized for an outer part increases, the rate of diffusion bonding area increases. Consequently, the initial inner part diameter over sized is an important factor in controlling the bonding area. When it is increased too much, however, there is a risk of cracking in the outer part. Tests showed that no cracking occurred when the initial inner part diameter over sized was increased to 0.335 mm. Thus the maximum inner part diameter over sized was estimated by calculation.

Asaka[4] has defined the maximum inner part diameter over sized for when a tapered shaft is inserted into an outer part green compact of Fe-Cu-C material with a density of 6.7 g/cm^3. According to this, the rate of rupture of the outer part will be 100% when the inner part diameter over sized is –75 μm for an outer part with an inside diameter of 30 mm. It was determined, therefore, that rupture results when the initial inner part diameter over sized is 0.25% of the inside diameter of the outer part. The inner part diameter over sized was calculated to be 0.360 mm when the inside diameter of the outer part was 144 mm, taking the shape of the rotor into consideration, and this was inferred to be the maximum inner part diameter over sized. With the present developed material, however, the outer part is made of Fe material, so the composition is different from Asaka's specimen. The density, however, is high at 6.9–7.0 g/cm^3, so Asaka's test results were used as a reference for improving the strength of the green compact.

4.3. Rate of Diffusion Bonding Area

Fig. 15 shows the measurement results for the bonding area of the rotor that is diffusion bonded. This shows an expanded view of the bonding state of the bonding surfaces. Supersonic waves penetrate the diffusion bonded parts with very little reflection, and these are shown in white, blue, and green. The other parts indicated in yellow and red show where the diffusion bonding is inadequate.

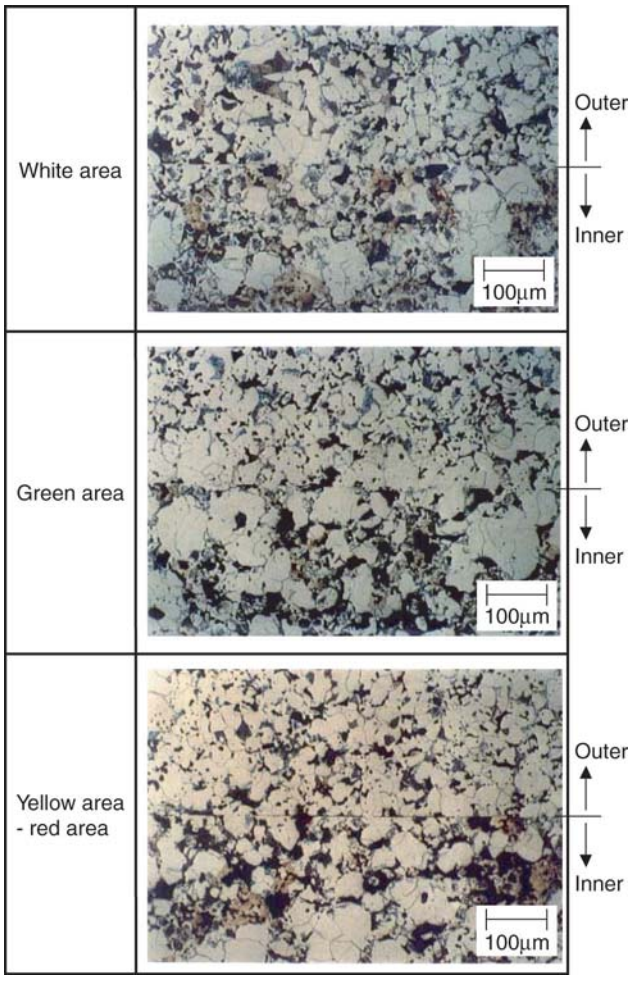


Fig. 16 Microstructure of boundary by diffusion bonding

When the rate of diffusion bonding area is 18%, the bonded parts shown from white to green appear in a regular laddered pattern. This occurs because the diffusion bonding is promoted mostly on the spokes of the inner part. During diffusion bonding, the quantity of thermal expansion becomes greater in the inner part than in the outer part. Since pressure is exerted on the outer part mainly from the spokes of the inner part, diffusion bonding is thought to be promoted in this part. In this state, however, the rate of diffusion bonding area is low. Consequently, when pressure due to the initial inner part diameter over sized is applied in addition to the difference in thermal expansion between the inner and outer parts, the bonding area increases from the center of the bonding surfaces, and rates of diffusion bonding area of 40–70% occur.

Fig. 16 shows the microstructure of boundary by diffusion bonding. The outer part displays a ferrite structure, while the inner part displays a mixed ferrite and pearlite structure. The diffusion bonded part (the white to green portions in Fig. 15 and Fig. 16) shows good ferrite grain growth extending beyond the bonding surfaces. The part that did not bond (the yellow to red portions in Fig. 15 and Fig. 16) was observed to form gaps of about 1 μm in the bonding surfaces.

5. Application to Motor Rotors

The knowledge obtained up to this point on sinter diffusion bonding technology will be illustrated below using application to motor rotors as an example.

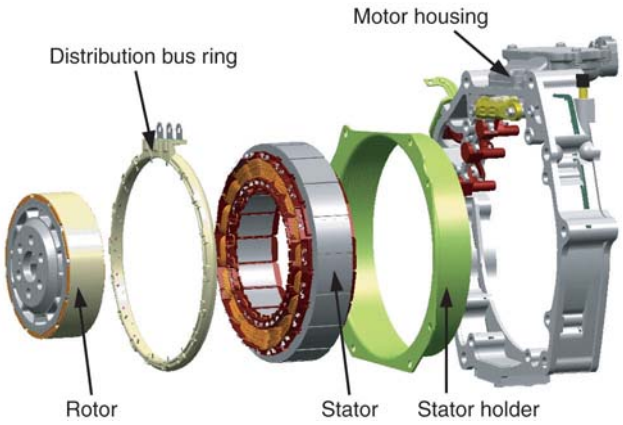


Fig. 17 Motor construction

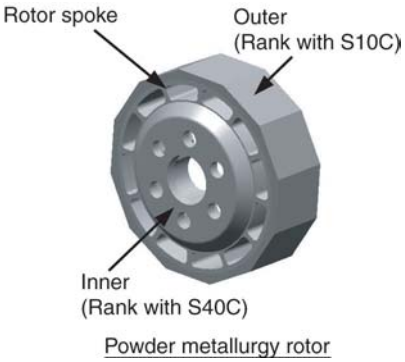


Fig. 18 Rotor construction

5.1. Structure of Sintered Rotor

Fig. 17 shows the construction of the motor. The stator is made up of a magnetic pole consisting of a divided concentrated winding of salient-pole and a bus ring molded by PPS, and a stator holder, which is a structural part that fixes the stator in place in the motor housing.[5] The outer circumference of the rotor has rare-earth sintered magnet (Nd-Fe-B) affixed to it with glass fiber. For compactness, it is made to be connected directly to the engine crankshaft. Fig. 18 shows the construction of the sintered rotor for the motor. It consists of different materials in the outer part, which is made of material selected for its magnetic properties, and the inner part, which requires strength.

5.2. Sintered Rotor Bonding Conditions

It is necessary to set the optimum bonding conditions that take account of factors such as density and sintering conditions in order for the sintered rotor to have both magnetic properties and mechanical properties at the same time. First, as a strength evaluation of the diffusion bonded portion, the equipment shown in Fig. 19 was used to conduct twist tests for durability of a sintered rotor that had a rate of diffusion bonding area of 36%. The results showed that the spokes ruptured first and the bonded portion did not. Consequently, the fatigue strength of the diffusion bonded portion can be said to be greater than that of the spokes.

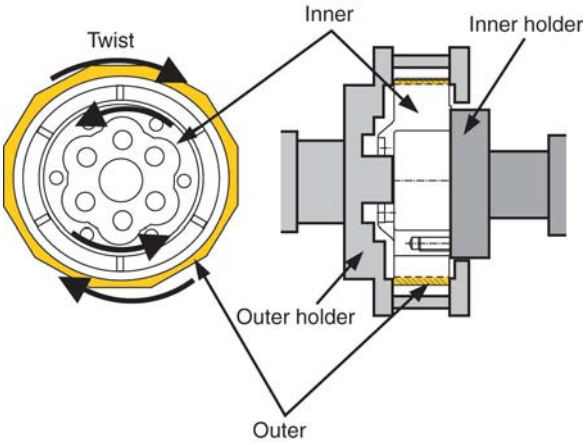


Fig. 19 Equipment of twist test for durability

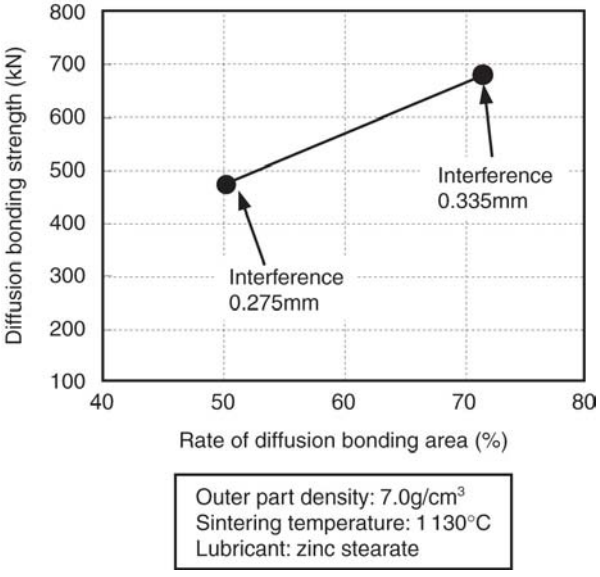


Fig. 20 Relationship between diffusion bonding strength and rate of diffusion bonding area

The safety for the rate of diffusion bonding area was set as the factor 1.3, and the lower limit of the rate of diffusion bonding area was set at 50% on the basis of those results. Fig. 20 shows the results from bonding strength tests of sintered rotors that were manufactured to satisfy these conditions. Sintered rotors displaying a rate of diffusion bonding area of 50% or over also had a higher bonding strength, and it was determined that they surpassed the guideline of 179 kN in engine tests for durability. The bonding conditions that will achieve sintered rotors with a rate of diffusion bonding area of 50% or over were selected as shown in Table 4 according to the density and sintering temperature of the inner and outer parts and the initial inner part diameter over sized. These yielded sintered rotors that joined different materials by diffusion bondings.

Table 4 Condition of diffusion bonding

Density (g/cm^3)	Outer	6.9 ~ 7.0
	Inner	6.4 ~ 6.6
Sintering temperature (°C)		1 120 ~ 1 140
Inner part diameter over sized by (mm)		0.275 ~ 0.335

5.3. Durability, Reliability, and Cost Effectiveness of Sintered Rotors

Next, the durability of the engine was evaluated by determining the fatigue strength of the spokes. The spoke fatigue strength was 190 MPa (3,432 N•m twisting torque), and this result yielded the fatigue limit diagram shown in Fig. 21. This shows that there is a 20-fold factor of safety relative to the maximum stress experienced in engine testing, and it was determined that the sintered rotor has adequate durability.

This sintered rotor also yielded near-net shape forming using sinter diffusion bonding, and significantly reduced the machining process. Therefore it achieved a 50% cost reduction over the rotor used in the Insight.

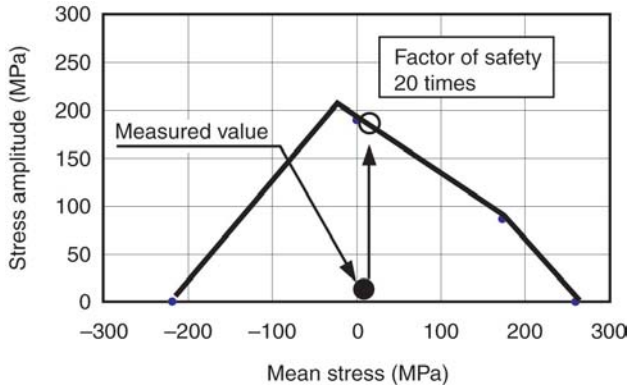


Fig. 21 Durability of boundary by diffusion bonding

6. Conclusion

Development of sinter diffusion bonding was conducted with a focus on the manufacturing of motor rotors using powder metallurgy methods to provide both magnetic properties and mechanical properties simultaneously. The following results were obtained:

(1) Techniques were developed for sinter diffusion bonding of green compacts of two types of material with different properties as a means of yielding both magnetic and mechanical properties simultaneously.
(2) It was determined that it is important for the sinter diffusion bonding of motor rotors to apply pressure by means of the initial inner part diameter over sized, in addition to the conventional pressure on the bonding surfaces resulting from the difference in thermal expansion.
(3) The application of diffusion bonding techniques satisfied the strength and durability requirements of actual engines, while near-net shape forming made it possible to provide motor rotors with a reduced machining process.

Motor rotors using this sinter diffusion bonding have been used in the Civic Hybrid since December 2001.

7. Acknowledgements

In conclusion, the authors express their profound gratitude to those persons involved at Hitachi Powdered Metals Co., Ltd. whose generous cooperation assisted greatly with the present development.

References

(1) Japan Powder Metallurgy Association, ed.: *Sintered Machine Parts*, Tokyo, Gijutsu Shoin, 1987, p. 279.

(2) Fujiki, A.: “Development of sintered parts and materials for high-performance engines,” *Journal of the Japan Society of Powder and Powder Metallurgy*, Vol. 46, No. 5, 1999, pp. 510–518.

(3) Otsuka, E., Ikushima, A., trans.: *Introduction to Chemistry of Materials 3: Mechanical Properties*, Tokyo, Iwanami Shoten, 1965, p. 26.

(4) Asaka, K.: “Research in diffusion bonding methods for combining green compacts,” degree thesis, Hiroshima University, 1997, pp. 61–62.

(5) Shimada, A., Ogawa, H., Nakajima, M., Shimada, H.: “Development of an ultra-thin DC brushless motor for the Insight hybrid car,” *Honda R&D Technical Review*, Vol. 12, No. 1, 2000, pp. 15–20.

■ Authors ■


Toshiyasu KOMATSU


Satoru SHINZAKI


Youichi NAKAHARA


Kazuo ASAKA

Date	Conference	Title	Author	Organization
2001/6/30 ～7/5	CNS 2001 Orgnizing Committee/Tenth Annual Computational Neuroscience Meeting CNS 2001 (San Francisco, USA)	A Computational Model of Attentive Visual System Induced by Cortical Neural Network	Takamasa Koshizen	Wako Research Center
			Koji Akatsuka	Wako Research Center
			Hiroshi Tsujino	Wako Research Center
		The Brain Like System Simulator BLISS	Marc-Oliver Gewaltig	Honda R&D Europe
2001/7/1	JSAE/JSAE Review Vol.22 No.3	Development of an ultra-thin DC brushless motor for a hybrid car	Akiyoshi Shimada	Tochigi R&D Center
			Hirohisa Ogawa	Tochigi R&D Center
			Minoru Nakajima	Tochigi R&D Center
		Energy efficiency improvement of series hybrid vehicle	Satoshi Aoyagi	Tochigi R&D Center
			Yusuke Hasegawa	Tochigi R&D Center
			Takahiro Yonekura	Tochigi R&D Center
			Hiroyuki Abe	Tochigi R&D Center
		Application of the Magic Formula Tire Model to Motorcycle Maneuverbilitv	Yoshitaka Tezuka	Asaka R&D Center
			Hidefumi Ishii	Asaka R&D Center
			Satoru Kiyota	Asaka R&D Center
2001/07/02 ～ 04	Institute of Meteorology and Physics/International Conference on Fatigue in the Very High Cycle Regime/(Wien,Austria)	Evaluation of giga-cycle fatigue properties of some maraging steels by intermittent ultrasonic fatigue testing	Hitoshi Ishii	Shizuoka Univ.
			Hirofumi Akagi	Tochigi R&D Center
			Tooru Yagasaki	Tochigi R&D Center
2001/7/7～ 11	GECCO/Genetic and Evolutionary Computation Conference/(San Francisco, USA)	Dynamic weighted aggregation for evolutionary multi-objective optimization : Why does it work and how?	Yaochu Jin	Honda R&D Europe
			Markus Olhofer	Honda R&D Europe
			Bernhard Sendhoff	Honda R&D Europe
2001/7/7	Kluwer Academic Publishers/Journal of Intelligent Robotic Systems	The Brain-Like Sensor : Motor Control System	Takamasa Koshizen	Wako Research Center
			Yugo Ueda	Wako Research Center
			Hiroshi Tsujino	Wako Research Center
2001/7/14 ～19	Conference Proceeding of IJCNN 2001/the International Neural Network Society & the IEEE Neural Network Council/(Washington DC, USA)	To Learn Location of Target using New Synchronous Sensorimotor Control System	Takamasa Koshizen	Wako Research Center
			Yugo Ueda	Wako Research Center
			Makoto Nakamura	Wako Research Center
			Hiroshi Tsujino	Wako Research Center
	Carbon 2001/American Carbon Society/(Lexington, USA)	Hydrogen Adsorption on Single Walled Carbon Nanotubes (SWNT)	Yoshiya Fujiwara	Wako Research Center
			B.K.Pradhan	Pennsylvania State Univ.
			A.R.Harutyunyan	Pennsylvania State Univ.
			G.U.Sumanasekera	Pennsylvania State Univ.
			P.C.Eklund	Pennsylvania State Univ.
		Hydrogen Storage in Tubular and Herringbone Carbon Nanofibers	A.R.Harutyunyan	Pennsylvania State Univ.
			B.K.Pradhan	Pennsylvania State Univ.
			Toshio Tokune	Wako Research Center
			Yoshiya Fujiwara	Wako Research Center
			P.C.Eklund	Pennsylvania State Univ.
2001/7/30 ～8/3	ICBP2001/4th International Conference on Biological Physics/(Kyoto)	Brain Science based on an Engineering approach	Hiroshi Tsujino	Wako Research Center
2001/8/20 ～24	International Association for Vehicle System Dynamics/The 17th IAVSD Symposium, The Dynamics of Vehicles on Road and Tracks/(Copenhagen, Denmark)	Stochastic Robustness Analysis and Synthesis of Nonlinear Vehicle Dynamics Controller	Shinichiro Horiuchi	Nihon Univ.
			Kazuyuki Okada	Nihon Univ.
			Shinya Notomi	Tochigi R&D Center

Date	Conference	Title	Author	Organization
2001/8/21 ～25	European Neural Network Society, Universidad Autó noma de Madrid, Ministerio de Ciencia y Tecnologí a, Instituto de Ingenierí a del Conocimiento/International Conference on Artificial Neural Networks 2001/(Vienna, Austria)	Using Maximal Recurrence in Linear Threshold Competitive Layer Networks	Heiko Wersing Helge Ritter	Honda R&D Europe University of Bielefeld
	The MIT Press/Neural Computation Vol.13, No.9 September 2001	Learning Optimized Features for Hierachical Models of Invariant Recognition	Heiko Wersing Edgar Koerner	Honda R&D Europe Honda R&D Europe
	Elsevier Science/Neural Networks Vol.14, 2001	Propagation of synchronous spiking activity in cortical networks.	Marc-Oliver Gewaltig	Honda R&D Europe
2001/09/06 ～07	AVL/Engine & Environmental Conference 2001/(Groz, Asutria)	Honda Fuel Cell Vehicle Development	Takashi Moriya	Wako Research Center
2001/9/14	Qinetiq /36th UK Group Conference on Human Response to Vibration/(Farnborough, UK)	ON A 3-D DYNAMIC FEM MODEL OF HUMAN BODY SEATED IN A PASSENGER CAR SEAT	Nobuharu Kuriki Sachiko Yamada Nobuaki Takata Mitsunori Kubo	Tochigi R&D Center Tochigi R&D Center Tochigi R&D Center Chiba Univ.
	DBF-2001/The 6th Tamagawa Dynamic Brain Forum DBF-2001/(Breisach, Germany)	Rubust recognition with learning from few samples by utilizing a hierarchical set of local alphabets	Edgar Koerner Heiko Wersing	Honda R&D Europe Honda R&D Europe
2001/09/30 ～10/04	ITS /8th World Congress on Intelligent Transport Systems/ (Australia, Sydney)	A study for early detection of pedestrians in the nighttime	Akio Takahashi Nobuyoshi Asanuma	Tochigi R&D Center Tochigi R&D Center
2001/10/1	IEEE/IEEE Transactions on Speech & Audio Processing Vol.9, No.7	Active Control System for Low-Frequency Road Noise Combined with an Audio System	Hisashi Sano Toshio Inoue Akira Takahashi Kenichi Terai Yoshio Nakamura	Tochigi R&D Center Tochigi R&D Center Tochigi R&D Center Matsushita Electric Industrial Co.,Ltd. Matsushita Electronic Components Co., Ltd.
	SAE/Automotive and Transportation Technology Congress & Exhibition 2001/(Spain, Barcelona)	Description of the hybrid technology mounted to production model	Shinobu Ochiai Yasumichi Ohnuki	Tochigi R&D Center Tochigi R&D Center
2001/10/4	JSAE/JSAE Review vol.22, No.4	Numerical Analysis of optimal vehicle trajectories for emergency obstacle avoidance	Shinichiro Horiuchi Kazuyuki Okada Shinya Notomi	Nihon Univ. Nihon Univ. Tochigi R&D Center
2001/10/18	ESI Group/Europam2001/(Heidelberg, Germany)	Development and Application of the simulation model of BioRID II Dummy	Koji Sano Yasuhiro Dokko Tsukasa Goto Koshiro Ono	Tochigi R&D Center Tochigi R&D Center Japan Automobile Research Institute Japan Automobile Research Institute
2001/10/20 ～ 2001/10/24	Electric Vehicle Association of the Americas/The International Electric Vehicles Symposium & Exhibition/(Berlin, Germany)	Development of simultaneous analytial system in motor performance measurement	Hirofumi Atarashi Yoshinari Murayama Makoto Kishida Hirokazu Yamashita	Tochigi R&D Center Tochigi R&D Center Tochigi R&D Center Tochigi R&D Center
2001/10/29 ～31	The Surface Finishing Society of Japan/Frontiers of Surface Engineering 2001 Conference/(Nagoya)	Entropy control and surface analysis of energy storage systems for advanced vehicles	Noboru Sato	Tochigi R&D Center

Date	Conference	Title	Author	Organization
2001/10/31	3M UNITEK (DIVISION OF 3M HEALTH CARE LTD.), W. S. ATKINS CONSULTANTS LTD., EUROPEAN SOCIETY OF ENGINEERING AND MEDICINE G & B, MEMBER OF TAYLOR & FRANCIS GROUP, SMITH & NEPHEW WELSH DEVELOPMENT AGENCY, WALES, UK, UNIVERSITY OF WALES COLLEGE OF MEDICINE,	A Computational Framework for Analysis of Control Strategies in Human Augmentation Devices	Behzad Dariush	Honda R&D Americas
2001/11/06 ～09	SAE/The 11th International Pacific Conference on Automotive Engineering/(Shanghai, China)	Three-dimensional Simulation of Engine Intake Noise	Tooru Takabayashi Yasuaki Hotozuka	Tochigi R&D Center Tochigi R&D Center
		The influence of body lateral bending on the handling characteristics	Kaoru Kusaka Masaki Nagahisa Tetsuji Nishimura	Tochigi R&D Center Tochigi R&D Center Tochigi R&D Center
		Development of new 2.0L lean-burn engine	Aruto Hayashi Tomonori Niizato	Tochigi R&D Center Tochigi R&D Center
		Development of a Virtual Road Simulator for Motorcycles	Makoto Hasegawa Hideki Yamaguchi	Asaka R&D Center Asaka R&D Center
2001/11/07 ～09	The Instrumentation Systems and Automation Society, Japan Electric Measuring Instruments Manufactures' Association, The Society of Instrument and Control Engineers/INTERMAC2001 Joint Technical Conference/(Tokyo)	Development of Simultaneous Analytical System in Motor Performance Measurement	Makoto Kishida Hirokazu Yamashita	Tochigi R&D Center Tochigi R&D Center
2001/11/12 ～14	SAE/Environmental Sustainability Conference/(Graz, Austria)	Reduction of Life Cycle CO^2 Emissions-The Example of Honda Insight	Tadayoshi Hayashi	Tochigi R&D Center
2001/11/14 ～16	Japan Society for the Promotion of Science/International Symposium Nanocarbons 2001 Nagano/(Nagano)	A characteristic of alkaline mesophase based carbon for Electrochemical Capaciter	Takeshi Fujino Shigeki Oyama Naohiko Oki Minoru Noguchi Kenji Sato Morinobu Endo Yong-Jung Kim	Wako Research Center Wako Research Center Wako Research Center Wako Research Center Wako Research Center Shinshu Univ. Shinshu Univ.
2001/11/15 ～17	JSME/The JSME International Conference on Motion and Power Transmissions MPT2001/(Fukuoka)	Fatigue Failure of Synchronous Belts for Automobile under Fluctuating Torque	Kiyohisa Tomono Hideaki Takahashi Hiroshi Iizuka	Tochigi R&D Center Tochigi R&D Center Yamagata Univ.
2001/11/26 ～27	L'Institut Francais du Petrole/IFP International Congress/(Paris, France)	Activated Radical Combustion in A High-Speed High-Power Pneumatic Direct Injection Two Stroke Engine	Yoichi Ishibashi Kenji Nishida Masahiro Asai	Asaka R&D Center Asaka R&D Center Asaka R&D Center
2001/11/28 ～30	SAE/2001 Small Engine Technology & Exposition/(Pisa, Italy)	Development of a 1.6L VTEC-E engine for the 2001 Civic	Katsushi Watanabe Masato Matsuki	Tochigi R&D Center Tochigi R&D Center
		Reducing Vibration of a 2-Cylinder Outboard Motor by the Pendulum Motion Mount Method	Kazuyuki Shiomi Takeshi Okada Michiharu Ohkawa Tetsuro Ikeno	Asakahigashi R&D Center Asakahigashi R&D Center Asakahigashi R&D Center Asakahigashi R&D Center
		A New Analysis Approach for Motorcycle Brake Squeal Noise and Its Adaptation	Hiroyuki Nakata Kiyoshi Kobayashi Masashi Kajita	Asaka R&D Center Tochigi R&D Center Asaka R&D Center
		Study on the Life Cycle Assessment Application to	Yposhihiko Tatemichi Takeshi Yoshida	Asaka R&D Center Asaka R&D Center
		Virtual Assessment of Motorcycle Vibrations	Hiroyuki Kuwahara Yoji Fukui P. Mas	Asaka R&D Center Asaka R&D Center LMS International

Date	Conference	Title	Author	Organization
			B. Vandenolas	LMS International
		Study on the Process of Backfiring	Shinji Saito Masaya Adachi	Asaka R&D Center Asaka R&D Center
		Development of 7003 Aluminum Extrusions for Motorcycle Frame Applications	Rowdy Joseph Junichi Ueda	Honda R&D Americas Asaka R&D Center
2001/11/29	Material Research Society/2001 Fall Meeting/(Boston, USA)	Large Cryogenic Storage of Hydrogen in Carbon Nanotubes at Low Pressures	B.K.Pradhan A.Harutyunyan D.Stojkovic J.Grossman P.Zhang M.W.Cole V.Crespi Hajime Goto Yoshiya Fujiwara P.C.Eklund	Pennsylvania State Univ. Pennsylvania State Univ. Pennsylvania State Univ. Pennsylvania State Univ. Pennsylvania State Univ. Pennsylvania State Univ. Pennsylvania State Univ. Wako Research Center Wako Research Center Pennsylvania State Univ.
2001/12/3 ～8	The NIPS 2001/Neural Information Processing Systems 2001/(Vancouver, Canada)	Learning Methods for Perceptual Grouping Lateral Interactions	Heiko Wersing	Honda R&D Europe
		Density formulation of I&F population dynamics	Julian Eggert Berthold Baeuml	Honda R&D Europe DLR
		Categorization by Learning and Combining Object Parts	Bernd Heisele	Honda R&D Americas
		Face Recognition for intelligent robots and smart cars	Ming-Hsuan Yang	Honda R&D Americas
2001/12/9	IEEE/IEEE Computer Society Conference on Computer Vision and Pattern Recognition/(Lihue , USA)	Feature Redection and Hierarchy of Classifiers for Fast Object Detection in Video Images	Bernd Heisele	Honda R&D Americas
2001/12/10	Kookmin University/International Conference on Automotive Engineering/(Seoul. Korea)	VGS (Variable Gear ratio Steering) System	Toshitake Kawai Yasuji Shibahata Yasuo Shimizu Fumio Kawano Shoichi Sano	Tochigi R&D Center Tochigi R&D Center Tochigi R&D Center Tochigi R&D Center Tokyo Denki Univ.

Editor's Postscript

The *Honda R&D Technical Review* has now entered its 14th year, and already three years have passed since we changed to a twice-yearly publication schedule. For this issue (Vol. 14, No.1), we have looked into the changes in numbers of submissions to previous issues.

The concern when we changed to the schedule of twice-yearly publication was that there would not be enough articles submitted. When the *Review* was an annual publication, the average number of submissions per issue was 25.1 (including the F-1 special edition in 1993). By contrast, the average since the *Review* went twice-yearly has been 25.3 submissions per issue, which is very much on a par with the earlier figure. There is also a measure for the substance of those submissions. Writing these articles is work that has to be carried out with a very effective use of the narrow time intervals that open up during product development. Despite those conditions, we receive enough submissions to fill two issues a year, and this indication of the tremendous energy to be found among our authors and the other people involved fills us with admiration.

At present, English-language translations of the *Review* articles have been made available for reading on our intranet. The access system allows full-text searching, so the required articles can be retrieved very quickly. Hits on this site are recorded, so we know that the Japanese-language site (original article versions) is accessed 600 times per month, while the English-language versions are accessed 200 times per month.

It may be that making the *Review* available for examination in this way has had a stimulating effect, since recently we have been receiving more submissions from overseas Honda research organizations.

In light of these circumstances, we can conclude that the *Review* is achieving its purpose, which is to serve as a communication tool for our engineers, The *Review's* function as a tool to pass on engineering expertise is becoming well established.

Publication activity at Honda, and particularly the in-house information program of the *Review*, requires steady, persevering activity. For those of us involved in this publication program, however, the greatest encouragement is to see how the *Review* is becoming an established, widespread presence as a communication tool for engineers here at Honda.

(Masatoshi Akagi, Asaka R&D Center)

Honda R&D Technical Review English Version Vol.14 No.1
The following associates provided us with their cooperation and expertise:

Karen	Arneson	American Honda Motor Co., Inc.	
Bill	Bezilla	Honda R&D Americas, Inc.	North Carolina Center
Jeff	Brown	Honda R&D Americas, Inc.	Ohio Center
Mary	Christopherson	American Honda Motor Co., Inc.	
Koichi	Funatsu	Honda R&D Americas, Inc.	Ohio Center
Lee	Goldring	American Honda Motor Co., Inc.	
Kaoru	Ichihashi	Honda R&D Americas, Inc.	Ohio Center
Rowdy	Joseph	Honda R&D Americas, Inc.	Ohio Center
Shigeaki	Kagami	Honda R&D Americas, Inc.	Ohio Center
Ted	Klaus	Honda R&D Americas, Inc.	Ohio Center
Michael	Koening	Honda R&D Americas, Inc.	Ohio Center
Toshiyuki	Makino	Honda R&D Americas, Inc.	Ohio Center
Elie	Merheb	Honda R&D Americas, Inc.	Ohio Center
Dale	Motzko	Honda R&D Americas, Inc.	Ohio Center
Kazuhiro	Nakahara	Honda R&D Americas, Inc.	Ohio Center
Brian	Nutwell	Honda R&D Americas, Inc.	Ohio Center
Chris	Osborne	Honda R&D Americas, Inc.	North Carolina Center
Jason	Ray	Honda R&D Americas, Inc.	Ohio Center
Alan	Seid	Honda R&D Americas, Inc.	Ohio Center
Chris	Thomas	Honda R&D Americas, Inc.	Ohio Center
Chuck	Thomas	Honda R&D Americas, Inc.	Ohio Center
Hideki	Wakamatsu	Honda R&D Americas, Inc.	Ohio Center
William	Willen	American Honda Motor Co., Inc.	
Yoshio	Yamamoto	Honda R&D Americas, Inc.	Ohio Center
Atsuko	Yamazaki	Honda R&D Americas, Inc.	Ohio Center

